



Universitat de Girona

SYNTHESIS, STRUCTURE AND REACTIVITY OF NOVEL Cu I, Cu II, Cu III COMPLEXES CONTAINING TRIAZA AND HEXAAZA MACROCYCLIC LIGANDS

Xavi RIBAS SALAMAÑA

ISBN: 84-8458-123-3

Dipòsit legal: Gi.68-2002

<http://hdl.handle.net/10803/8020>

ADVERTIMENT. L'accés als continguts d'aquesta tesi doctoral i la seva utilització ha de respectar els drets de la persona autora. Pot ser utilitzada per a consulta o estudi personal, així com en activitats o materials d'investigació i docència en els termes establerts a l'art. 32 del Text Refós de la Llei de Propietat Intel·lectual (RDL 1/1996). Per altres utilitzacions es requereix l'autorització prèvia i expressa de la persona autora. En qualsevol cas, en la utilització dels seus continguts caldrà indicar de forma clara el nom i cognoms de la persona autora i el títol de la tesi doctoral. No s'autoritza la seva reproducció o altres formes d'explotació efectuades amb finalitats de lucre ni la seva comunicació pública des d'un lloc aliè al servei TDX. Tampoc s'autoritza la presentació del seu contingut en una finestra o marc aliè a TDX (framing). Aquesta reserva de drets afecta tant als continguts de la tesi com als seus resums i índexs.

ADVERTENCIA. El acceso a los contenidos de esta tesis doctoral y su utilización debe respetar los derechos de la persona autora. Puede ser utilizada para consulta o estudio personal, así como en actividades o materiales de investigación y docencia en los términos establecidos en el art. 32 del Texto Refundido de la Ley de Propiedad Intelectual (RDL 1/1996). Para otros usos se requiere la autorización previa y expresa de la persona autora. En cualquier caso, en la utilización de sus contenidos se deberá indicar de forma clara el nombre y apellidos de la persona autora y el título de la tesis doctoral. No se autoriza su reproducción u otras formas de explotación efectuadas con fines lucrativos ni su comunicación pública desde un sitio ajeno al servicio TDR. Tampoco se autoriza la presentación de su contenido en una ventana o marco ajeno a TDR (framing). Esta reserva de derechos afecta tanto al contenido de la tesis como a sus resúmenes e índices.

WARNING. Access to the contents of this doctoral thesis and its use must respect the rights of the author. It can be used for reference or private study, as well as research and learning activities or materials in the terms established by the 32nd article of the Spanish Consolidated Copyright Act (RDL 1/1996). Express and previous authorization of the author is required for any other uses. In any case, when using its content, full name of the author and title of the thesis must be clearly indicated. Reproduction or other forms of for profit use or public communication from outside TDX service is not allowed. Presentation of its content in a window or frame external to TDX (framing) is not authorized either. These rights affect both the content of the thesis and its abstracts and indexes.



Universitat de Girona

Departament de Química
Àrea de Química Inorgànica

TESI DOCTORAL

Synthesis, structure and reactivity of novel Cu^{I} , Cu^{II} and
 Cu^{III} complexes containing triaza and hexaaza macrocyclic
ligands

XAVI RIBAS SALAMAÑA

Desembre 2001



Universitat de Girona

Departament de Química

El sotasignat Antoni Llobet i Dalmases, Professor Catedràtic del Departament de Química de la Universitat de Girona,

CERTIFICA que la memòria que porta per títol "Synthesis, structure and reactivity of novel Cu^{I} , Cu^{II} and Cu^{III} complexes containing triaza and hexaaza macrocyclic ligands" aplega el treball realitzat sota la meva direcció per en Xavi Ribas Salamaña, llicenciat en Ciències Químiques, i constitueix la seva memòria de Tesi Doctoral per aspirar al grau de Doctor en Ciències, especialitat Química.

I perquè així consti signo el present certificat el dia 3 d'octubre de l'any 2001.

Prof. Dr. Antoni Llobet i Dalmases

Agraïments

Buff!, no sé per on començar. Haig d'agraïr el suport i la confiança a tanta gent que se'm fa difícil saber com fer-ho.

Em deixaré d'ortodòxies i vull començar per agrair el suport que des del primer dia m'ha donat en Miquel Costas. Aquest prototip de químic despistat ha estat i és un fenomen de la química, tant per la seva afició per devorar informació com per la seva capacitat de sacrifici i devoció al seu treball. Crec que una petita part d'aquest esperit se m'ha impregnat i això li agrairé tota la vida. Tot això a part del seu caràcter, és un tros de pa que es fa difícil no collonar-lo a totes hores!. Tota la sort per tu, noi!

L'Elena Plantalech ha estat aquella amiga i companya de laboratori, molt treballadora, que sempre va per feina i es deixa estar d'hòsties, i que ha donat un exemple de pragmatisme per tothom alhora d'espavilar-se per trobar una bona feina quan en el seu moment les coses han anat maldades.

En Josep Maria, cas apart. Un treballador nat, un polític precoç i amb molt de futur (sempre des de l'ombra, clar), i un amic que desitjo que continui disfrutant de la vida com ara.

No em vull oblidar de la Montse, la Carme, la Silvia, en Raül, la Cristina, en Nadal, en Pep Duran, la Nuri, i tots els que han passat per inorgànica, que m'han hagut de suportar d'alguna manera a mi i a la meva poiata plena de vials!

Als tots els orgànics, en Xevi Serrat, en Santi, en Font, la Cabarroques, en David, en Juan Carlos, la Pilar,... per les converses i els dinars i sopars plegats. Especial menció a l'Ayats, que ha revolucionat tota la facultat amb la seva energia. Sempre hi haurà un abans i un després de

l'Ayats a la facultat i a qualsevol lloc a on vagi a petar en el futur. A l'Anna, la orgànica-inorgànica compartida, una gran amiga a qui li desitjo el millor dels futurs.

I a molts d'altres del departament o la facultat, que no tinc espai per anomenar, però que conec, hem coincidit o m'han ajudat en algun moment.

Agraeixo a en Toni els consells rebuts i que em donés la oportunitat a treballar en el que m'apassiona. A l'Alfons, la Marisa, la M^a Ángeles, l'Anna Roglans, en Bardagí, i molts d'altres pels consells que m'han donat. A l'Anna Costa, per la paciència que ha tingut amb mi. A en Miquel Solà, per la seva dedicació i ajuda amb els càlculs teòrics.

En la meva estada a Basel, a en Zuberbühler per acollir-me al seu laboratori, i a la Susan, en Michael, en Christian i en Jerry, per l'amistat que mantenim.

En l'estada a Stanford, a l'Stack per dedicar-me tantes hores i per fer-me veure una nova manera d'interpretar i discutir sobre química. A en Geraud, el gigoló gabatxo (amb alguna similitud amb l'Ayats!) i bon amic, i a la resta de gent del laboratori (Liviu, Russell, Vish, Chris).

A la Deanne, pels EXAFS, a en Mahía i en Bruno per les difraccions, a en Vieri Fusi per la col·laboració en el sistema H₂m. A en Teo, per els NMR's i per la confiança.

A en Larry Que pel Raman de l'intermedi.

Tema "cuartos": agraeixo a la Generalitat de Catalunya per la beca predoctoral que m'ha permès sobreviure durant els quatre anys que ha durat.

Uff, em falta molta gent encara! Els següents no han tingut relació directa amb la feina, sinó que són amics i família que m'han ajudat a veure la vida amb pragmatisme, a tocar de peus a terra i a estar conveçut que la química no ho és tot. A en Jordi i la Tana i Genís, la família Fornos que tanta confiança i estimació (ei, mariconades només en casos

excepcionals!) ens tenim. A l'Enric i en Ferran, per l'amistat que ens tenim. Als meus pares i la meva àvia, per suportar-me (molt difícil a vegades, ho reconec!), recolzar-me i estimar-me. A l'Antonia i en Josep, per confiar en mi des del principi i per fer-me tocar de peus a terra.

La Brenda: el meu "fenomenu" petit, la meva vida. Per aguantar-me, estimar-me i per ser tant valenta i aguantar el que està passant. Estic convençut que valdrà la pena i que el futur serà tranquil i feliç.

No voldria deixar-me als meus avis Quim i Carme, que me'ls estimo molt i que m'han ensenyat moltes coses de la vida. Els trobo a faltar.

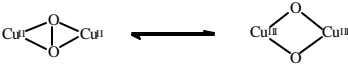
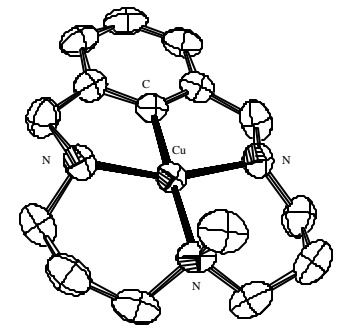
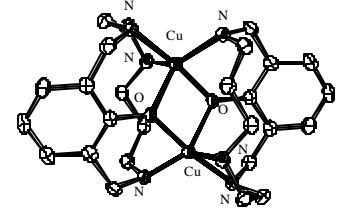
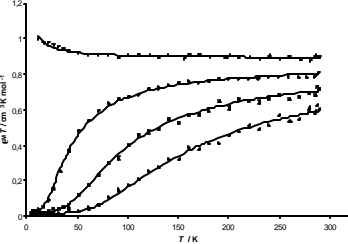
Finalment, a la gent del Ressò, tots els amics i companys de Santa Coloma per fer-me viure i disfrutar del meu poble. Per acabar, al mar, per fer-me sentir petit, i als peixos i pops, per deixar-se pescar!

.....

Ei, ja ho he dit, però volia tornar a agrair a la Brenda la nostra vida plegats. Ens necessitem com el pa que mengem!

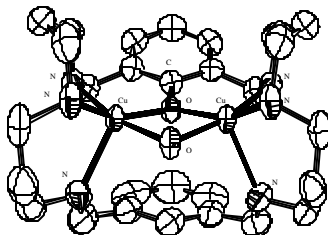
A la meva família,
A la meva nina,

GRAPHICAL ABSTRACTS

<p>Chapter 1</p> <p>Introduction to bioinorganic chemistry of copper</p>		<p>A global overview of O₂ activation and C-H bond activation involving copper species is presented.</p>
<p>Chapter 2</p> <p>Objectives</p>		<p>Objectives of the present work are the study of O₂ activation capability of novel copper complexes and their reactivity.</p>
<p>Chapter 3</p> <p>A Novel Twist on Copper Disproportionation: Room Temperature Aryl-C-H Activation by Cu^{II} to Form Novel Organometallic Aryl-Cu^{III} species</p>		<p>New disproportionation reaction of Cu^{II} complexes with novel triazamacrocyclic ligands yield novel air-stable organocopper(III) compounds. Full characterization of products and approaches to reaction mechanism are described.</p>
<p>Chapter 4</p> <p>Aryl-Cu^{III} complexes reactivity. New intermediates in aromatic hydroxylation</p>		<p>Reactivity of Aryl-Cu^{III} species in front basic/aqueous conditions leads to intramolecular hydroxylation of the ligand to obtain bis(phenoxo)copper(II) final products. O₂ activation by Cu^I systems is shown to be linked to an aryl-Cu^{III} pathway mechanism.</p>
<p>Chapter 5</p> <p>Magneto-structural correlation of novel bis(phenoxo) Cu^{II} complexes</p>		<p>Magnetic behavior description of new bis(phenoxo)Cu^{II} complexes. Subtle structural differences explain different magnetic properties.</p>

Chapter 6

Competitive O₂ activation reactivity driven by steric limitations. Aromatic hydroxylation vs CO₂ fixation by new macrocyclic dinuclear copper complexes



Capability of dinuclear hexaazamacrocyclic copper complexes of performing intramolecular aromatic monohydroxylation is presented along with the ability of atmospheric CO₂ fixation in certain experimental conditions.

Chapter 7

Conclusions

Conclusions for each chapter and general conclusions are exposed.

TABLE OF CONTENTS

ABBREVIATIONS.....	1
CRYSTAL STRUCTURE DATA FILES.....	5
CHAPTER 1 – INTRODUCTION TO BIOINORGANIC CHEMISTRY OF COPPER.....	7
1.1 BIOINORGANIC CHEMISTRY: METALLOENZYMES AND SYNTHETIC MODELS	9
1.2 THE BIOLOGICAL ROLE OF COPPER.....	10
1.2.1 COPPER METALLOPROTEINS.....	12
1.2.2 HEMOCYANIN	17
1.2.3 TYROSINASE	19
1.3 BIOMIMETIC MODELING AND MOLECULAR O₂ ACTIVATION.....	22
1.3.1 MODELING ACTIVE SITES	23
1.3.2 INTERMEDIATE CHARACTERIZATION.....	23
1.3.2.1 <i>Superoxo complexes</i>	25
1.3.2.2 <i>Peroxo complexes</i>	27
1.3.2.2.1 <i>Transperoxo complexes</i>	27
1.3.2.2.2 <i>Terminal peroxo complexes</i>	29
1.3.2.2.3 <i>μ-η²:η² side-on peroxo complexes</i>	31
1.3.2.3 <i>Bis(μ-oxo) complexes</i>	35
1.3.2.4 <i>Bis (μ₃-oxo) complexes</i>	39
1.4 BIOMIMETIC MODELING OF TYROSINASE AND CATHECOLOXIDASE	
REACTIVITY	41
1.4.1 WHAT IS THE HYDROXYLATING ACTIVE SPECIES? PROPOSED MECHANISMS	42
1.4.1.1 <i>O-O bond breaks after the attack on the aromatic ring</i>	42
1.4.1.2 <i>O-O bond breaks along with the attack on the aromatic ring</i>	43
1.4.1.3 <i>O-O bond breaks prior to the attack on the aromatic ring</i>	46
1.4.1.4 <i>The hydroxylating active species: μ-η²:η²-peroxo side-on versus bis(μ-oxo)</i>	48
1.5 C-H ACTIVATION: A CHALLENGING TARGET	51
1.5.1 OXIDATION OF ALKANES.....	51
1.5.2 MECHANISM OF THE SHILOV REACTION	56
1.5.3 GIF SYTEMS: A METHANO MONOOXYGENASE (MMO) SYNTHETIC MODEL	59
1.5.4 ORGANOCOPPER SPECIES	62
1.5.5 CU ^{III} COMPLEXES	64
1.6 REFERENCES	66

TABLE OF CONTENTS

CHAPTER 2 – OBJECTIVES	77
CHAPTER 3 –A NOVEL TWIST ON COPPER DISPROPORTIONATION: ROOM TEMPERATURE ARYL-C-H ACTIVATION BY Cu^{II} TO FORM NOVEL ORGANOMETALLIC ARYL-Cu^{III} SPECIES	81
3.1 ABSTRACT	83
3.2 INTRODUCTION	85
3.3 RESULTS	87
3.3.1 SYNTHESIS	87
3.3.1.1 <i>The ligands</i>	87
3.3.1.2 <i>Cu^{I} complexes</i>	88
3.3.1.3 <i>Cu^{III} complexes</i>	89
3.3.2 X-RAY STRUCTURES	90
3.3.3 SPECTROSCOPIC PROPERTIES.....	97
3.3.3.1 <i>X-Ray Absorption Spectroscopy (XAS)</i>	97
3.3.3.2 <i>NMR Characterization</i>	99
3.3.3.2.1 <i>NMR of Aryl-Cu^{III} complexes</i>	99
3.3.3.2.2 <i>NMR of Cu^{I} complexes</i>	103
3.3.3.3 <i>UV-VIS Spectroscopy</i>	104
3.3.4 ELECTROCHEMISTRY OF ARYL- Cu^{III} COMPLEXES	105
3.4 DISCUSSION	108
3.4.1 STRUCTURE AND REACTIVITY	108
3.4.1.1 <i>Disproportionation reaction</i>	108
3.4.1.2 <i>XAS experiment</i>	109
3.4.1.3 <i>Other systems reactivity</i>	110
3.4.2 MECHANISTIC DISCUSSION.....	112
3.4.3 H/D EXCHANGE IN $\text{H33M}/\text{Cu}^{\text{I}}$ SYSTEM. SYNTHESIS OF H33M(D)	118
3.4.4 AN ARYL- Cu^{II} ISOLATED COMPLEX.....	120
3.4.5 AROMATIC C-H ACTIVATION BY NICKEL(II).....	122
3.4.6 THEORETICAL CALCULATIONS.....	122
3.5 SUMMARY	127
3.6 EXPERIMENTAL SECTION	129
3.7 REFERENCES	142
SUPPORTING INFORMATION FOR CHAPTER 3	147

CHAPTER 4 – ARYL-CU^{III} COMPLEXES REACTIVITY. NEW INTERMEDIATES IN AROMATIC HYDROXYLATION.....	199
4.1 ABSTRACT	201
4.2 INTRODUCTION	203
4.3 RESULTS.....	205
4.3.1 SYNTHESIS.....	205
4.3.1.1 <i>The ligands</i>	205
4.3.1.2 <i>Cu^I complexes</i>	205
4.3.1.3 <i>Cu^{III} complexes</i>	205
4.3.1.4 <i>Cu^I complexes</i>	206
4.3.1.5 <i>Cu^{III} colored intermediates</i>	208
4.3.2 X-RAY STRUCTURES OF BISPHENOXO COMPLEXES	209
4.3.3 SPECTROSCOPIC PROPERTIES.....	218
4.3.3.1 <i>X-Ray Absorption Spectroscopy (XAS) of 1b-2b</i>	218
4.3.3.2 <i>¹H NMR characterization of intermediates 1b-3b</i>	219
4.3.3.3 <i>UV-Vis Spectroscopy of intermediates 1b-3b</i>	221
4.3.3.4 <i>Raman spectroscopy of intermediate 3b</i>	222
4.4 DISCUSSION.....	223
4.4.1 HYDROXYLATION REACTION DETAILS	223
4.4.2 DIOXYGEN ACTIVATION BY CU ^I COMPLEXES	225
4.4.3 MECHANISTIC STUDIES	231
4.4.4 THE H22M SYSTEM.....	235
4.4.5 OXIDANT CHARACTER OF ARYL-CU ^{III} COMPLEXES (1-3).....	235
4.5 EXPERIMENTAL SECTION.....	236
4.6 REFERENCES	245
SUPPORTING INFORMATION FOR CHAPTER 4.....	247
CHAPTER 5 – MAGNETO-STRUCTURAL CORRELATION OF NOVEL BISPHENOXO CU^{II} COMPLEXES.....	267
5.1 ABSTRACT	269
5.2 INTRODUCTION	271

TABLE OF CONTENTS

5.3 RESULTS	273
5.3.1 STRUCTURAL SUMMARY OF BISPHENOXO COMPLEXES 1C-3C, 5C	273
5.3.2 MOLECULAR ORBITAL CALCULATIONS	276
5.3.3 MAGNETIC PROPERTIES.....	279
5.4 DISCUSSION	282
5.4.1 MAGNETOSTRUCTURAL CORRELATIONS	282
5.5 EXPERIMENTAL SECTION	288
5.6 REFERENCES	289
CHAPTER 6 – COMPETITIVE O₂ ACTIVATION REACTIVITY DRIVEN BY STERIC LIMITATIONS. AROMATIC HYDROXYLATION VS CO₂ FIXATION BY NEW MACROCYCLIC DINUCLEAR COPPER COMPLEXES	291
6.1 ABSTRACT	293
6.2 INTRODUCTION	295
6.3 RESULTS	297
6.3.1 COMPLEX SYNTHESIS	298
6.3.2 CRYSTAL STRUCTURES	300
6.3.2.1 $[(\mu\text{-H33+33mO})\text{Cu}^{\text{II}}_2(\mu\text{-OH})](\text{PF}_6)_2\cdot\text{CH}_3\text{CN}$ (11-(PF ₆) ₂ ·CH ₃ CN)	302
6.3.2.2 $[(\text{H33+33m})_2\text{Cu}^{\text{II}}_4(\mu\text{-CO}_3)_2](\text{ClO}_4)_4\cdot 4\text{H}_2\text{O}\cdot 2\text{CH}_3\text{COCH}_3$ (12-(ClO ₄) ₄ ·4H ₂ O·2CH ₃ COCH ₃).....	306
6.3.2.3 $[(\text{H33+33m})\text{Cu}^{\text{II}}_2(\text{CH}_3\text{CN})_4](\text{ClO}_4)_4\cdot 2\text{H}_2\text{O}$ (14-(ClO ₄) ₄ ·2H ₂ O)	309
6.3.3 MAGNETIC PROPERTIES.....	311
6.3.3.1 $[(\mu\text{-H33+33mO})\text{Cu}^{\text{II}}_2(\mu\text{-OH})](\text{PF}_6)_2\cdot\text{CH}_3\text{CN}$ (11-(PF ₆) ₂ ·CH ₃ CN)	311
6.3.3.2 $[(\text{H33+33m})_2\text{Cu}^{\text{II}}_4(\mu\text{-CO}_3)_2](\text{ClO}_4)_4\cdot 4\text{H}_2\text{O}\cdot 2\text{CH}_3\text{COCH}_3$ (12-(ClO ₄) ₄ ·4H ₂ O·2CH ₃ COCH ₃).....	312
6.4 DISCUSSION	313
6.4.1 MODULATION OF REACTIVITY.....	313
6.4.2 CRYSTAL STRUCTURES	314
6.4.3 STRUCTURE-REACTIVITY CORRELATION	315
6.4.4 CO ₂ FIXATION CAPABILITY	316
6.4.5 ANTIFERROMAGNETIC COMPOUNDS.....	318
6.4.5.1 $[(\mu\text{-H33+33mO})\text{Cu}^{\text{II}}_2(\mu\text{-OH})](\text{PF}_6)_2\cdot\text{CH}_3\text{CN}$ (11-(PF ₆) ₂ ·CH ₃ CN)	318
6.4.5.2 $[(\text{H33+33m})_2\text{Cu}^{\text{II}}_4(\mu\text{-CO}_3)_2](\text{ClO}_4)_4\cdot 4\text{H}_2\text{O}\cdot 2\text{CH}_3\text{COCH}_3$ (12-(ClO ₄) ₄ ·4H ₂ O·2CH ₃ COCH ₃).....	319
6.4.6 NEW LIGAND H33+33MOH	320

TABLE OF CONTENTS

6.4.7	THEORETICAL CALCULATIONS: POSTULATING A PEROXO INTERMEDIATE	320
6.4.8	CONCLUDING REMARKS	323
6.5	EXPERIMENTAL SECTION.....	324
6.6	REFERENCES	331
	SUPPORTING INFORMATION FOR CHAPTER 6.....	337
	CHAPTER 7 - CONCLUSIONS.....	347

ABBREVIATIONS

ADF	Amsterdam Density Functional
Bipy	Bipyridine
BQPA	bis(2-quinolylmethyl)(2-pyridylmethyl)amine
BPMAN	2,7-bis[bis(2-pyridylmethyl)aminomethyl]- 1,8-naphthyridine
BPQA	bis(2-pyridylmethyl)(2-quinolylmethyl)amine
CA	Carbonic Anhydrase
CD	Circular Dichroism
COase	Catecholoxidase
COSY	Correlation Spectroscopy
CV	Cyclic Voltammetry
DABCO	1,4-Diazabicyclo[2.2.2]octane
DeoxyHc	DeoxyHemocyanin
DFT	Density Functional Theory
DKIE	Deuterium Kinetic Isotope Effect
EA	Elemental Analysis
EH	Extended Hückel
EPR	Electron Paramagnetic Resonance
ESI-MS	ElectroSpray Ionization Mass spectrometry
ET	Electron Transfer
EXAFS	Extended X-Ray Absorption Fine Structure
FAB-MS	Fast-Atom Bombardment Mass Spectrometry
FT-IR	Fourier Transform Infra-Red spectroscopy
HA	Hydrogen Abstraction
Hc	Hemocyanin
His	Histidine
HMBC	Heteronuclear Multiple Bond Correlation
HOMO	Highest Occupied Molecular Orbital
I.P.D.S	Imaging Plate Diffraction System
KIE	Kinetic Isotope Effect
L-66	α,α' -bis{bis[2-(1'-methyl-2'-benimidazolyl)]}

ABBREVIATIONS

	ethylamino}- <i>m</i> -xylene
LC	Liquid Chromatography
LDA	Local Density Approximation
LMCT	Ligand-to-Metal Charge Transfer
LUMO	Lowest Unoccupied Molecular Orbital
MM	Molecular Mechanics
MMCT	Metal-to-Metal Charge Transfer
MMO	Methano MonoOxygenase
MO	Molecular Orbital
MOOP	Molecular Orbital Overlap Population
MT-Cu	Metal transport proteins of Cu
NADH	Nicotinamide adenine dinucleotide
NCP	N-Confused Porphyrin
NMR	Nuclear Magnetic Resonance
NOESY	Nuclear Overhauser Spectroscopy
OxyHc	OxyHemocyanin
OxyTyr	OxyTyrosinase
PDB	Protein Data Bank
PDL	Peralkylated Diamine Ligand
Phen	1,10-phenanthroline
QM	Quantum Mechanics
R.T.	Room Temperature
RDS	Rate Determining Step
ROP	Reduced Overlap Population
SE	Electrophilic Substitution
SLAC	Stanford Synchotron Radiation Laboratory
SSCE	Saturated NaCl Calomelans Electrode
TACN	Triazacyclononane
TBAP	Tetrabutylamonium perchlorate
THF	Tetrahydrofurane
TMPA	tris-[(2-pyridil)methyl]amine
TMPAE	TMPA with a -C(O)OCH ₃ ester substituent in the 5-position of one pyridyl group
TMS	Tetramethylsilane

Ts	Tosyl
Tyr	Tyrosinase
UV-Vis	Ultraviolet-Visible spectroscopy
XAS	X-Ray Absorption Spectroscopy
XRD	X-Ray Diffraction

CRYSTAL STRUCTURE DATA FILES

The following Cif files for each crystal structure presented within this thesis are listed below and can be found in the attached CD.

Crystal structure	Cif file
$[(\text{H32m-C})\text{Cu}^{\text{III}}](\text{ClO}_4)_2$ (1 - $(\text{ClO}_4)_2$)	(1)_(H32m-C)Cu(III).cif
$[(\text{H}_2\text{Me33m-C})\text{Cu}^{\text{III}}](\text{ClO}_4)_2$ (2 - $(\text{ClO}_4)_2$)	(2)_(H2Me33m-C)Cu(III).cif
$[(\text{H33m-C})\text{Cu}^{\text{III}}](\text{OTf})_2$ (3 - $(\text{OTf})_2$)	(3)_(H33m-C)Cu(III).cif
$[(\text{H33m-C})\text{Cu}^{\text{III}}(\text{Cl})](\text{ClO}_4)$ (4 - (ClO_4))	(4)_(H33m-C)Cu(III)(Cl).cif
$[(\text{H33m-C})\text{Cu}^{\text{II}}]_2(\mu\text{-Cl})](\text{PF}_6)_2 \cdot 6\text{H}_2\text{O} \cdot \text{CH}_2\text{Cl}_2$ (6 - $(\text{PF}_6)_2 \cdot 6\text{H}_2\text{O} \cdot \text{CH}_2\text{Cl}_2$)	(6)_(H33m-C)2Cu(II)2(Cl).cif
$[(\text{H32mO})_2\text{Cu}^{\text{II}}]_2(\text{OTf})_2$ (1c - $(\text{OTf})_2$)	(1c(OTF)2)_(H32mO)2Cu2.cif
$[(\text{H}_2\text{Me33mO})_2\text{Cu}^{\text{II}}]_2(\text{ClO}_4)_2 \cdot \text{CH}_3\text{CN}$ (2c - $(\text{ClO}_4)_2 \cdot \text{CH}_3\text{CN}$)	(2c(ClO4)2)_(H2Me33mO)2Cu2.cif
$[(\text{H33mO})_2\text{Cu}^{\text{II}}]_2(\text{PF}_6)_2$ (3c - $(\text{PF}_6)_2$)	(3c(PF6)2)_(H33mO)2Cu2.cif
$[(\text{H}_2\text{Me33mO})_2\text{Cu}^{\text{II}}]_2(\text{Cl})_2$ (2d)	(2d)_(H2Me33mO)2Cu2(Cl)2.cif

[(H₂Me33mO)₂Cu^{II}₂] (Cl) (PF₆) · 2H₂O · 0.5CH₃OH (2c(Cl)(PF₆))_(H2Me33mO)2Cu2.cif
(2c-(Cl)(PF₆)·2H₂O·0.5CH₃OH)

[(H22mO)₂Cu^{II}₂] (PF₆)₂ (5c-(PF₆)₂) (5c(PF₆)₂_(H22mO)2Cu2.cif

[(μ-H33+33mO)Cu^{II}₂(μ-OH)] (PF₆)₂ · CH₃CN (11- (11)_(H33+33mO)Cu2(OH).cif
(PF₆)₂·CH₃CN)

[(H33+33m)₂Cu^{II}₄(μ-CO₃)₂] (ClO₄)₄ (12)_(H33+33m)2Cu4(CO3)2.cif
· 4H₂O · 2CH₃COCH₃ (12-(ClO₄)₄·4H₂O
· 2CH₃COCH₃)

[(H33+33m)Cu^{II}₂(CH₃CN)₄] (ClO₄)₄ (14)_(H33+33m)Cu2(CH3CN)4.cif
· 2H₂O (14-(ClO₄)₄·2H₂O)

CHAPTER 1

Introduction to bioinorganic chemistry of copper

1.1	BIOINORGANIC CHEMISTRY: METALLOENZYMES AND SYNTHETIC MODELS.....	9
1.2	THE BIOLOGICAL ROLE OF COPPER.....	10
1.2.1	COPPER METALLOPROTEINS.....	12
1.2.2	HEMOCYANIN	17
1.2.3	TYROSINASE	19
1.3	BIOMIMETIC MODELING AND MOLECULAR O₂ ACTIVATION	22
1.3.1	MODELING ACTIVE SITES.....	23
1.3.2	INTERMEDIATE CHARACTERIZATION.....	23
1.3.2.1	<i>Superoxo complexes</i>	25
1.3.2.2	<i>Peroxo complexes</i>	27
1.3.2.2.1	Transperoxo complexes	27
1.3.2.2.2	Terminal peroxo complexes	29
1.3.2.2.3	μ - η^2 : η^2 side-on peroxo complexes	31
1.3.2.3	<i>Bis(moxo) complexes</i>	35
1.3.2.4	<i>Bis(m-oxo) complexes</i>	39
1.4	BIOMIMETIC MODELING OF TYROSINASE AND CATHECOLOXIDASE REACTIVITY.....	41
1.4.1	WHAT IS THE HYDROXYLATING ACTIVE SPECIES? PROPOSED MECHANISMS	42
1.4.1.1	<i>O-O bond breaks after the attack on the aromatic ring</i>	42
1.4.1.2	<i>O-O bond breaks along with the attack on the aromatic ring</i>	43
1.4.1.3	<i>O-O bond breaks prior to the attack on the aromatic ring</i>	46
1.4.1.4	<i>The hydroxylating active species: $m\eta^2:h^2$-peroxo side-on versus bis(moxo)</i>	48
1.5	C-H ACTIVATION: A CHALLENGING TARGET.....	51
1.5.1	OXIDATION OF ALKANES.....	51
1.5.2	MECHANISM OF THE SHILOV REACTION.....	56
1.5.3	GIF SYSTEMS: A METHANO MONOOXYGENASE (MMO) SYNTHETIC MODEL	59
1.5.4	ORGANOCOPPER SPECIES.....	62
1.5.5	Cu ^{III} COMPLEXES	64
1.6	REFERENCES.....	66

1.1 Bioinorganic chemistry: metalloenzymes and synthetic models

Approximately, half of all protein crystal structures in Protein DataBank (PDB) contain transition metal ions, that usually correspond to only 1% in weight for a wide range of proteins. Transition metals located in the active sites of enzymes play a crucial role on the organisms. Chemical reactions catalyzed by enzymes occur in the active sites, and are responsible for the biological function of each enzyme.^{1,2,3,4} In the enzyme molecule, the cofactor is the non-amino acid fragment required for catalysis or other functions, and it is named prosthetic group when it is tightly bound to the polyaminoacid chain (apoenzyme).⁵ There are two basic types of prosthetic groups in bioinorganic chemistry: metal ions (or clusters of metal ions bridged by oxide or sulfide ligands) and the N-heterocycle complexes, that include a tightly bound metal ion due to chelate effect and present extensive π delocalization into tetrapyrrole porphyrinic ligand.

Reactivity of the active site is dependent on many factors: a) the nature of the metal, b) the nature of ligands, c) the local geometry of the metal, d) relative geometric disposition of the metal centers in metalloproteins containing two or more metal centers in close proximity and e) the tridimensional conformation of the polyaminoacid chain that forms the apoenzyme. These factors determine the metal ion capability towards substrate coordination, the capability to stabilize different oxidation states and also the formation of tridimensional cavities that can control substrate accessibility to the metal center. Therefore, the catalytic activity displayed by a redox enzyme is directly related to stabilization of different oxidation states and

to space flexibility in order to adapt structural changes in front of changes in oxidation state and reversible coordination of substrates-products.⁶

Bioinorganic chemistry focuses its work into structural characterization of active sites, study of their reactivity, and the synthesis of low molecular weight chemical models capable of reproducing the spectroscopic and catalytic properties of the original enzymes.⁷ Synthetic models are usually discrete transition metal complexes with electronic and steric effects resembling the properties of corresponding active sites.

1.2 The biological role of Copper

Cu is a first row transition metal found in trace amounts in organisms, but indispensable for life. Its unique reactivity properties convert copper into a bioessential metal. Enzymes containing Cu in their active sites present diverse biological functions, from O₂-transport carried out by hemocyanin in mollusks and arthropods,⁸ O₂ activation and substrate oxidation in tyrosinase^{3,9} and dopamine β -monooxygenase,¹⁰ and also the reduction of nitrite in nitrite reductase,¹¹ among others (see Figure 1).

Copper belongs to 11th group of the Periodic Table and can be found in organisms as +1 and +2 oxidation state. However, high oxidation state +3 has been postulated in many reaction mechanisms.¹²

The Cu^{II} ion, with a d⁹ electronic configuration, presents coordination numbers from 4 to 6.¹³ Jahn-Teller distortions are generally explained by a different e_g (d_{z²} and d_{x²-y²}) orbitals occupation when a d⁹ ion is subjected to an octahedral crystal field. The common result of this effect is the axial elongation of the octahedron (4 short and 2

long bonds) as expected if d_{z^2} copper orbital is occupied and $d_{x^2-y^2}$ is half-occupied. The extreme example of Jahn-Teller effect is the elongation until complete loss of axial ligands, leaving an square-planar complex. The orbital mixing determines if axial elongation is favored in front axial contraction.

The Cu^{I} species, with a d^{10} full-shell configuration, is diamagnetic and pale-colored or colorless. In aqueous solution, Cu^{I} is unstable because disproportionation reaction occurs to form Cu^{II} and Cu^0 , due to high hydration energy of divalent ion.^{13,1} In spite of that, Cu^{I} species can be stabilized as not very soluble complexes or by complexation with π -acceptor ligands. The most common geometry for Cu^{I} is tetrahedral as in complexes $[\text{Cu}(\text{CN})_4]^{3-}$, $[\text{Cu}(\text{py})_4]^+$ and $[\text{Cu}(\text{L-L})_2]^+$ (L-L = bipy, phen), but tricoordinated complexes are known as in $\text{K}[\text{Cu}(\text{CN})_2]$ (trigonal polymeric $\text{Cu}(\text{CN})_3$ units in the solid state), and also linear complexes as $[\text{CuCl}_2]^-$, that forms by dissolving CuCl in HCl .

One of the most relevant aspects of Cu^{I} chemistry is its affinity to coordinate molecular oxygen O_2 , that is activating an inert gas into a reactive form useful to perform a wide variety of reactions. There are two other well-characterized O_2 activation centers: the system Fe^{II} high spin (four unpaired electrons in 3d orbitals) and the 1,5-dihydroflavin system, formally antiaromatic.¹⁴ The Cu^{I} affinity for the triplet ground state dioxygen $^3\text{O}_2$ is based on the empty 4s and 4p orbital participation and the possible formation of hybrid 3d/4s and 3d/4p orbitals,¹⁵ as well as the resulting activation from the metal-ligand and metal-metal interactions.¹⁶

1.2.1 Copper metalloproteins

Copper versatility is reflected in the high diversity of biological functions that catalyze and in the variety of Cu ions contained in each enzyme's active site. The copper metal can be present as mononuclear, dinuclear or trinuclear complex, sharing the active site with other metals as Fe and Zn, and forming clusters.^{1,6} The standard classifications of Cu active sites were useful to correlate the biological function with spectroscopic and magnetic properties, and types 1, 2 and 3 were defined.^{2,3} Updated classification includes three more categories (Table 1): type (2+3) trimer, type Cu_A and type MT-Cu.

Table 1. Classification of different Cu-containing active sites.¹

	Type 1	Type 2	Type 3	Type (2+3) trimer	Cu _A	MT-Cu
Aggregation state	Mononuclear	mononuclear	dinuclear	Trinuclear	dinuclear	Mononuclear or clusters
Biological function	Electron transfer	Catalysis and redox reactivity	O ₂ activation for transport and oxygenation	O ₂ activation for oxidase function	Electron transfer	Regulation, storage and transport
Examples	Blue protein (plastocyanin, azurin, stellacyanin)	Amine oxidase, galactose oxidase, superoxide dismutase, cytochrome c oxidase (Cu _B)	Hemocyanin and tyrosinase	Ascorbate oxidase, laccase	N ₂ O reductase, cytochrome c oxidase	CUP2, metalotionein (MT), transport Cu ATPase
Coordination geometry for Cu	3, trigonal - planar +1 axial	4 or 5, square-planar or square-based pyramid	Cu ^I : 3, trigonal - planar	Cu ^I : 3, trigonal Cu ^{II} : 4	4	3, trigonal - planar

Focusing on structural and spectroscopic characteristics for each type, it is found that Type 1 active sites show a coordination environment for Cu with a S- cysteine residue, two histidinic N and one S residue from a methionine in the axial position. EPR spectrum for oxidized form shows a hyperfine splitting (A_{II}) and a low g factor (g_{II}). A ligand-to-metal charge transfer (LMCT: $\text{Cys}^- \rightarrow \text{Cu}^{II}$) is responsible for intense absorption at the visible region in the electronic spectrum.

In Type 2, the metal is coordinated to three histidinic N, with a fourth available coordination site, suitable for ligands as organic radicals or other adjacent metal centers. The oxidized form presents a typical Cu^{II} EPR spectrum and only ligand field forbidden transitions are observed, without intense absorption bands.

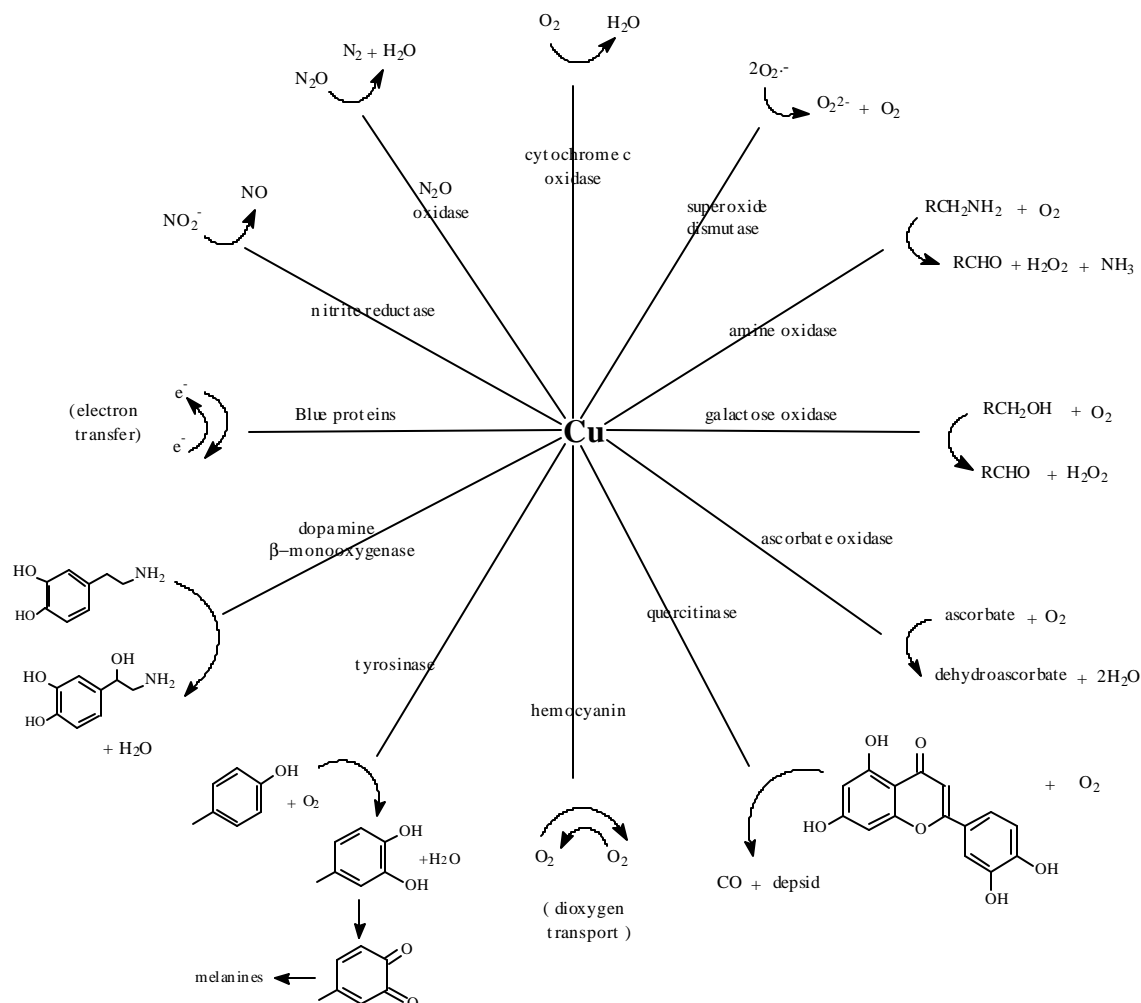
In copper active sites of Type 3, each metal center is coordinated to three histidinic N and to the peroxo bridging group in a side-on geometry fashion for the oxidized form.²³ The latter is EPR silent due to strong antiferromagnetic coupling between copper centers through the peroxo bridge, and shows intense UV-Vis absorptions due to LMCT ($\text{O}_2^{2-} \rightarrow \text{Cu}^{II}$).

In Type (2+3) trimer centers, the three Cu are coordinated to histidinic N, and activation of O_2 is mediated by a hydroperoxo group bound to one of the Cu centers.¹⁷ Typical EPR spectrum for Cu^{II} is found and large absorptions at the electronic spectrum are due to LMCT ($\text{O}_2^{2-} \rightarrow \text{Cu}^{II}$).

Type Cu_A active centers present a coordination of two S cysteine residues, two histidinic N and one methioninic S or peptide O to both Cu centers. Equivalence of Cu atoms is reflected in a minor hyperfine splitting on the EPR. Absorption near the infra-red region is due to metal-to-metal charge transfer (MMCT).

Proteins with Type MT-Cu active sites present a coordination of three cysteinic S per Cu atom. Their function is copper transport and no oxidized form is found.

Figure 1. Reaction catalyzed by Cu-containing proteins¹



The present work will focus on proteins involved in dioxygen processing, that can be classified depending on specific function (Table 2): O_2 transport, monooxygenation, dioxygenation and dehydrogenation reactions.

Table 2. Cu protein involved on O₂ processing⁶ and superoxide dismutation.

<i>Function</i>	<i>Protein</i>
O ₂ -carrier $\text{Hc} + \text{O}_2 \rightleftharpoons \text{oxyHc}$	Hemocyanin
Monooxygenation $\text{S} + \text{O}_2 + 2\text{e}^- + 2\text{H}^+ \rightarrow \text{SO} + \text{H}_2\text{O}$	Tyrosinase dopamine- b -monooxygenase phenylalanine monooxygenase peptidylglycine- α -amidating enzyme metano monooxygenase amonium monooxygenase
Dioxygenation $\text{S} + \text{O}_2 \rightarrow \text{SO}_2$	Quercitinase 2,3-dihydroxibenzoate 2,3-dioxygenase indole dioxygenase
oxidation $2\text{SH}_2 + \text{O}_2 \rightarrow 2\text{S} + 2\text{H}_2\text{O}$ $\text{SH}_2 + \text{O}_2 \rightarrow \text{S} + \text{H}_2\text{O}_2$	galactose oxidase amine oxidase ascorbate oxidase laccase
reduction $\text{O}_2 + 4\text{e}^- + 4\text{H}^+ \rightarrow \text{H}_2\text{O}$	cytochrome c oxidase
Superoxide dismutation $2\text{O}_2^- + 2\text{H}^+ \rightarrow \text{O}_2 + \text{H}_2\text{O}_2$	Cu-Zn superoxide dismutase

1.2.2 Hemocyanin

Hemocyanin is the protein responsible for O₂ transport in arthropods and mollusks principally, but also in higher entity creatures such as lobsters and squids.⁸

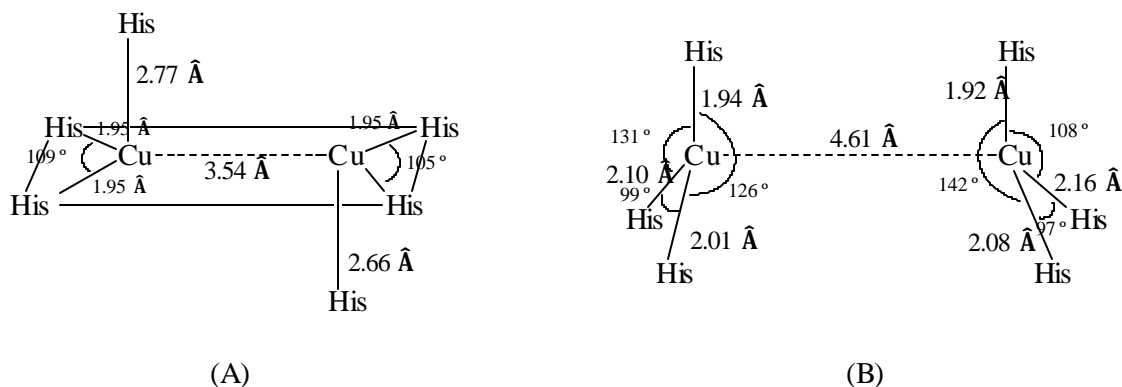
Protein dimensions are in a 4.5 a 90x10⁵ Da range, and are constituted by different cooperating subunits. In the active site of each of these subunits, two Cu atoms are coordinated to three histidine residues per copper,¹⁸ allowing the reversible coordination of dioxygen in the peroxide form O₂²⁻.

Initially, the coordination environment proposed for oxyhemocyanin (oxyHc) was a cis-1,2-end-on peroxy bridging group with a H₂O or OH⁻ molecule as exogenous ligand,¹⁹ but resolution of crystalline structure of a dinuclear copper complex with a bridging $\mu\text{-}\eta^2\text{:}\eta^2\text{-side-on}$ peroxy by Kitajima and co-workers in 1989,^{20,21} that showed spectroscopic similarities with oxyHc, focused the attention of the scientific community to this new coordination mode,²² that was confirmed in 1993 by Magnus and co-workers with the crystalline structure resolution of oxyhemocyanin from *Limulus polyphemus*.²³

Deoxyhemocyanin is a colorless protein that bears a dinuclear Cu^I complex in the active site, where each Cu atoms is coordinated to the imidazole group from three histidine residues. The crystal structure of deoxyHc from *P. Interruptus*¹⁸ shows a pseudo-tetrahedral geometry for each Cu center, with an available fourth coordination site. Two of the Cu-N bond distances are 1.95 Å, and the third bond is weaker (2.77 Å). Cu-Cu distance is 3.54 Å. Four histidinic N atoms and both Cu centers lie in the same plane, whereas the two apical N present a *trans* disposition.

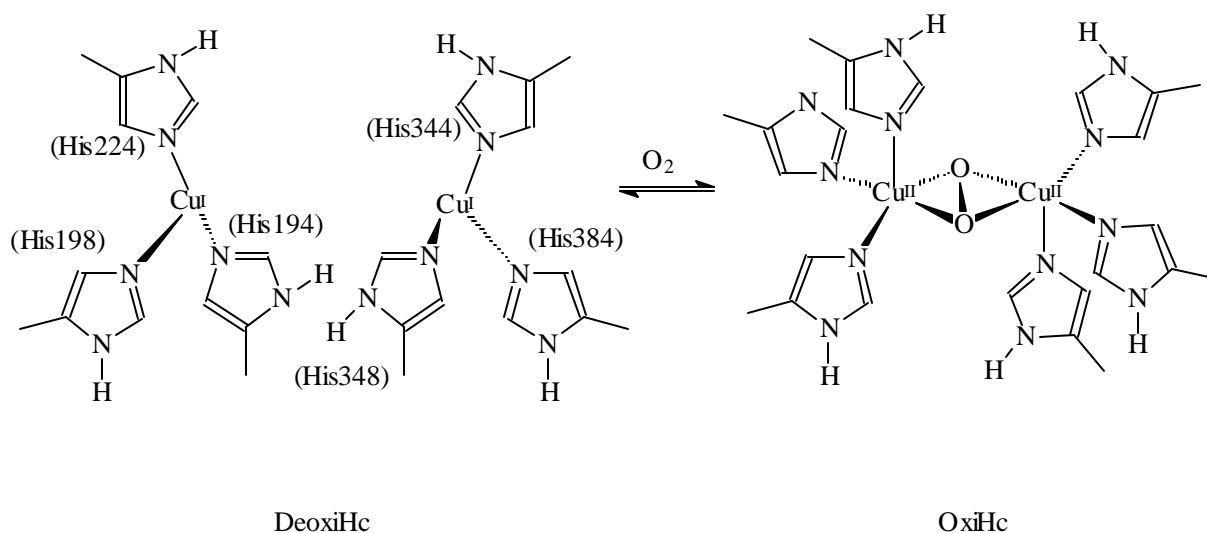
Recently, deoxyHc structure for *Limulus polyphemus*²⁴ was obtained and it is remarkably different compared to *P. Interruptus*. Cu-Cu distance is larger in the former (4.61 Å), each copper presents a slightly distorted plane-trigonal geometry with Cu-N bond distances from 1.92 to 2.16 Å, and no elongation of any of Cu-N bonds is found. The longer Cu-Cu distance implied an important structural reorganization on the O₂ activation step. Actually, it is the 3-D α -helix structure of the apoenzyme that modulates its conformation to allow a normal peroxide coordination.

Figure 2. Active sites of deoxyHc: (A) in *P. interruptus* and (B) in *L. polyphemus*



Magnus and co-workers finally confirmed the μ - η^2 : η^2 -side-on peroxo coordination mode in oxyHc with its crystal structure in *L. Polyphemus*.²³ The Cu-Cu distance shortens to 3.6 Å and O-O bond distance is 1.4 Å, very similar to what was found in Kitajima's model.²⁵

Figure 3. DeoxyHc active site in *P. Interruptus* and activation of O₂.



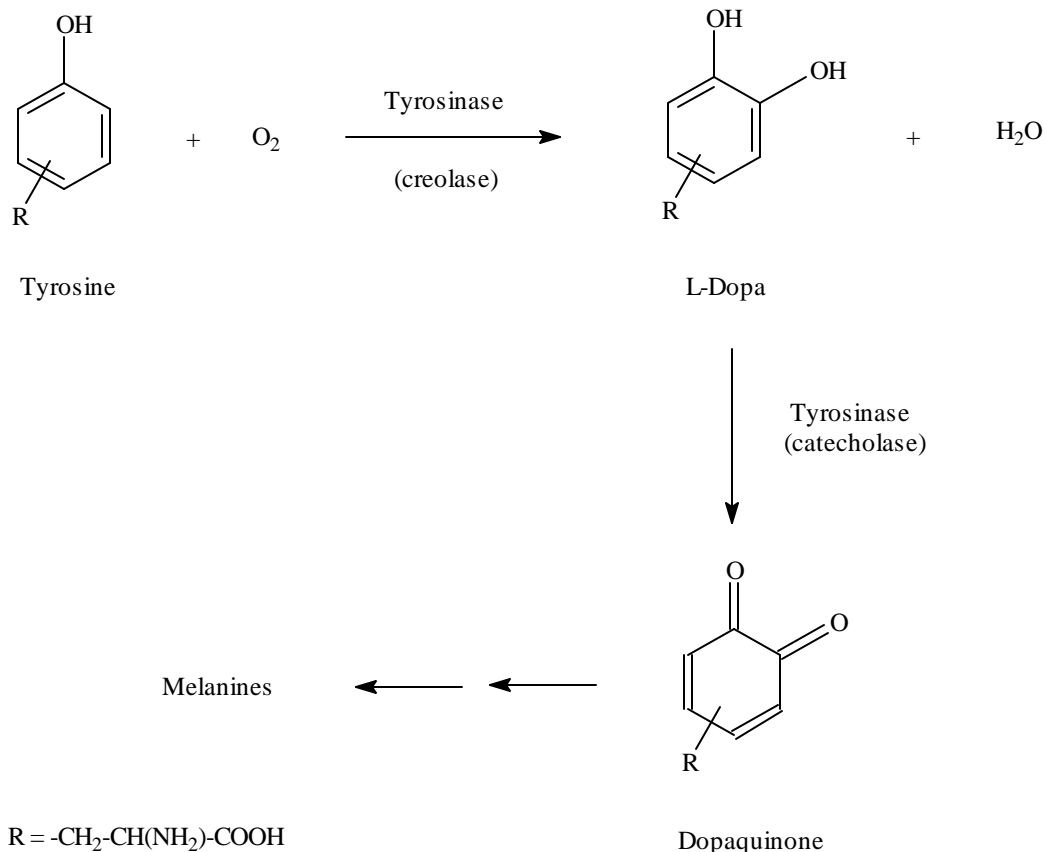
OxyHc shows two absorption bands at the UV-Vis spectrum centered at $\lambda_{\text{max}} = 350 \text{ nm}$ ($\epsilon \approx 20000/2\text{Cu M}^{-1}\text{cm}^{-1}$) and $\lambda = 580 \text{ nm}$ ($\epsilon \approx 1000$), both due to LMCT ($\text{O}_2^{2-} \rightarrow \text{Cu}^{\text{II}}$).

OxyHc shows a characteristic vibration $\nu(\text{O-O})$ at 750 cm^{-1} in the Raman spectrum, as well as a band at 450 nm detected by circular dichroism spectroscopy (CD). OxyHc is EPR silent due to strong antiferromagnetic coupling, behaving as formally diamagnetic species at room temperature.

1.2.3 Tyrosinase

Tyrosinase (Tyr) is a monooxygenase enzyme usually found in bacteria, fungi, plants and mammals, and is responsible of melanogenesis.²⁶ The enzyme catalyzes the hydroxylation of monophenols to obtain *ortho*-diphenols (catechols) in a first step, and reoxidizes the latter to *o*-quinones in a second step (Figure 4).⁹

Figure 4. Biological function of tyrosinase towards the final synthesis of melanines²⁶



OxyTyr active site structure has not been solved by X-Ray diffraction studies, but spectroscopic analysis including EXAFS measurements^{3,27,28} indicate a very similar structure compared to oxyHc. Two factors are proposed to explain the different reactivity in both enzymes: the accessibility of phenolic substrates to the active site, modulated by the polipeptidic chain,²⁹ and different coordination structures for Cu atoms in each enzyme.³⁰

Thus, tyrosinase's active site contains two Cu atoms coordinated to three histidinic N each, that are able to activate molecular dioxygen and coordinate it as the

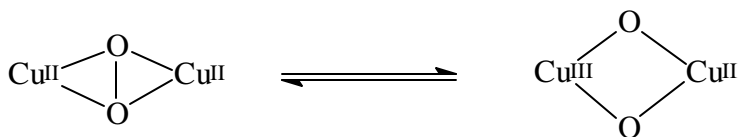
bridging $\mu\text{-}\eta^2\text{:}\eta^2\text{-}$ side-on peroxo group, responsible for the monooxygenase activity of the enzyme.

Synthesis of chemical "Tyr-like" models has helped on obtaining more information about the hydroxylation process performed by tyrosinase. The first synthetic model with hydroxylating activity was reported by Karlin and co-workers, using the R-XYL-H ligand series,^{31,32} and obtaining an aromatic hydroxylation at the ortho position of the ring. Hydroxylations have also been found in xylyl modified systems of Schiff base^{33,34} and others developed by Tolman and co-workers.³⁵

The $\mu\text{-}\eta^2\text{:}\eta^2\text{-}$ side-on peroxo group is thought to be the active species for hydroxylation step, through an addition of the electrophilic peroxide oxygen to the π -system of the aromatic ring, mechanism supported by frontier molecular orbital analysis.³⁶

Very recently, Tolman and co-workers have demonstrated the coexistence of $\mu\text{-}\eta^2\text{:}\eta^2\text{-}$ side-on peroxo and bis- $\mu\text{-oxo}$ cores in rapid equilibrium³⁷ and therefore, both species may be active towards aromatic hydroxylation.³⁸

Figure 5. Equilibrium of $\mu\text{-}\eta^2\text{:}\eta^2\text{-}$ side-on peroxo and bis- $\mu\text{-oxo}$ coordination modes



The hydroxylation reaction mechanism will be studied in detail in section 1.4.1.

1.3 Biomimetic modeling and molecular O₂ activation

The scientific community has spent great efforts to understand the reaction mechanisms that govern the molecular O₂ activation by metalloproteins and their reactivity. It has been over the past 15 years when mechanistic details of Cu-O₂ interactions have been established.

The synthesis of mono- and dinuclear copper complexes with simple ligands has allowed the characterization of a wide variety of coordination modes for the activated forms of molecular dioxygen O₂ (see Figure 8). The identification of these Cu-O₂ intermediates has been crucial to propose mechanisms for reactions performed by natural enzymes.^{25,37,39,40} Other trinuclear complexes⁴¹ have been synthesized as models for ascorbate oxidase and laccase activities (i.e. 4 electron reduction of O₂ to H₂O).

Early works from Karlin and co-workers⁴² set the bases to obtain synthetic models designed to simulate structural, spectroscopic and reactivity characteristics of Type 3 dinuclear cuproproteins (hemocyanin and tyrosinase).

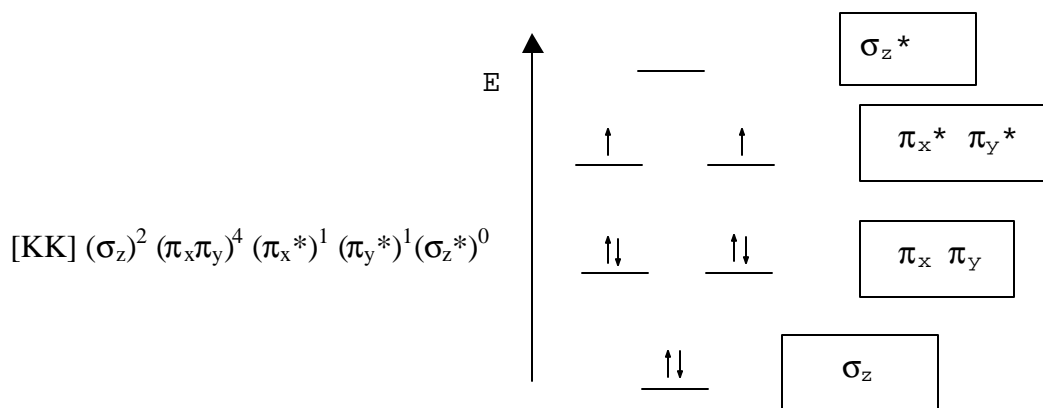
In 1992, Kitajima and co-workers obtained the first X-Ray structure for the $\mu\text{-}\eta^2\text{:}\eta^2\text{-peroxo}$ side-on core, in 1993 Karlin and co-workers isolated a trans-1,2-peroxo core³⁹ and Tolman and co-workers crystallized a bis($\mu\text{-oxo}$)Cu^{III}₂ in 1996,⁴³ at the same time that demonstrated the equilibrium between $\mu\text{-}\eta^2\text{:}\eta^2\text{-peroxo}$ side-on and bis($\mu\text{-oxo}$) cores.³⁷

1.3.1 Modeling active sites

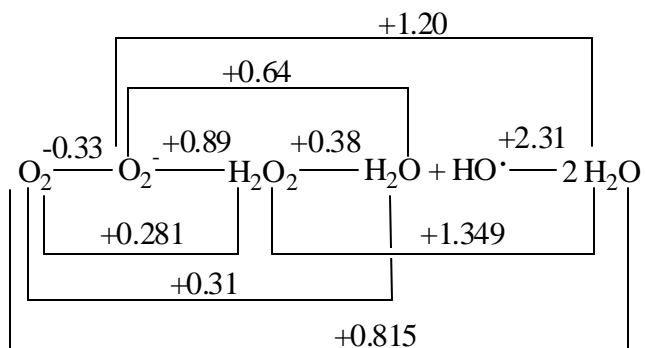
Synthesis of chemical models of natural enzymatic active sites requires a careful analysis of all structural, spectroscopic and reactivity data available to design the ligands that will be used to synthesize the chemical models. The donating atoms ligated to Cu centers are crucial to obtain a complex capable of simulate the chemical and spectroscopic parameters of the natural site. Substituents in donating heteroatoms, distance between them, coordination numbers, and also bridging groups and metal-metal distances in dinuclear complexes are determining factors to obtain good model complexes.⁴² Subtle changes in heteroatom substituents are magnified in O₂ activation behavior, as reflected in studies perform with different families of ligands.^{43,44,45,46}

1.3.2 Intermediate characterization

The interaction of a O₂ molecule with Cu^I implies a partial or total reduction of dioxygen and the oxidation of the metal. The majority of reactions with O₂ have a favorable enthalpy ($\Delta H < 0$), but some factors difficult the interaction. Dioxygen molecule ground state is a triplet and spin conservation rules allow the interaction of dioxygen (triplet) with other systems with unpaired electrons. The reaction of the triplet O₂ with a diamagnetic molecule will only proceed if the final product has an easily accessible triple state.^{47,48}

Figure 6. Orbital diagram for ${}^3\text{O}_2$ 

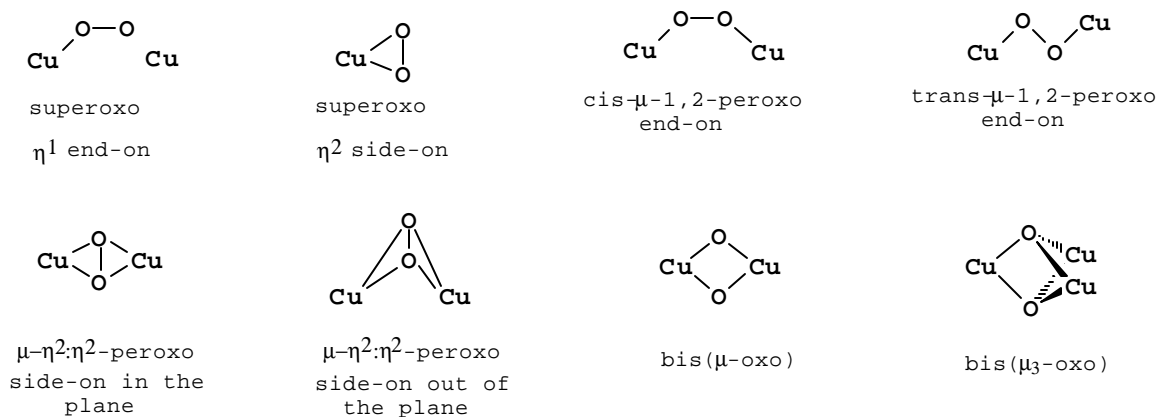
These rules create kinetic barriers for the reaction with dioxygen. Enthalpically, reactions are limited for the unfavorable reduction of O_2 to superoxide O_2^- , even though the 2 and 4 electron reduction to peroxide and water respectively are favorable.⁴⁵

Figure 7. Latimer diagram of dioxygen species dissolved in H_2O at pH=7 at 1 atm of O_2 

The dioxygen molecule behaves as σ -donor and π -acceptor ligand when reacts with Cu^I . Spin-orbit coupling, that reduces the potential barrier for the spin change, and the interaction with the metal, that supplies the necessary energy to overcome the barrier, are the factors that allow the reaction to occur.^{49,50}

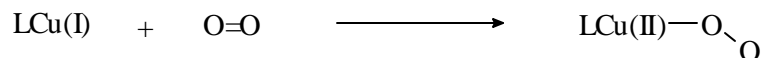
The different coordination modes described in the literature for $\text{Cu}_n\text{-O}_2$ cores are depicted in Figure 8.

Figure 8. Different $\text{Cu}_n\text{-O}_2$ coordination modes.



1.3.2.1 Superoxo complexes

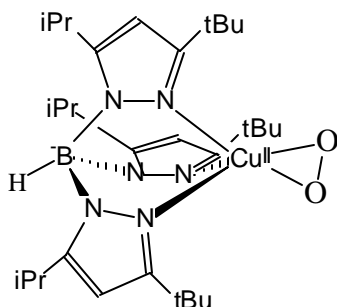
Mononuclear complexes 1:1 Cu-O_2 are clue intermediates postulated in many biological and catalytic processes.⁶ The reaction of a Cu^{I} complex with dioxygen undergoes towards the formation of a superoxo Cu^{II} complex, as a first step of the dioxygen activation process. Superoxo species are unstable and transform to other intermediate species.



The superoxocomplex molecule rapidly reacts with a second Cu^{I} complex molecule to form new peroxocomplexes (see next sections). There are few superoxocomplexes well characterized due to their rapid formation and short half-lives. Its detection is usually achieved by UV-Vis and Raman spectroscopy at low temperatures. There is only one

superoxocomplex characterized by X-Ray diffraction to date, described by Kitajima in 1994,⁵¹ where trispyrazolyl hydroborate ligand with bulky substituents was used. Its design prevents the reaction of superoxo intermediate with other Cu^{I} molecules, allowing its isolation. The complex presents a η^2 side-on type of coordination, whereas the majority of UV-Vis detected superoxo intermediates are thought to present end-on coordination.⁴⁴

Figure 9. Crystal structure of superoxocomplex $[\text{Cu}^{\text{II}}(\text{O}_2^-)(\text{HB}(3\text{-tBu-5-}i\text{Prpz})_3)]$.⁵¹



Complex $[\text{Cu}^{\text{II}}(\text{O}_2^-)(\text{HB}(3\text{-tBu-5-}i\text{Prpz})_3)]$ presents a brown-reddish color in CH_2Cl_2 at $-50\text{ }^\circ\text{C}$, with two characteristic bands at 352 nm (ϵ 2330 $\text{M}^{-1}\text{cm}^{-1}$) and 510 nm (230), with a minor shoulder at 660 nm. Strong coupling between Cu^{II} and superoxo group (both with spin $\frac{1}{2}$) is reflected in the diamagnetic behavior (sharp signals on the NMR spectrum are obtained).

Karlin and co-workers have detected spectroscopically superoxo complexes as reaction intermediates with TMPA ligand and derivatives.^{44,45}

Recently, UV-Vis studies at low temperatures with Cu^{I} complexes using the ligands $i\text{Pr}_3\text{-TACN}$,³⁷ and dinucleant ligands formed by TACN units linked with $-\text{CH}_2\text{CH}_2-$ ⁵² or $-\text{Xylyl}-$ ³⁵ also postulated the existence of superoxo complexes as intermediates of the reaction with O_2 .

Harata and co-workers reported the crystal structure of a η^1 end-on superoxo complex,⁵³ but a better resolution of the structure finally determined that it was a hydroperoxo complex.⁵⁴ Therefore, a careful analysis of the X-Ray diffraction data is required to avoid important confusions.

1.3.2.2 Peroxo complexes

Reaction of a superoxo complex molecule ($\text{LCu}^{\text{II}}\text{-O}_2^-$) with a Cu^{I} complex molecule generates a peroxo complex $\text{LCu}^{\text{II}}\text{-(O}_2^{2-})\text{-Cu}^{\text{II}}\text{L}$. At least four different coordination modes for peroxo intermediates have been characterized (see Figure 8), generally highly unstable species characterized by low temperature Raman and UV-Vis spectroscopy.

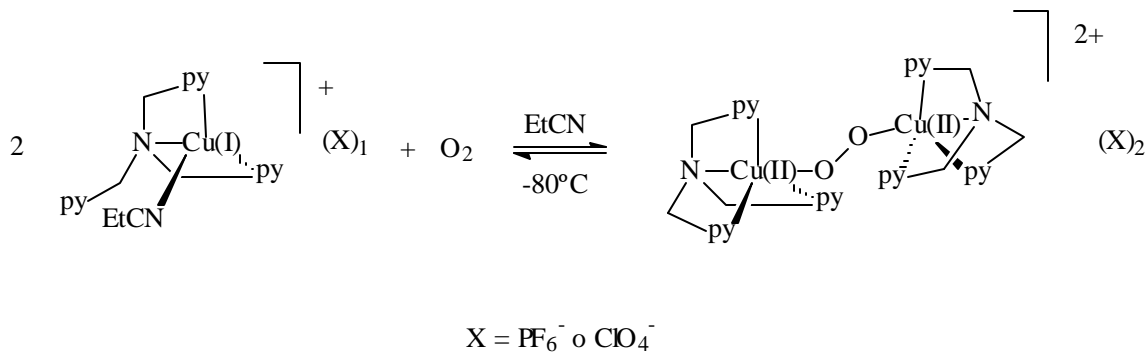
Peroxo complexes are clue intermediates in the mechanism of the Cu-O_2 interaction and major attention is dedicated to them in the O_2 activation field. Besides, peroxo complexes are thought to be the active species in several catalytic reactions⁶ and therefore, the complete determination of their properties is of importance.

1.3.2.2.1 Transperoxo complexes

There is only one crystal structure of a *trans*- μ -1,2-peroxo end-on complex, described by Karlin and co-workers,³⁹ and corresponds to the interaction of complex $[(\text{TMPA})\text{Cu}^{\text{I}}(\text{EtCN})](\text{X})$ ($\text{X} = \text{PF}_6^-$, ClO_4^-) with O_2 at -80°C . This peroxocomplex was considered initially a synthetic model

for hemocyanin, as the reaction of Cu^{I} and O_2 at -80°C is reversible, but spectroscopic differences and longer Cu-Cu distances discarded the hypothesis.

Figure 10. Reversible formation of peroxo complex $[(\text{TMPA})_2\text{Cu}^{\text{II}}_2(\text{O}_2)](\text{X})_2$



UV-Vis spectrum of the complex, and generally for other transperoxo complexes, presents three characteristic absorption bands at 440 nm (shoulder, $\epsilon = 2000 \text{ M}^{-1}\text{cm}^{-1}$), 525 nm (11500) and 600 nm (shoulder, 7600), that confer the typical deep-violet color to these intermediates.

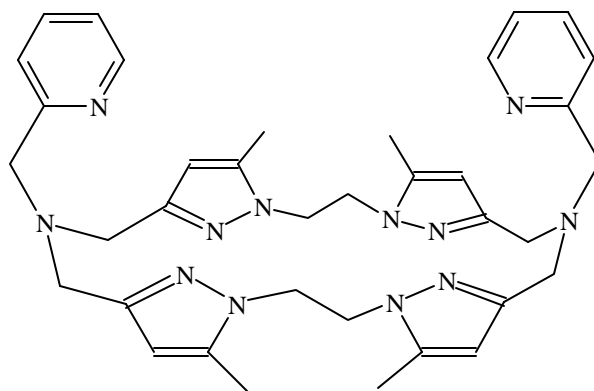
Studies done by Karlin and co-workers allowed the detection and spectroscopic characterization of transperoxo complexes at low temperatures with TMPA derivative ligands, such as the mononucleant BPQA, BQPA⁴⁴, TMPAE⁵⁵ and tris(3-*t*-Bu-2-pyridylmethyl)amine⁴⁵ or the dinucleant D^{I} ,⁵⁵ consisting in two TMPA units linked by a $-\text{CH}_2\text{CH}_2-$ group.

Lippard and co-workers have published an interesting transperoxo complex in a recent report, which shows typical spectroscopic properties but a very short Cu-Cu distance (2.84 Å, determined by EXAFS),⁵⁶ compared to 4.36 Å for complex $[(\text{TMPA})_2\text{Cu}^{\text{II}}_2(\text{O}_2)]$. The ligand BPMAN used is a dinucleating derivative of 1,8-naphthyridine and the short

transperoxo complex obtained may be a model for key intermediates in the formation of $\mu\text{-}\eta^2\text{:}\eta^2$ side-on peroxo structures in dicopper systems and in the conversion of ($\mu\text{-}1,2\text{-peroxo}$) to bis($\mu\text{-oxo}$) species in dioxygen activation by diiron centers.⁵⁷

Reedijk and co-workers have designed a dinucleant ligand MEPY22PZ capable of generating the corresponding $\text{Cu}_2\text{-O}_2$ intermediate as a stable *trans*- $\mu\text{-}1,2\text{-peroxo}$ at room temperature in protic media (the most stable reported to date, $t_{1/2} = 200$ s).⁵⁸

Figure 11. The dinucleant macrocyclic ligand MEPY22PZ



MEPY22PZ

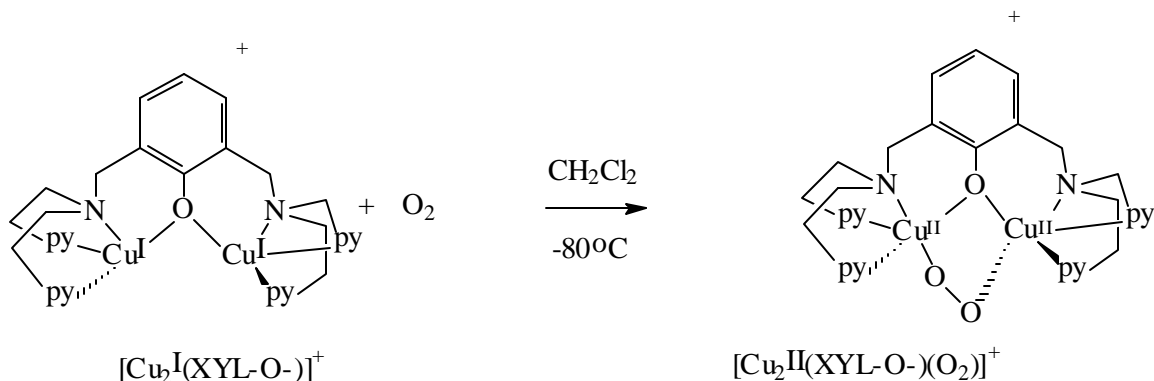
The ligand coordination environment is designed to protect the Cu_2O_2 core and enhance its stability.

1.3.2.2.2 Terminal peroxo complexes

A dinuclear Cu^{I} complex with a XYLYL derivative with a phenoxo group has been reported to react quasi-reversibly with O_2 by the formation of a peroxo complex.⁵⁹

Designed by Karlin and co-workers, the peroxy group showed distinct spectroscopic features that generated some controversy when the work was published. Raman experiments excluded a *cis-μ-1,2-end-on* coordination mode, giving support to a $\mu-1,1$ -terminal peroxy. On the contrary, the latter demands a Cu-Cu distance shorter than 3.15 Å, whereas Cu...Cu distance in complex $[\text{Cu}^{\text{II}}(\text{XYL-O-})(\text{O}_2)]^+$ is 3.3 Å. It was finally concluded that an asymmetric peroxy coordination mode with a weak interaction with the second Cu center was operating in this system.

Figure 12. Formation of a terminal asymmetric peroxy complex $[\text{Cu}^{\text{II}}(\text{XYL-O-})(\text{O}_2)]^+$



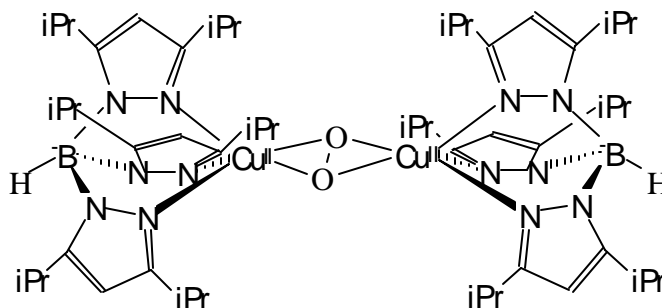
The complex shows electronic absorption bands at 385 nm (2900), 505 (6000) and 787 (700) with a shoulder at 610 nm. The band centered at 385 nm is assigned to a phenoxo $\rightarrow \text{Cu}^{\text{II}}$ LMCT, whereas the band at 787 nm corresponds to d-d transitions for Cu^{II} ion. The maximum at 505 nm corresponds to LMCT ($\text{O}_2^{2-} \rightarrow \text{Cu}^{\text{II}}$).

Some modifications to the -XYL-O- ligand structure have been applied^{60,6} and it is concluded that terminal peroxy coordination mode only forms when at least one pyridil group is bound to each Cu.

1.3.2.2.3 $m-h^2:h^2$ side-on peroxo complexes

This new coordination mode was first discovered and reported by Kitajima and co-workers with the resolution of the X-Ray crystal structure of $[(Tp^{iPr_2}Cu)_2(O_2)]$ complex (Tp^{iPr_2} = tris(3,5-diisopropylpyrazolyl)hydroborate).²⁵ The $\mu-\eta^2:\eta^2$ - side-on peroxo bridging group is symmetric and all atoms of the Cu_2O_2 core lie in the same plane. The resolution of this crystal structure determined the coordination mode in oxyHc, prior to crystallization of the natural active site (see section 1.2.2).⁸

Figure 13. Structure of $\mu-\eta^2:\eta^2$ - side-on peroxo complex $[(Tp^{iPr_2}Cu)_2(O_2)]$.²⁵



UV-Vis spectrum of peroxo complex $[(Tp^{iPr_2}Cu)_2(O_2)]$ shows two characteristic bands at 349 nm (20800) and 551 nm (790), conferring the violet color to this species. The intermediate is virtually diamagnetic at room temperature due to strong antiferromagnetic coupling between metal centers. Raman spectrum presents a signal at 741 cm^{-1} , typical for $\nu(O-O)$ vibration in this coordination mode. The decomposition of the intermediate to form bis(μ -hydroxo)

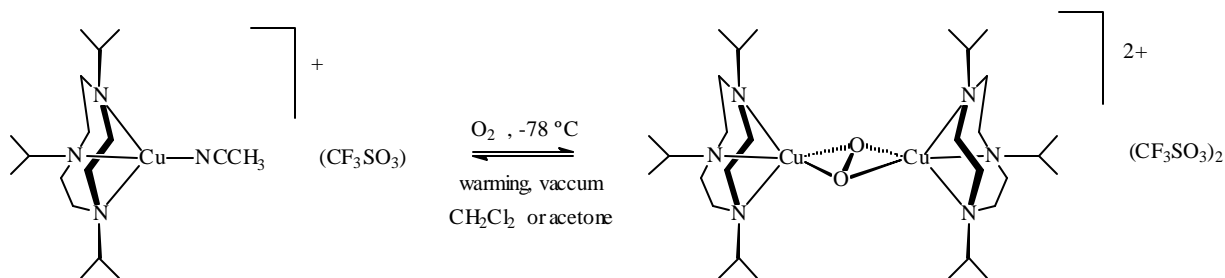
species follows first-order kinetics at 25°C with a rate constant value of $1.83 \times 10^{-3} \text{ s}^{-1}$.

Tp^{iPr_2} ligand derivatives like Tp^{Ph_2} or Tp^{Me_2} have been proved to also form same intermediates for the reaction of their Cu^{I} complexes with O_2 .^{20,25}

Recently, Tolman and co-workers have developed new Cu^{I} complexes using the triazacyclononane (TACN) ligand and derivatives,⁶¹ capable of molecular dioxygen activation to form side-on peroxo intermediates, which are much more unstable than Kitajima's systems, and characterized in solution below -70°C.

Peroxocomplex $[((i\text{-Pr}_3\text{TACN})\text{Cu}^{\text{II}})_2(\text{O}_2)](\text{O}_3\text{SCF}_3)_2$ bears a $\mu\text{-}\eta^2:\eta^2\text{-}$ side-on coordination mode as deduced from EPR, UV-Vis and Raman spectroscopy.

Figure 14. Formation of peroxo complex $[((i\text{-Pr}_3\text{TACN})\text{Cu}^{\text{II}})_2(\text{O}_2)](\text{O}_3\text{SCF}_3)_2$



The complex presents two characteristic absorption bands in the UV-Vis spectrum, one at 365 nm ($11000 \text{ M}^{-1}\text{cm}^{-1}$) and the second one at 510 nm (1000), it is EPR silent (virtually diamagnetic), and shows a Raman signal at 722 cm^{-1} corresponding to the $\nu(\text{O-O})$ vibration.

The same scientific team synthesized dinucleant ligands based on TACN units, using $-\text{CH}_2\text{CH}_2-$ or $-\text{Xylyl}-$ linkers, also capable of $\mu\text{-}\eta^2:\eta^2\text{-}$ peroxo side-on intermediate formation. For example, peroxo complexes $[(m-$

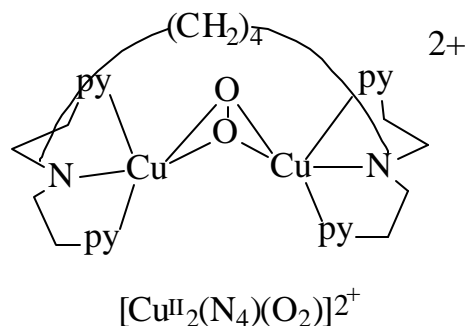
$\text{XYL}^{\text{iPr}_4}\text{Cu}^{\text{II}}_2(\text{O}_2)](\text{X})_2$ ($\text{X} = \text{ClO}_4^-$, SbF_6^- , CF_3SO_3^-) are characterized even though their formation is very sensitive to experimental conditions.^{35,38,52}

Karlin and co-workers have also characterized this type of $\text{Cu}_2\text{-O}_2$ coordination cores when using a family of mononucleant tridentate RPY2 ligands.^{62,63} However, a mixture of $\mu\text{-}\eta^2\text{:}\eta^2\text{-peroxo}$ side-on and bis($\mu\text{-oxo}$) species is found in coexistence (90:10 relation respectively). This system is an example of the facile interconversion between both isomeric species.^{37,63,64}

Karlin *et al.* already identified this coordination mode in complexes bearing R-XYL- ($\text{R} = \text{H}$, NO_2 or F) type ligands, that ultimately lead to aromatic hydroxylation product.^{32,65}

An structurally distinct variant of this coordination mode was firstly described by Zuberbühler and co-workers, and consists in the bent or butterfly $\mu\text{-}\eta^2\text{:}\eta^2\text{-side-on peroxo}$ core.⁴⁰ In these examples, ligand constrains imposes a bent Cu_2O_2 core to release tension of the system.

Figure 15. Bent $\mu\text{-}\eta^2\text{:}\eta^2\text{-side-on peroxo}$ corresponding to complex $[(\text{N}_4)\text{Cu}^{\text{II}}_2(\text{O}_2)]^{2+}$

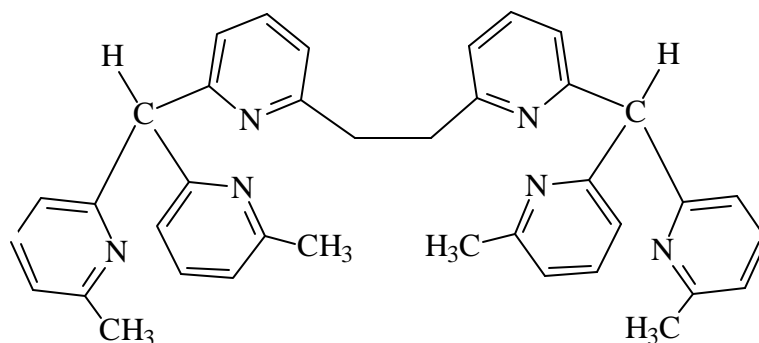


UV-Vis spectrum for intermediate $[(\text{N}_4)\text{Cu}^{\text{II}}_2(\text{O}_2)]^{2+}$ presents maximums at 360 nm ($\epsilon = 16000 \text{ M}^{-1} \text{ cm}^{-1}$) and 456 nm. EXAFS studies determines a $\text{Cu}\cdots\text{Cu}$ distance of 3.4 Å, slightly shorter than the 3.5 Å described by plane coordination mode

in oxyHc^8 or $[(\text{Tp}^{\text{iPr}_2}\text{Cu})_2 (\text{O}_2)]$.²⁵ Complexes from same family of ligands but different length of linker $(-\text{CH}_2)_n-$ ($n=3-5$) also form the same bent peroxy side-on intermediates.^{66,29,40}

Same bulky ligand strategy to stabilize *trans*- μ -1,2-peroxy at room temperature was used to design a dinucleant ligand derived from tripy (tris-(6-methyl-2-pyridyl)methane), which consists in two tripy units linked with the $-\text{CH}_2\text{CH}_2-$ capable of real stabilization of a bent μ - $\eta^2:\eta^2$ - side-on peroxy intermediate at room temperature ($t_{1/2} = 25.5$ hours) in CH_2Cl_2 .⁶⁷

Figure 16. Dinucleant ligand derivative of tripy designed to stabilize a μ - $\eta^2:\eta^2$ - side-on peroxy intermediate



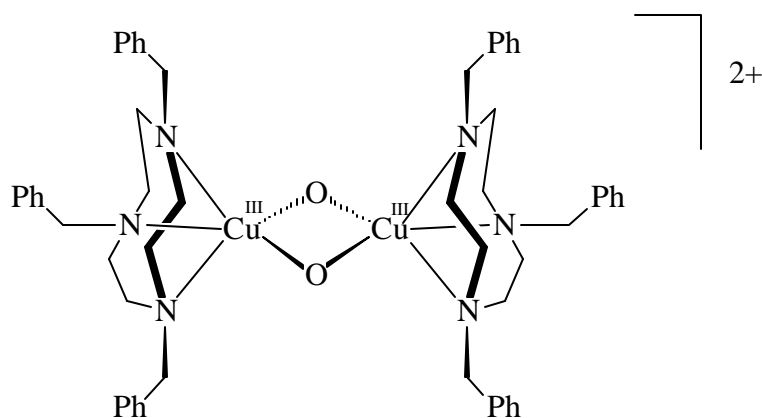
This is the most stable peroxy intermediate ever reported, coordination of O_2 is fully reversible and therefore, constitutes one of the better models for hemocyanin. Butterfly Cu_2O_2 peroxy plays an important role in reversibility aspects of O_2 coordination,⁶⁸ and the bent core is formed to accommodate the slightly short Cu-Cu distance in the complex ($\text{Cu}\cdots\text{Cu}$ 3.477 Å).⁶⁹

1.3.2.3 Bis(μ -oxo) complexes

The first $\text{Cu}^{\text{III}}-(\mu\text{-O})_2\text{-Cu}^{\text{III}}$ core was reported by Tolman in 1995,⁷⁰ and it presents completely different spectroscopic features compared to the rest of $[\text{Cu}_n\text{O}_2]$ intermediates. Actually, the bis(μ -oxo) coordination mode represents an step forward to the resolution of the $\text{Cu}_2\text{-O}_2$ interaction mechanism and to the reactivity pathways to oxidation products as well (O-O bond is already broken).

The electronic spectrum of complex $[(\text{Bn}_3\text{-TACN})\text{Cu}^{\text{I}}(\text{CH}_3\text{CN})](\text{SbF}_6)$ after reaction with O_2 at -80°C in CH_2Cl_2 showed distinct and characteristic absorption bands. The intermediate is unstable above -80°C , and it was characterized in solution by ESI-MS, ^1H -RMN, and O_2 uptake manometry. Only Raman and EXAFS studies allowed the assignment of the complex to a bis(μ -oxo) coordination mode for comparison to spectroscopic characteristics of similar intermediates in Fe or Mn complexes.⁷¹ Importantly, EXAFS data determined a short Cu-Cu distance (2.86 Å), unreliable for a $\mu\text{-}\eta^2\text{:}\eta^2\text{-}$ side-on peroxo (3.6 Å), and therefore, giving support to the new coordination mode.

Figure 17. Bis(μ -oxo) complex $[(\text{Bn}_3\text{-TACN})\text{Cu}^{\text{III}}]_2(\mu\text{-O}_2)(\text{SbF}_6)_2$



The obtention of crystals at low temperature suitable for X-Ray diffraction confirmed the bis(μ -oxo) core,⁴³ with Cu...Cu distance of 2.794 Å and O...O distance of 1.81 Å. The copper coordination sphere is an square-based pyramid slightly distorted at the axial position. Short Cu-O bonds (1.8 Å) are in line with copper oxidation state +3 and agree with bis(μ -oxo) complexes of Fe⁷² and Mn³⁸ with high oxidation states.

The UV-Vis spectrum of complexes [((Bn₃-TACN)Cu^{III})₂(μ -O₂)](X)₂ (X= ClO₄⁻ or SbF₆⁻) show two bands centered at 318 nm (ϵ = 12000 M⁻¹cm⁻¹) and 430 nm (14000), that confers the characteristic orange-brown color to it. The complex is diamagnetic due to d⁸ electronic configuration for Cu^{III} (EPR silent, ¹H NMR with fine structure). Raman spectrum (λ_{ex} = 457.9 nm) presents two signals at 602 and 612 cm⁻¹, that collapse to a single peak at 584 cm⁻¹ when ¹⁸O₂ is used.

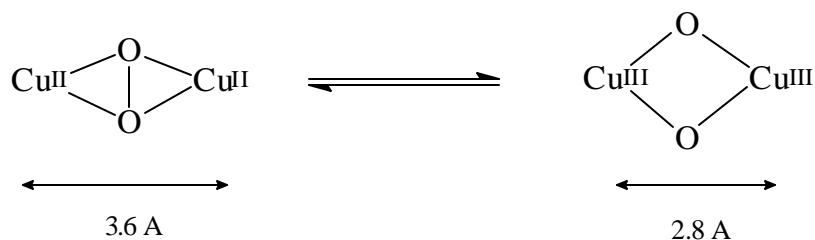
One of the major contributions from Tolman and co-workers was the demonstration of the rapid equilibrium between μ - $\eta^2:\eta^2$ -peroxo side-on and bis(μ -oxo) electronic isomers,³⁷ when using TACN derivative ligands (with variable *i*Pr and Bn group substitution on the coordinating N atoms). The equilibrium is very sensitive to experimental conditions, being solvent and counteranion nature the factors that control the displacement of the equilibrium towards one side.⁴³ The interaction of Cu^I complex [(*i*-Pr₃TACN)Cu^I(CH₃CN)](X) with O₂ at -80 °C formed the bis(μ -oxo) species when using THF and counterions X = ClO₄⁻ or PF₆⁻, while if using CH₂Cl₂ as solvent, reaction was directed to μ - $\eta^2:\eta^2$ -peroxo side-on species with all the counterions. The peroxo intermediate was also obtained if reaction was done in acetone or THF with BPh₄⁻, SbF₆⁻, O₃SCF₃⁻ counteranions.

It has not been established yet the exact influence of counterions and solvent towards displacement of the equilibrium to any of the two isomers. Some theoretical calculations have been performed in $[(\text{NH}_3)_3\text{Cu}]_2(\mu\text{-}\eta^2:\eta^2\text{-O}_2)]^{2+}$ and $[(\text{NH}_3)_3\text{Cu}]_2(\mu\text{-O})_2]^{2+}$ model systems in the gas phase. It is deduced that bis(μ -oxo) core is slightly more stabilized than peroxy core.³⁸ Calculations using solvents with dielectric constant $\epsilon = 10$ indicate that solvation also favors the bis(μ -oxo) core. However, the studies do not take into account the interactions of cores with the first coordination solvent sphere and counterions.

Focusing in ligand modification effects on the equilibrium, Tolman and co-workers concluded that steric characteristics of ligands determine which of the isomers will form.³⁸ When substituent groups on N atoms of TACN ligands present a tertiary carbon in the α position, $\mu\text{-}\eta^2:\eta^2$ -peroxy side-on core is formed (longer Cu...Cu distance), whereas if secondary carbon is found in the α position, bis(μ -oxo) core is formed (shorter Cu...Cu distance). It can be deduced from these data that steric problems imposed by a tertiary α carbon maintains the copper centers at longer distance and therefore the short distance in bis(μ -oxo) core is unachievable. However, solvation can overcome this effect as mentioned before.

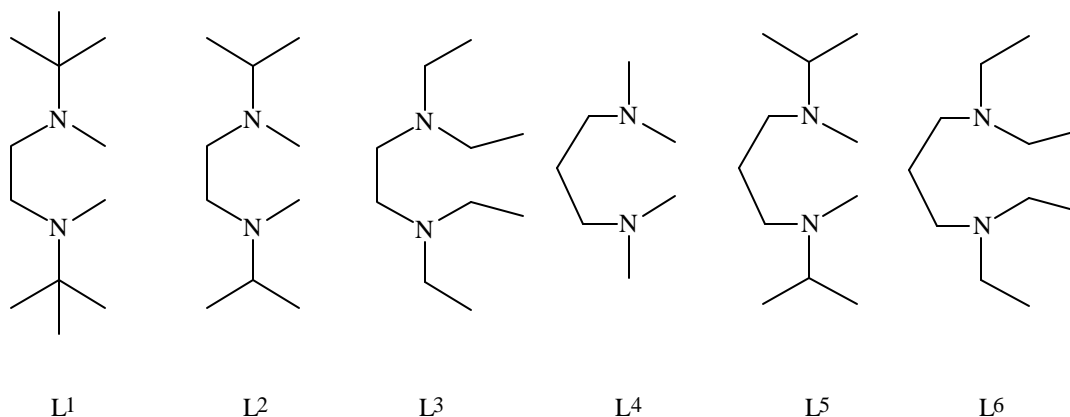
Ligand structure also imposes one of the isomers in the dinuclear TACN derivatives with $\text{-CH}_2\text{CH}_2\text{-}$ or -Xylyl- linkers. Ethyl linker maintains copper atoms close together and bis(μ -oxo) core is formed, whereas -Xylyl- linker is longer and peroxy core is obtained.

Figure 18. Cu...Cu distance for $\mu\text{-}\eta^2\text{:}\eta^2\text{-peroxo}$ side-on and bis($\mu\text{-oxo}$) cores



Stack and co-workers have developed a new way of generating $\mu\text{-}\eta^2\text{:}\eta^2\text{-peroxo}$ side-on and bis($\mu\text{-oxo}$) species with simple binucleating commercial peralkylated diamine ligands (PDLs).^{30,73,74} Regarding the weak coordination of the axial N in $\mu\text{-}\eta^2\text{:}\eta^2\text{-peroxo}$ side-on reported previously,^{8,25,67} compared to strong equatorial Cu-Neq bonds described, they decided to test bidentate chelation on Cu^I complexes towards O₂ activation. They have found that peralkylated diamine ligands provide sufficient Cu^I ligation for O₂ activation and, at the same time, substrate access to the peroxo or oxo cores is available. Thus, these simple systems are designed to prepare catalysts for potential oxidation reactions performed by the Cu_n-O₂ intermediates.

Figure 19. Peralkylated diamine ligands (PDLs) for Cu^{I} complexes capable of O_2 activation.



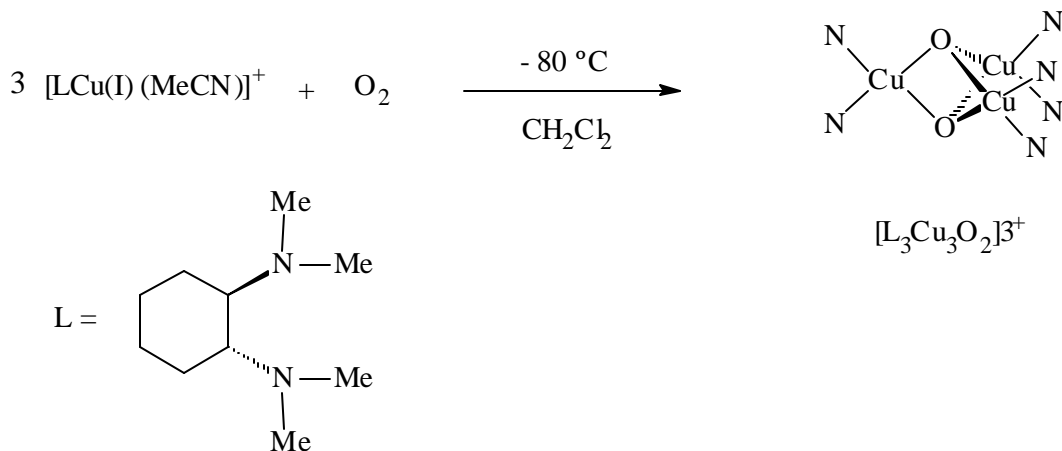
Larger N-alkyl substituents, at parity of diamine backbone, bias the equilibrium towards peroxo core, as already seen by Tolman systems.³⁸ The trends observed indicate interligand steric interactions as the major determinant of the equilibrium. Stack and co-workers also determined in this work that peroxo and oxo isomers can also be interconverted by temperature, solvent and the nature of counteranions.⁷³

1.3.2.4 Bis (μ_3 -oxo) complexes

This new coordination mode has only been characterized in one mixed-valence trinuclear copper cluster bearing the core $(\text{Cu}_3\text{O}_2)^{3+}$,⁴¹ where two copper atoms are formally divalent Cu^{II} and the third is trivalent Cu^{III} .⁷⁵ The ligand used is a permethylated (1R,2R)-cyclohexanediamine chosen for its preorganized structure ideal for binding one Cu atom. The small steric problems of this ligand allowed the

formation of the cluster after reaction with O₂ (in a 3:1 complex:O₂ relation) at -80°C in CH₂Cl₂.

Figure 20. Synthesis of new bis (μ₃-oxo) coordination mode in complex [L₃Cu₃O₂](O₃SCF₃)₃



The O···O distance is 2.37 Å and each copper atom achieves an optimal square-planar geometry. Only one of them presents short Cu-O bonds (1.83 Å), as a reflection of its higher oxidation state (Cu^{III}; similar distances are found in similar complex bearing bis(μ-oxo) core).⁷⁴

Electronic spectrum registered at -80°C in CH₂Cl₂ shows absorption bands centered at 290 nm (ε 12500 M⁻¹cm⁻¹), 355 (15000), 480 (1400) and 620 (800), conferring a brown color to it. Bands at 290 and 355 nm are attributed to O²⁻ → Cu^{III} LMCT, and their high intensity is a reflection of the degree of covalency for the Cu^{III}-O bond.

The mixed-valence cluster may be envisioned as the addition of a Cu^I complex molecule to an already formed bis(μ-oxo) core (Cu₂^{III}O₂).³⁸

1.4 Biomimetic modeling of tyrosinase and catecholoxidase reactivity

The catalysis of oxygenation and oxidation reactions by tyrosinase and catecholoxidases (COases) is currently one of the most intriguing fields in bioinorganic chemistry. Phenol oxidation reaction to *ortho*-diphenols and subsequent oxidation to *ortho*-quinones are known for over a century, but those reaction are still far from being understood at a molecular level. Tyrosinase is the only Type 3 copper protein that has not been characterized by X-Ray diffraction studies. This lack of structural data has been overcome by full spectroscopic characterization: similar hemocyanin active site structure is proposed, as well as similar intermediate $\mu\text{-}\eta^2\text{:}\eta^2\text{-peroxo}$ side-on species are formed on the oxyTyr form.^{6,29}

Importantly, the growing structural insight into tyrosinase activity is complemented in great manner by a continuous publication of chemical and mechanistic information obtained from the study of relatively simple synthetic models.^{32,36,76} After exposure of all the $\text{Cu}_n\text{-O}_2$ coordination modes in the previous sections, we will focus on the intrinsic mechanism of *ortho*-hydroxylation of phenols (monooxygenase activity, see Figure 4). Different proposed mechanism for aromatic hydroxylation in synthetic low molecular weight models and in tyrosinase natural site will be discussed in the following sections.

1.4.1 What is the hydroxylating active species? Proposed mechanisms

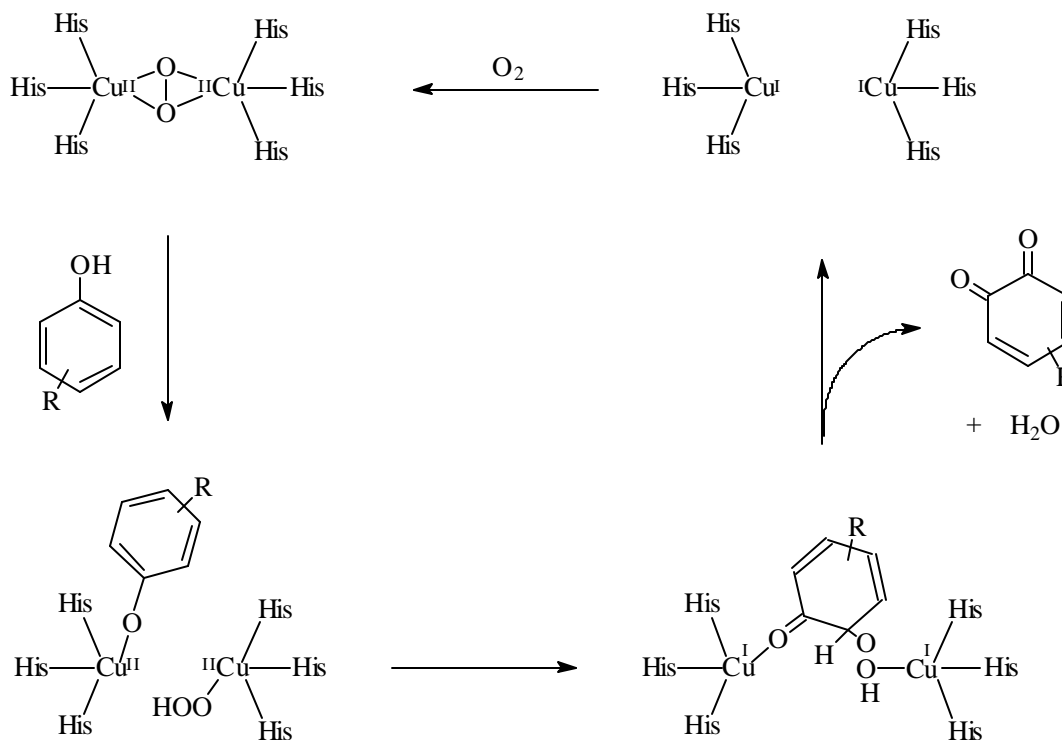
Assuming that the observed $\text{Cu}_2\text{-O}_2$ intermediate in tyrosinase active site is the well characterized $\mu\text{-}\eta^2\text{:}\eta^2\text{-}$ peroxo side-on, and considering that final product comes from the aromatic hydroxylation of the phenolic substrate, a question arises at this point: when does the O-O bond break? Does it break prior to, along with or after the attack by the oxygen to the aromatic ring?^{27,77}

The three possibilities are considered and their chance to be involved in the operating mechanism is evaluated.

1.4.1.1 O-O bond breaks after the attack on the aromatic ring

This was one of the earliest mechanisms proposed to be operating in tyrosinase activity.^{6,7} Once the $\mu\text{-}\eta^2\text{:}\eta^2\text{-}$ peroxo side-on core is formed, the following step would be the nucleophilic attack of the substrate hydroxo group to one of the Cu atoms. Homolysis of a Cu-O bond leads to formation of a phenoxide and an hydroperoxide groups. Concerted coupling of both species forms the intermediate hydroperoxibenzoquinone species. Final release of benzoquinone and a water molecule regenerates the dinuclear Cu^{I} active site ready to catalyze again the reaction.

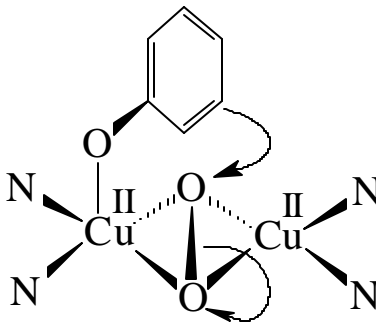
Figure 21. Proposed mechanism for hydroxylation reaction when O-O bond breaks after attack on the aromatic ring.



1.4.1.2 O-O bond breaks along with the attack on the aromatic ring

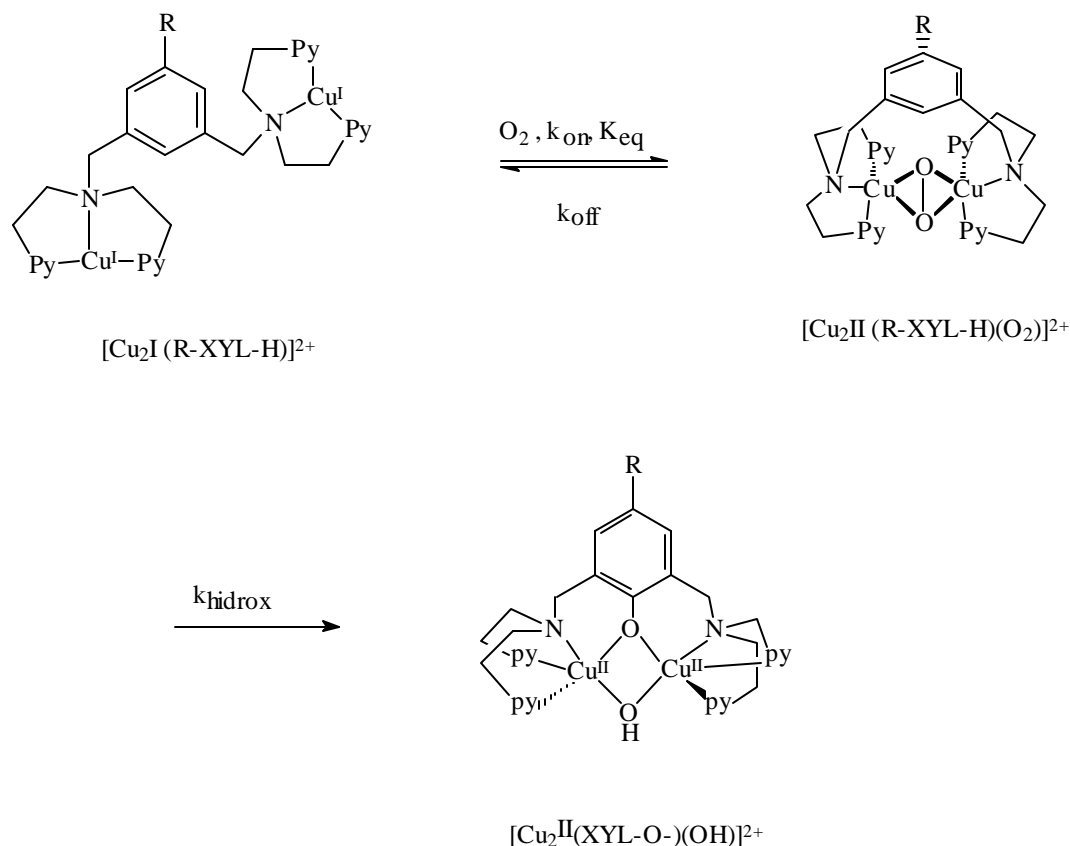
This mechanism would represent a case of electrophilic aromatic substitution (SE) by peroxide with the π system being activated for this reaction by the first OH group. The electrophilic character of the bridging side-one peroxide group is explained by a large amount of charge donation into the Cu^{II} centers, converting it as a suitable target for nucleophilic attack from the aromatic ring.^{78,79}

Figure 22. Proposed mechanism for hydroxylation reaction when O-O bond breaks along with the attack on the aromatic ring.



A typical and very representative example for this reactivity is the family of binuclear copper complexes $[\text{Cu}_2^{\text{I}}(\text{R-XYL-H})]^{2+}$ developed by Karlin and co-workers.^{32,80} In the binucleating ligand series R-XYL-H, two bis[2-(2-pyridyl)ethyl]-amino (PY2) tridentate units are linked by a xylyl spacer which is hydroxylated upon reaction of the corresponding Cu^{I} complex with O_2 . It has been demonstrated that the $\text{Cu}_2\text{-O}_2$ intermediate species is a $\mu\text{-}\eta^2\text{:}\eta^2\text{-peroxo}$ side-on. Reactivity depending on different electron withdrawing R- groups is in line with an electrophilic attack of the peroxide. For example, when $\text{R} = \text{F}^-$, the reaction becomes less favorable due to less nucleophilic character of the aromatic group. The lack of Deuterium Kinetic Isotope Effect (DKIE) also agrees with the electrophilic mechanism proposed, so the aromatic C-H bond breaking is not the Rate Determining Step (RDS) of the reaction.

Figure 23. Reaction pathway for intramolecular ligand hydroxylation with the model systems $[\text{Cu}_2^{\text{I}}(\text{R-XYL-H})]^{2+}$



R = H, t-Bu, F, CN, NO₂

Theoretical calculations have been performed on this system,³⁶ and within a frontier orbital approach, two distinct orbital pathways for electrophilic attack are considered. The highest occupied molecular orbital (HOMO) of the arene ring can either interact with the lowest unoccupied molecular orbital (LUMO) of the side-on peroxo group, which has a π^* character, or with the next unoccupied orbital at higher energy, which is σ^* type. Geometric and electronic considerations favoured the former possibility, namely the π^* pathway.

A considerable amount of examples can be found in the literature reporting aromatic hydroxylation performed by

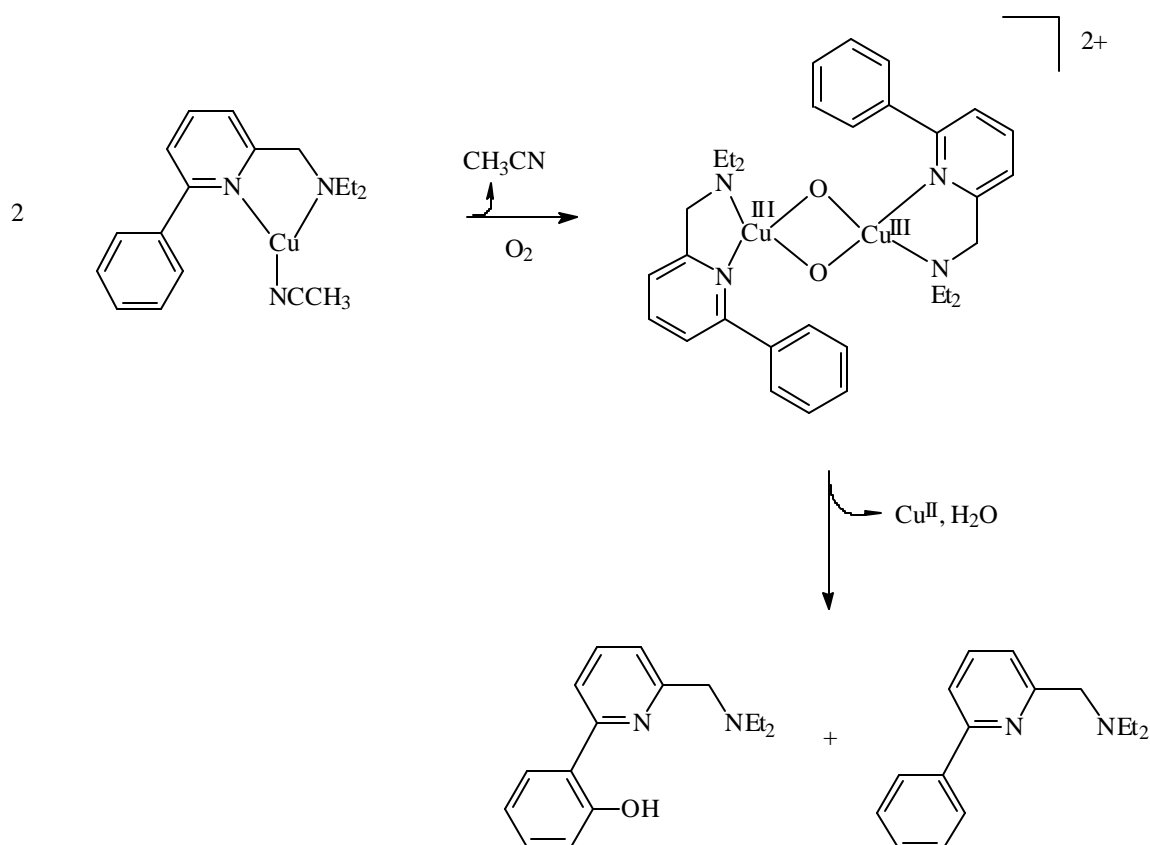
Cu^I complexes.^{35,38,52,81,82,83,84,85} None of them has been as exhaustively studied as Karlin's system, probably due to the fact that it is the cleaner example of this type of reactivity found in synthetic models so far. However, in all of them a close proximity of the peroxo core to the arene ring is demanded to achieve aromatic hydroxylation.

1.4.1.3 O-O bond breaks prior to the attack on the aromatic ring

A crucial question arised when the bis(μ -oxo) core was characterized⁷⁰ and specifically, when the interconversion equilibrium between μ - η^2 : η^2 -peroxo side-on and bis(μ -oxo) isomers was discovered:³⁷ was bis(μ -oxo) the active species responsible for the aromatic hydroxylation instead of side-on peroxo? Although the bis(μ -oxo) core has not been detected in proteins, an equilibrium displaced towards the peroxo side can not be excluded.^{64,65,86} Therefore, a small amount of bis(μ -oxo) could be the active form for hydroxylation without being actually detected neither by crystallography nor by spectroscopy in the natural systems. However, synthetic models have helped importantly in answering the question of whether the bis(μ -oxo) core itself is able to perform aromatic hydroxylation. Early studies with copper systems capable of O₂ activation to form bis(μ -oxo) intermediates did not perform aromatic hydroxylation but intermediate decomposition under N-dealkylation of the respective ligand was usually found.^{35,38} Actually, bis(μ -oxo) cores are typically active towards H atom abstraction rather than electrophilic attack.^{35,87,88} Experimental evidence for the fact that bis(μ -oxo)Cu₂^{III} cores are able to oxygenate an aromatic

substrate has recently been provided by Tolman and co-workers.⁸⁶ Cu^{I} complex with ligand 2-diethylamino-methyl-6-phenylpyridine react with O_2 in CH_3CN to generate a well-characterized bis(μ -oxo) intermediate at low temperatures. After warming the reaction solution hydroxylation of the aromatic ring contained within the ligand system occurs.

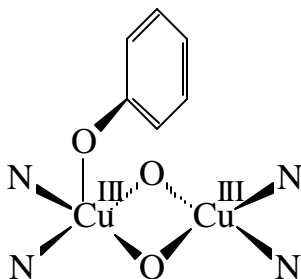
Figure 24. Reaction pathway for intramolecular ligand hydroxylation with the model system designed by Tolman.⁸⁶



The rate of hydroxylation and the relative amounts of hydroxylated versus non-hydroxylated ligand strongly depend on the substituents in the phenyl ring in a way that suggests an electrophilic substitution mechanism. The H

atom abstraction process can be excluded in this specific system as no KIE is found. The novel proposed active species in tyrosinase natural system would be the one depicted in the following figure.

Figure 25. Proposed active intermediate for hydroxylation reaction when O-O bond breaks prior to the attack on the aromatic ring.



1.4.1.4 The hydroxylating active species: $m-h^2:h^2$ -peroxo side-on versus bis(m -oxo)

As deduced from recently resolved X-Ray structure of a COase of sweet potato⁸⁹ and from phenolic substrate coordination in activated hemocyanins^{90,91} a coordination of the phenol to one of the two Cu centers (CuA) is envisioned as the first step of the reaction.⁷⁷ Substrate bonding geometry would agree with an electrophilic substitution by interaction of the HOMO of the arene ring and the LUMO of the side-on peroxo group. Although the most plausible mechanism seems to be the latter, some factors may turn to be counterproductive. For example, a primary coordination of the phenol to center CuA would mean a ligand-to-metal charge transfer, that in turn would diminish the nucleophilic character of the aromatic ring towards the

attack over the peroxo group. Moreover, upon coordination of the phenolic substrate the charge donation of peroxide to copper would decrease and peroxo group would become less electrophilic. Besides, it can not be ruled out the possibility of existence of small amounts of the other isomer, respectively, although not detected experimentally. Modeling exogenous substrate oxidations, only one bis(μ -oxo) Cu^{III}_2 complex among a large amount of related ligands (PDLs) has been demonstrate to be efficient in the oxidation of alcohols to aldehydes (>70% conversion), and reactivity is well correlated to Cu accessibility for proper coordination of exogenous substrate.⁹²

Therefore, the active species has not been completely defined so far. Apart from the unknown active site doubts, questions such as whether the phenolic substrate really binds to one Cu center of the Cu_2O_2 unit, and if it does, whether this is before, after or along with hydroxylation should be addressed in the future.

Radical mechanisms have also been considered and even proposed to be operative,^{6,93} so the most important conclusion that can be obtained from published work to date is that no clear mechanism can be yet determined for tyrosinase activity, and possible novel mechanisms will be proposed in the future to rationalize one of the most exciting topics in bioinorganic chemistry.

1.4.2 Intermolecular hydroxylation

Casella and coworkers have recently found the first system capable of both aromatic ortho-hydroxylation and catechol oxidation to quinones of exogenous substrates.⁸⁵ The reaction of complex $[\text{Cu}^{\text{I}}_2(\text{L-66})]^{2+}$ with O_2 at $-80\text{ }^\circ\text{C}$ yields

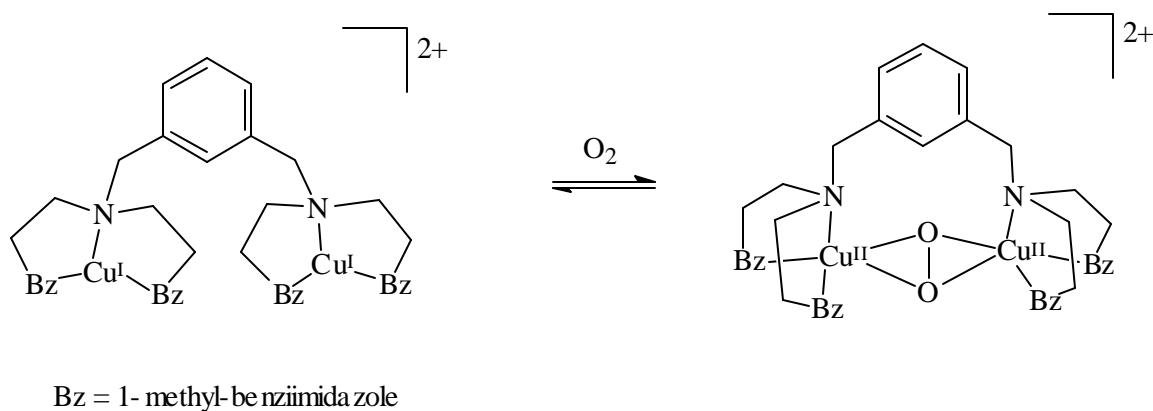
a $\mu\text{-}\eta^2\text{:}\eta^2\text{-peroxo}$ side-on $[\text{Cu}^{\text{II}}_2(\text{L-66})(\text{O}_2)]^{2+}$ complex. The oxygenation can be fully reversed upon application of vacuum (Figure 26).

Addition of sodium 4-carbomethoxyphenolate to a solution of $[\text{Cu}^{\text{II}}_2(\text{L-66})(\text{O}_2)]^{2+}$ in acetone at -60°C triggers the reaction to finally obtain the catechol product. Moreover, the oxidation of catechol to quinone is demonstrated by the reaction of the complex $[\text{Cu}^{\text{II}}_2(\text{L-66})(\text{O}_2)]^{2+}$ with 3,5-di-*tert*-butylcatechol at -60°C .

Complex $[\text{Cu}^{\text{I}}_2(\text{L-66})]^{2+}$ resembles Karlin's system $[\text{Cu}^{\text{I}}_2(\text{H-XYL})]^{2+}$, with the difference of two benzimidazole residues per copper atom instead of two pyridines. However, reactivity is completely different, as high unstability of the peroxo and fast intramolecular hydroxylation is observed in oxygenation of $[\text{Cu}^{\text{I}}_2(\text{H-XYL})]^{2+}$ (see section 1.4.1.2 and Figure 23).

The dinuclear $[\text{Cu}^{\text{I}}_2(\text{L-66})]^{2+}$ system has been called the first true tyrosinase model.

Figure 26. Reversible oxygenation of complex $[\text{Cu}^{\text{I}}_2(\text{L-66})]^{2+}$



1.5 C-H activation: a challenging target

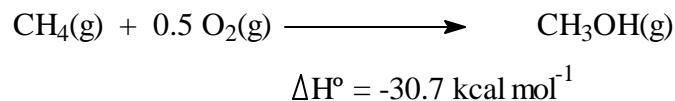
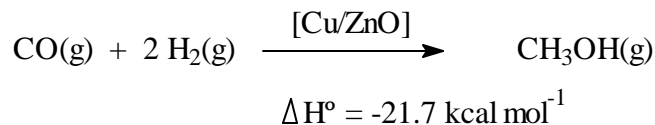
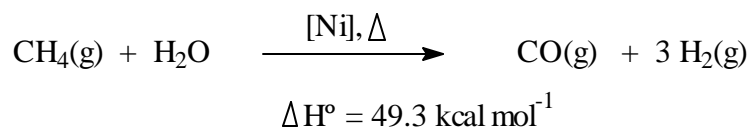
As exposed in the previous sections, tyrosinase reactivity is one of the natural models for functionalization of substrates, and for aromatic hydroxylation specifically. Chemical industry has been using expensive and environmental non-friendly procedures to functionalize hydrocarbons, and therefore, incorporation of synthetically designed catalysts is one of the major challenges to reduce costs and become an environmentally sustainable industry. A general overview to chemical processes to achieve C-H activation will be presented in the following sections.

1.5.1 Oxidation of alkanes

Although alkanes are the most abundant and least expensive hydrocarbon feedstocks available in earth, olefins are the general starting material in many commercial processes to produce commodity organic chemicals. Unfortunately, very few industrial methods exist for the selective conversion of alkanes to more valuable products. Furthermore, several desirable reactions using alkanes are not thermodynamically favorable at reasonable temperatures. For example, alkanes are used in the generation of synthesis gas "syngas" ($\text{CO} + \text{H}_2$) by the "steam reforming" of methane, which is in turn the primary component of natural gas. Syngas may be then used directly in industrial reactions such as hydroformylation of olefins, but it is often converted to methanol for use as fuel or as a chemical feedstock. However, the direct oxidation of methane represents a much more efficient pathway for methanol synthesis (Figure 27).⁹⁴

Attempts to selectively oxidize alkanes encounter two important problems. First, with respect to chemoselectivity, the initial product of alkane oxidation is often more reactive than the alkane itself; for example, the C-H bond in methanol is 11 kcal mol⁻¹ weaker than in methane (93 and 104 kcal mol⁻¹, respectively). Consequently, if methane oxidation involves the abstraction of a hydrogen atom, with a reaction rate usually governed by C-H bond strength, overoxidation of methanol (leading to CO₂ if completed) will dramatically reduce the desired product yield.⁹⁵ The second problem is regioselectivity of alkane oxidation: both radical and electrophilic reagents preferentially attack tertiary over primary and secondary C-H bonds (3° > 2° > 1°).^{96,97} However, the selectivity is not high and preferences usually are in the opposite direction, that is towards selective oxidation of primary C-H bonds.

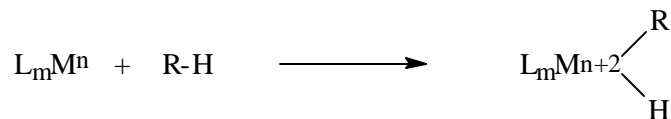
Figure 27. Syngas synthesis equation, and two routes for the obtention of methanol.



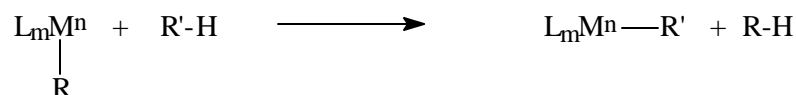
Recent work suggests that homogeneous organometallic systems can overcome some of these selectivity problems.^{96,97,98,99,100,101} Moreover, the large amount of examples of organometallic alkane oxidation (referring to the formation of a metal-carbon bond in the C-H activation step) suggest that a reversed regioselective pattern (i.e., $1^\circ > 2^\circ > 3^\circ$) can be attained. Furthermore, strong C-H bonds can be activated selectively in the presence of weaker C-H bonds (for example, aromatic C-H bonds are activated before benzylic C-H bonds in toluene).¹⁰² Several approaches to organometallic activation reactions are shown in Figure 28. Despite the success in this area, few systems are capable of subsequent substrate functionalization and regeneration of the metal fragment as required for a good catalytic turnover. In most cases the reactive metal species responsible for alkane activation is incompatible with oxidants required for catalysis (O_2 , H_2O_2).

Figure 28. Various pathways discovered for the activation of alkane C-H bonds (stoichiometry is specified in the reactions).

Oxidative addition



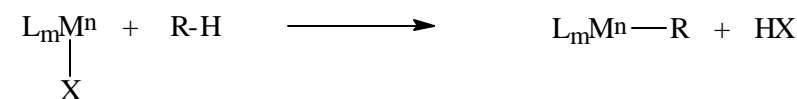
σ -bond metathesis



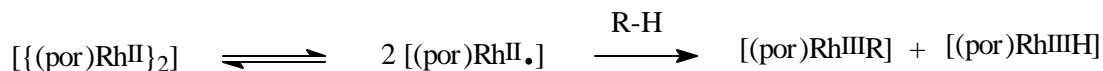
1,2-addition



electrophilic activation



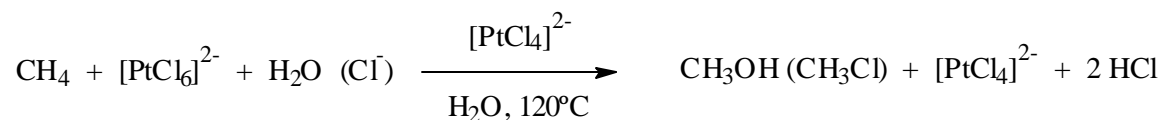
metalloradical activation



An important exception to this limitation is the reaction of alkanes with chloroplatinum salts in aqueous solution. Interestingly, this was one of the earliest examples of C-H activation: Shilov and co-workers observed the incorporation of deuterium into alkanes in solutions of $K_2[PtCl_4]$ in $D_2O/[D^1]$ acetic acid.¹⁰³ The same group reported in 1972 that addition of $H_2[PtCl_6]$ to the reaction mixture generated oxidized alkane products RCl and ROH (see

Equation 1).¹⁰⁴ Opposite to extremely air and moisture sensitivity in organometallic reagents shown in Figure 28, the platinum complexes are soluble in water and the reactions are unaffected by the presence of O₂, becoming a remarkably robust system.

Equation 1. Shilov's chloroplatinum system for the oxidation of methane to methanol.



The doubly solvated complex $[\text{PtCl}_2(\text{H}_2\text{O})_2]$ has been proposed to be the active catalytic species, and the observed selectivity patterns are parallel to other organometallic activation systems ($1^\circ > 2^\circ > 3^\circ$).⁹⁹

In recent years, several new alkane oxidations that utilize electrophilic late transition metals in strongly acidic media (CF₃COOH, H₂SO₄) have been discovered, and significant similarities to the platinum chemistry have been noticed. Periana and co-workers discovered the Hg^{II}-mediated system (as triflate, hydrogensulfate or trifluoroacetate salts), capable of catalytically oxidize CH₄ to CH₃OSO₃H in 43% yield in pure H₂SO₄ as solvent.¹⁰⁵ Similar reactivity was observed in trifluoromethanesulfonic and sulfuric acids in the presence of Tl^{III}, Au^I, Pd^{II} and Pt^{II}/Pt^{IV}, but no efficient catalysis was observed. In a recent report, a bipyrimidine Pt^{II} complex is used as the catalyst, obtaining the final CH₃OSO₃H product in a 70% yield.¹⁰⁶ Sen and co-workers reported a Pd^{II}-acetate mediated catalytic oxidation to CF₃CO₂CH₃ in trifluoroacetic

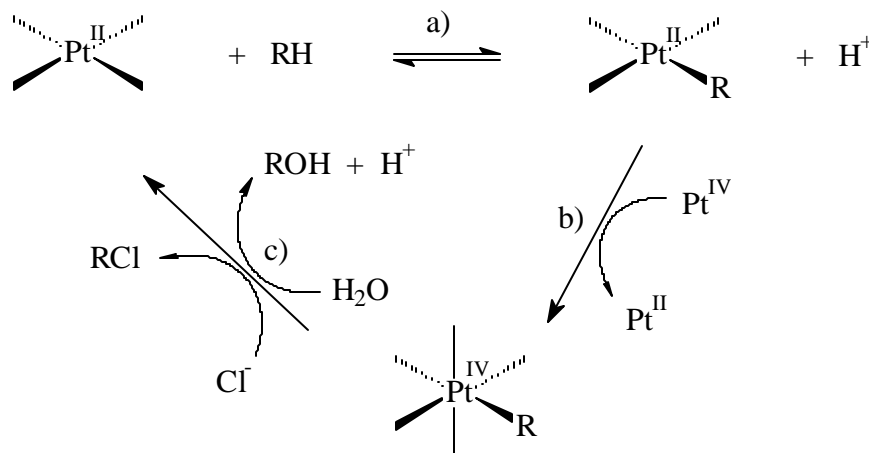
anhydride with H_2O_2 as stoichiometric oxidant.¹⁰⁷ The same group observed the selective oxidation of methane and other lower alkanes by O_2 , when employing 5% Pd/C and soluble Cu^{II} salts in a mixture of trifluoroacetic acid and water, obtaining methanol as the major product.^{108,109} Carbon monoxide was found necessary to be present in order to maintain selectivity in the reaction. Authors suggest that CO reduces O_2 to H_2O_2 , which then oxidizes alkanes in the presence of transition metals. The necessity of a coreductant in the reaction strongly resembles monooxygenase enzymes reactivity such as cytochrome P450, which require a reducing agent (NADH) to activate O_2 and then produce substrate oxidation.^{5,94}

Cobalt(III) ions in trifluoroacetic acid are also effective in the oxidation of methane to $\text{CF}_3\text{CO}_2\text{CH}_3$ at 180°C , and addition of O_2 increases the catalytic behavior of the reaction, suggesting reoxidation of Co^{II} by O_2 .¹¹⁰ Similarly, Rh^{III} salts also catalyze the methane oxidation in trifluoroacetic acid using H_2O_2 as the stoichiometric oxidant.¹¹¹

1.5.2 Mechanism of the Shilov Reaction

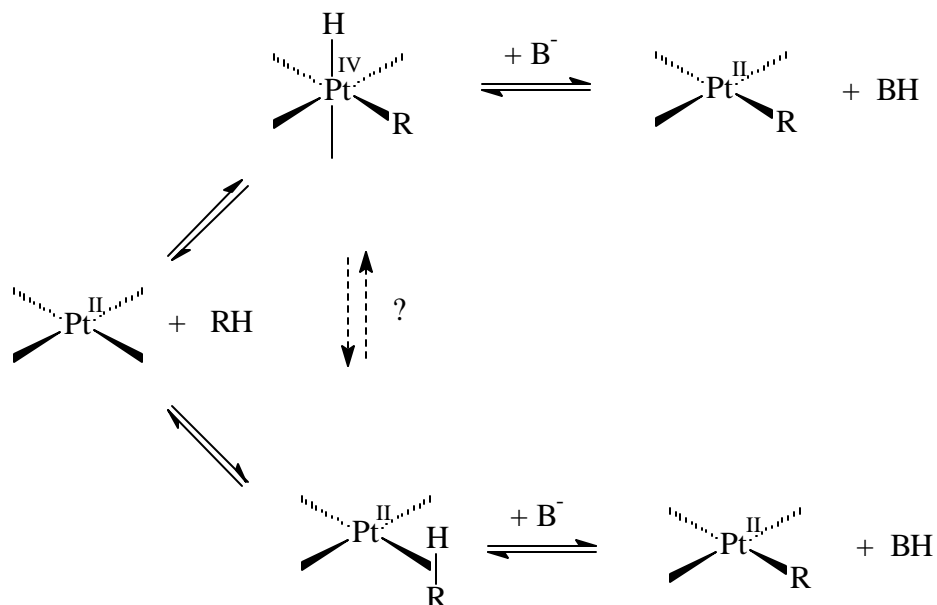
In 1983 Shilov proposed a mechanism for platinum catalyzed alkane oxidation consisting in three basic transformations (Figure 29):¹¹² a) activation of the alkane by Pt^{II} to generate an alkylplatinum(II) intermediate, b) two-electron oxidation of the latter intermediate to generate an alkylplatinum(IV) species, and c) reductive elimination of RX ($\text{X} = \text{Cl}$ or OH) to liberate the oxidized alkane and the Pt^{II} catalyst.

Figure 29. Proposed catalytic cycle for the platinum catalyzed oxidation of alkanes in aqueous solution.



The discussion of this mechanism has generated a large amount of studies where the most controversial and still unresolved step to date is the process involving the C-H activation of the alkane (step a). Nevertheless, this step often dictates both the rate and selectivity of the alkane oxidation. The major discussion about the C-H activation is whether it is via oxidative addition of the C-H bond at Pt^{II} yielding an alkyl(hydrido)platinum(IV) complex which is subsequently deprotonated, or on the contrary, via deprotonation of an intermediate Pt^{II}-alkane σ adduct (Figure 30).^{95,113}

Figure 30. Two possible pathways for alkane C-H activation by Pt^{II} : oxidative C-H addition and subsequent deprotonation of the Pt^{IV} hydride, or formation and subsequent deprotonation of an alkane σ adduct



Deposition of platinum metal and reaction conditions (>100 °C) preclude a detailed mechanistic study and detection of intermediates. Thus, theoretical studies have become a useful tool to understand experimental questions. However, calculations can not exclude any of the above mentioned mechanism, in spite of favoring a H atom transfer from a methane σ complex, first to a neighboring Cl ligand (best described as a σ bond metathesis) and then to solvent water.¹¹³

While oxidative addition of the C-H bond may be operative in the Pt^{II} -mediated reaction,¹¹⁴ this is not a viable pathway for many of the other systems. For example, it seems not reliable for Hg^{II} or Co^{III} because of unknown existence of $\text{M}^{\text{n}+2}$ species that would be formed as intermediates in an oxidative addition process.

The role of strongly acidic solvent appears to be crucial in these catalytic systems. Polarity of solvents or capability to alter alkane redox potentials are two parameters argued to be important, as well as esterification of alcohols produced in the reaction in order to deactivate them to prevent overoxidation.

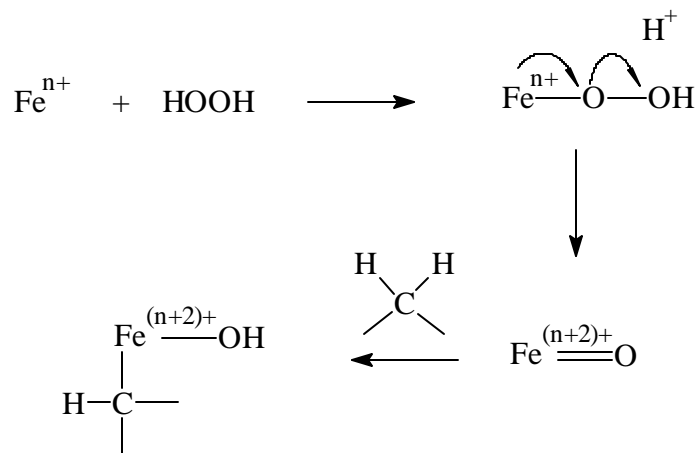
1.5.3 Gif systems: a Methano Monooxygenase (MMO) synthetic model

Methano monooxygenase is an iron containing enzyme that catalyzes the oxidation of methane to methanol under normal living conditions of temperature and pressure. Gif systems have been proposed to be synthetic models of MMO due to similarities in reactivity and structural coordination to the iron center.^{115,116} Therefore, detailed studies on this systems may proportionate mechanistic clues for the methane oxidation pathways in MMO.

With the former idea of imitating the reductive conditions existing on earth 3800 million years ago, Barton and co-workers dissolved metallic iron Fe^0 and H_2S in acetic acid, and added adamantane in air atmosphere. Surprisingly, adamantane was oxidized to the corresponding ketone with reasonable yields and selectively at the secondary carbon position. This was called the Gif(III) system.¹¹⁷ System modifications were applied over the years and modern Gif systems^{118,119} utilize Fe^{II} or Fe^{III} salts with either H_2O_2 or Fe^{II} /superoxide with picolinic acid as the ligand, in pyridine as solvent. Those systems are capable of alkane oxidation in 75% yield without destruction of the catalyst,¹²⁰ although none of them is sufficiently good for industrial applications.

As mentioned, Gif systems show a high selectivity for secondary in front tertiary carbons.¹²⁰ This selectivity along with the lack of KIE in the cyclohexane oxidation reaction do not favor a C-H bond activation pathway via hydrogen atom abstraction.^{121,122} Similar reactivity has been found if Cu^{I} salts are used, indicating the same C-H activation mechanism for Fe and Cu.¹²³ Mechanistic studies indicate the existence of two intermediates: one of them has been proved to be an alkylhydroperoxide^{124,125} or metalalkylperoxide,¹²⁶ depending on the presence of pycolinic acid acting as ligand, but the nature of the other intermediate remains unclear. Barton et al. postulates the formation of an organometallic Fe-C species (see Figure 31).^{119,124,127}

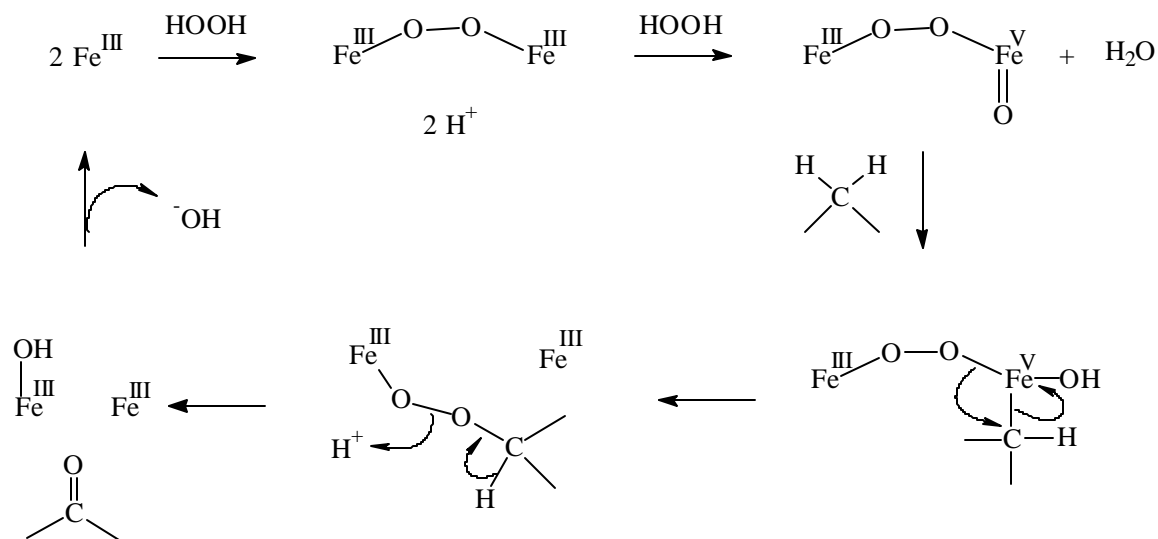
Figure 31. Postulated alkane C-H activation pathway in Gif systems using indistinctively Fe^{II} or Fe^{III} .



The reactivity of $\text{Fe}^{\text{IV}}-\text{CHR}_2$ species is thought to proceed through homolysis to yield Fe^{III} and the carbon centered radical $\cdot\text{CHR}_2$. In presence of $\text{Fe}^{\text{III}}-\text{Cl}$, the radical can be trapped to give the corresponding alkylchloride ClCHR_2 . On

the contrary, the organometallic intermediate species formed in the $\text{Fe}^{\text{III}}\text{-Fe}^{\text{V}}$ mechanism do not homolytically break to give Fe^{IV} and a carbon centered radical. The chemistry shown has been probed to be non-radicalary and the mechanism proposed to be operative with the presence of picolinic acid is depicted in Figure 32.

Figure 32. Alkane ketonization mechanism in $\text{Fe}^{\text{III}}/\text{Fe}^{\text{V}}$ Gif systems (picolinic acid present)

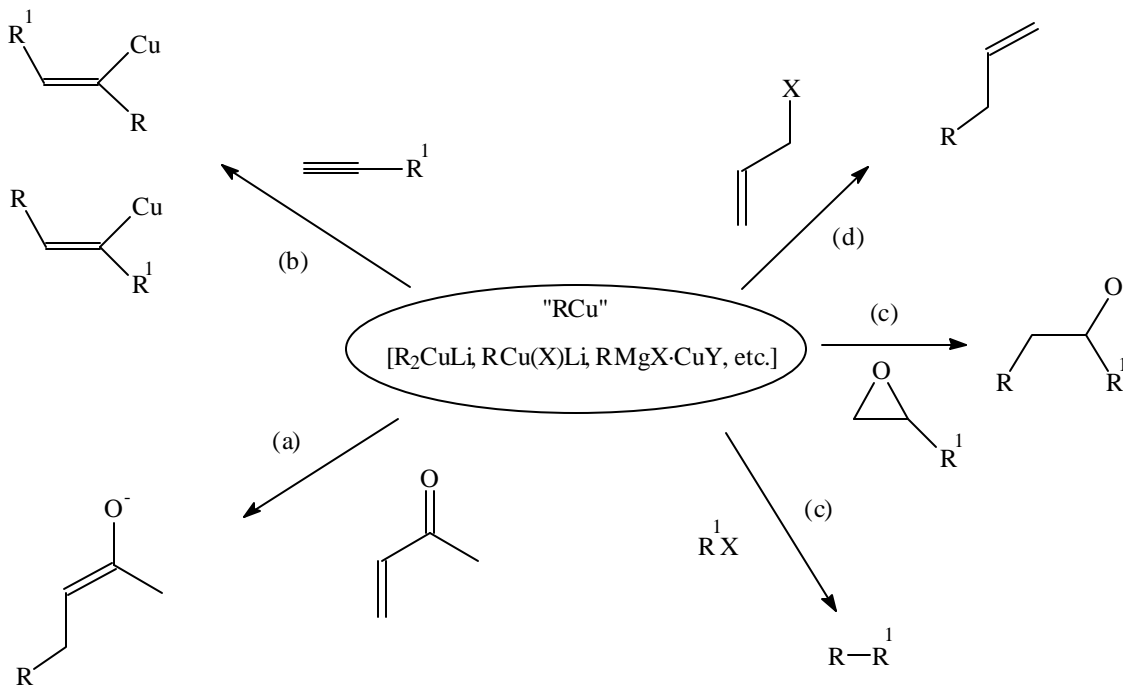


The presence of carboxylic acids with a N atom in the α position, such as picolinic acid, is essential to perform alkane oxidation.¹²⁰ NMR studies have concluded that each Fe^{III} center bears two picolinic acid ligand,¹¹⁸ and recent reports demonstrated that pyridinic solvents are necessary (systems where acetonitrile as solvent is used do not show Gif chemistry).¹²⁸ The rate limiting step for the latter reaction appears to be after the formation of the organometallic Fe-C bond.

1.5.4 Organocopper species

The most important utility of copper in organic chemistry is in the form of nucleophilic organocopper(I) reagents (R_2CuM) for the delivery of hard carbanions to electrophilic carbon centers.¹²⁹ Conjugate additions (a),¹³⁰ carbocupration (b),¹³¹ alkylation (c)¹³² and allylation (d)¹³³ represent the reactions that can be achieved readily with organocuprate reagents but not with other transition metal organometallic complexes (Figure 33).

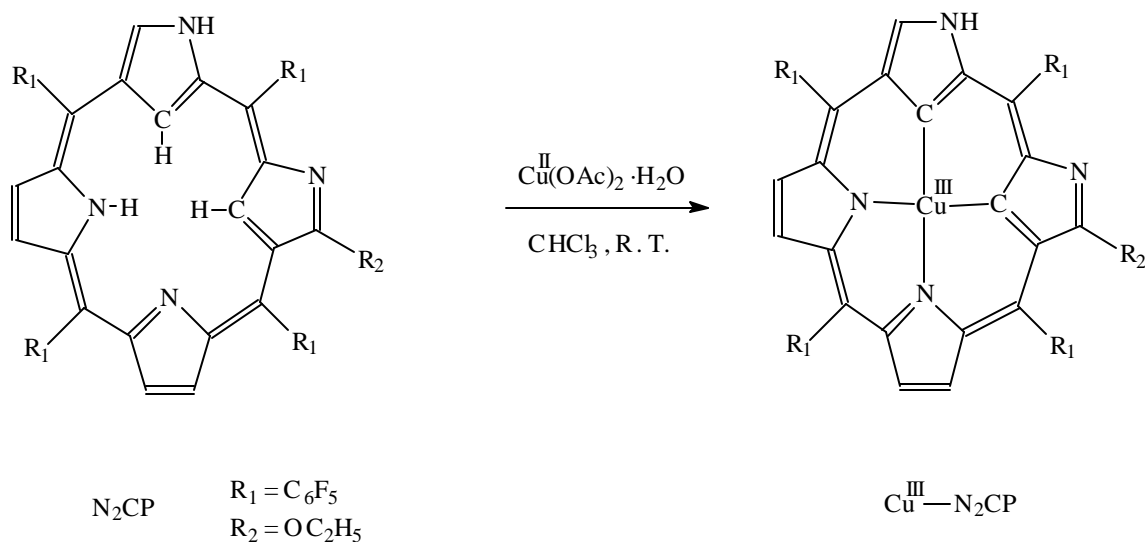
Figure 33. Nucleophilic reactivities of organocopper(I) reagents RCu ($R = sp^2, sp^3$ carbon anionic centers; $X, Y =$ halogens, etc.).



However, mechanistic information about these reactions has not been addressed until recent theoretical reports from Nakamura, Morokuma and co-workers were published,¹³⁴ more than 50 years after Kharasch and co-workers reported the first organocuprate species.¹³⁵ In all proposed mechanisms, organocopper(III) R_3Cu^{III} species have been postulated to exist as intermediates,¹²⁹ although no example was exhaustively characterized until crystal structures were reported in the late 1980s (three complexes bearing CF_3^- groups in order to stabilize the high oxidation state - Cu^{III-}).¹³⁶

There are now four crystal structures of discrete organocopper(III) species. The most interesting one is the complex reported by Furuta and co-workers in the year 2000,¹³⁷ consisting in a doubly N-confused Porphyrin (NCP) ligand capable of stabilize a Cu^{III} center (see Figure 34).

Figure 34. Synthesis of the doubly N-confused porphyrin Cu^{III} complex.



The most striking point of this complex is the synthesis itself. Cu^{II} salts were mixed with the corresponding NCP ligand in CHCl_3 at room temperature overnight and the organocopper(III) complex was obtained as final product. No mechanistic details are proposed in Furuta's work so far, but oxidation of Cu^{II} to Cu^{III} and C-H bond activation are two processes that deserve to be explained. Similar reactivity is observed when Ag^{I} is used (obtaining an organosilver(III) complex),¹³⁷ as well as Ni^{II} (obtaining organonickel(III) species).¹³⁸ Chmielewski and co-workers reported a similar C-H activation with NCP using Cu^{II} salts and obtaining organocopper(II) final species,¹³⁹ although the first organometallic Cu^{II} crystal structure has been published this year (2001) by Furuta's group.¹⁴⁰

C-H bond cleavage performed by a variety of metals with NCP ligands under mild conditions opens the scope of C-H activation studies and may lead to design of new catalyst capable of C-H bond activation in the future. Moreover, unexplored reactivity of these new carbon pre-activated organocopper(III) species may guide to new reaction pathways for hydrocarbon functionalization.

1.5.5 Cu^{III} complexes

Oxidative potential of Cu^{III} species has been considered in monooxygenase activity, and bis(μ -oxo) Cu^{III} intermediates have been proposed to be the active species in aromatic hydroxylation performed by tyrosinase. Same intermediates can undergo aliphatic hydroxylation as shown by Tolman and co-workers.⁸⁸ However, scarce studies have been done on exploring the oxidative potential of other more stable non-oxygen containing Cu^{III} complexes. Mayer and co-workers used

two well established Cu^{III} complexes to show their capability of oxidizing C-H in dihydroanthracene to anthracene (complex $[\text{Cu}^{\text{III}}(\text{Pre})]^+$), and 2,4-di-*t*-butylphenol to the corresponding coupling product (complex $[\text{Cu}^{\text{III}}(\text{H-}_3\text{Aib}_3)]$), both reactions at room temperature.¹⁴¹

1.6 REFERENCES

- ¹ W. Kaim, J. Rall, *Angew. Chem. Int. Ed. Engl.* **1996**, *35*, 43-60
- ² S. J. Lippard, J. M. Berg, *Principles of Bioinorganic Chemistry*, University Science Books, Mill Valley, **1994**
- ³ E. I. Solomon, M. J. Baldwin, M. D. Lowery, *Chem Rev.* **1992**, *92*, 521
- ⁴ R. H. Holm, P. Kennepohl, E. I. Solomon, *Chem. Rev.* **1996**, *96*, 2239-2314.
- ⁵ A. L. Lehninger, *Principles of Biochemistry*, Worth Publishers, Inc., NY, **1982**
- ⁶ N. Kitajima, Y. Moro-oka, *Chem. Rev.* **1994**, *94*, 737-757
- ⁷ N. Kitajima, T. Koda, Y. Iwata, Y. Moro-oka, *J. Am. Chem. Soc.* **1990**, *112*, 8833-8839
- ⁸ K. A. Magnus, H. Ton-That, J. E. Carpenter, *Chem. Rev.* **1994**, *94*, 727
- ⁹ D. E. Wilcox, A. G. Porras, Y. T. Hwang, K. Lerch, M. E. Winkler, E. I. Solomon, *J. Am. Chem. Soc.* **1985**, *107*, 4015
- ¹⁰ L. C. Stewart, J. P. Klinman, *Ann. Rev. Biochem.* **1988**, *57*, 551
- ¹¹ B. A. Averill, *Chem. Rev.* **1996**, *96*, 2951-2964
- ¹² J. P. Klinman, *Chem. Rev.* **1996**, *96*, 2541-2561
- ¹³ N. N. Greenwood, A. Eanrshaw, *Chemistry of the Elements*, Pergamon Press, Oxford, **1986**
- ¹⁴ V. Massey, *J. Biol. Chem.* **1994**, *269*, 2459
- ¹⁵ J. A. Guckert, M. D. Lowery, E. I. Solomon, *J. Am. Chem. Soc.* **1995**, *117*, 2817
- ¹⁶ K. M. Merz, R. Hoffmann, *Inorg. Chem.* **1988**, *27*, 2120
- ¹⁷ A. Messerschmidt, H. Luecke, R. Huber, *J. Mol. Biol.* **1993**, *230*, 997
- ¹⁸ A. Volbeda, W. G. J. Hol, *J. Mol. Biol.* **1989**, *209*, 249-279

- ¹⁹ R. S. Himmelwright, N. C. Eickman, C. D. LuBein, E. I. Solomon, *J. Am. Chem. Soc.* **1980**, *102*, 5378
- ²⁰ N. Kitajima, T. Koda, S. Hashimoto, T. Kitagawa, Y. Moro-oka, *J. Chem. Soc., Chem. Commun.* **1988**, 151
- ²¹ N. Kitajima, K. Fujisawa, Y. Moro-oka, K. Toriumi, *J. Am. Chem. Soc.* **1989**, *111*, 8975
- ²² N. Kitajima, T. Koda, Y. Iwata, Y. Moro-oka, *J. Am. Chem. Soc.* **1990**, *112*, 8833-8839
- ²³ K. A. Magnus, H. Ton-That, J. E. Carpenter, *Bioinorganic Chemistry of Copper*; K. D. Karlin, Z. Tyeklar, Eds.; Chapman & Hall: New York, 1993; p 143
- ²⁴ B. Hazes, K. A. Magnus, C. Bonaventura, J. Bonaventura, Z. Dauter, K. H. Kalk, W. G. J. Hol, *J. Protein Sci.* **1993**, *2*, 597
- ²⁵ N. Kitajima, K. Fujisawa, C. Fujimoto, Y. Moro-oka, S. Hashimoto, T. Kitagawa, K. Toriumi, K. Tatsumi, A. Nakamura, *J. Am. Chem. Soc.* **1992**, *114*, 1277-1291
- ²⁶ *Copper Proteins and Copper Enzymes*, R. Lontie, Eds., CRC Press, Boca Raton, FL, **1984**, Vol. 1-3
- ²⁷ E. I. Solomon, U. M. Sundaram, T. E. Machonkin, *Chem. Rev.* **1996**, *96*, 2563
- ²⁸ E. I. Solomon, M. D. Lowery, *Science* **1993**, *259*, 1575
- ²⁹ K. D. Karlin, S. Kaderli, A. D. Zuberbühler, *Acc. Chem. Res.* **1997**, *30*, 139-147
- ³⁰ V. Mahadevan, J. L. DuBois, B. Hedman, K. O. Hodgson, T. P. D. Stack, *J. Am. Chem. Soc.*, **1999**, *121*, 5583-5584
- ³¹ R. W. Cruse, S. Kaderli, K. D. Karlin, A. D. Zuberbühler, *J. Am. Chem. Soc.* **1988**, *110*, 6882
- ³² K. D. Karlin, M. S. Nasir, B. I. Cohen, R. W. Cruse, S. Kaderli, A. D. Zuberbühler, *J. Am. Chem. Soc.* **1994**, *116*, 1324

- ³³ L. Casella, E. Monzani, M. Gullotti, D. Caravagnoni, G. Cerina, L. Santagostini, R. Ugo, *Inorg. Chem.* **1996**, *35*, 7516
- ³⁴ R. Menif, A. E. Martell, P. J. Squattrito, A. Clearfield, *Inorg. Chem.* **1991**, *29*, 4723
- ³⁵ S. Mahapatra, S. Kaderli, A. Llobet, Y. M. Neuhold, T. Palanché, J. A. Halfen, V. G. Young, Jr., T. A. Kaden, L. Que, Jr., A. D. Zuberbühler, W. B. Tolman, *Inorg. Chem.* **1997**, *36*, 6343-6356
- ³⁶ E. Pidcock, H. V. Obias, C. X. Zhang, K. D. Karlin, E. I. Solomon, *J. Am. Chem. Soc.* **1998**, *120*, 7841-7847
- ³⁷ J. A. Halfen, S. Mahapatra, E. C. Wilkinson, S. Kaderli, V. G. Young, Jr., L. Que, Jr., A. D. Zuberbühler, W. B. Tolman, *Science* **1996**, *271*, 1397-1400
- ³⁸ W. B. Tolman, *Acc. Chem. Res.* **1997**, *30*, 227-237
- ³⁹ Z. Teyklár, R. R. Jacobson, N. Wei, N. N. Murthy, J. Zubieta, K. D. Karlin, *J. Am. Chem. Soc.* **1993**, *115*, 2677-2689
- ⁴⁰ B. Jung, K. D. Karlin, A. D. Zuberbühler, *J. Am. Chem. Soc.* **1996**, *118*, 3763-3764
- ⁴¹ A. P. Cole, D. E. Root, P. Mukherjee, E. I. Solomon, T. P. D. Stack, *Science* **1996**, *276*, 1848
- ⁴² K. D. Karlin, Y. Gultneh, *J. Chem. Educ.* **1985**, *62*, 983-990
- ⁴³ S. Mahapatra, J. A. Halfen, E. C. Wilkinson, G. Pan, X. Wang, V. G. Young, Jr., C. J. Cramer, L. Que, Jr., W. B. Tolman, *J. Am. Chem. Soc.* **1996**, *118*, 11555-11574
- ⁴⁴ K. D. Karlin, N. Wei, B. Jung, S. Kaderli, P. Niklaus, A. D. Zuberbühler, *J. Am. Chem. Soc.* **1993**, *115*, 9506
- ⁴⁵ M. Costas, *Doctoral Thesis*, University of Girona, February **1999**
- ⁴⁶ The work presented in this thesis

- ⁴⁷ *Free Radicals*, J. K. Kochi, Eds.; John Wiley & Sons: New York, 1973
- ⁴⁸ L. L. Ingraham, D. L. Meyer, *Biochemistry of Dioxigen*, Plenum Press, New York, 1985
- ⁴⁹ R. A. Sheldon, J. K. Kock, *Metal-Catalyzed oxidation of Organic Compounds*, Academic Press, New York, **1981**
- ⁵⁰ E. C. Niederhoffer, J. H. Timmons, A. E. Martell, *Chem. Rev.* **1984**, *84*, 137-203
- ⁵¹ K. Fujisawa, M. Tanaka, Y. Moro-oka, N. Kitajima, *J. Am. Chem. Soc.* **1994**, *116*, 12079-12080
- ⁵² S. Mahapatra, V. G. Young, Jr., S. Kaderli, A. D. Zuberbühler, W. B. Tolman, *Angew. Chem., Int. Ed. Engl.* **1997**, *36*, 130-133
- ⁵³ M. Harata, K. Jitsukawa, H. Masuda, H. Einaga, *J. Am. Chem. Soc.* **1994**, *116*, 10817-10818
- ⁵⁴ L. M. Berreau, S. Mahapatra, J. A. Halfen, V. G. Young, Jr., W. B. Tolman, *Inorg. Chem.* **1996**, *35*, 6339-6342
- ⁵⁵ D. H. Lee, N. Wei, N. N. Murthy, Z. Teyklár, K. D. Karlin, S. Kaderli, B. Jung, A. D. Zuberbühler, *J. Am. Chem. Soc.* **1995**, *117*, 12498
- ⁵⁶ C. He, J. L. DuBois, B. Hedman, K. O. Hodgson, S. J. Lippard, *Angew. Chem. Int. Ed.* **2001**, *40*, 1484-1487.
- ⁵⁷ B. J. Wallar, J. D. Lipscomb, *Chem. Rev.* **1996**, *96*, 2625-2657.
- ⁵⁸ J. E. Bol, W. L. Driessen, R. Y. N. Ho, B. Maase, L. Que, Jr., J. Reedijk, *Angew. Chem. Int. Ed. Engl.* **1997**, *36*, 998
- ⁵⁹ K. D. Karlin, R. W. Cruse, Y. Gultneh, A. Farooq, J. Hayes, J. Zubieta, *J. Am. Chem. Soc.* **1987**, *109*, 2668
- ⁶⁰ T. N. Sorrell, V. A. Vankai, *Inorg. Chem.* **1990**, *29*, 1687
- ⁶¹ S. Mahapatra, J. A. Halfen, E. C. Wilkinson, L. Que, Jr., W. B. Tolman, *J. Am. Chem. Soc.* **1994**, *116*, 9785-9786

- ⁶² L. Sanyal, M. Mahroof-Tahir, M. S. Nasir, P. Ghosh, B. I. Cohen, Y. Gultneh, R. W. Cruse, A. Farooq, K. D. Karlin, J. Zubieta, *Inorg. Chem.* **1992**, *31*, 4322
- ⁶³ H. V. Obias, Y. Lin, N. N. Murthy, E. Pidcock, E. I. Solomon, M. Ralle, N. J. Blackburn, Y. M. Neuhold, A. D. Zuberbühler, K. D. Karlin, *J. Am. Chem. Soc.* **1998**, *120*, 12960-12961
- ⁶⁴ E. Pidcock, S. DeBeer, H. V. Obias, B. Hedman, K. O. Hodgson, K. D. Karlin, E. I. Solomon, *J. Am. Chem. Soc.* **1999**, *121*, 1870-1878
- ⁶⁵ E. Pidcock, H. V. Obias, C. X. Zhang, K. D. Karlin, E. I. Solomon, *J. Am. Chem. Soc.* **1998**, *120*, 7841-7847
- ⁶⁶ K. D. Karlin, Z. Tyeklár, A. D. Zuberbühler, *Bioinorganic Catalysis*; J. Reedijk, Ed.; Marcel Dekker, Inc.; New York, 1993; pp 261-315
- ⁶⁷ M. Kodera, K. Katayama, Y. Tachi, K. Kano, S. Hirota, S. Fujinami, M. Suzuki, *J. Am. Chem. Soc.* **1999**, *121*, 11006-11007.
- ⁶⁸ K. D. Karlin, Z. Tyeklár, A. Farooq, M. S. Haka, P. Ghosh, R. W. Cruse, Y. Gultneh, J. C. Hayes, P. J. Toscano, *Inorg. Chem.* **1992**, *31*, 1436.
- ⁶⁹ E. Pidcock, H. V. Obias, M. Abe, H. C. Liang, K. D. Karlin, E. I. Solomon, *J. Am. Chem. Soc.* **1999**, *121*, 1299.
- ⁷⁰ S. Mahapatra, J. A. Halfen, E. C. Wilkinson, G. Pan, C. J. Cramer, L. Que, Jr., W. B. Tolman, *J. Am. Chem. Soc.* **1995**, *117*, 8865-8866
- ⁷¹ Y. Dong, H. Fujii, M. P. Hendrich, R. A. Leising, G. Pan, C. R. Randall, E. C. Wilkinson, Y. Zang, L. Que, Jr., B. G. Fox, K. Kauffmann, E. Münck, *J. Am. Chem. Soc.* **1995**, *117*, 2778-2792
- ⁷² L. Shu, J. C. Nesheim, K. Kauffmann, E. Münck, J. D. Lipscomb, L. Que, Jr., *Science* **1997**, *275*, 515-518

- ⁷³ V. Mahadevan, M. J. Henson, E. I. Solomon, T. D. P. Stack, *J. Am. Chem. Soc.* **2000**, *122*, 10249-10250
- ⁷⁴ V. Mahadevan, Z. Hou, A. P. Cole, D. E. Root, T. K. Lal, E. I. Solomon, T. D. P. Stack, *J. Am. Chem. Soc.* **1997**, *119*, 11996-11997
- ⁷⁵ D. E. Root, M. J. Henson, T. Machonkin, P. Mukherjee, T. D. P. Stack, E. I. Solomon, *J. Am. Chem. Soc.* **1998**, *120*, 4982-4990.
- ⁷⁶ P. L. Holland, W. B. Tolman, *Coord. Chem. Rev.* **1999**, *190-192*, 855-859.
- ⁷⁷ H. Decker, R. Dillinger, F. Tuczek, *Angew. Chem. Int. Ed.* **2000**, *39*, 1591-1595.
- ⁷⁸ E. I. Solomon, F. Tuczek, D. E. Root, C. A. Brown, *Chem. Rev.* **1994**, *94*, 827-856.
- ⁷⁹ P. K. Ross, E. I. Solomon, *J. Am. Chem. Soc.* **1991**, *113*, 3246-3259.
- ⁸⁰ M. Suzuki, H. Furutachi, H. Okawa, *Coord. Chem. Rev.* **2000**, *200-202*, 105-129.
- ⁸¹ S. Ryan, H. Adams, D. E. Fenton, M. Becker, S. Schindler, *Inorg. Chem.* **1998**, *37*, 2134-2140
- ⁸² D. Ghosh, R. Mukherjee, *Inorg. Chem.* **1998**, *37*, 6597-6605
- ⁸³ A. Llobet, A. E. Martell, M. A. Martínez, *J. Mol. Catal. A* **129** **1998**, 19-26
- ⁸⁴ G. Alzuet, L. Casella, M. L. Villa, O. Carugo, M. Gullotti, *J. Chem. Soc., Dalton Trans.* **1997**, 4789-4794
- ⁸⁵ L. Santagostini, M. Gullotti, E. Monzani, L. Casella, R. Dillinger, F. Tuczek, *Chem. Eur. J.* **2000**, *6*, 519-522
- ⁸⁶ P. L. Holland, K. R. Rodgers, W. B. Tolman, *Angew. Chem. Int. Ed.* **1999**, *38*, 1139-1142.
- ⁸⁷ I. Blain, M. Giorgi, I. D. Riggi, M. Réglie, *Eur. J. Inorg. Chem.* **2001**, 205-211.

- ⁸⁸ S. Itoh, M. Taki, H. Nakao, P. Holland, W. B. Tolman, L. Que, Jr., S. Fukuzumi, *Angew. Chem. Int. Ed.* **2000**, *39*, 398-400.
- ⁸⁹ T. Klabunde, C. Eicken, J. C. Sacchettini, B. Krebs, *Nat. Struct. Biol.* **1998**, *5*, 1084-1090.
- ⁹⁰ H. Decker, T. Rimke, *J. Biol. Chem.* **1998**, *273*, 25889-25892.
- ⁹¹ B. Salvato, M. Santamaria, M. Beltramini, G. Alzuet, L. Casella, *Biochemistry* **1998**, *37*, 14065-14077.
- ⁹² V. Mahadevan, R.J.M..K. Gebbink, T. D.P. Stack, *Curr. Opin. Chem. Bio.* **2000**, 228-234.
- ⁹³ T. Lind, P. E. M. Siegbahn, R. H. Crabtree, *J. Phys. Chem B* **1999**, *103*, 1193-1202.
- ⁹⁴ S. S. Stahl, J. A. Labinger, J. E. Bercaw, *Angew. Chem. Int. Ed.* **1998**, *37*, 2180-2192.
- ⁹⁵ R. H. Crabtree, *Chem. Rev.* **1995**, *95*, 987-1007.
- ⁹⁶ *Activation and Functionalization of Alkanes* (Eds.: C. L. Hill), Wiley, New York, **1989**.
- ⁹⁷ *Selective Hydrocarbon Activation* (Eds.: J. A. Davies, P. L. Watson, J. F. Liebman, A. Greenberg), VCH, New York, **1990**.
- ⁹⁸ B. A. Andertsen, R. G. Bergman, T. A. Mobley, T. H. Peterson, *Acc. Chem. Res.* **1995**, *28*, 154-162.
- ⁹⁹ A. E. Shilov, *Activation of Saturated Hydrocarbons by Transition Metal Complexes*, Riedel, Dordrecht, **1984**.
- ¹⁰⁰ J. A. Labinger, *Fuel Process. Technol.* **1995**, *42*, 325-338.
- ¹⁰¹ A. E. Shilov, G. B. Shul'pin, *Chem. Rev.* **1997**, *97*, 2879-2932.
- ¹⁰² J. M. Buchanan, J. M. Stryker, R. G. Bergman, *J. Am. Chem Soc.* **1986**, *108*, 1537-1550.

- ¹⁰³ N. F. Gol'dshleger, M. B. Tyabin, A. E. Shilov, A. A. Shteinman, *Zh. Fiz. Khim. (Engl. Transl.)* **1969**, 43, 1222-1223.
- ¹⁰⁴ N. F. Gol'dshleger, V. V. Es'kovba, A. E. Shilov, A. A. Shteinman, *Zh. Fiz. Khim. (Engl. Transl.)* **1972**, 46, 785-786.
- ¹⁰⁵ R. A. Periana, D. J. Taube, E. R. Evitt, D. G. Liffler, P. R. Wentrcek, G. Voss, T. Masuda, *Science* **1993**, 259, 340-343.
- ¹⁰⁶ R. A. Periana, D. J. Taube, S. Gamble, H. Taube, T. Satoh, H. Fujii, *Science* **1998**, 280, 560-564.
- ¹⁰⁷ L.-C. Kao, A. C. Hutson, A. Sen, *J. Am. Chem. Soc.* **1991**, 113, 700-701.
- ¹⁰⁸ M. Lin, A. Sen, *J. Am. Chem. Soc.* **1992**, 114, 7307-7308.
- ¹⁰⁹ M. Lin, T. Hogan, A. Sen, *J. Am. Chem. Soc.* **1997**, 119, 6048-6053.
- ¹¹⁰ M. N. Vargaftik, I. P. Stolarov, I. I. Moiseev, *J. Chem. Soc., Chem. Commun.* **1990**, 1049-1050.
- ¹¹¹ S. Nomura, S. Uemura, *J. Chem. Soc., Chem. Commun.* **1994**, 129-130.
- ¹¹² L. A. Kushch, V. V. Lavrushko, Y. S. Misharin, A. P. Moravsky, A. E. Shilov, *Nouv. J. Chim.* **1983**, 7, 729-733.
- ¹¹³ P. E. M. Siegbahn, R. H. Crabtree, *J. Am. Chem. Soc.* **1996**, 118, 4442-4450.
- ¹¹⁴ L. Johansson, M. Tilset, J. A. Labinger, J. E. Bercaw, *J. Am. Chem. Soc.* **2000**, 122, 10846-10855.
- ¹¹⁵ D. H. R. Barton, A. H. Beck, D. K. Taylor, *Tetrahedron*, **1995**, 51, 5245-5254.
- ¹¹⁶ D. H. R. Barton, E. Cshuhai, E. Doller, N. Ozbalik, G. Balavoire, *Proc. Natl. Acad. Sci. USA* **1990**, 87, 3401-3404.
- ¹¹⁷ D. H. R. Barton, M. J. Gastiger, W. B. Motherwell, *J. Chem. Soc., Chem. Commun.* **1983**, 41-43.

- ¹¹⁸ D. H. R. Barton, B. Hu, R. U. RojasWahl, D. Taylor, *New J. Chem.* **1996**, *20*, 121-124.
- ¹¹⁹ D. H. R. Barton, D. Taylor, *Pure & Appl. Chem.* **1996**, *68*, 497-504.
- ¹²⁰ D. H. R. Barton, B. Hu, R. U. RojasWahl, D. Taylor, *J. Chem. Soc., Perkin Trans. II* **1996**, 1031-1041.
- ¹²¹ D. H. R. Barton, D. Doller, Y. V. Gelletti, *Tetrahedron Lett.* **1991**, *32*, 3811-3814.
- ¹²² D. H. R. Barton, J. Boivin, M. Gastiger, J. Morzycki, R. S. Hay-Motherwell, W. B. Motherwell, N. Ozbalik, K. M. Schwartzentruber, *J. Chem. Soc., Perkin Trans. II* **1986**, 947-955.
- ¹²³ D. H. R. Barton, S. D. Bévière, W. Chavasiri, E. Csuhai, D. Doller, *Tetrahedron*, **1992**, *48*, 2895-2910.
- ¹²⁴ a) D. H. R. Barton, D. Doller, *Acc. Chem. Res.* **1992**, *25*, 504-512; b) D. H. R. Barton, S. D. Bévière, W. Chavasiri, E. Csuhai, D. Doller, W. -W. Liu, *J. Am. Chem. Soc.* **1992**, *114*, 2147-2156.
- ¹²⁵ D. H. R. Barton, E. Csuhai, D. Doller, G. Balavoine, *J. Chem. Soc., Chem. Commun.* **1990**, 1787-1789.
- ¹²⁶ D. H. R. Barton, S. D. Bévière, D. Doller, *Tetrahedron Lett.* **1991**, *32*, 4671-4674.
- ¹²⁷ D. H. R. Barton, F. Halley, N Ozbalik, M. Schmitt, E. Young, G. Balavoine, *J. Am. Chem. Soc.* **1989**, *111*, 7144-7149.
- ¹²⁸ D. H. R. Barton, B. Hu, T. Li, J. MacKinnon, *Tetrahedron Lett.* **1996**, *37*, 8329.
- ¹²⁹ E. Nakamura, S. Mori, *Angew. Chem. Int. Ed.* **2000**, *39*, 3750-3771.
- ¹³⁰ P. Perlmutter, *Conjugate Addition Reactions in Organic Synthesis*, Pergamon, Oxford, **1992**.
- ¹³¹ J. F. Normant, *Synthesis* **1981**, 841-870.

- ¹³² J. M. Klunder, H. H. Posner in *Comprehensive Organic Synthesis, Vol 3* (Eds.: B. M. Trost, I. Fleming), Pergamon, Oxford, **1991**, 207-239.
- ¹³³ J. A. Marshall, *Chem. Rev.* **1989**, *89*, 1503-1511.
- ¹³⁴ a) E. Nakamura, S. Mori, M. Nakamura, K. Morokuma, *J. Am. Chem. Soc.* **1997**, *119*, 4887-4899; b) S. Mori, E. Nakamura, K. Morokuma, *J. Am. Chem. Soc.* **2000**, *122*, 7294-7307; c) E. Nakamura, M. Yamanaka, S. Mori, *J. Am. Chem. Soc.* **2000**, *122*, 1826-1827.
- ¹³⁵ M. S. Karasch, P. O. Tawney, *J. Am. Chem. Soc.* **1941**, *63*, 2308-2315.
- ¹³⁶ a) M. A. Willert-Porada, D. J. Burton, N. C. Baenziger, *J. Chem. Soc., Chem. Commun.* **1989**, 1633-1634; b) D. Naumann, T. Roy, K. F. Tebbe, W. Crump, *Angew. Chem.* **1993**, *105*, 1555; *Angew. Chem. Ed. Engl.* **1993**, *32*, 1482-1483; c) R. Eujen, B. Hoge, D. J. Brauer, *J. Organomet. Chem.* **1996**, *519*, 7-20.
- ¹³⁷ H. Furuta, H. Maeda, A. Osuka, *J. Am. Chem. Soc.* **2000**, *122*, 803-807.
- ¹³⁸ H. Furuta, T. Ogawa, Y. Uwatoko, K. Araki, *Inorg. Chem.* **1999**, *38*, 2676-2682.
- ¹³⁹ P. J. Chmielewski, L. Latos-Grazynski, I. Schmidt, *Inorg. Chem.* **2000**, *39*, 5475-5482.
- ¹⁴⁰ H. Furuta, T. Ishizuka, A. Osuka, Y. Uwatoko, Y. Ishikawa, *Angew. Chem. Int. Ed.* **2001**, *40*, 2323-2325.
- ¹⁴¹ M. A. Lockwood, T. J. Blubaugh, A. M. Collier, S. Lovell, J. M. Mayer, *Angew. Chem. Int. Ed.* **1999**, *38*, 225-227.

CHAPTER 2

Objectives

2.1 OBJECTIVES

- I. Synthesis of low molecular weight chemical models of catalytic active sites of metalloproteins involved in the activation of molecular dioxygen.
- II. Study of the intrinsic mechanisms of O₂ activation, focusing on intermediates and final products.
- III. Test the capability of the new copper complexes synthesized to oxidize substrates catalytically.
- IV. Investigation of the mechanism of substrate C-H bond activation and subsequent oxidation.

CHAPTER 3

A Novel Twist on Copper Disproportionation: Room Temperature ArylC-H Activation by Cu^I to Form Novel Organometallic Aryl-Cu^{III} species

3.1	ABSTRACT.....	83
3.2	INTRODUCTION.....	85
3.3	RESULTS	87
3.3.1	SYNTHESIS.....	87
3.3.1.1	<i>The ligands.....</i>	87
3.3.1.2	<i>Cu^I complexes.....</i>	88
3.3.1.3	<i>Cu^{III} complexes.....</i>	89
3.3.2	X-RAY STRUCTURES.....	90
3.3.3	SPECTROSCOPIC PROPERTIES.....	97
3.3.3.1	<i>X-Ray Absorption Spectroscopy (XAS).....</i>	97
3.3.3.2	<i>NMR Characterization.....</i>	99
3.3.3.2.1	<i>NMR of Aryl-Cu^{III} complexes.....</i>	99
3.3.3.2.2	<i>NMR of Cu^I complexes.....</i>	103
3.3.3.3	<i>UV-VIS Spectroscopy.....</i>	104
3.3.4	ELECTROCHEMISTRY OF ARYL-CU ^{III} COMPLEXES.....	105
3.4	DISCUSSION.....	108
3.4.1	STRUCTURE AND REACTIVITY	108
3.4.1.1	<i>Disproportionation reation.....</i>	108
3.4.1.2	<i>XAS experiment.....</i>	109
3.4.1.3	<i>Other systems reactivity.....</i>	110
3.4.2	MECHANISTIC DISCUSSION.....	112
3.4.3	H/D EXCHANGE IN H ³³ M/CU ^I SYSTEM. SYNTHESIS OF H ³³ M(D).....	118
3.4.4	AN ARYL-CU ^{II} ISOLATED COMPLEX	120
3.4.5	AROMATIC C-H ACTIVATION BY NICKEL(II).....	122
3.4.6	THEORETICAL CALCULATIONS.....	122
3.5	SUMMARY.....	127
3.6	EXPERIMENTAL SECTION	129
3.7	REFERENCES.....	142

CHAPTER 3

A Novel Twist on Copper Disproportionation: Room Temperature Aryl-C-H Activation by Cu^{II} to Form Novel Organometallic Aryl- Cu^{III} species

3.1 ABSTRACT

Cu^{II} complexes containing triazamacrocyclic ligands **L** (**H32m**, **H₂Me33m** and **H33m**) undergo a disproportionation reaction at room temperature in CH_3CN that yields diamagnetic Cu^{I} and Cu^{III} species in a 1:1 molar relation. Cu^{III} complexes have been isolated and structurally characterized by X-ray Diffraction, XAS and NMR as novel organometallic Aryl- Cu^{III} species ($[(\text{H32m-C})\text{Cu}^{\text{III}}]^{2+}$ (**1**), $[(\text{H}_2\text{Me33m-C})\text{Cu}^{\text{III}}]^{2+}$ (**2**), $[(\text{H33m-C})\text{Cu}^{\text{III}}]^{2+}$ (**3**)), with a slightly distorted square-planar geometry for Cu centers. Organocopper(III) complexes **1**, **2** and **3** are stable under protic media and aerobic conditions at ambient temperatures. Formation of Aryl- Cu^{III} complexes (**1-3**) constitutes an example of aromatic C-H bond activation at room temperature and its kinetics and mechanism have been studied by UV-Vis monitoring of the Cu^{I} d-d transition bands decay. Theoretical calculations show a clear agostic interaction between the Cu^{I} center and the C-H bond. Data obtained from these studies is suggestive of a heterolytic C-H cleavage and subsequent electron transfer for the disproportionation reaction mechanism, with the C-H bond cleavage as the RDS.

3.2 INTRODUCTION

Selective activation of C-H bonds is important to achieve further functionalization of organic moieties, and running these reactions under mild conditions is one of the major goals for synthetic chemists.¹ There are two main mechanisms known to achieve activation of C-H bonds by a single metal:^{2,3} one is the heterolytic activation, where an electrophilic metal is capable of activate C-H bonds ($M^{n+} + R-H \rightarrow M^{n+}-R + H^{\dagger}$). One of the first examples proposed to undergo through electrophilic C-H bond activation was Shilov's system,⁴ where alkanes can be oxidized with chloroplatinium salts in aqueous solutions. This system is still today subjected to controversial mechanistic discussions.⁵ Oxidation of alkanes mediated by electrophilic metal ions in strong acidic conditions has gained attention recently.⁶ In these reactions, metals are in high oxidation state (Hg^{II} , Co^{III} , Pd^{II} , Rh^{III}).⁷

The second one is the oxidative addition reaction, which proceeds through formation of agostic C-H- M^{n+} bonds,⁸ to finally form C- M^{n+2} -H species. Intramolecular oxidative additions, also named as cyclometallations,⁹ are widely known, but intermolecular reactions (i.e. activation of desired hydrocarbons) are scarce due to the propensity of the reductive elimination reverse reaction.^{2,10} The majority of the oxidative addition reactions are driven by late transition metal complexes or by rare earth complexes, both known to form strong bonds to carbon,¹¹ but examples are known for other metals, such as Pd, Ru, Rh (2nd row Transition Metals),¹² Ni and Co (1st row Transition Metals).¹³

Very recently, C-H activation on N-Confused Porphyrins (NCP) ligands by Cu^{II} salts has been reported.^{14,15} One or two pyrrolic C-H groups can be activated to form the

corresponding organometallic Cu^{II} or Cu^{III} species. Similar reactivity is found with NCP ligands by using Ni^{II} and Ag^I.^{16,14} However, no mechanistic studies are reported to rationalize these C-H activation reactions.

In this study a novel Cu chemistry is presented, where a Cu^{II} metal center is capable of intramolecular insertion to an aryl-C-H bond at room temperature and form an organoaryl copper(III) compound.

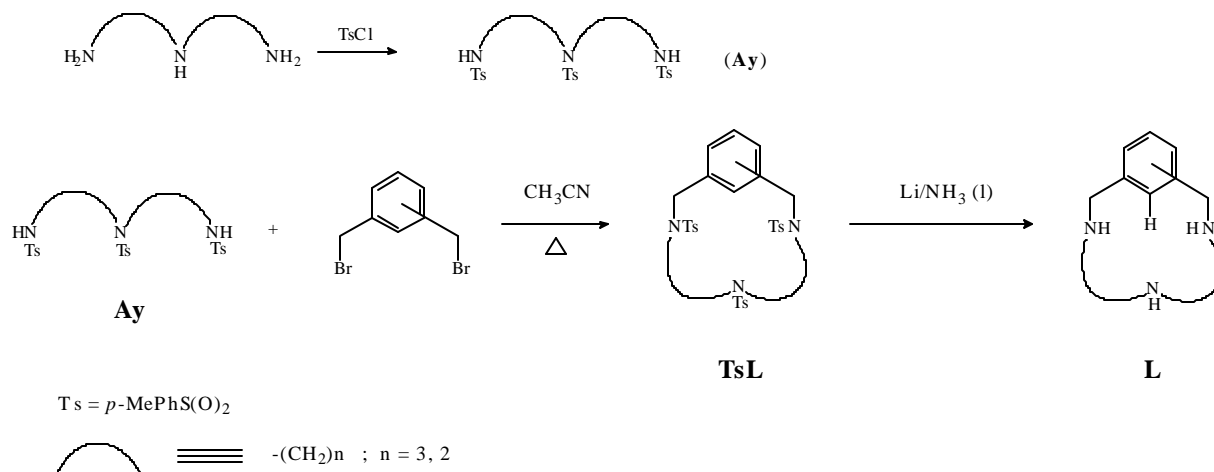
3.3 RESULTS

3.3.1 Synthesis

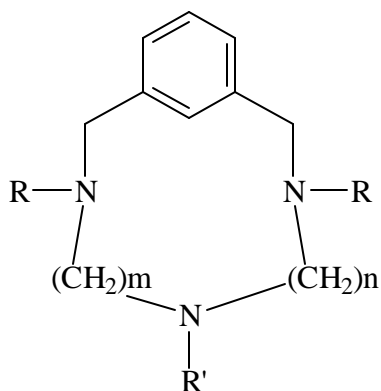
3.3.1.1 The ligands

All ligands have been obtained by the same general method (Scheme 1). Cyclization of tosylated amines and dibromomethylene derivatives allowed the formation in good yield (> 80%) of tosylated triaza macrocycles.¹⁷ Detosylation was achieved by reduction with Li/liquid ammonia,¹⁸ to give final products in yields from 60 to 80%. Tosylated ligands NMR characterization is shown in Figure S1.

Scheme 1. Synthetic general procedure for the isolation of macrocyclic ligands



A wide variety of ligands have been synthesized by modifying the methylenic chain and/or the aromatic substitution (Scheme 2). Ligand NMR characterization is shown in Figure S2.

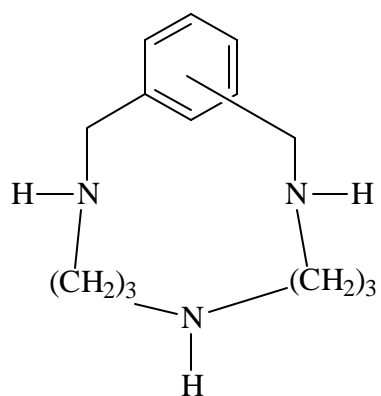
Scheme 2. Triazamacrocyclic ligands synthesized

H32m : R, R' = H; m = 3, n = 2

H₂Me33m : R = H, R' = CH₃; m, n = 3

H33m : R, R' = H; m, n = 3

H22m : R, R' = H; m, n = 2

Me33m : R, R' = CH₃; m, n = 3

H33p : para- xylyl

H33o : orto- xylyl

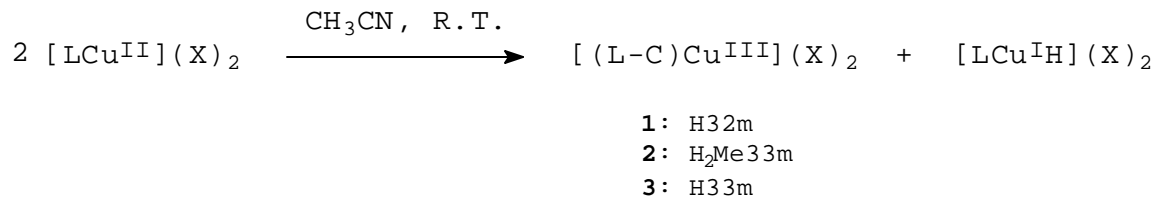
3.3.1.2 Cu^I complexes

Mixing equimolar amounts of ligand L (L = H32m, H₂Me33m, H33m, H22m) and [Cu^I(CH₃CN)₄](X) (X = PF₆⁻, OTf⁻, ClO₄⁻) in dry CH₃CN or CH₂Cl₂ under controlled anaerobic atmosphere allow the formation of Cu^I complexes [(L)Cu^I](X). Isolation is achieved by precipitation with diethyl ether and filtration. Vacuum is applied to dry the compounds which are finally stored under Ar.

3.3.1.3 Cu^{III} complexes

The anaerobic reaction of equimolar amounts of Cu^{II}(X)₂ (X = OTf⁻, ClO₄⁻) and ligand (L= H32m, H₂Me33m, H33m) in CH₃CN at room temperature results in a 50% yield of a novel organometallic Cu^{III} complex that is stable in aerobic, protic media (MeOH, H₂O). The remaining 50% of the starting material is converted to [(LH)Cu^I](X)₂ (see Scheme 3 and section 3.3.3.2.2).

Scheme 3. Cu^{II} disproportionation reaction



L = H32m, H₂Me33m, H33m

X = ClO₄⁻, OTf⁻

The overall reaction is a quantitative disproportionation of Cu^{II} to give equimolar amounts of Cu^{III} and Cu^I species. All Cu^{III} complexes have been characterized by Elemental Analyses, IR (Figure S3) and ESI-MS (see Figure S4), NMR studies (see section 3.3.3.2.1). X-Ray Diffraction analyses were performed on single crystals of complexes [(H32m-C)Cu^{III}](ClO₄)₂ (**1**-(ClO₄)₂), [(H₂Me33m-C)Cu^{III}](ClO₄)₂ (**2**-(ClO₄)₂), [(H33m-C)Cu^{III}](OTf)₂ (**3**-(OTf)₂) and [(H33m-C)Cu^{III}(Cl)](ClO₄) (**4**-(ClO₄)) (see section 3.3.2).

3.3.2 X-Ray structures

Crystal structures as shown in Figure 1-4. Crystal data is listed in Table 1 and selected bond lengths and angles in Table 2.

Cu^{III} complexes [(H32m-C)Cu^{III}](ClO₄)₂ (**1**-(ClO₄)₂), [(H₂Me33m-C)Cu^{III}](ClO₄)₂ (**2**-(ClO₄)₂), [(H33m-C)Cu^{III}](OTf)₂ (**3**-(OTf)₂) and [(H33m-C)Cu^{III}(Cl)](ClO₄) (**4**-(ClO₄)) present distorted square planar geometry (Figures 1-4), typical of d⁸ electronic configuration, where Cu^{III} is bound to the aromatic C1 carbon and to the three aminic nitrogen centers.

All Cu^{III} compounds present short Cu-N and Cu-C1 distances due to high oxidation state of the metal center, and those are specially short for complex **1**-(ClO₄)₂ (see Table 2).

Table 1. Crystal data and structure refinement of Cu^{III} complexes.

	1 -(ClO ₄) ₂	2 -(ClO ₄) ₂	3 -(OTf) ₂	4 -(ClO ₄)	6 -(PF ₆) ₂ ·6H ₂ O ·CH ₂ Cl ₂
empirical formula	C ₁₃ H ₂₀ Cl ₂ CuN ₃ O ₈	C ₁₅ H ₂₂ Cl ₂ CuN ₃ O ₈	C ₁₆ H ₂₂ Cu ₁ F ₆ N ₃ O ₆ S ₂	C ₂₈ H ₄₄ Cu ₂ N ₆ O ₈ Cl ₄	C ₂₉ H ₅₈ Cu ₂ N ₆ O ₆ Cl ₃ P ₁ F ₆
fw	480.76	506.80	594.03	861.70	965.21
space group	P-1	P(2)1/n	P21/c	Pbca	P2(1)/n
<i>a</i> , Å	8.0892(8)	8.831(1)	9.603(2)	16.9591(10)	9.64440(10)
<i>b</i> , Å	8.6971(8)	12.439(1)	8.777(2)	18.0884(15)	21.2311(3)
<i>c</i> , Å	13.9751(15)	18.361(1)	26.476(5)	22.4408(12)	19.87780(10)
a , deg	90.043(12)	90	90	90	90
b , deg	74.168(12)	93.1550(10)	98.08(3)	90	95.2530(10)
g , deg	67.401(11)	90	90	90	90
<i>V</i> , Å ³	867.07(15)	2013.8(2)	2209.4(8)	6884.0(8)	4053.11(7)
<i>Z</i>	2	4	4	8	4
Data collection	STOE imaging plate	Bruker SMART CCD	STOE imaging plate	STOE imaging plate	Bruker SMART CCD
instrument					
<i>T</i> , K	180(2)	298(2)	160(2)	160(2)	298(2)
I Mo-K α , Å	0.71073	0.71073	0.71073	0.71073	0.71073
r (calcd), g cm ⁻³	1.841	1.672	1.786	1.663	1.582
μ mm ⁻¹	1.619	1.399	1.268	1.604	1.361
<i>R</i> / <i>R</i> _w ^a	0.0428/0.1024	0.0587/0.1583	0.0295/0.0765	0.0548/0.0895	0.0507/0.0956

^a $R = \sum |F_0 - F_c| / \sum F_0$ and $R_w = \{ \sum [w(F_0^2 - F_c^2)^2] / \sum [w(F_0^2)^2] \}^{1/2}$

Figure 1. ORTEP diagram of complex $[(H_{32m}-C)Cu^{III}](ClO_4)_2$ ($1-(ClO_4)_2$) (50% probability thermal ellipsoids) and geometric environment for Cu.

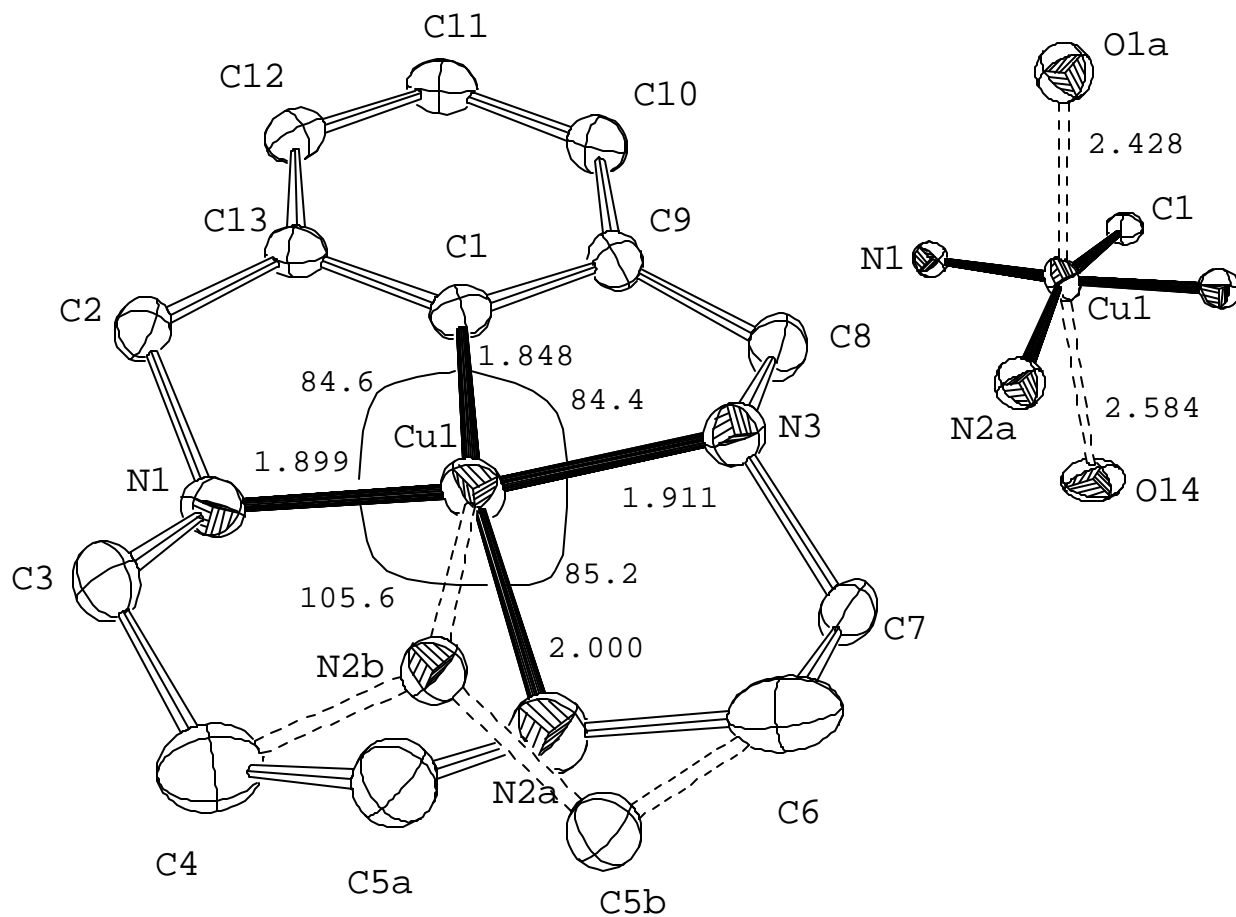


Figure 2. ORTEP diagram of complex $[(H_2Me33m-C)Cu^{III}](ClO_4)_2$ ($2-(ClO_4)_2$) (50% probability thermal ellipsoids) and geometric environment for Cu.

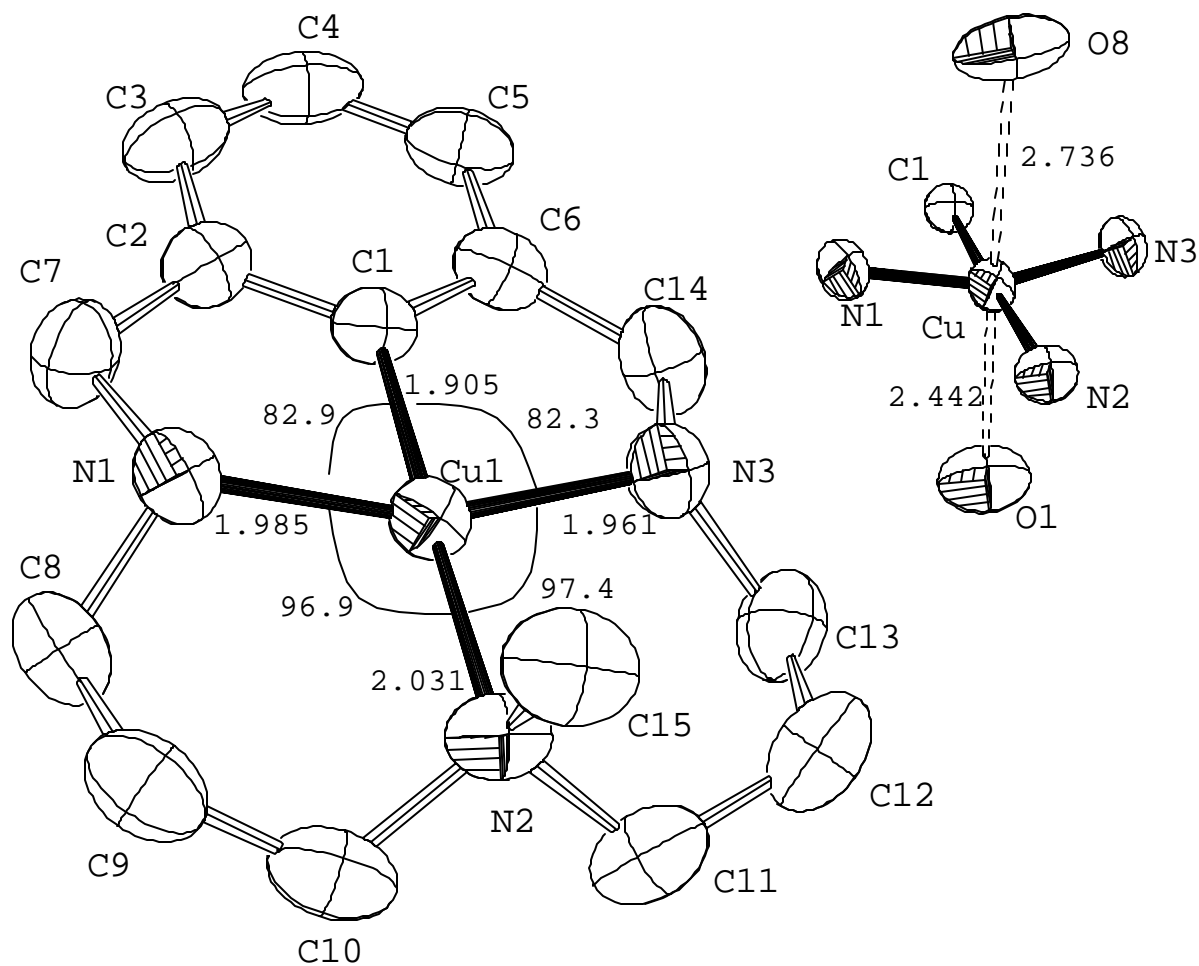


Figure 3. ORTEP diagram of complex $[(\text{H33m-C})\text{Cu}^{\text{III}}](\text{OTf})_2$ ($3-(\text{OTf})_2$) (50% probability thermal ellipsoids) and geometric environment for Cu.

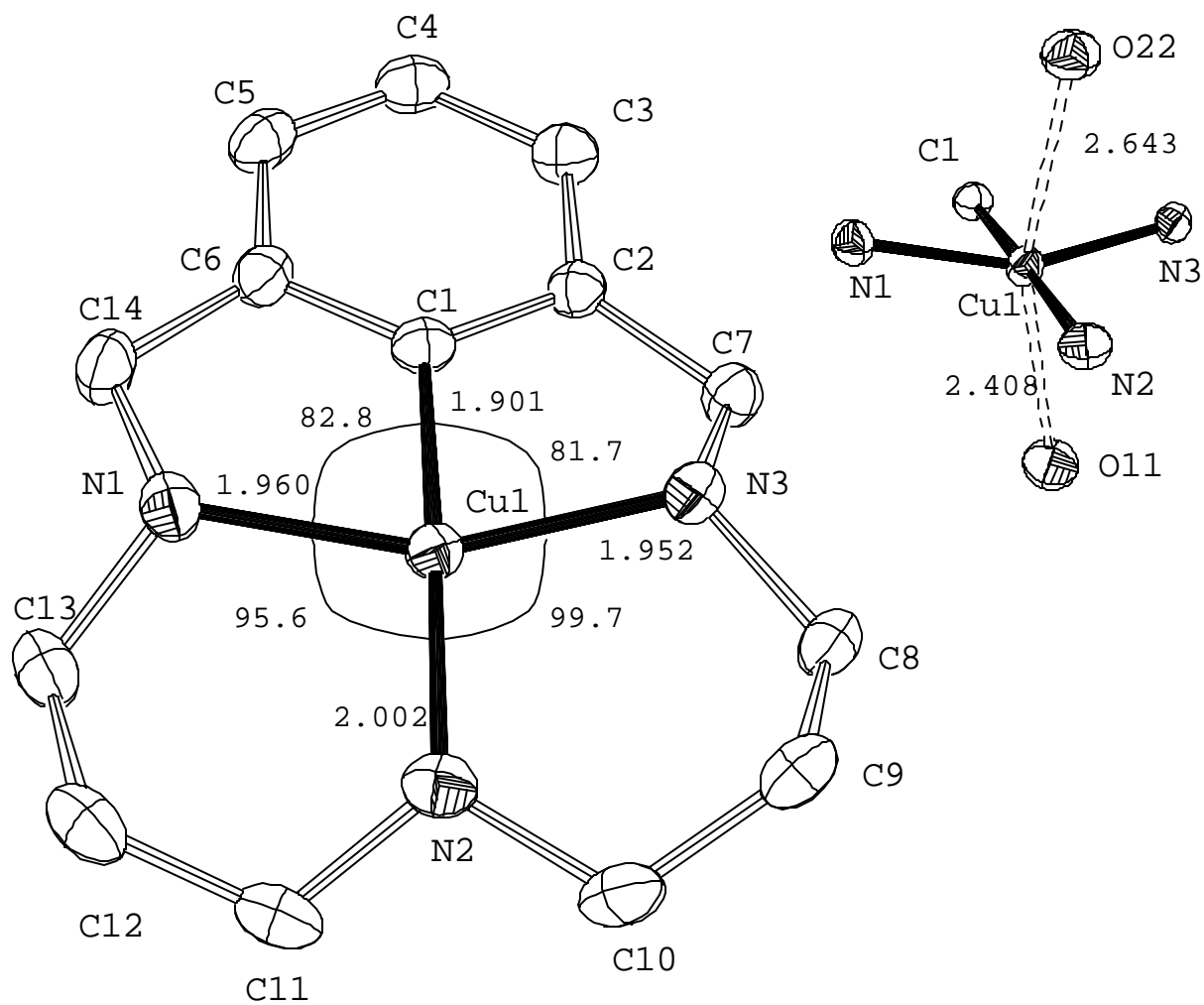


Figure 4. ORTEP diagram of complex $[(\text{H33m-C})\text{Cu}^{\text{III}}(\text{Cl})](\text{ClO}_4)$ ($4-(\text{ClO}_4)$) (50% probability thermal ellipsoids) and geometric environment for Cu.

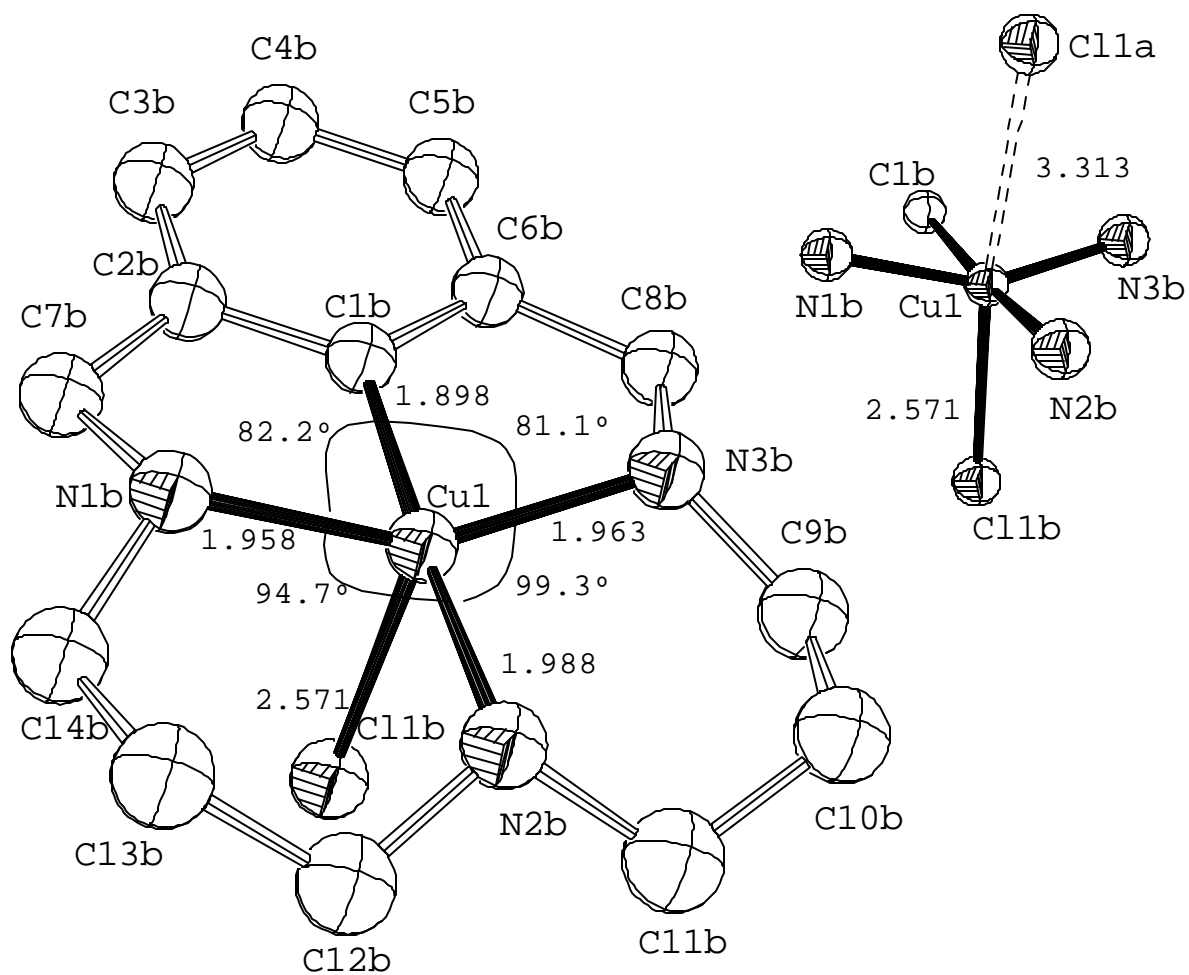


Table 2. Comparison of selected bond distances (Å) and angles (deg) for Cu^{III} structures.

	1 -(ClO ₄) ₂	2 -(ClO ₄) ₂	3 -(OTf) ₂	4 -(ClO ₄)
C1-Cu1	1.848	1.905	1.901	1.898
N1-Cu1	1.899	1.985	1.960	1.958
N2-Cu1	2.000	2.031	2.002	1.988
N3-Cu1	1.911	1.961	1.952	1.963
C1-Cu1-N1	84.6	82.9	82.8	82.2
C1-Cu1-N3	84.4	82.3	81.7	81.1
N1-Cu1-N2	105.6	96.9	95.6	94.7
N2-Cu1-N3	85.2	99.7	99.7	99.3
C1-Cu1-N2	163.5	177.6	178.4	171.9
N1-Cu1-N3	169.0	160.7	157.2	154.5
Cu-O (short)	2.428	2.442	2.408	-
Cu-O (long)	2.584	2.736	2.643	-
Cu-Cl (short)	-	-	-	2.571
Cu-Cl (long)	-	-	-	3.313
O-Cu-O	170.9	177.3	156.6	-
Cl-Cu-Cl	-	-	-	161.6

Statistic disorder has been found in complex [(H32m-C)Cu^{III}]²⁺ (**1**) for the atoms labeled N2 and C5, which have been located on two sites with a ratio of occupancy close to 50% (see Figure 1). The coordination sphere for Cu is very dependent on the ligand backbone; thus, the smallest ligand H32m (13-membered ring) contributes to a more distorted environment for Cu in complex **1**. On the other hand, the 14-membered cycle exhibited by ligands H₂Me33m and H33m, allows copper to be positioned in a less tensioned manner (approximately 0.05 Å longer distances compared to **1**, and C1-Cu1-N2 angles close to linearity). Complexes **1-3** present weak electrostatic interactions between the Cu center and the O atom from ClO₄⁻ and OTf⁻ at

long distances (>2.4 Å) (see Figure S5a-c for crystal packing of each complex).

Interestingly, different substituents on N2 (i.e. methyl in ligand H₂Me33m) or different counteranions (ClO₄⁻, OTf⁻) do not affect the bond distances but significantly influence bond angles. Crystal packing view for complex [(H33m-C)Cu^{III}(Cl)](ClO₄) (**4**-(ClO₄)) shows the moderate interactions of copper(III) centers with Cl⁻ atoms in a pseudo-chain mode (see Figure S5d), with one short covalent bond (Cu-Cl 2.571 Å) and one long ionic interaction (Cu-Cl 3.313 Å).

NH hydrogens in complex **1** are dispositioned in *anti* (N1-H and N2-H down, N3-H up; Figure 1) and 6-membered cycle formed due to coordination of Cu to N1 and N2 present a chair conformation. On the contrary, complexes **2**, **3** and **4** show a *syn* NH disposition, with two 6-membered cycles per complex in a chair conformation. Crystal cell for **4** contains two asymmetric molecules with very similar bond distances and slightly different bond angles.

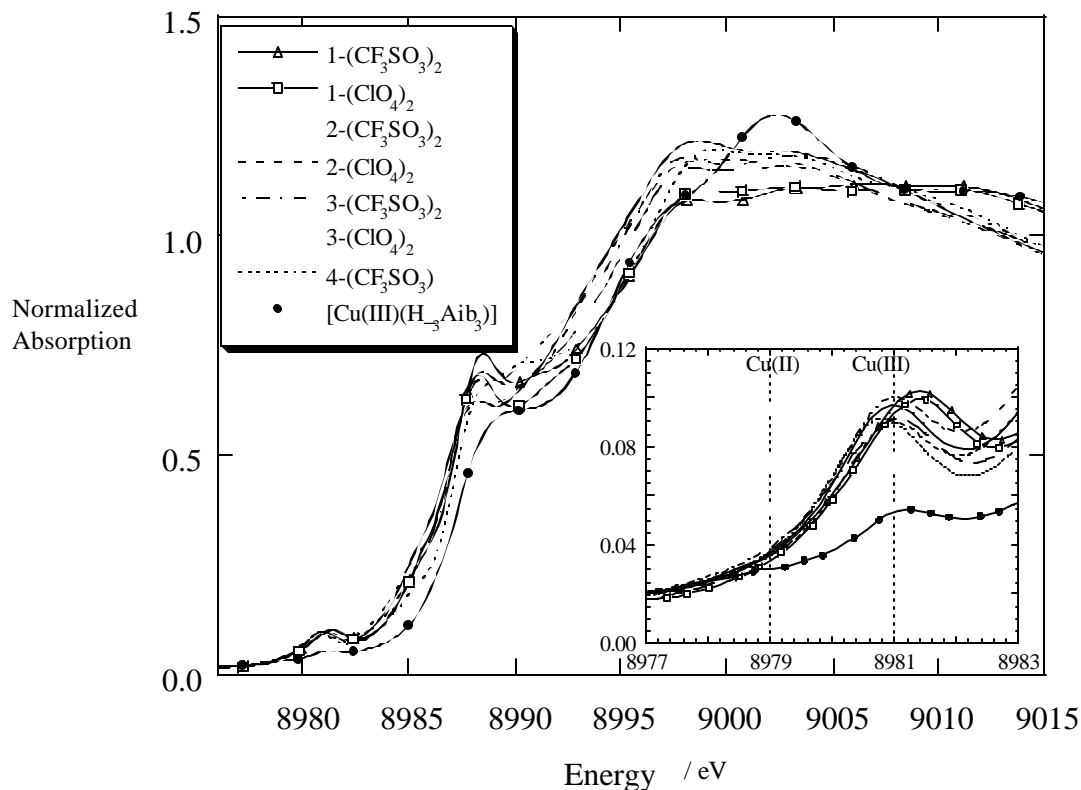
3.3.3 Spectroscopic properties

3.3.3.1 X-Ray Absorption Spectroscopy (XAS)

XAS spectra for Cu^{III} complexes are depicted in Figure 5. All data suggested copper center in +3 oxidation state and it was also confirmed by Cu K-Edge X-Ray Absorption Spectroscopy (XAS).¹⁹ Preedge features on XAS spectra of solid samples of [(H32m-C)Cu^{III}]²⁺ (**1**), [(H₂Me33m-C)Cu^{III}]²⁺ (**2**), [(H33m-C)Cu^{III}]²⁺ (**3**) with ClO₄⁻ and OTf⁻ counterions provides direct spectroscopic evidence for Cu^{III}. These complexes exhibit a very intense transition at 8981 ± 0.5 eV, which has been demonstrated to be indicative of the 1s

3d transition of Cu^{III} compounds.¹⁹ Similar intense preedge feature is found for complex $[(\text{H33m-C})\text{Cu}^{\text{III}}(\text{Cl})]^{2+}$ (4).

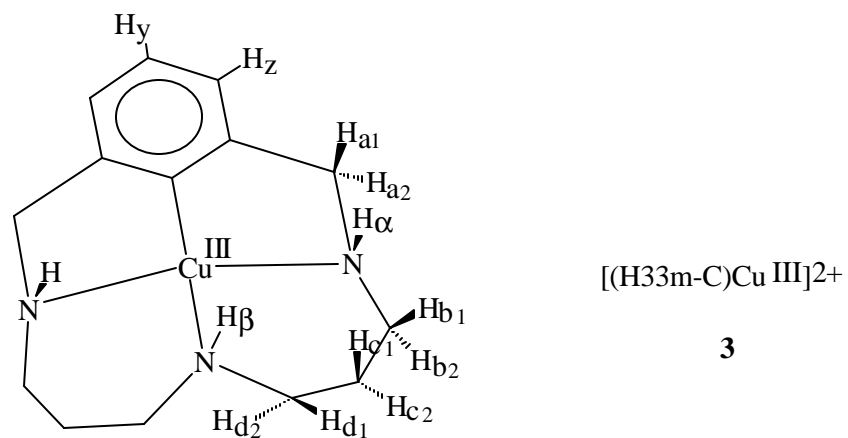
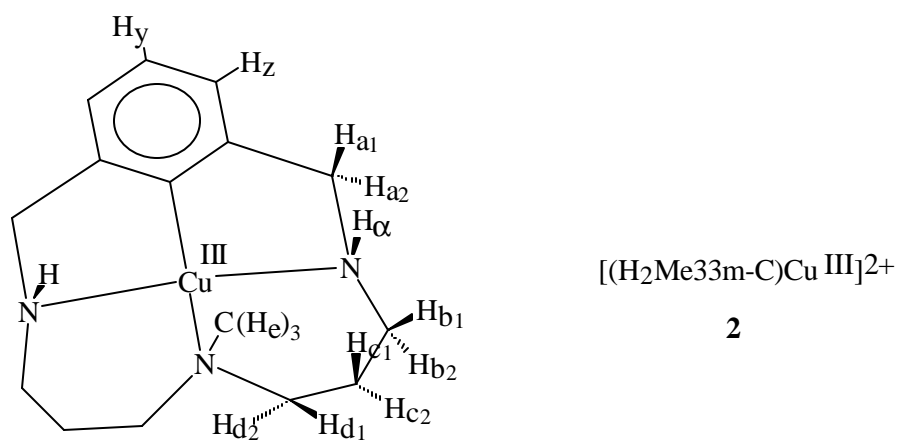
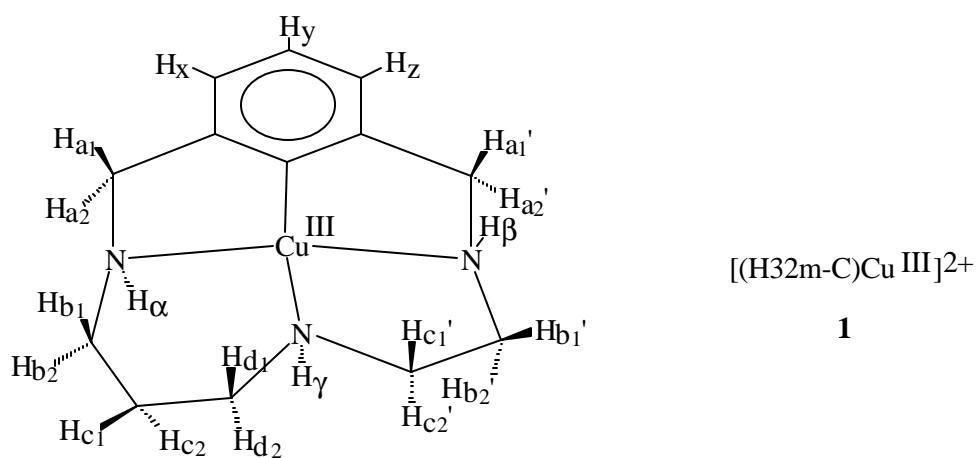
Figure 5. Cu K-edges for Cu^{III} complexes **1**- $(\text{CF}_3\text{SO}_3)_2$, **1**- $(\text{ClO}_4)_2$, **2**- $(\text{ClO}_4)_2$, **2**- $(\text{CF}_3\text{SO}_3)_2$, **3**- $(\text{ClO}_4)_2$, **3**- $(\text{CF}_3\text{SO}_3)_2$, **4**- (CF_3SO_3) and $[\text{Cu}^{\text{III}}(\text{H}_3\text{Aib}_3)]$. Inset shows the amplified preedge region (i.e. location of 1s → 3d transition)(8976–8983 eV).



3.3.3.2 NMR Characterization

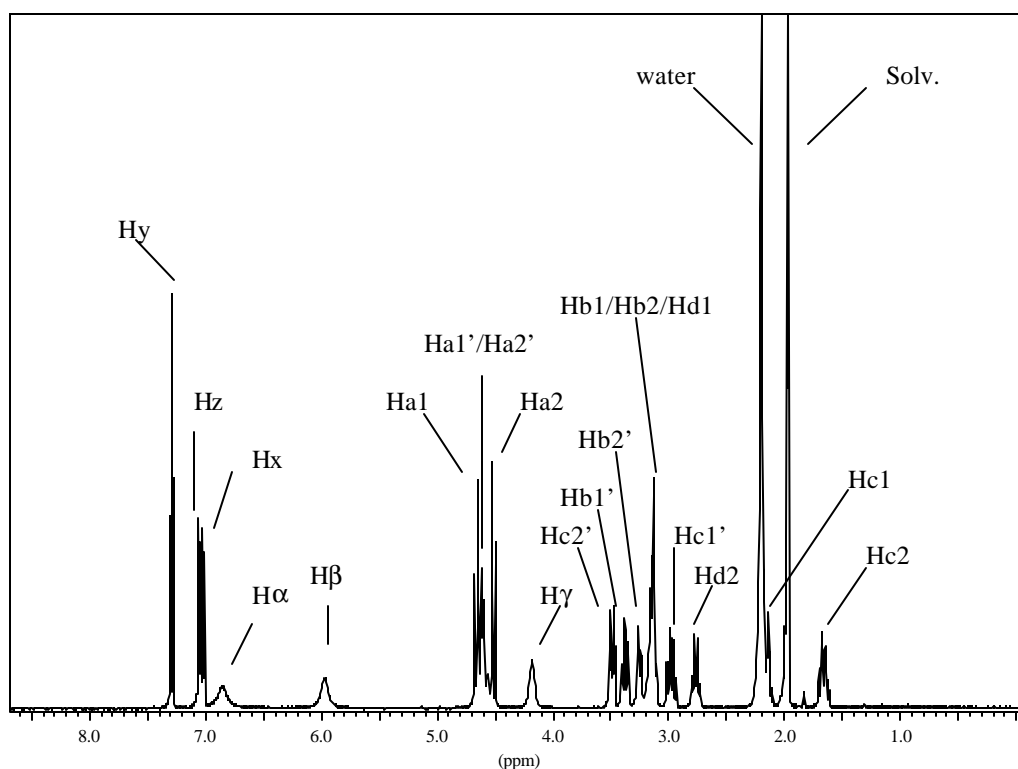
3.3.3.2.1 NMR of Aryl-Cu^{III} complexes

NMR spectra are shown in Figure 6 and Figures S6a-n (proton labeling and proton shifts for each complex are shown in Scheme 4 and Table 3, respectively). Cu^{III} presents a d⁸ electronic configuration and diamagnetic behavior was expected for these complexes. Structures of complexes [(H32m-C)Cu^{III}]²⁺ (**1**), [(H₂Me33m-C)Cu^{III}]²⁺ (**2**) and [(H33m-C)Cu^{III}]²⁺ (**3**) with perchlorate (ClO₄⁻) counterions have been fully characterized in solution by NMR studies in CD₃CN. ¹H, ¹³C, COSY, NOESY and HMBC techniques have been employed to establish the solution structure of these systems (see Figures S6a-n). Complexes **2** and **3** present a symmetry plane in solution that contain the C1-Cu1-N2 atoms. This symmetry is broken in system **1** due to asymmetry of ligand H32m and thus all protons become magnetically distinguishable in the ¹H NMR spectrum (see Scheme 4). Very characteristic signals of these complexes are the assigned to benzylic protons. The conformation adopted is highly rigid even in solution and it does not interconvert with other potential conformations. Therefore, protons Ha1 and Ha2 are not equivalent and they couple to each other, giving rise to a hyperfine structured benzylic signal on the ¹H NMR. A very unique feature for these complexes is the ¹³C signal for C1 carbon, as it appears at very high shifts (179.4 ppm in **1**, 184.7 in **2** and 183.2 in **3** compared to signal in ligands H32m, H₂Me33m, H33m typically at ~125 ppm), due to high deshielding caused by the bonded Cu^{III} atom.

Scheme 4. Proton labeling for NMR characterization studies.

Complex $[(H32m-C)Cu^{III}](ClO_4)_2$ ($1-(ClO_4)_2$): asymmetry causes unequivalency in all protons. H_γ appears as a triplet at 7.28 ppm, whereas H_x (NOE with H_{a1}) and H_z (NOE with $H_{a1'}$) appear as doublets at 7.01 and 7.03 ppm respectively. Equatorial H_{a1} appears as a doublet at 4.65 ppm, whereas axial H_{a2} appears at 4.51, also as a doublet. $H_{a1'}$ and $H_{a2'}$ appear as a double doublet (dd) at 4.60 ppm.

Figure 6. Proton assignment in 1H NMR for complex $[(H32m-C)Cu^{III}]^{2+}$ (**1**) in CD_3CN .



Interestingly, asymmetry also allows differentiation of all three NH hydrogen atoms. H_α and H_β appear as broad signals at 6.85 and 5.96 ppm respectively, both with exchange signals with water at NOESY spectrum indicating the highly acidic character of these amine protons. On the contrary, H_γ does not present exchange signals neither with the other NH nor with water, indicating its low acidic character and

it appears at 4.18 ppm. See Table 3 for the rest of proton shifts and Figure 6.

Table 3. Chemical Shifts (ppm) for ^1H NMR signals of Cu^{III} complexes.

	1-(ClO₄)₂	2-(ClO₄)₂	3-(ClO₄)₂
Hy	7.28	7.27	7.27
H _z	7.03	6.95	6.95
H _x	7.01	-	-
H α	6.85	6.33	6.12
H β	5.96	-	3.14
H γ	4.18	-	-
Ha1	4.65	4.67	4.61
Ha2	4.51	4.52	4.49
Ha1'	4.60	-	-
Ha2'	4.60	-	-
Hb1	3.13	3.05	3.09
Hb2	3.13	2.66	3.09
Hb1'	3.37	-	-
Hb2'	3.24	-	-
Hc1	2.17	2.15	1.77
Hc2	1.65	1.95	2.04
Hc1'	2.97	-	-
Hc2'	3.48	-	-
Hd1	3.13	3.08	2.99
Hd2	2.75	3.24	2.63
He	-	2.73	-

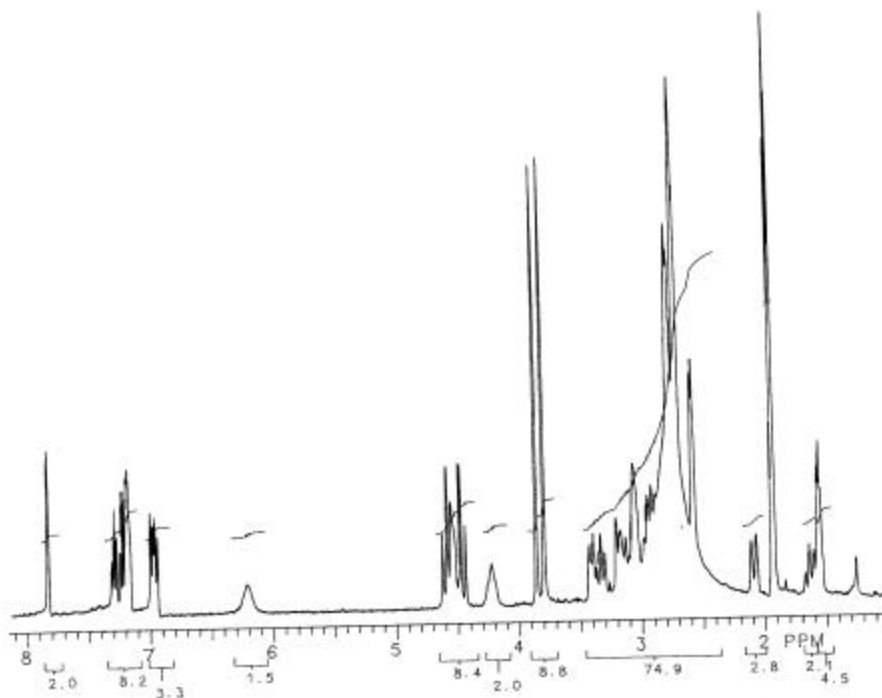
Complex $[(H_2Me33m-C)Cu^{III}](ClO_4)_2$ (**2**- $(ClO_4)_2$): axial benzylic proton H_{a1} appear at 4.67 ppm as a doublet (NOE with NH_α) and equatorial H_{a2} at 4.52 ppm, also as a doublet. Aminic protons H_α appear as a broad band at 6.33 ppm. Exchange signals with water at NOESY spectrum indicate the highly acidic character of these amine protons. See Table 3 for the rest of proton shifts.

Complex $[(H33m-C)Cu^{III}](ClO_4)_2$ (**3**- $(ClO_4)_2$): axial benzylic proton H_{a1} appear at 4.61 ppm as a double doublet (NOE with NH_α) and H_{a2} at 4.49 also as a dd. Aminic protons H_α appear as a broad band at 6.12 ppm. Exchange signals with water at NOESY spectrum indicates the highly acidic character of these amine protons. Low acidic character for central NH_β is found, similarly as in complex **1**, and H_β appears at 3.14 ppm. 1H NMR show small signals attributed to another conformation in solution, in equilibrium with the major one. This side conformation is considered minority and has not been studied in detail. See Table 3 for the rest of proton shifts.

3.3.3.2.2 NMR of Cu^I complexes

Isolation of Cu^I complexes $[(LH)Cu^I]^{2+}$ obtained from disproportionation has been elusive. However, final reaction mixture 1H NMR spectra demonstrate the intact existence of the aromatic C-H bond for the 50% fraction corresponding to $[(LH)Cu^I]^{2+}$ (L = H32m, H_2Me33m , H33m) (see Figure 7 and Figure S7). Besides, splitting of benzylic singlet in systems with ligands H32m and H_2Me33m suggests protonation of one benzylic NH (the amine is proposed to be the basic group responsible for proton abstraction, see mechanistic discussion).

Figure 7. ^1H NMR (400 MHz) spectrum for final reaction mixture $[(\text{H}32\text{m-C})\text{Cu}^{\text{III}}]^{2+}/[(\text{H}32\text{mH})\text{Cu}^{\text{I}}]^{2+}$ 1/1 in CD_3CN .



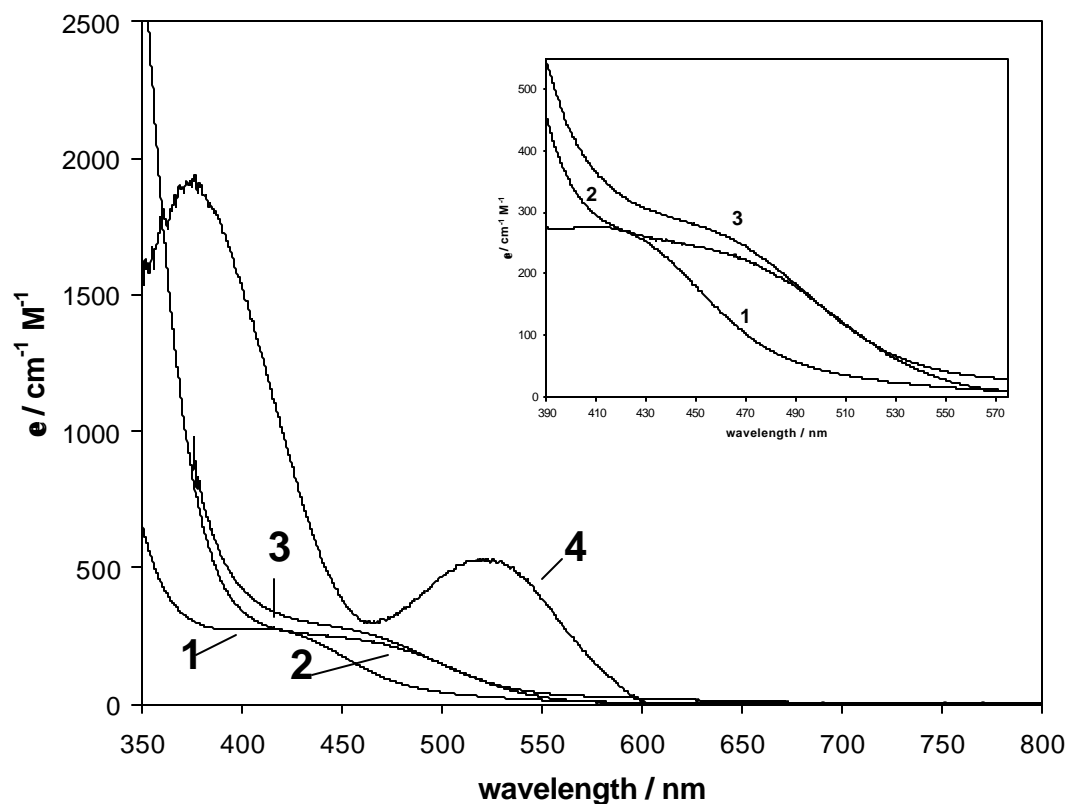
Only $[\text{Cu}^{\text{I}}(\text{CH}_3\text{CN})_4](\text{OTf})$ salt could be crystallized out from solution after diethyl ether diffusion (see section 3.4.1.1).

3.3.3.3 UV-VIS Spectroscopy

UV-Vis spectrum of Aryl- Cu^{III} complexes $[(\text{H}32\text{m-C})\text{Cu}^{\text{III}}]^{2+}$ (**1**), $[(\text{H}_2\text{Me}33\text{m-C})\text{Cu}^{\text{III}}]^{2+}$ (**2**) and $[(\text{H}33\text{m-C})\text{Cu}^{\text{III}}]^{2+}$ (**3**) with ClO_4^- counteranions in CH_3CN is presented in Figure 8. The three species present a weak shoulder peak centered at 409 nm ($\epsilon = 280 \text{ M}^{-1}\text{cm}^{-1}$) for **1**, 440 nm (250) for **2** and 448 nm (280) for **3**. On the contrary, complex $[(\text{H}33\text{m-C})\text{Cu}^{\text{III}}(\text{Cl})]^+$ (**4**) shows intense LMCT bands at 375 nm (1900) and 522 nm (540) due to covalent bonding with Cl atom, placed at the apical position of the square-planar pyramid presented by the Cu^{III} complex environment. Covalency on $\text{Cu}^{\text{III}}\text{-Cl}$ bond is also

reflected on the relatively short bond length (2.571 Å) found by X-Ray diffraction.

Figure 8. Electronic spectra of Aryl-Cu^{III} complexes **1**, **2**, **3** and **4** as perchlorate salts in CH₃CN.

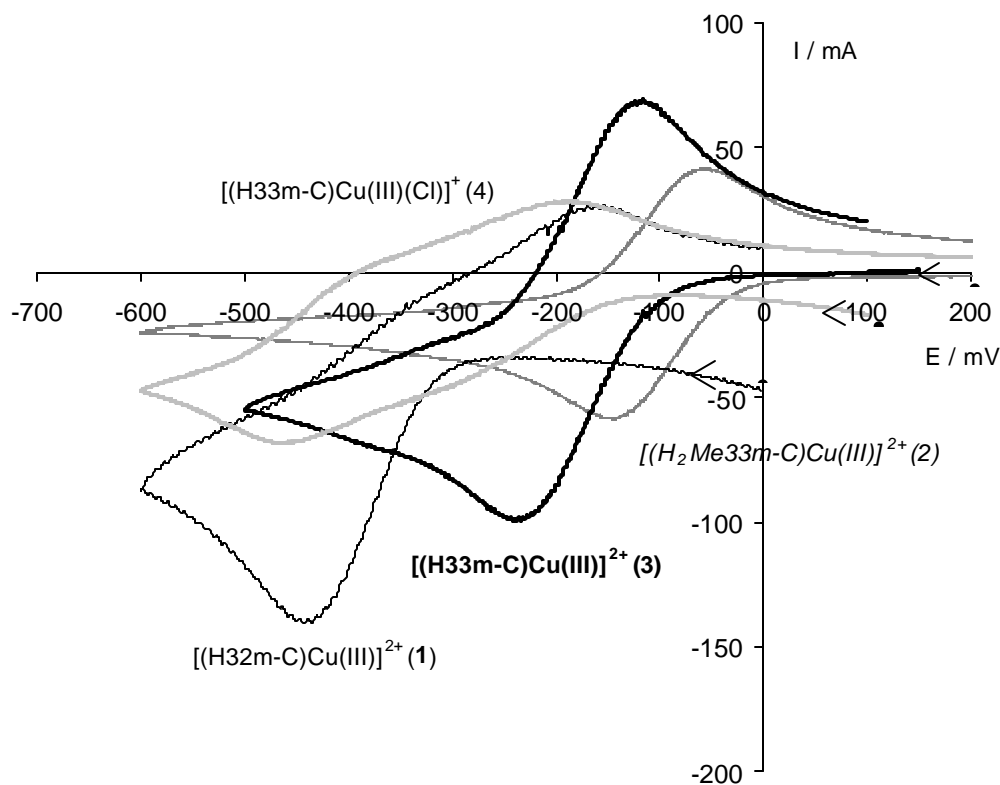


3.3.4 Electrochemistry of Aryl-Cu^{III} complexes

Electrochemical characterization of complexes [(H32m-C)Cu^{III}]²⁺ (**1**), [(H₂Me33m-C)Cu^{III}]²⁺ (**2**), [(H33m-C)Cu^{III}]²⁺ (**3**) and [(H33m-C)Cu^{III}(Cl)]⁺ (**4**) by Cyclic Voltammetry (CV), shown in Figure 9. CV experiments have been performed in CH₃CN using a complex concentration of approximately 2 mM. Complexes **2** and **3** show a chemically reversible 1 e⁻ wave at E_{1/2} = -103 mV (E_{pa} = -60 mV, E_{pc} = -146 mV, ΔE = 86 mV) and -181 mV (E_{pa} = -124 mV, E_{pc} = -238 mV, ΔE = 118 mV) versus

SSCE respectively, whereas complex **1** presents an irreversible wave at even more negative potentials, $E_{pc} = -444$ mV (vs SSCE). Ferrocene was used as an internal reference displaying a 1 e⁻ reversible wave at $E_{1/2} = 371$ mV vs SSCE.

Figure 9. Cyclic Voltammeteries for complexes [(H32m-C)Cu^{III}](ClO₄)₂ (**1**-(ClO₄)₂), [(H₂Me33m-C)Cu^{III}](OTf)₂ (**2**-(OTf)₂), [(H33m-C)Cu^{III}](ClO₄)₂ (**3**-(ClO₄)₂) and [(H33m-C)Cu^{III}](Cl)(OTf) (**4**-(OTf)). Scan rate = 100 mV, TBAP 0.2 M, CH₃CN, R.T.



Plot of i_p vs $v^{1/2}$ gives a straight line with slope of 0.18489 ($R^2=0.999$) for **2** and 0.28134 ($R^2=0.998$) for **3** (see Figures S10-13) following the Randles-Sevcik equation,²⁰ eq 1 :

$$i_p = (2.69e+5)n^{3/2}AD_0^{1/2}C_0v^{1/2} \quad (\text{eq 1})$$

Diffusion coefficient D_0 is deduced from the equation, being $D_0 = 7.358$ cm²/s for **2** and 9.488 cm²/s for **3**.

Coulometry experiment at an applied potential ($E_{\text{app}} = -0.25$ V) for complex $[(\text{H33m-C})\text{Cu}^{\text{III}}]^{2+}$ (**3**) showed $2e^-$ transfer, and allowed full reduction to Cu^{I} species (Figure S16). Solution changes from orange to colorless and final solution was titrated with 1,10-phenanthroline, also confirming the existence of Cu^{I} species in quantitative yield. CV experiments in a -1.5 V to 1.5 V range showed a second irreversible reduction at -1.1 V for complex **3** if scan rate is higher than 200 mV/s (Figure S14), but additional peaks appeared if scan rate used was lower than 60 mV/s (Figure S15). This suggests either a $2e^-$ transfer to Cu^{I} followed by a chemical reaction to form $[\text{Cu}^{\text{I}}(\text{CH}_3\text{CN})_4]^+$, or a $1e^-$ transfer followed by a chemical reaction generating a new species that, under this potential, is further reduced to Cu^{I} forming $[\text{Cu}^{\text{I}}(\text{CH}_3\text{CN})_4]^+$ (Figure S17).

Electrochemical experiments show an important degree of instability of Aryl- Cu^{II} species, as it can be expected from the disproportionation itself. However, complex $[(\text{H33m-C})\text{Cu}^{\text{III}}(\text{Cl})](\text{OTf})$ (**4**-(OTf)) shows two reversible and consecutive waves at $E_{1/2} = -250$ mV ($E_{\text{pa}} = -190$ mV, $E_{\text{pc}} = -310$ mV, $\Delta E = 120$ mV) and -427 mV ($E_{\text{pa}} = -392$ mV, $E_{\text{pc}} = -462$ mV, $\Delta E = 70$ mV), which have been assigned to $\text{Cu}^{\text{III}}/\text{Cu}^{\text{II}}$ and $\text{Cu}^{\text{II}}/\text{Cu}^{\text{I}}$ redox couples respectively. No other reduction waves appear below -1.5 V (see Figure S18). The different redox behavior of complex **4** versus **1-3** might be due to the apical coordination of the chloro atom in this complex.

3.4 DISCUSSION

3.4.1 Structure and reactivity

A wide variety of ligands have been synthesized (see Scheme 2) to understand the different parameters that govern the metal insertion to the aromatic ring.

3.4.1.1 Disproportionation reaction

Experimental conditions for disproportionation (see Scheme 3) reaction of Cu^{II} with ligands H32m, $\text{H}_2\text{Me33m}$ and H33m are remarkably mild (room temperature), reaction is specially fast (it can be completed in less than 1 minute) and final products are highly stable.

The Cu^{I} complexes $[(\text{LH})\text{Cu}^{\text{I}}]^{2+}$ obtained from the disproportionation reaction have not been isolated but their ^1H NMR spectra have been registered from reaction mixture in deuterated acetonitrile (see section 3.3.3.2.2). Final yields were determined as 50% through titration with 1,10-phenanthroline²¹ and ^1H NMR signal integration of $[(\text{LH})\text{Cu}^{\text{I}}]^{2+}$ (see Figure 7 and Figure S7). The latter shows distinct ^1H NMR spectrum compared to LCu^{I} complex directly synthesized in CH_3CN (see Figure S8). However, the monoprotection of the ligand and the affinity of Cu^{I} for acetonitrile displace the equilibrium to form $[\text{Cu}^{\text{I}}(\text{CH}_3\text{CN})_4]^+$ when its isolation is attempted with diethyl ether diffusion,²² indicating the lability of the monoprotectioned complex $[(\text{LH})\text{Cu}^{\text{I}}]^{2+}$ towards dissociation. CV of $\text{Cu}^{\text{I}}/\text{Cu}^{\text{III}}$ reaction mixture show typical intense adsorption wave corresponding to $[\text{Cu}^{\text{I}}(\text{CH}_3\text{CN})_4]^+$ species, and similar CV

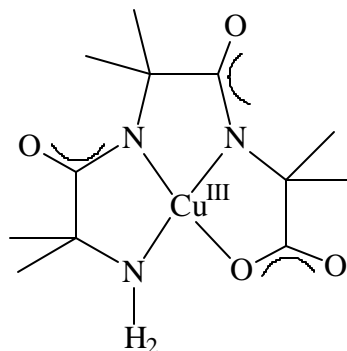
pattern at ~ 0.25 V is obtained when complex $[(\text{H32m})\text{Cu}^{\text{I}}]^+$ is treated with 1 equivalent of triflic acid (see Figure S9).

Cu^{III} -aryl species $[(\text{H32m-C})\text{Cu}^{\text{III}}]^{2+}$ (**1**), $[(\text{H}_2\text{Me33m-C})\text{Cu}^{\text{III}}]^{2+}$ (**2**) and $[(\text{H33m-C})\text{Cu}^{\text{III}}]^{2+}$ (**3**) are thermally stable in protic media at acidic and neutral pH. In basic conditions, complexes **1**, **2** and **3** react to give intensively colored intermediates (characterized by ESI-MS to be amine deprotonated Cu^{III} complex) that in presence of H_2O undergo oxygen insertion to form a final bis(μ -phenoxo) Cu^{II}_2 compound (see Chapter 4).

3.4.1.2 XAS experiment

The large intensity of the transition at 8981 ± 0.5 eV for complexes **1-3**-(X)₂ (X = ClO_4^- , OTf^-) and **4**-(OTf) (see Figure 5) compared with other Cu^{III} complexes such as $[\text{Cu}^{\text{III}}(\text{H-}_3\text{Aib}_3)]$ (depicted in Figure 10) may be attributed to extensive mixing of the 3d and 4p metal orbitals.¹⁹ This intensity, as well as the shift to slightly higher energy of complexes **1**-(CF_3SO_3)₂ and **1**-(ClO_4)₂, is being studied in further detail. Note that a change of counterion does not affect the intensity or energy shift of the transition. The effect of chloride atom in the preedge feature shown by complex $[(\text{H33m-C})\text{Cu}^{\text{III}}(\text{Cl})](\text{OTf})$ (**4**) is reflected on the shift to lower energy in 0.2 eV.

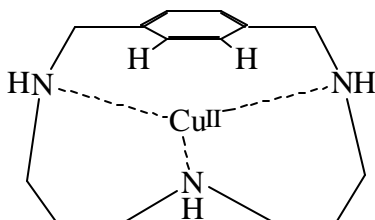
Figure 10. Complex $[\text{Cu}^{\text{III}}(\text{H}_3\text{Aib}_3)]$ used as the Cu^{III} complex of reference for comparing XAS preedge data (H_3Aib_3 is a tripeptide trianionic ligand)



3.4.1.3 Other systems reactivity

Ligands H33p and H33o do not react with Cu^{II} to form an organocopper(III) complex. This result is expected for H33o, as no aromatic C-H bond are placed close to the metal center due to its *ortho* ring substitution. For the *para* substituted ligand H33p, even though there are two aromatic C-H bonds inside the macrocyclic ring cavity, they can not adopt the right geometry to interact to the metal center, as can be observed in Figure 11. The aromatic ring tends to be positioned perpendicularly to the macrocyclic cavity.

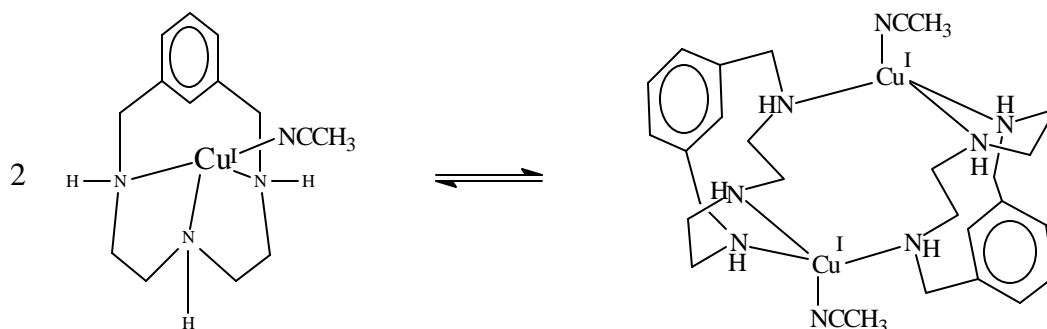
Figure 11. Model plot for geometry of $[(\text{H33p})\text{Cu}^{\text{II}}]^{2+}$ complex.



When the 12-membered macrocyclic ligand H22m is used, too constrained environment for copper(II) is created and reaction does not proceed readily. Cu^{I} studies performed

with this ligand showed a tendency of dimerize due to ligand conformational restrictions (Figure 12): ^1H NMR spectrum of complex $[(\text{H22m})\text{Cu}^{\text{I}}](\text{PF}_6)$ in CD_2Cl_2 shows a splitting of the benzylic proton signal in two different broad bands (Figure S19),²³ that do not collapse or sharpen at low temperatures (240–300 K range). This behavior is not observed for Cu^{I} complexes with ligands H33m, $\text{H}_2\text{Me33m}$ or H32m (see Figure S8c); ESI-MS spectrum for $[(\text{H22m})\text{Cu}^{\text{I}}](\text{PF}_6)$ in CH_3CN presents peaks for high molecular fragments with patterns corresponding to dinuclear Cu species (Figure S19). Therefore, a similar dimerization equilibrium may be expected when Cu^{II} is used. In spite of this apparent unsuccessful reaction, Cu^{III} formation in some extent may be postulated with H22m, as its reaction with Cu^{II} leads to oxygen insertion on aromatic C1 position under certain conditions (see section 3.4.2).

Figure 12. Dimerization equilibrium for complex $[(\text{H22m})\text{Cu}^{\text{I}}]^+$ in solution.



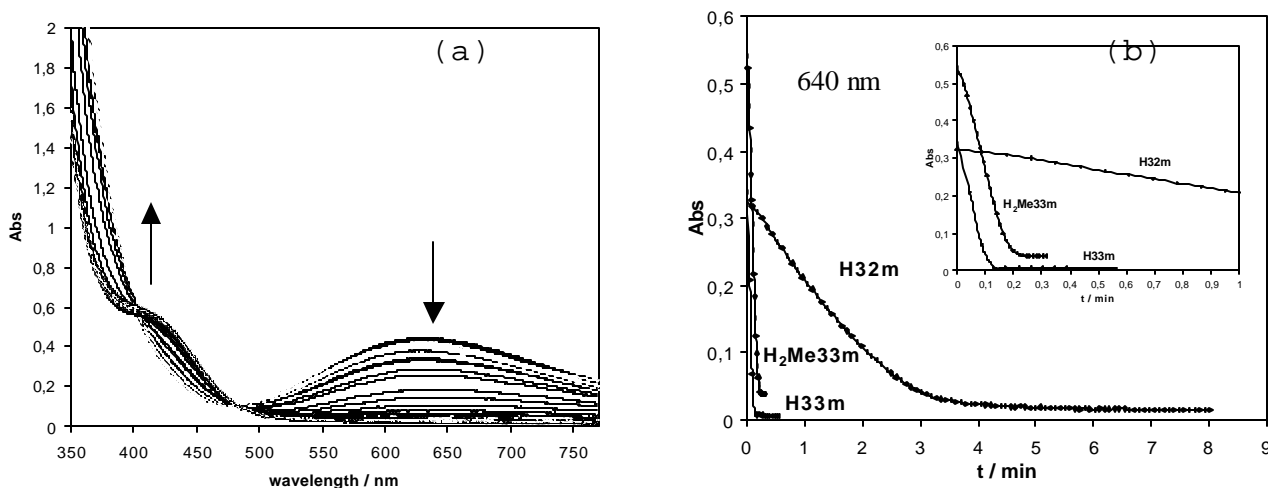
Ligand Me33m has the same ring size as $\text{H}_2\text{Me33m}$ and H33m, but it has three tertiary amines as coordinating atoms. Reaction with Cu^{II} does not lead to the organocopper(III) complex and therefore, the presence of N-H groups should be considered when discussing the mechanistic details of the disproportionation reaction. Moreover, it has been

described that tertiary amines stabilize Cu^{I} centers and non formation of Cu^{III} species was expected with ligand Me33m.²⁴

3.4.2 Mechanistic discussion

The disproportionation reaction can be monitored by UV-Vis spectroscopy, where full decay of Cu^{II} d-d transition bands can be followed. The reaction is considered to be finished when d-d bands completely disappear, since neither Cu^{I} nor Cu^{III} absorb at this region of the spectrum. The reaction has been monitored for complexes $[(\text{H32m-C})\text{Cu}^{\text{III}}]^{2+}$ (**1**), $[(\text{H}_2\text{Me33m-C})\text{Cu}^{\text{III}}]^{2+}$ (**2**), $[(\text{H33m-C})\text{Cu}^{\text{III}}]^{2+}$ (**3**) with triflate as counteranions at different concentrations and temperatures. The reaction is rapidly accomplished at room temperature in CH_3CN , and it takes only a few seconds to obtain complexes **2** and **3** whereas the H32m ligand reacts with Cu^{II} approximately one order of magnitude slower (reaction is finished in 4 minutes)(see Figure 13).

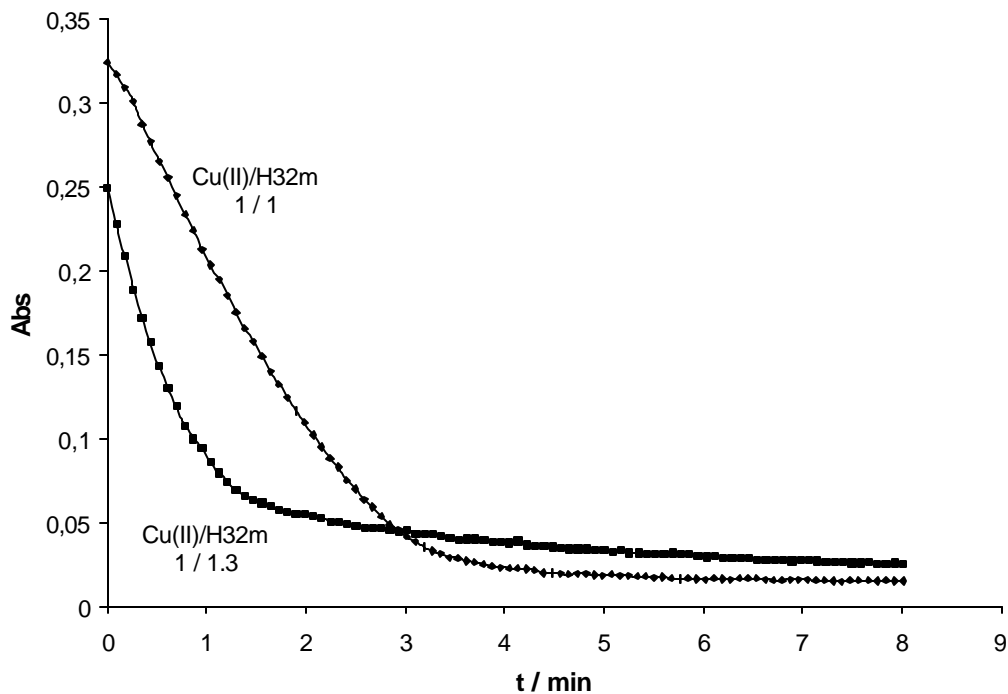
Figure 13. UV-Vis monitoring experiments of Cu^{II} disproportionation reaction in CH_3CN . (a) Full-range spectra for reaction at R.T for ligand H32m + Cu^{II} at $[\text{H32m}] = [\text{Cu}^{\text{II}}] = 4.56 \text{ mM}$ (1 scan/5 seconds); (b) Decay of Cu^{II} d-d band at 640 nm for reactions with H32m, $\text{H}_2\text{Me33m}$, H33m at R.T.



The decay of Cu^{II} d-d transition bands shows an induction period type of profile that precludes simple data treatment and rate constant determination for all systems 1-3. This can be related to an auto-catalytic type of behavior,²⁵ where many steps may be involved.

However, by changing reaction conditions it was found that switching from a 1 to 1 equivalent L/ Cu^{II} relation to a small excess of ligand (1.3 L/1 Cu^{II}) situation (L = H32m, H₂Me33m, H33m), the induction period is suppressed and reaction becomes faster, giving a simple first-order kinetics decay (see Figure 14).

Figure 14. Comparison of the kinetic profiles for disproportionation reaction with ligand H32m and Cu^{II} at different molar relations (Cu^{II} d-d transition decay at 640 nm). $[\text{Cu}^{\text{II}}] = 2.5 \text{ mM}$, R.T., CH_3CN .



Kinetic data analysis has been performed using Specfit program (Spectrum Software Ass.).

Focusing on H32m/Cu^{II} and H₂Me33m/Cu^{II} systems, a similar clean behavior is observed in the temperature range 263–298 K using concentrations from 0.5 to 2.5 mM (see Table 4). Thus, Eyring equation has been plotted and thermodynamic parameters have been calculated for the reaction formation of complexes **1** and **2** (see Figures S20–23).

Table 4. Kinetic and thermodynamic parameters for disproportionation reaction with ligands H32m ([Cu^{II}]= 1.25 mM; [H32m]/[Cu^{II}] = 1.28) and H₂Me33m ([Cu^{II}]= 1.21 mM; [H₂Me33m]/[Cu^{II}] = 1.28) in the 263–298 K temperature range.

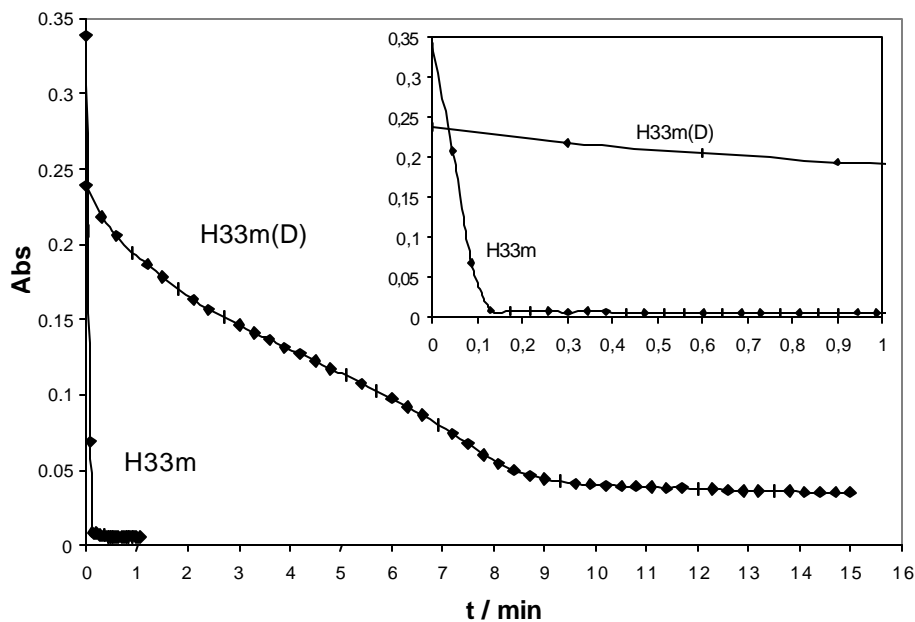
	H32m / Cu ^{II}	H ₂ Me33m / Cu ^{II}
	k _{obs} (s ⁻¹) A → B	k _{obs} (s ⁻¹) A → B
263 K	-	1.454 x 10 ⁻²
273 K	1.379 x 10 ⁻³	2.607 x 10 ⁻²
285 K	8.851x 10 ⁻³	5.242 x 10 ⁻²
298 K	2.078 x 10 ⁻²	1.886 x 10 ⁻¹
ΔH* (Kcal mol ⁻¹)	16.98	10.62
ΔS* (cal mol ⁻¹ K ⁻¹)	-6.92	-24.05

Similar reaction profiles are found when a small excess of a base such as NEt₃ is added instead of ligand itself, suggesting that the role of the excess ligand is to act as a base. On the contrary, an excess of Cu^{II} in a 1.0 H32m / 2.0 Cu^{II} relation stops the reaction and no disproportionation products are detected.

Two major events must be explained to understand the mechanism of this disproportionation reaction: the first one is the aromatic C-H activation (C-H bond breaking), and the second is the electron transfer from one Cu^{II} center to another one to finally obtain the equimolar Cu^{III} and Cu^I

products. Despite all kinetic and thermodynamic information, none of these explains which is the Rate Determining Step (RDS). Importantly, Kinetic Isotope Effect (KIE) is a definitive parameter to understand the mechanism in greater detail and therefore, the synthesis of a deuterated ligand becomes mandatory. Isolation of deuterated H33m(D) ligand has been achieved and its synthesis is described in section 3.4.3. As a result, reaction of equimolar amounts of deuterated H33m(D) ligand with $\text{Cu}^{\text{II}}(\text{OTf})_2$ reacts significantly more slowly than reaction of H33m/ Cu^{II} . Kinetic profile also shows an induction period that does not disappear when small excess of ligand is used (see Figure 15 and Figure S25). In spite of that, KIE can be estimated by comparison of rate constant values obtained from $\text{A} \rightarrow \text{B}$ reaction simulation: $k_1 = 0.7553 \text{ s}^{-1}$ for H33m system and $k_1' = 0.2169 \text{ min}^{-1}$ for H33m(D) system ($[\text{Cu}^{\text{II}}] = 2.5 \text{ mM}$, R.T., CH_3CN). As all experimental conditions are the same for H33m and H33m(D), a rough estimation of the KIE value can be extracted by direct comparison of total time to complete the reaction. Then, reaction with deuterated ligand takes about 10 minutes whereas with ligand H33m takes about 10 seconds, so a KIE value may be estimated to be $\text{KIE} > 50$. Thus, it can be unequivocally concluded that breaking the C-H bond is the RDS of the disproportionation reaction.

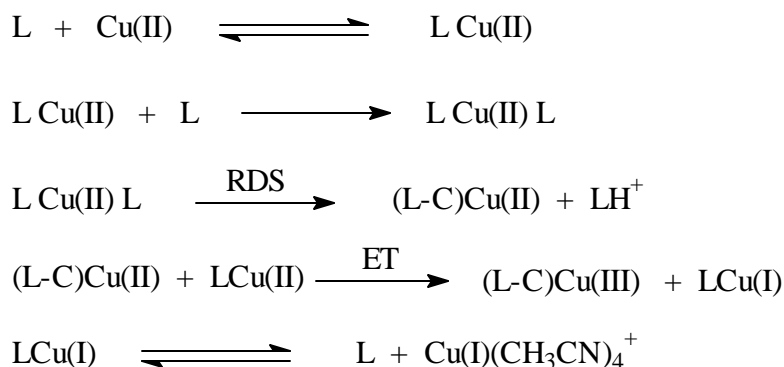
Figure 15. Comparison of Kinetic isotope effect on 640 nm band (Cu^{II} d-d transition) decay. Conc Cu^{II} = 2.5 mM, R.T., CH_3CN , for H33m/H33m(D).



A possible mechanism is depicted in Scheme 5. An outer-sphere electron transfer process is thought to be proceeding rapidly once the Cu-C bond is formed. The reason is to stabilize the system because Aryl- Cu^{II} species are less stable than final Aryl- Cu^{III} , as shown by Coulometry experiments (*vide supra*).

First order kinetics when small excess of ligand (base as well) and a significant KIE value for the C-H bond activation step are two reaction characteristics accommodated by the mechanism proposed. The excess of ligand necessary for this reaction under first order clean kinetics is also supported by experimental data,²² and agrees with an heterolytic type of C-H activation. Excess of Cu^{II} captures all ligand in solution and therefore stops the reaction.

Scheme 5. Proposed general mechanism for the disproportionation reaction



Ligand Me33m does not display same reactivity with Cu^{II} . The presence of benzylic secondary amines NH may be a requisite for these complexes to undergo aromatic copper insertion. Steric problems with tertiary amines on the base approximation step to pull out the aromatic proton may be argued to explain this behavior. Electronic effects as well may be considered due to known stabilization of Cu^{I} by tertiary amines.²⁴

CV experiments (see section 3.3.4) indicate an electrochemically less reversible reduction wave at lower potentials for complex $[(\text{H32m-C})\text{Cu}^{\text{III}}]^{2+}$ (**1**) compared to complexes $[(\text{H}_2\text{Me33m-C})\text{Cu}^{\text{III}}]^{2+}$ (**2**) and $[(\text{H33m-C})\text{Cu}^{\text{III}}]^{2+}$ (**3**). Complex **1** is thus more stable thermodynamically because is harder to reduce. However, **1** forms more slowly than **2** and **3**. The reason is that the formation reaction is controlled by kinetic parameters (ligand H32m is smallest than $\text{H}_2\text{Me33m}$ and H33m, and its steric characteristics must be seen as the cause of its slower formation), but once the organocopper(III) complex is formed, also the smaller size and the short bonds found on its X-Ray structure (see Table

2) explain the higher thermodynamic stability of complex **1** relative to complexes **2** and **3**.

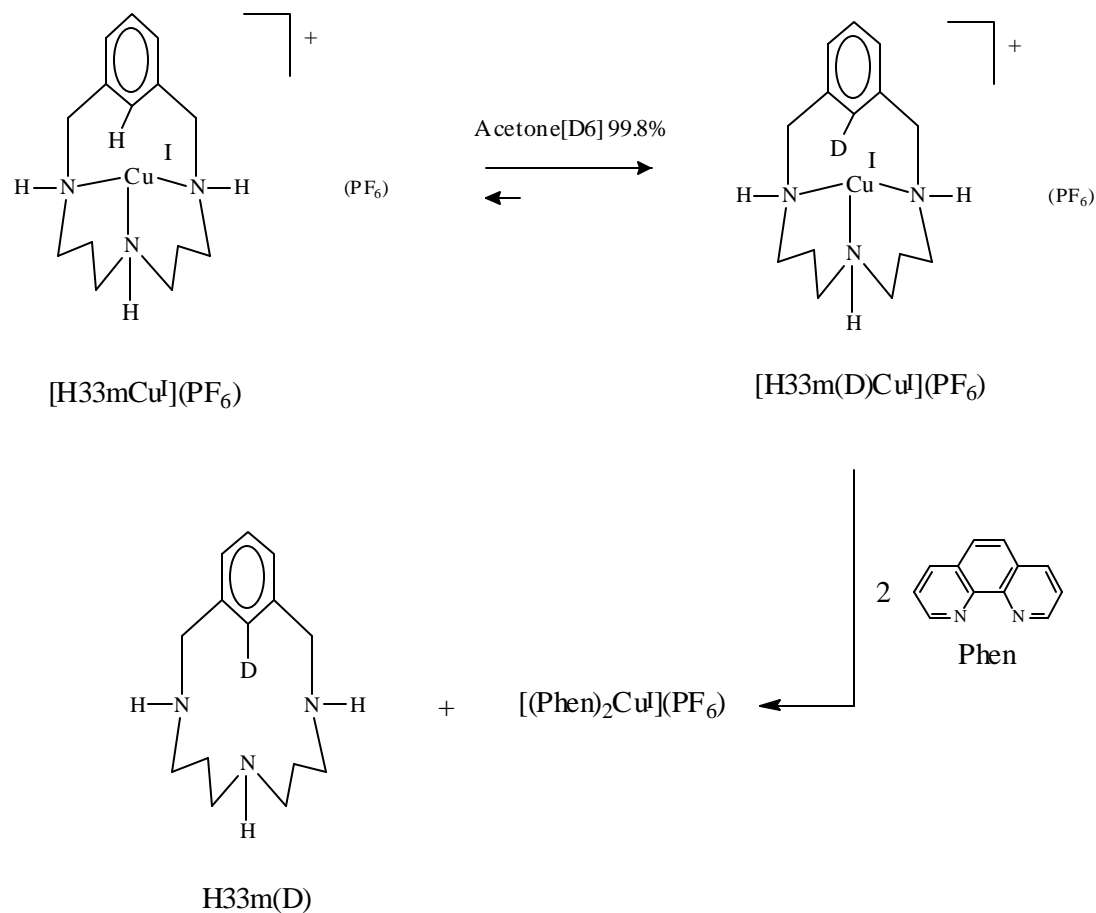
Ligand H22m is a particular case of this family of complexes for its tendency of dimerization.²³ No reactivity in a same time scale as ligands H32m/H₂Me33m/H33m is observed when equimolar amounts of ligand and Cu^{II} are mixed, but when little excess of ligand is used, the system undergoes similar type of C-H activation, although Cu^{III} isolation has been elusive. Nevertheless, excess of ligand (base) (1.3 H22m/ 1 Cu^{II}) and traces of water contamination allowed the formation of bisphenoxo complex [(H22mO)₂Cu₂](OTf)₂ (see Chapter 4). An explanation for this reaction can be a Cu^{III} intermediate similar to complexes **1-3**. However, the elusiveness of [(H22m-C)Cu^{III}]²⁺ complex may be an expected result: sterical constrains in complex [(H32m-C)Cu^{III}](ClO₄)₂ (**1**-(ClO₄)₂) were already very important, so reducing the size even more with ligand H22m (12-membered cycle) is possibly excessive to stabilize an Aryl-Cu^{III} complex similar to complexes **1-3**. On the other hand, C-H activation exists as final Oxygen insertion product formation demonstrates.

3.4.3 H/D exchange in H33m/Cu^I system. Synthesis of H33m(D)

Copper(I) complexes with ligands H32m-H₂Me33m-H33m are stable in acetonitrile as observed with NMR studies, but a proton/deuterium exchange exists in a displaced equilibrium towards the deuterated form when LCu^I complexes (L = H32m, H₂Me33m, H33m) are synthesized in deuterated acetone[D₆] (see Scheme 6). NMR studies are very useful to monitor the reaction, as decay of the specific singlet at 7.95 ppm on the H33m/Cu^I system can be integrated and used as a measure of the extent of the reaction (see Figures S25-26). In the

case of complex $[(\text{H}33\text{m})\text{Cu}^{\text{I}}]^+$ (**9**), reaction is finished in 8-10 hours at room temperature. After this time, complex is stable and does not suffer further chemical reactions. ESI-MS confirmed the NMR suspicion of H/D exchange with a peak for fragments $[(\text{H}33\text{m}(\text{D}))\text{Cu}^{\text{I}}]^+$ ($m/z = 297$) and $\text{H}33\text{m}(\text{D})+\text{H}^+$ ($m/z = 235$) (see Figure S27).

Scheme 6. H/D exchange reaction and synthesis of H33m(D)



As a first approach, we believe that deuterium comes from equilibrium of deuterated acetone[D6] with D^+ and $^-\text{CD}_2\text{COCD}_3$ ($\text{pK}_a \sim 20$). The latter will act as a base to abstract the proton from the aromatic ring. However, it can not be excluded the possibility that the equilibrium of D_2O (being

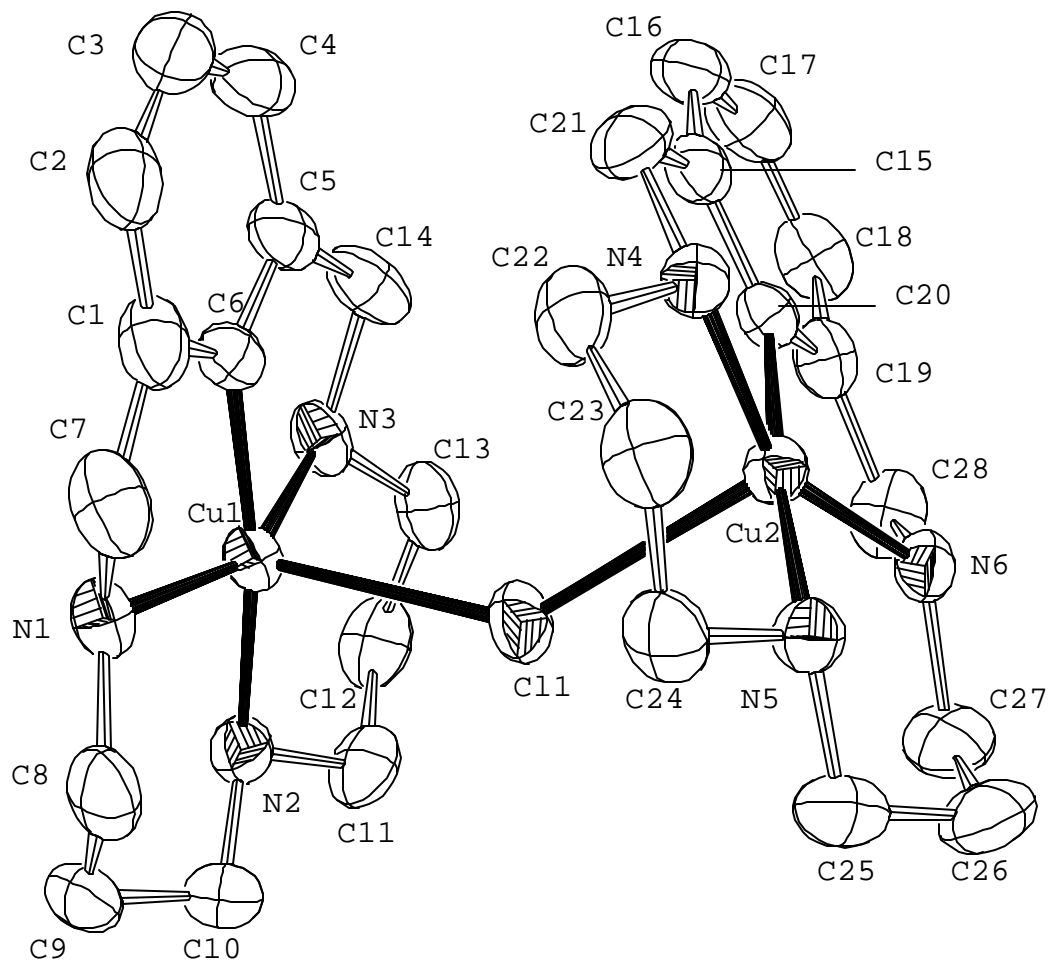
a 0.2% impurity in deuterated acetone-d₆ used) with D⁺ and ⁻OD could be the source of D⁺.

Specific experiment to isolate the deuterated ligand H33m(D) was performed with 40 mg of starting ligand H33m. Four days stirring at room temperature under Ar atmosphere allowed complete exchange of aromatic proton for deuterium. Addition of 1,10-phenanthroline (phen) (2.5 eq.) captured all Cu^I to form the stable complex [(phen)₂Cu^I](PF₆), leaving the ligand H33m(D) in solution (see Scheme 6). Partial precipitation of phen complex helped on its elimination but column chromatography was needed to finally obtain H33m(D) ligand in high purity (NMR, ESI-MS; see Figure S28).

3.4.4 An Aryl-Cu^{II} isolated complex

As explained on the Electrochemistry section, aryl-Cu^{II} complexes can only be stabilized by an strong electron donor such as Cl⁻. A novel aryl-Cu^{II} complex has been isolated from an alternative synthesis, and is presented here as the demonstration that organometallic Cu^{II} species can also be isolated and characterized. X-Ray diffraction analysis was performed on block orange crystals of dinuclear complex [((H33m-C)Cu^{II})₂(μ-Cl)](PF₆)·6H₂O·CH₂Cl₂ (**6**-(PF₆)·6H₂O·CH₂Cl₂) (see Figure 16). Crystal data is listed in Table 1. This complex has been obtained by reaction of copper(I) complex [(H33m)Cu^I](PF₆) (**9**-(PF₆)) with CH₂Cl₂ solvent in very low yields. Mechanism of this reaction is under current investigation. However, this is the second example of an organocopper(II) complex ever reported.^{26,27} Crystal packing plot is depicted in Figure S29.

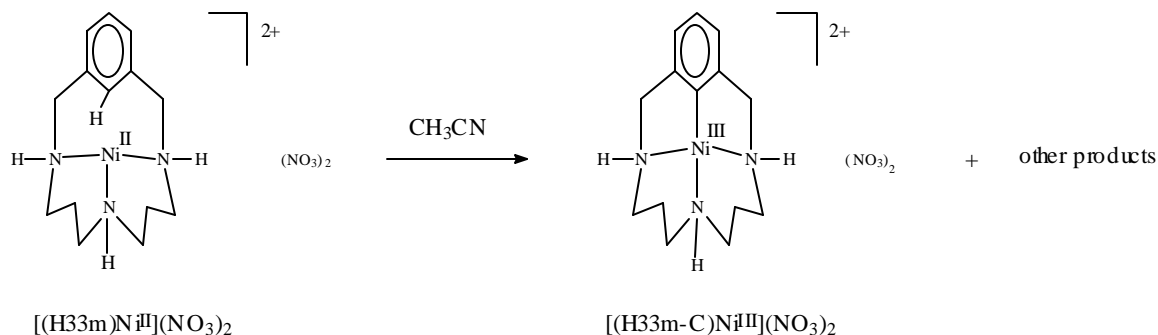
Figure 16. ORTEP diagram of complex $[(\text{H}33\text{m-C})\text{Cu}^{\text{II}}]_2(\mu\text{-Cl})(\text{PF}_6) \cdot 6\text{H}_2\text{O} \cdot \text{CH}_2\text{Cl}_2$ (**6-PF₆**) (50% probability thermal ellipsoids). Selected bond lengths [Å] and angles [°]: Cu1-C6 1.905(4), Cu1-N1 1.958(3), Cu1-N3 1.963(3), Cu1-N2 2.011(3), Cu1-Cl1 2.585(1), Cu2-Cl1 2.630(1), Cu1-Cu2 4.981(1), C6-Cu-N2 169.9(2), N1-Cu-N3 154.7(1), C6-Cu-Cl1 94.6(1), Cu1-Cl1-Cu2 139.4(1).



3.4.5 Aromatic C-H activation by Nickel(II)

Ni^{II} also performs a similar reaction, although it reacts much more slowly (overnight reaction). Green solution of Ni^{II}/H33m system turns orange in roughly 12 hours at room temperature to obtain an organometallic Ni^{III} species (characterized by IR, Elemental Analysis and ESI-MS)(see Scheme 7). The electronic configuration for Ni^{III} is d⁷, paramagnetic, and no signals were observed within the 30/-15 ppm NMR window.

Scheme 7. Organonickel(III) synthesis reaction.



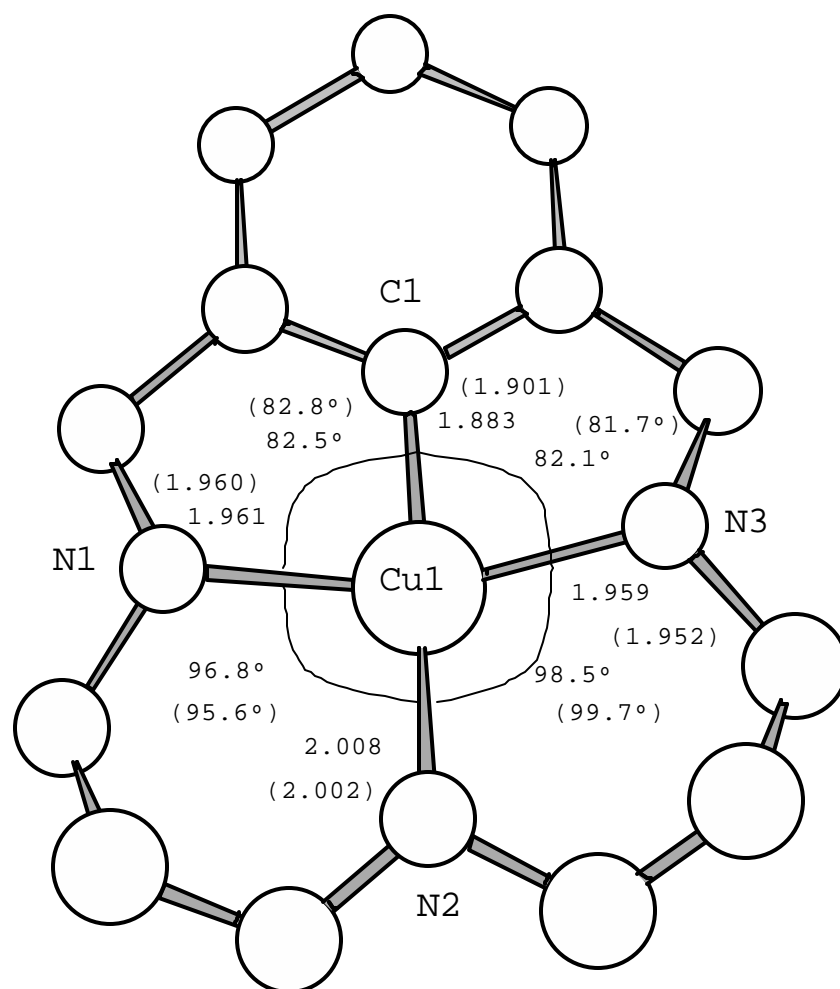
3.4.6 Theoretical calculations

Theoretical calculation were performed in order to gain insight into the nature of the intermediate species in the C-H activation by Cu^{II} metal.

Theoretical calculations at the DFT level³⁴ have been performed on different systems: as a first approach, the accuracy of these calculations for our copper complexes was first checked, and complex $[(\text{H33m-C})\text{Cu}^{\text{III}}]^{2+}$ was optimized considering the molecule as a singlet with total charge of +2. Highly accurate result was obtained as shown in Figure 17 compared to crystal geometry obtained by X-Ray

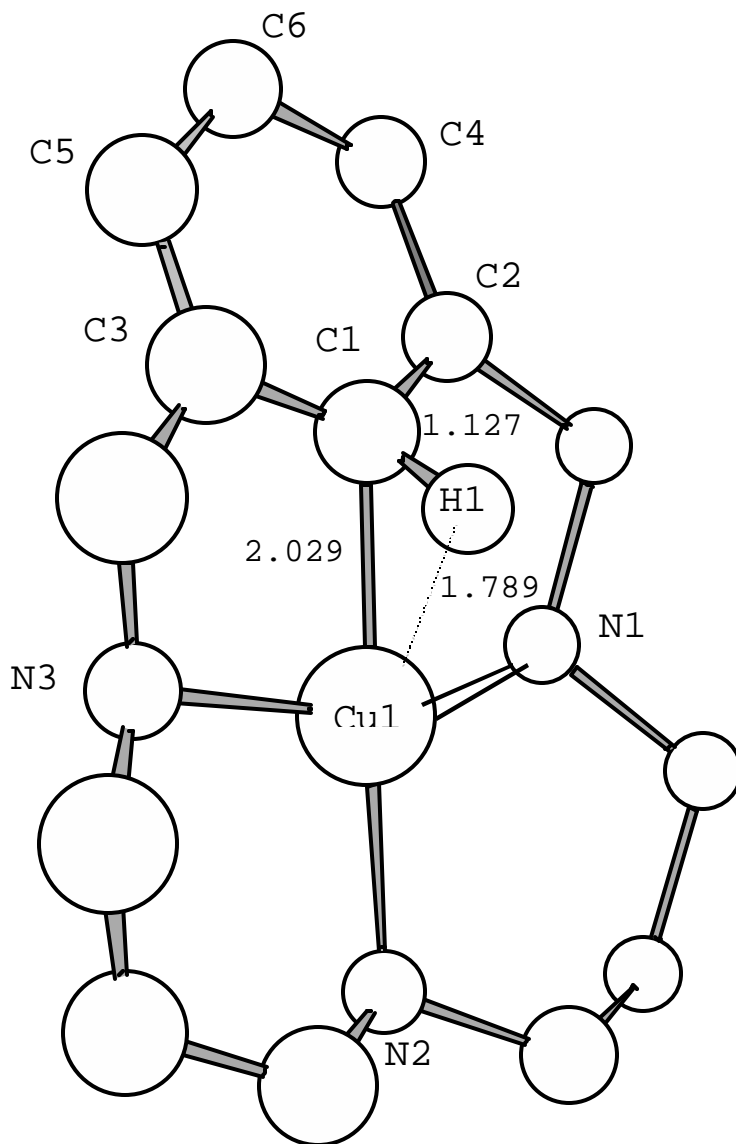
Diffraction (see Figure 3). Same calculation was performed on Cu^{III} system, but considering it as a triplet with total charge +2. Significant distortions were found (C1-Cu1-N2 168° and bent aryl ring) and those are reflected on the $39.6 \text{ Kcal mol}^{-1}$ higher energy value for the triplet compared to the singlet.

Figure 17. Chem3D plot of theoretical calculated geometry for $[(\text{H33m-C})\text{Cu}^{\text{III}}]^{2+}$ (calculated as singlet with total charge +2). Experimental X-Ray diffraction values are in parenthesis. Selected angles [$^\circ$]: C1-Cu-N2 179.2 (178.4), N1-Cu-N3 159.8 (157.2).



Once it was known that calculations were suitable for our systems, the aromatic C-H activation reaction by Cu^{II} was studied, and system $[(\text{H33m})\text{Cu}^{\text{II}}]^{2+}$ was analyzed. Final optimized geometry shows a significant enlargement of C-H bond in a $\text{C-H}\rightarrow\text{M}$ agostic⁸ type of bond (see Figure 18). Moreover, H1 is placed out of the arene plane showing a significant torsion angle of 40.8° .

Figure 18. Chem3D view of theoretical calculated geometry for activated intermediate $[(\text{H33m})\text{Cu}^{\text{II}}]^{2+}$ (calculated as doublet with total charge +2). Selected bond lengths (Å) and angles [$^\circ$]: Cu1-N3 2.010, Cu1-N1 2.139, Cu1-N2 2.002, C1-Cu-N2 170.7, Cu1-C1-C3-C5 26.3, H1-C1-C2-C4 40.9.



Similar η^2 C-H agostic species has been reported recently by Milstein and coworkers with Rhodium arene complexes.²⁸

This enlargement, up to 1.127 Å compared to the calculated C-H bond length of 1.101 Å for the ligand H33m (calculated as a singlet with neutral charge), would explain the increased acidity of the proton, which allows its abstraction by the action of a base, as observed experimentally. Subsequent electron transfer is thought to undergo to further stabilize the system as final [(H33m-C)Cu^{III}]²⁺ species.

Theoretical calculations also explain the H/D exchange reaction with [(H33m)Cu^I]⁺ system (singlet, +1) in acetone. Slightly longer C-H bond up to 1.110 Å is found in final optimized geometry, and that would explain its increased sensitivity to exchange with deuterium. Calculations on system [(H33m)Cu^I(CH₃CN)]⁺ (singlet, +1) (i.e. simulating the reaction in CH₃CN as solvent), also is in line with the experimentally observed and no significant C-H bond length differences are found (up to 1.103 Å compared to 1.101 Å of ligand H33m), so no reactivity is expected. Moreover, the acetonitrile group coordinated to Cu center may prevent H removal due to steric impediments (see Figures S30-31). See Table 5 for optimized bond distances and angles of calculated systems.

Table 5. Comparison of selected bond distances (Å) and angles (deg) for optimized geometries of calculated systems (X-Ray diffraction values for complex [(H33m-C)Cu^{III}]²⁺ (3) in parentheses).

	[(H33m-C) Cu ^{III}] ²⁺	[(H33m)Cu ^{II}] ²⁺	[(H33m)Cu ^I] ⁺	[(H33m)Cu ^I (CH ₃ CN)] ⁺	Ligand H33m
C1-Cu1	1.883 (1.901)	2.029	2.232	2.388	-
N1-Cu1	1.961 (1.960)	2.139	2.046	2.090	-
N2-Cu1	2.008 (2.002)	2.002	2.034	2.074	-
N3-Cu1	1.959 (1.952)	2.010	2.047	2.087	-
C1-H1	-	1.127	1.110	1.103	1.101
Cu1··H1	-	1.789	2.130	2.080	-
Cu1-NCCH3	-	-	-	1.843	-
C1-Cu1-N2	179.2 (178.4)	170.7	-	-	-

3.5 SUMMARY

A novel disproportionation reaction has been described and fully characterized for Cu^{I} , as well as the products of this reaction: equimolar amounts of Cu^{III} -aryl $[(\text{L}-\text{C})\text{Cu}^{\text{III}}]^{2+}$ complex and $[(\text{LH})\text{Cu}^{\text{I}}]^{2+}$ ($\text{L} = \text{H32m}, \text{H}_2\text{Me33m}, \text{H33m}$). Copper(III) complexes have been described in literature as thermally unstable species and often their crystal structure characterization has been elusive. The novelty of organocopper(III) complexes $[(\text{H32m}-\text{C})\text{Cu}^{\text{III}}]^{2+}$ (**1**), $[(\text{H}_2\text{Me33m}-\text{C})\text{Cu}^{\text{III}}]^{2+}$ (**2**) and $[(\text{H33m}-\text{C})\text{Cu}^{\text{III}}]^{2+}$ (**3**) is highly remarkable when we compare these structures with what has been reported in literature. Organometallic copper(III) species had been only stabilized by strong donor groups, mainly CF_3^- , and three crystals structures are reported with this ligand.²⁹ More recently, an organometallic Cu^{III} complex has been stabilized by N-Confused Porphyrin (NCP) type of ligands, those containing 2 C^- and one N^- groups to stabilize the metal in oxidation state +3.¹⁴ On the contrary, the complexes described here only present the aryl anionic group as strong donor to stabilize the Cu^{III} center, further helped by three aminic nitrogen atoms that place the metal in a square-planar geometry.

However, this new family of complexes clearly show that right conditions allow their facile formation and right coordinating environment for Cu^{III} stabilize them, even in protic media at room temperature. H/D exchange exemplifies the C-H activation provoked by the presence of a metal center close enough to the C-H bond. The present experimental and theoretical evidence supports an heterolytic type of C-H activation over an oxidative addition, because the latter would imply a transient $\text{C}-\text{Cu}^{4+}-\text{H}$ intermediate.

As shown with the Ni case, the type of chemistry described in the present chapter could also be carried out with other transition metals, particularly of the first row, to stabilize otherwise unstable high oxidation states.

3.6 EXPERIMENTAL SECTION

General Information. Diethylenetriamine, N-(3-Aminopropyl)-1,3-propanediamine, N-(2-Aminoethyl)-1,3-propanediamine, 3,3'-Diamino-N-methyldipropylamine, α,α' -dibromo-*m*-xylene, α,α' -dibromo-*o*-xylene, $\text{Cu}^{\text{II}}(\text{OTf})_2$, $\text{Cu}^{\text{II}}(\text{ClO}_4)_2 \cdot 6\text{H}_2\text{O}$ were purchased from Aldrich, α,α' -dibromo-*p*-xylene was from Fluka, and all of them used without further purification. Analytical grade solvents were purchased from SDS and dried and distilled under Ar before use. IR, Elemental Analyses, UV-Vis, ESI-MS, FAB-MS and NMR spectra were measured on Mattson Satellite FT-IR, Fisons EA-1108, Varian Cary-50 Scan / Polytec PI X-DAP-06, Thermo Quest Finigan Navigator LC/MS, Fisons VG-Quattro, Bruker DPX-200 MHz and Avance-500 MHz instruments, respectively. Electrochemistry was studied with a EG&G Princeton Applied Research 263A potentiostat.

Warning: Although we have experienced no problems with the compounds reported herein, perchlorate salts are potentially explosive, and should only be handled in small quantities and never heated in the solid state.

Ligand synthesis. **Ligand H32m** (3,6,10-Triaza-bicyclo[10.3.1] hexadeca-1(16),1,14-triene): N-(2-Aminoethyl)-1,3-propanediamine (3.0 g, 24.8 mmol) is tosylated with TsCl (14.45 g, 74.5 mmol) in THF/H₂O (200 mL) in presence of NaOH (3.97g, 99.3 mmol) at 60°C overnight to give a 27% yield of tritosylated amine 32Ts (3.88, 6.69 mmol) after purification by column chromatography (silica gel, CH₂Cl₂/ethyl acetate 92/8). Reaction of α,α' -dibromo-*m*-xylene (0.78 g, 6.70 mmol) with 32Ts (3.88, 6.69 mmol) in CH₃CN (250 mL) at reflux for 24 hours gives, prior column chromatography purification with silica gel, CH₂Cl₂/ethyl acetate 98/2, the desired cycled

product Ts32m (3.98g, 5.83 mmol) in 87% yield. Detosylation of Ts32m is achieved by reduction with Li in liquid ammonia (approx. 250 mL) at -70°C . Lithium metal is added until solution turns deep blue. After 1 hour of reaction, NH_4Cl (15g, 0.28 mol) is added and NH_3 is carefully evaporated. Extraction with CHCl_3/HCl 1M, evaporation of the aqueous phase, basification with NaOH 30%, extraction with CHCl_3 and final purification with silica gel, $\text{CH}_2\text{Cl}_2/\text{MeOH}/\text{NH}_4\text{OH}$ 80/20/5, yielded 0.70 g (55% yield, 3.19 mmol) of ligand H32m.

H32m: IR (KBr pellet, cm^{-1}): 3305 (s), 3023 (m), 2913 (s), 1446 (s), 1119 (s), 703 (s). $^1\text{H-NMR}$ (**d** in CDCl_3 , ppm): 7.76 ppm (s, 1H, C-**CH**-C ar), 7.20 (t, $^3J(\text{H,H})=6$ Hz, 1H, CH-**CH**-CH ar), 7.03 (d, $^3J(\text{H,H})=6$ Hz, 2H, C-**CH**-CH ar), 3.85 (s, 4H, Ar-**CH**₂-NH), 2.79 (m, 4H, Ar-**CH**₂-N-**CH**₂CH₂), 2.57 (m, 4H, CH₂-**CH**₂-N-**CH**₂-CH₂), 1.74 (s, 3H, NH), 1.54 (q, $^3J(\text{H,H})=6$ Hz, 2H, CH₂**CH**₂CH₂). $^{13}\text{C-RMN}$ (**d** in CDCl_3 , ppm): 142.5, 141.9, 128.1, 126.4, 126.0, 125.6, 52.3, 52.2, 49.4, 48.1, 46.2, 45.1, 30.1. ESI-MS: $m/z=220$ ($\text{M}+\text{H}^+$)

Similar procedure is used to synthesize the rest of ligands.

H₂Me33m (7-Methyl-3,7,11-triaza-bicyclo[11.3.1]Heptadeca-1(16),13(17),14-triene): 65% yield in detosylation step. IR (KBr pellet, cm^{-1}): 3321 (s), 3052 (m), 2922 (s), 2787 (s), 1451 (s), 1129 (s), 771 (s). $^1\text{H-NMR}$ (**d** in CDCl_3 , ppm): 7.62 ppm (s, 1H, C-**CH**-C ar), 7.20 (t, $^3J(\text{H,H})=6$ Hz, 1H, CH-**CH**-CH ar), 7.02 (d, $^3J(\text{H,H})=8$ Hz, 2H, C-**CH**-CH ar), 3.91 (s, 4H, Ar-**CH**₂-NH), 2.58 (t, $^3J(\text{H,H})=6$ Hz, 4H, Ar-**CH**₂-N-**CH**₂CH₂), 2.41 (t, $^3J(\text{H,H})=6$ Hz, 4H, CH₂-**CH**₂-N-**CH**₂-CH₂), 2.01 (s, 3H, CH₃), 1.77 (s, 2H, NH), 1.63 (q, $^3J(\text{H,H})=6$ Hz, 4H, CH₂**CH**₂CH₂). $^{13}\text{C-RMN}$ (**d** in CDCl_3 , ppm): 140.6, 128.0, 126.3, 124.4, 55.9, 52.8, 45.0, 40.9, 27.5. ESI-MS: $m/z=248$ ($\text{M}+\text{H}^+$).

H33m (3,7,11-Triaza-bicyclo[11.3.1]heptadeca-1(16),13(17),14-triene): 76% yield in detosylation step.

IR (KBr pellet, cm^{-1}): 3299 cm^{-1} (NH), 3050, 3024 (C-H arom.), 1450 (C=C ar). ^1H -RMN (CDCl_3 , 298 K): δ = 7.70 ppm (s, 1H, C-**CH**-C ar), 7.23-7.02 (m, 3H, arom.), 3.88 (s, 4H, Ar-**CH**₂-NH), 2.77 (t, J= 3Hz, 4H, Ar-CH₂-N-**CH**₂CH₂), 2.54 (t, J= 3Hz, 4H, CH₂-**CH**₂-N-**CH**₂-CH₂), 1.70 (m, 7H, CH₂**CH**₂CH₂ (4H), NH (3H)). ^{13}C -RMN (CDCl_3 , 298 K): δ = 141.25 ppm (ar**C**-CH₂), 127.97, 126.97, 124.60 (arom.), 52.89 (Ar-**CH**₂-NH), 46.54 (ArCH₂-NH-**CH**₂), 44.11 (CH₂**CH**₂NH**CH**₂CH₂) 29.10 (CH₂**CH**₂CH₂). Elemental analysis calcd for C₁₄N₆H₂₃.0.5H₂O: C 69.4 N 17.3 H 10.0; found: C 69.8 N 17.2 H 10.4. MS (FAB): m/z = 234.0 (M+H⁺)

H22m (3,6,9-Triaza-bicyclo[9.3.1]pentadeca-1(14),11(15),12-triene): 70% yield in detosylation step. IR (KBr pellet, cm^{-1}): 3301 cm^{-1} , 3215 (NH), 3052, 3024 (C-H arom.), 1446 (C=C ar). ^1H -RMN (CDCl_3 , 298 K): δ = 8.26 ppm (s, 1H, C-**CH**-C ar), 7.26-6.99 (m, 3H, arom.), 3.90 (s, 4H, Ar-**CH**₂-NH), 2.71 (t, J= 3Hz, 4H, Ar-CH₂-N-**CH**₂CH₂), 2.08 (m, 4H, CH₂-**CH**₂-NH-**CH**₂-CH₂), 2.01 (s, 3H, NH). ^{13}C -RMN (CDCl_3 , 298 K): δ = 142.28 ppm (ar**C**-CH₂), 127.64, 126.39, 125.87 (arom.), 53.41 (Ar-**CH**₂-NH), 48.39, 47.56 (NH-**CH**₂). MS (FAB): m/z = 206 (M+H⁺).

H33p (3,7,11-triaza-bicyclo[11.2.2]heptadeca-1(16),13(17),14-triene): 79 % yield in detosylation step. ^1H -NMR (**d** in CDCl_3 , ppm): 7.32 ppm (s, 4H, **CH** ar), 3.72 (s, 4H, Ar-**CH**₂-NH), 2.48 (t, $^3J(\text{H,H})=6$ Hz, 4H, Ar-CH₂-N-**CH**₂CH₂), 2.16 (t, $^3J(\text{H,H})=6$ Hz, 4H, CH₂-**CH**₂-N-**CH**₂-CH₂), 1.38 (q, $^3J(\text{H,H})=6$ Hz, 4H, CH₂**CH**₂CH₂), 1.10 (s, 3H, NH). ^{13}C -RMN (**d** in CDCl_3 , ppm): 140.3, 129.3, 53.1, 45.5, 41.7, 30.2. ESI-MS: m/z= 234 (M+H⁺)

H33o (6,7,8,9,10,11,12,13,14,15-Decahydro-5H-6,10,14-triaza-benzocyclotridecene): 63% yield in detosylation step. IR (KBr pellet, cm^{-1}): 3357 (s), 3016 (m), 2919 (s), 2813 (s), 1468 (s), 1115 (s), 744 (s). $^1\text{H-NMR}$ (**d** in CDCl_3 , ppm): 7.26 (m, 4H, **CH** ar), 3.77 (s, 4H, Ar-**CH**₂-NH), 2.73 (m, 8H, N-**CH**₂CH₂), 2.41 (t, $^3J(\text{H,H})=6$ Hz, 4H, CH₂-**CH**₂-N-**CH**₂-CH₂), 2.34 (s, 3H, NH), 1.70 (q, $^3J(\text{H,H})=6$ Hz, 4H, CH₂**CH**₂CH₂). $^{13}\text{C-RMN}$ (**d** in CDCl_3 , ppm): 139.1, 131.1, 127.6, 53.6, 48.1, 48.0, 27.7. ESI-MS: $m/z = 234$ ($\text{M}+\text{H}^+$).

Me33m (3,7,11-Trimethyl-3,7,11-triaza-bicyclo[11.3.1]heptadeca-1(16),13(17),14-triene): ligand H33m (0.35g, 1.5 mmol) is dissolved in 4.8 mL of formaldehyde 35-40% and 3.5 mL of formic acid 85%. Solution is refluxed for 24 hours, solvent is evaporated and extraction with $\text{CHCl}_3/\text{NaOH}(\text{aq})30\%$ and column chromatography purification (silica gel, $\text{CH}_2\text{Cl}_2/\text{MeOH}/\text{NH}_4\text{OH}$ 99/1/0.5) gives 0.23 g (0.85 mmol) of ligand Me33m (56% yield).

IR (KBr): 3055 cm^{-1} (C-H arom.), 2779 (**CH**₃-N), 1456 (C=C ar)
 $^1\text{H-RMN}$ (CDCl_3 , 298 K): $\delta = 7.64$ ppm (s, 1H, C-**CH**-C ar), 7.26-7.05 (m, 3H, arom.), 3.53 (s, 4H, Ar-**CH**₂-N-), 2.36 (s, 6H, Ar-CH₂-N-**CH**₃), 2.25 (m, 8H, CH₂-**CH**₂-N-), 1.96 (s, 3H, CH₂CH₂N(**CH**₃)CH₂CH₂), 1.52 (m, 4H, CH₂**CH**₂CH₂). $^{13}\text{C-RMN}$ (CDCl_3 , 298 K): $\delta = 139.22$ ppm (**arC**-CH₂), 128.97, 127.64, 127.31 (arom.), 63.29 (Ar-**CH**₂-N-), 55.04 (Ar-CH₂-N-**CH**₃), 52.58 (Ar-CH₂-N-**CH**₂-), 43.57 (CH₂**CH**₂N(**CH**₃)**CH**₂CH₂), 42.50 (CH₂CH₂N(**CH**₃)CH₂CH₂), 25.00 (CH₂**CH**₂CH₂). MS(FAB): $m/z = 276$ ($\text{M}+\text{H}^+$)

Synthesis of complexes. [(H32m-C)Cu^{III}](ClO₄)₂ (**1**-(ClO₄)₂). Equimolar amounts of ligand H32m (0.03 g, 1.4x10⁻⁴ mol) and Cu^{II}(ClO₄).6H₂O (0.051 g, 1.4x10⁻⁴ mol) are dissolved in CH₃CN (3 mL). After 30 minutes, the yellow solution was filtered through Celite®. Slow diffusion of diethyl ether into the filtrated solution allowed the formation of yellow crystals in 49% isolated yield (0.032 g, 7x10⁻⁵ mol) after 24 hours. Same procedure can be used with Cu^{II}(OTf)₂ salt obtaining same isolated yield. X-Ray quality crystals of **1**-(ClO₄)₂ were obtained by recrystallization in CH₃CN/ether and its XRD registered.

Complexes [(H₂Me33m-C)Cu^{III}](ClO₄)₂ (**2**-(ClO₄)₂) and [(H33m-C)Cu^{III}](ClO₄)₂ (**3**-(ClO₄)₂) are obtained with same procedure and yields, and are isolated as orange crystals. X-Ray quality crystals were also obtained for **2**-(ClO₄)₂ and **3**-(OTf)₂.

[(H32m-C)Cu^{III}](ClO₄)₂ (**1**-(ClO₄)₂). ESI-MS (CH₃CN): 380 [(1-(ClO₄)]⁺; UV/Vis (CH₃CN): λ_{max} (ε) = 273 (6900), 409 nm (280); ¹H NMR (500 MHz, CD₃CN, 25 °C): δ = 7.28 (t, ³J(H,H)=7.5 Hz, 1H; Hy), 7.03 (d, ³J(H,H)=2.5 Hz, 1H; Hx), 7.01 (d, ³J(H,H)=2.5 Hz, 1H; Hx), 6.85 (m, 1H; Hα), 5.96 (m, 1H; Hβ), 4.65 (d, ²J(H,H)=15.3 Hz, 1H; Ha1), 4.60 (m, 2H; Ha1', Ha2'), 4.51 (d, ²J(H,H)=15.3 Hz, 1H; Ha2), 4.18 (m, 1H; Hy), 3.48 (dt, ³J(H,H)=4.2 Hz, ²J(H,H)=12.6 Hz, 1H; Hc2'), 3.37 (td, ³J(H,H)=4 Hz, ²J(H,H)=9 Hz, 1H; Hb1'), 3.24 (dd, ³J(H,H)=3.5 Hz, ²J(H,H)=9 Hz, Hb2'), 3.13 (m, 3H; Hb1, Hb2, Hd1), 2.97 (qd, ³J(H,H)=4.2 Hz, ²J(H,H)=8.6 Hz, 1H; Hc1'), 2.75 (q, ³J(H,H)=12 Hz, 1H; Hd2), 2.17 (m, 1H; Hc1), 1.65 (m, 1H; Hc2); elemental analysis calcd for C₁₃H₂₀N₃CuCl₂O₈ (%): C 32.5 H 4.2 N 8.7; found: C 32.9 H 4.0 N 8.6.

[(H₂Me33m-C)Cu^{III}](ClO₄)₂ (2-(ClO₄)₂). ESI-MS (CH₃CN): 408 [2-(ClO₄)]⁺; UV/Vis (CH₃CN): λ_{max} (ϵ) = 291 (7500), 440 nm (sh, 250); ¹H NMR (500 MHz, CD₃CN, 25 °C): δ = 7.27 (t, ³J(H,H)=6.5 Hz, 1H; H_Y), 6.95 (d, ³J(H,H)=6.5 Hz, 2H; H_Z), 6.33 (m, 2H; H α), 4.67 (d, ²J(H,H)=16 Hz, 2H; H_{a1}), 4.52 (d, ²J(H,H)=16 Hz, 2H; H_{a2}), 3.24 (m, 2H; H_{d2}), 3.08 (m, 2H; H_{d1}), 3.05 (m, 2H; H_{b1}), 2.73 (s, 3H; H_e), 2.66 (dt, ³J(H,H)=3.3 Hz, ²J(H,H)= 13.3 Hz, 2H; H_{b2}), 2.15 (m, 2H; H_{c1}), 1.95 (m, 2H; H_{c2}); elemental analysis calcd for C₁₅H₂₄N₃CuCl₂O₈ (%): C 35.4 H 4.7 N 8.3; found: C 35.7 H 4.4 N 8.4.

[(H33m-C)Cu^{III}](ClO₄)₂ (3-(ClO₄)₂). ESI-MS (CH₃CN): 394 [3-(ClO₄)]⁺; UV/Vis (CH₃CN): λ_{max} (ϵ) = 280 (8200), 448 nm (sh, 280); ¹H NMR (500 MHz, CD₃CN): δ = 7.27 (t, ³J(H,H)=7.5 Hz, 1H; H_Y), 6.95 (d, ³J(H,H)=7.5 Hz, 2H; H_Z), 6.12 (m, 2H; H α), 4.61 (dd, ³J(H,H)= 5Hz, ²J(H,H)=16 Hz, 2H; H_{a1}), 4.49 (dd, ³J(H,H)=7.9 Hz, ²J(H,H)=16 Hz, 2H; H_{a2}), 3.14 (m, 1H; H β), 3.09 (m, 4H; H_{b1}, H_{b2}), 2.99 (dq, ³J(H,H)= 3.5 Hz, ²J(H,H)=12.7, 2H; H_{d1}), 2.63 (dq, ³J(H,H)=1.9 Hz, ²J(H,H)= 12.9 Hz, 2H; H_{d2}), 2.04 (m, 2H; H_{c2}), 1.77 (m, 2H; H_{c1}); elemental analysis calcd for C₁₄H₂₃N₃CuCl₂O₈ (%): C 33.9 H 4.7 N 8.5; found: C 34.1 H 4.7 N 8.4.

[(H33m-C)Cu^{III}(Cl)](OTf) (4-(OTf)): 0.022 g (0.037 mmol) of complex **3**-(OTf)₂ were dissolved in 2 mL of CH₃CN and 1 equivalent of NaCl (0.0022 g) was added in H₂O. Solution turns from orange to red instantaneously. After 30 min stirring, solution is filtered and diethyl ether diffusion allowed the formation of red crystals in 73 % isolated yield. IR (KBr pellet, cm⁻¹): 3126, 3090, 3033, 2926, 2854, 1459, 1423, 1144, 1116, 1078, 627. UV/Vis (CH₃CN): λ_{max} (ϵ) = 375 nm (1900), 522 (540); ¹H NMR (400 MHz, CD₃CN, 25 °C): δ

= 7.12 (t, $^3J(\text{H,H}) = 7.5$ Hz, 1H), 6.81 (d, $^3J(\text{H,H}) = 3.6$ Hz, 2H), 6.07 (m, 2H; NH), 4.38 (m, 2H), 4.25 (m, 2H), 3.14 (m, 3H), 2.80 (m, 6H), 1.89 (m, 1H), 1.70 (m, 2H). ^{13}C NMR (400 MHz, CD_3CN , 25 °C): $\delta = 179.5, 145.6, 128.4, 121.9, 61.9, 51.6, 48.2, 26.4$.

Crystals suitable for X-Ray diffraction were obtained for complex $[(\text{H33m-C})\text{Cu}^{\text{III}}(\text{Cl})](\text{ClO}_4)$ (**4-(ClO₄)**), synthesized by same procedure.

$[(\text{H33m-C})\text{Cu}^{\text{II}}]_2(\text{m-Cl})](\text{PF}_6) \cdot 6\text{H}_2\text{O} \cdot \text{CH}_2\text{Cl}_2$ (**6-(PF₆)**) $\cdot 6\text{H}_2\text{O} \cdot \text{CH}_2\text{Cl}_2$): Ligand H33m (0.038 g, 0.163 mmol) and $[\text{Cu}^{\text{I}}(\text{CH}_3\text{CN})_4](\text{PF}_6)$ (0.061 g, 0.163 mmol) were dissolved with 2 mL of anhydrous CH_2Cl_2 under Ar atmosphere. White powder is filtered out and dichloromethane solution is stored at 248 K for 2 weeks, until the appearance of small crystals of complex **6** (<5% yield). IR (KBr pellet, cm^{-1}): 3217, 3130, 1507, 1465, 1423, 1072, 841, 557. Crystals suitable for X-Ray Diffraction.

$[(\text{H32m})\text{Cu}^{\text{I}}](\text{OTf})$ (**7-OTf**): synthesis was carried out under N_2 or Ar. Equimolar amounts of ligand H32m (0.03 g, 1.36×10^{-4} mol) and $\text{Cu}^{\text{I}}(\text{CH}_3\text{CN})_4(\text{OTf})$ (0.052 g, 1.4×10^{-4} mol) are dissolved in 2 mL CH_3CN . After 15 minutes stirring, white compound is precipitated by addition of diethyl ether. Solid is filtered out and dried under vacuum in 95% yield (0.056 g). Same procedure is used to synthesize complex $[(\text{H}_2\text{Me33m})\text{Cu}^{\text{I}}](\text{OTf})$ (**8-OTf**), $[(\text{H33m})\text{Cu}^{\text{I}}](\text{OTf})$ (**9-OTf**) as well complexes **7-9** with PF_6^- and ClO_4^- counteranions.

Complex (**7-OTf**). ^1H NMR (500 MHz, CD_3CN , 25°C): 7.94 (s, 1H; CH), 7.27 (t, $^3J(\text{H,H}) = 9.5$ Hz, 1H; CH), 7.14 (d, $^3J(\text{H,H}) = 10$ Hz, 1H; CH), 7.06 (d, $^3J(\text{H,H}) = 9$ Hz, 1H; CH), 3.86 (s, 2H; CH_2), 3.84 (s, 2H, CH_2), 2.88 (m, 2H; CH_2),

2.77 (m, 4H; CH₂), 2.60 (m, 3H; NH), 2.57 (m, 2H; CH₂), 1.48 (q, ³J(H,H)= 6.9 Hz, 2H; CH₂).

[(H₂Me33m)Cu^I](OTf) (8-OTf). ¹H NMR (200 MHz, CD₃CN, 25 °C): 7.77 (s, 1H; CH), 7.28 (t, ³J(H,H)=8 Hz, 1H; CH), 7.13 (d, ³J(H,H)= 8 Hz, 2H; CH), 3.88 (s, 4H; CH₂), 2.60 (m, 4H; CH₂), 2.50 (t, ³J(H,H)= 6 Hz, 4H; CH₂), 2.27 (s, 3H; NH), 2.07 (s, 3H; CH₃), 1.62 (q, ³J(H,H)= 6 Hz, 4H; CH₂).

[(H33m)Cu^I](OTf) (9-PF₆). ¹H NMR (200 MHz, CD₃CN, 25 °C): 7.89 (s, 1H; CH), 7.32 (t, ³J(H,H)=8 Hz, 1H; CH), 7.16 (d, ³J(H,H)= 8 Hz, 2H; CH), 3.88 (s, 4H; CH₂), 2.83 (m, 4H; CH₂), 2.73 (m, 4H; CH₂), 2.61 (s, 3H; NH), 1.64 (q, ³J(H,H)= 6 Hz, 4H; CH₂).

[(H22m)₂Cu^I]₂(PF₆)₂: synthesis was carried out under N₂ or Ar. Equimolar amounts of ligand H22m (0.03 g, 1.46x10⁻⁴ mol) and Cu^I(CH₃CN)₄(OTf) (0.054 g, 1.46x10⁻⁴ mol) are dissolved in 2 mL CH₂Cl₂. After 15 minutes stirring, white compound is precipitated by addition of diethyl ether. Solid is filtered out and dried under vacuum in 80% yield (0.048 g). ¹H NMR (500 MHz, CH₂Cl₂, 300 K): 8.80 (s, 1H), 7.27 (t, 1H), 7.14 (d, 1H), 4.25 (s, 2H), 3.50 (s, 2H), 2.75 (s, 2H), 2.45 (s, 2H), 2.25 (s, 2H), 1.50 (s, 2H).

[(H33m(D))Cu^I](PF₆). **H/D exchange reaction.** Ligand H33m (0.04 g, 0.17 mmol) and [Cu^I(CH₃CN)₄](PF₆) (0.064 g, 0.17 mmol) were dissolved in 3 mL of deuterated acetone[D6] and stirred under Ar atmosphere for 5 days. Complete H/D exchange is determined by ¹H NMR, so quantitative formation is estimated. Complex has been characterized in situ by ¹H-NMR and ESI-MS.

¹H NMR (200 MHz, CDCl₃, 25 °C): δ = 7.30 (t, 1H), 7.20 (d, 2H), 3.94 (s, 4H), 3.24 (m, 4H), 2.92 (m, 4H), 1.82 (m,

4H), 2.80 (m, 6H), 1.89 (m, 1H), 1.70 (m, 2H). ESI-MS (CH_3CN , m/z): 297 $[(\text{H}33\text{m}(\text{D}))\text{Cu}^{\text{I}}]^+$, 235 $\text{H}33\text{m}(\text{D})+\text{H}^+$.

H33m(D) synthesis. Complex $[(\text{H}33\text{m}(\text{D}))\text{Cu}^{\text{I}}](\text{PF}_6)$ formed in situ in acetone- d_6 (0.17 mmol H33m and 0.17 mmol $[\text{Cu}^{\text{I}}(\text{CH}_3\text{CN})_4](\text{PF}_6)$) was treated with 2.5 equivalents of 1,10-phenanthroline (phen) (0.077 g, 0.429 mmol) dissolved in 1 mL CH_2Cl_2 . Partial precipitation of complex $[(\text{phen})_2\text{Cu}^{\text{I}}](\text{PF}_6)$ was filtered out and solution dried under vacuum. Column chromatography on silica gel ($\text{CH}_2\text{Cl}_2/\text{CH}_3\text{OH}/\text{NH}_4\text{OH}$ 70/30/5) was performed to purify H33m(D) from phen complex and excess phen, obtaining 0.018 g (0.077 mmol, 45% isolated yield).

^1H NMR (200 MHz, CDCl_3 , 25 °C): δ = 7.21 (t, $^3J(\text{H},\text{H})=6$ Hz, 1H), 7.04 (d, $^3J(\text{H},\text{H})=8$ Hz, 2H), 3.88 (s, 4H), 2.81 (t, $^3J(\text{H},\text{H})=6$ Hz, 4H), 2.57 (t, $^3J(\text{H},\text{H})=6$ Hz, 4H), 2.06 (s, 3H), 1.70 (q, $^3J(\text{H},\text{H})=6$ Hz, 4H). ESI-MS (CH_3CN , m/z): 235 $\text{H}33\text{m}(\text{D})+\text{H}^+$.

$[(\text{H}33\text{m}-\text{C})\text{Ni}^{\text{III}}](\text{NO}_3)_2$. Ligand H33m (0.021 g, 0.086 mmol) and $\text{Ni}^{\text{II}}(\text{NO}_3)_2 \cdot 6\text{H}_2\text{O}$ (0.026, 0.086 mmol) were dissolved in 2 mL of CH_3CN and stirred under Ar. Solution changes from green to orange gradually. After 12 hours, diethyl ether diffusion allowed formation of yellow-orange microcrystalline powder of organonickel(III) complex in 30% isolated yield (0.011 g, 0.027 mmol).

IR (KBr pellet, cm^{-1}): 3187 (NH), 1460, 1427 (C=C ar), 1383 (NO_3). Elemental analysis calcd for $\text{C}_{14}\text{H}_{22}\text{N}_5\text{NiO}_6$ (%): C 40.5 H 5.3 N 16.9; found: C 40.7 H 5.5 N 16.8. ESI-MS (CH_3CN , m/z): 352 $[(\text{H}33\text{m}-\text{C})\text{Ni}^{\text{III}}](\text{NO}_3)^+$.

Mass Spectrometry. ESI-MS spectra were performed with a Thermo Quest Finigan Navigator LC/MS, that bears an atmospheric pressure ionization source (API-MS), and using

the positive ionization mode (ESI⁺). Typical experimental conditions were: solvent = CH₃CN 100%, source voltage = 30 eV, temperature = 170 °C, Flux = 150 μl/min, mass range = 100-1000, 10-15 scans per LC peak and registration under profile peak format.

FAB-MS spectra were performed with a Fisons VG-Quattro (Cs tube, 10 kV voltage, 3-nitrobenzylalcohol matrix).

NMR Spectroscopy. Bruker DPX200 Model Avance (4.7 T) was used to obtain ¹H and ¹³C NMR spectra of all ligands. NMR data of diamagnetic copper complexes were registered in a Bruker Avance-500. Sensitive copper samples were treated under controlled Ar atmosphere using rubber septa for NMR tubes.

UV-Vis experimental procedure. A Varian Cary-50 Scan and Polytec PI X-DAP-06 spectrophotometers were used to perform electronic spectra. Custom-designed immersible quartz fiber-optic probe (Hellma) in custom designed sample cells (ChemGlass) were used to perform experiments under anhydrous/anoxic conditions. Stock solutions of ligands were injected to the cell under continuous stirring and electronic spectra simultaneously registered. Cell temperature was thermostated with a FTS and a Huber CC180 cryostats. Experiments were focused on 640 nm band attributed to Cu^{II} d-d transitions. Its decay has been used to measure the extent of the disproportionation reaction in all systems studied.

Electrochemical experiments. CV experiments have been performed using a glassy-carbon disc as working electrode (0.07 cm²), a calomelans SSCE reference electrode and a Pt wire as auxiliary electrode. Experiments were performed in

acetonitrile solution of TBAP 0.2 M (supporting electrolyte) under controlled Ar atmosphere.

Coulometry experiments were performed in a similar way but using a graphite electrode as working electrode.

X-Ray Diffraction Analysis. Analyses on a block yellow crystal of **1**-(ClO₄)₂, a orange crystal of **3**-(OTf)₂ and a parallepiped dark red crystal of **4**-(ClO₄) was carried out on a STOE imaging plate diffraction system (I.P.D.S) with graphite monochromated Mo K α radiation (λ = 0.71073 Å) operating in the *j* scan method. Cell measurement temperature was 180(2) K for **1**-(ClO₄)₂, and 160(2) for **3**-(OTf)₂ and **4**-(ClO₄). Structures were solved by direct methods using the SIR92³⁰ and refined by least-squares procedures on a F² with the aid of SHELXL97.³¹

Statistical disorder has been found in complex **1** for the atoms labeled N2 and C5, which have been located on two sites with a ratio of occupancy close to 50%. Disordered perchlorate O atoms are found in complex **4**-(ClO₄), which contains two almost identical molecules of chloride complex.

Analyses on a block orange crystal of **2**-(ClO₄)₂ and a block pale orange crystal of **6**-(PF₆)₂·6H₂O·CH₂Cl₂ was carried out on a Bruker SMART CCD area detector single crystal diffractometer with graphite monochromated Mo K α radiation (λ = 0.71073 Å) operating in the *w* scan method. Cell measurement temperature was 298(2) K for **2** and **7**. Data reduction, Lorentz, polarization and empirical absorption corrections were performed with the Sadabs package. Structures were solved by direct methods using SHELXS-86³² and refined by full-matrix least-squares analysis with SHELXL-93.³³ Disordered hexafluorophosphate F atoms are found in complex **6**-(PF₆)₂.

A summary of the crystallographic data is given in Table 1.

XAS Analysis. Dry solid samples were diluted in boron nitride and the mixtures ground to fine powder. The mixtures were pressed into 1 mm thick aluminum spacers lined with Mylar tape (X-Ray transparent) windows. X-Ray absorption spectra were measured on unfocused wiggler beamline 7-3 at the Stanford Synchrotron Laboratory (SSRL), with the ring operating at 3 GeV and 50-100 mA. Samples were maintained at 10 K inside an Oxford Instruments CF-1208 liquid helium continuous flow cryostat. A Si(220) double-crystal monochromator was used, detuned 50% at 9868 eV to minimize contamination of the radiation by higher harmonics. Vertical 1 mm pre-monochromator slits were used to define beam size, minimizing beam divergence. K-edge and EXAFS data were measured, for all samples, over the energy range 8650-9868 eV. The monochromator step size in the edge region (8970-9020 eV) was 0.1-0.2 eV, to enhance resolution over this range. Spectra were collected in transmission mode, using N₂ filled ionization chambers to measure the intensity on incident and transmitted radiation. The spectrum of a Cu foil was collected concomitantly, allowing for internal energy calibration of the spectra. The first inflection point for the Cu foil spectra was set to 8980.3 eV. The spectrometer energy resolution was approximately 1.4 eV, with reproducibility in the determination of edge position of <0.2 eV. Two to four scans were averaged for each data set.

Computational details. All calculations were performed with the Amsterdam Density Functional (ADF) program system.³⁴ An uncontracted triple- ξ STO basis set³⁵ was used for copper (cf. Basis set IVA)³⁶. The ligand atoms were represented by a double- ξ STO basis set³⁵ extended with 3d polarization function. The 1s electrons for C and N as well as the 1s,

2s, and 2p electrons on Cu were considered as core electrons and treated by the frozen-core approximation.³⁴ In order to fit the molecular density and to present Coulomb and exchange potentials accurately, a set of auxiliary s, p, d, f, and g STO functions, centered on all nuclei, was introduced.^{37,36}

Geometries were fully optimized with the local density approximation (LDA), which includes the $X\alpha$ exchange³⁸ ($\alpha = 2/3$), together with the electron gas correlation functional (in the Vosko-Wilk-Nusair parametrization³⁹), where according to Stoll *et al.*⁴⁰ Only the correlation between electrons of different spin is used. The molecular geometries were optimized using the analytical energy gradients implemented by Versluis and Ziegler.⁴¹

3.7 REFERENCES

- ¹ B. A. Arndtsen, R. G. Bergman, T. A. Mobley, T. H. Peterson, *Acc. Chem. Res.* **1995**, *28*, 154.
- ² J. P. Collman, L. S. Hegedus, J. R. Norton, R. G. Finke, *Principles and Applications of Organotransition Metal Chemistry*, University Science Books, Sausalito, **1987**, pp. 279-355.
- ³ R. H. Crabtree, *Chem. Rev.* **1995**, *95*, 987-1007.
- ⁴ a) N. F. Gol'dshleger, V. V. Es'kova, A. E. Shilov, A. A. Shteinman, *Zh. Fiz. Khim. (Engl. Transl.)* **1972**, *46*, 785-786; b) A. E. Shilov, G. B. Shul'pin, *Chem. Rev.* **1997**, *97*, 2879-2932.
- ⁵ P. E. M. Siegbahn, R. H. Crabtree, *J. Am. Chem. Soc.* **1996**, *118*, 4442-4450.
- ⁶ S. S. Stahl, J. A. Labinger, J. E. Bercaw, *Angew. Chem.* **1998**, *110*, 2298-2311; *Angew. Chem. Int. Ed.* **1998**, *37*, 2180-2192.
- ⁷ a) R. A. Periana, D. J. Taube, E. R. Evitt, D. G. Loffler, P. R. Wentrcek, G. Voss, T. Masuda, *Science* **1993**, *259*, 340-343; b) M. N. Vargaftik, I. P. Storalov, I. I. Moiseev, *J. Chem. Soc. Chem. Commun.* **1990**, 1049-1050; c) A. Sen, *Acc. Chem. Res.* **1988**, *21*, 421-428; d) S. Nomura, S. Uemura, *J. Chem. Soc. Chem. Commun.* **1994**, 129-130.
- ⁸ M. Brookhart, M. L. H. Green, *J. Organomet. Chem.* **1983**, *250*, 395-408.
- ⁹ E. C. Constable, *Polyhedron* **1984**, *3*, 1037.
- ¹⁰ A. H. Janowicz, R. G. Bergman, *J. Am. Chem. Soc.* **1983**, *105*, 3929.
- ¹¹ a) J. A. Ibers, R. DiCosimo, G. M. Whitesides, *Organometallics* **1982**, *1*, 13; b) M. J. Buchanan, J. M. Styker, R. G. Bergman, *J. Am. Chem. Soc.* **1986**, *108*, 1537-1550.

- ¹² a) J. Chatt, J. M. Davidson, *J. Chem. Soc.* **1965**, 843; b) W. D. Jones, F. J. Feher, *J. Am. Chem. Soc.* **1984**, 106, 1650.
- ¹³ a) J. P. Kleiman, M. Dubeck, *J. Am. Chem. Soc.* **1963**, 85, 1544; b) S. Horie, S. Murahashi, *Bull. Chem. Soc. Jpn.* **1960**, 23, 247.
- ¹⁴ H. Furuta, H. Maeda, A. Osuka, *J. Am. Chem. Soc.* **2000**, 122, 803-807.
- ¹⁵ P. J. Chmielewski, L. Latos-Grazynski, I. Schmidt, *Inorg. Chem.* **2000**, 39, 5475-5482.
- ¹⁶ H. Furuta, T. Ogawa, Y. Uwatoko, K. Araki, *Inorg. Chem.* **1999**, 38, 2676-2682.
- ¹⁷ A. Bencini, M. I. Burguete, E. Garcia-Espana, S. V. Luis, J. F. Miravet, C. Soriano, *J. Org. Chem.* **1993**, 58, 4749-4753.
- ¹⁸ C. Bazzicalupi, A. Bencini, A. Bianchi, V. Fusi, E. Garcia-Espana, P. Paoletti, P. Paoli, B. Valtancoli, *Inorg. Chem.* **1993**, 32, 4900.
- ¹⁹ J. L. DuBois, P. Mukherjee, T. D. P. Stack, B. Hedman, E. I. Solomon, K. O. Hodgson, *J. Am. Chem. Soc.* **2000**, 122, 5775-5787.
- ²⁰ G. A. Mabbot, *J. Chem. Educ.*, **1983**, 60, 697.
- ²¹ 1,10-phenanthroline is an excellent ligand for Cu^I to form the stable [(phen)₂Cu^I]⁺ complex. This complex presents an absorption band at 436 nm ($\epsilon = 5400 \text{ M}^{-1}\text{cm}^{-1}$).
- ²² ESI-MS of the reaction mixture shows clear signals for the fragment [Cu^I(CH₃CN)₂]⁺ and for the ligand H32m+H⁺. No signal corresponding to [(H32mH)Cu^I]²⁺ is found, indicating dissociation of Cu^I complex when the ligand is monoprotonated under ESI-MS experimental conditions. 1H NMR spectrum of final reaction mixture resembles the monoprotonated ligand H32mH spectrum as well as 1H NMR of

complex [(H32m)Cu^I]⁺ after treatment with 1 eq of triflic acid (see Figure S8).

²³ V. Fusi, A. Llobet, J. Mahía, M. Micheloni, P. Paoli, X. Ribas, P. Rossi, in press.

²⁴ G. Golub, H. Cohen, A. Paleotti, L. Bencini, E. Messori, I. Bertini, D. Meyerstein, *J. Am. Chem. Soc.* **1995**, *117*, 8353

²⁵ J. N. Figlar, D. M. Stanbury, *J. Phys. Chem. A* **1999**, *103*, 5732-5741.

²⁶ H. Furuta, T. Ishizuka, A. Osuka, Y. Uwatoko, Y. Ishikawa, *Angew. Chem. Int. Ed.* **2001**, *40*, 2323-2325.

²⁷ E. Nakamura, S. Mori, *Angew. Chem. Int. Ed.* **2000**, *39*, 3750-3771.

²⁸ A. Vigalok, O. Uzan, L. J. W. Shimon, Y. Ben-David, J. M. L. Martin, D. Milstein, *J. Am. Chem. Soc.* **1998**, *120*, 12539-12544.

²⁹ a) M. A. Willert-Porada, D. J. Burton, N. C. Baenziger, *J. Chem. Soc., Chem. Commun.* **1989**, 1633-1634; b) D. Neumann, T. Roy, K. F. Tebbe, W. Crump, *Angew. Chem.* **1993**, *105*, 1555; *Angew. Chem. Ed. Engl.* **1993**, *32*, 1482-1483; c) R. Eujen, B. Hoge, D. J. Brauer, *J. Organomet. Chem.* **1996**, *519*, 7-20.

³⁰ A. Altomare, G. Cascarano, G. Giacovazzo, A. Guagliardi, M. C. Burla, G. Polidori, M. Camalli, SIR92 - a program for automatic solution of crystal structures by direct methods. *J. Appl. Cryst.* **1994**, *27*, 435.

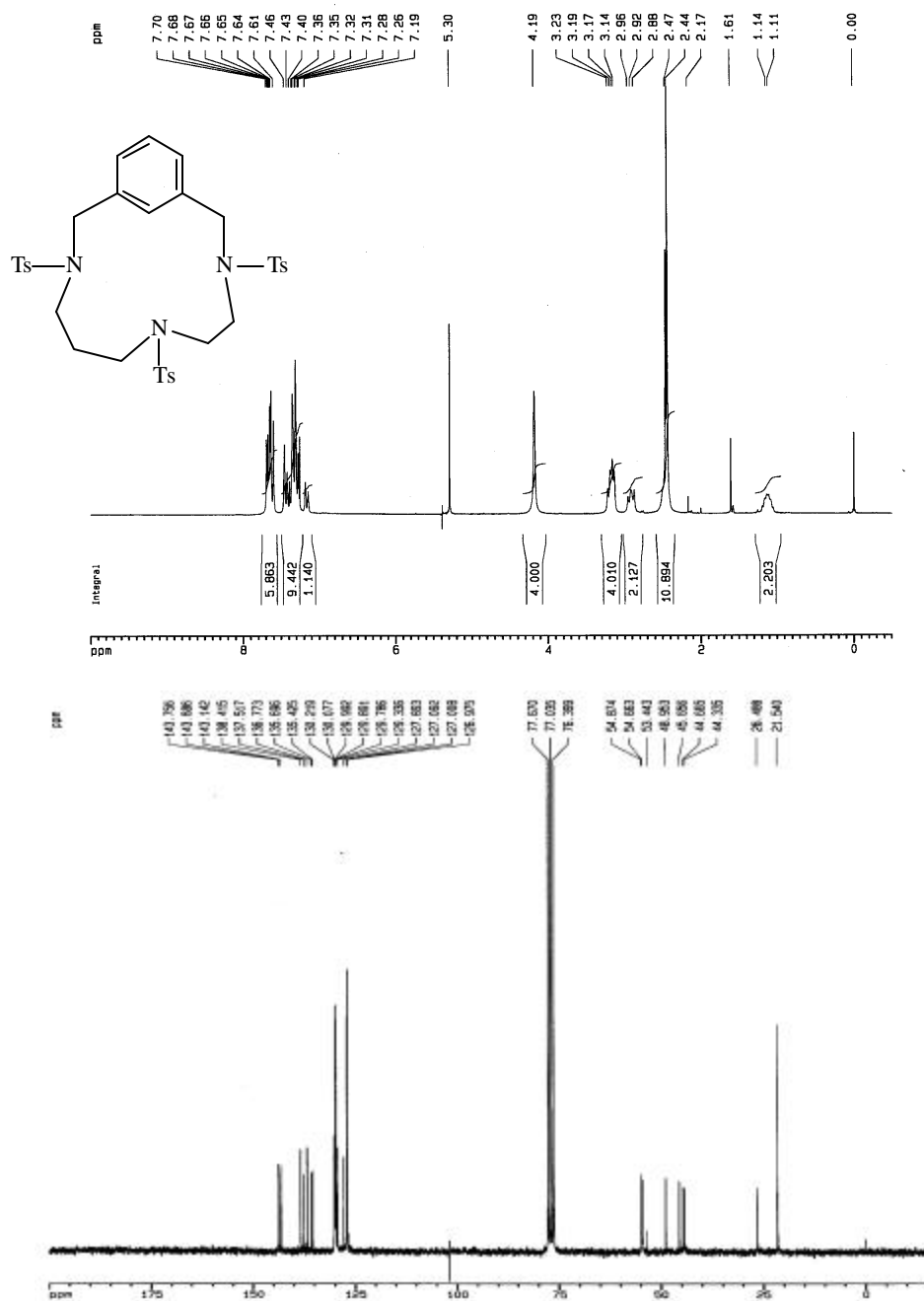
³¹ G. M. Sheldrick, *SHELXS-97*, Computer Program for Crystal Structure Refinement; University of Göttingen, Germany, 1997..

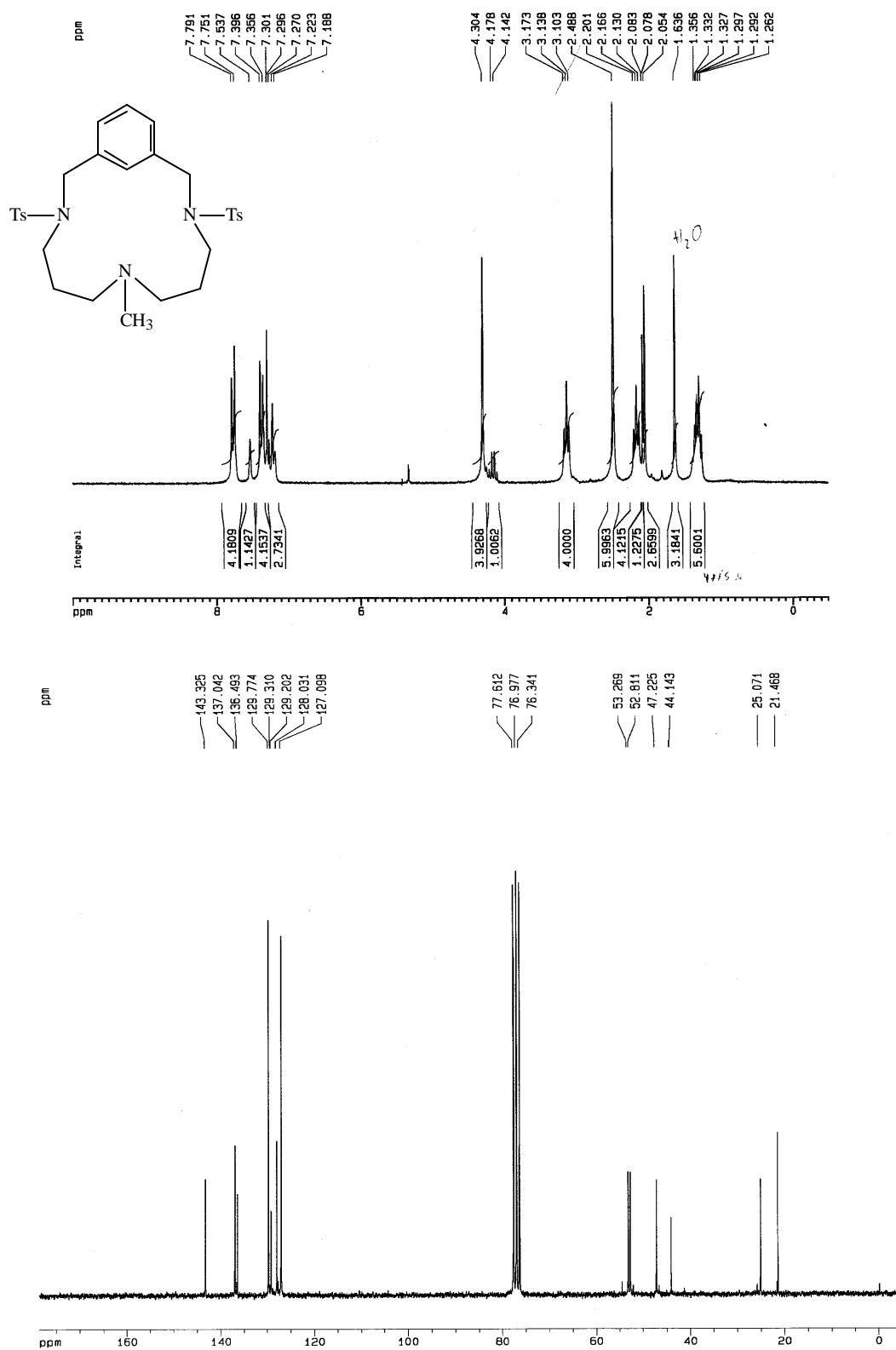
³² G. M. Sheldrick, *SHELXS-86: Program for the Solution of Crystal Structures*; University of Göttingen, Germany, 1986.

³³ G. M. Sheldrick, *SHELXS-93*; University of Göttingen, Germany, 1986.

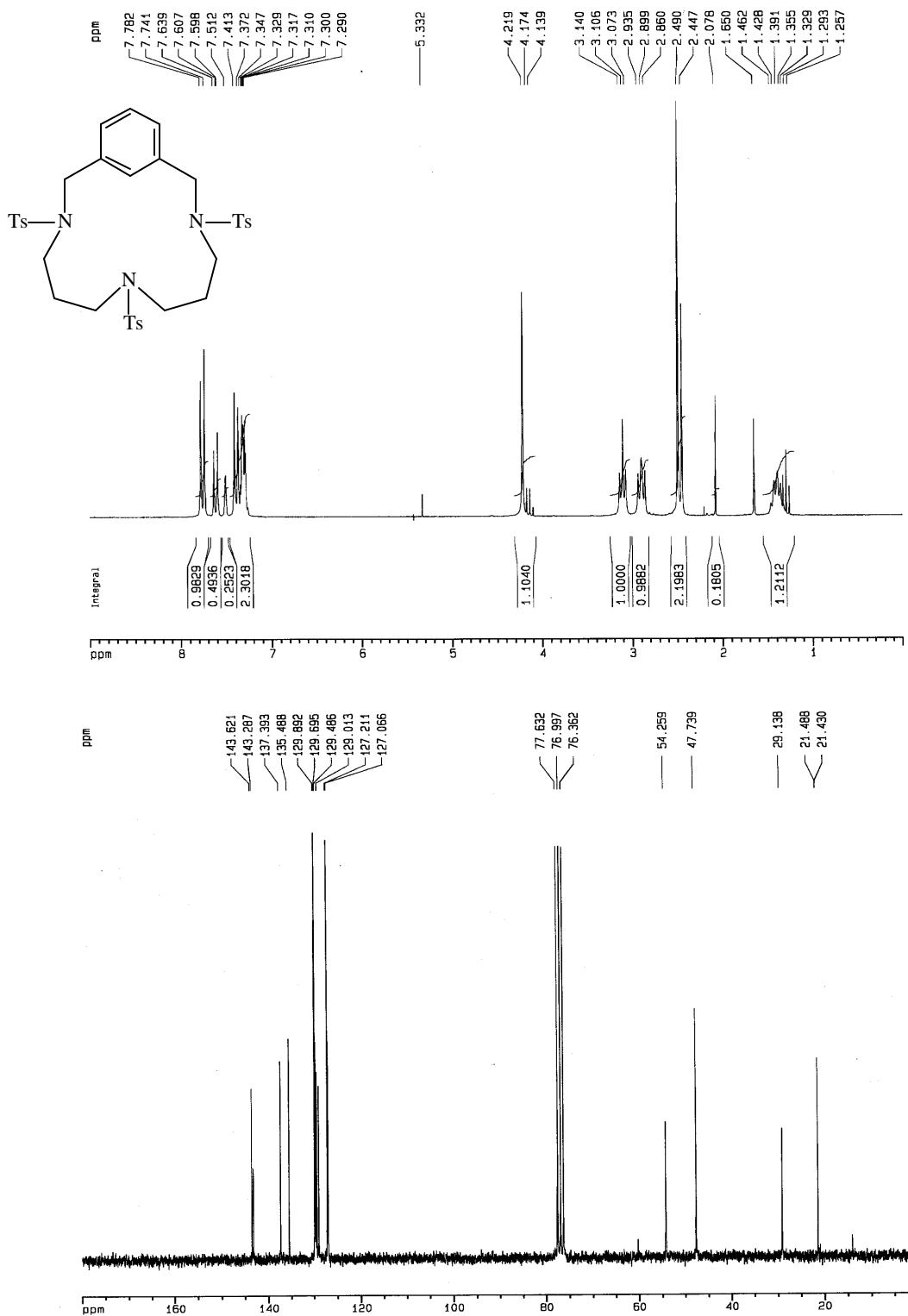
-
- ³⁴ a) E. J. Baerends, D. E. Ellis, P. Ros, *Chem. Phys.* **1973**, 2, 41; b) P. M. Boerrigter, G. te Velde, E. J. Baerends, *Int. J. Quant. Chem.* **1988**, 33, 87; c) G. te Velde, E. J. Baerends, *J. Comput. Phys.* **1992**, 99, 84.
- ³⁵ a) J. G. Snijders, E. J. Baerends, P. Vernooijs, *At. Nucl. Data Tables* **1982**, 26, 483; b) P. Vernooijs, J. G. Snijders, E. J. Baerends, Slater type basis functions for the whole periodic system. Internal report; Free University of Amsterdam, The Netherlands, 1981.
- ³⁶ A. Rosa, A. W. Ehlers, E. J. Baerends, J. G. Snijders, G. te Velde, *J. Phys. Chem.* **1996**, 100, 5690.
- ³⁷ J. Krijn, E. J. Baerends, Fit functions in the HFS-method. Internal report; Free University of Amsterdam, The Netherlands, 1981.
- ³⁸ J. C. Slater, *Quantum Theory of Molecules and Solids*; McGraw-Hill: New York, 1974; Vol. 4.
- ³⁹ S. H. Vosko, L. Wilk, M. Nusair, *Can. J. Phys.* **1980**, 58, 1200.
- ⁴⁰ H. Stoll, E. Golka, H. Preuss, *Theor. Chim. Acta* **1980**, 55, 29.
- ⁴¹ L. Versluis, T. Ziegler, *J. Chem. Phys.* **1988**, 28, 322.

SUPPORTING INFORMATION FOR CHAPTER 3

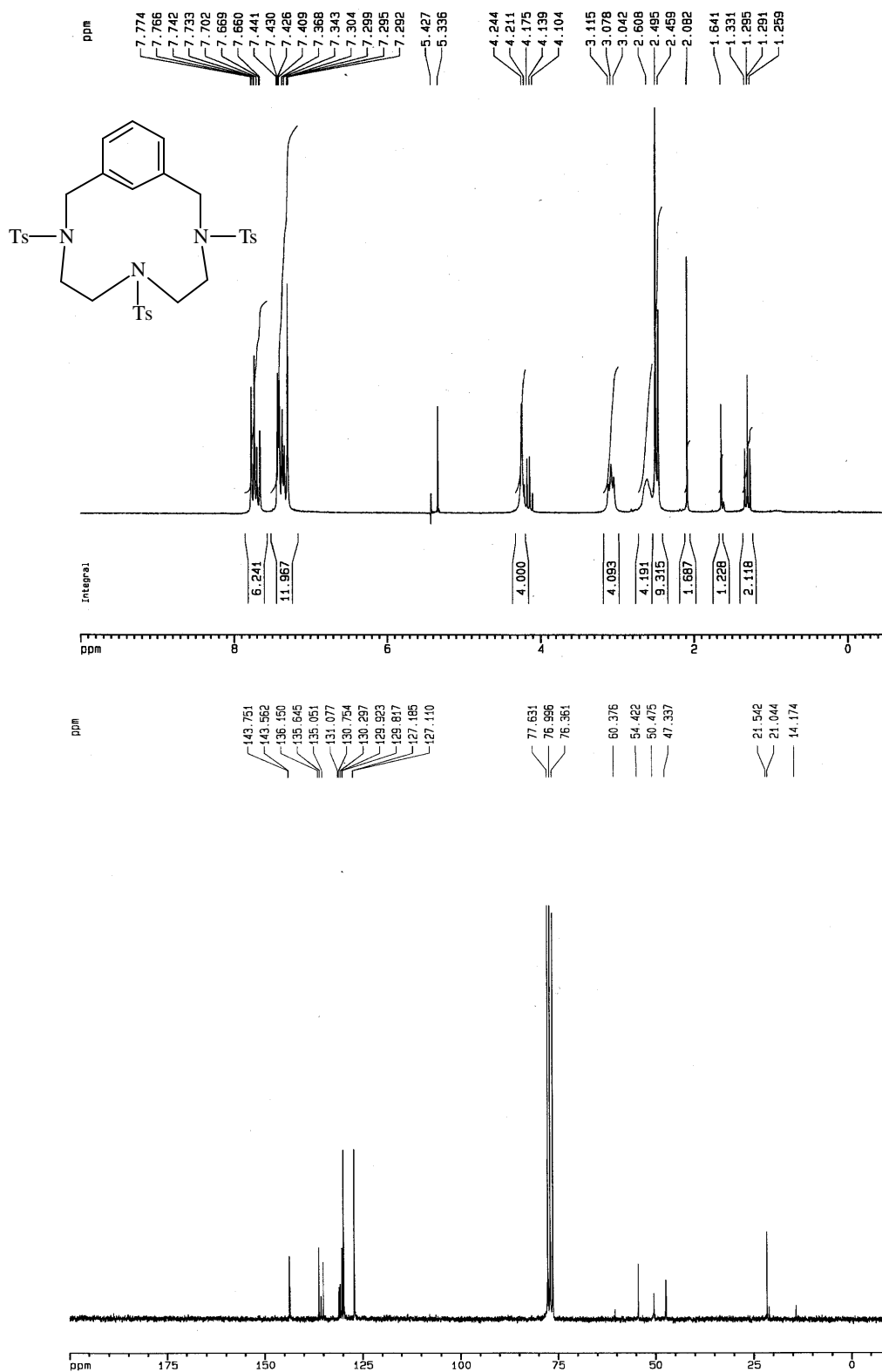
Figure S1. ^1H and ^{13}C characterization of tosylated ligands TsL in CDCl_3 .**Ligand Ts32m**

Ligand Ts₂Me33m

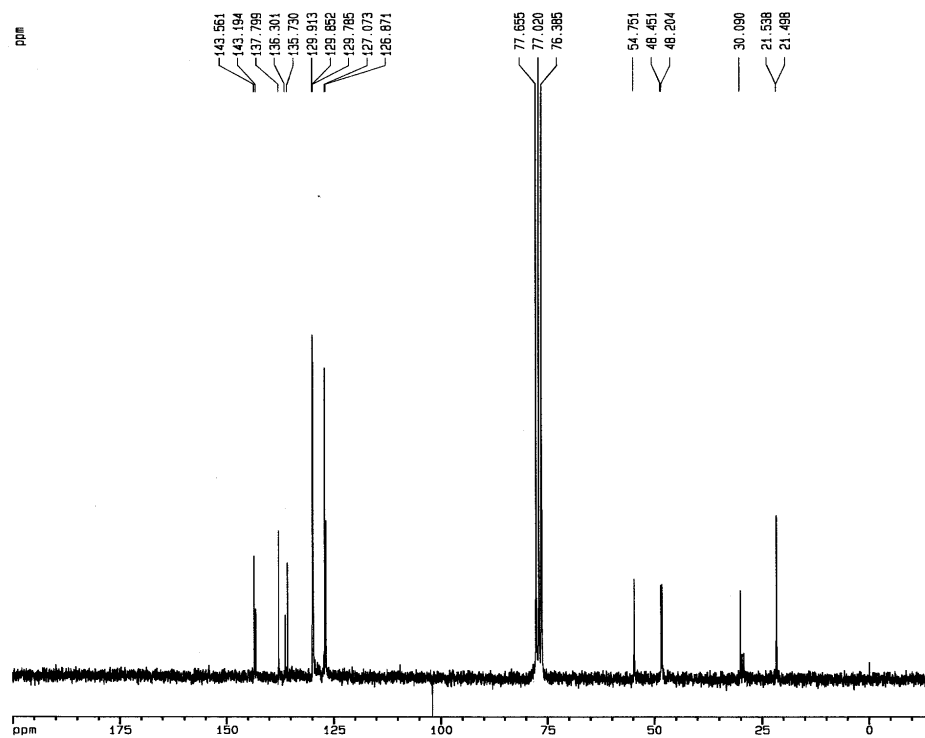
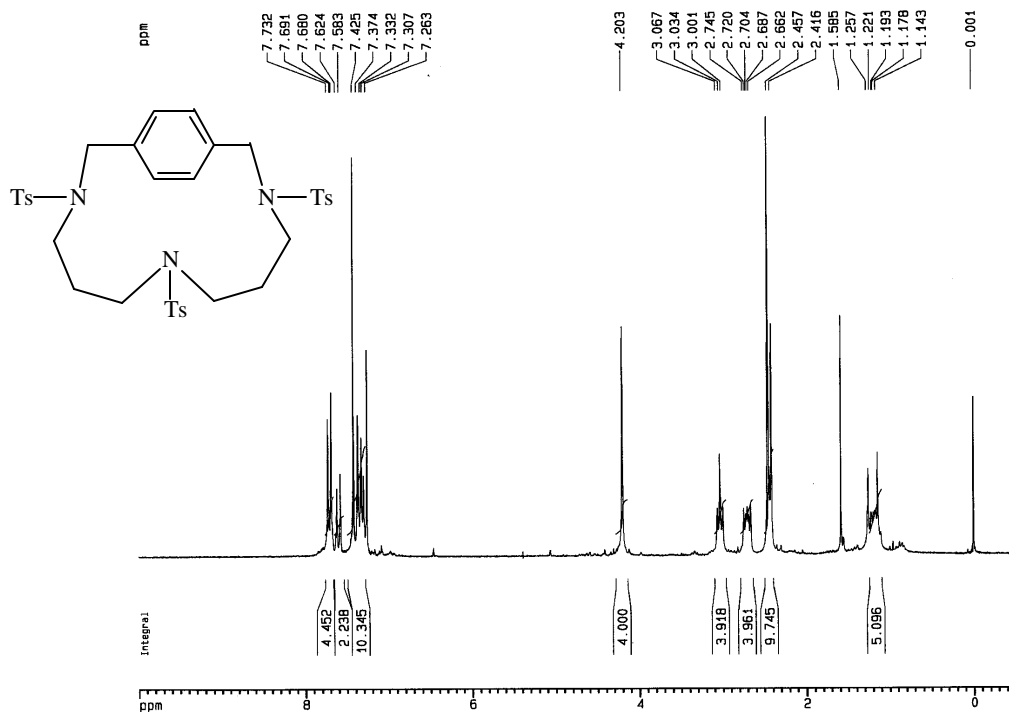
Ligand Ts33m



Ligand Ts22m



Ligand Ts33p



Ligand Ts33o

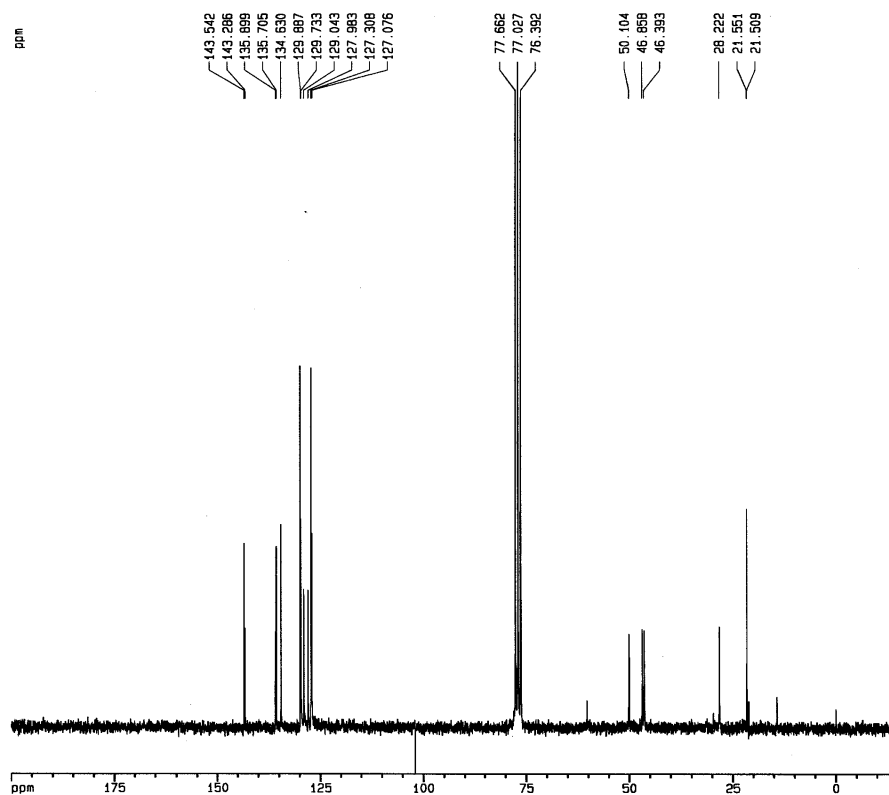
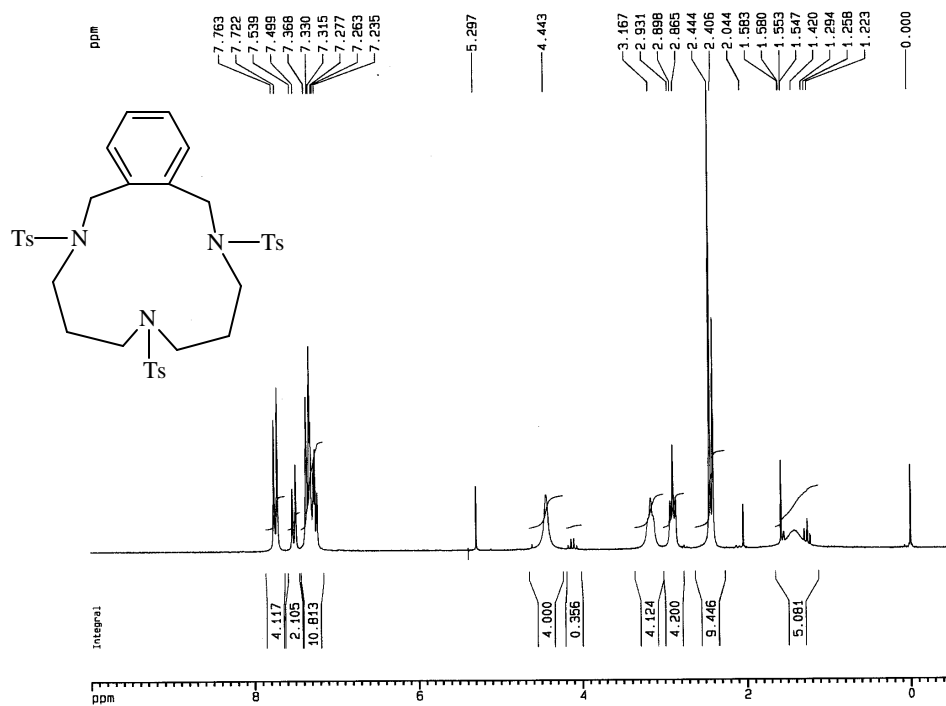
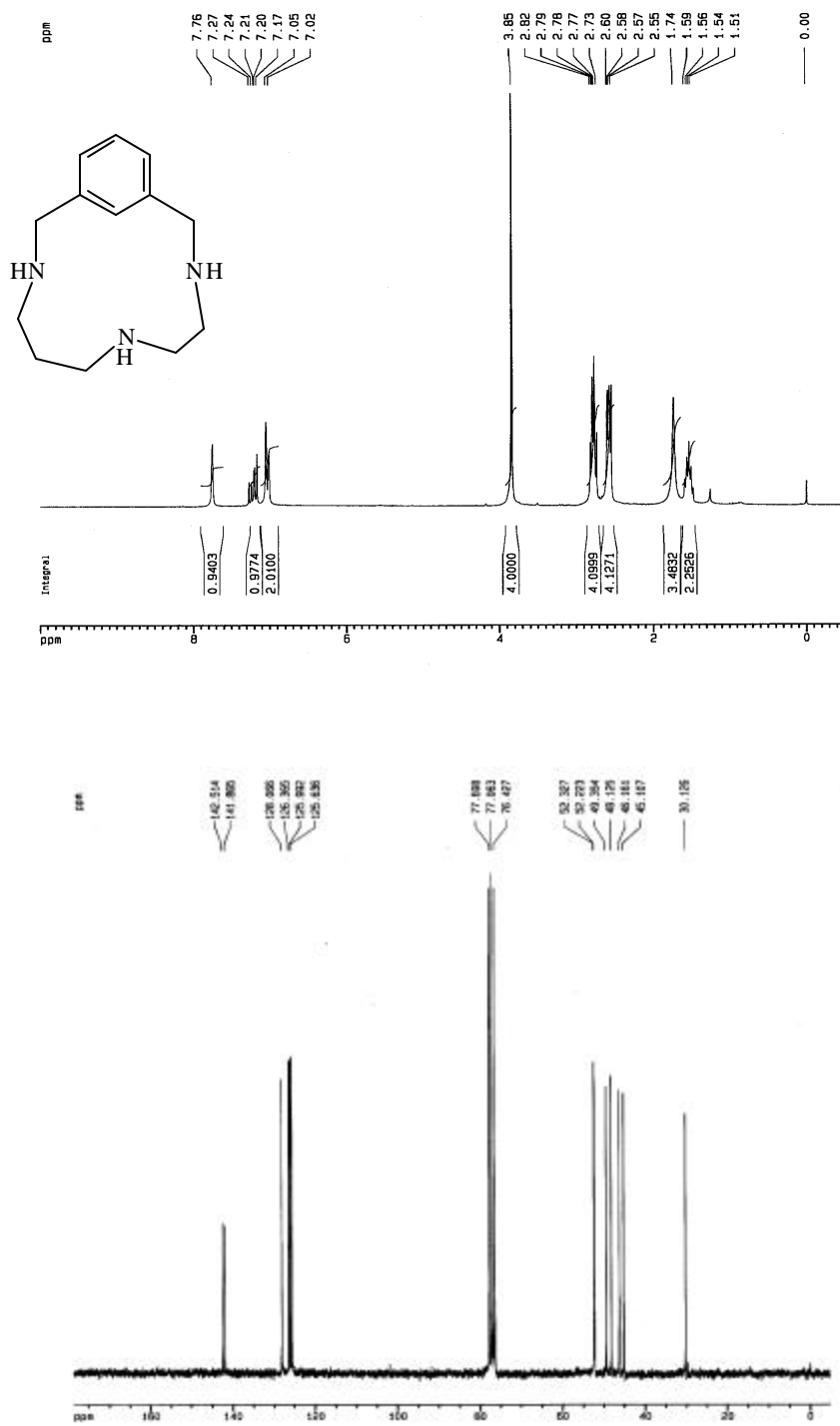
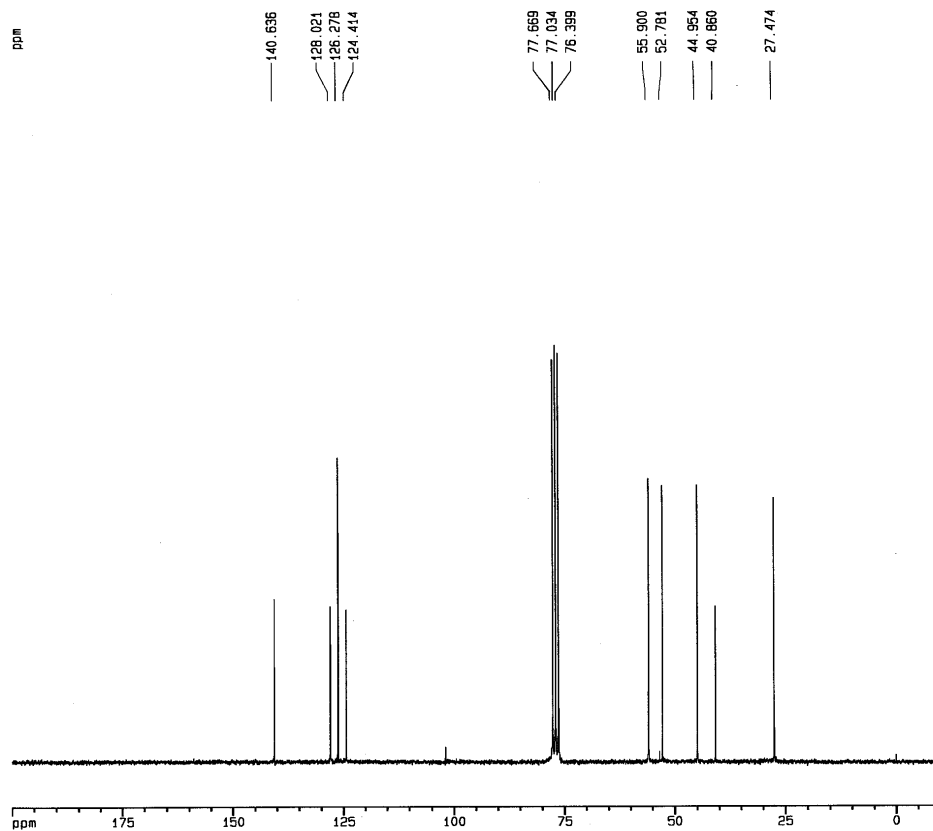
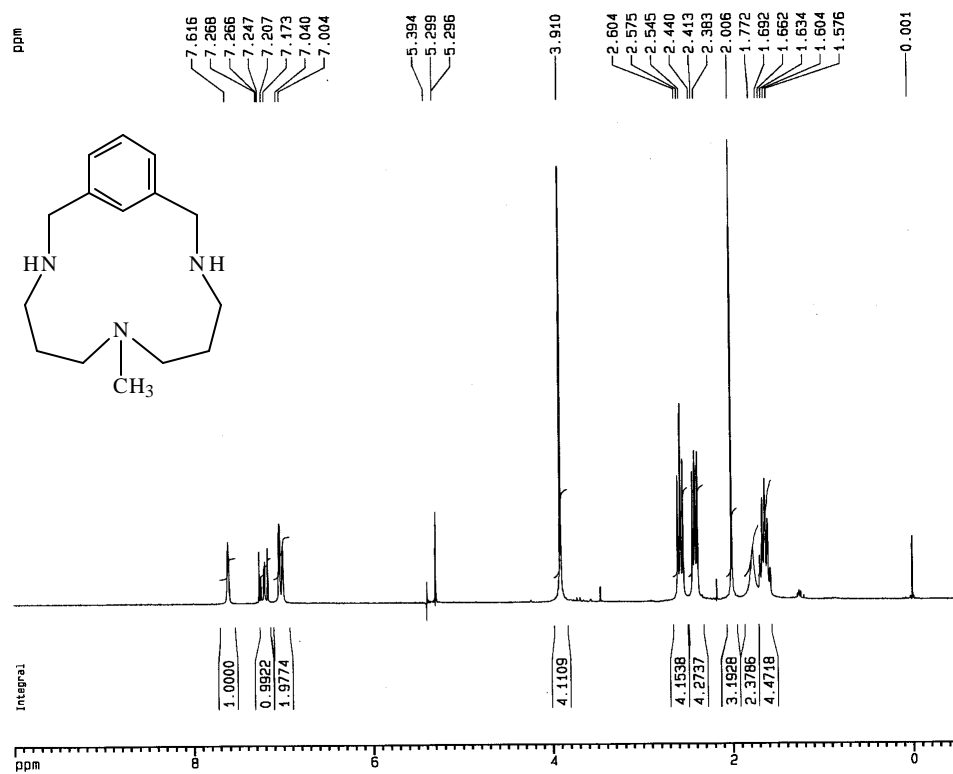


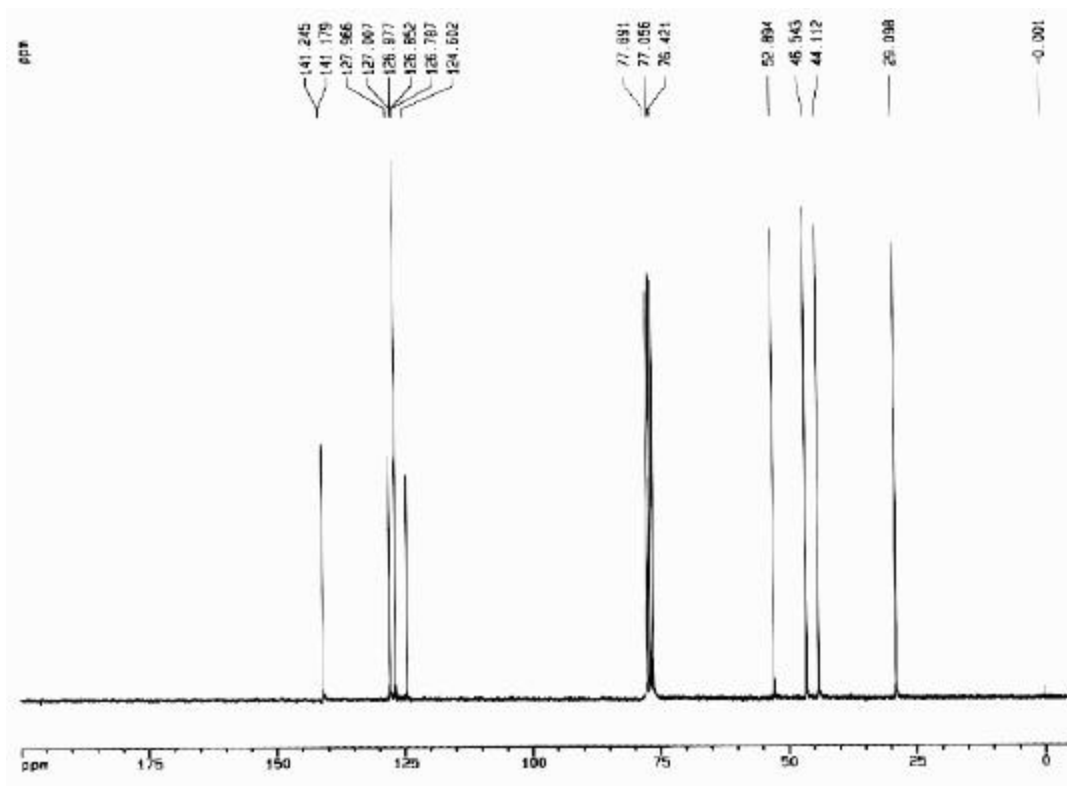
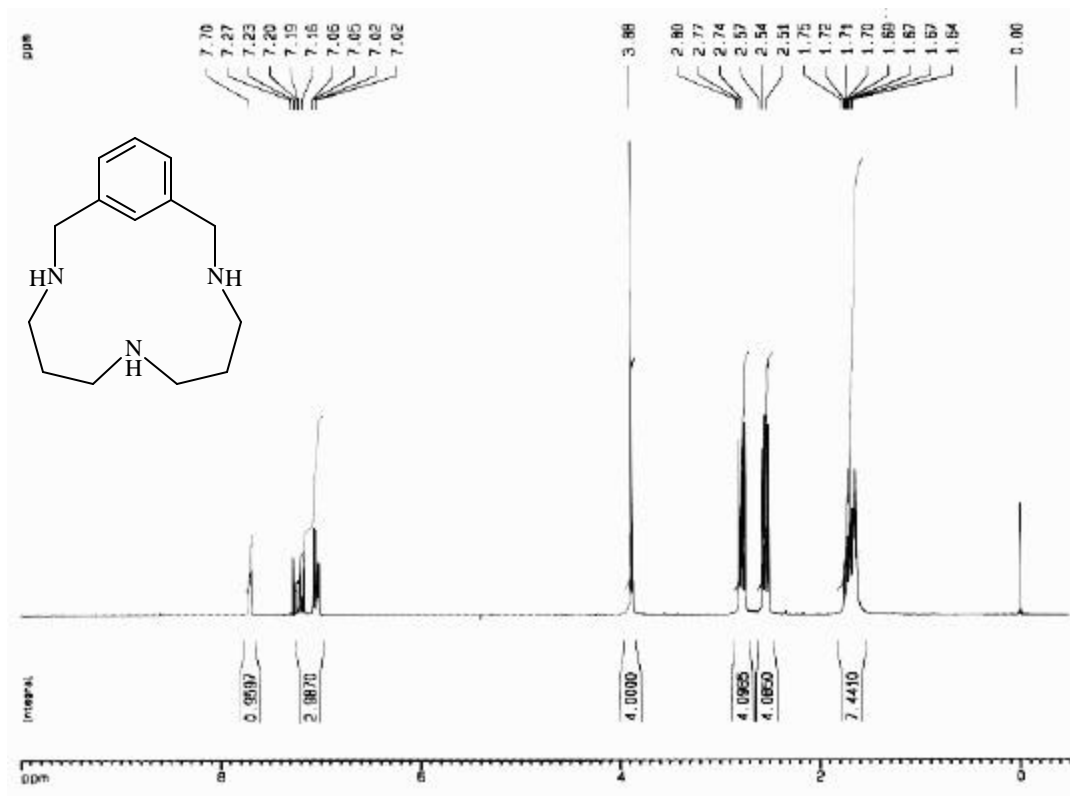
Figure S2. ^1H and ^{13}C NMR characterization of ligands L in CDCl_3 .

Ligand H32m

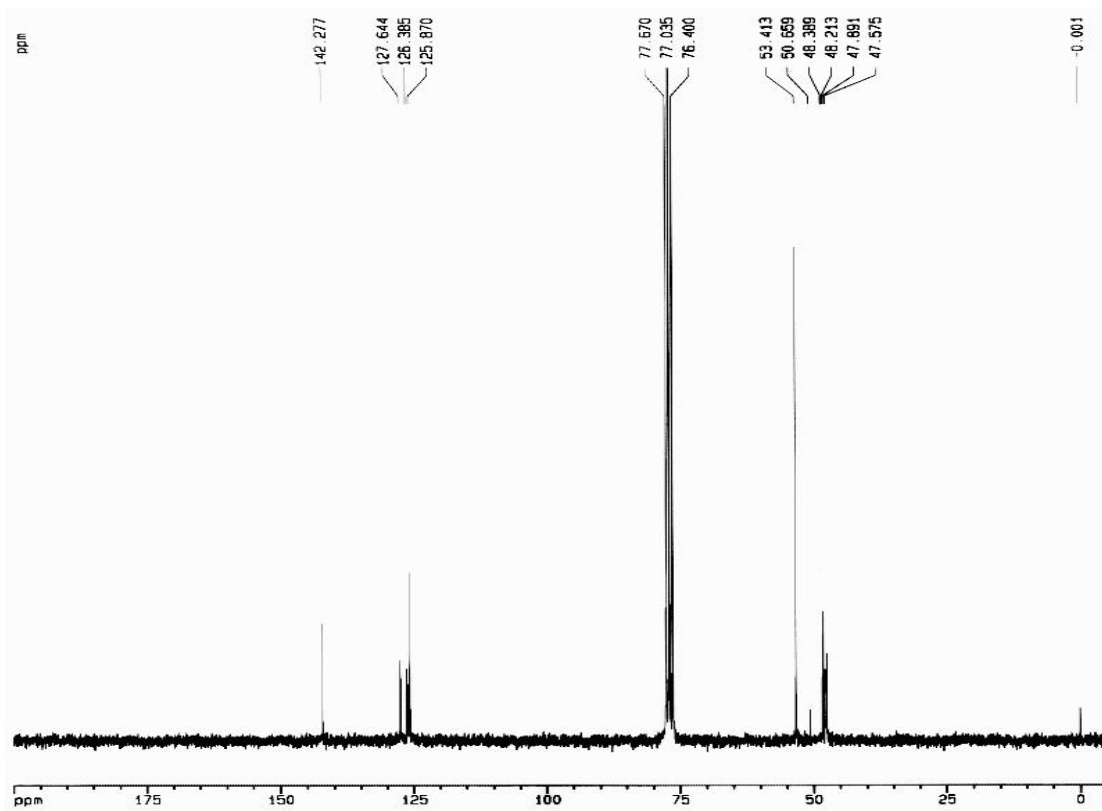
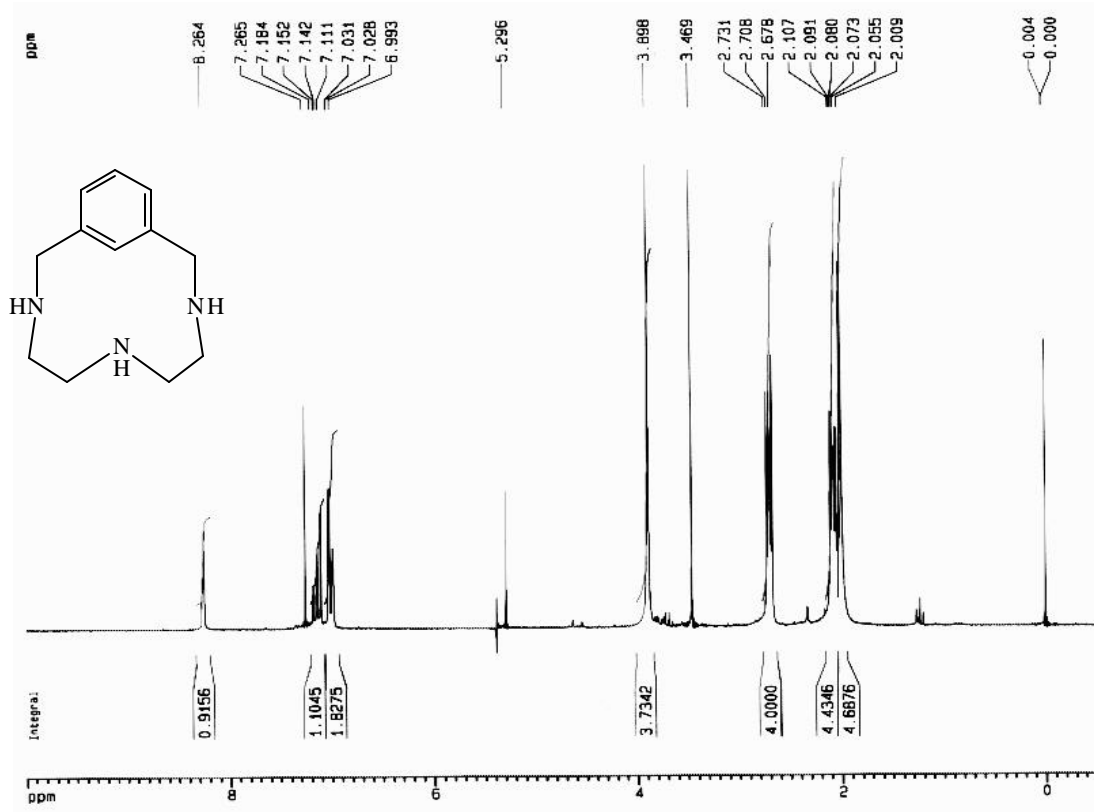


Ligand H₂Me33m

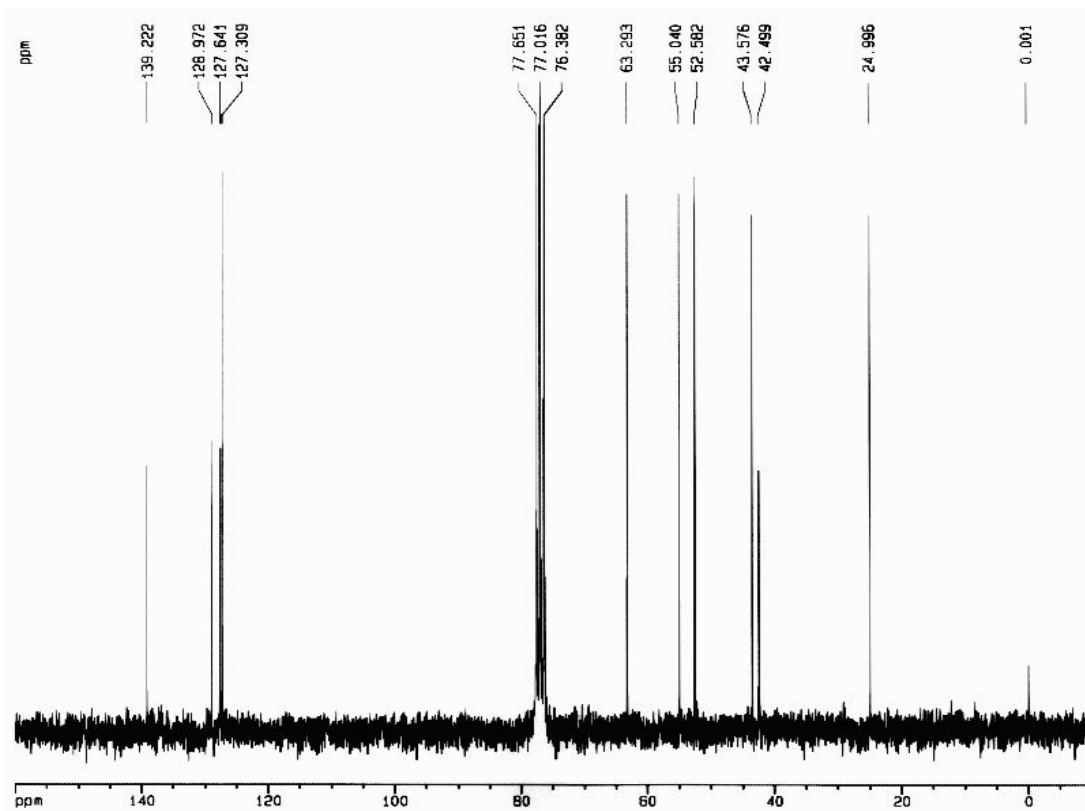
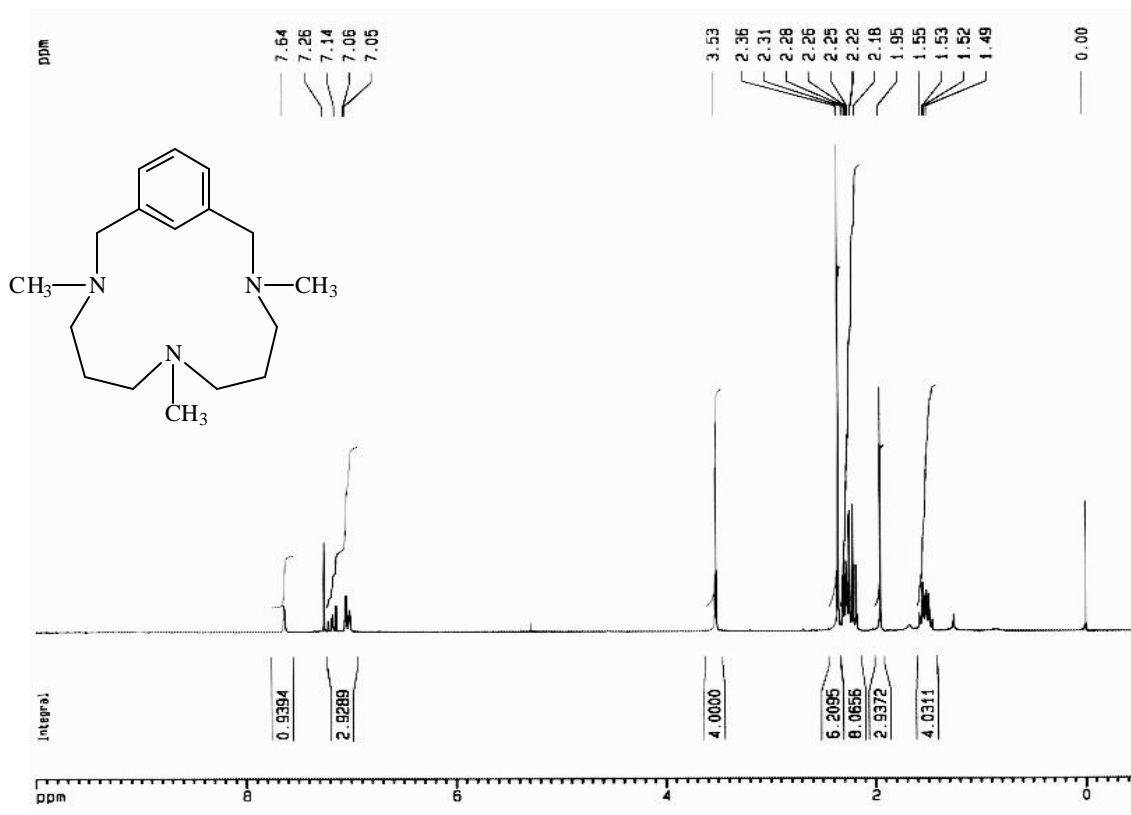
Ligand H33m



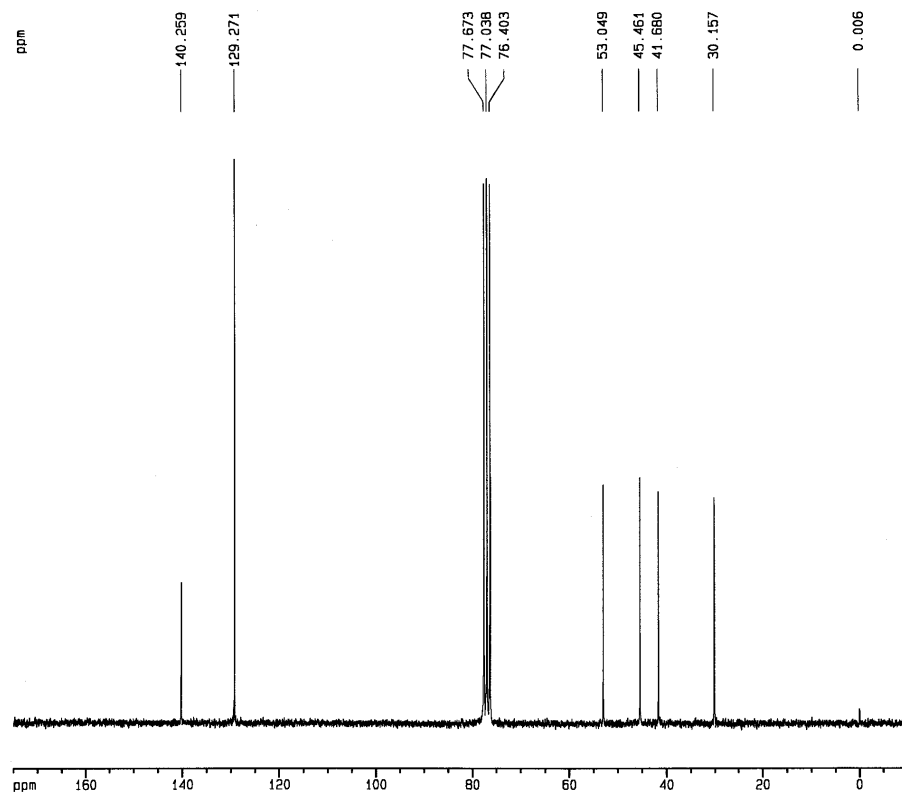
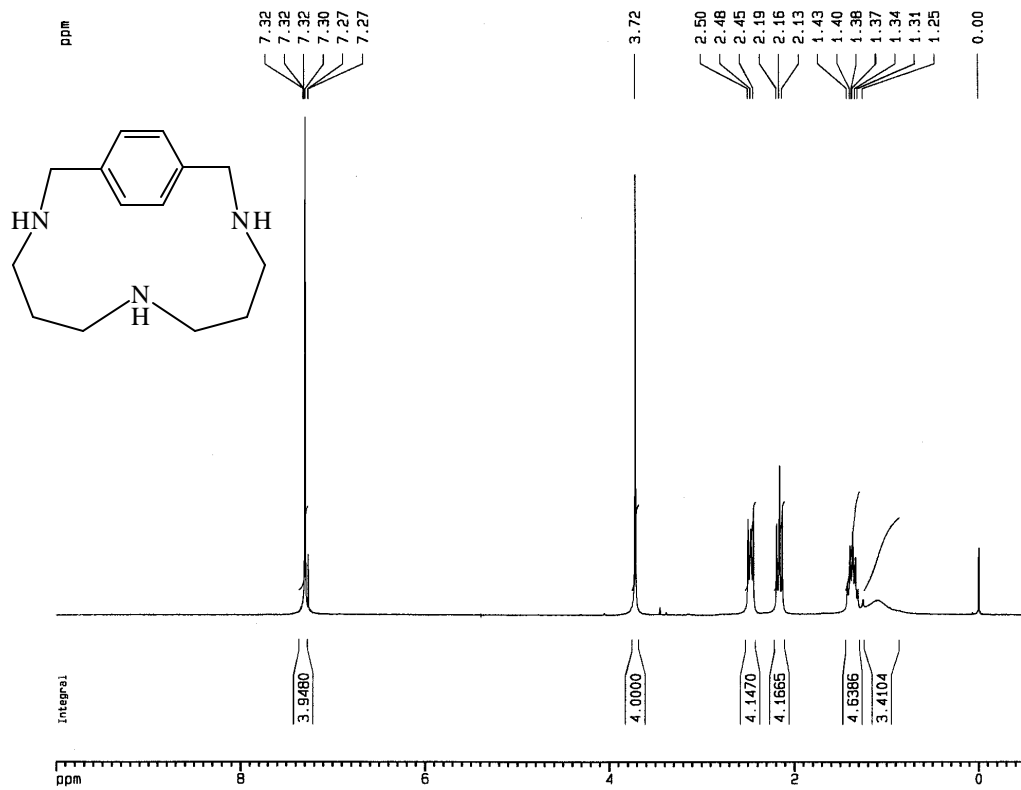
Ligand H22m



Ligand Me33m



Ligand H33p



Ligand H33o

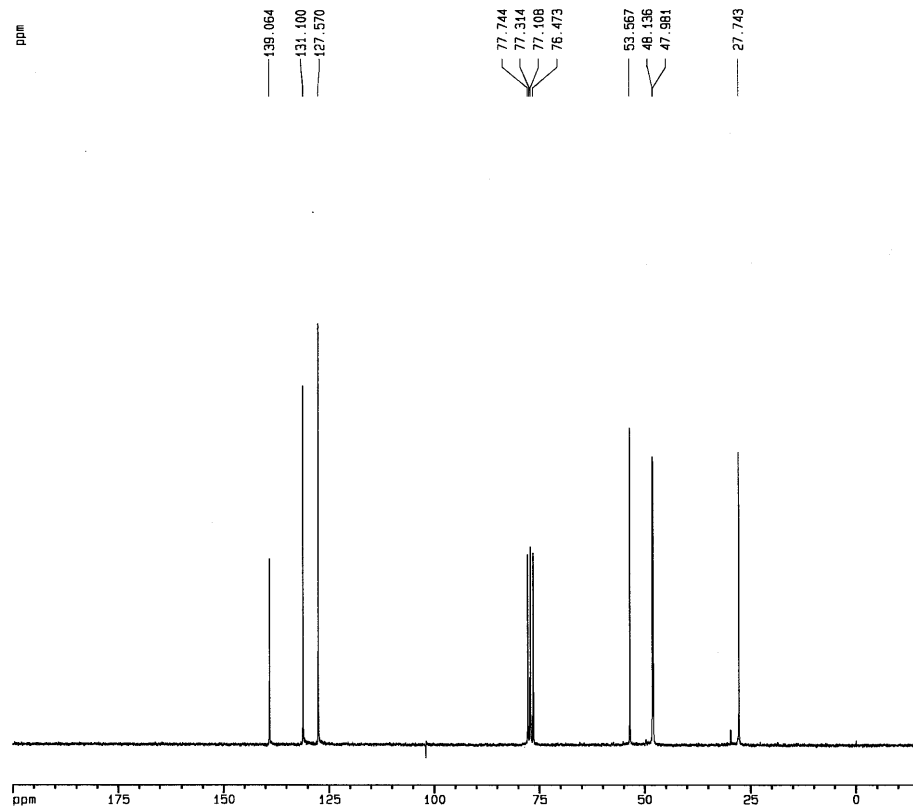
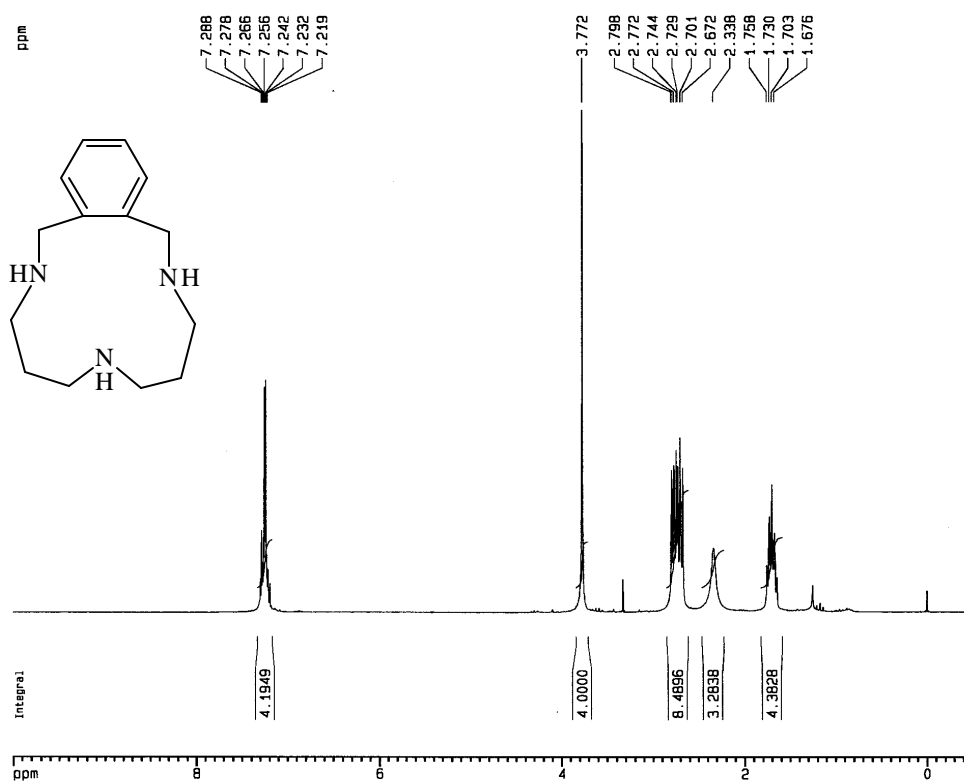
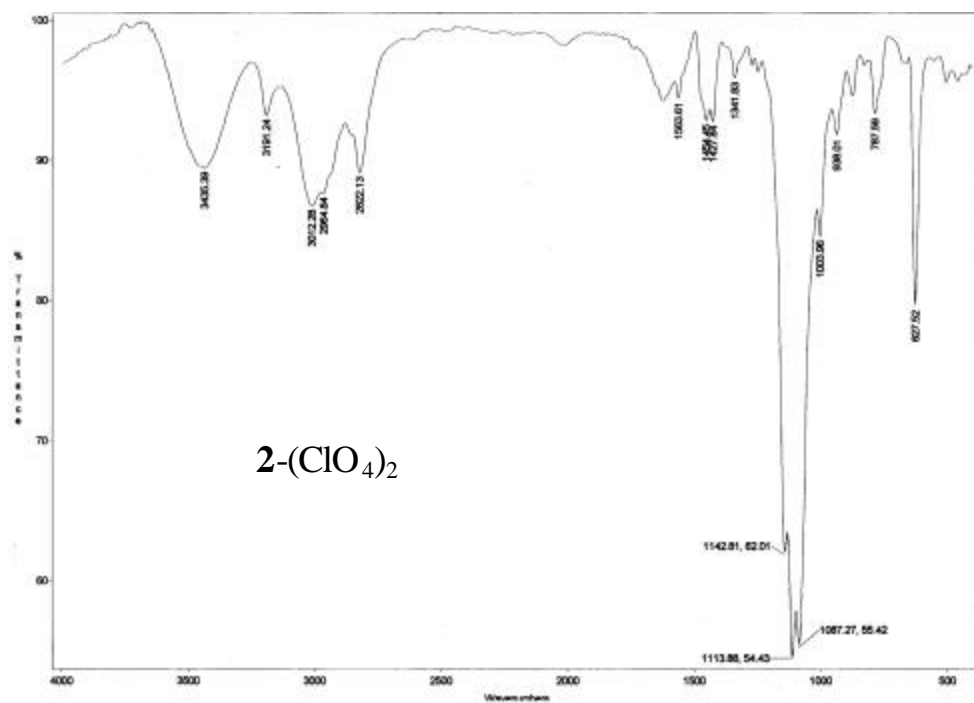
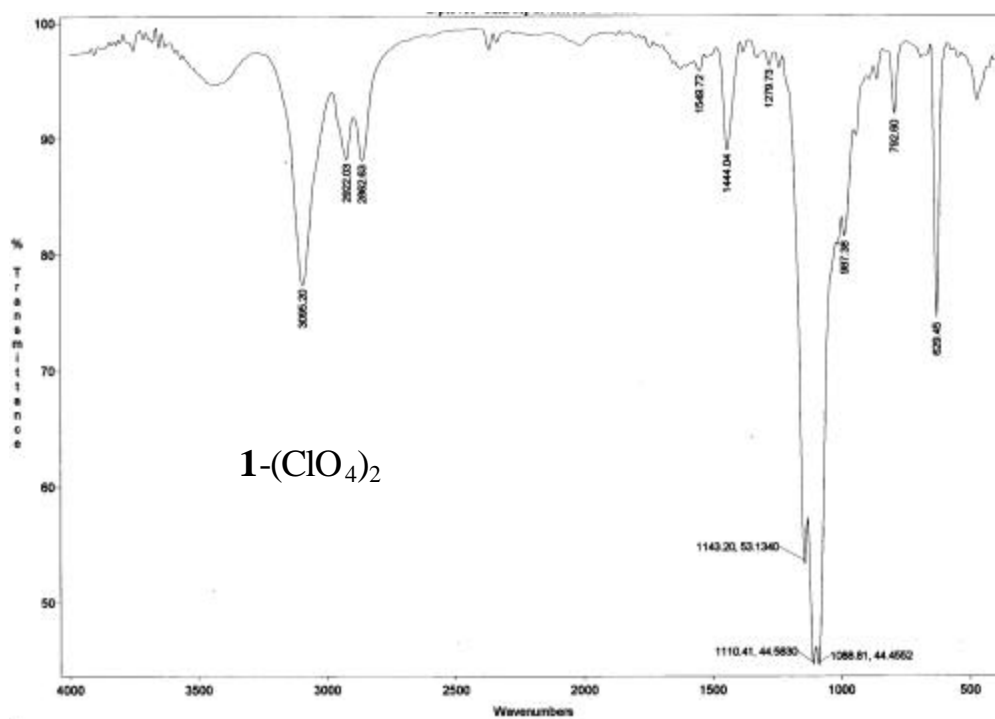


Figure S3. IR spectra of organocopper(III) complexes.

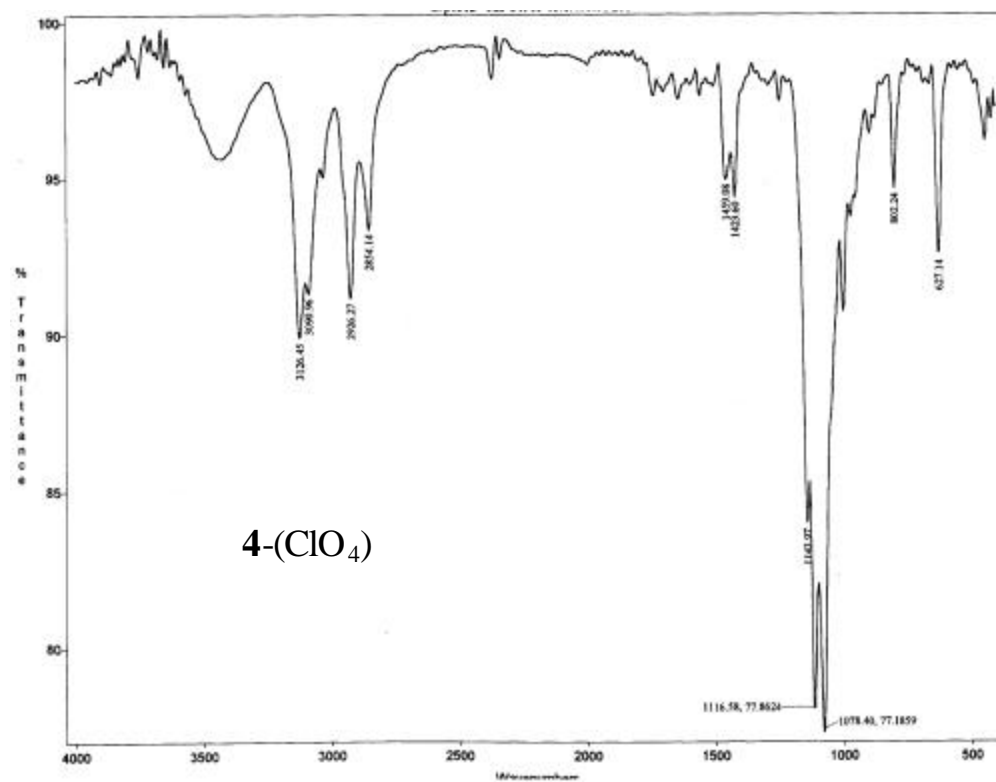
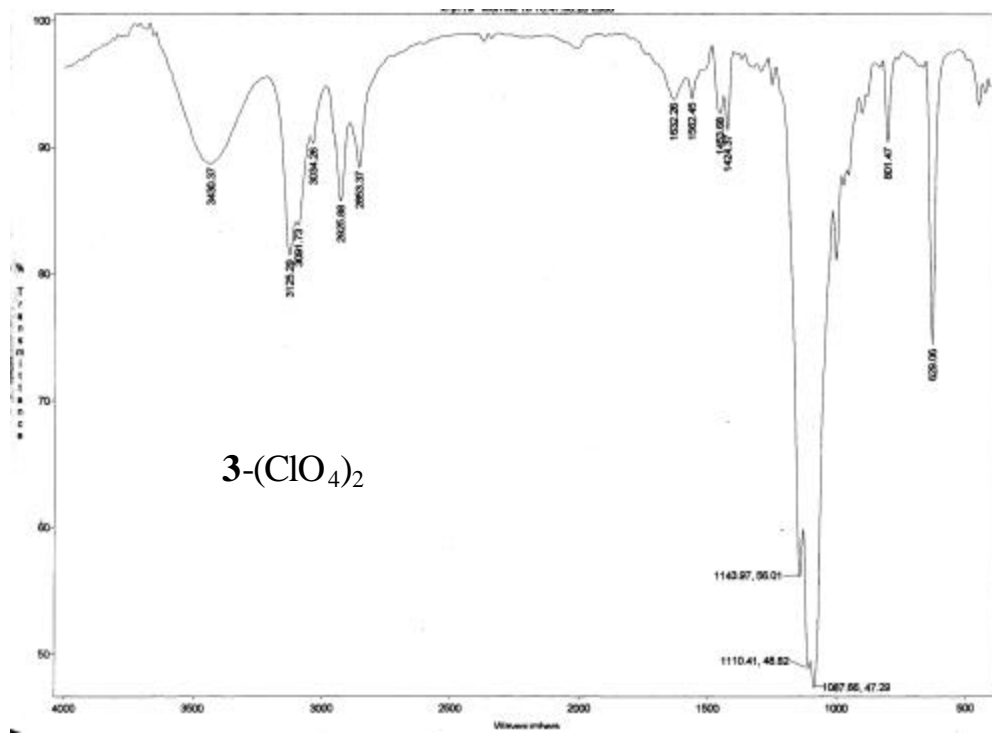
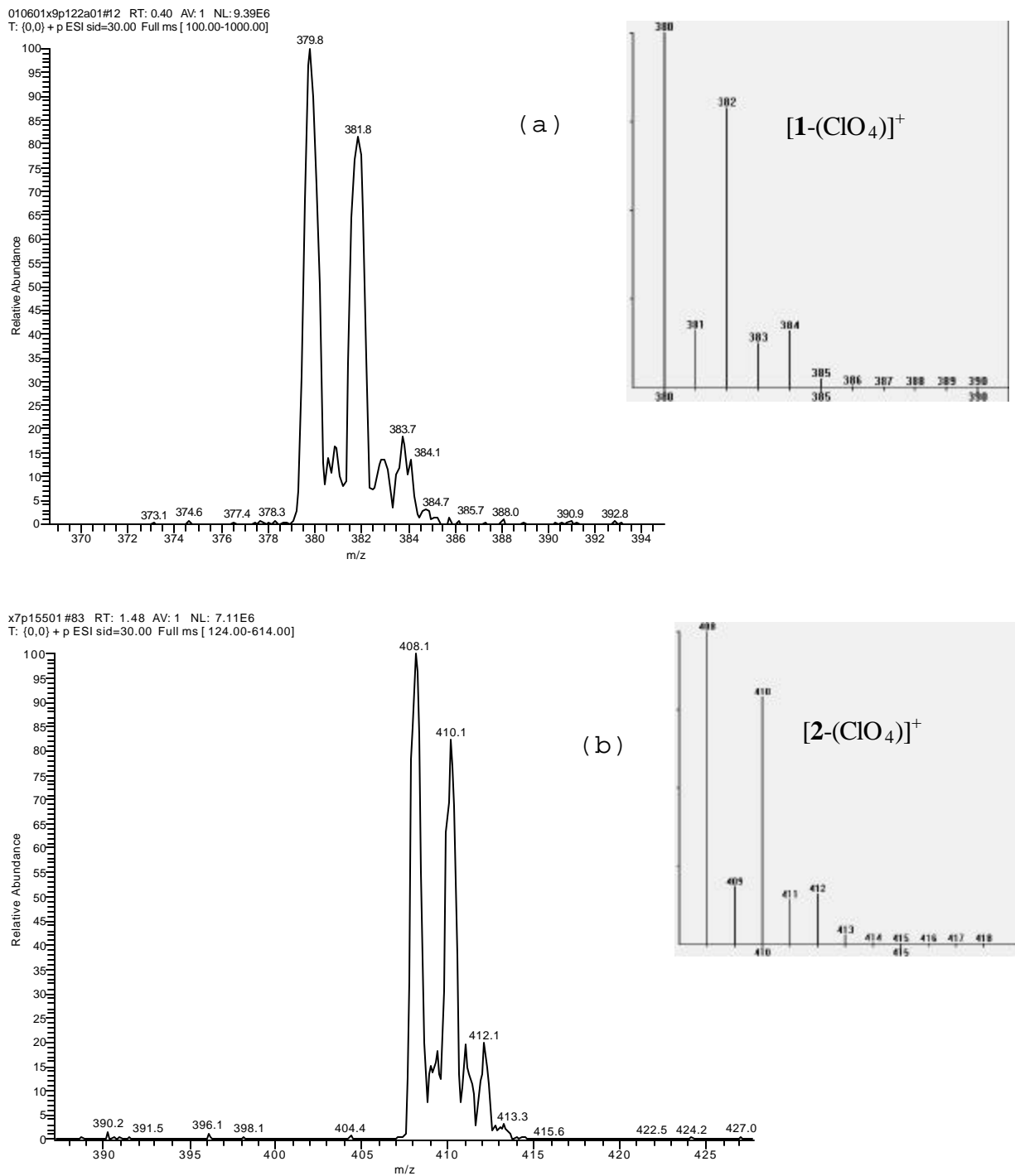


Figure S4. ESI-MS spectra of Cu^{III} complexes (a) $[(\text{H}32\text{m-C})\text{Cu}^{\text{III}}](\text{ClO}_4)_2$ (**1**- $(\text{ClO}_4)_2$), (b) $[(\text{H}_2\text{Me}33\text{m-C})\text{Cu}^{\text{III}}](\text{ClO}_4)_2$ (**2**- $(\text{ClO}_4)_2$) and (c) $[(\text{H}33\text{m-C})\text{Cu}^{\text{III}}](\text{ClO}_4)_2$ (**3**- $(\text{ClO}_4)_2$). Insets: simulation of corresponding fragment peaks.



x7p16101#108 RT: 2.01 AV: 1 NL: 1.31E7
T: (0,0) + p ESI sid=30.00 Full ms [101.00-614.00]

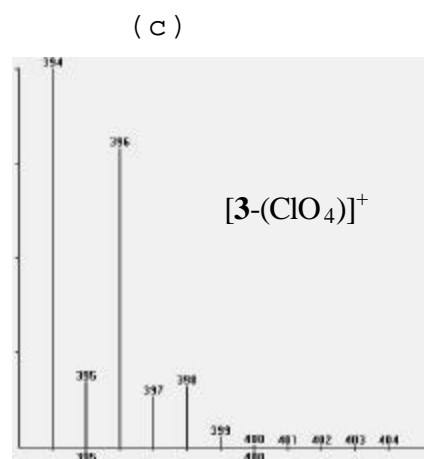
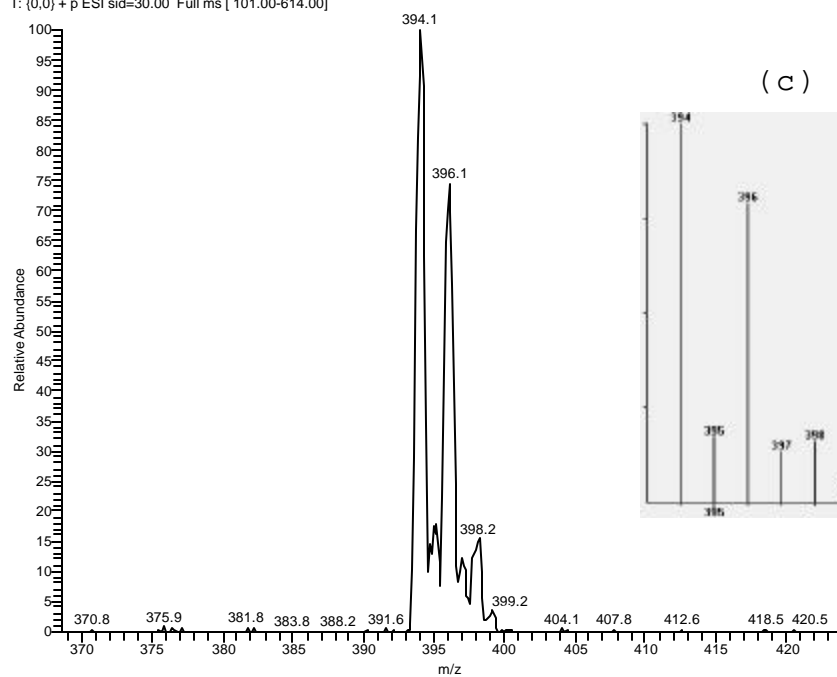
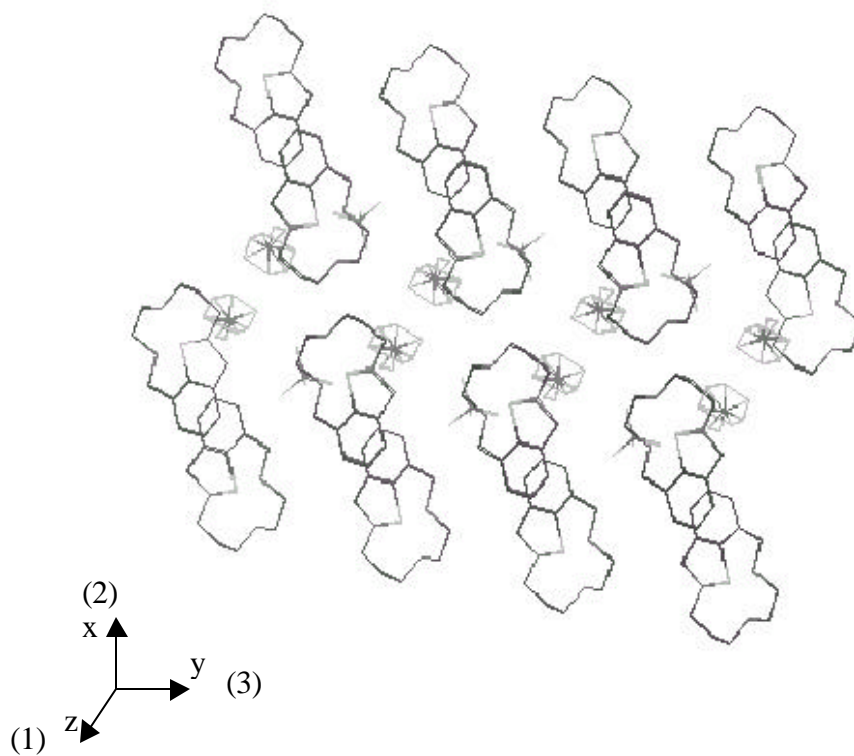
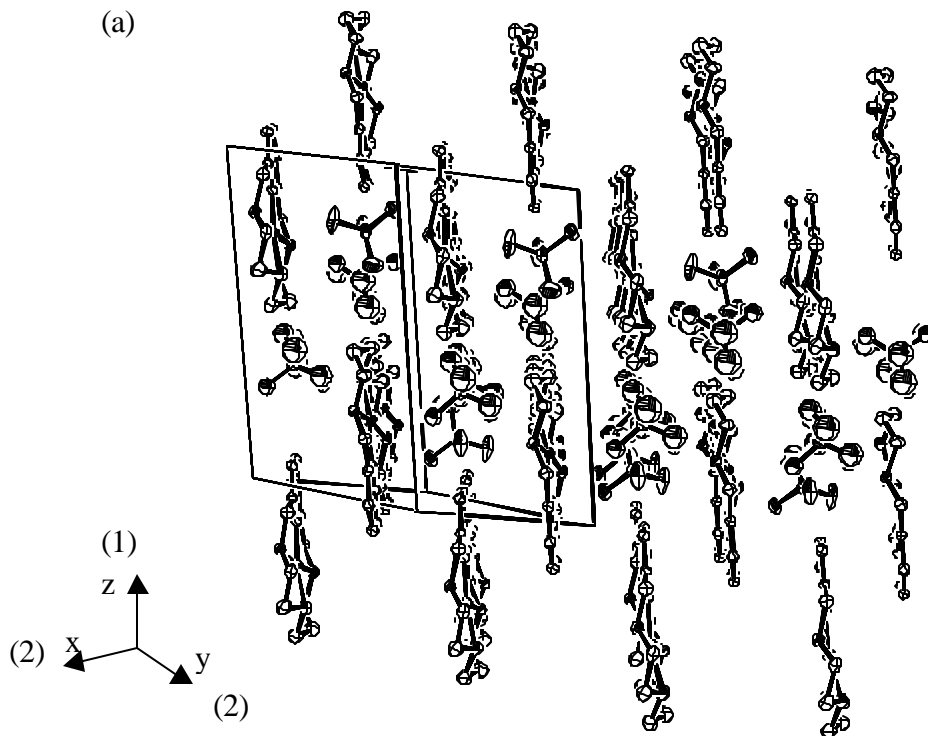
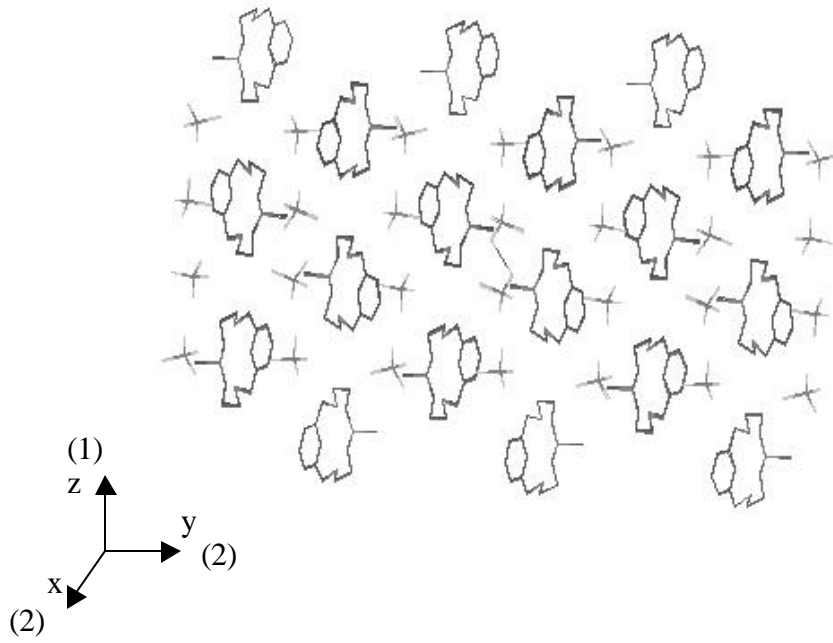
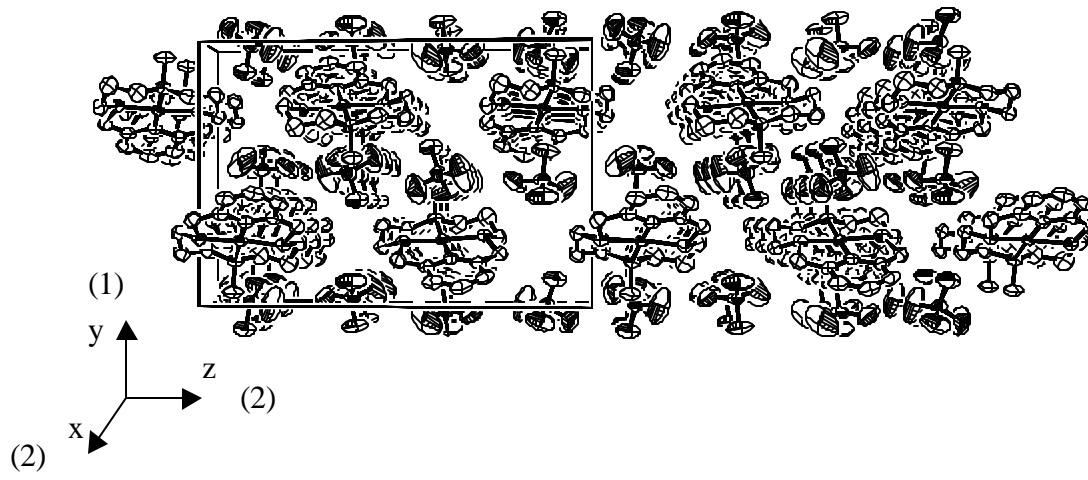


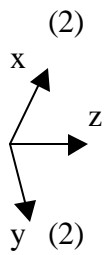
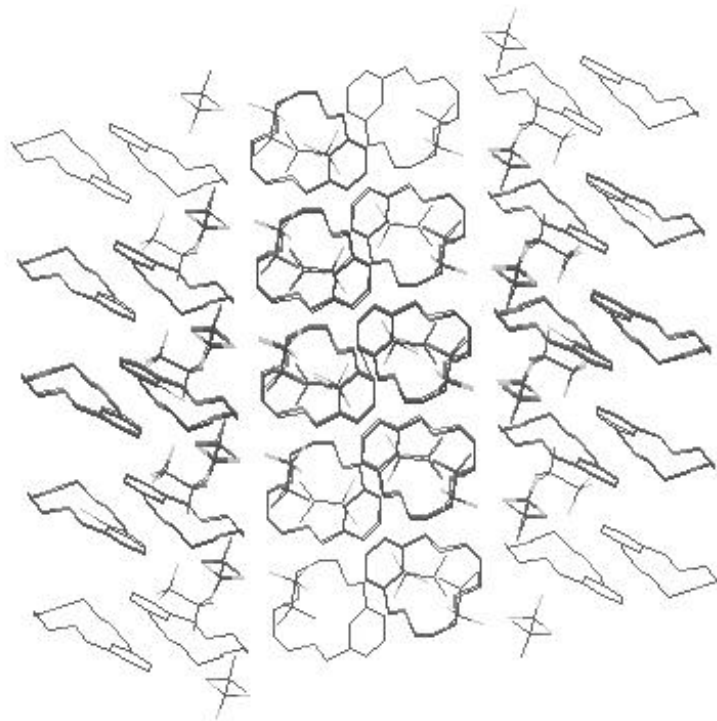
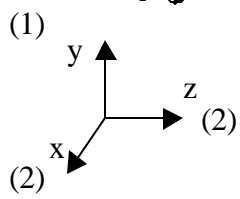
Figure S5. ORTEP and wireframe plots of packing cells for structures of complexes (a) $[(\text{H}32\text{m-C})\text{Cu}^{\text{III}}](\text{ClO}_4)_2$ (**1**- $(\text{ClO}_4)_2$), (b) $[(\text{H}_2\text{Me}33\text{m-C})\text{Cu}^{\text{III}}](\text{ClO}_4)_2$ (**2**- $(\text{ClO}_4)_2$), (c) $[(\text{H}33\text{m-C})\text{Cu}^{\text{III}}](\text{OTf})_2$ (**3**- $(\text{OTf})_2$) and (d) $[(\text{H}33\text{m-C})\text{Cu}^{\text{III}}(\text{Cl})](\text{ClO}_4)$ (**4**- (ClO_4)). Enclosure boxes in each axis indicated in brackets.



(b)



(c)



(d)

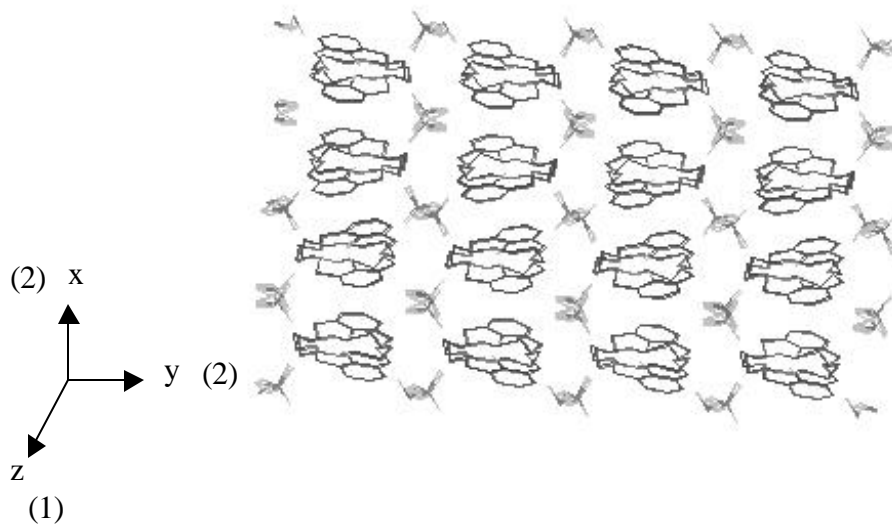
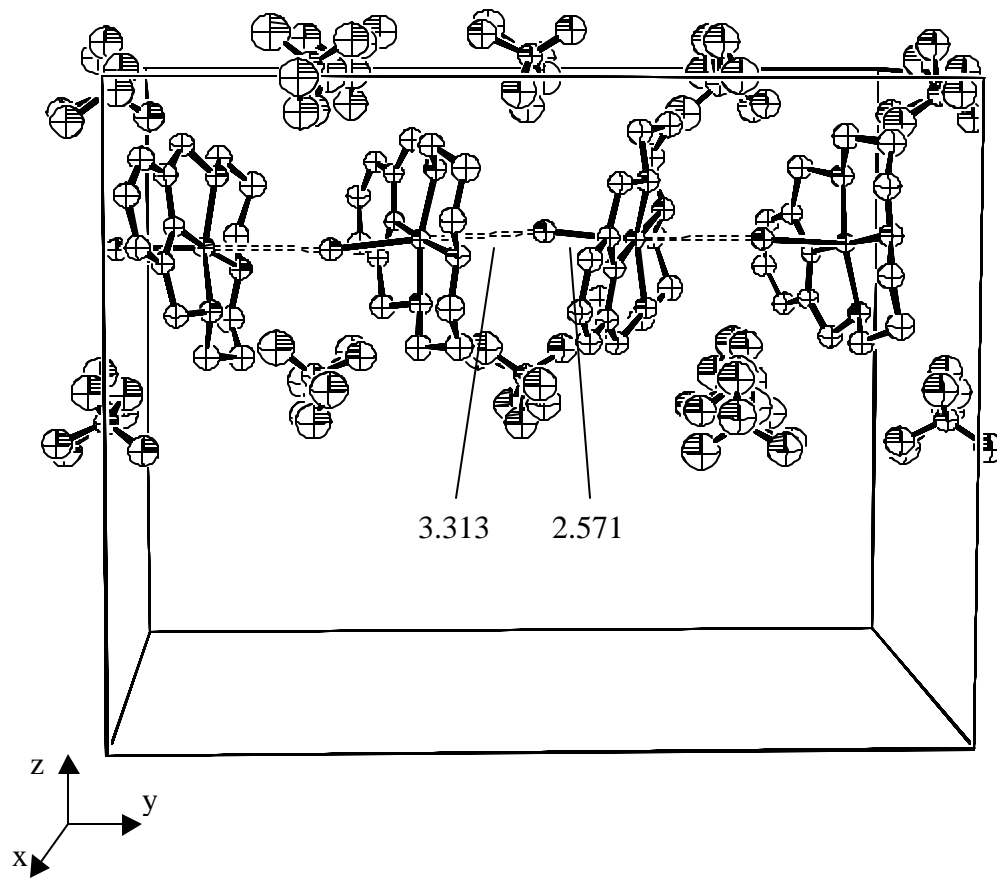
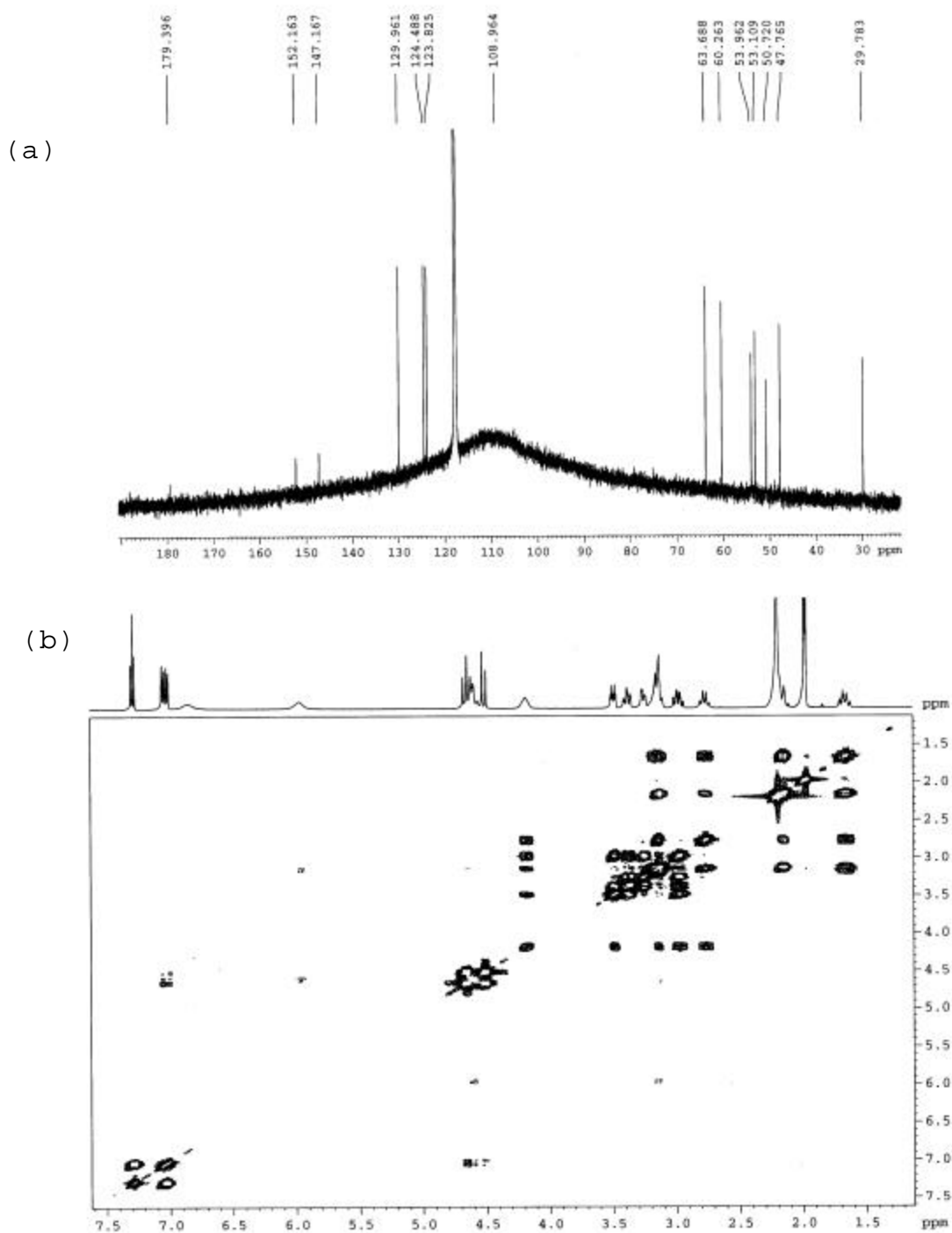


Figure S6a-d. NMR (500 MHz, 298 K, CD₃CN) spectra for complex [(H32m-C)Cu^{III}](ClO₄)₂ (**1**-(ClO₄)₂): (a) ¹³C NMR, (b) COSY, (c) NOESY, (d) HMBC. See ¹H NMR spectrum in Figure 6 (Discussion Chapter 3).



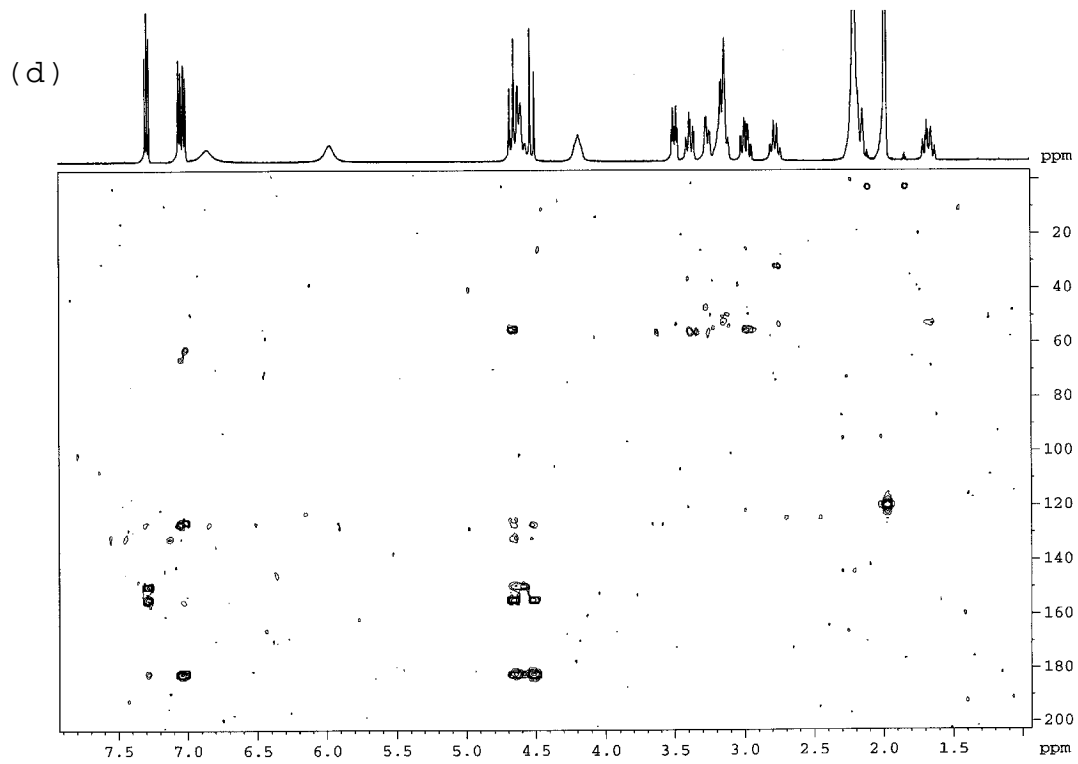
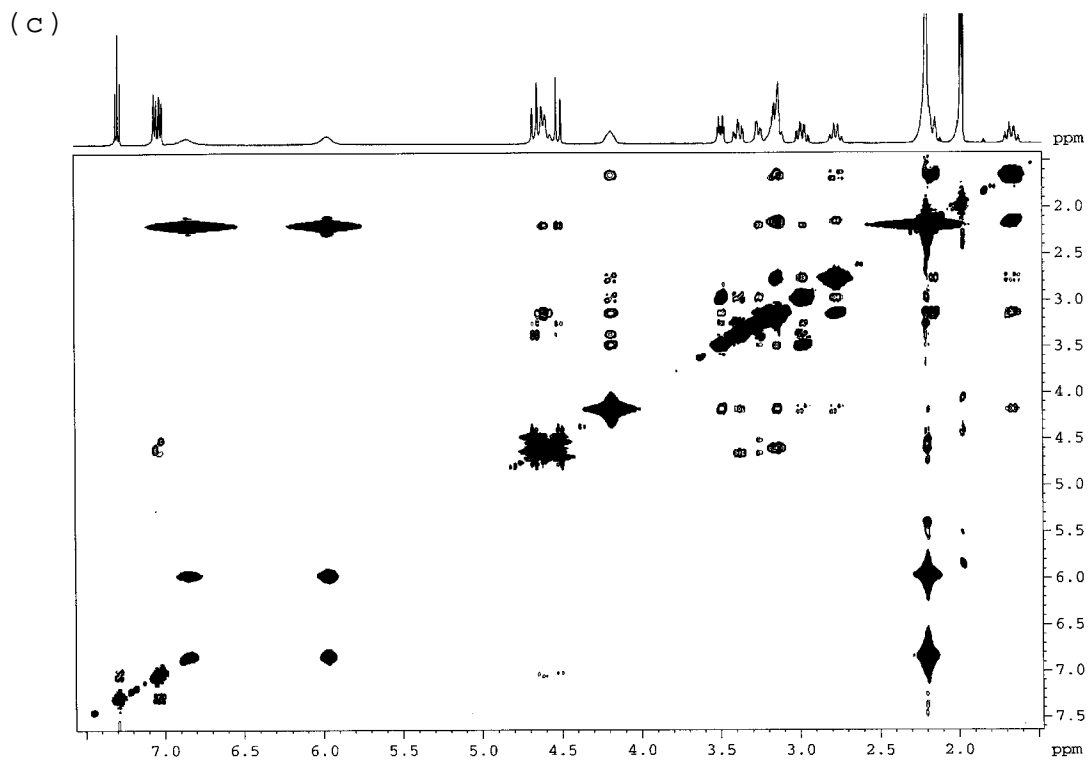
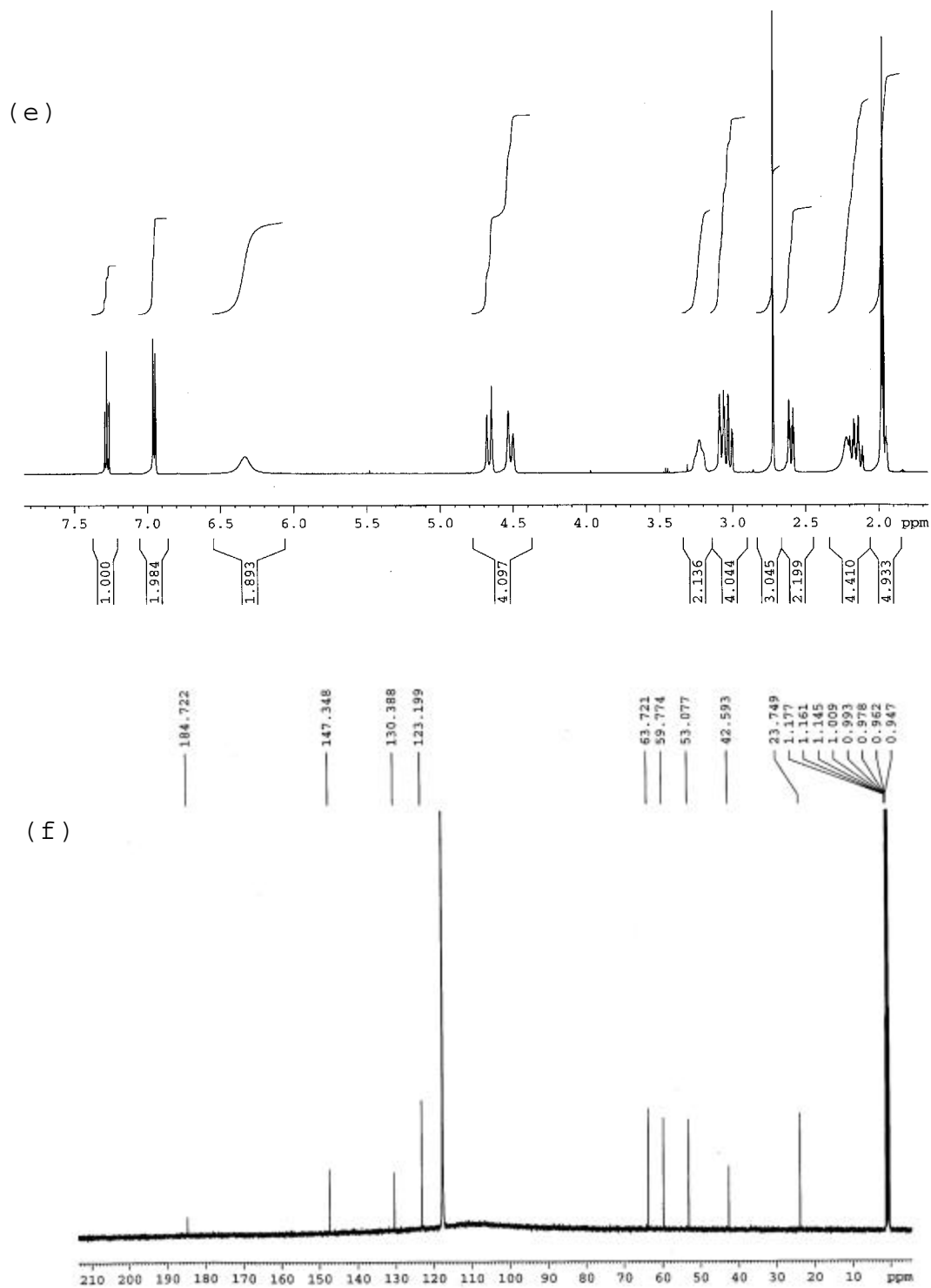
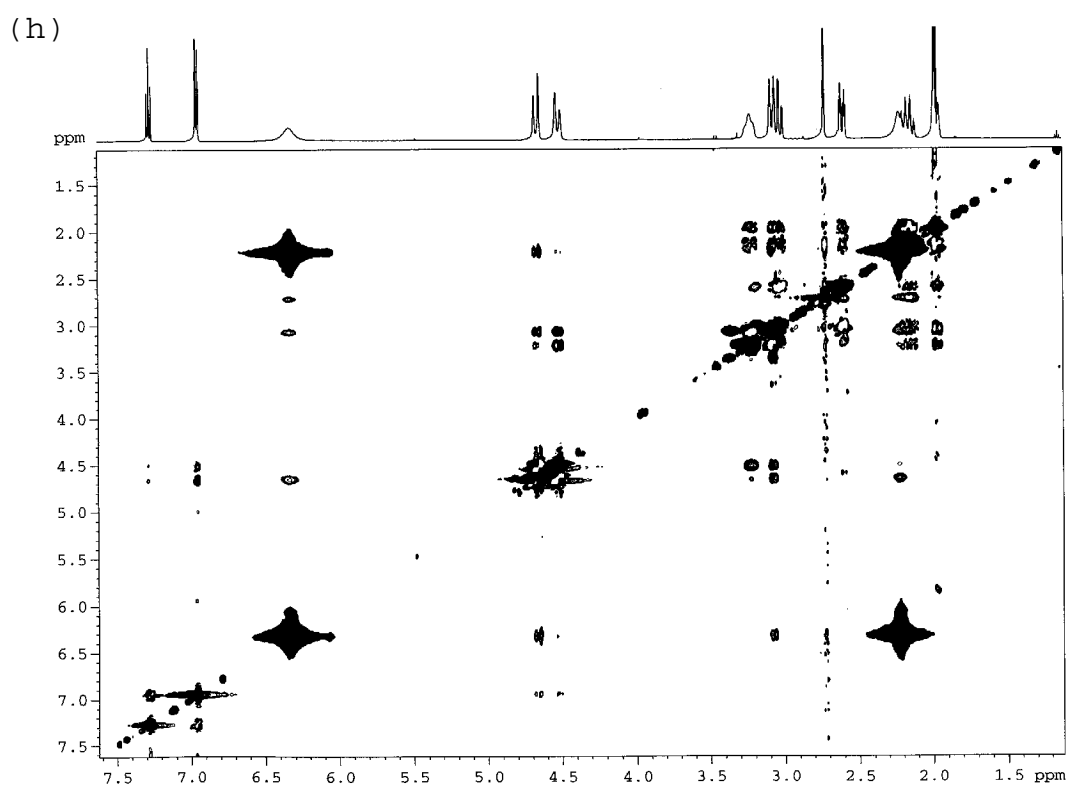
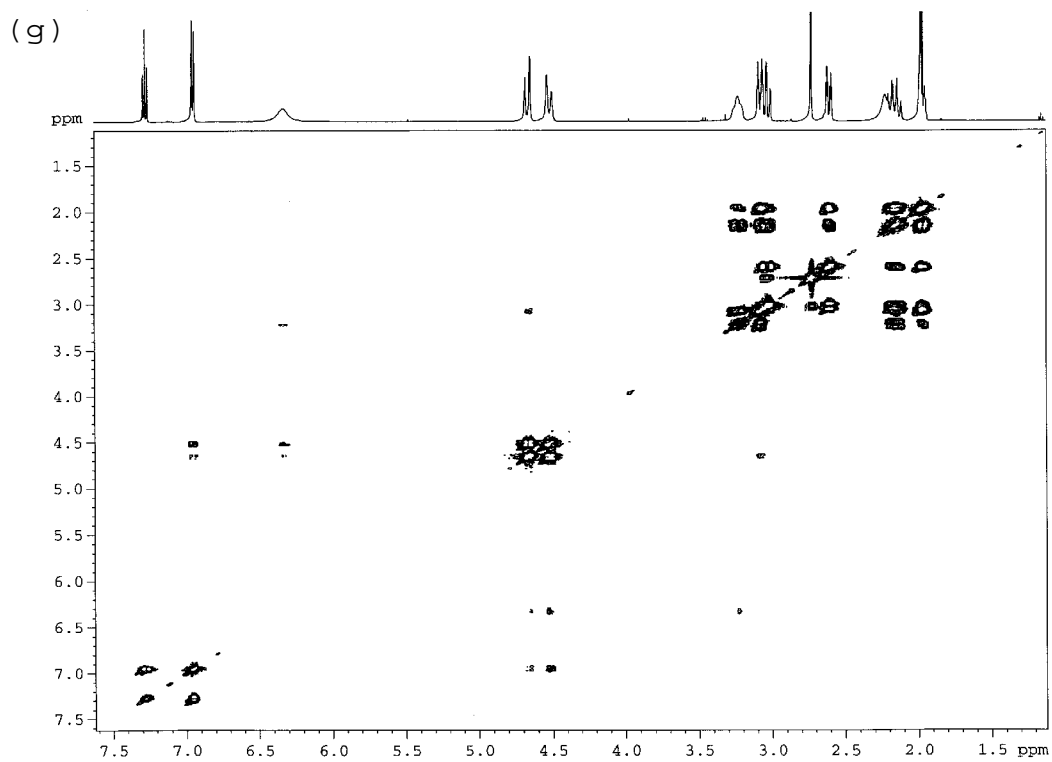


Figure S6e-i. NMR (500 MHz, 298 K, CD₃CN) spectra for complex [(H₂Me33m-C)Cu^{III}](ClO₄)₂ (2-(ClO₄)₂): (e) ¹H NMR, (f) ¹³C NMR, (g) COSY, (h) NOESY, (i) HMBC.





(i)

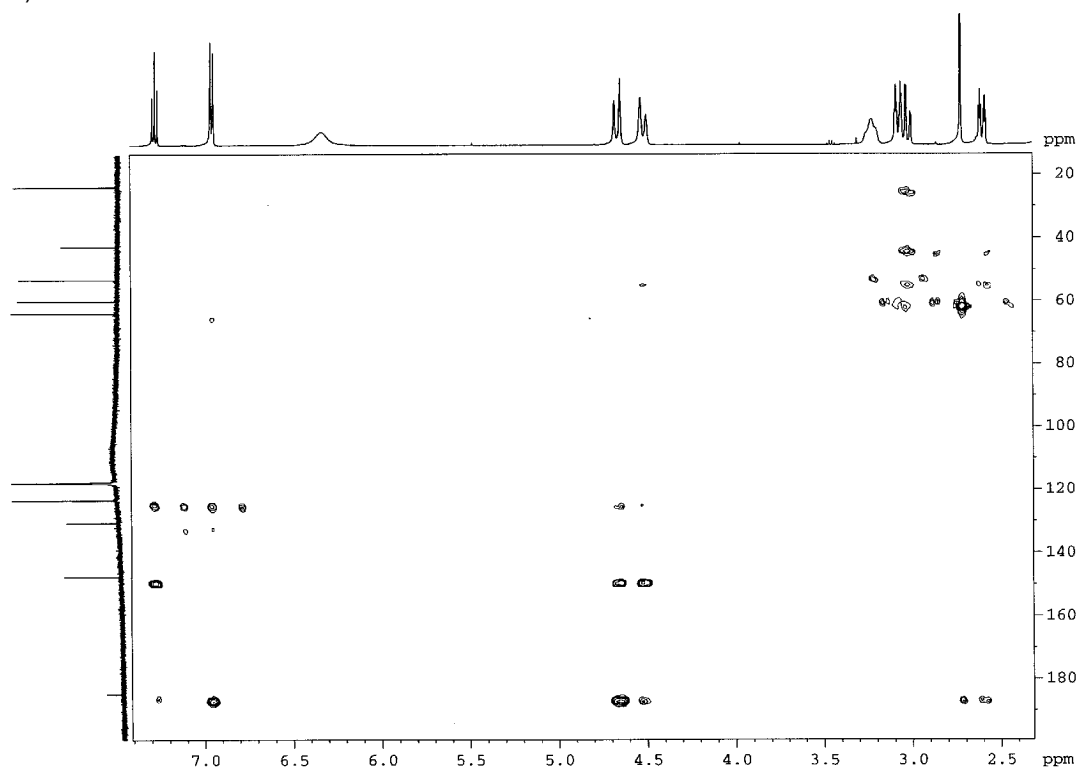
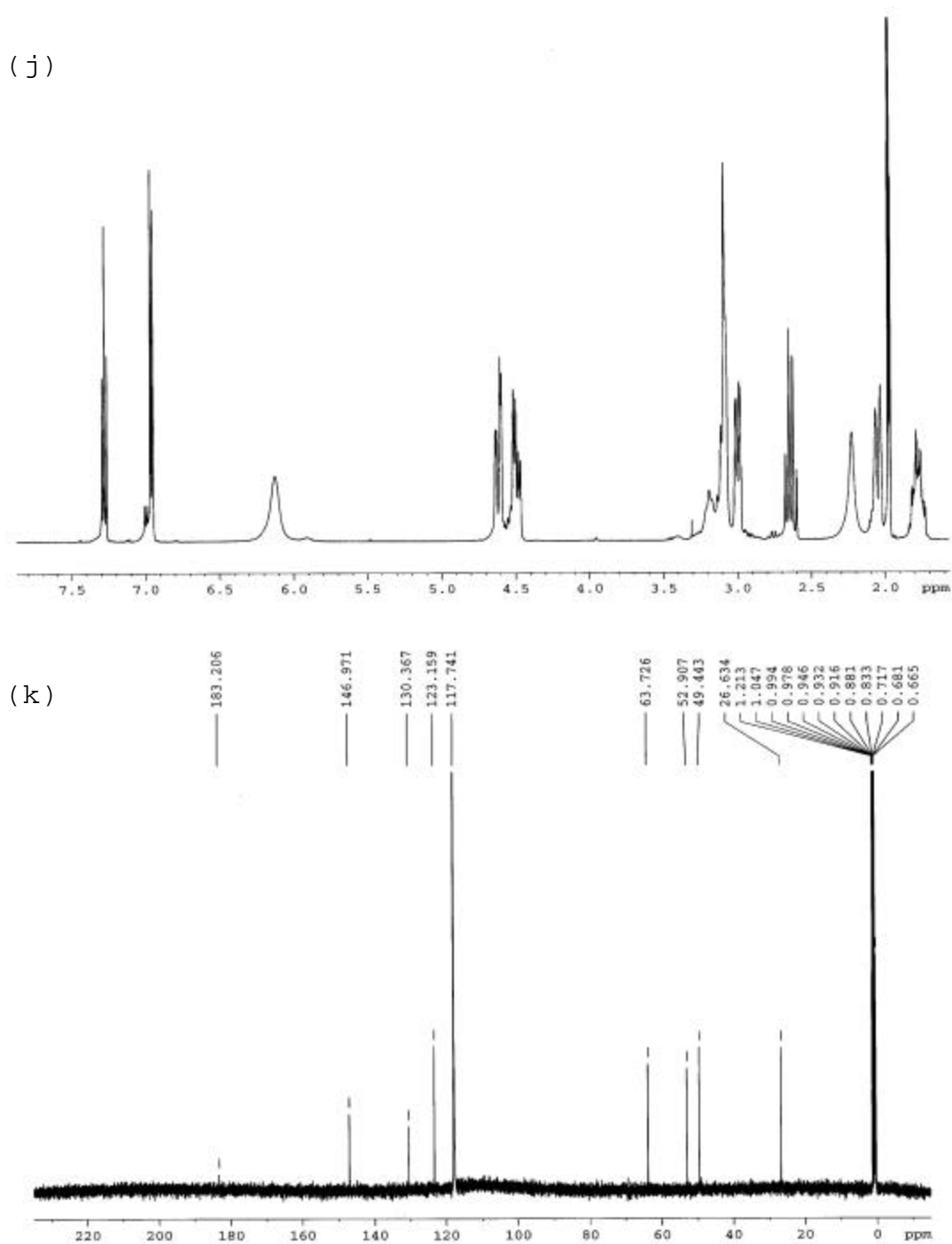
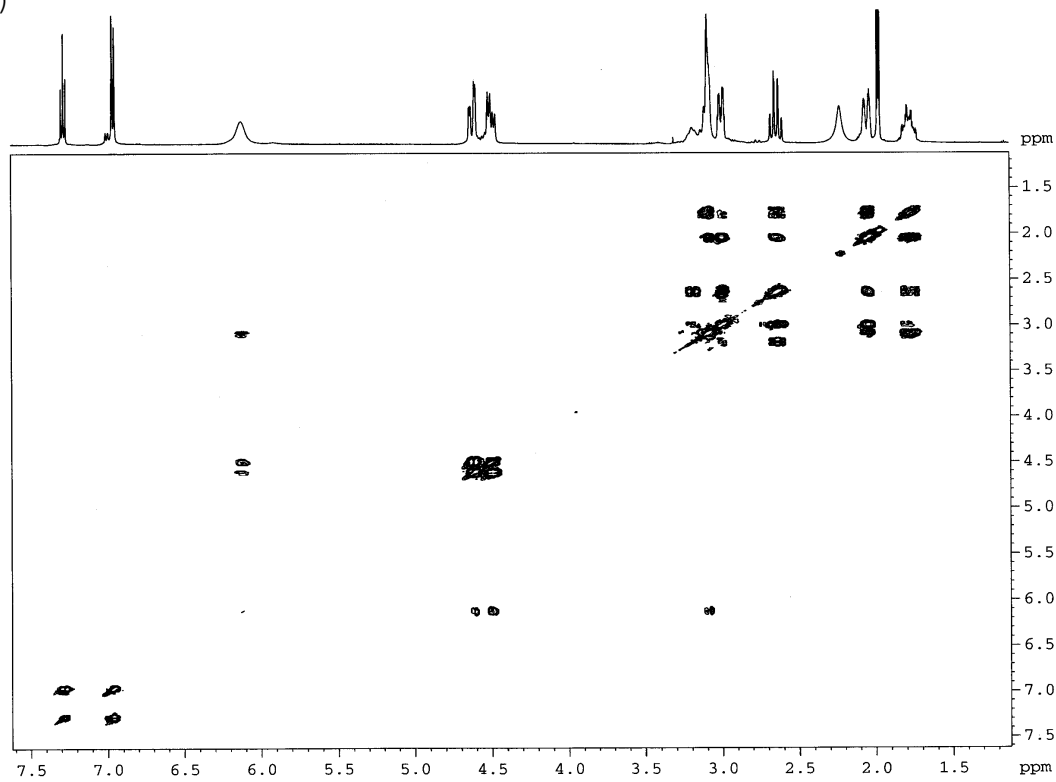


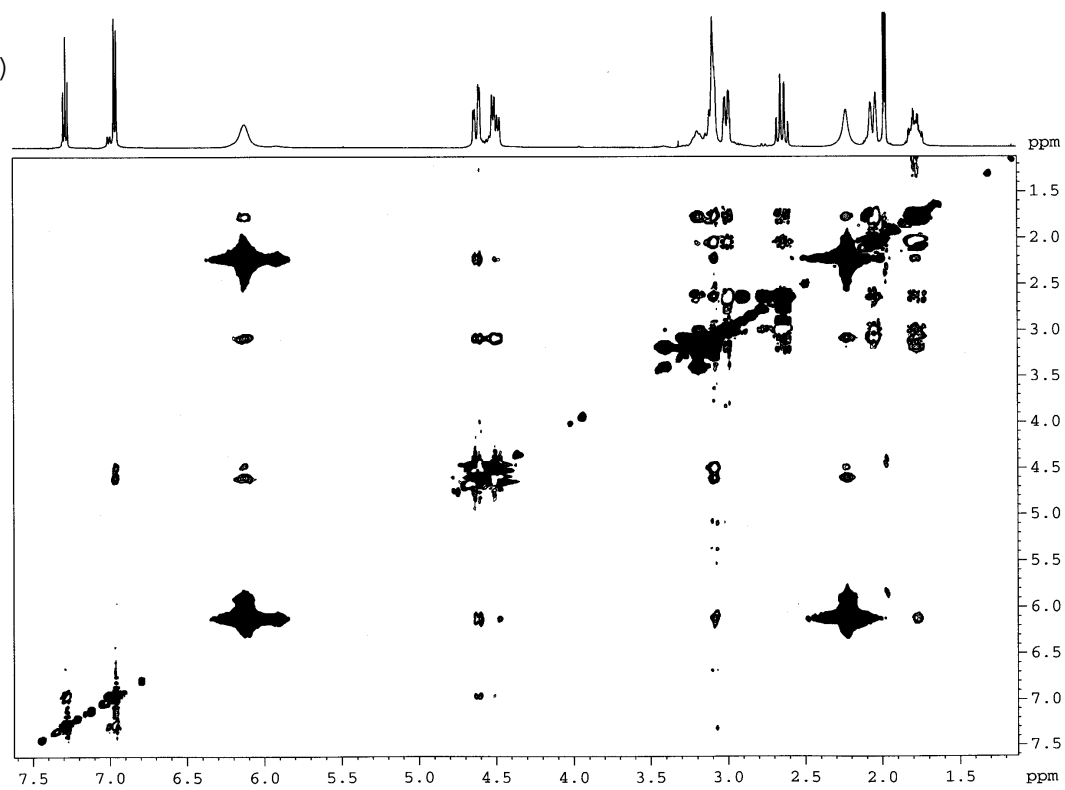
Figure S6j-n. NMR (500 MHz, 298 K, CD₃CN) spectra for complex [(H33m-C)Cu^{III}](ClO₄)₂ (**3**-(ClO₄)₂): (j) ¹H NMR, (k) ¹³C NMR, (l) COSY, (m) NOESY, (n) HMBC.



(1)



(m)



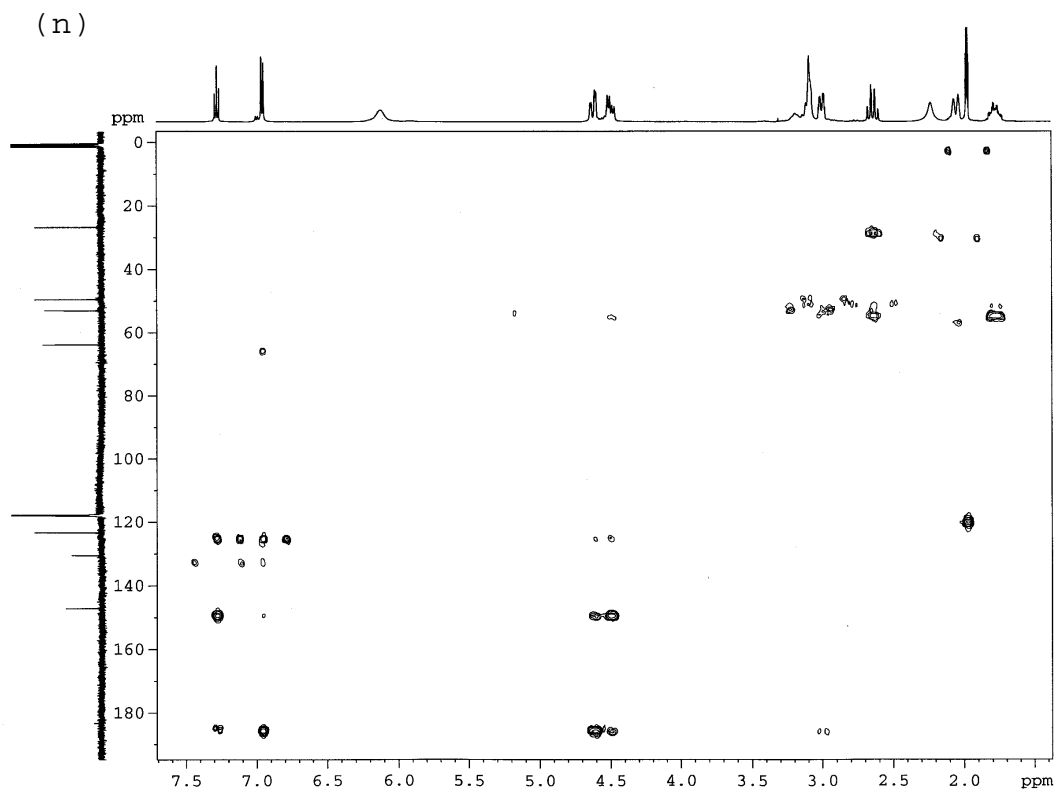


Figure S7. ^1H NMR (400 MHz, 298 K, CD_3CN) spectra for final disproportionation reaction mixture for (a) $[(\text{H}_2\text{Me33m-C})\text{Cu}^{\text{III}}]^{2+}/[\text{Cu}^{\text{I}}(\text{CH}_3\text{CN})_4]^+ / [\text{H}_2\text{Me33mH}]^+$ and (b) $[(\text{H33m-C})\text{Cu}^{\text{III}}]^{2+}/[\text{Cu}^{\text{I}}(\text{CH}_3\text{CN})_4]^+ / [\text{H33mH}]^+$.

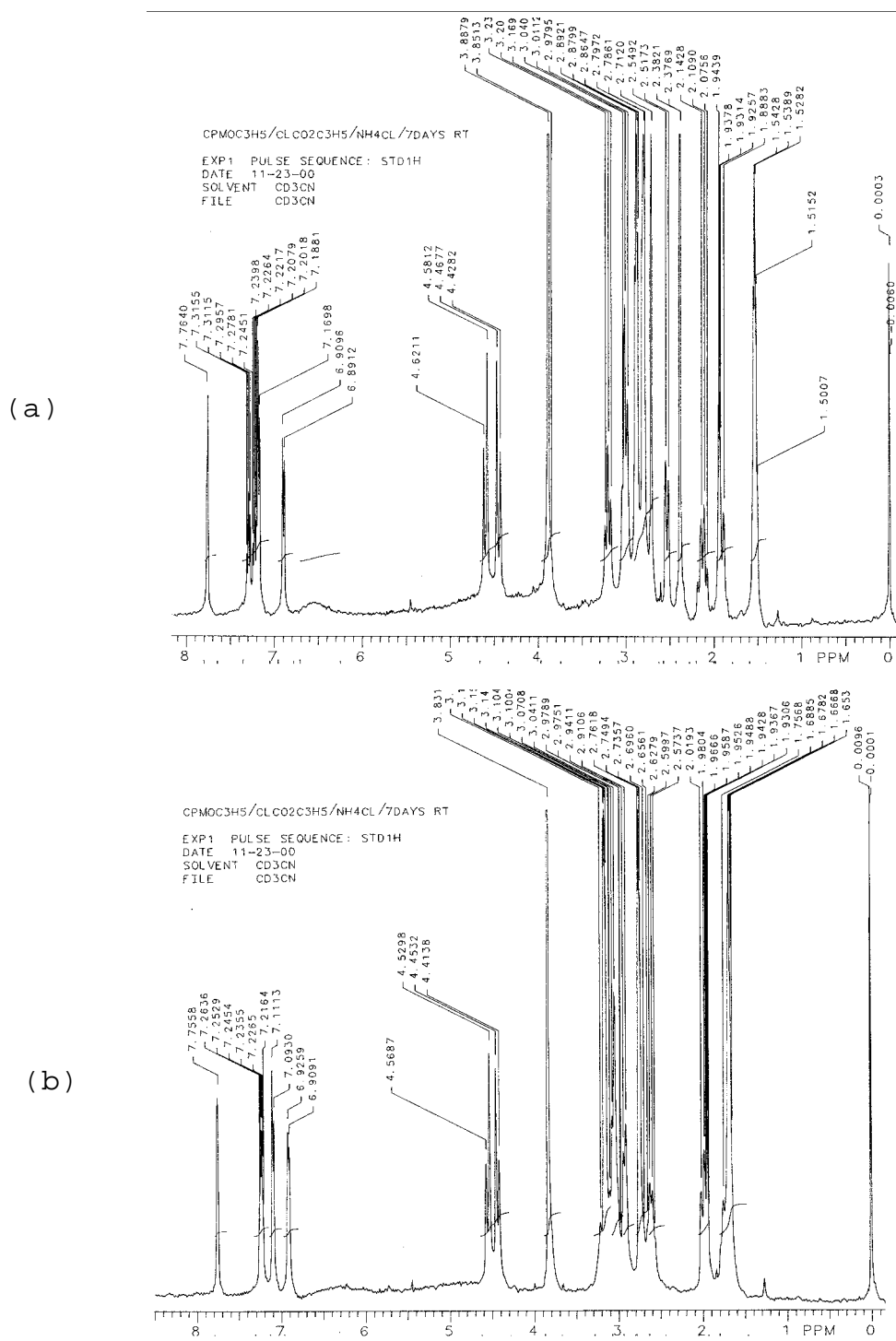
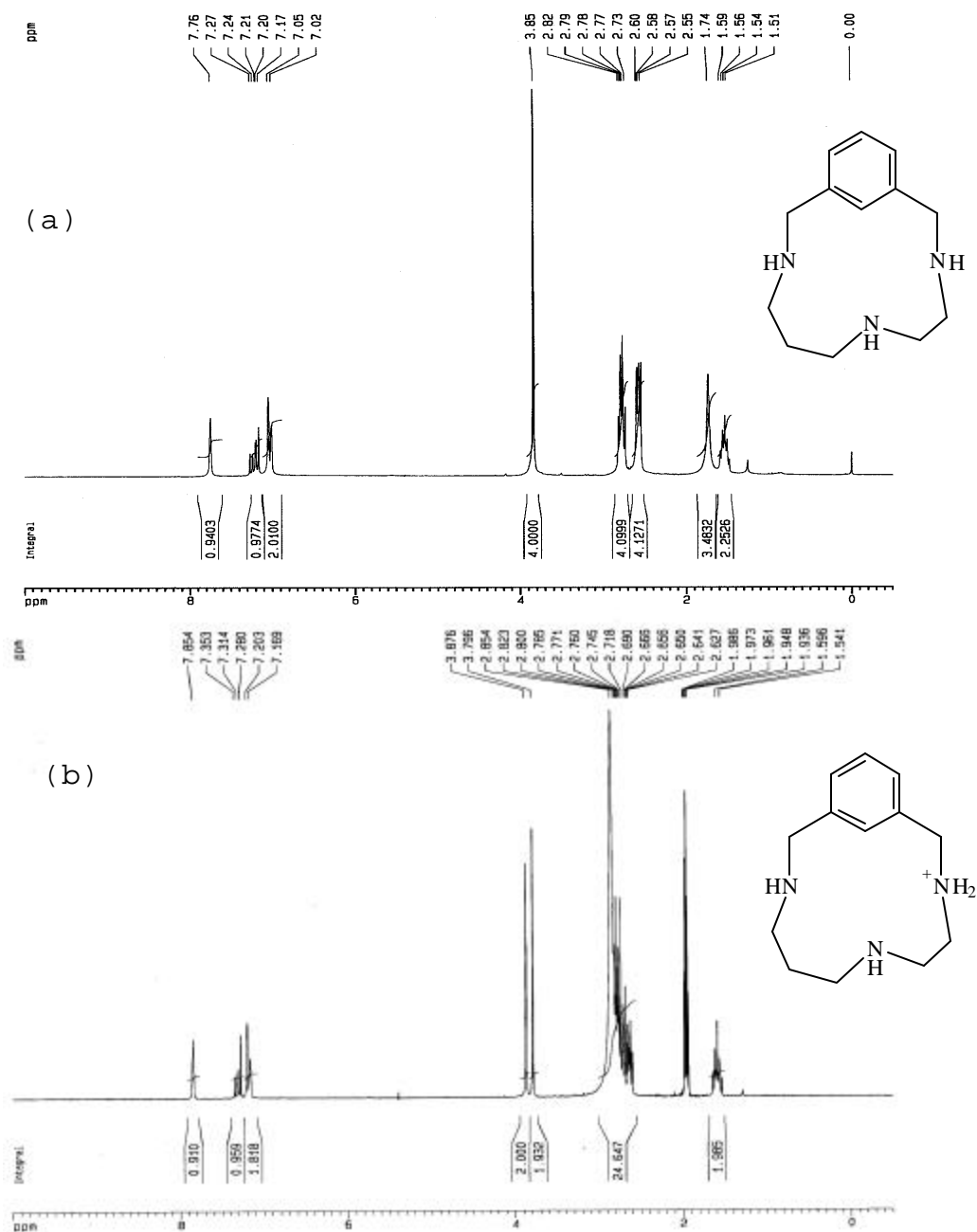
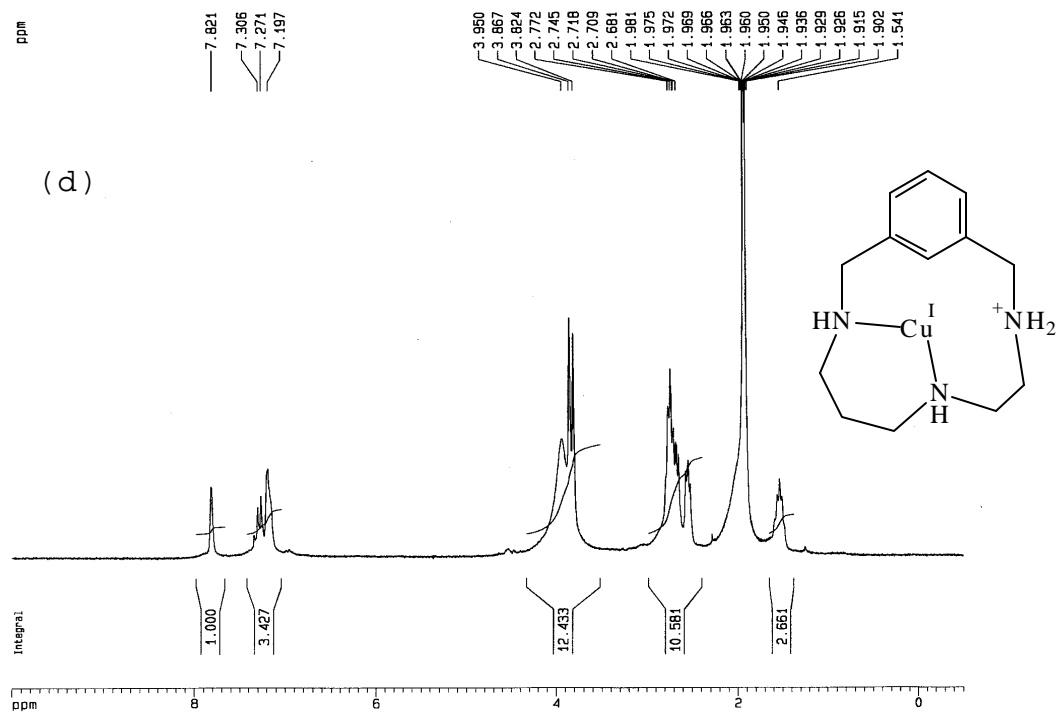
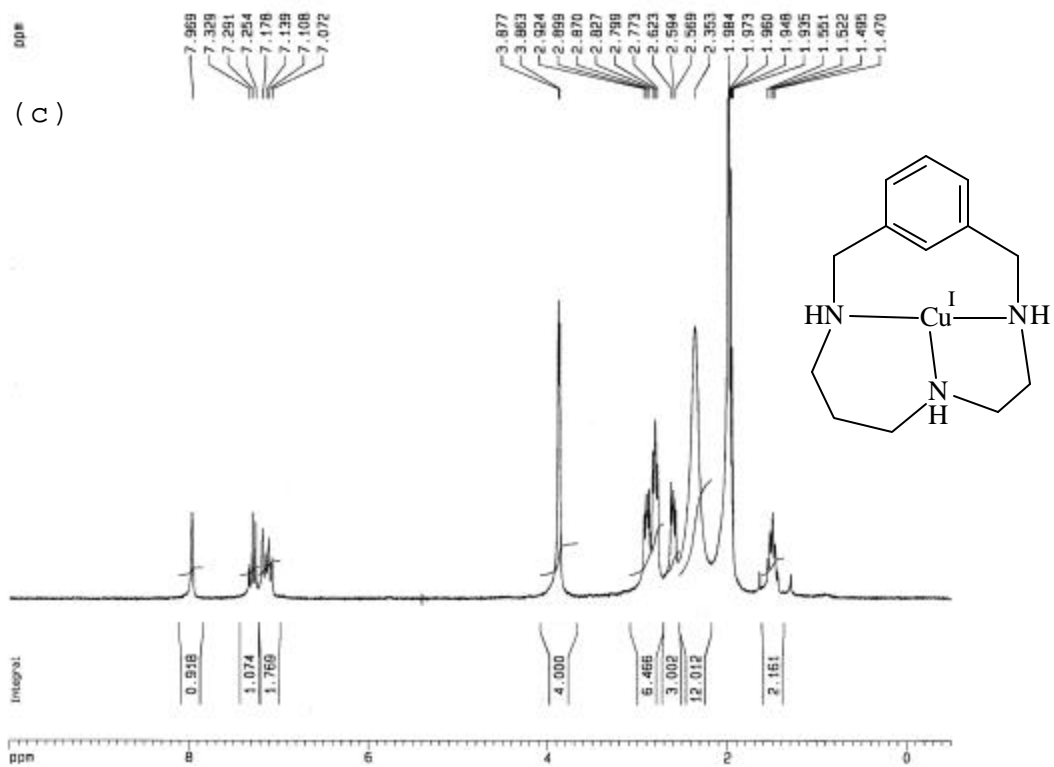


Figure S8. ^1H NMR spectra for (a) Ligand H32m in CDCl_3 , (b) monoprotonated $[\text{H32mH}]^+$ ligand with 1 eq of HClO_4 (in CDCl_3), (c) complex $[(\text{H32m})\text{Cu}^{\text{I}}]$ in CD_3CN at 300 K and (d) monoprotonation of Cu^{I} complex $[(\text{H32m})\text{Cu}^{\text{I}}]$ with 1 eq. of $\text{CF}_3\text{SO}_3\text{H}$. (e) ESI-MS spectrum for final reaction mixture $[(\text{H32m-C})\text{Cu}^{\text{III}}](\text{ClO}_4)_2 / [\text{Cu}^{\text{I}}(\text{CH}_3\text{CN})_4]^+ / [\text{H32mH}]^+$.





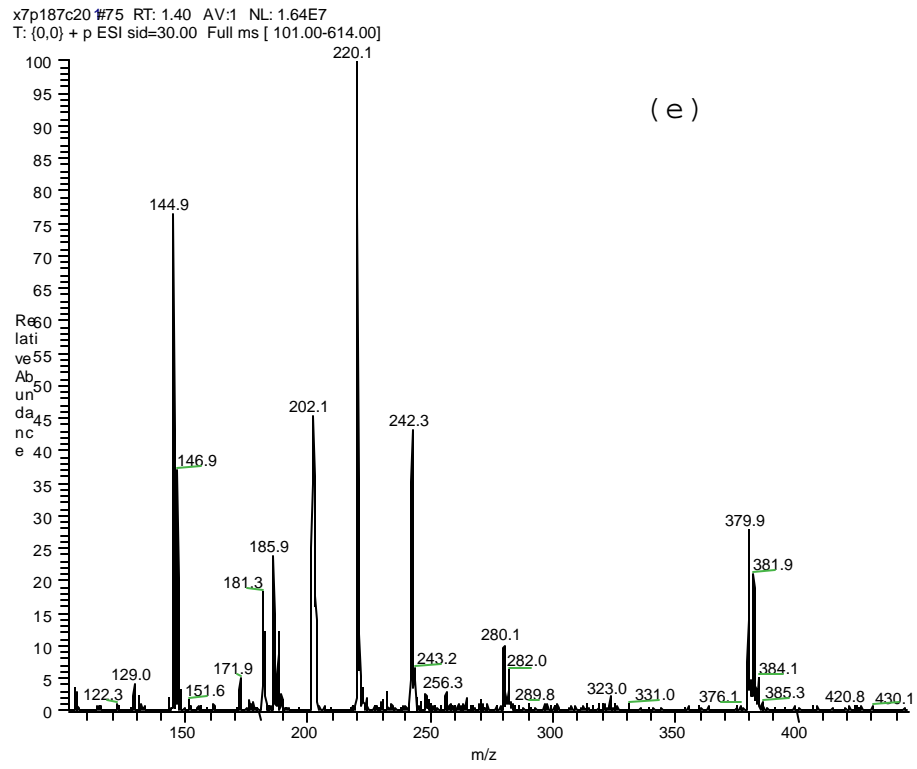


Figure S9. CV of (a) final reaction mixture [(H32m-C)Cu^{III}](ClO₄)₂/[Cu^I(CH₃CN)₄]⁺/[H32mH]⁺ and (b) complex [(H32m)Cu^I]⁺ after treatment with 1 eq of triflic acid (CH₃CN, TBAP 0.2 M, R.T.).

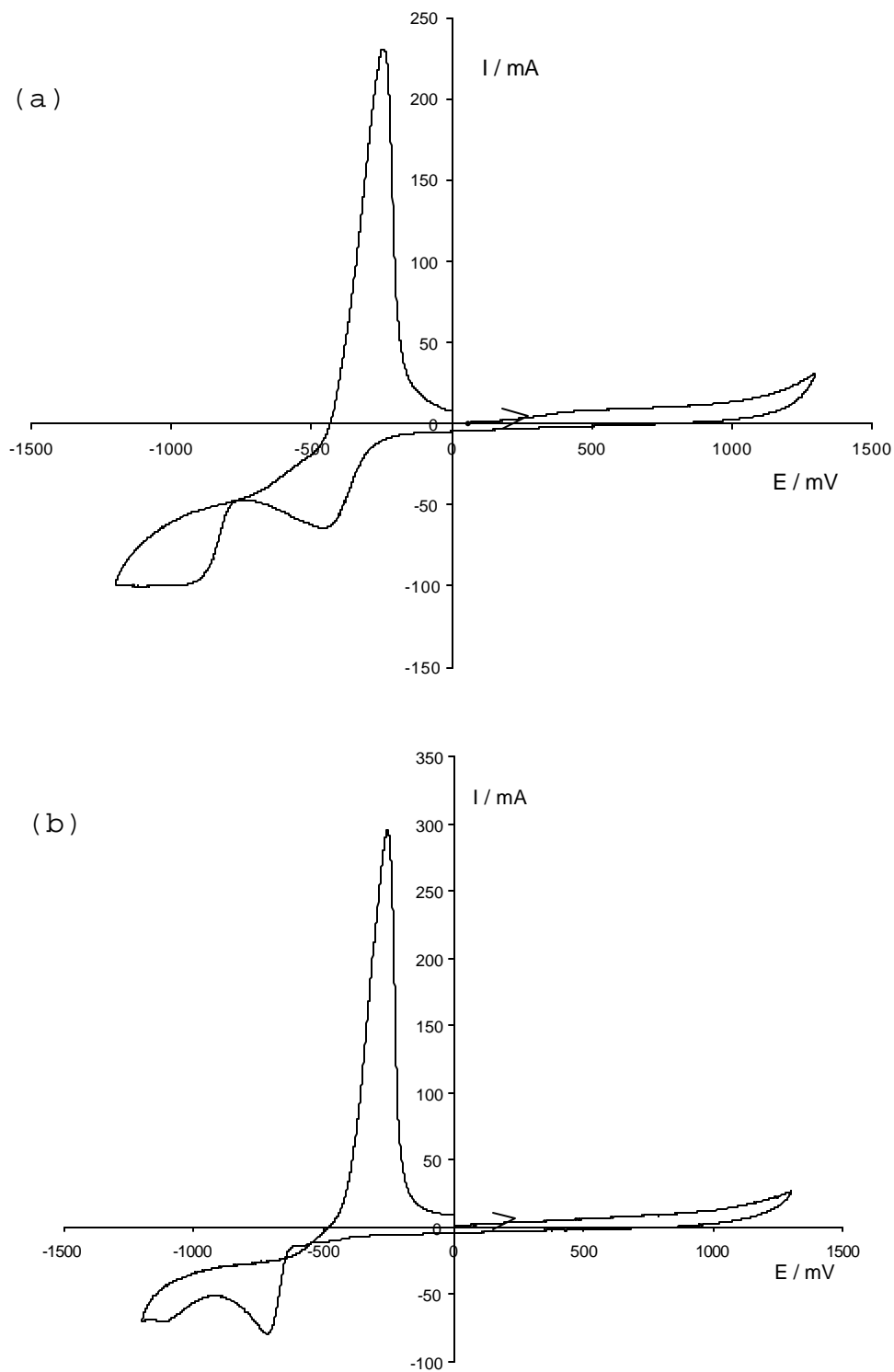


Figure S10. Cyclic Voltammetry for complex $[(H_2Me_3m-C)Cu^{III}](OTf)_2$ ($2-(OTf)_2$) at different scan rates (mV/s): (a) 400, (b) 300, (c) 200, (d) 150, (e) 100, (f) 80, (g) 60, (h) 40, (i) 20. ($[2] \approx 2mM$, CH_3CN , R.T.).

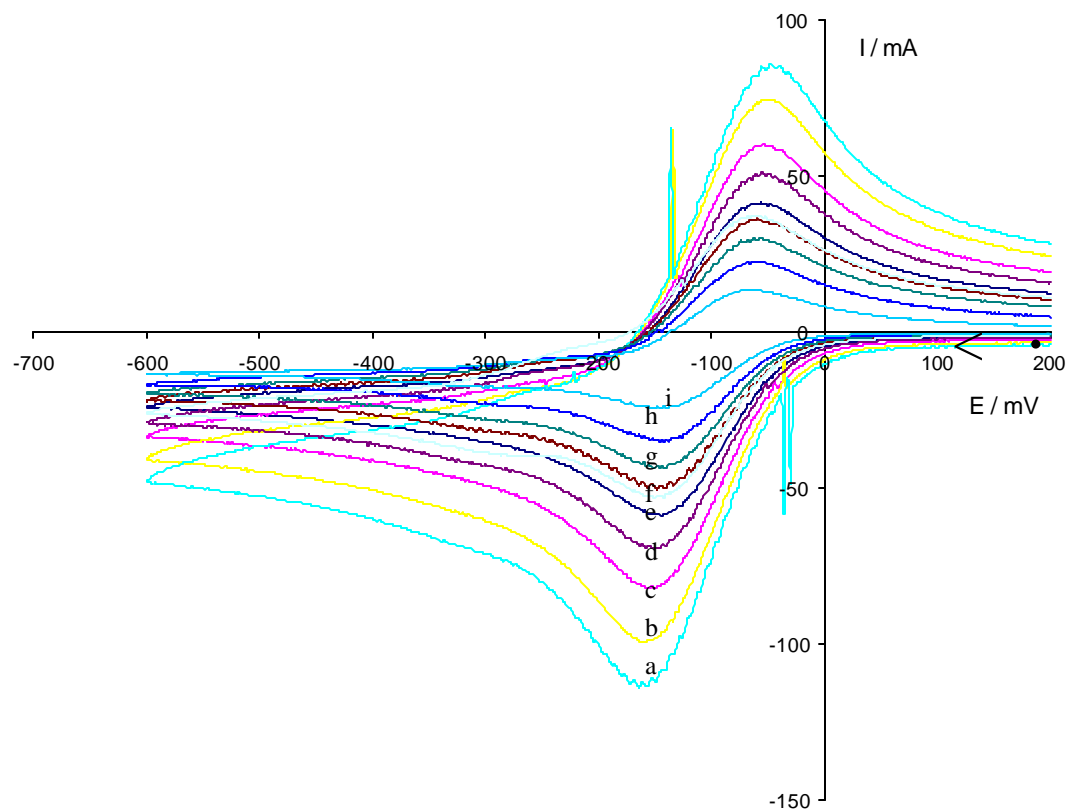


Figure S11. Plot of I_p vs $v^{1/2}$ of $2-(OTf)_2$ system (Randles-Sevcik equation: $i_p = (2.69e+5)n^{3/2}AD_o^{1/2}C_o v^{1/2}$ where $v^{1/2}$ (V/s) $^{1/2}$, I_p (A), A (cm 2), D_o (cm 2 /s), C_o (mol/mL), n (electrons transferred)). Data extracted from previous Figure S10.

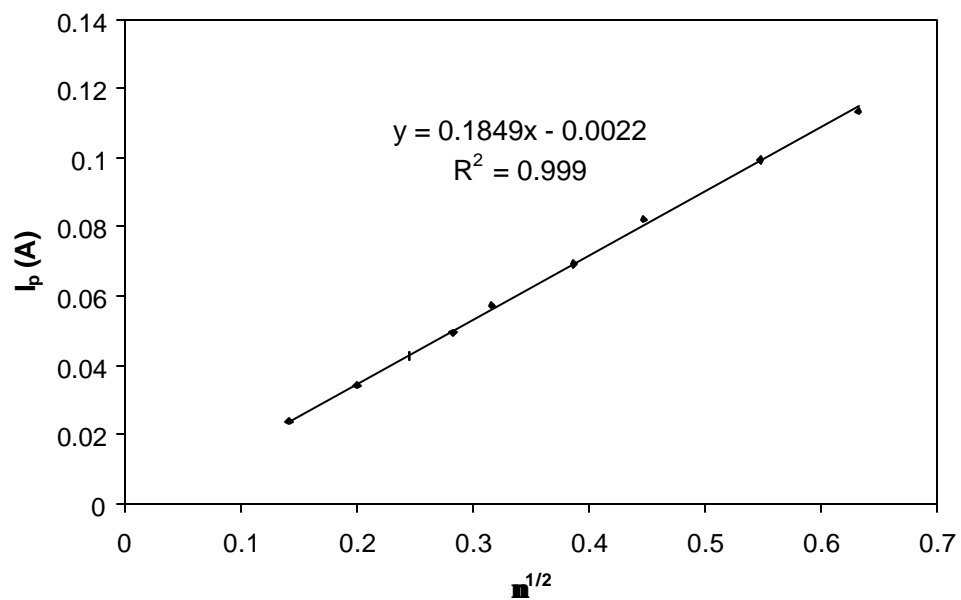


Figure S12. Cyclic Voltammetry for complex $[(\text{H33m-C})\text{Cu}^{\text{III}}](\text{ClO}_4)_2$ ($3-(\text{ClO}_4)_2$) at different scan rates (mV/s): 400, 300, 200, 150, 100, 80, 60, 40, 20. Ferrocene is used as internal reference ($[\mathbf{3}] \approx [\text{ferrocene}] \approx 2\text{mM}$, CH_3CN , R.T.).

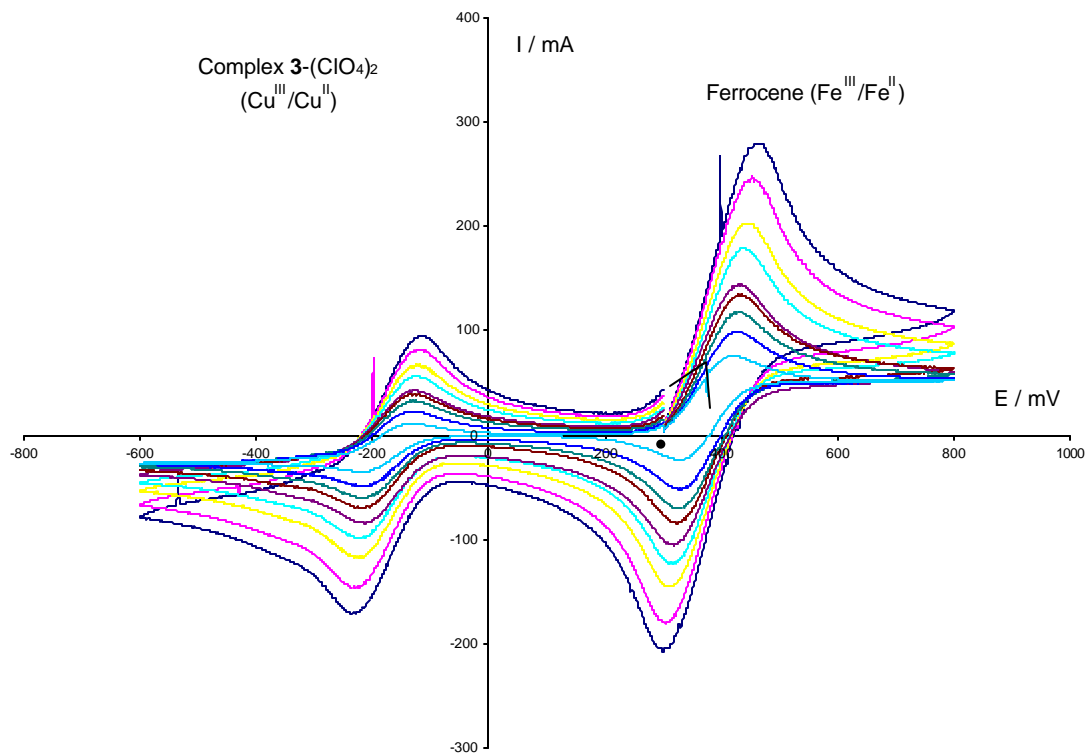


Figure S13. Plot of I_p vs $v^{1/2}$ of 3-(ClO₄)₂ system (Randles-Sevcik equation: $i_p = (2.69e+5)n^{3/2}AD_o^{1/2}C_o v^{1/2}$ where $v^{1/2}$ (V/s)^{1/2}, I_p (A), A (cm²), D_o (cm²/s), C_o (mol/mL), n (electrons transferred)). Data extracted from previous Figure S12.

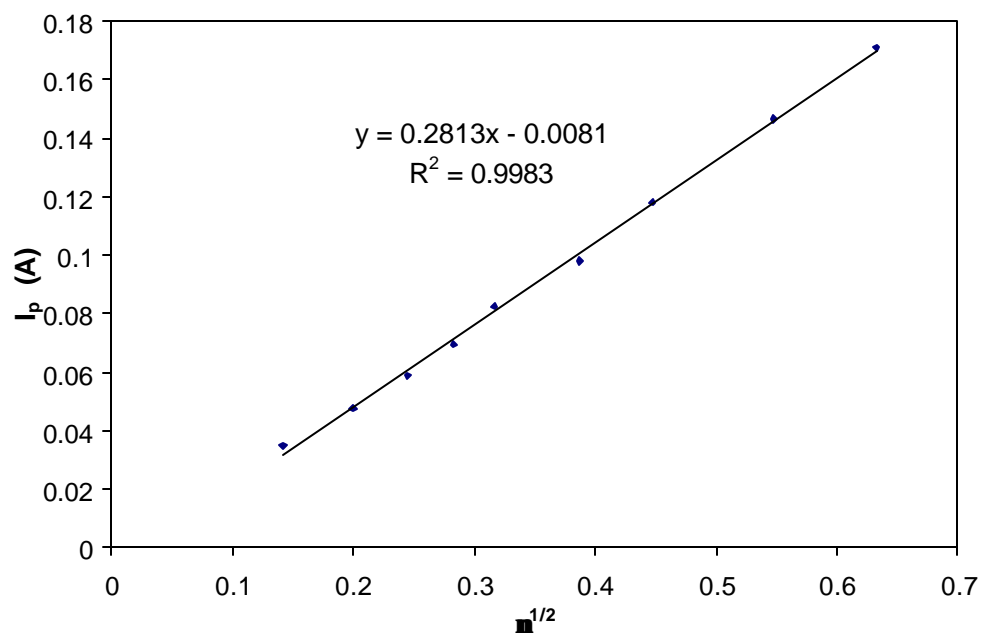


Figure S14. Cyclic Voltammetry of complex $[(\text{H33m-C})\text{Cu}^{\text{III}}](\text{OTf})_2$ ($\mathbf{3}-(\text{OTf})_2$). Scan rate = 400 mV/s, $[\mathbf{3}] \approx 2\text{mM}$, TBAP 0.2 M, CH_3CN , R.T.

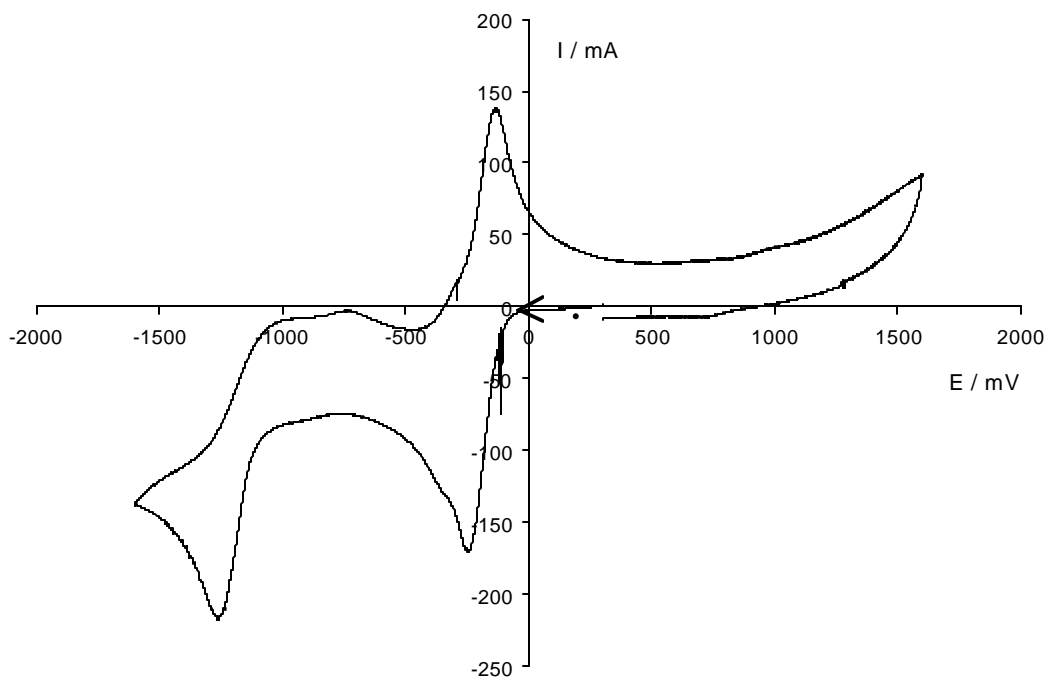


Figure S15. Cyclic Voltammetry of complex $[(\text{H33m-C})\text{Cu}^{\text{III}}](\text{OTf})_2$ ($\mathbf{3}-(\text{OTf})_2$). Scan rate = 10 mV/s, $[\mathbf{3}] \approx 2\text{mM}$, TBAP 0.2 M, CH_3CN , R.T. .

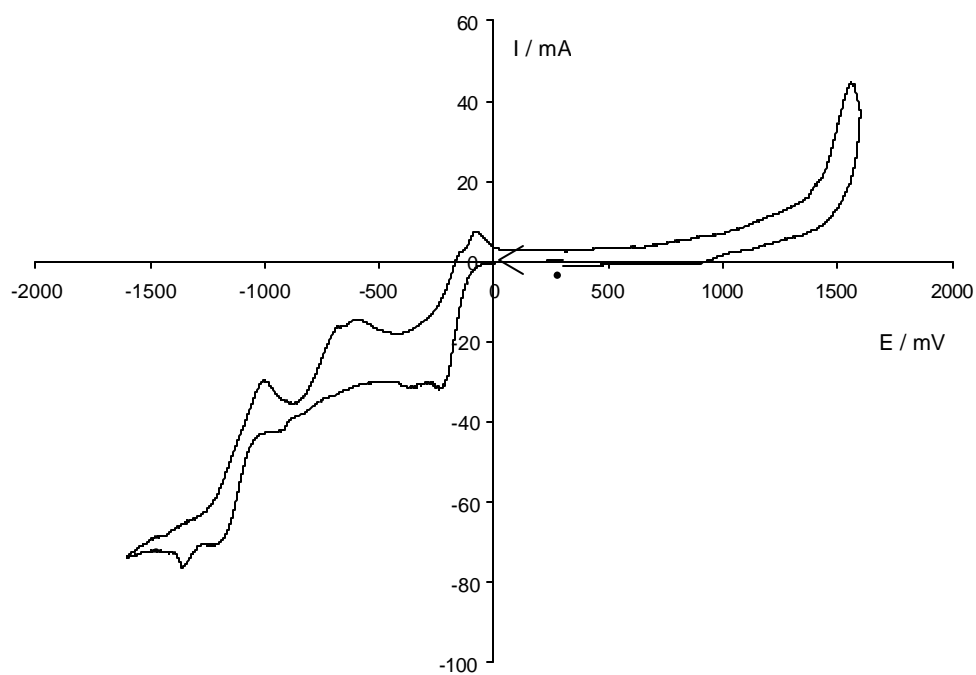


Figure S16. Coulometry at $E = -0.25$ V applied potential for complex $[(\text{H33m-C})\text{Cu}^{\text{III}}](\text{OTf})_2$ ($\mathbf{3}-(\text{OTf})_2$) ($[\mathbf{3}] = 1.18$ mM, CH_3CN , R.T.).

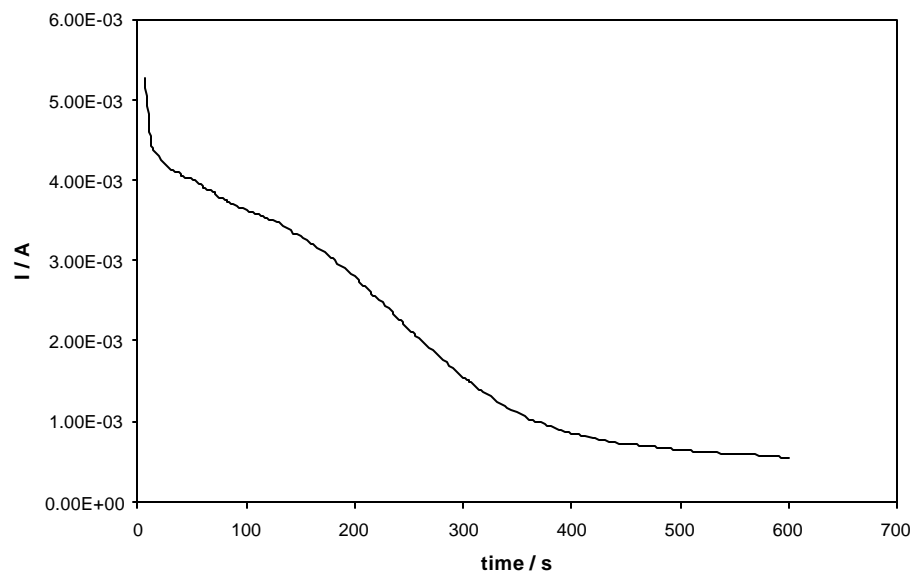


Figure S17. Cyclic Voltammetry for final colorless solution after coulometry experiment at -0.25 V applied potential on complex $[(\text{H33m-C})\text{Cu}^{\text{III}}](\text{OTf})_2$ ($\mathbf{3}-(\text{OTf})_2$), corresponding to $[\text{Cu}^{\text{I}}(\text{CH}_3\text{CN})_4]^+$ ($[\mathbf{3}] = 1.18$ mM, CH_3CN , R.T.).

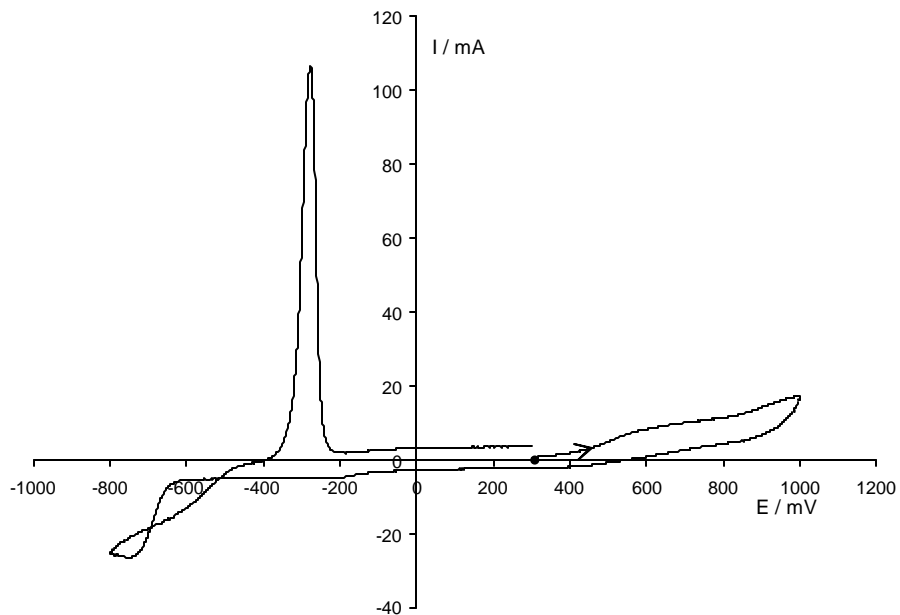


Figure S18. Cyclic Voltammetry of complex [(H33m-C)Cu^{III}(Cl)](OTf) (**4**-(OTf)). Scan rate = 100 mV/s, [**4**] ≈ 2 mM, TBAP 0.2 M, CH₃CN, R.T. (ferrocene as internal reference).

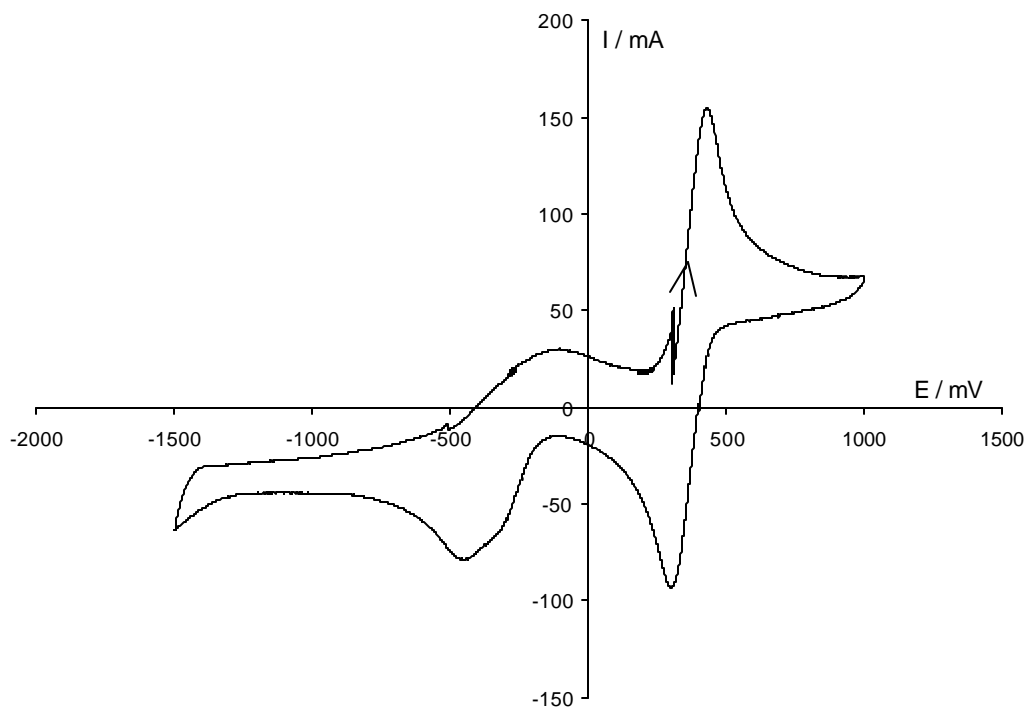


Figure S19. (a) ^1H NMR spectrum for Cu^{I} complex $[(\text{H}22\text{m})\text{Cu}^{\text{I}}](\text{PF}_6)$ in CD_2Cl_2 at 300 K and (b) ESI-MS of same complex in CH_3CN (inset shows the simulation for fragment $[(\text{H}22\text{m})\text{Cu}^{\text{I}}(\text{CH}_3\text{CN})]^+$).

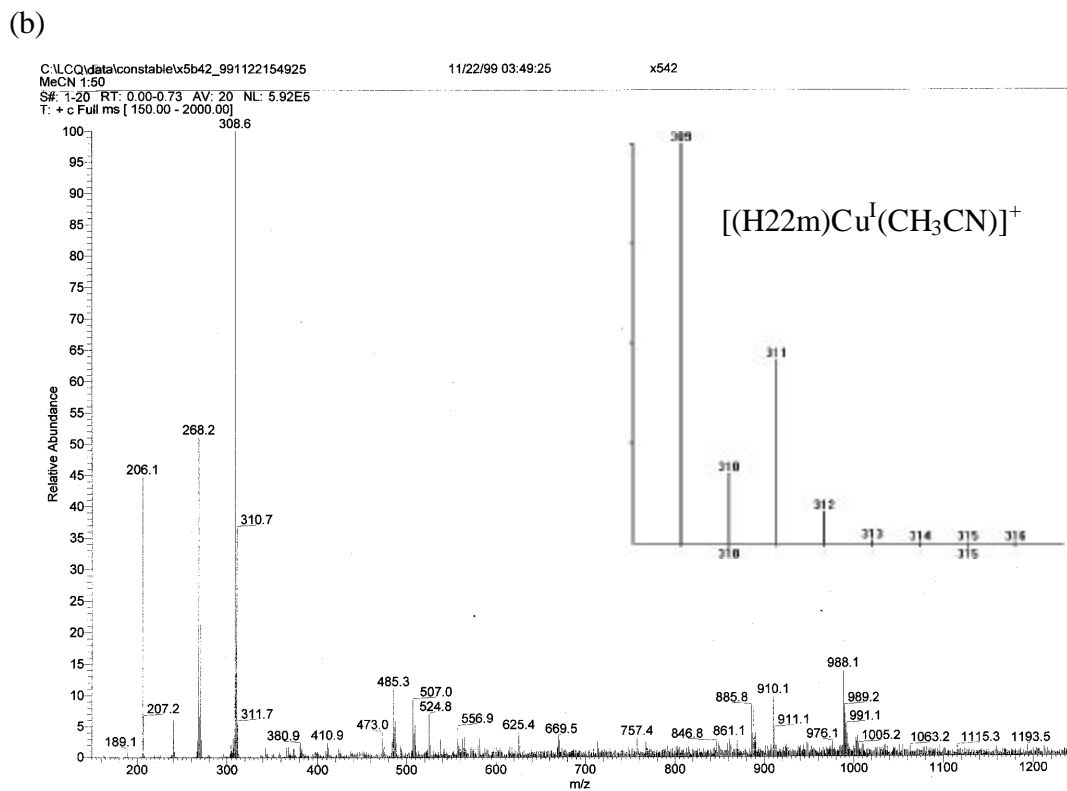
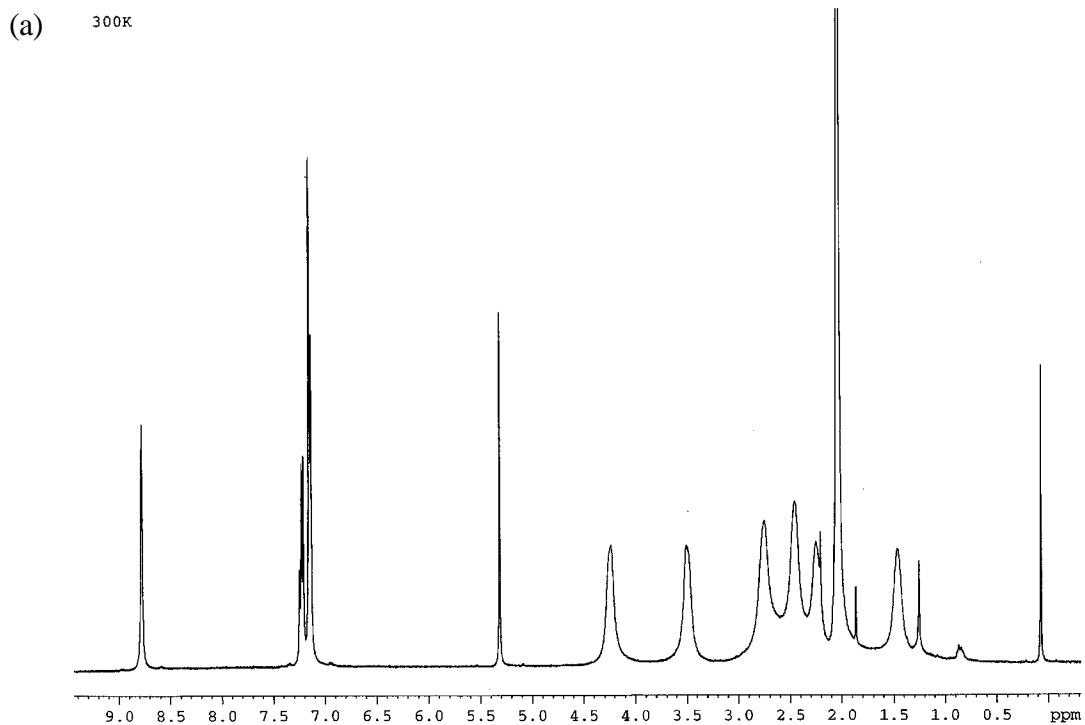


Figure S20. Electronic spectra for the decay of Cu^{II} d-d band at 640 nm for complex [(H32m)Cu^{II}](OTf)₂ ([Cu^{II}]_i = 1.27 mM, [H32m]_i = 1.62 mM, CH₃CN, 25°C, 1 scan/ 1 second).

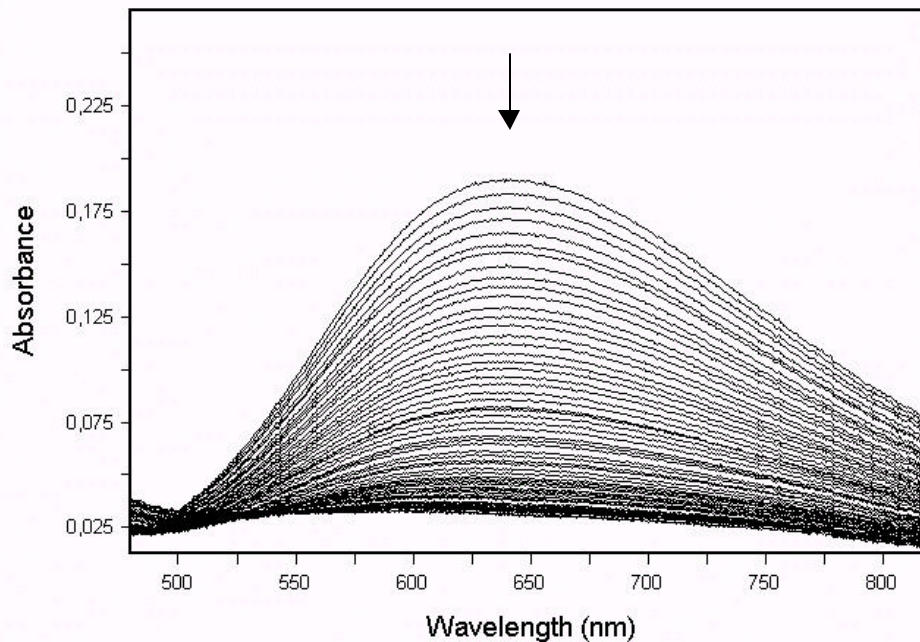


Figure S21. Eyring plot ($\ln(k_{\text{obs}})$ vs $1/T$) from kinetic data for [(H32m)Cu^{II}](OTf)₂ ([Cu^{II}]_i = 1.25 mM, [H32m]_i = 1.60 mM, CH₃CN) in a Temperature Range from 0 to 25°C.

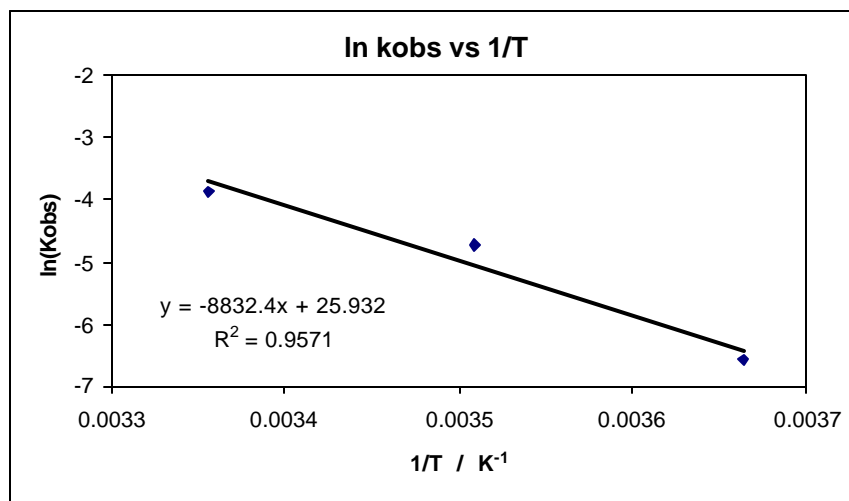


Figure S22. Electronic spectrum for the decay of Cu^{II} band at 420nm, known to be associated to the d-d band, for complex $[(\text{H}_2\text{Me33m})\text{Cu}^{\text{II}}](\text{OTf})_2$ ($[\text{Cu}^{\text{II}}]_i = 2.47 \text{ mM}$, $[\text{H32m}]_i = 3.15 \text{ mM}$, CH_3CN , 25°C , 1 scan / 0.5 seconds).

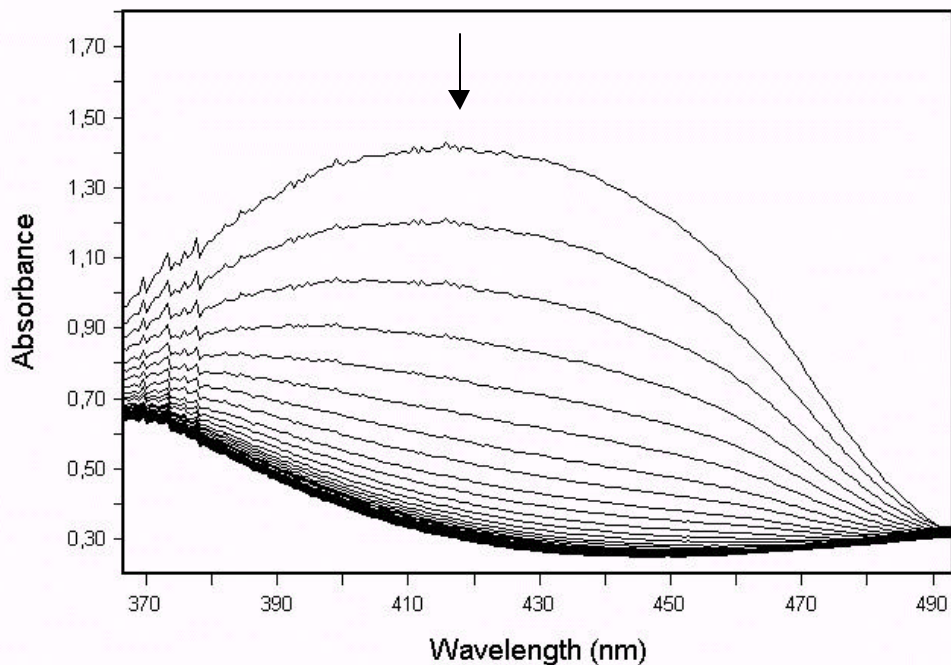


Figure S23. Eyring plot ($\ln(k_{\text{obs}})$ vs $1/T$) from kinetic data for $[(\text{H}_2\text{Me33m})\text{Cu}^{\text{II}}](\text{OTf})_2$ ($[\text{Cu}^{\text{II}}]_i = 1.21 \text{ mM}$, $[\text{H32m}]_i = 1.55 \text{ mM}$, CH_3CN) in a Temperature Range from -10 to 25°C .

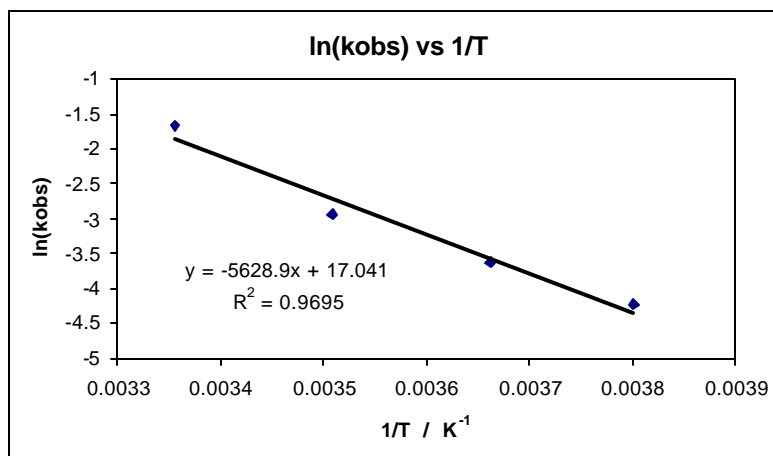


Figure S24. Cu^{II} complex bands decay for 1.2 H33m(D)/ Cu^{II} experiment and decay profile at 640 nm for H33m/ Cu^{II} , H33m(D)/ Cu^{II} and 1.2 H33m(D)/ Cu^{II} (Conc Cu^{II} = 2.5 mM, R.T., CH_3CN).

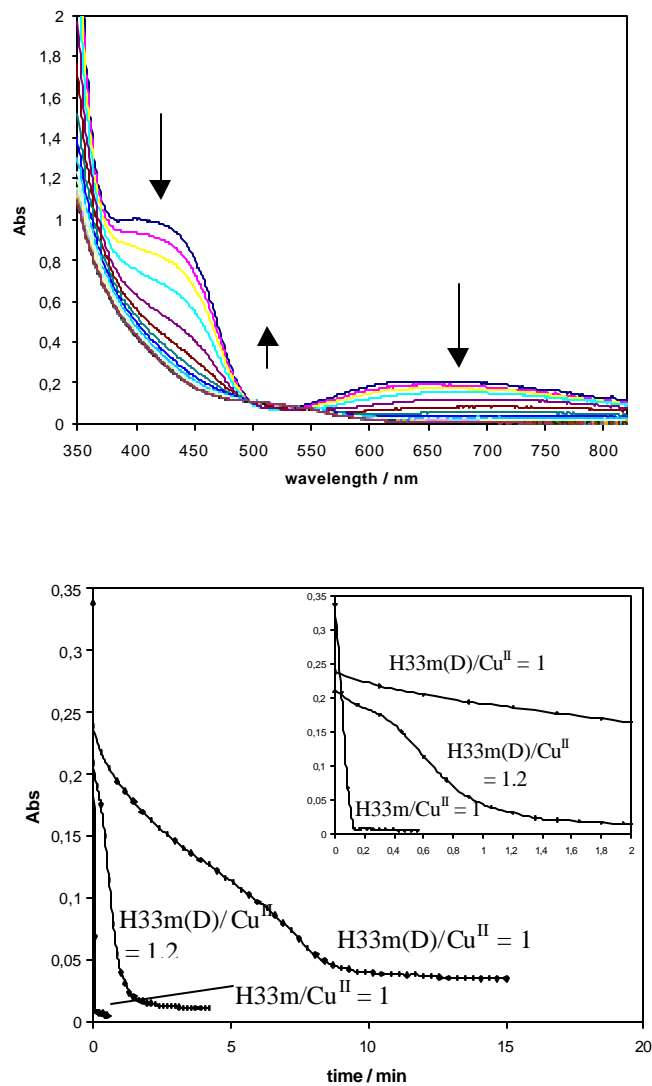
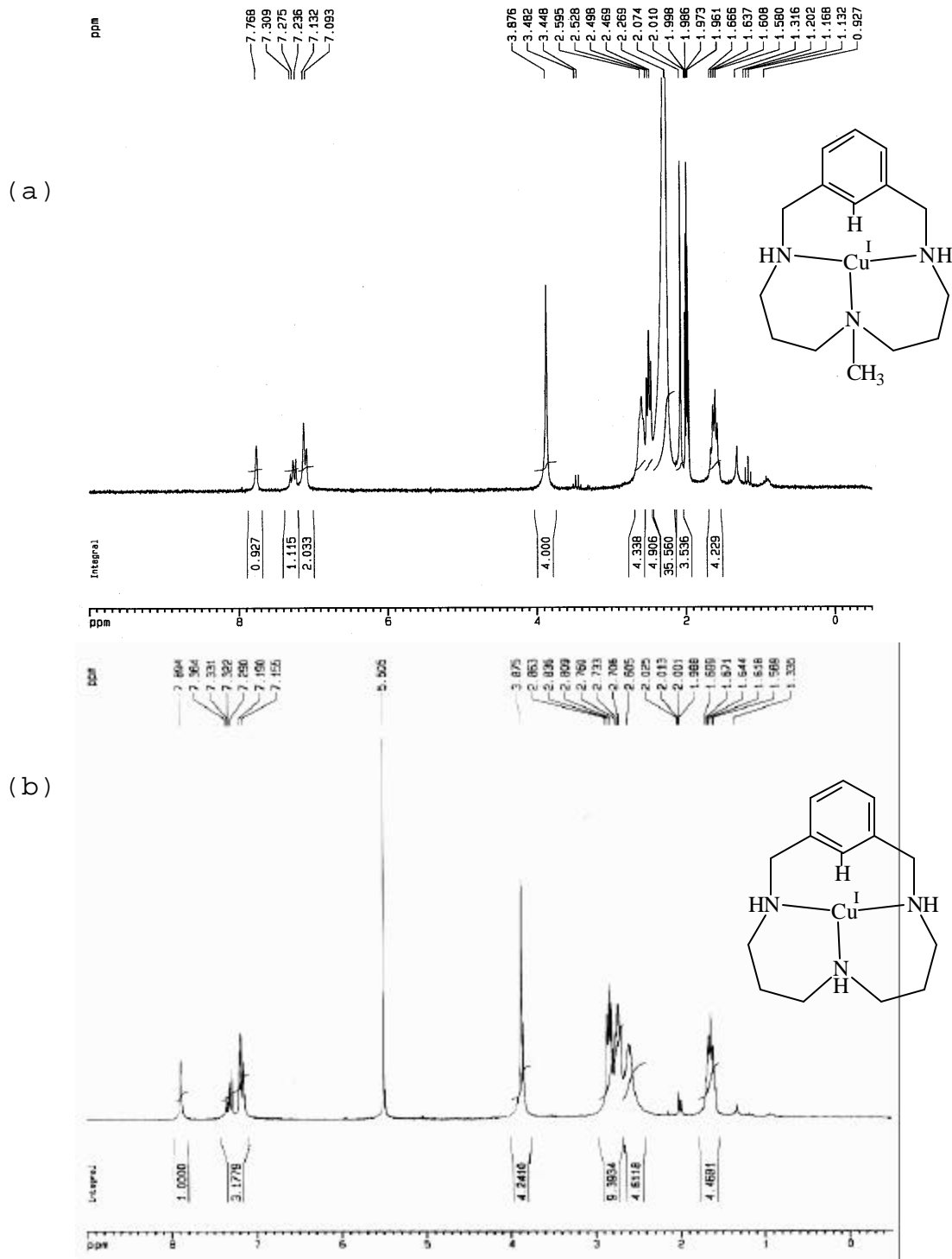


Figure S25. ^1H NMR spectra of Cu^{I} complexes (a) $[(\text{H}_2\text{Me33m})\text{Cu}^{\text{I}}]^+$ and (b) $[(\text{H33m})\text{Cu}^{\text{I}}]^+$ in CD_3CN (see $[(\text{H32m})\text{Cu}^{\text{I}}]^+$ in Figure S8c), and final Deuterated Cu^{I} complexes in Acetone- $[\text{D}_6]$ after full H/D exchange: (c) $[(\text{H}_2\text{Me33m}(\text{D}))\text{Cu}^{\text{I}}]^+$ and (d) $[(\text{H33m}(\text{D}))\text{Cu}^{\text{I}}]^+$.



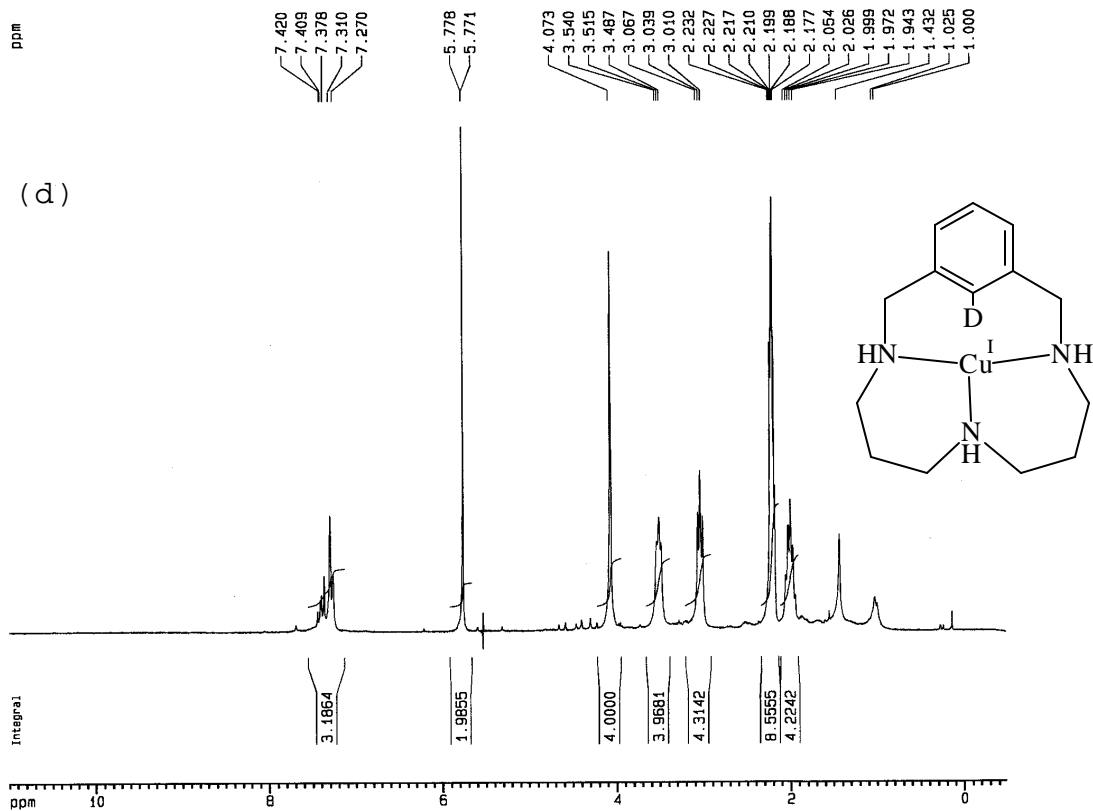
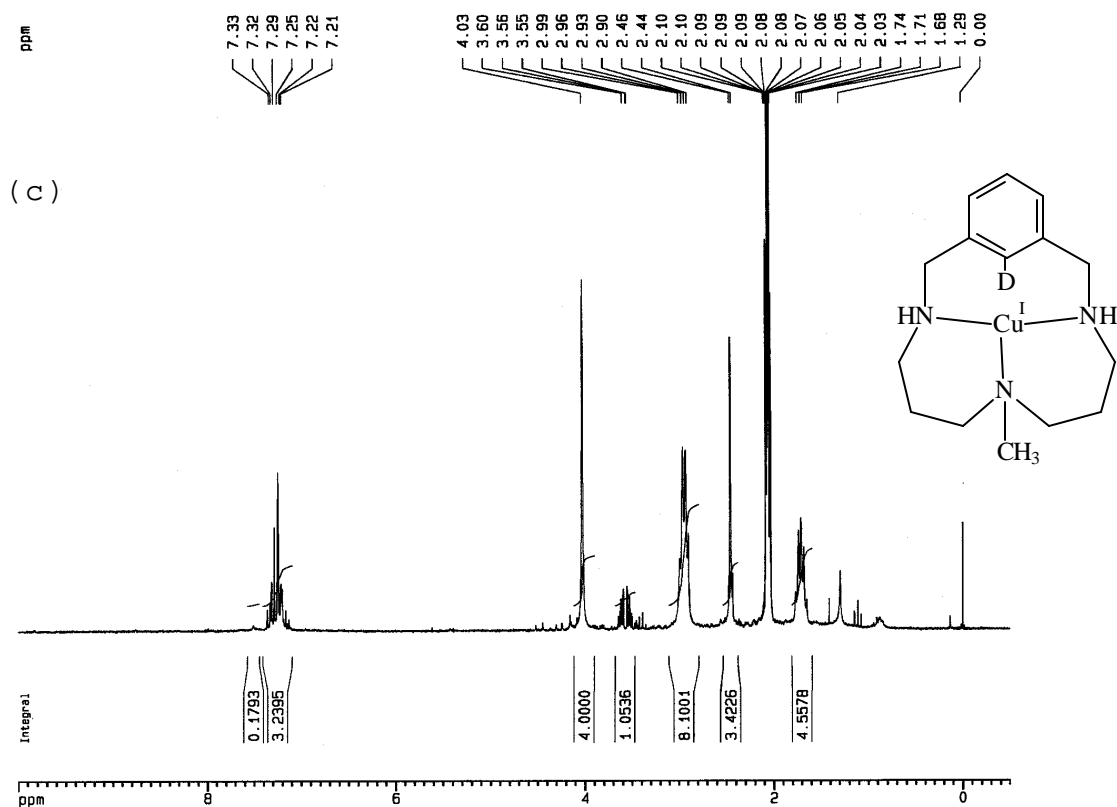


Figure S26. H/D exchange profile for systems with H32m, H₂Me33m, H33m. Plot of aromatic proton ¹H NMR integration vs time.

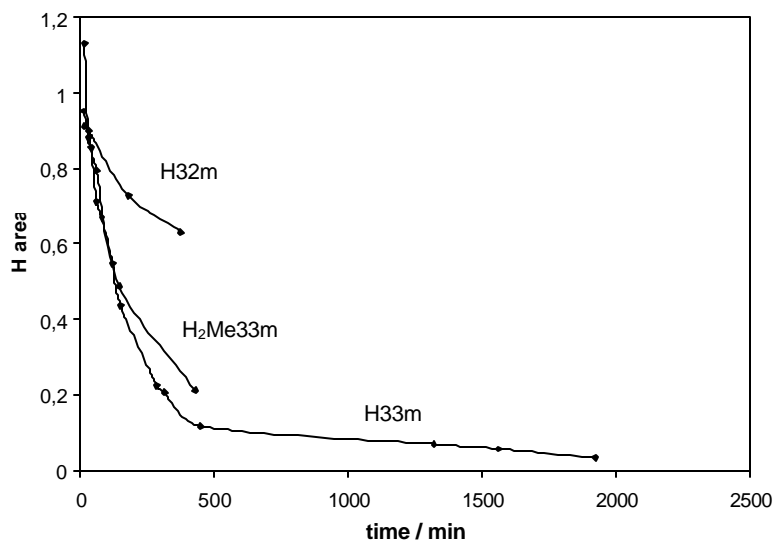


Figure S27. ESI-MS of deuterated complex [(H33m(D))Cu^I]⁺.

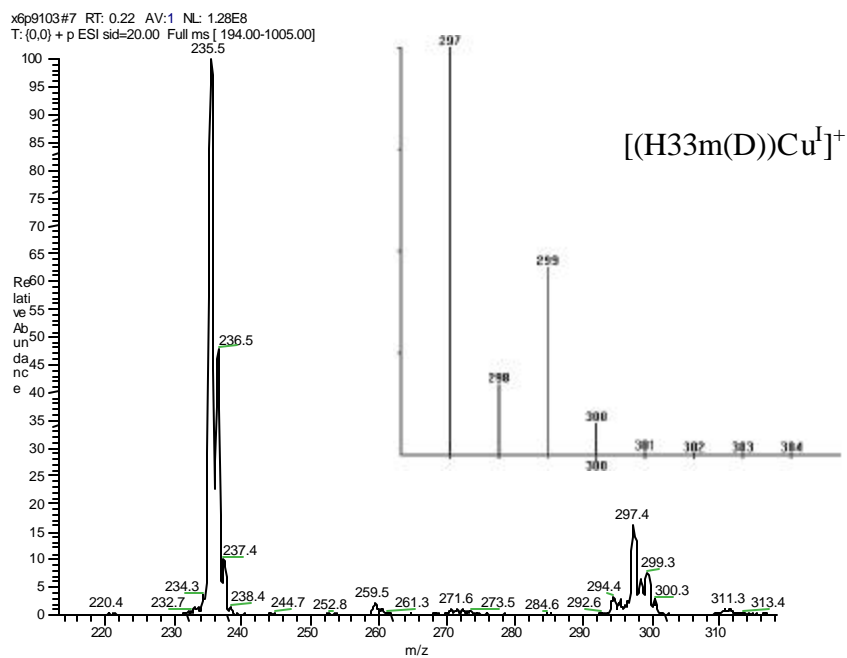


Figure S28. (a) ESI-MS of deuterated ligand H33m(D) and (b) ^1H NMR (200 MHz, CDCl_3 , 300 K) of H33m(D).

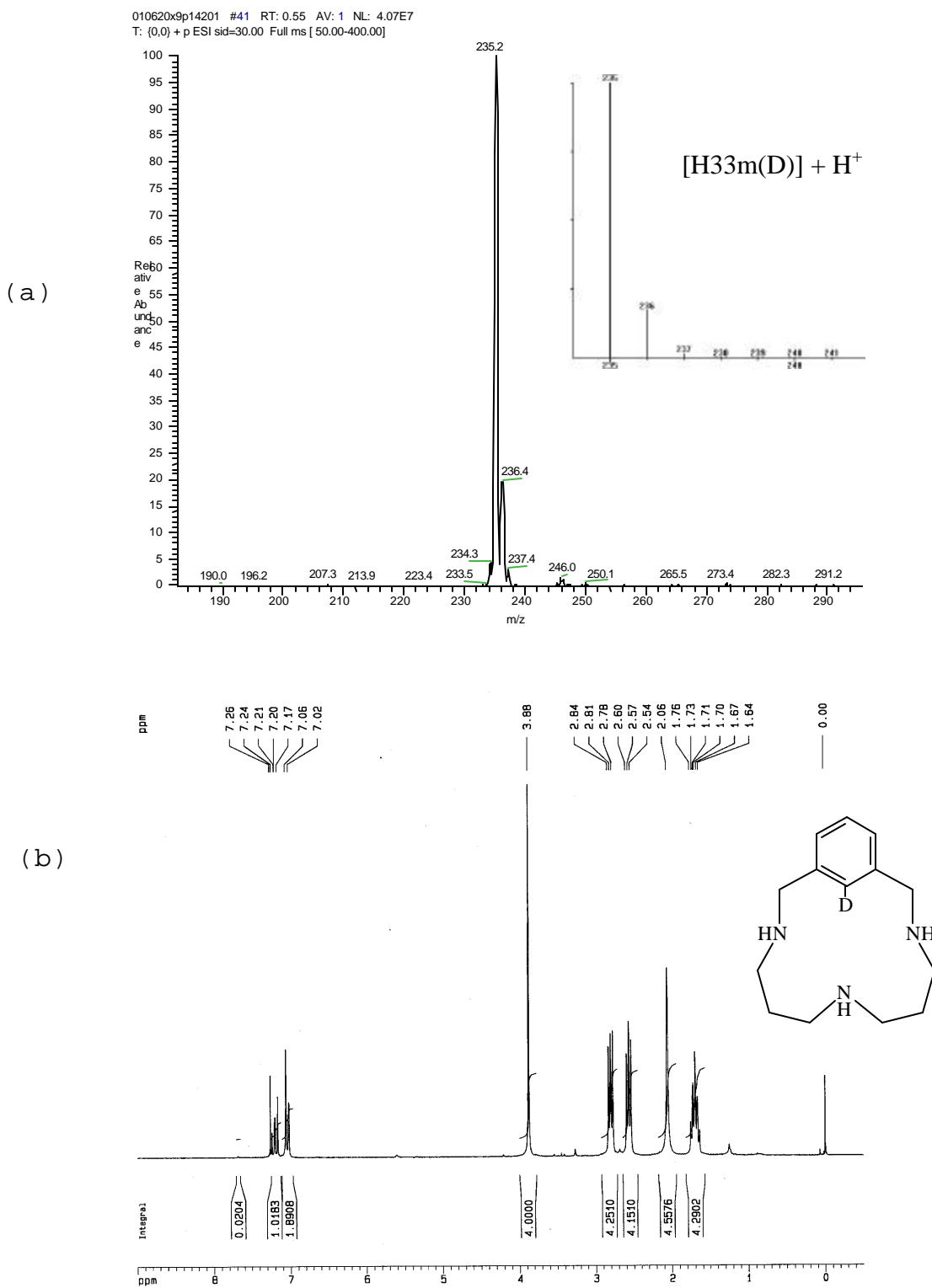


Figure S29. ORTEP and wireframe plot of packing cell for aryl- Cu^{II} complex $[((\text{H33m-C})\text{Cu}^{\text{II}})_2(\mu\text{-Cl})](\text{PF}_6) \cdot 6\text{H}_2\text{O} \cdot \text{CH}_2\text{Cl}_2$ (**6**- $\text{PF}_6 \cdot 6\text{H}_2\text{O} \cdot \text{CH}_2\text{Cl}_2$). Enclosure boxes in each axis indicated in brackets.

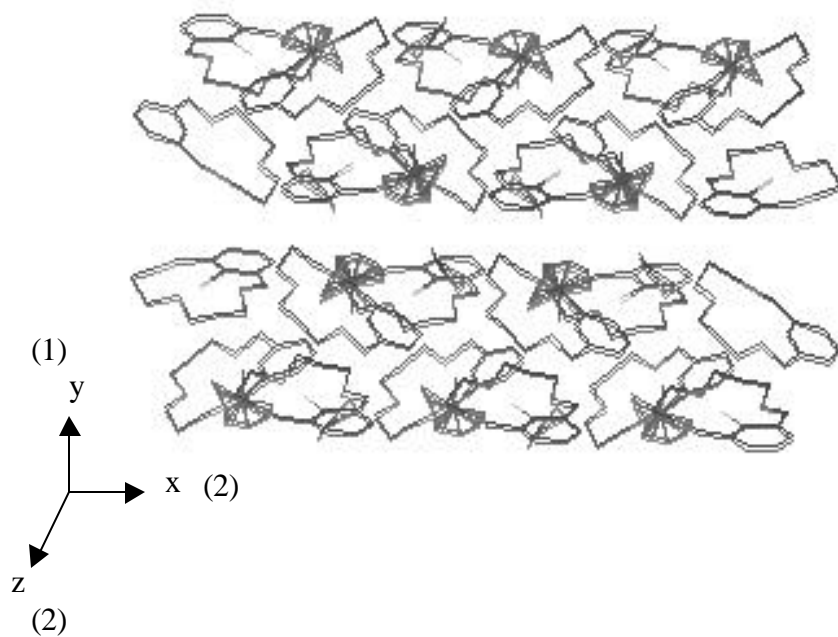
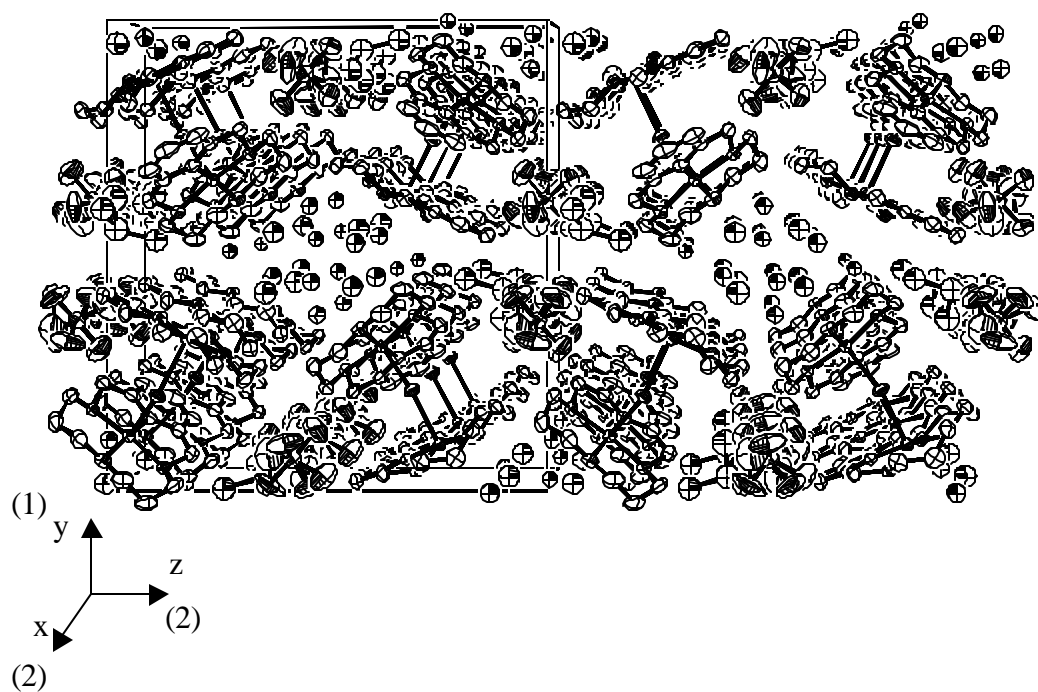


Figure S30. Chem3D view of optimized geometry for system $[(\text{H33m})\text{Cu}^{\text{I}}]^+$.

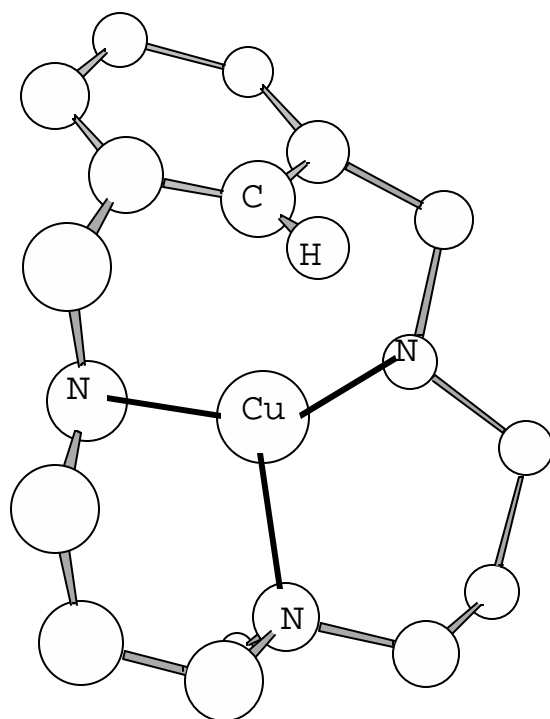
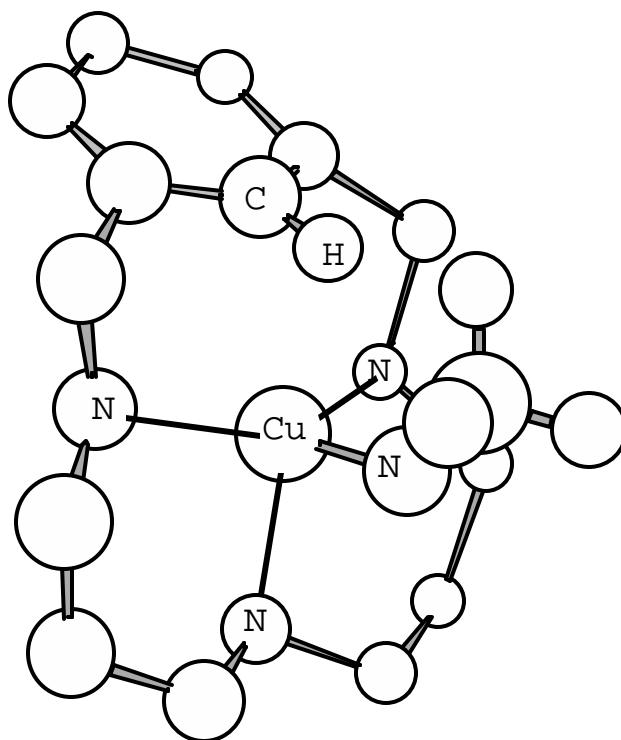


Figure S31. Chem3D view of optimized geometry for system $[(\text{H33m})\text{Cu}^{\text{I}}(\text{CH}_3\text{CN})]^+$.



CHAPTER 4

Aryl-Cu^{III} complexes reactivity. New intermediates in
aromatic hydroxylation

4.1	ABSTRACT	201
4.2	INTRODUCTION	203
4.3	RESULTS	205
4.3.1	SYNTHESIS.....	205
4.3.1.1	<i>The ligands</i>	205
4.3.1.2	<i>Cu^I complexes</i>	205
4.3.1.3	<i>Cu^{III} complexes</i>	205
4.3.1.4	<i>Cu^{II} complexes</i>	206
4.3.1.5	<i>Cu^{III} colored intermediates</i>	208
4.3.2	X-RAY STRUCTURES OF BISPHENOXO COMPLEXES.....	209
4.3.3	SPECTROSCOPIC PROPERTIES.....	218
4.3.3.1	<i>X-Ray Absorption Spectroscopy (XAS) of 1b-2b</i>	218
4.3.3.2	<i>¹H NMR characterization of intermediates 1b-3b</i>	219
4.3.3.3	<i>UV-Vis Spectroscopy of intermediates 1b-3b</i>	221
4.3.3.4	<i>Raman spectroscopy of intermediate 3b</i>	222
4.4	DISCUSSION	223
4.4.1	HYDROXYLATION REACTION DETAILS.....	223
4.4.2	DIOXYGEN ACTIVATION BY Cu ^I COMPLEXES.....	225
4.4.3	MECHANISTIC STUDIES.....	231
4.4.4	THE H22M SYSTEM	235
4.4.5	OXIDANT CHARACTER OF ARYL-Cu ^{III} COMPLEXES (1-3)	235
4.5	EXPERIMENTAL SECTION	236
4.6	REFERENCES	245

CHAPTER 4

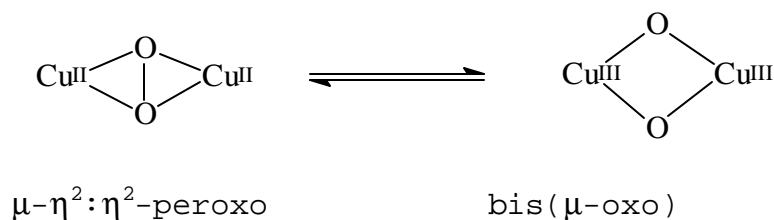
Aryl-Cu^{III} complexes reactivity. New intermediates in aromatic hydroxylation

4.1 ABSTRACT

Reactivity of Aryl-Cu^{III} complexes **1-3** has been studied under different conditions. Reaction with non-coordinating bases in presence of water affords the formation of novel dinuclear bisphenoxo complexes $[(H32mO)_2Cu^{II}_2]^{2+}$ (**1c**), $[(H_2Me33mO)_2Cu^{II}_2]^{2+}$ (**2c**) and $[(H33mO)_2Cu^{II}_2]^{2+}$ (**3c**), which have been structurally characterized by XRD. The insertion of the oxygen atom to the previously activated aromatic carbon takes place through colored intermediates $[(L-C)'Cu^{III}]^+$ (**1b-3b**) characterized as the amine deprotonated form of Aryl-Cu^{III} species. The aromatic hydroxylation reaction performed from isolated Cu^{III} species **1-3** is directly related to the reactivity presented by Cu^I complexes $[(L)Cu^I]^+$ (L= H32m, H₂Me33m, H33m; **7, 8, 9**) with molecular dioxygen. O₂ activation occurs at low temperature in CH₃CN to form a side-on peroxo intermediate, capable of rearranging to the same colored Cu^{III} intermediates **1b-3b** at room temperature. Final products of the Cu^I/O₂ reaction are again the bisphenoxo complexes **1c-3c**. Reactivity studies and isolation of complexes $[(H22mO)_2Cu^{II}_2]^{2+}$ (**5c**) and $[(H_2Me33mO)_2Cu^{II}_2(Cl)_2]$ (**2d**) are helpful to propose a plausible mechanism for the aromatic hydroxylation reaction.

4.2 INTRODUCTION

Metal-mediated activation of hydrocarbon C-H bonds are of interest due to their involvement in metalloenzymes reactivity and industrial oxidations. Oxidations conducted by copper metalloenzymes such as tyrosinase¹ and dopamine β -hydroxylase² are widely studied, and many chemical models have been synthesized.³ In the particular case of tyrosinase, the dinuclear Cu active site activates dioxygen to form a $(\mu:\eta^2:\eta^2\text{-peroxo})\text{dicopper(II)}$ intermediate, which is considered one of the possible active species in aromatic hydroxylation of tyrosine. Chemical models of tyrosinase reactivity present intramolecular ligand hydroxylation through a generally accepted electrophilic peroxide oxygen attack to the π -system of the aromatic ring.^{3,4} However, some questions still remain unanswered,⁵ and one of them is when does the O-O bond break. Cu^{III} has been invoked in many reaction mechanisms,^{6,7} and since the equilibrium between $(\mu:\eta^2:\eta^2\text{-peroxo})\text{dicopper(II)}$ and $\text{bis}(\mu\text{-oxo})\text{dicopper(III)}$ isomers was discovered,⁸ chemists have indeed focused deeply in Cu^{III} intermediates to be responsible of reactions such as aromatic hydroxylation in tyrosinase.⁹ It is known that both $\text{bis}(\mu\text{-oxo})$ and $\mu:\eta^2:\eta^2\text{-peroxo}$ dicopper species are capable of intramolecular ligand hydroxylation of phenyl groups and no KIE is found,^{3,9} as in tyrosinase.



On the other hand, aliphatic chain hydroxylation has only been observed with bis(μ -oxo) intermediates through Hydrogen Abstraction (HA) mechanism, and significant isotopic effect is found.¹⁰ Thus, the last reaction sequence for the aromatic hydroxylation mechanism suggested in literature is first breaking the O-O bond in peroxy core to form the bis(oxo) core, and the latter being responsible of hydroxylation through electrophilic attack on the arene ring. However, experiments can not rule out the coexistence of both isomers in rapid preequilibrium and it has not been determined unequivocally which one is the active species.^{5,9}

New aryl-Cu^{III} complexes obtained from a new type of disproportionation in copper chemistry are reported in Chapter 3, along with an aromatic C-H bond activation reaction.¹¹ The purpose of the present work is to study the reactivity of these Aryl-Cu^{III} complexes under different conditions to synthesize new bisphenoxo Cu^{II} complexes, and to give some light to possible mechanisms for the hydroxylation reaction that takes place, as well as the link of this reactivity with the known aromatic hydroxylation reaction of tyrosinase-like copper(I) models using dioxygen.

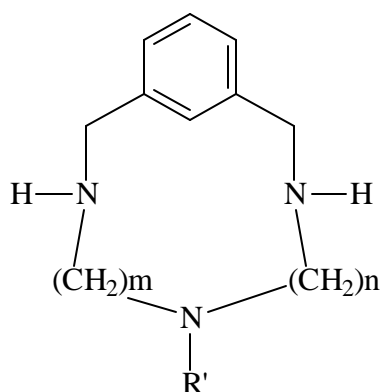
4.3 RESULTS

4.3.1 Synthesis

4.3.1.1 The ligands

Synthesis of ligands used in this work (see Scheme 1) have been described in Chapter 3.¹¹

Scheme 1. Ligands used in the present work



H32m : R' = H; m = 3, n = 2

H₂Me33m : R' = CH₃; m, n = 3

H33m : R' = H; m, n = 3

H22m : R' = H; m, n = 2

4.3.1.2 Cu^I complexes

Synthesis of complexes [(L)Cu^I](X) (L = H32m, H₂Me33m, H33m, H22m; X = PF₆⁻, OTf⁻, ClO₄⁻) have been described in Chapter 3.

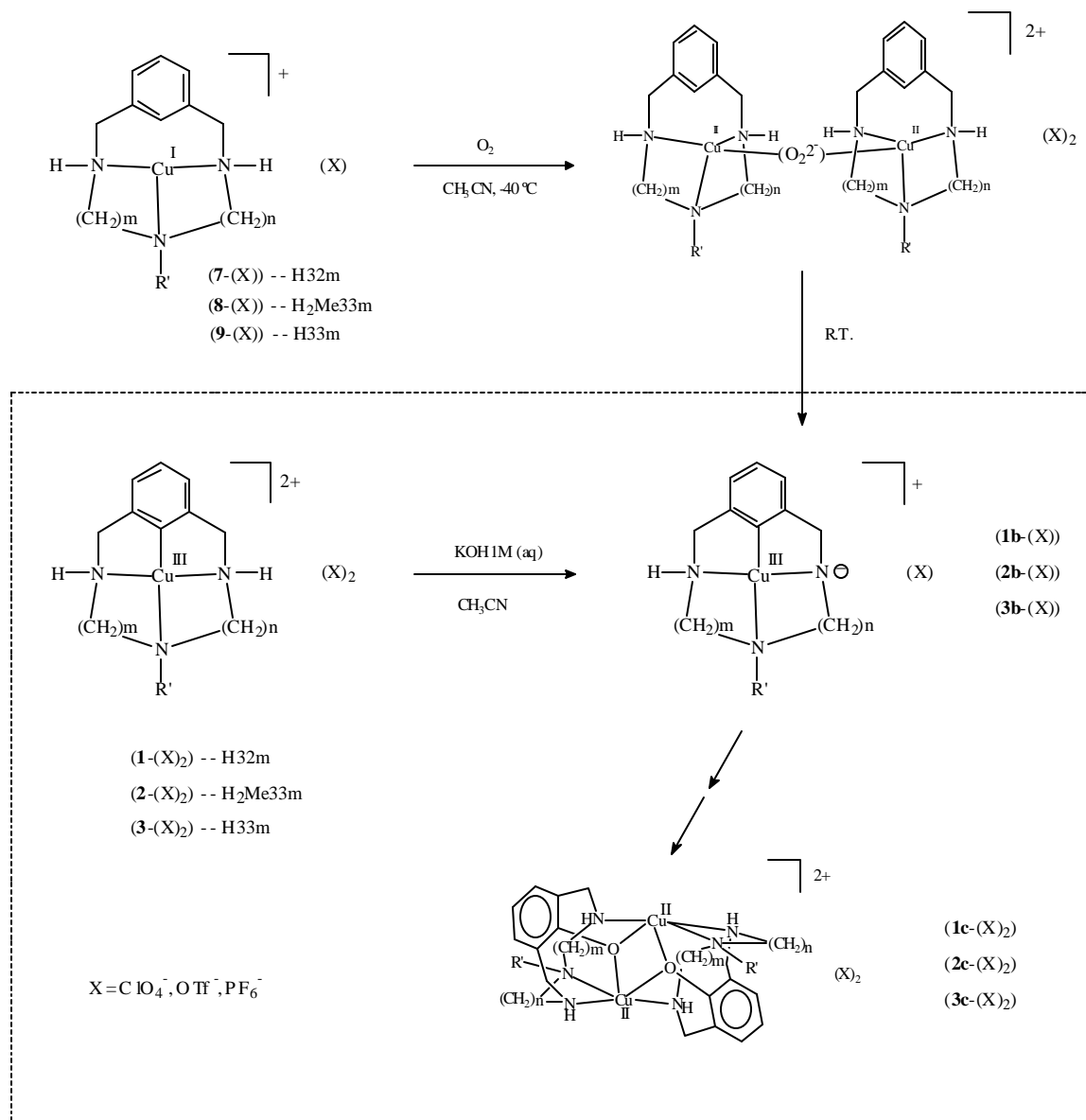
4.3.1.3 Cu^{III} complexes

Synthesis of Aryl-Cu^{III} complexes [(H32m-C)Cu^{III}](X)₂ (**1**-(X)₂), [(H₂Me33m-C)Cu^{III}](X)₂ (**2**-(X)₂) and [(H33m-C)Cu^{III}](X)₂ (**3**-(X)₂) (X = ClO₄⁻, OTf⁻) are reported in Chapter 3.

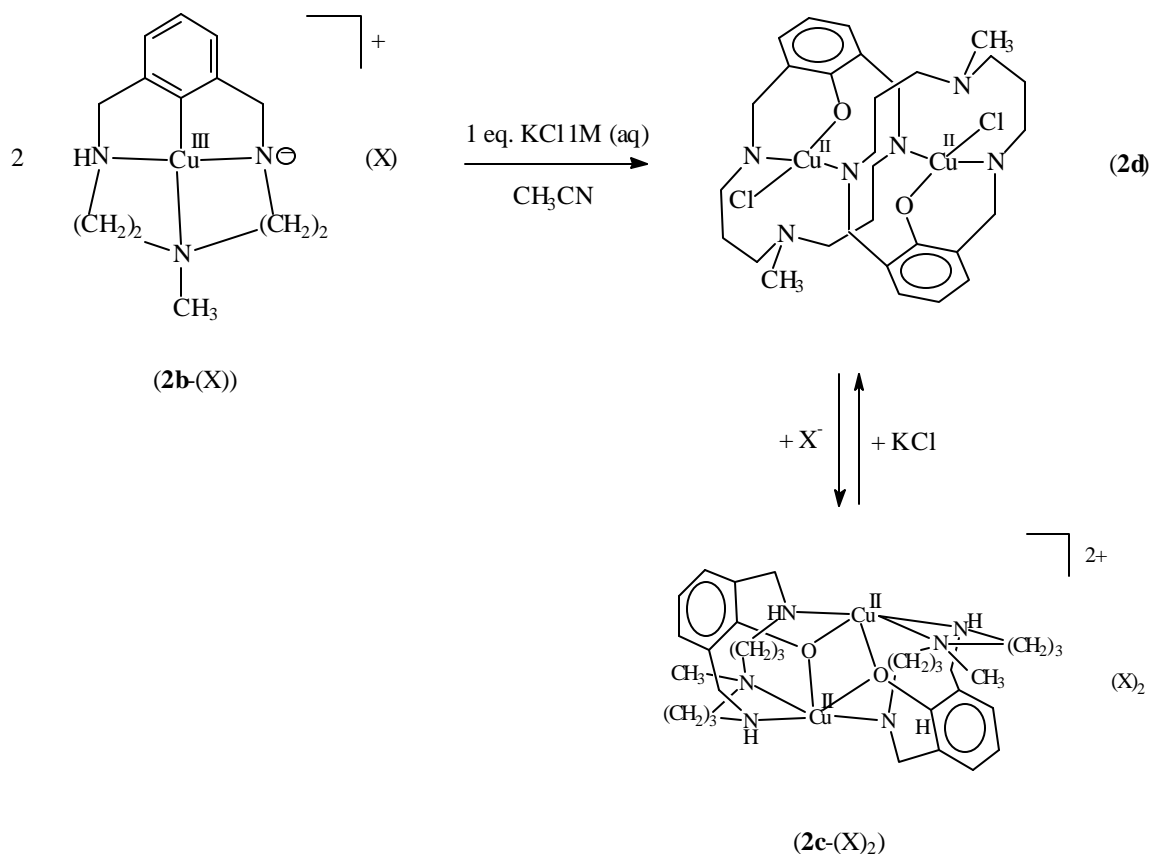
4.3.1.4 Cu^{II} complexes

Complexes [(H32m-C)Cu^{III}](X)₂ (**1**-(X)₂), [(H₂Me33m-C)Cu^{III}](X)₂ (**2**-(X)₂) and [(H33m-C)Cu^{III}](X)₂ (**3**-(X)₂) (X= ClO₄⁻, OTf⁻) dissolved in CH₃CN react with 1 equivalent of aqueous KOH 1M at room temperature to give colored intermediates. Solution acquires a red-brown (when cation **1** used) or deep violet color (when cation **2** and **3** used) corresponding to intermediates **1b**, **2b** and **3b** respectively (see section 4.3.1.5), which fade to obtain final green solutions. Intermediate **1b** takes more than 24 hours to totally fade to green products, whereas **2b** and **3b** only take 2-3 hours. Slow diethyl ether diffusion leads to the final bisphenoxo complexes: [(H32mO)₂Cu^{II}]₂(X)₂ (**1c**-(X)₂) in 30% isolated yield, [(H₂Me33mO)₂Cu^{II}]₂(X)₂ (**2c**-(X)₂) in 65% yield and [(H33mO)₂Cu^{II}]₂(X)₂ (**3c**-(X)₂) in 60% yield (X= ClO₄⁻, OTf⁻). Bisphenoxo complex synthesis is depicted in Scheme 2. Same bisphenoxo complexes **1c**, **2c** and **3c** can be obtained from the reaction of Cu^I complexes [(H32m)Cu^I]⁺ (**7**), [(H₂Me33m)Cu^I]⁺ (**8**) and [(H33m)Cu^I]⁺ (**9**) with molecular dioxygen in CH₃CN solvent. The reaction undergoes at room temperature under similar colored intermediates observed with the Aryl-Cu^{III}/base reaction (Scheme 2). Bisphenoxo complex [(H22mO)₂Cu^{II}]₂²⁺ (**5c**) can be isolated in low yields after reaction of the corresponding Cu^I complex with dioxygen. However, despite the fact that aryl-Cu^{III} species with ligand H22m can not be isolated (see Chapter 3), hydroxylation occurs when mixing H22m and Cu^{II} salt in a 1.3 to 1 relation in CH₃CN solvent and ambient temperature to obtain 22% yield of complex **5c**. No distinct colored intermediate is observed and water traces present in the reaction may be the source for oxygen atoms demanded for hydroxylation.

Scheme 2. Synthesis of bisphenoxo complexes from Aryl-Cu^{III} compounds and dioxygen activation by Cu^I complexes and further aromatic hydroxylation through **1b-3b** intermediates



Addition of 1 equivalent of KCl 1M to a solution of $[(H_2Me33m-C)Cu^{III}]^{2+}$ (**2**) already treated with base yields crystals of complex $[(H_2Me33m-O)_2Cu^{II}_2(Cl)_2]$ (**2d**). However, complex **2d** can also be obtained by treating complex **2c** with 1 eq. of KCl 1M, although it rearranges again to **2c** in the acetonitrile solution after 48 hours (Scheme 3).

Scheme 3. Synthesis of complex $[(H_2Me33m-O)_2Cu^{II}_2(Cl)_2]$ (**2d**)

All complexes have been characterized by IR, A.E., ESI-MS, UV-Vis and crystal structures have been obtained for all of them (see section 4.3.2).

4.3.1.5 Cu^{III} colored intermediates

Intermediate colored complexes $[(H32m-C)'Cu^{III}](X)$ (**1b**-(X)), $[(H_2Me33m-C)'Cu^{III}](X)$ (**2b**-(X)) and $[(H33m-C)'Cu^{III}](X)$ (**3b**-(X)) ($X = ClO_4^-$, OTf^-) obtained from reaction of Aryl- Cu^{III} **1-3** with KOH (see Scheme 2) have been studied by ESI-MS, NMR (See section 4.3.3.2), UV-Vis (section 4.3.3.3) and X-Ray Absorption Spectroscopy (XAS) in solution (section 4.3.3.1), since their solid isolation have been elusive.

ESI-MS spectra for **1b-3b** show an intense peak for the fragment $[(L-C)'Cu^{III}]^+$ at $m/z = 280, 308, 294$ for $L = H32m, H_2Me33m, H33m$ respectively (see Figure S1), corresponding to the deprotonated amine Aryl-Cu^{III} complex. Colored species **1b-3b** are diamagnetic (see section 4.3.3.2), also in line with an square-planar low spin d^8 Cu^{III} magnetic properties.

Same intermediates **1b-3b** can be obtained by reaction of aryl-Cu^{III} **1-3** with *N,N,N',N'*-Tetramethyl-naphthalene-1,8-diamine (Proton Sponge®). Proton Sponge reactant was selected as an strong non-coordinating base to support the deprotonation reaction of aryl-Cu^{III} complexes. Other bases such as Et₃N or nBu₃N also generates the colored intermediates when react with aryl-Cu^{III} complexes.

4.3.2 X-Ray Structures of bisphenoxo complexes

Crystal structures of dinuclear Cu^{II} complexes $[(H32mO)_2Cu^{II}_2](OTf)_2$ (**1c**-(OTf)₂), $[(H_2Me33mO)_2Cu^{II}_2](ClO_4)_2$ (**2c**-(ClO₄)₂), $[(H33mO)_2Cu^{II}_2](PF_6)_2$ (**3c**-(PF₆)₂), $[(H_2Me33mO)_2Cu^{II}_2(Cl)_2]$ (**2d**) and $[(H22mO)_2Cu^{II}_2](PF_6)_2$ (**5c**-(PF₆)₂) are presented and discussed. All crystal data and refinement parameters are listed in Table 1.

Crystal structure for complex $[(H32mO)_2Cu^{II}_2](OTf)_2$ (**1c**-(OTf)₂) was obtained, and its ORTEP diagram is shown in Figure 1. The molecule sits on a center of symmetry that transforms one macrocyclic ligand into the other. Each copper metal atom has a strongly distorted trigonal bipyramidal towards a square-planar pyramidal geometry (with a τ factor of 0.56),¹² and can be considered a mixture of both. Copper centers share coordinative sites with both ligands. Each copper atom is coordinated to a

phenoxo O atom and a N atom from one of the macrocyclic ligands, and to the phenoxo O atom and two N atoms from the second macrocyclic ligand. The copper metal centers become doubly bridged by each macrocyclic ligand. The oxygen atoms of the phenoxo groups are bridging the copper metal centers so that the axial oxygen atom from one pyramid also occupies a position in the trigonal base of the other pyramid. The Cu_2O_2 core atoms lie in a plane forming a rhomboidal arrangement (Cu-O 1.930(2) Å, 2.174(2) Å), Cu...Cu 3.085 Å and O...O 2.718 Å) (see Table 2). Packing cell ORTEP plot for **1c** is depicted in Figure S2.

Figure 1. ORTEP Diagram for complex $[(\text{H}32\text{mO})_2\text{Cu}^{\text{II}}_2](\text{OTf})_2$ (**1c**- $(\text{OTf})_2$)

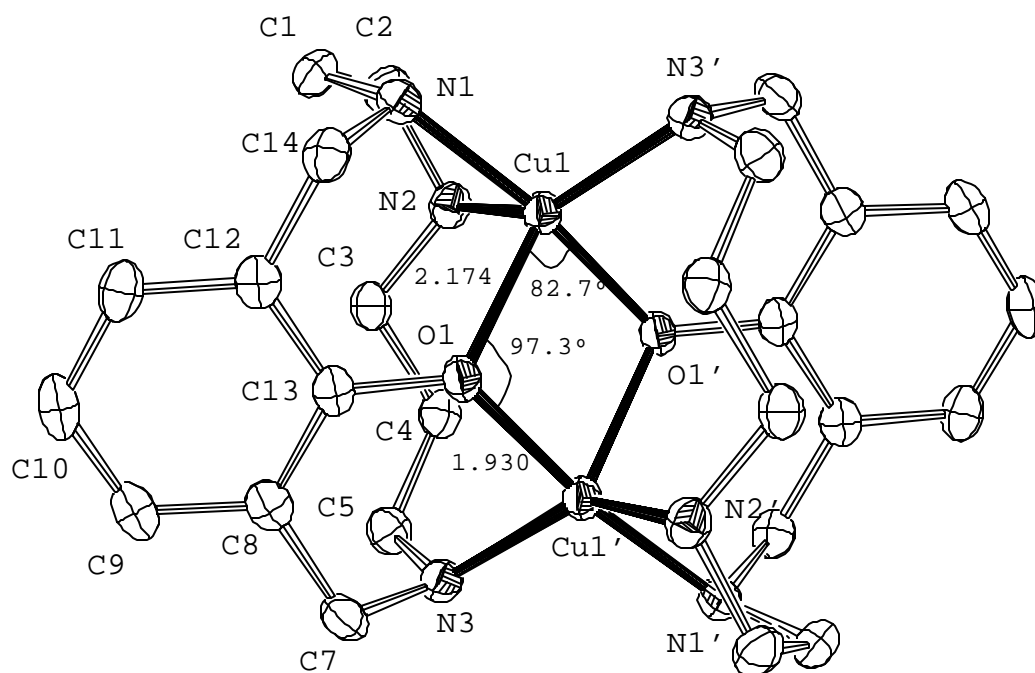


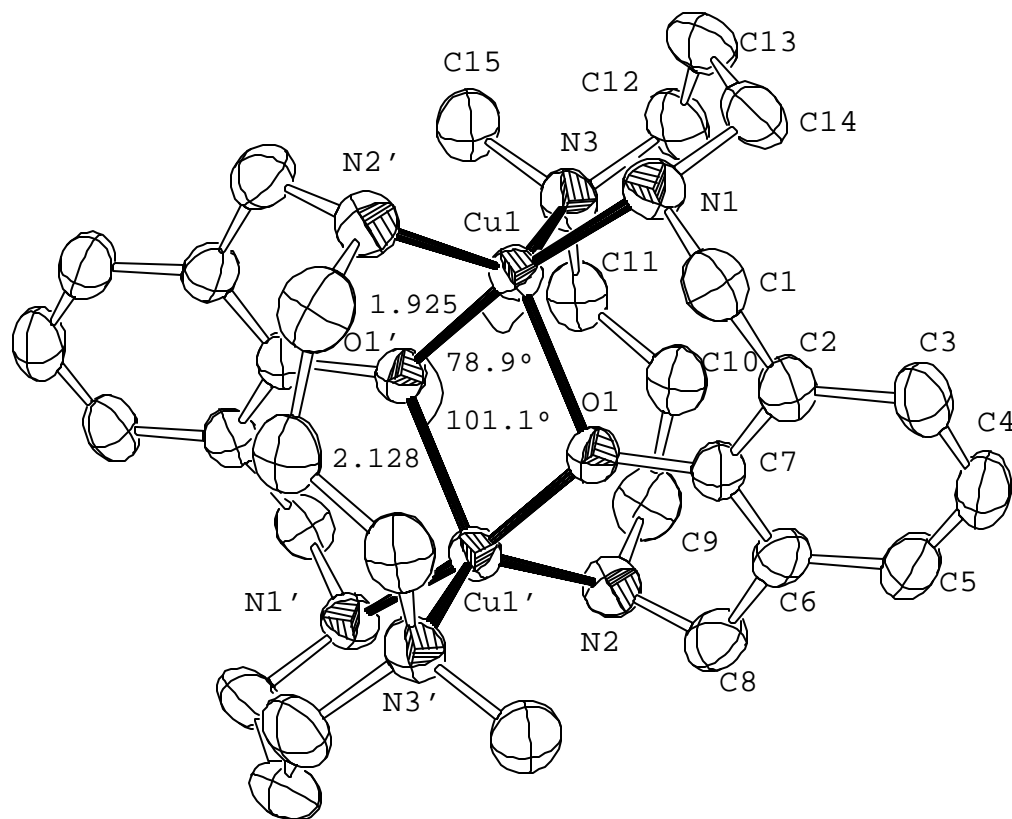
Table 1. Crystal Data and Structure Refinement of dinuclear bisphenoxo copper(II) complexes

	1c -(OTf) ₂	2c -(ClO ₄) ₂ ·CH ₃ CN	2c - (Cl)(PF ₆) ·2H ₂ O ·0.5CH ₃ OH	3c -(PF ₆) ₂	5c -(PF ₆) ₂	2d
Empirical formula	C ₂₈ H ₄₀ Cu ₂ N ₆ O ₈ F ₆ S ₂	C ₃₂ H ₅₁ Cl ₂ Cu ₂ N ₇ O ₁₀	C _{30.5} H ₅₄ Cu ₂ N ₆ O _{4.5} F ₆ PCl	C ₂₈ H ₄₄ Cu ₂ N ₆ O ₂ P ₂ F ₁₂	C ₂₄ H ₃₆ Cu ₂ F ₁₂ N ₆ O ₂ P ₂	C ₃₀ H ₄₈ Cl ₂ Cu ₂ N ₆ O ₂
Fw	893.86	889.27	878.25	913.71	857.61	722.74
space group	P21/n	P-1	P21/n	P-1	P(-1)(No.2)	P-1
<i>a</i> , Å	11.302(5)	9.2947(9)	10.1412(19)	10.0473(11)	8.818(4)	9.264(1)
<i>b</i> , Å	12.467(5)	10.4355(12)	21.650(3)	10.5034(12)	9.696(3)	9.549(1)
<i>c</i> , Å	13.464(5)	11.3621(12)	17.087(3)	10.6524(12)	10.801(6)	10.793(2)
<i>a</i> , deg	90	73.676(12)	90	113.438(2)	113.89(5)	80.948(2)
<i>b</i> , deg	114.458(5)	85.965(12)	98.85(2)	100.351(2)	113.20(2)	65.182(2)
<i>g</i> , deg	90	76.743(12)	90	111.460(2)	90.28(3)	75.057(2)
<i>V</i> , Å ³	1726.9(12)	1029.43(19)	3706.9(11)	887.56(17)	761.0(6)	835.9(2)
<i>Z</i>	4	2	4	1	1	2
Data collection	STOE imaging plate	STOE imaging plate	STOE imaging plate	CCD Siemens SMART	CCD Siemens SMART	CCD Siemens SMART
instrument						
<i>T</i> , K	160(2)	293(2)	160(2)	293(2)	173(2)	273(2)
<i>I</i> Mo-K _α , Å	0.71073	0.71073	0.71073	0.71073	0.71073	0.71073
<i>r</i> (calcd), g cm ⁻³	1.719	1.505	1.574	1.709	1.871	1.436
<i>m</i> , mm ⁻¹	1.443	1.226	1.338	1.389	1.613	1.468
<i>R/Rw</i> ^a	0.0299 /0.0757	0.0330 /0.0894	0.0447 /0.1127	0.0452 /0.1302	0.0429 /0.0952	0.0888 /0.1100

^a $R = \sum |F_0 - F_c| / \sum F_0$ and $Rw = \{\sum [w(F_0^2 - F_c^2)^2] / \sum [w(F_0^2)^2]\}^{1/2}$

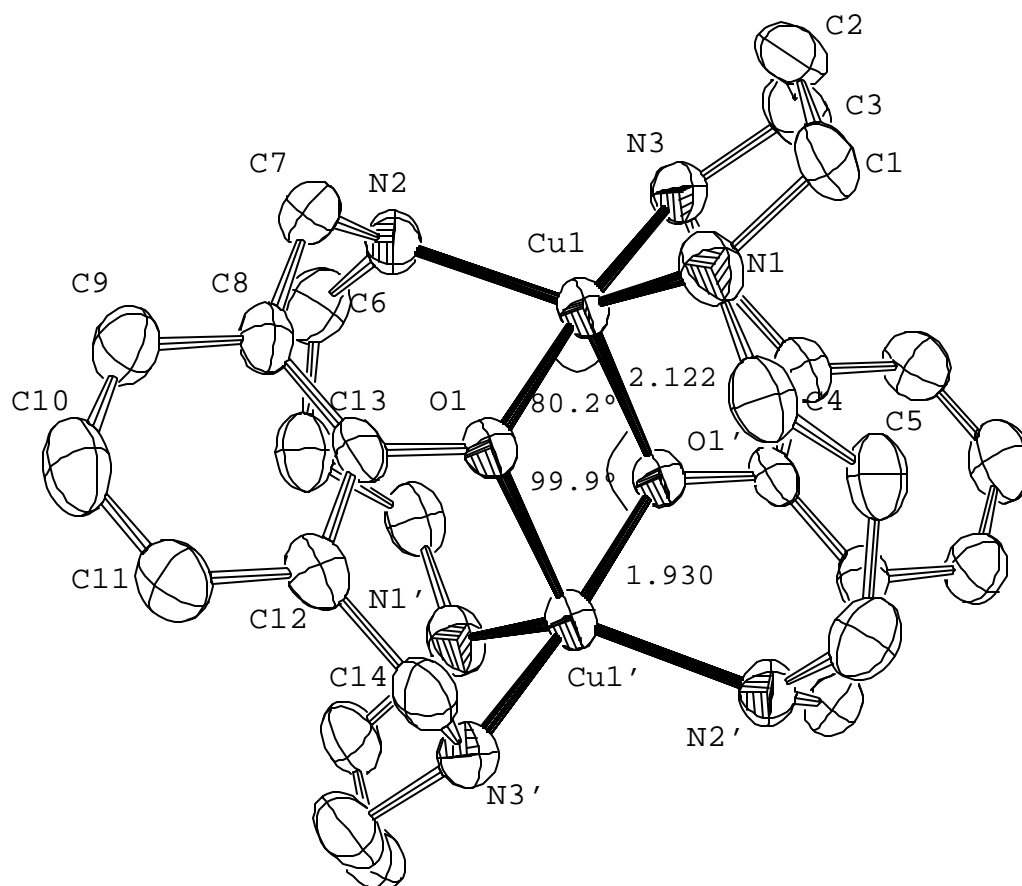
Structures of complexes $[(\text{H}_2\text{Me33mO})_2\text{Cu}^{\text{II}}_2](\text{ClO}_4)_2$ (**2c**- $(\text{ClO}_4)_2$) (see Figure 2), $[(\text{H33mO})_2\text{Cu}^{\text{II}}_2](\text{PF}_6)_2$ (**3c**- $(\text{PF}_6)_2$) (Figure 3) were also determined by X-Ray Diffraction. Crystal data and refinement parameters for each structure are listed in Table 1. Both dinuclear structures **2c** and **3c** bear the same ligand-donor set N_3O_2 per Cu atom and copper metal centers become doubly bridged by each macrocyclic ligand, as the previously described complex **1c**. Each copper metal atom in complexes **2c** and **3c** has a strongly distorted trigonal bipyramidal towards a square-planar pyramidal geometry (with a τ factor of 0.61 for **2c** and 0.62 for **3c**).

Figure 2. ORTEP diagram of complex $[(\text{H}_2\text{Me33mO})_2\text{Cu}^{\text{II}}_2](\text{ClO}_4)_2 \cdot 0.1\text{CH}_3\text{CN}$ (**2c**- $(\text{ClO}_4)_2 \cdot \text{CH}_3\text{CN}$)



The oxygen atoms of the phenoxo groups in complex **2c** are bridging the copper metal centers so that the axial oxygen atom from one pyramid also occupies a position in the trigonal base of the other pyramid. The Cu_2O_2 core atoms lie in a plane forming a rhomboidal arrangement (Cu-O 1.925(1) Å, 2.128(2) Å), Cu···Cu 3.132 Å and O···O 2.581 Å) (see Table 2). A rhomboidal arrangement of the Cu_2O_2 core is also found for complex **3c** (Cu-O 1.930(3) Å, 2.122(3) Å), Cu···Cu 3.103 Å and O···O 2.613 Å) (see Table 2). Packing cell ORTEP plots for **2c** and **3c** are depicted in Figure S2.

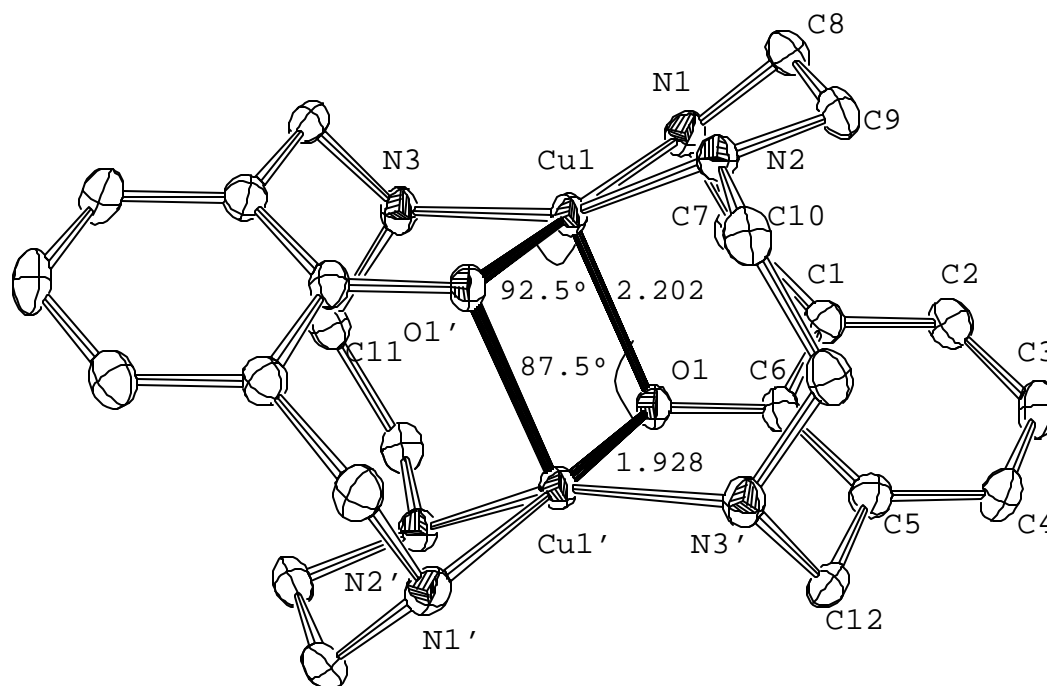
Figure 3. ORTEP diagram of complex $[(\text{H33mO})_2\text{Cu}^{\text{II}}]_2(\text{PF}_6)_2$ (**3c**- $(\text{PF}_6)_2$)



Crystal structure of complex $[(H22mO)_2Cu^{II}_2](PF_6)_2$ (**5c**-(PF_6)₂) is depicted in Figure 4. Crystal data and refinement parameters are listed in Table 1. The molecule sits on a center of symmetry that transform one macrocyclic ligand into the other. Each copper atom has the same ligand-donor set N_3O_2 as in complexes 1c-3c, and are also double bridged by each macrocyclic ligand, but presenting a slightly distorted square-planar pyramidal geometry (with a τ factor of 0.21). The oxygen atoms of the phenoxo groups are bridging the copper metal centers so that the axial oxygen atom from one pyramid also occupies a position in the square-planar base of the other pyramid. The Cu_2O_2 core atoms lie in a plane forming a pseudo-rectangular arrangement (Cu-O 1.928(2) Å, 2.202(2) Å), Cu...Cu 2.854 Å and O...O 2.988 Å) (see Table 2).

Packing cell ORTEP plot for **5c** is depicted in Figure S2.

Figure 4. ORTEP diagram of complex $[(\text{H22mO})_2\text{Cu}^{\text{II}}_2](\text{PF}_6)_2$ (**5c**- $(\text{PF}_6)_2$)

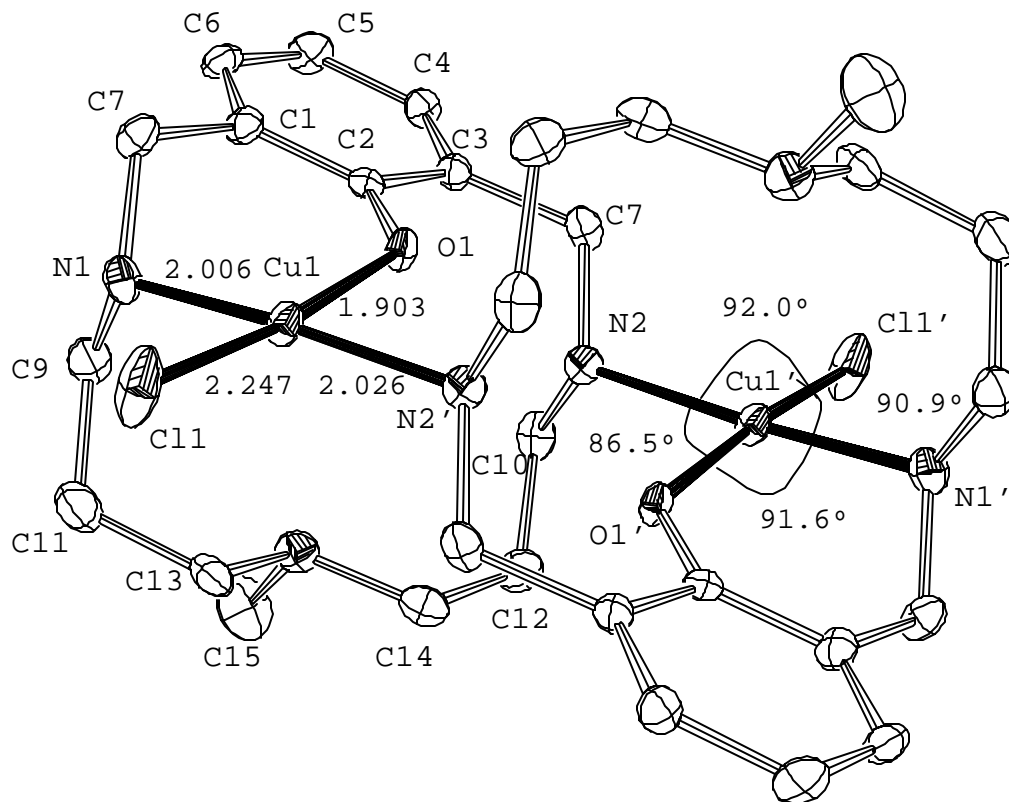


Comparison of crystal structures of complexes $[(\text{H32mO})_2\text{Cu}^{\text{II}}_2]^{2+}$ (**1c**), $[(\text{H}_2\text{Me33mO})_2\text{Cu}^{\text{II}}_2]^{2+}$ (**2c**) and $[(\text{H33mO})_2\text{Cu}^{\text{II}}_2]^{2+}$ (**3c**) shows same type of coordination sphere for each Cu atom with a more squared-rhomboidal Cu_2O_2 core for **1c** considering τ factor values: 0.56 for **1c**, 0.61 for **2c**, 0.62 for **3c** (see Table 2 for selected bond distances and angles). Geometry environment for copper is directly related to conformational constraints imposed by ligand backbone. Complex $[(\text{H22mO})_2\text{Cu}^{\text{II}}_2](\text{PF}_6)_2$ (**5c**- $(\text{PF}_6)_2$) still presents a more square-type Cu_2O_2 core (τ factor = 0.21). A trend can be envisioned for which the smaller the macrocycle ($\text{H22m} < \text{H32m} < \text{H}_2\text{Me33m} \sim \text{H33m}$), the more squared Cu_2O_2 core. Detailed structural description for bisphenoxo complexes **1c**, **2c**, **3c** and **5c** can be found in Chapter 5.

Table 2. Selected bond distances (Å) and angles (deg) for Cu₂O₂ bisphenoxo cores

	1c -(OTf) ₂	2c - (ClO ₄) ₂ ·CH ₃ CN	3c -(PF ₆) ₂	5c -(PF ₆) ₂
Cu-O _{equatorial}	1.930	1.925	1.930	1.928
Cu-O _{apical}	2.174	2.128	2.122	2.202
Cu-O-Cu	97.3	101.1	99.9	87.5
O-Cu-O	82.7	78.9	80.2	92.5
Cu···Cu	3.085	3.132	3.103	2.864
O···O	2.718	2.581	2.613	2.988
τ	0.556	0.611	0.616	0.212

Complex [(H₂Me₃mO)₂Cu^{II}₂(Cl)₂] (**2d**) structure was also determined by X-Ray Diffraction (see Figure 5). Crystal data and refinement parameters are listed in Table 1. The molecule sits on a center of symmetry that transform one macrocyclic ligand into the other. Each copper metal atom has a square-planar type of geometry, sharing coordinative sites with both ligands. Each copper atom is coordinated to a phenoxo O atom and a N atom from one of the macrocyclic ligands, to a N atom from the second macrocyclic ligand and to a terminal Cl atom. The methylated central N atom of each ligand remains uncoordinated (Cu···N3 3.891 Å). Copper and oxygen atoms stay far apart from each other (Cu···Cu 5.299 Å, O···O 3.623 Å). Cl are covalently bound to the Cu^{II} centers with a remarkably short bond (Cu-Cl 2.247(1) Å).

Figure 5. ORTEP Diagram of complex $[(\text{H}_2\text{Me33mO})_2\text{Cu}^{\text{II}}\text{Cl}_2]$ (**2d**)

Solution of complex **2d** in CH_3CN for a long period of time in presence of PF_6^- anions affords rearrangement of the structure to form final green crystals of complex $[(\text{H}_2\text{Me33mO})_2\text{Cu}^{\text{II}}](\text{Cl})(\text{PF}_6) \cdot 2\text{H}_2\text{O} \cdot 0.5\text{CH}_3\text{OH}$ (**2c**- $(\text{Cl})(\text{PF}_6) \cdot 2\text{H}_2\text{O} \cdot 0.5\text{CH}_3\text{OH}$), where the Cl^- atom covalently coordinated to Cu centers now act as non-coordinating counteranion. X-Ray Diffraction showed a quasi-identical geometry for copper atoms as the complex **2c**- $(\text{ClO}_4)_2$ (see .cif file, Table 1 and Figure S2).

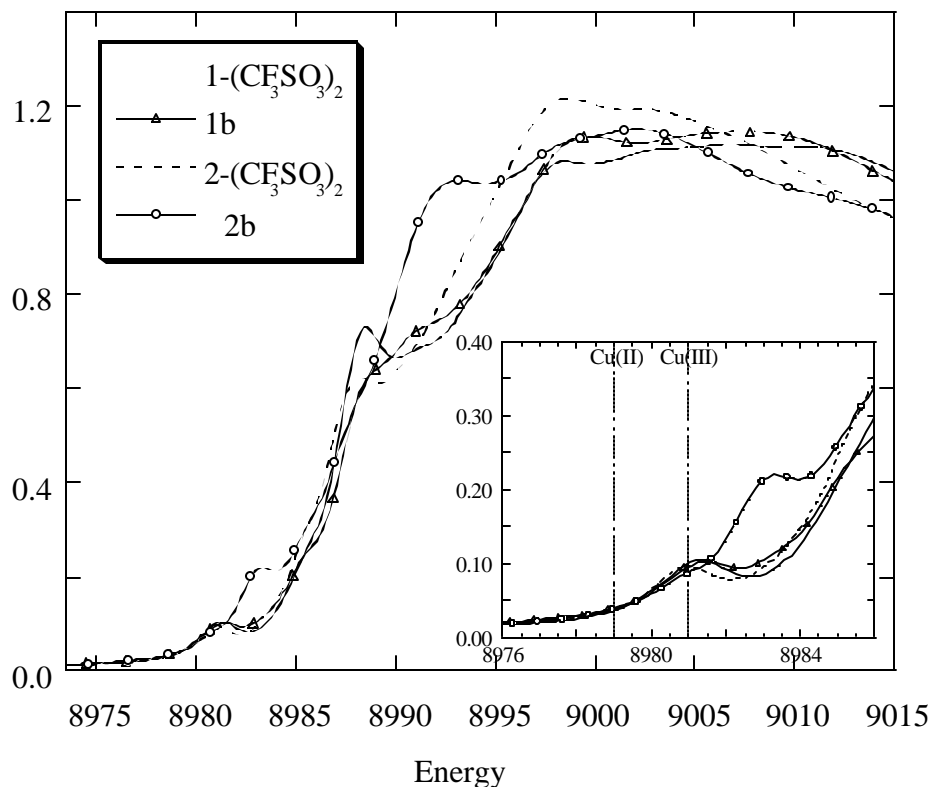
4.3.3 Spectroscopic properties

4.3.3.1 X-Ray Absorption Spectroscopy (XAS) of **1b-2b**

Cu K-Edge X-Ray Absorption Spectroscopy (XAS) experiments were performed on intermediates [(H32m-C)'Cu^{III}]⁺ (**1b**) and [(H₂Me33m-C)'Cu^{III}]⁺ (**2b**) generated in situ with proton sponge and analyzed at low temperatures. Preedge signal on **1b** spectrum shows a +3 oxidation state for Cu (see Figure 6).

On the other hand, intermediate **2b** shows Cu^{III} preedge signal with significant contamination of Cu^I species (feature at ~8983 eV, Figure 6). This unexpected contamination by Cu^I does not come from initial aryl-Cu^{III} **2** complex but is related to a side-reaction with Proton Sponge that will be discussed in section 4.4.5.

Figure 6. Cu K-edges for intermediates $[(\text{H}32\text{m-C})'\text{Cu}^{\text{III}}]^+$ (**1b**) and $[(\text{H}_2\text{Me}33\text{m-C})'\text{Cu}^{\text{III}}]^+$ (**2b**) with comparison to Cu K-edges for Cu^{III} complexes **1**- $(\text{CF}_3\text{SO}_3)_2$ and **2**- $(\text{CF}_3\text{SO}_3)_2$. Inset shows an amplification of preedge region (8976–8985 eV)

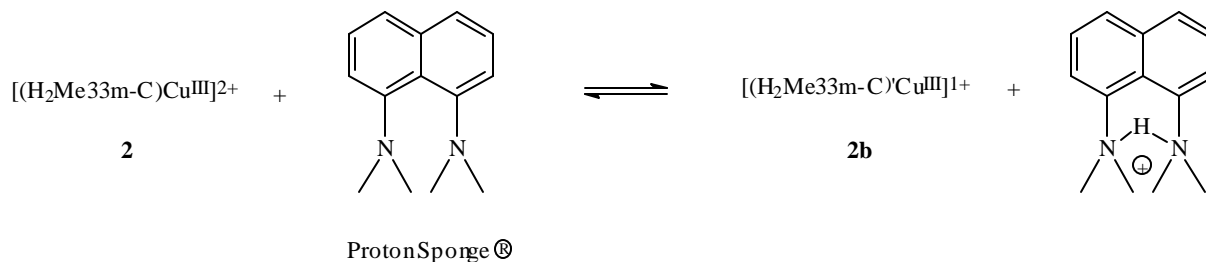


4.3.3.2 ^1H NMR characterization of intermediates **1b**-**3b**

^1H NMR of complex $[(\text{H}32\text{m-C})'\text{Cu}^{\text{III}}]^+$ (**1b**) is very similar to proton spectrum for initial aryl- Cu^{III} complex $[(\text{H}32\text{m-C})\text{Cu}^{\text{III}}]^{2+}$ (**1**) (see Figure S3). On the contrary, proton spectrum of complexes **2b** and **3b** obtained with KOH at room temperature present broad bands due to their instability. Same intermediates **1b**-**3b** can be reproduced by reaction of aryl- Cu^{III} **1**-**3** with Proton Sponge®. NMR studies at variable temperatures for the specific example of **2/2b** (system using

ligand H₂Me33m) suggested the existence of an equilibrium such as the one depicted in Scheme 4. Comparing corresponding signals for protonated form of Proton Sponge with signals for P.Sponge itself (see Figure S4), percentage of deprotonation of [(H₂Me33m-C)Cu^{III}]²⁺ (**2**) to obtain [(H₂Me33m-C)'Cu^{III}]⁺ (**2b**) can be calculated. Thus, equilibrium is totally displaced towards quantitative formation of **2b** at 320 K, 60-70% of **2b** is formed at 300 K and only 30% at 240 K (see Figure S4). In sharp contrast, reaction of aryl-Cu^{III} complex [(H32m-C)Cu^{III}]²⁺ (**1**) with Proton Sponge only generates 20-30% of deprotonated form [(H32m-C)'Cu^{III}]⁺ (**1b**) at 300 K as also deduced by ¹H NMR (see Figure S5).

Scheme 4. Equilibrium between aryl-Cu^{III} **2** and its deprotonated form **2b** by reaction with Proton Sponge in CH₃CN solution.

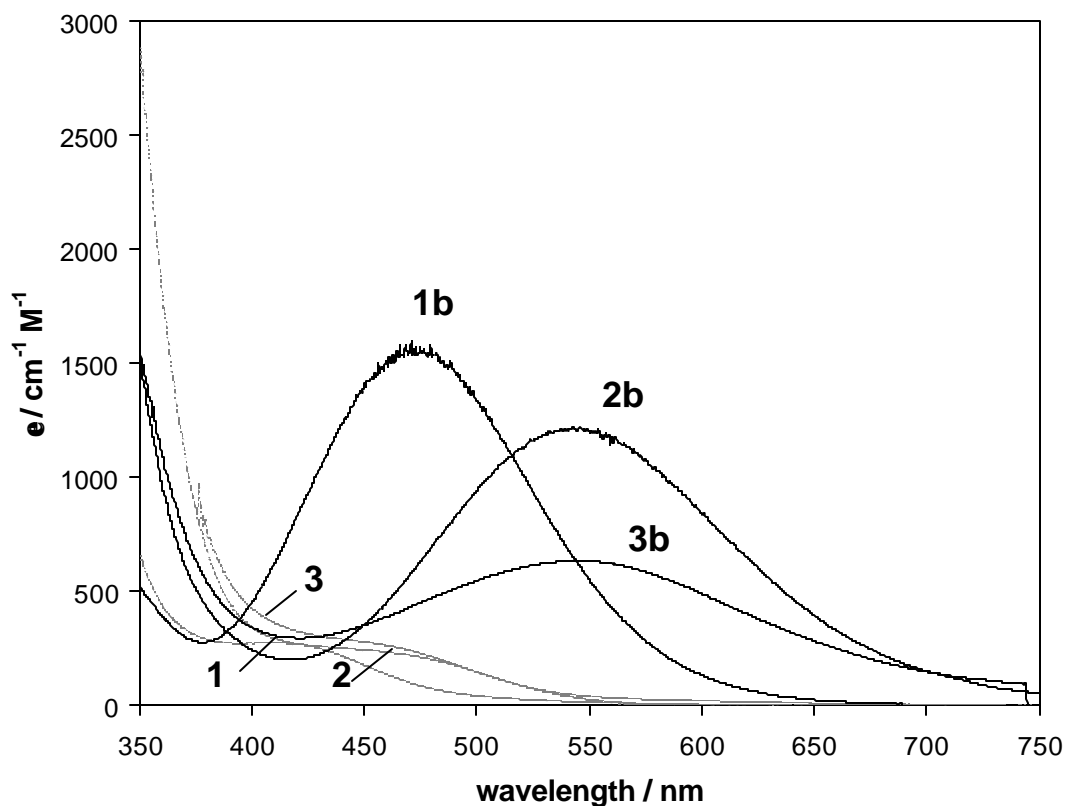


Intermediates **1b-3b** are drawn as deprotonated benzylic amines because, as predicted by NMR studies on aryl-Cu^{III} [(H32m-C)Cu^{III}]²⁺ (**1**) (see Chapter 3) and also by the ¹H NMR spectrum of [(H32m-C)'Cu^{III}]⁺ (**1b**) generated with proton sponge (Figure S5), the central secondary amine does not behave as an acidic proton at all and its signal neither exchange with water in NOESY spectrum of **1** (see Chapter 3, Figure 6) nor is affected by Proton Sponge.

4.3.3.3 UV-Vis Spectroscopy of intermediates 1b-3b

Red-brown intermediate $[(\text{H}32\text{m-C})'\text{Cu}^{\text{III}}]^+$ (**1b**) generated with KOH 1M presents a distinct LMCT band at 470 nm ($1550 \text{ M}^{-1}\text{cm}^{-1}$) on the electronic spectrum, whereas violet intermediate **2b** show a shifted LMCT band to 545 nm ($1250 \text{ M}^{-1}\text{cm}^{-1}$) and to 544 nm ($650 \text{ M}^{-1}\text{cm}^{-1}$) for **3b** (see Figure 7). To our knowledge these LMCT bands have not been reported for copper complexes in the literature before and may correspond to the electronic transition from the deprotonated secondary amine to the Cu^{III} center.

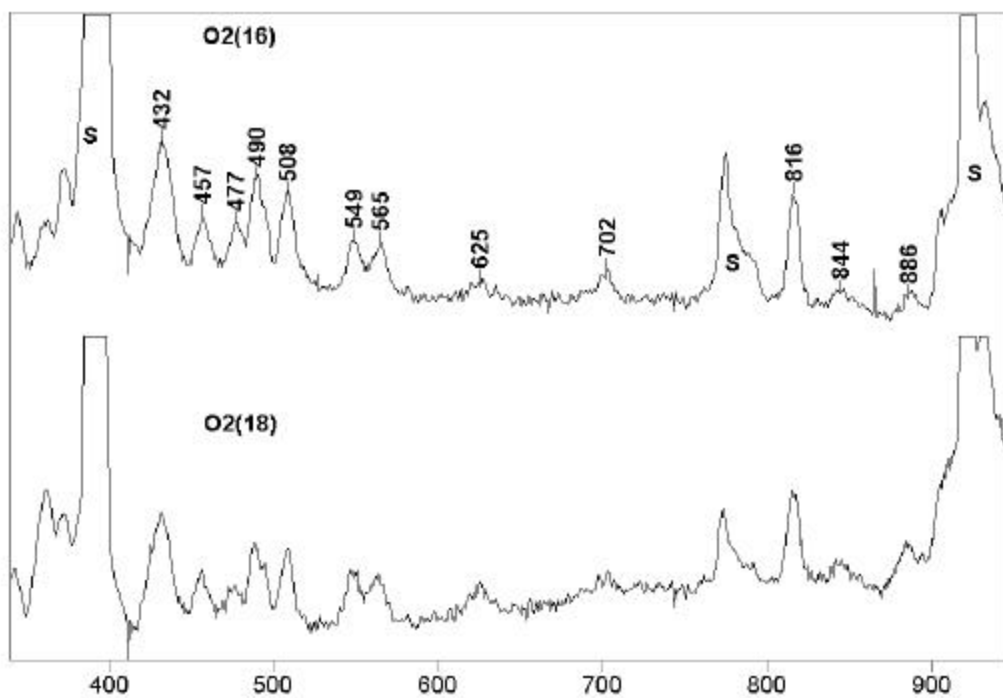
Figure 7. Electronic spectra of deprotonated Cu^{III} intermediates $[(\text{H}32\text{m-C})'\text{Cu}^{\text{III}}]^+$ (**1b**) and $[(\text{H}_2\text{Me}33\text{m-C})'\text{Cu}^{\text{III}}]^+$ (**2b**) and $[(\text{H}33\text{m-C})'\text{Cu}^{\text{III}}]^+$ (**3b**). UV-Vis plots for Aryl- Cu^{III} complexes **1**, **2** and **3** are also shown in the plot.



4.3.3.4 Raman spectroscopy of intermediate **3b**

Violet intermediate $[(\text{H33m-C})'\text{Cu}^{\text{III}}]^+$ (**3b**), generated by oxygenation of Cu^{I} complex $[(\text{H33m})\text{Cu}^{\text{I}}]^+$ (**9**) at room temperature in CH_3CN , presents several features between 430 and 900 cm^{-1} in the Raman spectrum (laser excitation at 568 nm). However, no changes were detected in the spectrum when intermediate **3b** was generated with $^{18}\text{O}_2$ (see Figure 8), and therefore, the possibility of a Cu-O or O-O bond vibration is excluded.

Figure 8. Resonance Raman spectra of intermediate **3b** in frozen solution with laser excitation at 568 nm, in CH_3CN generated with O_2^{16} (top) and O_2^{18} (bottom)



4.4 DISCUSSION

4.4.1 Hydroxylation reaction details

Apart from synthesis of bisphenoxo complexes depicted in Scheme 2, other synthetic conditions have been studied to perform the oxygen insertion into the aromatic ring. In principle, any aqueous base reagent instead of KOH 1M can be used to achieve final products $[(\text{H32mO})_2\text{Cu}^{\text{II}}]^{2+}$ (**1c**), $[(\text{H}_2\text{Me33mO})_2\text{Cu}^{\text{II}}]^{2+}$ (**2c**) and $[(\text{H33mO})_2\text{Cu}^{\text{II}}]^{2+}$ (**3c**) in different yields, as shown specifically for complex $[(\text{H}_2\text{Me33m-C})\text{Cu}^{\text{III}}]^{2+}$ (**2**) in Table 3.

Table 3. Different reactivity behavior of aryl-Cu^{III} complex $[(\text{H}_2\text{Me33m-C})\text{Cu}^{\text{III}}](\text{OTf})_2$ (**2**- $(\text{OTf})_2$) in front of different reagents. Typical experiment conditions: CH₃CN, [**2**] ≈ 15-20 mM, magnetic stirring, N₂ atmosphere, R.T.

	Reagents (equivalents)	Time of reaction (min)	Isolated Yield(%) of 2c
(a)	KOH (1 eq.), H ₂ O (54 eq.)	60 min	65 %
(b)	KOH (2 eq.), H ₂ O (108 eq.)	25 min	8 %
(c)	Proton Sponge (1 eq.), H ₂ O (7 eq.)	180 min	53 %
(d)	Proton Sponge (1 eq.)	60 min	0 %
(e)	Proton Sponge (1 eq.), O ₂ (excess)	240 min	20 %
(f)	H ₂ O ₂ (3% in H ₂ O) (1 eq.), H ₂ O (52 eq.), Et ₃ N (1 eq.)	10 min	31 %
(g)	H ₂ O ₂ (3% in H ₂ O) (1 eq.), H ₂ O (52 eq.)	60 min	0 %
(h)	DABCO.2H ₂ O ₂ (2 eq.)	45 min	15 %
(i)	DABCO.2H ₂ O ₂ (0.5 eq.)	40 min	40 %

Interestingly, other O-containing reagents as H_2O_2 also are able to perform the hydroxylation reaction. However, addition of H_2O_2 3% in water did not cause any change to copper(III) solution of $[(\text{H}_2\text{Me33m-C})\text{Cu}^{\text{III}}]^{2+}$ (**2**) until the base Et_3N was injected in the solution (see reactions (f) and (g) in Table 3).

From these series of reactions it may be concluded that addition of water or H_2O_2 do not affect the stability of organocopper(III) **2**, and only the presence of a base triggers the reaction to bisphenoxo complex $[(\text{H}_2\text{Me33mO})_2\text{Cu}^{\text{II}}]^{2+}$ (**2c**) formation through intermediate $[(\text{H}_2\text{Me33m-C})'\text{Cu}^{\text{III}}]^+$ (**2b**) complex. The presence of O_2 in solution in experiment (e) was tested to check if it had any influence in reaction time-scale or final yield. No quenching of violet intermediate was found but differences in final yield were noticeable: 20% yield for reaction (e) and 53% for (c) (see Table 3)

Same reactivity behavior is found for complex $[(\text{H33m-C})\text{Cu}^{\text{III}}]^{2+}$ (**3**), whereas significant differences are shown by complex $[(\text{H32m-C})\text{Cu}^{\text{III}}]^{2+}$ (**1**). For the latter, stability of red-brown intermediate $[(\text{H32m-C})'\text{Cu}^{\text{III}}]^+$ (**1b**) is much higher than **2b-3b**, and reaction is not finished in less than 24 hours when KOH 1M is added. Moreover, final isolated yield for complex $[(\text{H32mO})_2\text{Cu}^{\text{II}}]^{2+}$ (**1c**) was 30%. These results are also discussed in mechanistic section 4.4.3.

Studying the reactivity of complex $[(\text{H}_2\text{Me33m-C})\text{Cu}^{\text{III}}]^{2+}$ (**2**), we realized that a new type of bisphenoxo compound was obtained when treating the intermediate compound $[(\text{H}_2\text{Me33m-C})'\text{Cu}^{\text{III}}](\text{OTf})$ (**2b-(OTf)**) in acetonitrile with one equivalent of KCl 1M (aqueous solution). The violet color was quenched rapidly to red and dark red crystals precipitated from solution mixture. X-ray diffraction analysis gave the crystal structure of complex

$[(\text{H}_2\text{Me33mO})_2\text{Cu}^{\text{II}}_2(\text{Cl})_2]$ (**2d**). The ORTEP diagram for **2d** is shown in Figure 5.

This is an intermediate that is temporally stabilized by the presence of good σ -donor ligand such as chloride Cl^- , but is unstable in its absence towards the formation of the bisphenoxo complex $[(\text{H}_2\text{Me33mO})_2\text{Cu}^{\text{II}}_2](\text{OTf})_2$ (**2c**- $(\text{OTf})_2$). Furthermore, complex $[(\text{H}_2\text{Me33mO})_2\text{Cu}^{\text{II}}_2(\text{Cl})_2]$ (**2d**) can also be obtained if bisphenoxo complex **2c**- $(\text{OTf})_2$ is dissolved in CH_3CN and one equivalent (or slightly excess) of KCl 1M is added (see Figure S8 for ESI-MS comparison). Complex **2d** is not stable in solution and tends to rearrange to bisphenoxo **2c** complex over the course of 24-48 hours if PF_6^- or OTf^- are present in solution (see Scheme 3 and section 4.3.2).

4.4.2 Dioxygen activation by Cu^{I} complexes

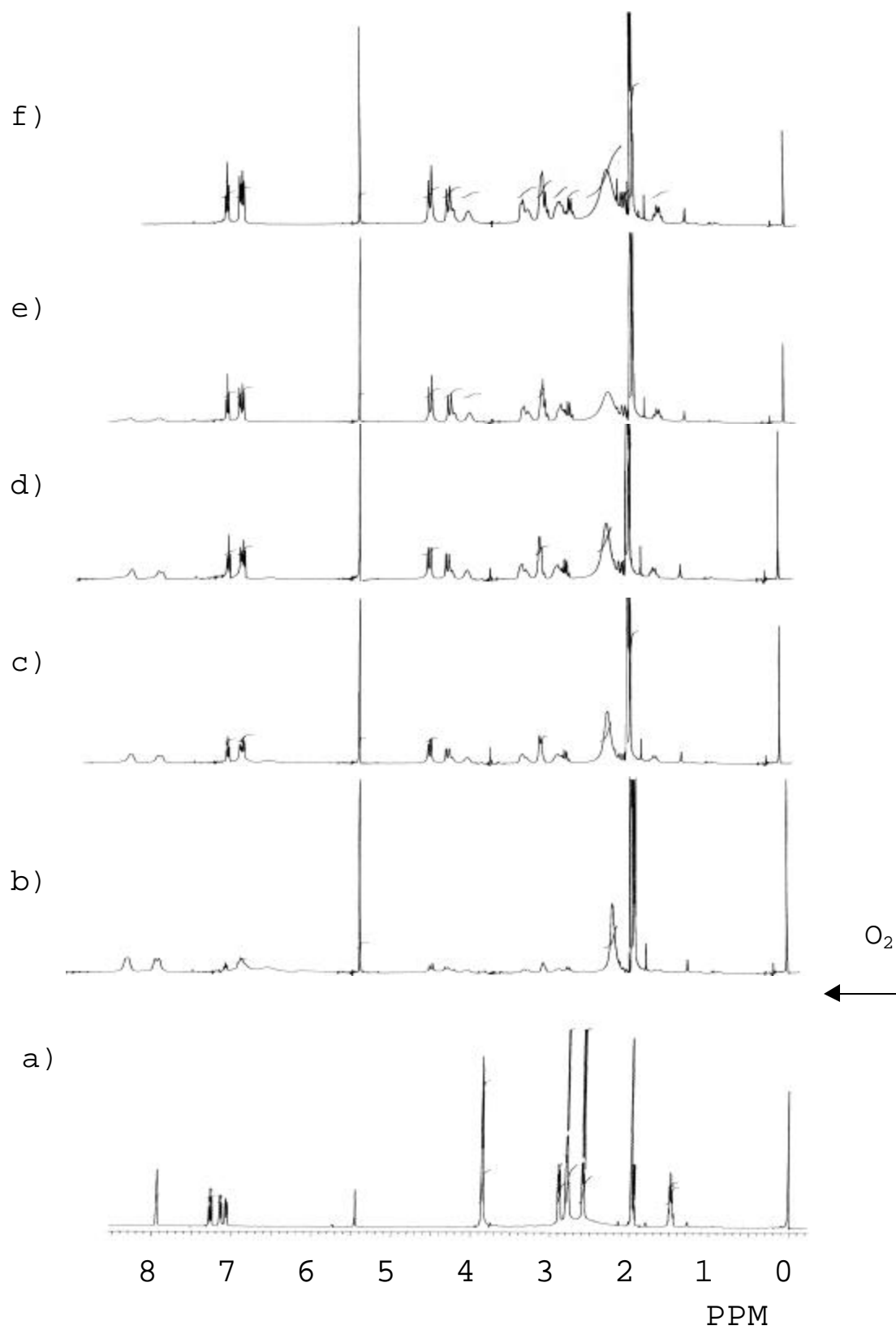
The study of dioxygen activation by Cu^{I} complexes synthesized with ligands H32m, $\text{H}_2\text{Me33m}$ and H33m gives another mechanistic perspective for aromatic hydroxylations. Bubbling O_2 to $[(\text{H32m})\text{Cu}^{\text{I}}](\text{X})$ (**7**- (X)), $[(\text{H}_2\text{Me33m})\text{Cu}^{\text{I}}](\text{X})$ (**8**- (X)) and $[(\text{H33m})\text{Cu}^{\text{I}}](\text{X})$ (**9**- (X)) ($\text{X} = \text{ClO}_4^-$, PF_6^- , OTf^-) at room temperature in CH_3CN caused the formation of intense colored intermediates resembling intermediates $[(\text{H32m-C})'\text{Cu}^{\text{III}}]^+$ (**1b**), $[(\text{H}_2\text{Me33m-C})'\text{Cu}^{\text{III}}]^+$ (**2b**) and $[(\text{H33m-C})'\text{Cu}^{\text{III}}]^+$ (**3b**), respectively (see Figure S6). Besides, decomposition of colored intermediates gives the same bisphenoxo copper complexes $[(\text{H32mO})_2\text{Cu}^{\text{II}}_2]^{2+}$ (**1c**), $[(\text{H}_2\text{Me33mO})_2\text{Cu}^{\text{II}}_2]^{2+}$ (**2c**) and $[(\text{H33mO})_2\text{Cu}^{\text{II}}_2]^{2+}$ (**3c**) as final products (see Scheme 2), although in lower yields. The detailed study of these reactions confirmed that hydroxylation was undergoing through the same aryl- Cu^{III} intermediates: UV-Vis spectra present same LMCT bands in each case, however with different intensities which is probably related to the lower yields obtained for final

bisphenoxo complexes (23% formation of **2b**, 25% final isolated yield for **2c** when obtained from $\text{Cu}^{\text{I}}/\text{O}_2$, compared to $\epsilon_{545} = 1070$ for **2b** and 65% yield for **2c** when obtained from aryl- Cu^{III} complex **2** with Proton Sponge).

ESI-MS spectrum for violet intermediate obtained from $[(\text{H}33\text{m})\text{Cu}^{\text{I}}](\text{PF}_6)$ (**9**-(PF_6)) plus O_2 shows a characteristic peak at $m/z = 294$ corresponding to the fragment $[(\text{H}33\text{m-C})'\text{Cu}^{\text{III}}]^+$ (**3b**) (see Figure S7).

^1H NMR experiment with $[(\text{H}32\text{m})\text{Cu}^{\text{I}}](\text{OTf})/\text{O}_2$ system was determinant to confirm the aryl- Cu^{III} intermediate pathway of the reaction: ^1H NMR for complex $[(\text{H}32\text{m})\text{Cu}^{\text{I}}](\text{OTf})$ (**7**-(OTf)) was registered in CD_3CN , O_2 bubbling was directly applied at the NMR tube and reaction was monitored by ^1H NMR (see Figure 9). After 15 min typical Aryl- Cu^{III} signals started to arise, and formation was complete in 2 hours. Under this conditions decomposition of intermediate was detected after 40 hours. Note that percentage of aryl- Cu^{III} intermediate $[(\text{H}32\text{m-C})'\text{Cu}^{\text{III}}](\text{OTf})$ (**1b**-(OTf)) formed can not be calculated because other paramagnetic species may be formed in solution but not seen in the NMR working window.

Figure 9. ^1H NMR changes in $[(\text{H}^{32}\text{m})\text{Cu}^{\text{I}}](\text{OTf})$ (**7**- (OTf)) complex spectrum after oxygenation in CD_3CN ; a) Cu^{I} complex **7**, b) 15 min reaction time, c) 40 min, d) 60 min, e) 130 min, f) 750 min.



Low temperature oxygenation studies of complex $[(\text{H}^{33}\text{m})\text{Cu}^{\text{I}}](\text{PF}_6)$ (**9**- (PF_6)) monitored by Stopped-Flow Uv-Vis Spectroscopy gave some insight into the mechanistic pathway from O_2 activation to the Aryl- Cu^{III} species detected. Reaction of complex **9** with O_2 in acetonitrile at -40°C allowed the formation of a compound with absorption bands characteristic of $(\mu:\eta^2:\eta^2\text{-peroxo})\text{dicopper}(\text{II})$ species (λ_{max} at 360 and 579 nm in a 10:1 intensity relation for this two bands)¹³. However, intensity of this bands was not corresponding to full-formation of peroxo intermediate and only a 10-20% formation is estimated from spectral data (see Figure 10). The incomplete formation of peroxo species may be attributable to either unknown side-reactions or, as described recently, to competition of CH_3CN solvent on the oxygenation step.¹⁴ A possible mechanism for aryl- Cu^{III} formation from $(\mu:\eta^2:\eta^2\text{-peroxo})\text{Cu}^{\text{II}}$ is discussed in section 4.4.3.

Monitoring experiments of this oxygenation at room temperature to directly obtain aryl- Cu^{III} intermediate turned out to be very dependent on complex and also O_2 concentration. The higher the factor $[\text{O}_2]/[\mathbf{9}]$, the faster the reaction to reach the maximum intermediate formation (but always incomplete), and the higher the $[\mathbf{9}]$, the higher formation of violet Cu^{III} intermediate (see Table 4 and Figure 11). Kinetic data treatment was not successful due to anomalous profiles obtained in the formation of the intermediates.

Figure 10. (a) Stopped-Flow UV-Vis spectral changes and (b) absorption profile at 356 nm for the oxygenation of complex $[(\text{H33m})\text{Cu}^{\text{I}}](\text{PF}_6)$ (**9**- (PF_6)) at -40.9°C (CH_3CN , $[\mathbf{9}] = 4.28\text{ mM}$, $[\text{O}_2] = 5.76\text{ mM}$).

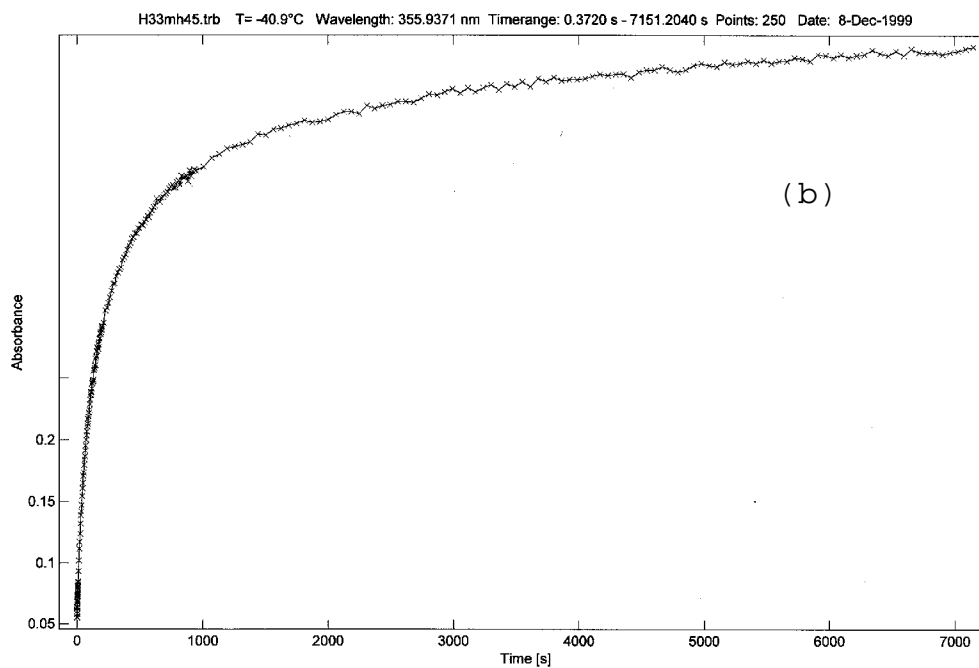
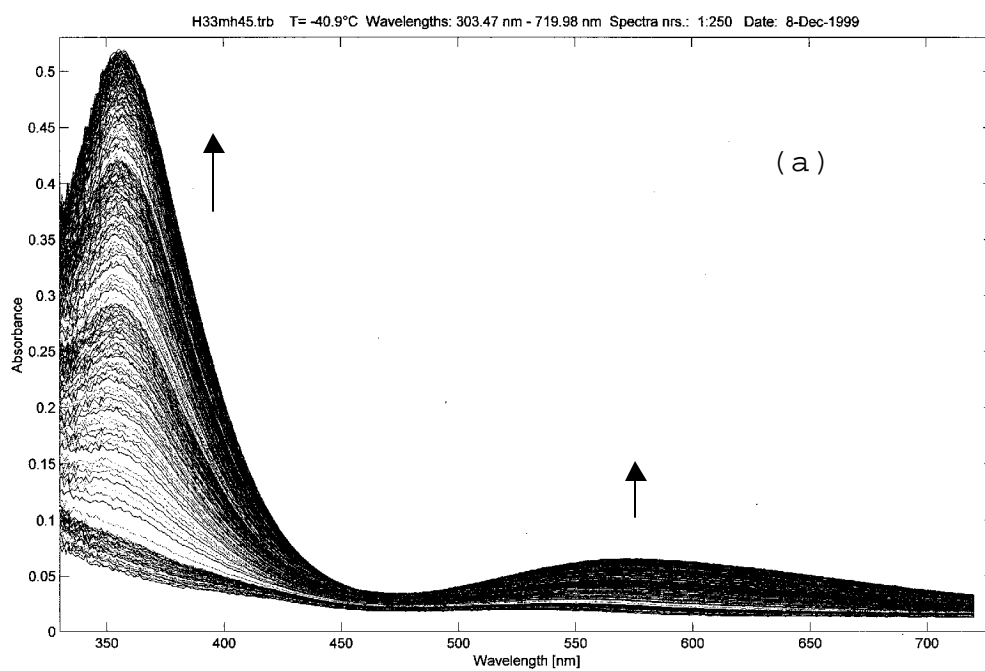


Figure 11. (a) Stopped-Flow UV-Vis spectral changes and (b) absorption profile at 551 nm for the oxygenation of complex $[(\text{H33m})\text{Cu}^{\text{I}}](\text{PF}_6)$ (**9**- (PF_6)) at 25.1 °C (CH_3CN , $[\mathbf{9}] = 4.28 \text{ mM}$, $[\text{O}_2] = 5.76 \text{ mM}$)

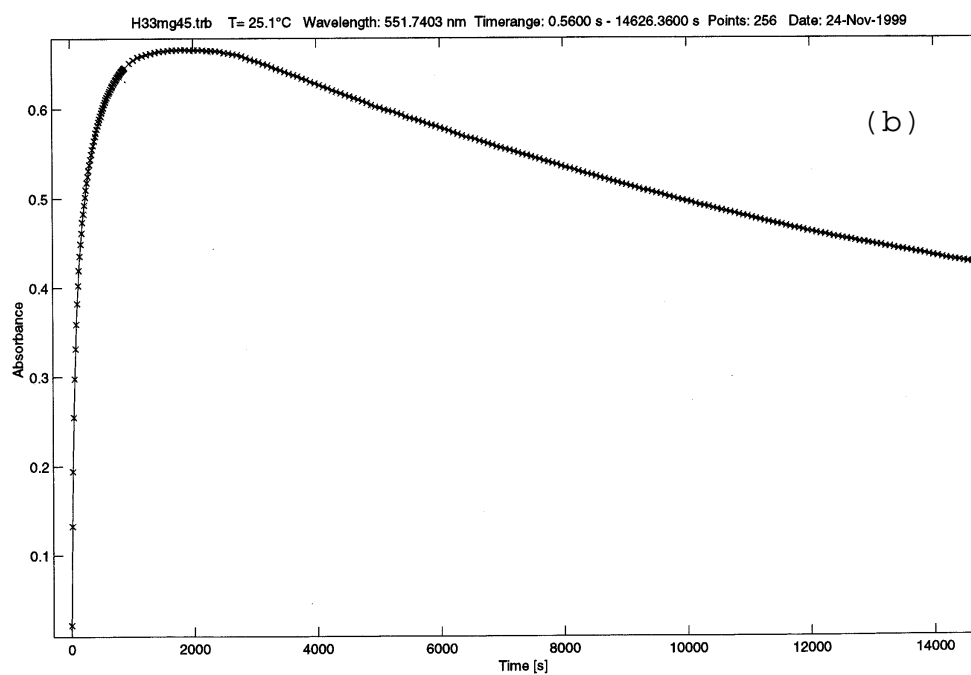
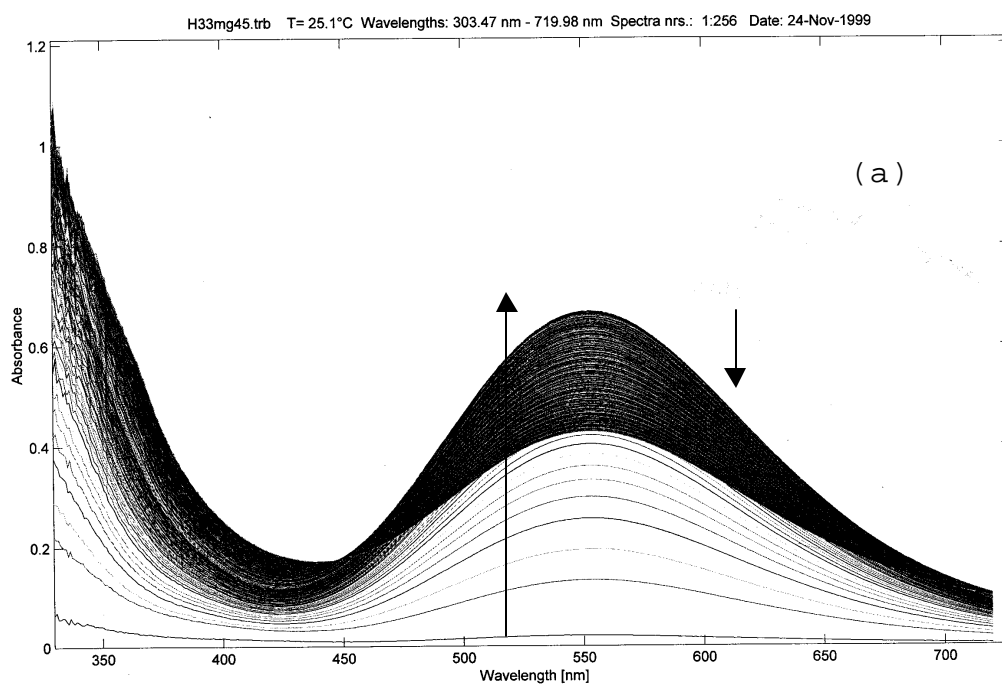


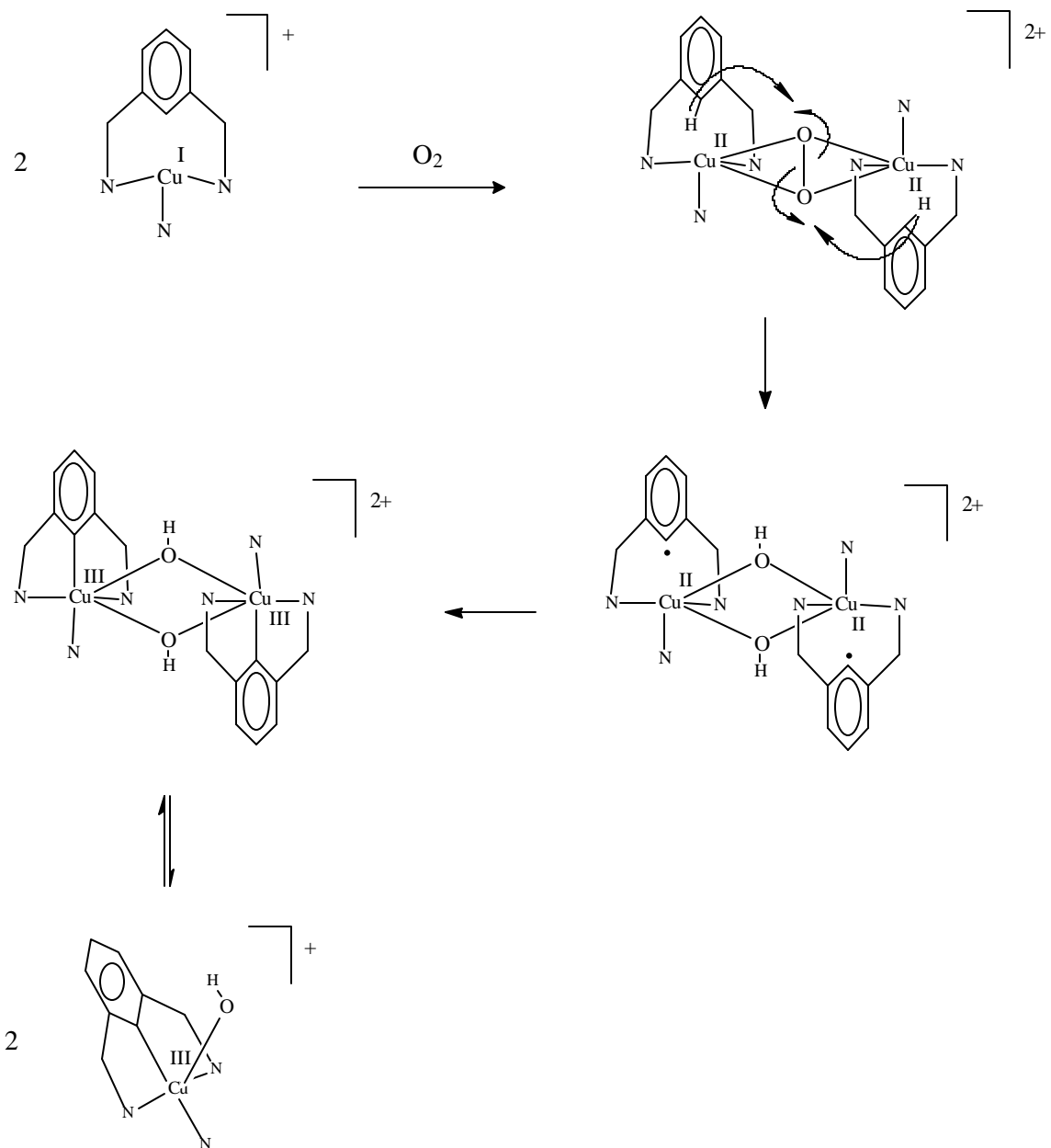
Table 4. Stopped-Flow UV-Vis monitoring experiments for oxygenation of complex [(H33m)Cu^I](PF₆) (**9**-(PF₆)) in CH₃CN at 25°C

	[9] (mM)	[O ₂] (mM)	[O ₂]/[9]	ϵ (M ⁻¹ cm ⁻¹) at 551 nm	Formation 3b (min)	3b decay (hours)
(a)	1.57	5.76	3.68	430	14	2
(b)	1.59	1.14	0.89	600	130	Very Stable
(c)	1.76	0.64	0.36	340	30	3
(d)	4.28	5.76	1.35	800	30	Stable
(e)	4.46	1.56	0.35	560	30	Stable

4.4.3 Mechanistic studies

All the experiments described so far are in agreement with the reaction mechanism outlined in Scheme 5 for the transformation of peroxo intermediate to aryl-Cu^{III}. On this mechanism, peroxo intermediate is proposed to interconvert to bishydroxo species coupled with Cu-C bond formation by oxidation of Cu^{II} to Cu^{III}. However, a first transformation of peroxo intermediate to bis(μ -oxo)Cu^{III} species can not be rule out,¹⁵ although the latter has not been detected by Stopped-Flow Uv-Vis studies at low temperature. If this was the active pathway, proton abstraction by oxo groups would then be the step towards aryl-Cu^{III} formation. Final aryl-Cu^{III}-(OH) species would ultimately insert in the mechanism pathway depicted in Scheme 6.

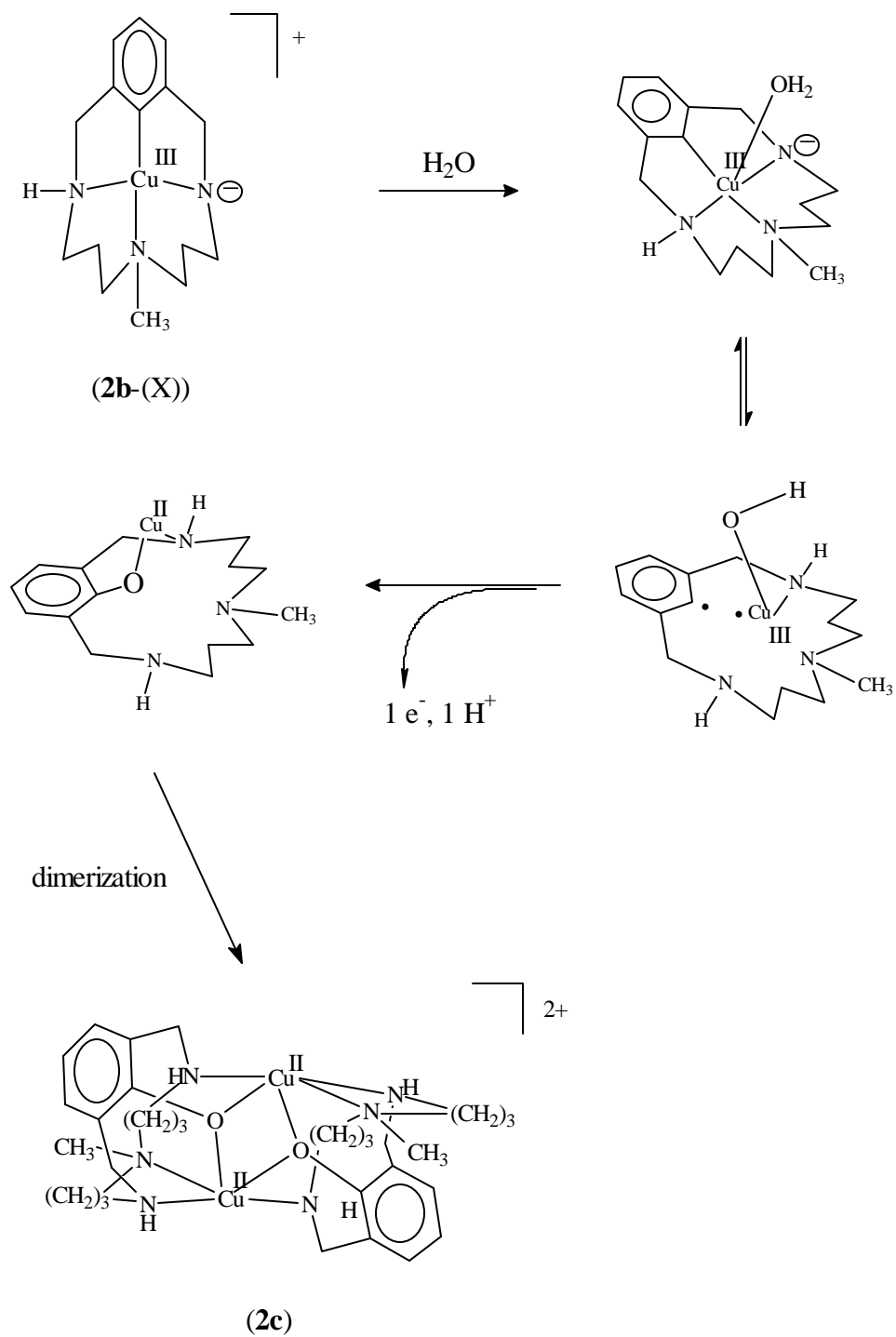
Scheme 5. Proposed general mechanism for aryl-Cu^{III} formation from ($\mu:\eta^2:\eta^2$ -peroxo)Cu^{II} intermediate



The mechanism for the hydroxylation reaction from aryl-Cu^{III} species is depicted in Scheme 6 and discussed in the concrete case of complex $[(H_2Me33m-C)Cu^{III}]^{2+}$ (**2**). From the reactions exposed so far, a general mechanism may be postulated. Once the intermediate $[(H_2Me33m-C)'Cu^{III}]^+$ (**2b**) is formed, H_2O must coordinate as an axial ligand to Cu^{III}

center. Subsequently, the deprotonated amine is basic enough to abstract a proton from the water molecule. The latter step is thought to be an equilibrium. Important conformational changes are demanded in this reaction, so two N coordinative sites should be lost in order to achieve normal and not extremely constrained arC-O-Cu bond distances and angles. The driving force for these changes can be attributed to the migration of OH group (strong σ -donor group) from an axial towards an equatorial position in order to stabilize the Cu^{III} center.¹⁶ Copper atom is leaving the central complex position and it is reasonable to consider at least 4 full coordination sites for Cu^{II}, so a second complex is required to supply good donors as N atoms (complex [(H₂Me33mO)₂Cu^{II}]₂)²⁺ (**2c**) is finally formed). Globally, a hydrogen atom is lost per copper center, which specifically consists in one electron used to reduce copper towards Cu⁰ (small amounts of copper metal Cu⁰ are formed in the reaction of **2**-(X)₂ with 1 eq. of KOH 1M) and one proton that protonates the free ligand generated. This mechanism is supported by the formation of the new type of bisphenoxo complex [(H₂Me33mO)₂(Cu^I)₂Cl₂] (**2d**) (see section 4.4.1), as it can be considered an intermediate step of hydroxylation reaction blocked by Cu^{II} stabilization properties of Cl⁻ anions.

Scheme 6. Proposed mechanism for aromatic hydroxylation through Cu^{III} intermediates



4.4.4 The H22m system

Ligand H22m chemistry with Cu^{I} and Cu^{II} has also been investigated. Although the aryl- Cu^{III} complex $[(\text{H22m-C})\text{Cu}^{\text{III}}](\text{X})_2$ has not been detected under similar reaction conditions as described,¹¹ activation of dioxygen by corresponding Cu^{I} complex is achieved and final bisphenoxo complex $[(\text{H22mO})_2\text{Cu}^{\text{II}}_2](\text{PF}_6)_2$ (**5c**- $(\text{PF}_6)_2$) is also obtained (see Figure 4).

Thus, performing the reaction of H22m and $\text{Cu}^{\text{II}}(\text{OTf})_2$ with a catalytic excess of ligand ($\text{H22m}/\text{Cu}^{\text{II}} = 1.3$, see Chapter 3) allowed the formation of complex $[(\text{H22mO})_2\text{Cu}^{\text{II}}_2](\text{OTf})_2$ (**5c**- $(\text{OTf})_2$) in 22% isolated yield. From these results similar aryl- Cu^{III} intermediates can be postulated to be responsible for the aromatic hydroxylation. Isolation of crystalline $[\text{Cu}^{\text{I}}(\text{CH}_3\text{CN})_4](\text{OTf})$ complex from the final solution supports the disproportionation reaction of initial Cu^{II} complex also proposed for this system. Complete formation and isolation of Cu^{III} complexes in this system is probably precluded by steric impediments of 12-membered cyclic ligand H22m and its tendency to dimerize (see Chapter 3).

4.4.5 Oxidant character of Aryl- Cu^{III} complexes (1-3)

High oxidation state of copper centers in these complexes promoted us to test their properties as oxidant reactants. Early Cyclic Voltammetry studies on aryl- Cu^{III} complexes $[(\text{H32m-C})\text{Cu}^{\text{III}}]^{2+}$ (**1**), $[(\text{H}_2\text{Me33m-C})\text{Cu}^{\text{III}}]^{2+}$ (**2**) and $[(\text{H33m-C})\text{Cu}^{\text{III}}]^{2+}$ (**3**) indicated that aryl- Cu^{II} complexes are not stable unless good electron-donor ligands were present (see Chapter 3).

Reduction of aryl- Cu^{III} **2** is chemically achieved by reaction with 2 equivalents of Proton Sponge in CH_3CN . Violet intermediate $[(\text{H}_2\text{Me33m-C})'\text{Cu}^{\text{III}}]^+$ (**2b**) forms immediately due

to deprotonation of **2** by the base. However, if no water is added into reaction mixture, violet solution fades to pale yellow-brown. Excess of 1,10-phenanthroline caused the instantaneous formation of an intense brown-reddish colored solution attributed to $[(\text{phen})_2\text{Cu}^{\text{I}}]^+$ complex. UV-Vis quantification confirmed a 84% conversion of Cu^{III} to Cu^{I} after 24 hours. ESI-MS spectrum also indicates the presence of Cu^{I} in the form of $[\text{Cu}^{\text{I}}(\text{CH}_3\text{CN})_4]^+$. Identification of chemical modifications on free ligand generated or Proton Sponge itself is currently under study.

Nevertheless, reactivity showed by complex **2** with Proton Sponge explains the Cu^{I} contamination found in XAS studies on violet intermediate **2b** (see section 4.3.3.1).

4.5 EXPERIMENTAL SECTION

Synthesis of ligands H32m, H₂Me33m, H33m and H22m, Cu^{III} complexes $[(\text{H32m-C})\text{Cu}^{\text{III}}](\text{X})_2$ (**1**-(X)₂), $[(\text{H}_2\text{Me33m-C})\text{Cu}^{\text{III}}](\text{X})_2$ (**2**-(X)₂) and $[(\text{H33m-C})\text{Cu}^{\text{III}}](\text{X})_2$ (**3**-(X)₂) (X= ClO_4^- , OTf^-), and Cu^{I} complexes $[(\text{H32m})\text{Cu}^{\text{I}}](\text{X})$ (**7**-(X)), $[(\text{H}_2\text{Me33m})\text{Cu}^{\text{I}}](\text{X})$ (**8**-(X)), $[(\text{H33m})\text{Cu}^{\text{I}}](\text{X})$ (**9**-(X)) (X= ClO_4^- , PF_6^- , OTf^-) and $[(\text{H22m})_2\text{Cu}^{\text{I}}_2](\text{PF}_6)_2$ are reported in Chapter 3.

General Information. Analytical grade solvents were purchased from SDS and dried and distilled under Ar before use. IR, Elemental Analyses, UV-Vis, ESI-MS and NMR spectra were measured on Mattson Satellite FT-IR, Fisons EA-1108, Varian Cary-50 Scan / Polytec PI X-DAP-06 / Tidas (J and M, 507 diodes) , Thermo Quest Finigan Navigator LC/MS, Bruker Avance-500 MHz instruments, respectively.

Warning: Although we have experienced no problems with the compounds reported herein, perchlorate salts are potentially explosive, and should only be handled in small quantities and never heated in the solid state.

Complex synthesis. [(H32m-C)'Cu^{III}](OTf) (**1b**-(OTf)): the synthesis was carried out under N₂ or Ar. To a solution of complex **1**-(OTf)₂ (0.03 g, 5.2x10⁻⁵ moles) in CH₃CN (1 mL) was added Proton Sponge® (0.011g, 5.2x10⁻⁵ moles) to give a red-brown solution. Complex couldn't be isolated as solid sample.

ESI-MS (CH₃CN): 430 [**1b**-(OTf) +H]⁺, 280 [**1b**]⁺; 1H NMR (400 MHz, CD₃CN, 25°C, generated with KOH 1M): 7.15 (t, 1H), 6.96 (dd, 2H), 4.51 (dd, 2H), 4.27 (dd, 2H), 3.30 (m, 2H), 3.07 (m, 3H), 2.89 (m, 2H), 2.71 (t, 1H), 2.03 (d, 1H), 1.59 (m, 1H); UV/Vis (CH₃CN): λ_{max} (ε)= 465 nm (950) (when complex generated with 1 eq. of KOH 1M: λ_{max} (ε)= 472 nm (1550))

[(H₂Me33m-C)'Cu^{III}](OTf) (**2b**-(OTf)): the synthesis was carried out under N₂ or Ar. To a solution of complex **2**-(OTf)₂ (0.03 g, 4.9x10⁻⁵ moles) in CH₃CN (1 mL) was added Proton Sponge® (0.0105g, 4.9x10⁻⁵ moles) to give a violet solution. Complex couldn't be isolated as solid sample.

ESI-MS (CH₃CN): 458 [**2b**-(OTf)+H]⁺, 308 [**2b**]⁺; UV/Vis (CH₃CN): λ_{max} (ε)= 545 nm (1070) (when complex generated with 1 eq. of KOH 1M: λ_{max} (ε)= 545 nm (1250)).

[(H33m-C)'Cu^{III}](OTf) (**3b**-(OTf)): the synthesis was carried out under N₂ or Ar. To a solution of complex **3**-(OTf)₂ (0.03 g, 5.05x10⁻⁵ moles) in CH₃CN (1 mL) was added Proton

Sponge® (0.0108g, 5.05×10^{-5} moles) to give a violet solution. Complex couldn't be isolated as solid sample.

ESI-MS (CH₃CN): 444 [**3b**-(OTf) +H]⁺, 294 [**3b**]⁺; UV/Vis (CH₃CN): λ_{\max} (ϵ) = 540 nm (540) (when complex generated with 1 eq. of KOH 1M: λ_{\max} (ϵ) = 544 nm (650)).

[(H32mO)₂Cu^{II}]₂(OTf)₂ (**1c**-(OTf)₂): the synthesis was carried out under N₂ or Ar. To a solution of complex **1**-(OTf)₂ (0.05 g, 8.7×10^{-5} moles) in CH₃CN (1 mL) was injected a KOH(aq) 1M (87 μ L, 8.7×10^{-5} moles). Reaction was stirred until the red-brown intermediate formed faded to green (48 hours). Diffusion of diethyl ether and overnight storing at -25°C allowed formation of green crystals in 30% isolated yield (0.012 g). ESI-MS (CH₃CN): 743 [**1c**-(OTf)]⁺, 297 [(H32mO)Cu^{II}]⁺; UV/Vis (CH₃CN): λ_{\max} (ϵ) = 394 (760), 699 (615); IR (KBr pellet, cm⁻¹): 3258 (m), 3121 (m), 2924 (w), 1591 (w), 1456 (m), 1285 (s), 1252 (s), 1165 (m), 1031 (m), 640 (m); elemental analysis calcd for C₂₆H₄₀N₆O₂Cu₂(C₂F₆S₂O₆) · 0.5CH₃CN (%): C 38.1, H 4.6, N 10.0, S 7.0; found: C 37.9, H 4.8, N 10.2, S 6.7.

Perchlorate complex **1c**-(ClO₄)₂ is synthesized in a similar manner. Complex **1c** can also be obtained by oxygenation of the Cu^I complex [(H32m)Cu^I](PF₆) (**7**-(PF₆)) (see synthesis of complex **3c**).

[(H₂Me33mO)₂Cu^{II}]₂(OTf)₂ (**2c**-(OTf)₂): synthesis was carried out under N₂ or Ar. To a solution of complex **2**-(OTf)₂ (0.03 g, 4.9×10^{-5} moles) in CH₃CN (2 mL) was injected a KOH(aq) 1M (50 μ L, 4.9×10^{-5} moles). Reaction was stirred until the violet intermediate formed faded to green (2-3 hours). Slow diffusion of diethyl ether allowed the formation of green crystals in 65% isolated yield (0.011 g). ESI-MS (CH₃CN): 799 [**2c**-(OTf)]⁺, 325 [(H₂Me33mO)Cu^{II}]⁺; UV/Vis (CH₃CN): λ_{\max}

(ϵ)= 411 nm (1000), 765 nm (610); IR (KBr pellet, cm^{-1}): 3258 (m), 3210 (m), 2931 (m), 2869 (m), 1592 (m), 1463 (s), 1282 (s), 1236 (s), 1162 (s), 1022 (s), 636 (s); elemental analysis calcd for $\text{C}_{30}\text{H}_{48}\text{N}_6\text{O}_2\text{Cu}_2(\text{C}_2\text{F}_6\text{S}_2\text{O}_6)$ (%): C 40.5, H 5.1, N 8.8, S 6.7 ; found: C 39.8, H 5.4, N 8.4, S 6.4.

Complex **2c**-(OTf)₂ can be also obtained generating intermediate **2b**-(OTf) followed by addition of 7 equivalents of H₂O. Perchlorate complex **2c**-(ClO₄)₂ is synthesized in a similar manner. X-Ray quality crystals were obtained for **2c**-(ClO₄)₂ · CH₃CN by recrystallization in CH₃CN/ether.

Oxygenation of Cu^I complex [(H₂Me33m)Cu^I](OTf) (**8**-(OTf)) also yield complex **3c**: Colorless solution of complex [(H₂Me33m)Cu^I](OTf) (**8**-(OTf)) (0.025 g, 5.4x10⁻⁵ mol) in 2 ml CH₃CN/CH₂Cl₂ 1/3 under Ar is treated with 1.75 mL of dioxygen O₂ (8.4x10⁻⁵ mol). Solution changes to violet slowly and after 3 hours stirring fades to green. Slow diffusion of diethyl ether allowed isolation of [(H₂Me33mO)₂Cu^{II}](OTf)₂ (**2c**-(OTf)₂) bisphenoxo complex in 25% isolated yield.

[(H33mO)₂Cu^{II}](OTf)₂ (**3c**-(OTf)₂): synthesis was carried out under N₂ or Ar. To a solution of complex **3**-(OTf)₂ (0.03 g, 5.05x10⁻⁵ moles) in CH₃CN (2 mL) was injected a KOH(aq) 1M (50 μL , 5.05x10⁻⁵ moles). Reaction was stirred until the violet intermediate formed faded to green (1-2 hours). Slow diffusion of diethyl ether allowed the formation of green crystals in 60% isolated yield (0.014 g). ESI-MS (CH₃CN): 771 [**3c**-(OTf)]⁺, 311 [(H33mO)Cu^{II}]⁺; UV/Vis (CH₃CN): λ_{max} (ϵ)= 436 nm (830), 756 nm (485); IR (KBr pellet, cm^{-1}): 3336 (m), 3294 (m), 1591 (m), 1465 (m), 1280 (s), 636 (s).

Complex **3c** can also be obtained from oxygenation of Cu^I complex **9**: colorless solution of complex [(H33m)Cu^I](PF₆) (**9**-PF₆) (0.025 g, 5.57x10⁻⁵ moles) in 2 ml CH₃CN/CH₂Cl₂ 1/3 under Ar is treated with excess O₂. Solution changes to

violet and slowly and after 3 hours stirring fades to green. Slow diffusion of diethyl ether allowed isolation of $[(\text{H33mO})_2\text{Cu}^{\text{II}}_2](\text{PF}_6)_2$ (**3c**-(PF_6)₂) bisphenoxo complex in 20% isolated yield. ESI-MS (CH_3CN): 767 [**3c**-(PF_6)]⁺, 311 $[(\text{H33mO})\text{Cu}^{\text{II}}]^+$. Elemental analysis calcd for $\text{C}_{28}\text{H}_{44}\text{N}_6\text{O}_2\text{Cu}_2\text{P}_2\text{F}_6$ (%): C 36.8, H 4.9, N 9.2; found: C 37.1, H 5.1, N 9.1.

$[(\text{H}_2\text{Me33mO})_2\text{Cu}^{\text{II}}_2\text{Cl}_2]$ (**2d**): to a 1 mL solution of complex **2b**-(OTf) (9.2 mM) in CH_3CN , a solution of KCl(aq) 1M (9 μL) is injected under stirring. Color changes from violet to red and crystals precipitate out from reaction mixture in 24 hours in 57% isolated yield.

ESI-MS (CH_3CN): 685 $[(\text{H}_2\text{Me33mO})_2\text{Cu}^{\text{II}}_2\text{Cl}]^+$, 325 $[(\text{H}_2\text{Me33mO})_2\text{Cu}^{\text{II}}_2]^{2+}$; IR (KBr pellet, cm^{-1}): 3214 (m), 2922 (m), 2861 (m), 2800 (m), 1594 (m), 1451 (s), 1279 (s), 1146 (m), 972 (m), 756 (m); UV/Vis (CH_3CN): λ_{max} (ϵ) = 422 nm (1170), 536 nm (470), 630 nm (375); elemental analysis calcd for $\text{C}_{30}\text{H}_{48}\text{N}_6\text{O}_2\text{Cu}_2\text{Cl}_2$ (%): C 50.0, H 6.7, N 11.6; found: C 49.7, H 6.6, N 11.7.

$[(\text{H22mO})_2\text{Cu}^{\text{II}}_2](\text{OTf})_2$ (**5c**-(OTf)₂). Ligand H22m (0.022 g, 0.106 mmol) and $\text{Cu}^{\text{II}}(\text{OTf})_2$ (0.0295 g, 0.082 mmol) are dissolved in 2 mL of CH_3CN and stirred under Ar for 5 hours. Diethyl ether diffusion allowed the formation of green crystals of desired complex in 22 % yield. ESI-MS (CH_3CN): 715 $[(\text{H22mO})_2\text{Cu}_2](\text{OTf})]^+$, 283 $[(\text{H22mO})\text{Cu}^{\text{II}}]^+$; IR (KBr pellet, cm^{-1}): 3258 (s), 3208 (s), 2932 (m), 1594 (m), 1457 (s), 1277 (s), 1258 (s), 1160 (s), 1030 (s), 638 (s); UV/Vis (CH_3CN): λ_{max} (ϵ) = 406 nm (540), 578 nm (325).

Complex (**5c**-(PF_6)₂) can be obtained from the oxygenation of the corresponding Cu^{I} complex: ligand H22m (0.020 g, 0.097 mmol) and $[\text{Cu}^{\text{I}}(\text{CH}_3\text{CN})_4]\text{PF}_6$ (0.0363 g, 0.097 mmol) are dissolved in 1 mL of anhydrous CH_3CN in anaerobic conditions, and after 5 minutes of magnetic stirring, O_2 is

bubbled for 5 minutes. Solution is filtered and slow diffusion of diethyl ether allows the isolation of green crystals of complex (**5c**-(PF₆)₂) in 20% yield. IR (KBr pellet, cm⁻¹): 3337 (s), 3291 (s), 2935 (m), 1595 (m), 1455 (s), 1297 (m), 843 (s), 559 (m); elemental analysis calcd for C₂₄H₃₆N₆O₂Cu₂P₂F₁₂ (%): C 33.6, H 4.2, N 9.8; found: C 34.0, H 4.6, N 9.7.

Mass Spectrometry. ESI-MS spectra were performed with a Thermo Quest Finigan Navigator LC/MS, that bears an atmospheric pressure ionization source (API-MS), and using the positive ionization mode (ESI⁺). Typical experimental conditions were: solvent = CH₃CN 100%, source voltage = 30 eV, temperature = 170 °C, Flux = 150 µl/min, mass range = 200-1000, 10-15 scans per LC peak and registration under profile peak format.

NMR Spectroscopy. Temperature-dependence ¹H NMR spectra of diamagnetic Cu^{III} intermediates **1a-2b** copper complexes were registered in a Bruker Avance-500. Sensitive copper samples were treated under controlled Ar atmosphere using rubber septa for NMR tubes.

UV-Vis experiments procedure. Temperature-dependence UV-Vis experiments were performed in CH₃CN with a SFL-21 variable temperature stopped-flow unit (Hi-Tech) connected to a Tidas 16 diode array spectrometer (J and M, 507 diodes). Five series of spectra were taken between 232.9 and 298 K. The concentration of complex used were in the 1.5-4.5 mM range. Dioxygen concentration was also adjusted in a range between 0.6 and 5.76 mM.

A Varian Cary-50 Scan spectrometer was also used to monitor intermediate formation and decay reactions of Cu^{III}

compounds. Temperature of the reaction cell was controlled by a Huber CC180 cryostat.

X-Ray Diffraction Analysis. Analyses on a parallelepiped green crystal of $[(\text{H32mO})_2\text{Cu}^{\text{II}}_2](\text{OTf})_2$ (**1c**- $(\text{OTf})_2$), a rod green crystal of $[(\text{H}_2\text{Me33mO})_2\text{Cu}^{\text{II}}_2](\text{ClO}_4)_2 \cdot \text{CH}_3\text{CN}$ (**2c**- $(\text{ClO}_4)_2 \cdot \text{CH}_3\text{CN}$) and a parallelepiped green crystal of $[(\text{H}_2\text{Me33mO})_2\text{Cu}^{\text{II}}_2](\text{Cl})(\text{PF}_6) \cdot 2\text{H}_2\text{O} \cdot 0.5\text{CH}_3\text{OH}$ (**2c**- $(\text{Cl})(\text{PF}_6) \cdot 2\text{H}_2\text{O} \cdot 0.5\text{CH}_3\text{OH}$) were carried out on a STOE imaging plate diffraction system (I.P.D.S) with graphite monochromated Mo $K\alpha$ radiation ($\lambda = 0.71073 \text{ \AA}$) operating in the *j* scan method. Cell measurement temperature was 160(2) K for **1c**- $(\text{OTf})_2$ and **2c**- $(\text{Cl})(\text{PF}_6) \cdot 2\text{H}_2\text{O} \cdot 0.5\text{CH}_3\text{OH}$, and 293(2) for **2c**- $(\text{ClO}_4)_2 \cdot \text{CH}_3\text{CN}$. Structures were solved by direct methods using the SIR92¹⁷ and refined by least-squares procedures on a F^2 with the aid of SHELXL97.¹⁸ Disordered perchlorate O atoms and CH_3CN crystallization molecule are found in **2c**- $(\text{ClO}_4)_2 \cdot \text{CH}_3\text{CN}$.

Analyses on a prismatic green crystal of $[(\text{H33mO})_2\text{Cu}^{\text{II}}_2](\text{PF}_6)_2$ (**3c**- $(\text{PF}_6)_2$), a block green crystal of $[(\text{H22mO})_2\text{Cu}^{\text{II}}_2](\text{PF}_6)_2$ (**5c**- $(\text{PF}_6)_2$) and a rhombic deep red crystal of $[(\text{H}_2\text{Me33mO})_2\text{Cu}^{\text{II}}_2\text{Cl}_2]$ (**2d**) were carried out on a Bruker Siemens SMART CCD area detector single crystal diffractometer with graphite monochromated Mo $K\alpha$ radiation ($\lambda = 0.71073 \text{ \AA}$) operating in the *j* and *w* scan method. Cell measurement temperature was 293(2) for **3c**- $(\text{PF}_6)_2$, 173(2) for **5c**- $(\text{PF}_6)_2$ and 273(2) K for **2d**. Data reduction, Lorentz, polarization and empirical absorption corrections were performed with the Sadabs package. Structures were solved by direct methods using SHELXS-86¹⁹ and refined by full-matrix least-squares analysis with SHELXL-93,²⁰ SHELXL-97,¹⁸ and teXsan for Windows.²¹

A summary of the crystallographic data is given in Table 1. Packing cell ORTEP plots for all crystals can be found in Figure S2.

XAS experiment. Air and thermally sensitive samples **1b** and **2b** were handled at low temperature (-78 °C) and under N₂ atmosphere throughout to prevent sample degradation. Samples were prepared starting with ≈ 20 mg of Aryl-Cu^{III} **1** and **2** and one equivalent of Proton Sponge. The mixtures were pressed into 1 mm thick aluminum spacers lined with Mylar tape (X-Ray transparent) windows. X-Ray absorption spectra were measured on unfocused wiggler beamline 7-3 at the Stanford Synchrotron Laboratory (SSRL), with the ring operating at 3 GeV and 50-100 mA. Samples were maintained at 10 K inside an Oxford Instruments CF-1208 liquid helium continuous flow cryostat. A Si(220) double-crystal monochromator was used, detuned 50% at 9868 eV to minimize contamination of the radiation by higher harmonics. Vertical 1 mm pre-monochromator slits were used to define beam size, minimizing beam divergence. K-edge and EXAFS data were measured, for all samples, over the energy range 8650-9868 eV. The monochromator step size in the edge region (8970-9020 eV) was 0.1-0.2 eV, to enhance resolution over this range. Spectra were collected in transmission mode, using N₂ filled ionization chambers to measure the intensity on incident and transmitted radiation. The spectrum of a Cu foil was collected concomitantly, allowing for internal energy calibration of the spectra. The first inflection point for the Cu foil spectra was set to 8980.3 eV. The spectrometer energy resolution was approximately 1.4 eV, with reproducibility in the determination of edge position of <0.2 eV. Two to four scans were averaged for each data set.

Raman Spectroscopy. Resonance Raman spectra were collected on an Acton AM-506 spectrometer (2400-groove grating) using a Kaiser Optical holographic supernotch filter with a Princeton Instruments liquid N₂-cooled (LN-1100PB) CCD detector with 4 cm⁻¹ spectral resolution. The laser excitation lines were obtained with a Spectra Physics 2030-15 argon ion laser and a 375B CW dye (Rhodamine 6G), or a spectra Physics BeamLok 2060-KR-V krypton ion laser. The Raman frequencies were referenced to indene. For the intermediate 3b, the spectra were obtained with 200 mW power at 77 K using a backscattering geometry on samples frozen on a gold-plated copper coldfinger in thermal contact with a dewar containing liquid N₂. Curve fits (Gaussian functions) and baseline corrections (polynomial fits) were carried out using Grams/32 Spectral Notebase Version 4.04 (Galactic).

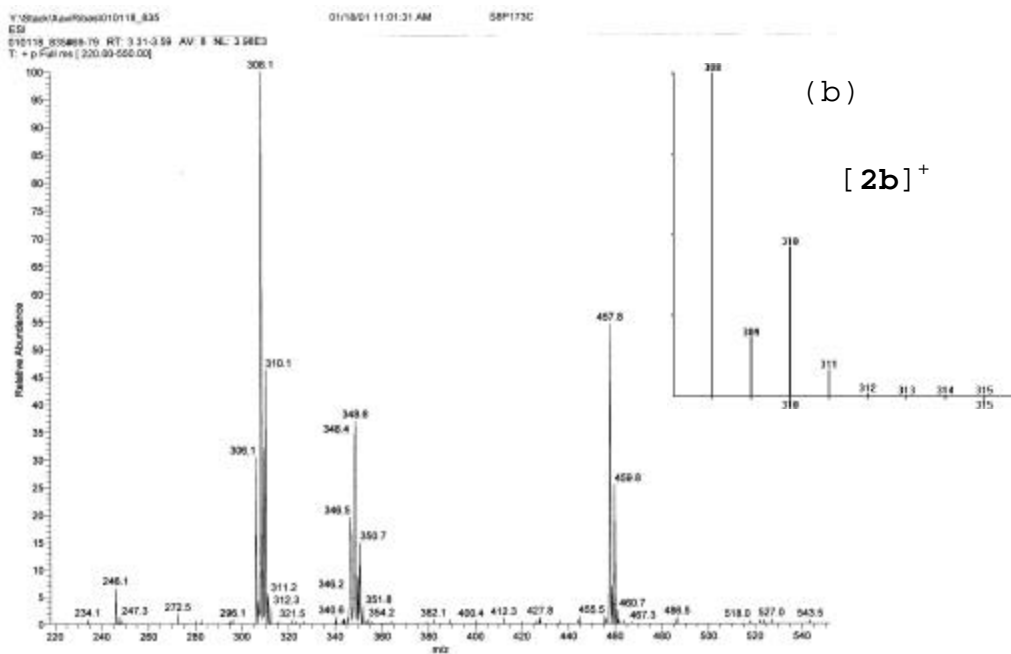
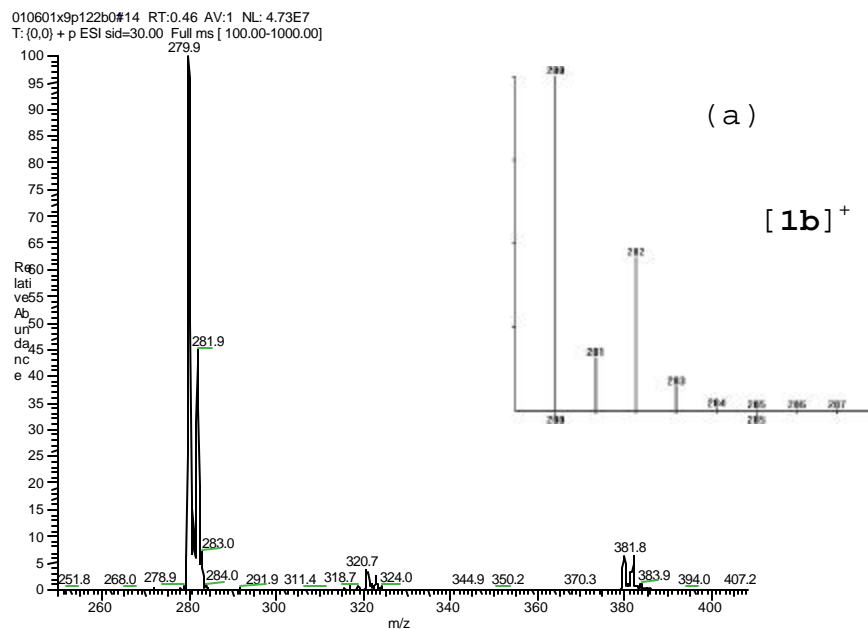
4.6 REFERENCES

- ¹ D.E. Wilcox, A.G. Porras, Y.T. Hwang, K. Lerch,; M.E. Winkler, E.I. Solomon, *J. Am. Chem. Soc.* **1985**, *107*, 4015
- ² J.P. Klinman, *Chem. Rev.* **1996**, *96*, 2541-2561
- ³ a) R.W. Cruse, S. Kaderli, K.D. Karlin, A.D. Zuberbühler, *J. Am. Chem. Soc.* **1988**, *110*, 6882; b) K.D. Karlin, M.S. Nasir, B.I. Cohen, R.W. Cruse, S. Kaderli, A.D. Zuberbühler, *J. Am. Chem. Soc.* **1994**, *116*, 1324; c) L. Casella, E. Monzani, M. Gullotti, D. Caravagnoni, G. Cerina, L. Santagostini, R. Ugo, *Inorg. Chem.* **1996**, *35*, 7516; d) R. Menif, A.E. Martell, P.J. Squattrito, A. Clearfield, *Inorg. Chem.* **1991**, *29*, 4723; e) S. Mahapatra, S. Kaderli, A. Llobet, Y.M. Neuhold, T. Palanché, J.A. Halfen, V. G. Young, Jr., T. A. Kaden, L. Que, Jr., A. D. Zuberbühler, W.B. Tolman, *Inorg. Chem.* **1997**, *36*, 6343-6356
- ⁴ E. Pidcock, H.V. Obias, C. X. Zhang, K. D. Karlin, E.I. Solomon, *J. Am. Chem. Soc.* **1998**, *120*, 7841-7847
- ⁵ V. Mahadevan, R. J. M. K. Gebbink, T. D. P. Stack, *Curr. Opin. Chem. Bio.* **2000**, 228-234
- ⁶ M. A. Lockwood, T. J. Blubaugh, A. M. Collier, S. Lovell, J. M. Mayer, *Angew. Chem.* **1999**, *111*, 178-180; *Angew. Chem. Int. Ed.* **1999**, *38*, 225-227.
- ⁷ E. Nakamura, S. Mori, *Angew. Chem.* **2000**, *112*, 3902-3924; *Angew. Chem. Int. Ed.* **2000**, *39*, 3750-3771.
- ⁸ J.A. Halfen, S. Mahapatra, E.C. Wilkinson, S. Kaderli, V.G. Young, Jr., L. Que, Jr., A.D. Zuberbühler, W.B. Tolman, *Science* **1996**, *271*, 1397-1400.
- ⁹ P. L. Holland, K. R. Rodgers, W. B. Tolman, *Angew. Chem.* **1999**, *111*, 1210-1213; *Angew. Chem. Int. Ed.* **1999**, *38*, 1139
- ¹⁰ a) V. Mahadevan, M. J. Henson, E. I. Solomon, T. D. P. Stack, *J. Chem. Am. Soc.* **2000**, *122*, 10249-10250; b) S. Itoh, M. Taki, H. Nakao, P. L. Holland, W. B. Tolman, L.

- Que, Jr., S. Fukuzumi, *Angew. Chem.* **2000**, *112*, 409-411;
Angew. Chem. Int. Ed. **2000**, *39*, 398-400.
- ¹¹ See Chapter 3 and references therein.
- ¹² A. W. Addison, T. N. Rao, J. Reedijk, J. V. Rijn, G. C. Verschoor, *J. Chem. Soc., Dalton Trans.* **1984**, 1349.
- ¹³ S. Mahapatra, J. A. Halfen, E. C. Wilkinson, L. Que, Jr., W. B. Tolman, *J. Am. Chem. Soc.* **1994**, *116*, 9785-9786.
- ¹⁴ H. C. Liang, K. D. Karlin, R. Dyson, S. Kaderli, B. Jung, A. D. Zuberbühler, *Inorg. Chem.* **2000**, *39*, 5884-5894.
- ¹⁵ J.A. Halfen, S. Mahapatra, E.C. Wilkinson, S. Kaderli, V.G. Young, Jr., L. Que, Jr., A.D. Zuberbühler, W.B. Tolman, *Science* **1996**, *271*, 1397-1400.
- ¹⁶ V. Mahadevan, Z. Hou, A. P. Cole, D. E. Root, T. K. Lal, E. I. Solomon, T. D. P. Stack, *J. Am. Chem. Soc.* **1997**, *119*, 11996-11997
- ¹⁷ Altomare, A., Cascarano, G., Giacovazzo G., Guagliardi A., Burla M.C., Polidori, G., Camalli, M. SIR92 - a program for automatic solution of crystal structures by direct methods. *J. Appl. Cryst.* **1994**, *27*, 435.
- ¹⁸ Sheldrick, G. M. *SHELXS-97*, Computer Program for Crystal Structure Refinement; University of Göttingen, Germany, 1997..
- ¹⁹ Sheldrick, G. M. *SHELXS-86: Program for the Solution of Crystal Structures*; University of Göttingen, Germany, 1986.
- ²⁰ Sheldrick, G. M. *SHELXS-93*; University of Göttingen, Germany, 1986.
- ²¹ Crystal Structure Analysis Package, Molecular Structure Corporation (1997).

SUPPORTING INFORMATION FOR CHAPTER 4

Figure S1. ESI-MS of complexes (a) $[(\text{H}32\text{m-C})'\text{Cu}^{\text{III}}](\text{OTf})$ (**1b**-(OTf)), (b) $[(\text{H}_2\text{Me}33\text{m-C})'\text{Cu}^{\text{III}}](\text{OTf})$ (**2b**-(OTf)) and (c) $[(\text{H}33\text{m-C})'\text{Cu}^{\text{III}}](\text{OTf})$ (**3b**-(OTf)), and corresponding simulation for fragment peaks.



(c)

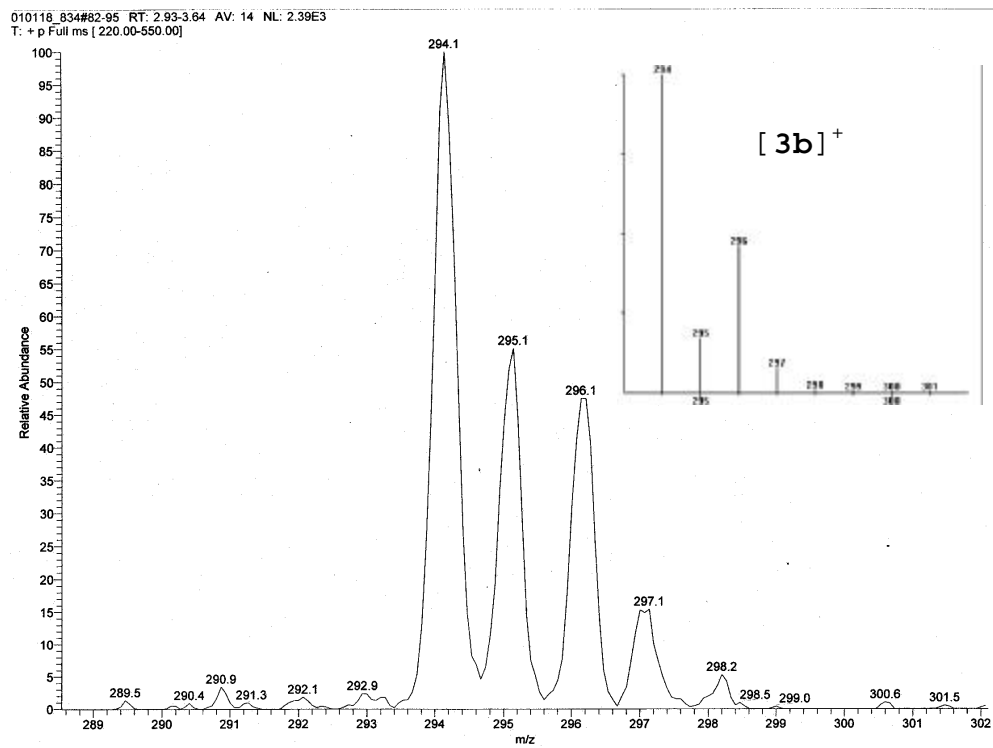
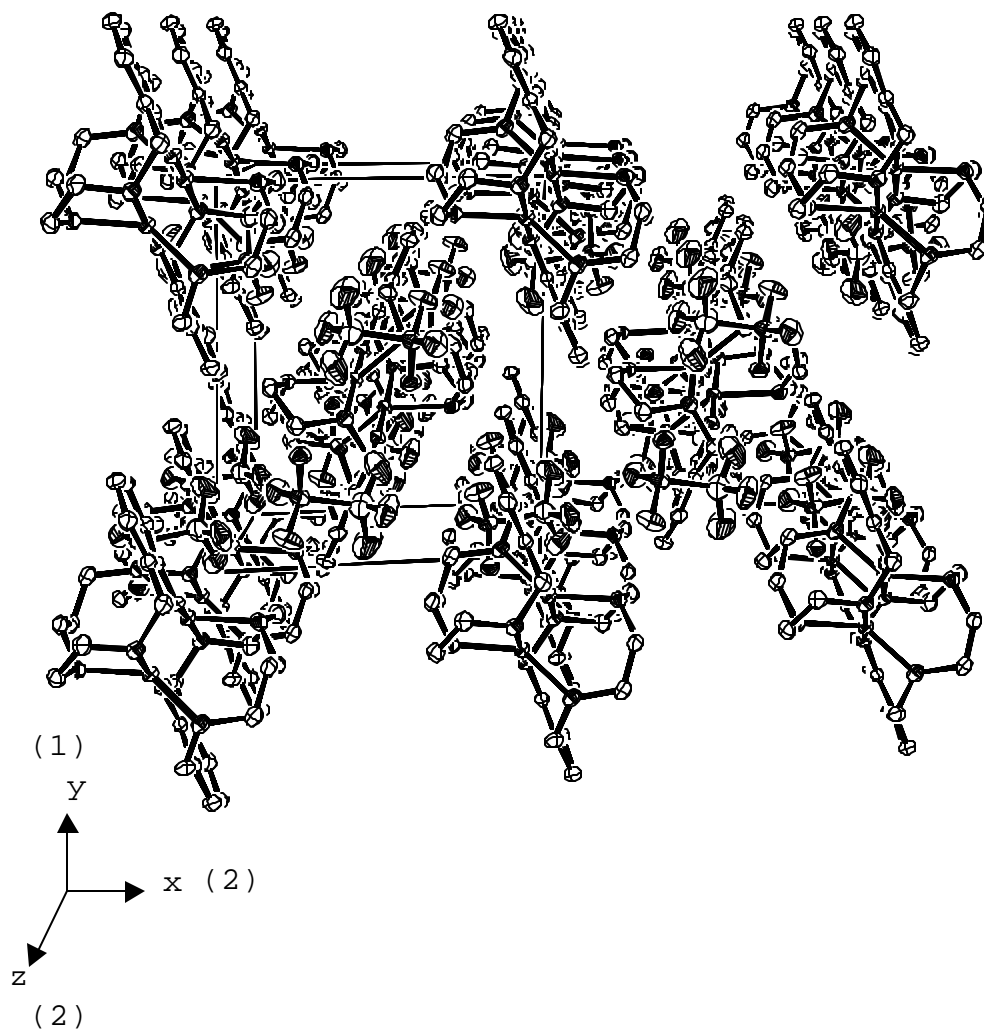
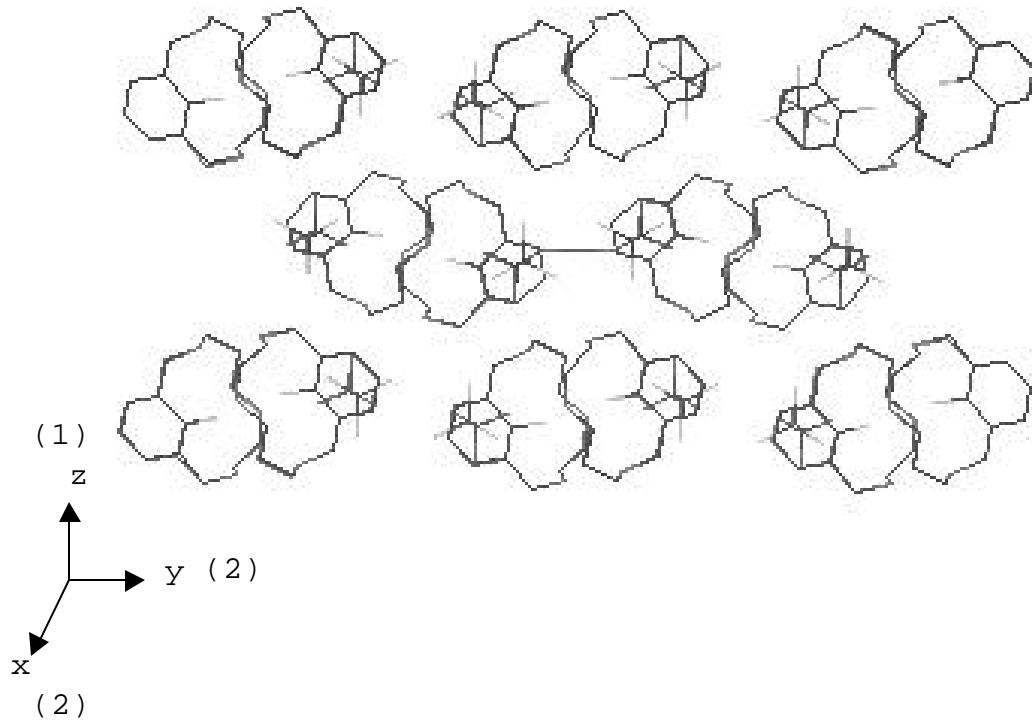


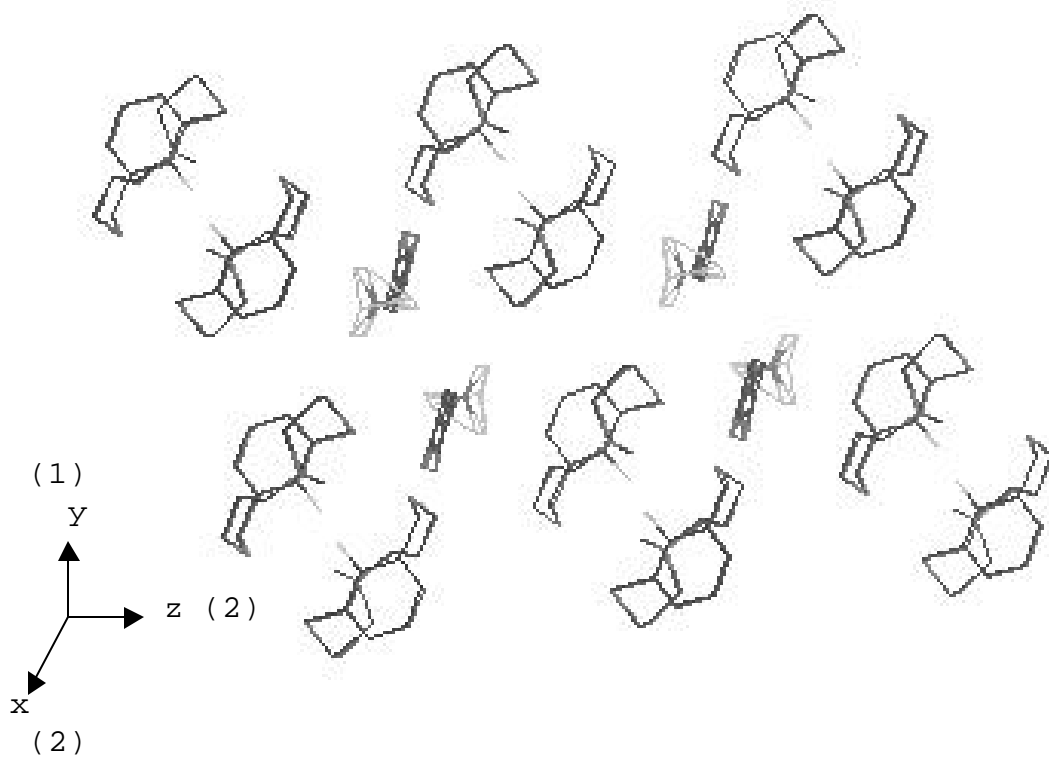
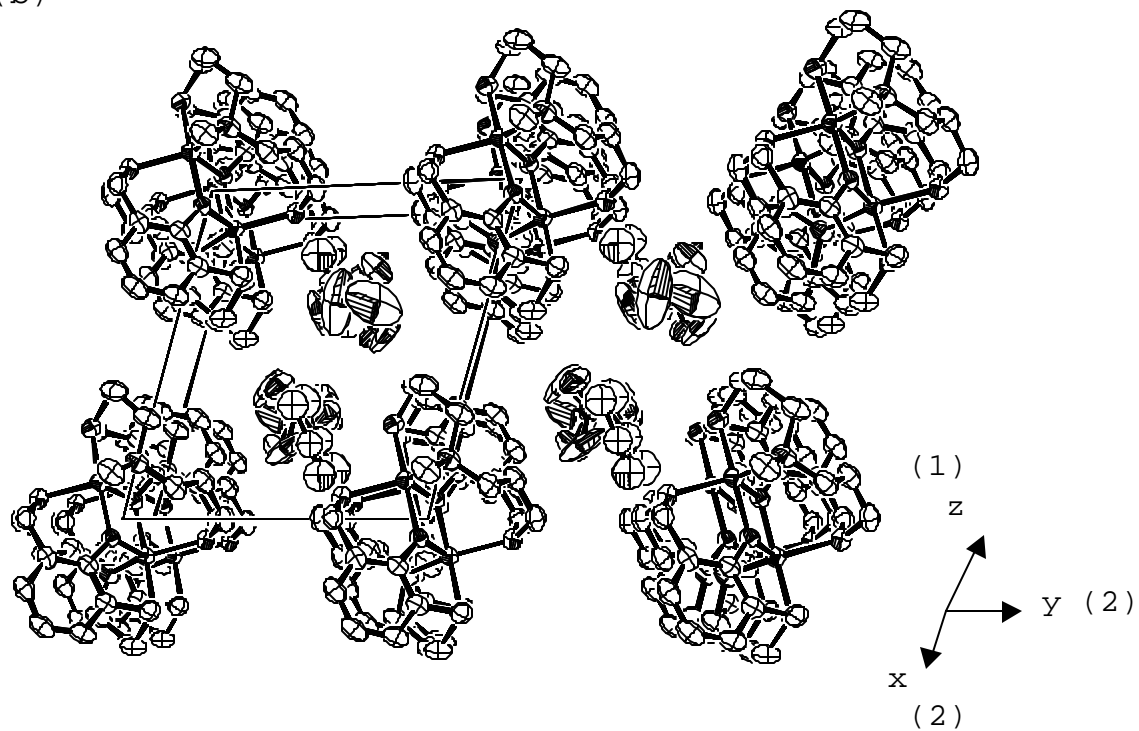
Figure S2. ORTEP and wireframe plots of packing cells for structures of complexes (a) $[(\text{H}32\text{mO})_2\text{Cu}^{\text{II}}](\text{OTf})_2$ (**1c**- $(\text{OTf})_2$), (b) $[(\text{H}_2\text{Me}33\text{mO})_2\text{Cu}^{\text{II}}](\text{ClO}_4)_2 \cdot \text{CH}_3\text{CN}$ (**2c**- $(\text{ClO}_4)_2 \cdot \text{CH}_3\text{CN}$), (c) $[(\text{H}33\text{mO})_2\text{Cu}^{\text{II}}](\text{PF}_6)_2$ (**3c**- $(\text{PF}_6)_2$), (d) $[(\text{H}22\text{mO})_2\text{Cu}^{\text{II}}](\text{PF}_6)_2$ (**4c**- $(\text{PF}_6)_2$), (e) $[(\text{H}_2\text{Me}33\text{mO})_2\text{Cu}^{\text{II}}\text{Cl}_2]$ (**2d**), (f) $[(\text{H}_2\text{Me}33\text{mO})_2\text{Cu}^{\text{II}}](\text{Cl})(\text{PF}_6) \cdot 2\text{H}_2\text{O} \cdot 0.5\text{CH}_3\text{OH}$ (**2c**- $(\text{Cl})(\text{PF}_6) \cdot 2\text{H}_2\text{O} \cdot 0.5\text{CH}_3\text{OH}$). Hydrogen atoms are omitted for clarity. Enclosure boxes in each axis indicated in brackets.

(a)

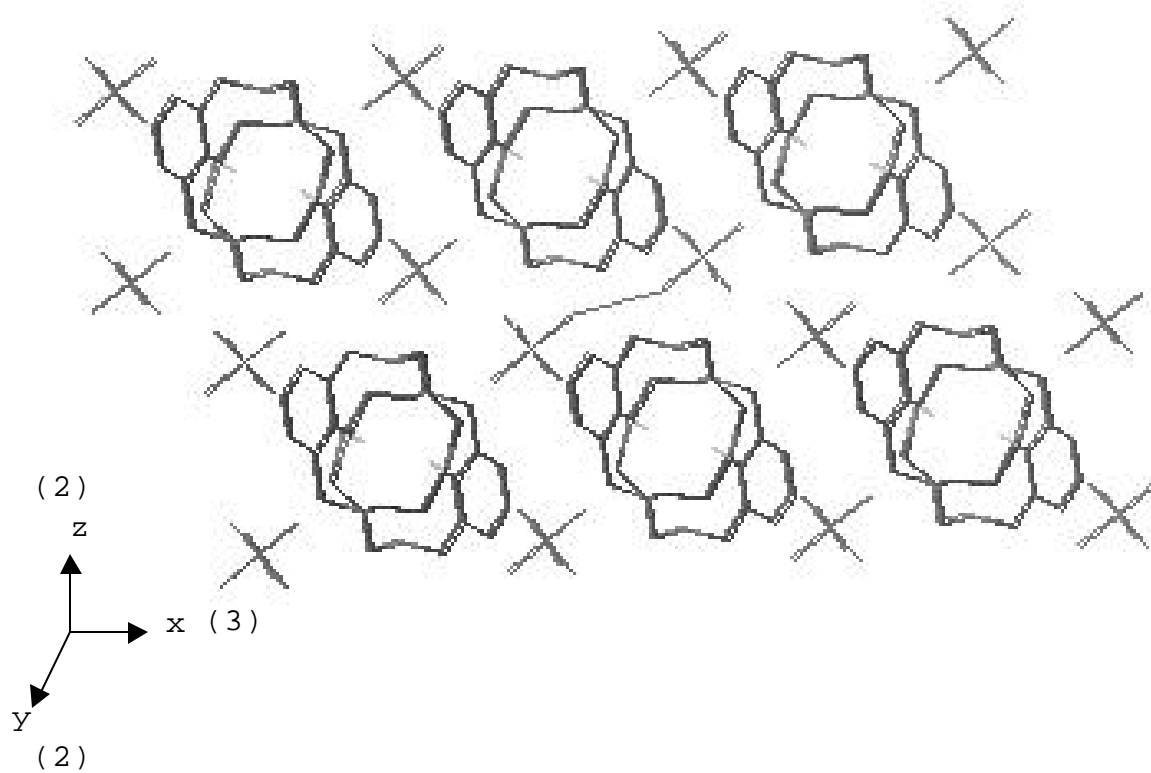
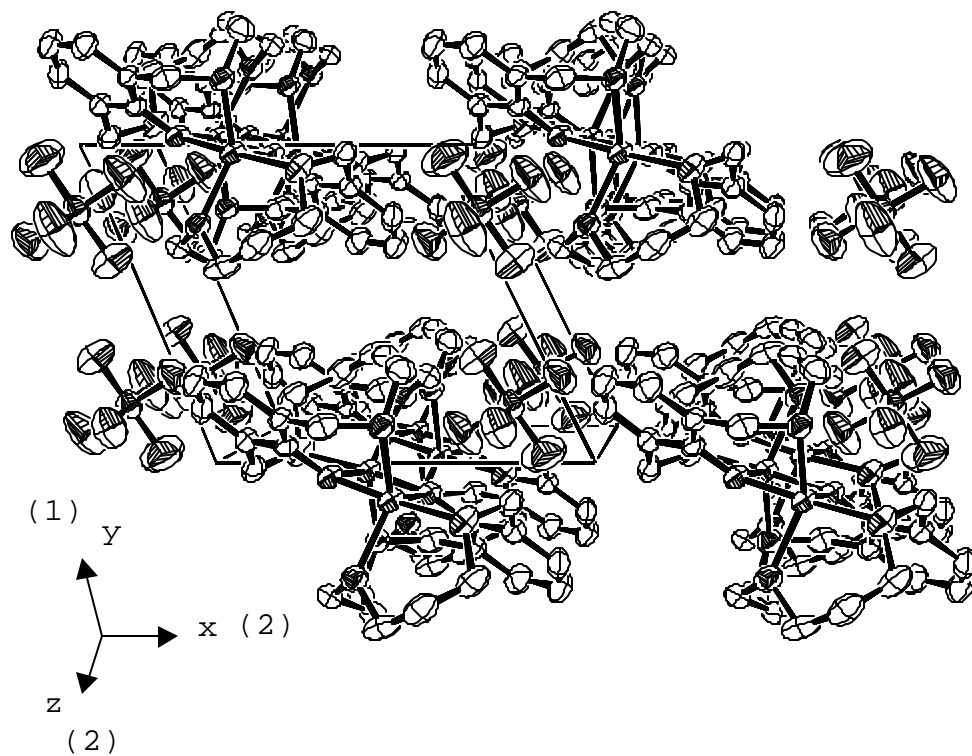


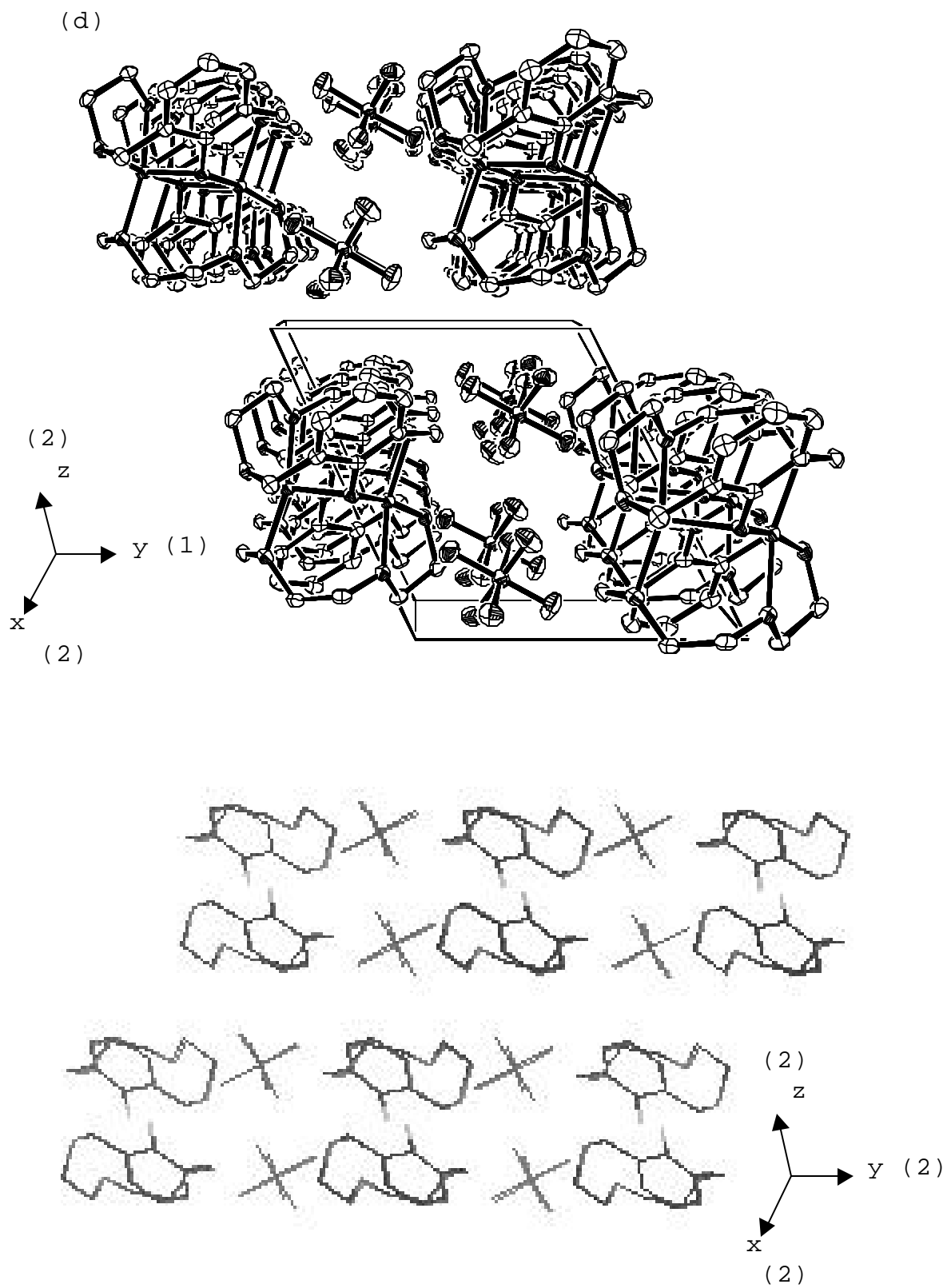


(b)

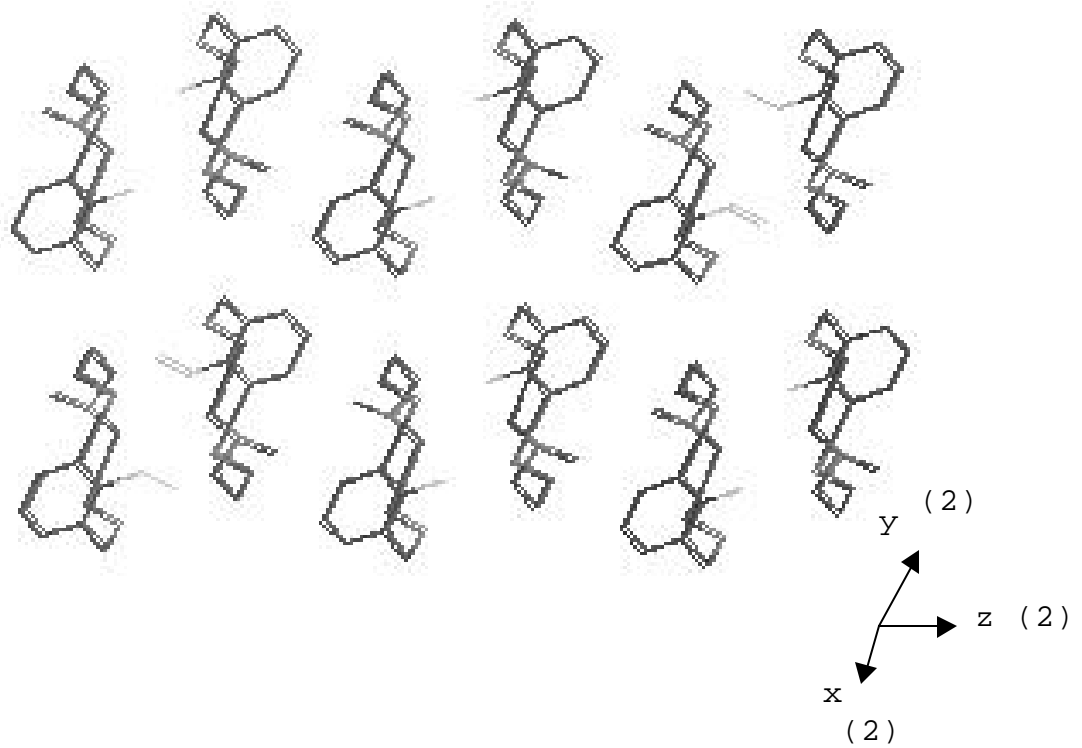
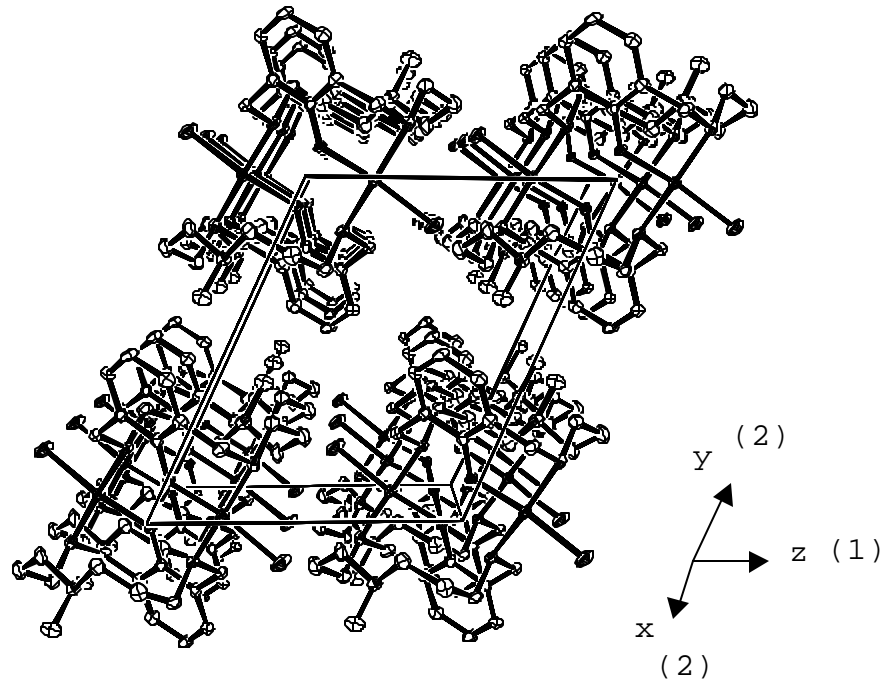


(c)





(e)



(f)

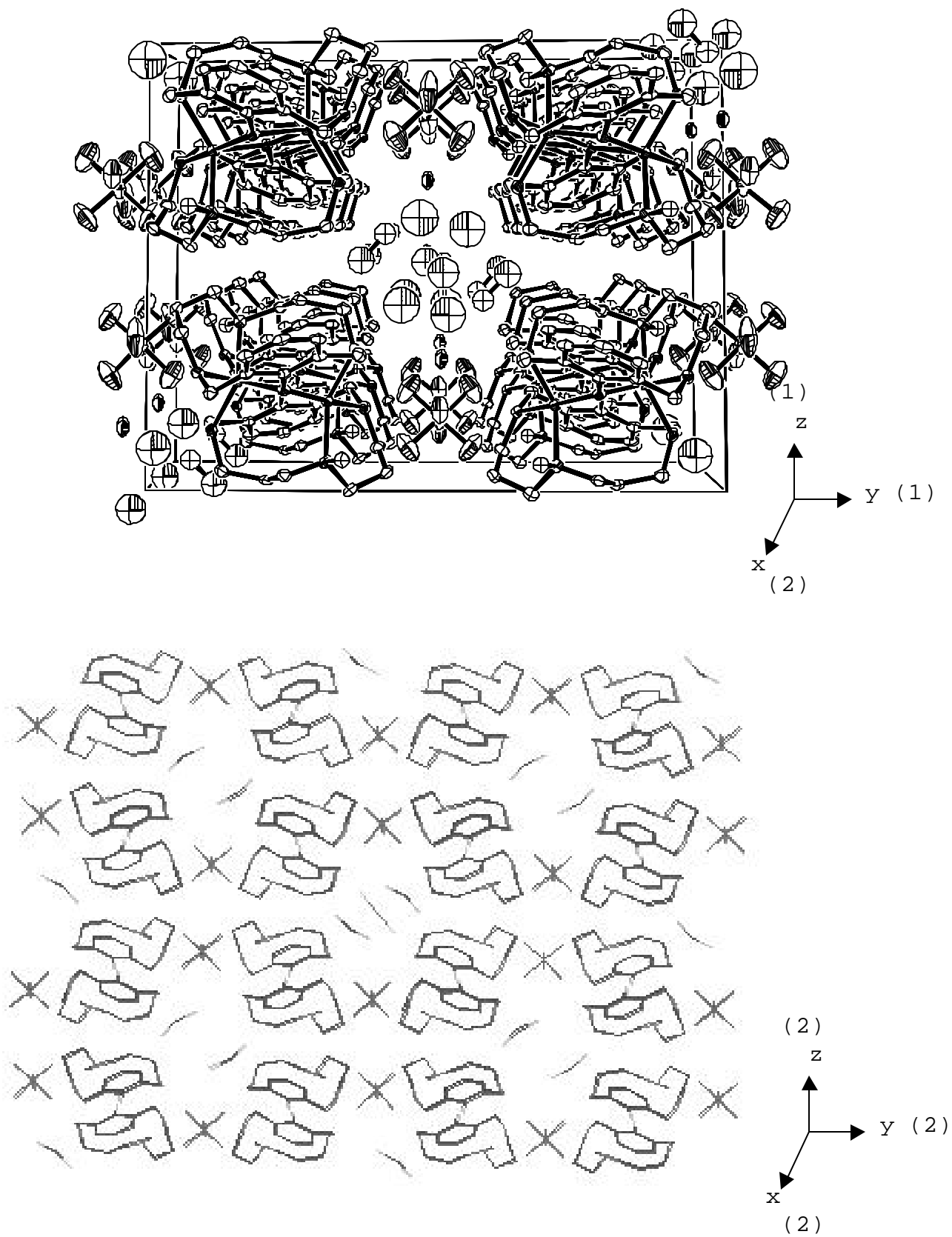


Figure S3. ^1H NMR spectra of (a) complex $[(\text{H32m-C})\text{Cu}^{\text{III}}]^{2+}$ (**1**) and (b) complex $[(\text{H32m-C})'\text{Cu}^{\text{III}}]^+$ (**1b**) obtained by reaction of **1** and KOH 1M. Conditions: CD_3CN , R.T.

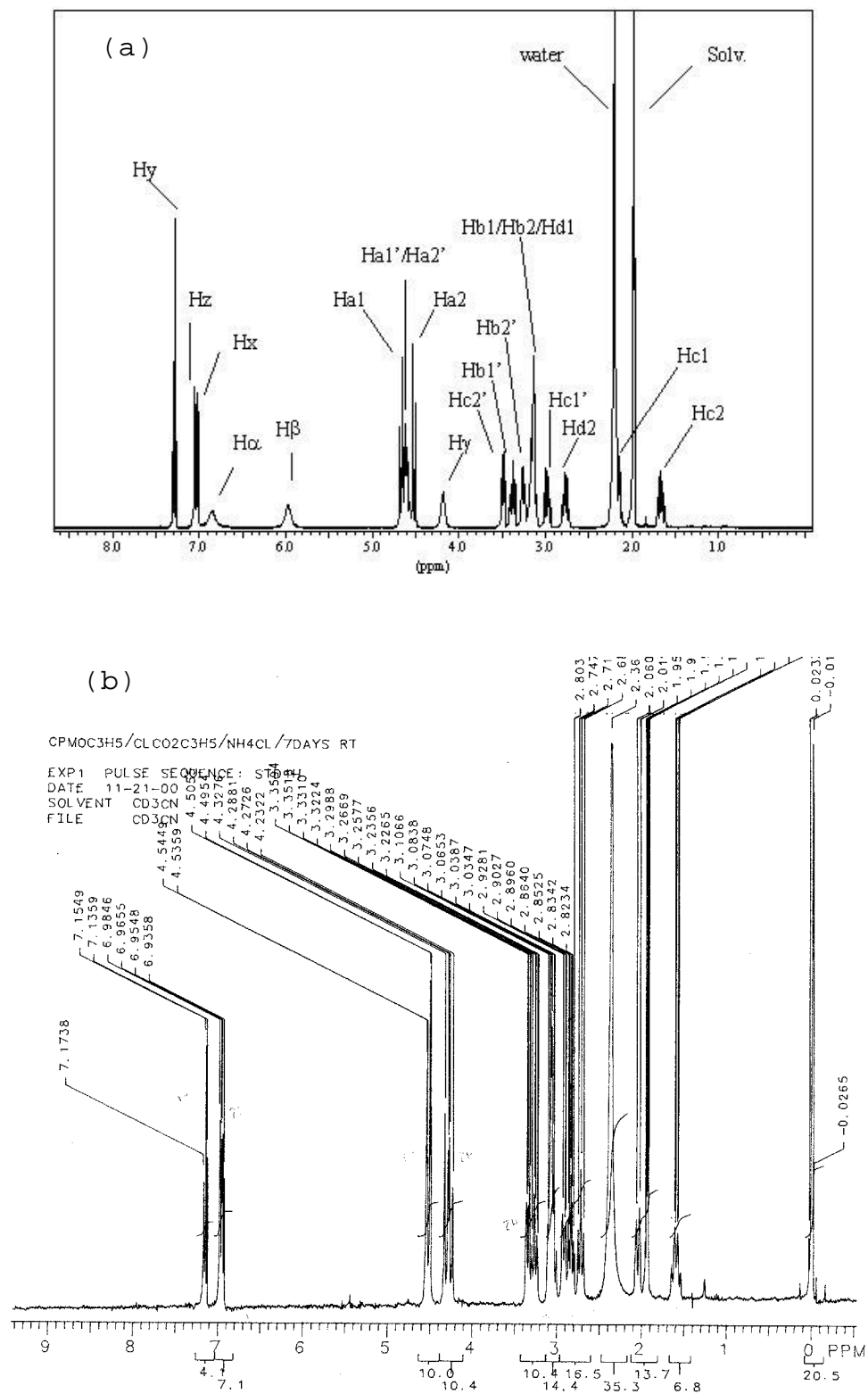
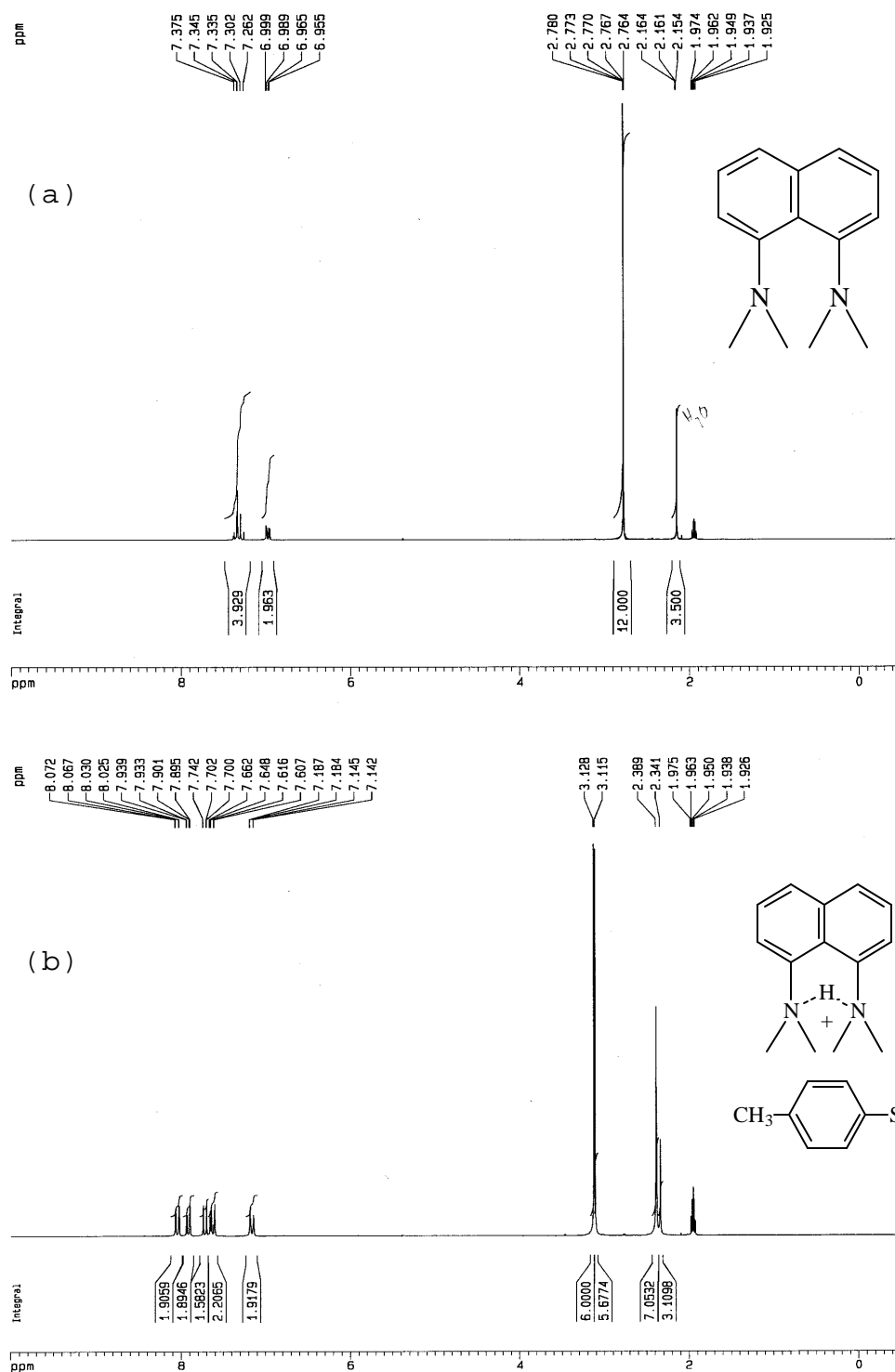
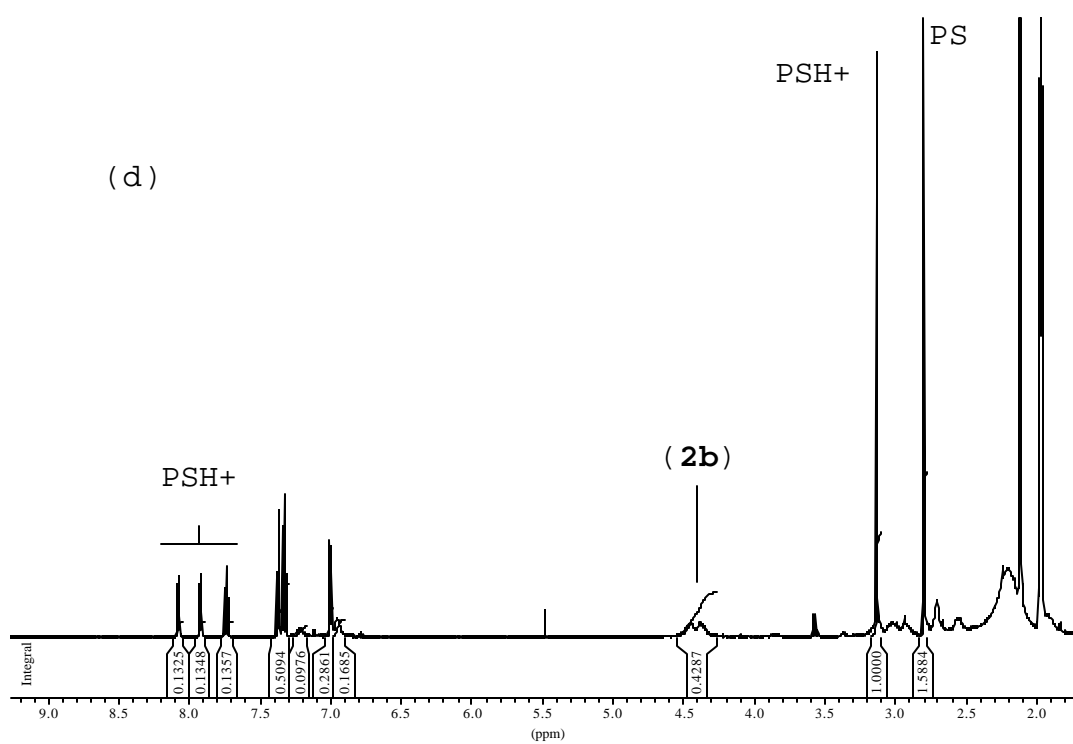
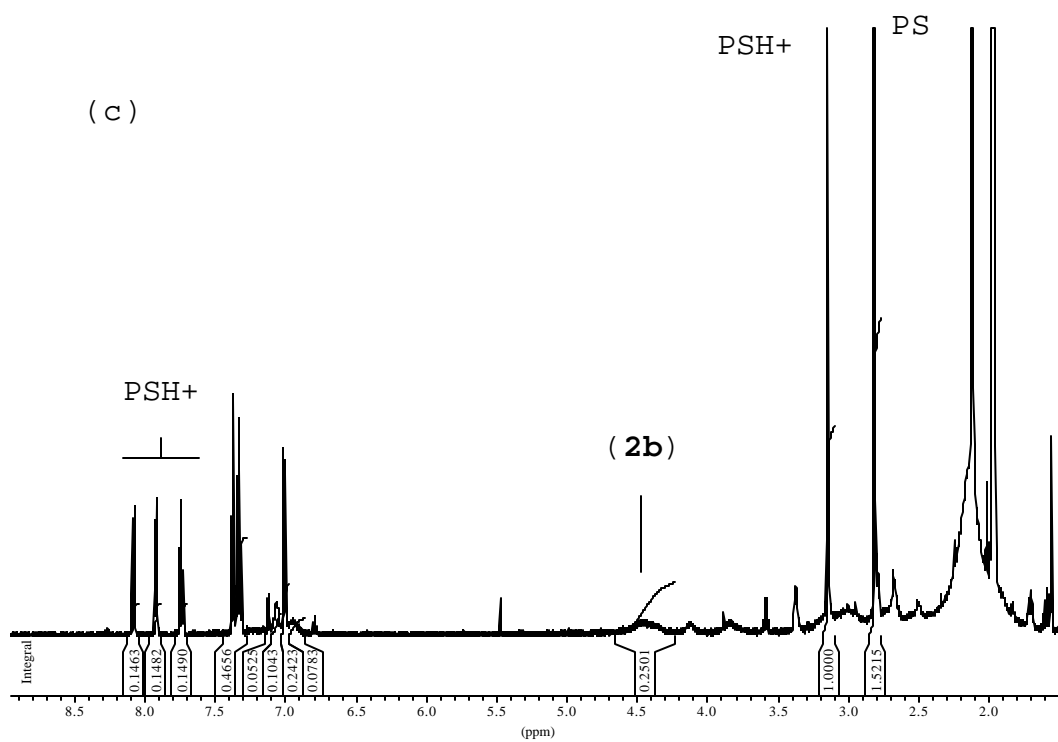


Figure S4. ^1H NMR (CD_3CN) spectra of (a) Proton Sponge® (PS), (b) Proton Sponge® protonated (PSH⁺) with 1 eq. *p*-toluenesulfonic acid, (c) complex $[(\text{H}_2\text{Me}33\text{m}-\text{C})'\text{Cu}^{\text{III}}]^{2+}$ (**2b**) obtained with 1 eq. of Proton Sponge® at 320 K, (d) at 300 K and (e) at 240 K.





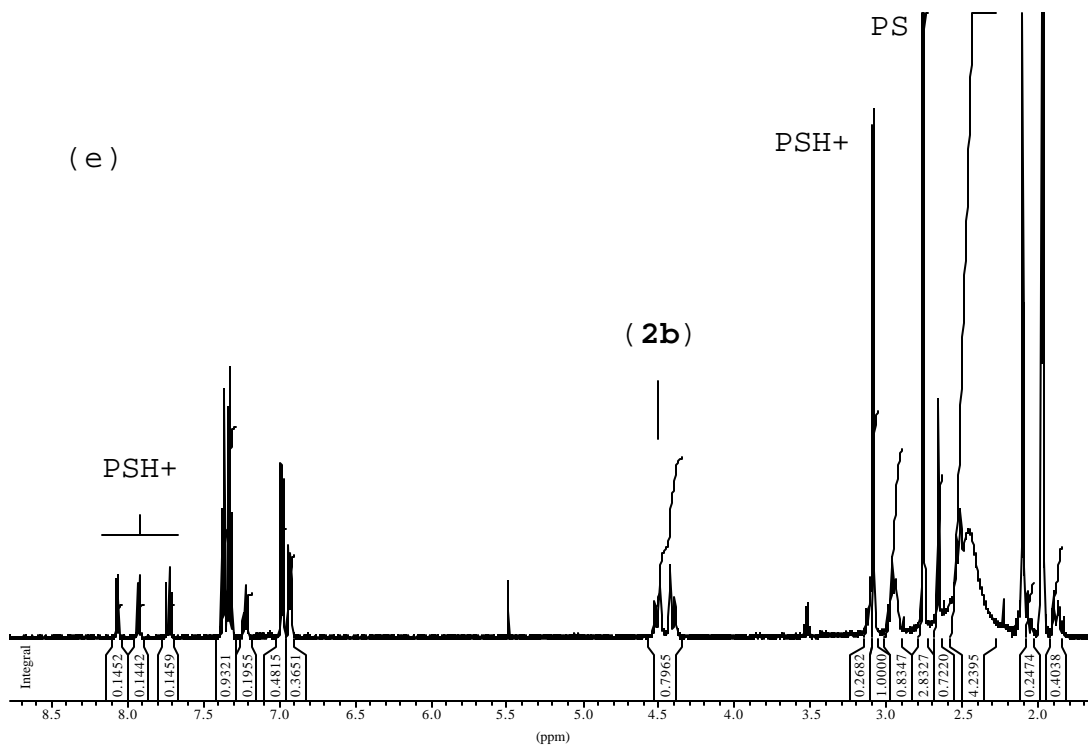


Figure S5. ^1H NMR spectrum of complex $[(\text{H}_{32}\text{m-C})'\text{Cu}^{\text{III}}]^+$ (**1b**) obtained by reaction of $[(\text{H}_{32}\text{m-C})\text{Cu}^{\text{III}}]^{2+}$ (**1**) and Proton Sponge® (1 eq.). Conditions: CD_3CN , R.T.

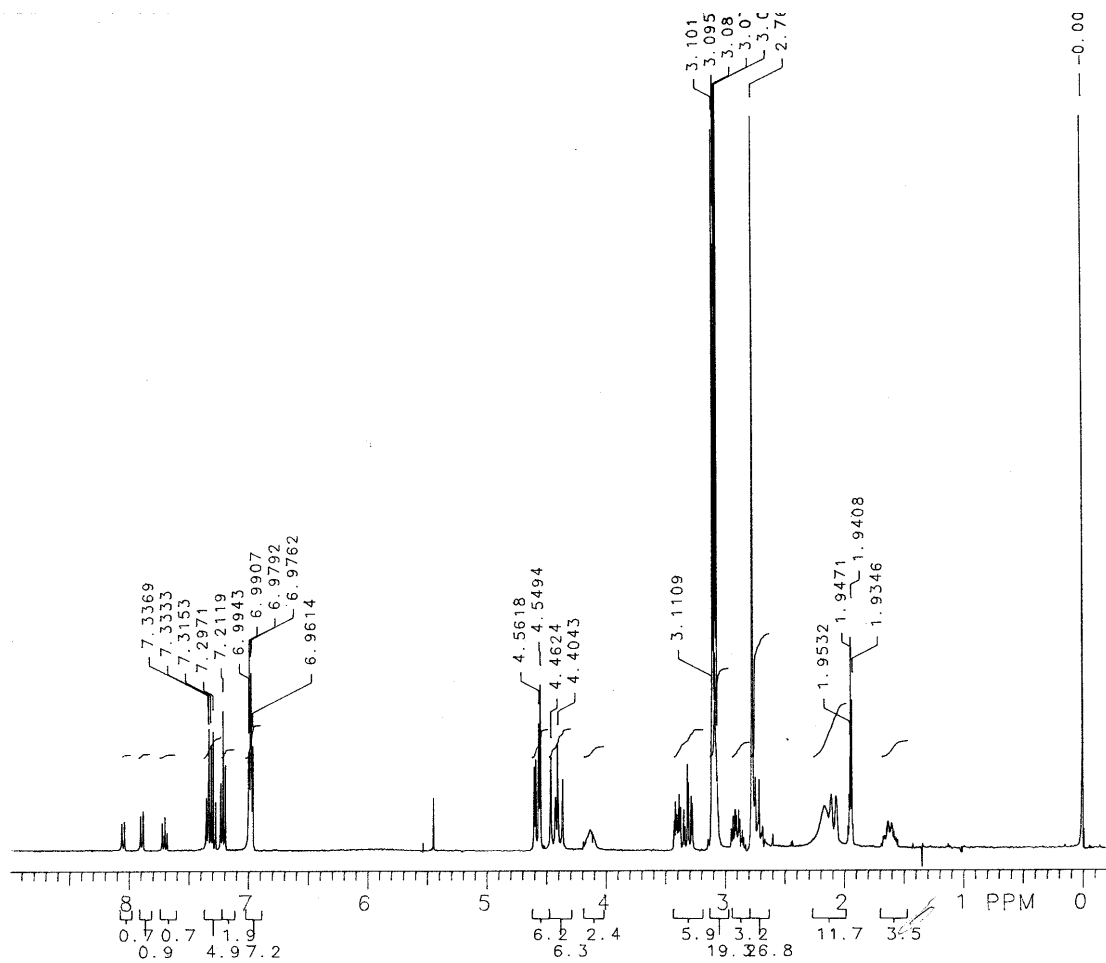
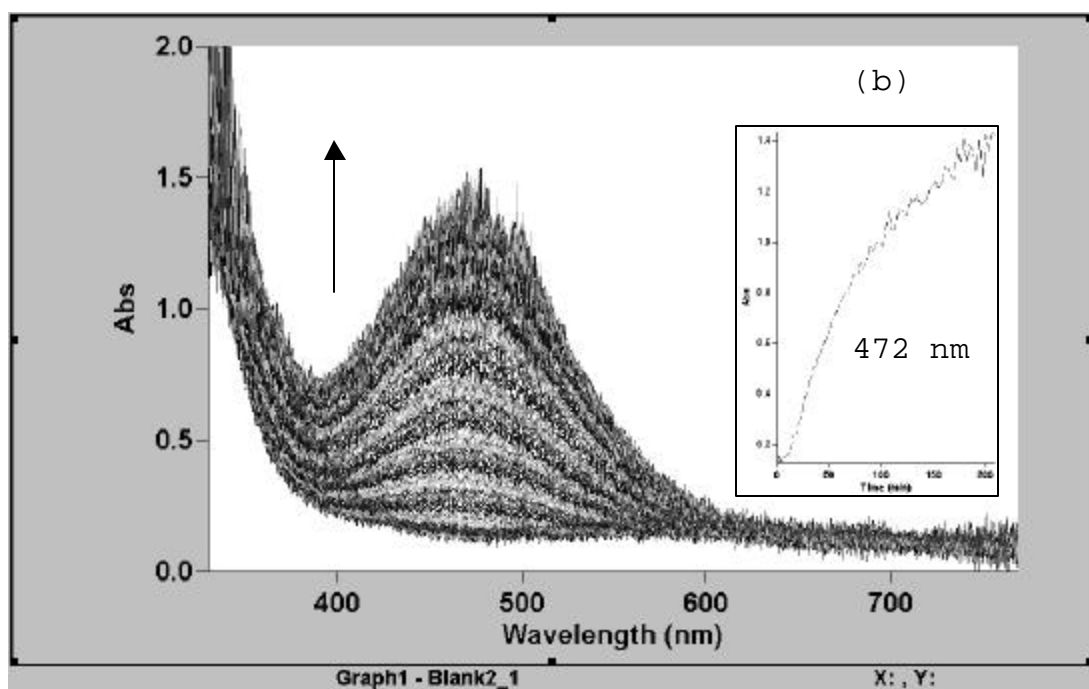
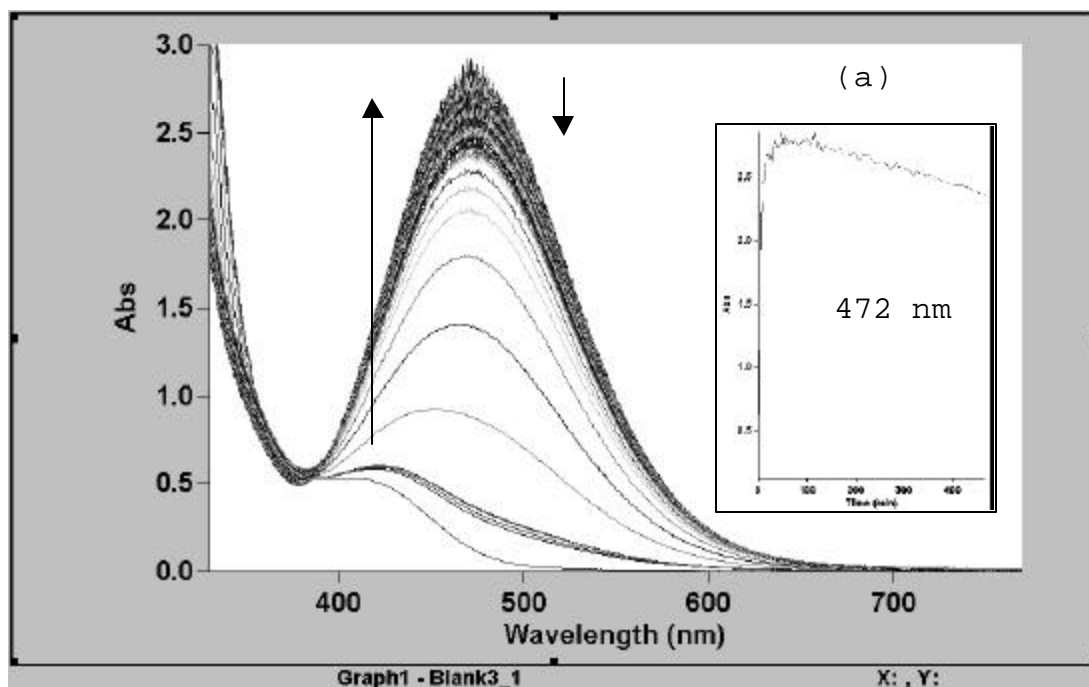


Figure S6. UV-Vis spectra for (a) reaction of Cu^{III} complex [(H32m-C)Cu^{III}]²⁺ (**1**) with 1 eq of KOH ([**1**] = 1.768 mM), (b) reaction of Cu^I complex [(H32m)Cu^I]⁺ (**7**) with O₂ ([**7**] = 1.915 mM), (c) reaction of Cu^{III} complex [(H₂Me33m-C)Cu^{III}]²⁺ (**2**) with 1 eq of KOH ([**2**] = 1.769 mM), (d) reaction of Cu^I complex [(H₂Me33m)Cu^I]⁺ (**8**) with O₂ ([**8**] = 1.139 mM). Experimental conditions: CH₃CN, R.T. Inset shows the Abs vs time plot at the corresponding wavelength.



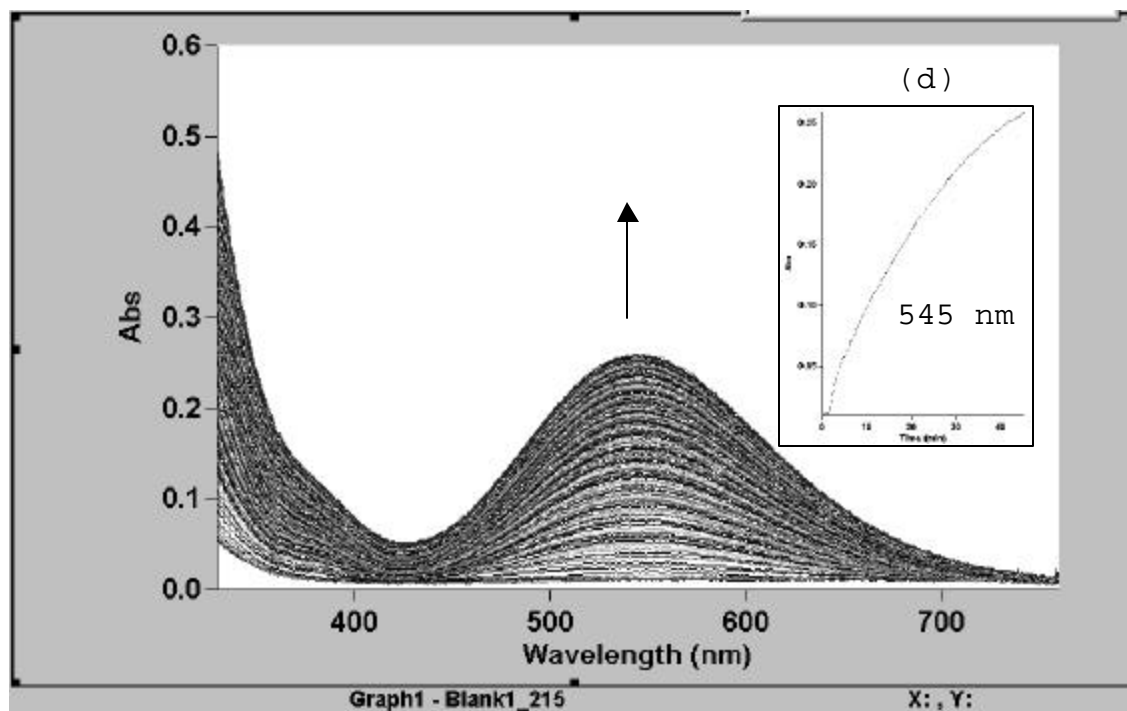
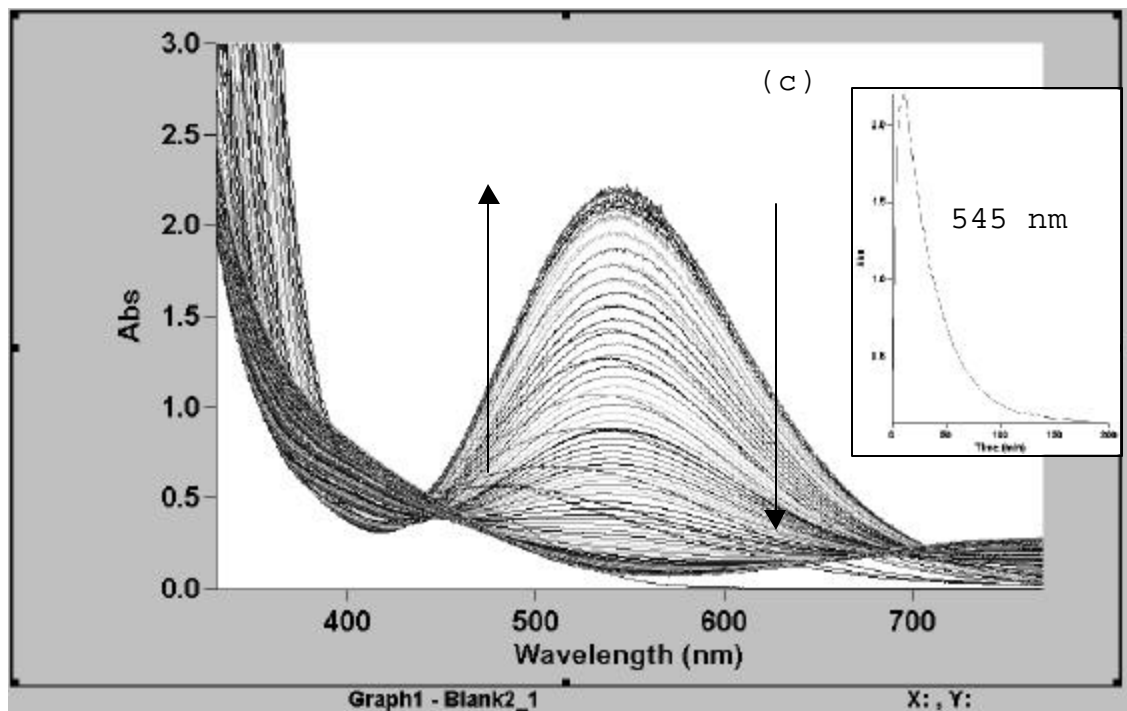


Figure S7. ESI-MS of complex $[(\text{H}^{33}\text{m-C})'\text{Cu}^{\text{III}}](\text{PF}_6)$ (**3b**- (PF_6)) obtained by reaction of $[(\text{H}^{33}\text{m})\text{Cu}^{\text{I}}]^+$ (**9**) + O_2 at R.T. in CH_3CN . Inset: simulated fragment peak.

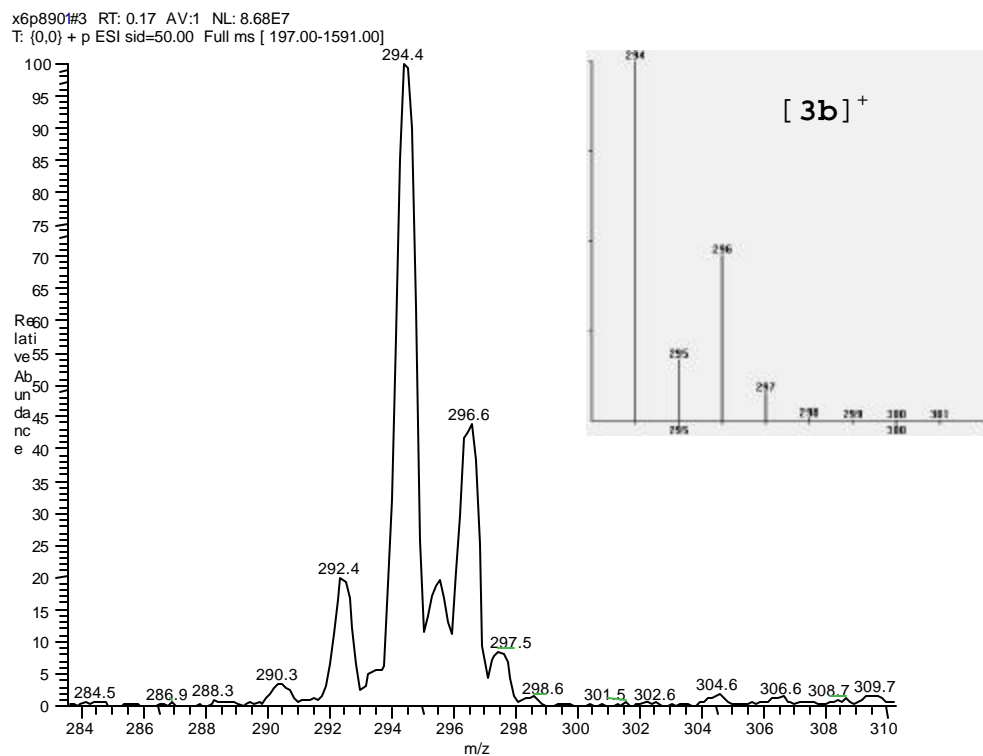
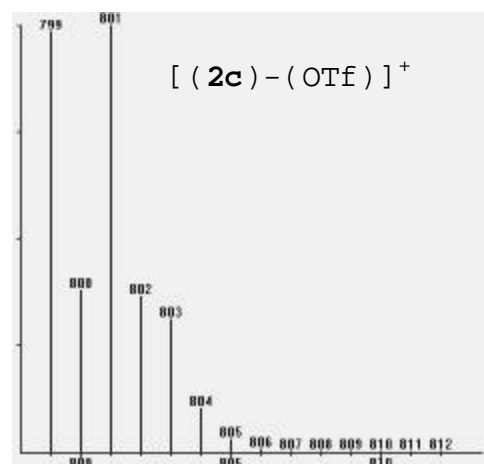
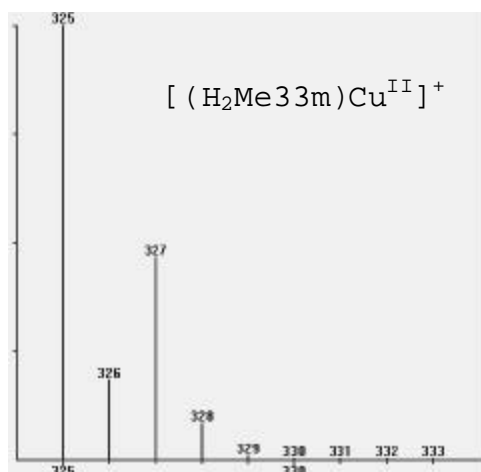
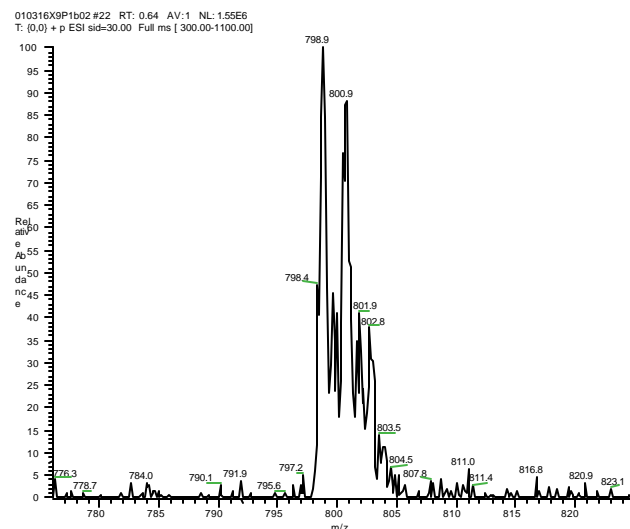
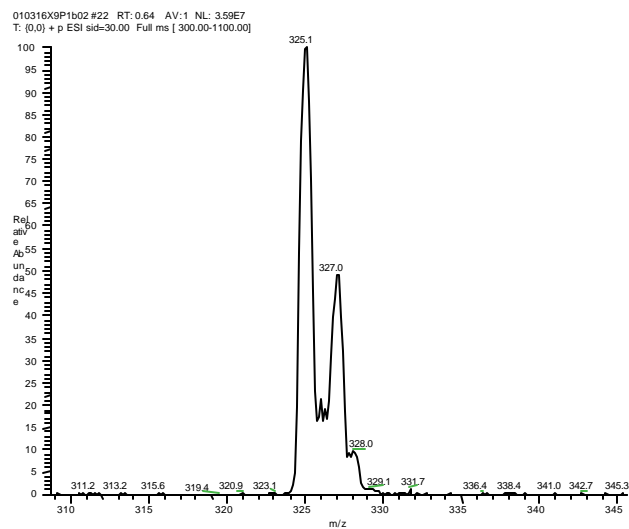


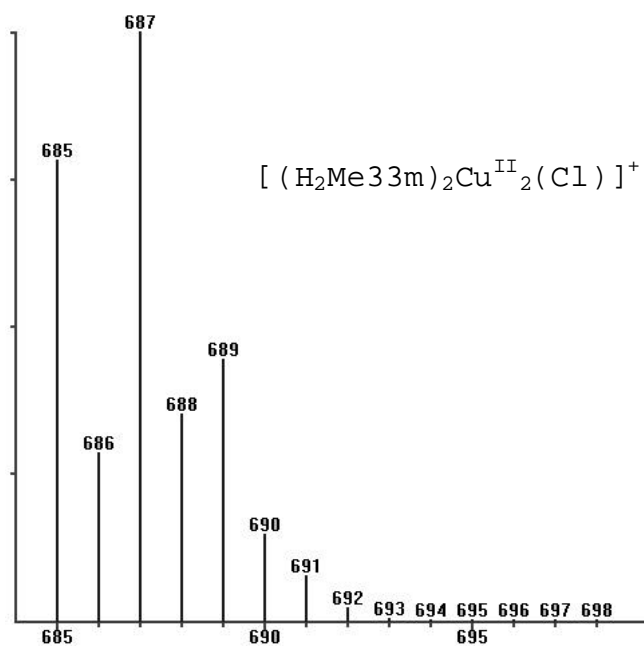
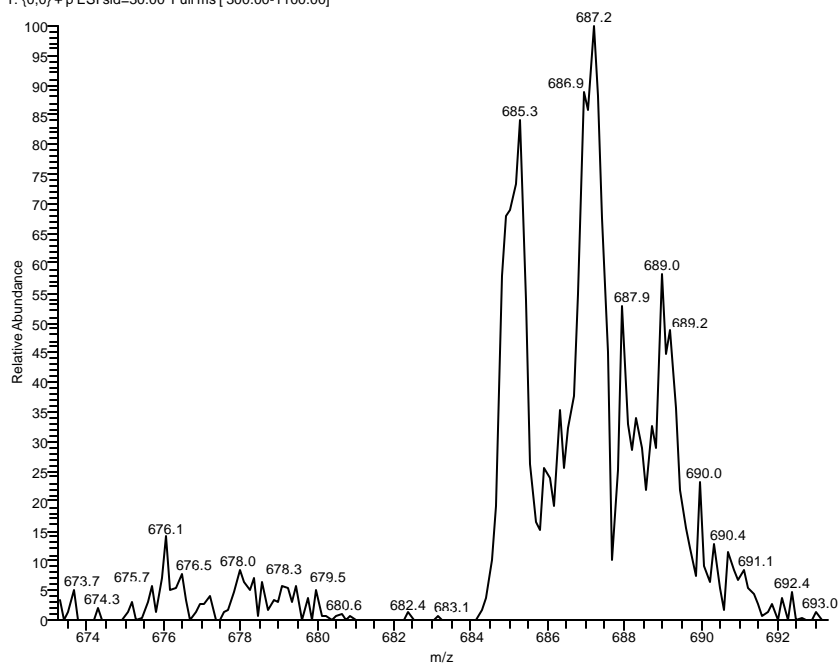
Figure S8. ESI-MS of (a) complex $[(H_2Me33mO)_2Cu^{II}](OTf)_2$ (**2c**- $(OTf)_2$) and (b) complex $[(H_2Me33mO)_2Cu^{II}Cl_2]$ (**2d**), and corresponding simulation for fragment peaks.

(a)



(b)

010316X9P1c01#22 RT: 0.64 AV: 1 NL: 1.91E6
T: {0,0} + p ESI sid=30.00 Full ms [300.00-1100.00]



CHAPTER 5Magneto-structural correlation of novel bisphenoxo Cu^{II}
complexes

5.1	ABSTRACT	269
5.2	INTRODUCTION	271
5.3	RESULTS	273
5.3.1	STRUCTURAL SUMMARY OF BISPHEOXO COMPLEXES 1C-3C, 5C.....	273
5.3.2	MOLECULAR ORBITAL CALCULATIONS.....	276
5.3.3	MAGNETIC PROPERTIES	279
5.4	DISCUSSION	282
5.4.1	MAGNETOSTRUCTURAL CORRELATIONS.....	282
5.5	EXPERIMENTAL SECTION	288
5.6	REFERENCES	289

CHAPTER 5

Magneto-structural correlation of novel bisphenoxo Cu^{II} complexes

5.1 ABSTRACT

Magnetic susceptibility measurements have been performed on bisphenoxo complexes [(H32mO)₂Cu^{II}]₂(OTf)₂ (**1c**-(OTf)₂), [(H₂Me33mO)₂Cu^{II}]₂(OTf)₂ (**2c**-(OTf)₂), [(H33mO)₂Cu^{II}]₂(PF₆)₂ (**3c**-(PF₆)₂), and [(H22mO)₂Cu^{II}]₂(ClO₄)₂ (**5c**-(ClO₄)₂). Detailed structural comparison and molecular orbital calculations focused on possible copper-copper magnetic interaction pathways are studied. Within a small range of Cu₂O₂ core distortion, wide differences in magnetic behavior are found, ranging from strong antiferromagnetic ($J = -208.29 \text{ cm}^{-1}$) for **2c** to slightly ferromagnetic ($J = 5.44 \text{ cm}^{-1}$) for **5c**.

5.2 INTRODUCTION

Dinuclear Cu^{II} complexes are of interest because of their magnetic properties, which result from a magnetic exchange (spin-spin interaction) between two paramagnetic ($s = 1/2$) cupric ions. Such magnetic interactions have received increased attention in the bioinorganic field since dinuclear copper centers were known to be part of the active site of several multicopper-containing proteins.¹

In dinuclear metal complexes, the coupling between electrons of the two metal ions leads to low-lying states of different spin multiplicities, which can be populated at thermal energies. The resulting magnetic behavior will be antiferromagnetic or ferromagnetic depending on whether the low-spin or high-spin state is the ground state, respectively. Systematic observations of these interactions have been interpreted in terms of a superexchange mechanism via ligand entities that bridge the two metal centers.² Both single-atom and multi-atom bridges are known to propagate exchange with the magnitude of exchange interaction being dependent upon the bridge identity, its length, the angle subtended at the bridge, the metal-bridging ligand bond lengths, the metal ion stereochemistry, etc.³

Relationship between magnetic properties and structure has been widely studied specially in dinuclear hydroxide⁹ and alkoxide⁴. Other studies have also been performed on monophenoxide/monohydroxide^{5,6} bridged dinuclear copper complexes and chloro bridged complexes⁷, but minor work has been reported with bis(phenoxide) bridge complexes.⁸

Magneto-structural correlations⁹ and theoretical calculations^{3,10} on hydroxide, alkoxide and phenoxide bridged complexes establish the relationship between the Cu-O-Cu bridge angle as the major factor controlling the

magnitude of the exchange coupling constant ($-J$). However, theoretical studies on alkoxides show that significant tetrahedral copper distortion and pyramidal distortion can lead to increased ferromagnetic contributions, which effectively reduce any antiferromagnetic term associated with the alkoxide bridges.^{4b,11}

A good linear relationship for the dihydroxide and alkoxide cases show that for Cu-O(R)-Cu angles around 97° , the exchange integral approaches zero (point called of accidental orthogonality by some authors).⁸ Hydroxide and alkoxide systems show a similar trend, but absolute values for $-J$ are larger for the alkoxides. Square-planar bridged bis(μ -phenoxide) complexes also show a linear correlation between Cu-O-Cu angle and J , with high antiferromagnetic coupling constants $J < -650 \text{ cm}^{-1}$ in a Cu-O-Cu angle range of 98.8 - 104.7° . Extrapolation of the line raises a $-J = 0$ point around 77° .¹¹

Scarce magnetic information is found in literature about bisphenoxide copper complexes and there has been no bisphenoxo complex with a $\text{Cu}_2\text{N}_6\text{O}_2$ chromophore described to date, where Cu centers share coordination sites with both macrocyclic ligands. Thus our phenoxide bridged complexes constitute an excellent family of compounds to establish the relationship between magnetic properties and structure. Magnetic susceptibility measurements for these complexes are presented along with a theoretical explanation derived from Extended Hückel calculations on X-Ray structures.

5.3 RESULTS

Synthesis and isolation of bisphenoxo complexes $[(\text{H}32\text{mO})_2\text{Cu}^{\text{II}}_2](\text{OTf})_2$ (**1c**-(OTf)₂), $[(\text{H}_2\text{Me}33\text{mO})_2\text{Cu}^{\text{II}}_2](\text{OTf})_2$ (**2c**-(OTf)₂), $[(\text{H}33\text{mO})_2\text{Cu}^{\text{II}}_2](\text{PF}_6)_2$ (**3c**-(PF₆)₂), and $[(\text{H}22\text{mO})_2\text{Cu}^{\text{II}}_2](\text{ClO}_4)_2$ (**5c**-(ClO₄)₂) are reported in Chapter 4.

5.3.1 Structural summary of bisphenoxo complexes **1c-3c**, **5c**

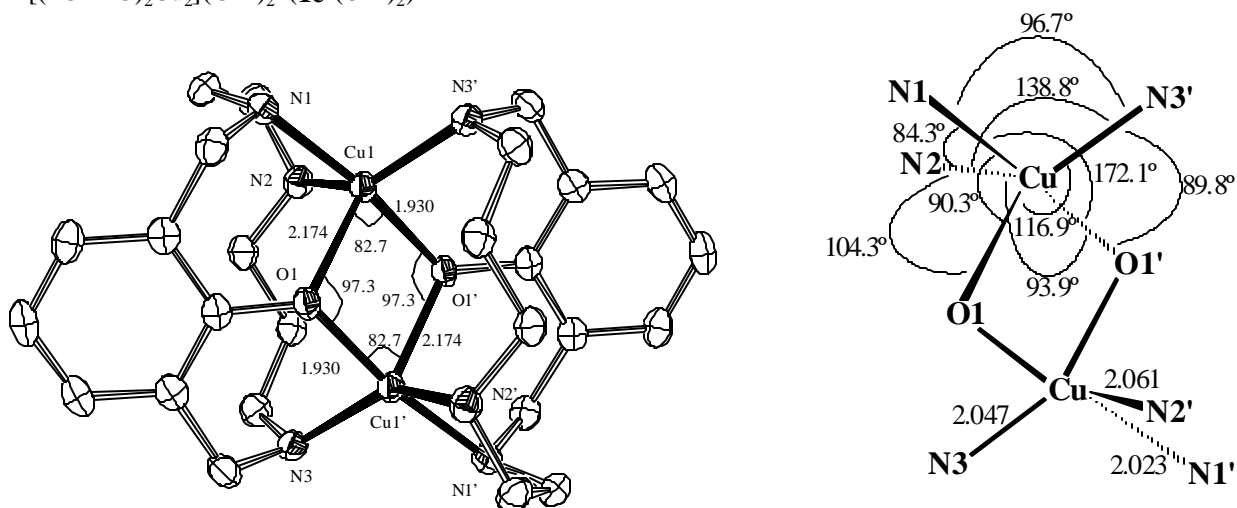
Structural differences in the Cu₂O₂ core have a determinant importance in magnetic behavior of bisphenoxo complexes. The most important ones are depicted in Figure 1 and listed in Table 1.

Table 1. Selected bond distances (Å) and angles (deg) for Cu₂O₂ bisphenoxo cores

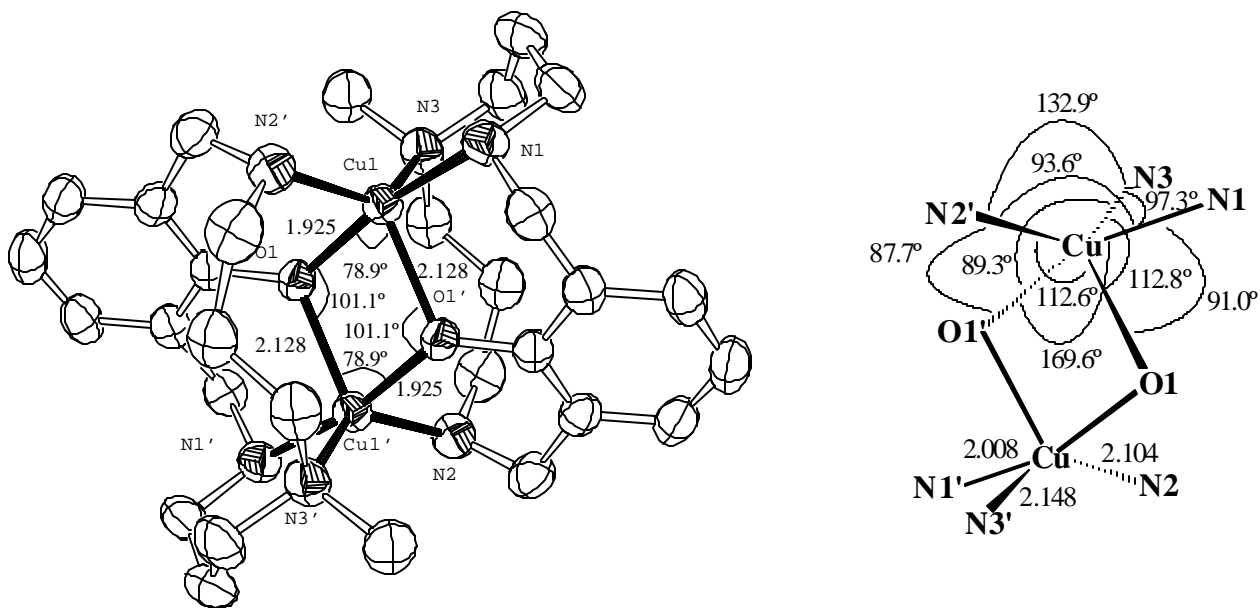
	$[(\text{H}32\text{mO})_2\text{Cu}^{\text{II}}_2]^{2+}$ 1c -(OTf) ₂	$[(\text{H}_2\text{Me}33\text{mO})_2\text{Cu}^{\text{II}}_2]^{2+}$ 2c -(ClO ₄) ₂	$[(\text{H}33\text{mO})_2\text{Cu}^{\text{II}}_2]^{2+}$ 3c -(PF ₆) ₂	$[(\text{H}22\text{mO})_2\text{Cu}^{\text{II}}_2]^{2+}$ 5c -(PF ₆) ₂
Cu-O _{equatorial}	1.930	1.925	1.930	1.928
Cu-O _{apical}	2.174	2.128	2.122	2.202
Cu-O-Cu	97.3	101.1	99.9	87.5
O-Cu-O	82.7	78.9	80.2	92.5
Cu···Cu	3.085	3.132	3.103	2.864
O···O	2.718	2.581	2.613	2.988
τ	0.556	0.611	0.616	0.212

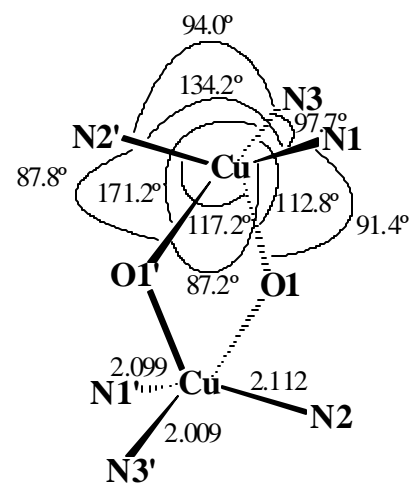
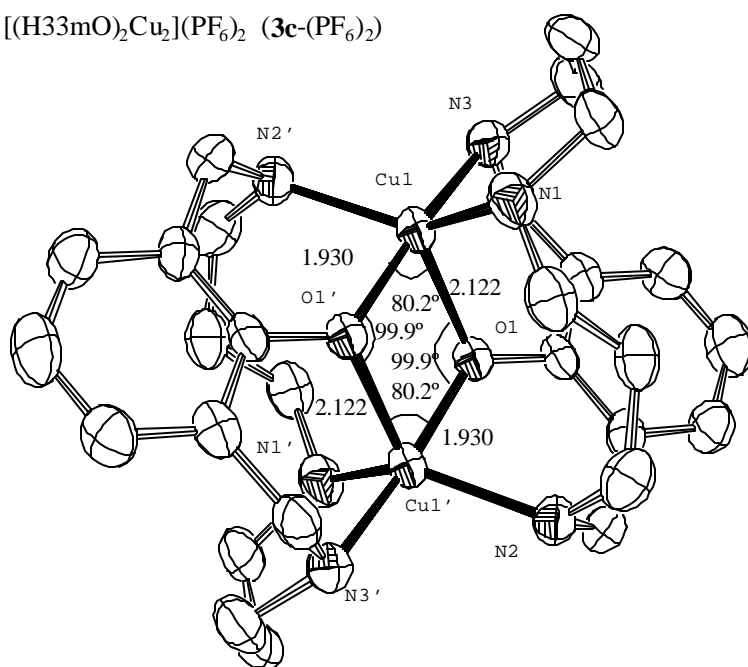
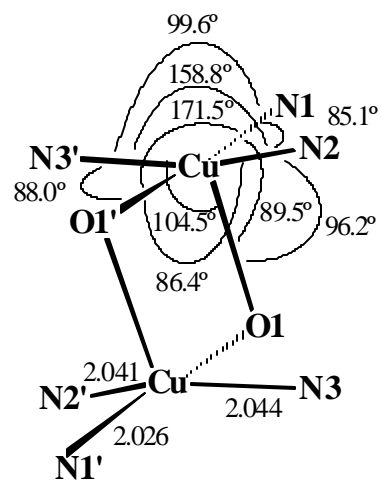
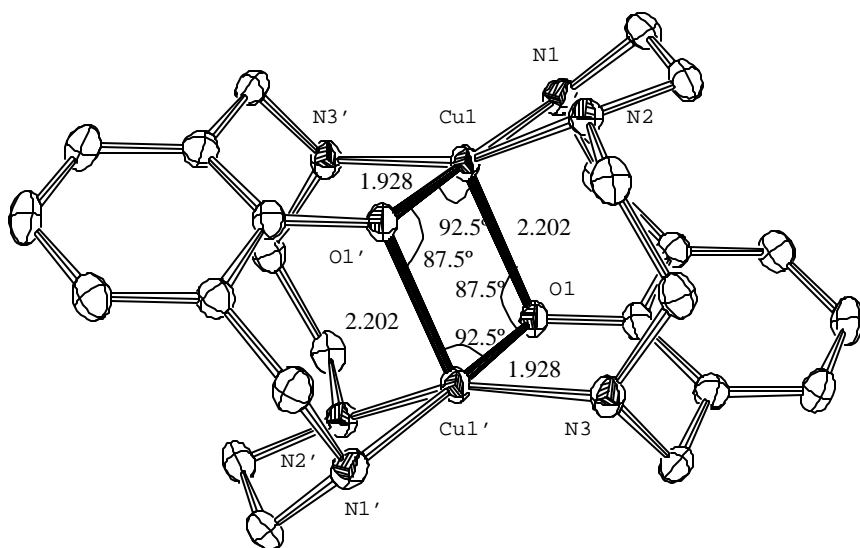
Figure 1. Structural differences between bisphenoxo complexes **1c**, **2c**, **3c** and **5c**.

$[(\text{H}32\text{mO})_2\text{Cu}_2](\text{OTf})_2$ (**1c**- $(\text{OTf})_2$)



$(\text{H}_2\text{Me}33\text{mO})_2\text{Cu}_2](\text{ClO}_4)_2$ (**2c**- $(\text{ClO}_4)_2$)



$[(\text{H}33\text{mO})_2\text{Cu}_2](\text{PF}_6)_2$ (**3c**- $(\text{PF}_6)_2$)

 $[(\text{H}22\text{mO})_2\text{Cu}_2](\text{PF}_6)_2$ (**5c**- $(\text{PF}_6)_2$)


5.3.2 Molecular orbital calculations

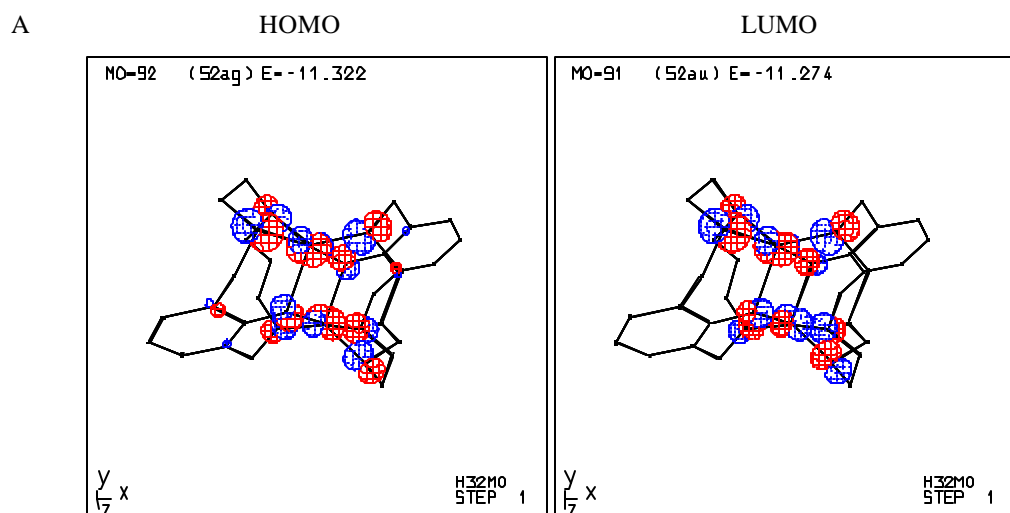
Extended Hückel (EH) calculations¹² have been performed with all systems to have a better understanding of the molecular orbitals that participate in the superexchange pathway. These orbitals have a crucial influence on the coupling constant J obtained from magnetic measurements. Cartesian coordinates obtained from crystal structures of complexes $[(\text{H32mO})_2\text{Cu}^{\text{II}}_2]^{2+}$ (**1c**), $[(\text{H}_2\text{Me33mO})_2\text{Cu}^{\text{II}}_2]^{2+}$ (**2c**), $[(\text{H33mO})_2\text{Cu}^{\text{II}}_2]^{2+}$ (**3c**) and $[(\text{H22mO})_2\text{Cu}^{\text{II}}_2]^{2+}$ (**5c**) have been used to obtain the HOMO and LUMO molecular orbitals for each system (see Figure 2).

In the particular case of complex $[(\text{H22mO})_2\text{Cu}^{\text{II}}_2]^{2+}$ (**5c**), calculations indicate the following orbital participation for the frontier orbitals: Cu d orbitals, 38-42%; N p orbitals, 44-46%; O p orbitals, 6-8% (see Table 2). As it can be observed in the graph of the HOMO and LUMO orbitals for **5c** in Figure 2, the Cu metal centers use d_{xz} and d_{xy} type orbitals for a σ^* interaction with p_N and p_O orbitals. The LUMO orbital is a symmetric $d_{Cu}-d_{Cu}$ orbital combination whereas the HOMO orbital is a $d_{Cu}-d_{Cu}$ antisymmetric combination.⁷

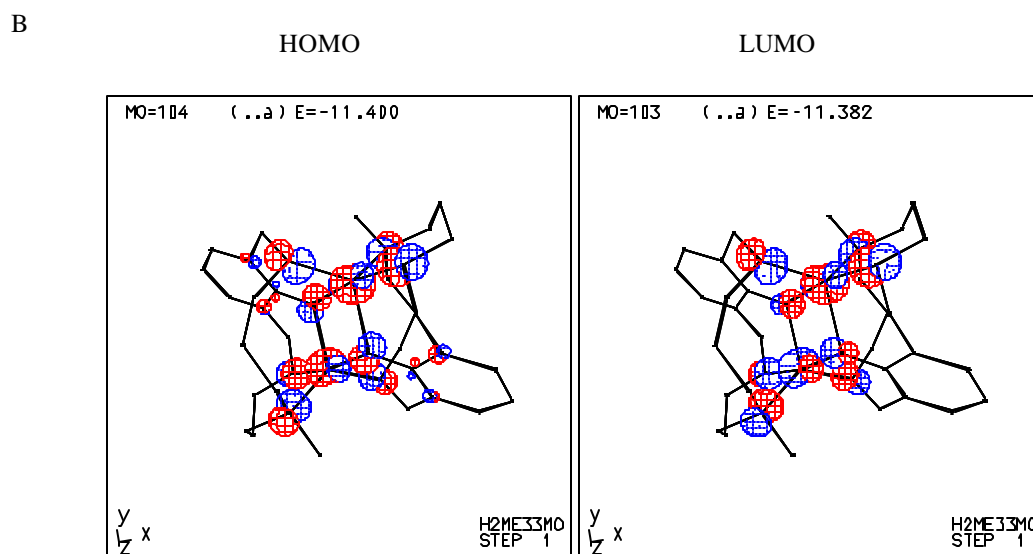
Different atomic orbital participation in HOMO and LUMO molecular orbitals for complexes **1c**, **2c** and **3c** are listed in Table 2 and drawings of frontier orbitals depicted in Figure 2. Comparing molecular orbitals between the four complexes, it is observed that complex $[(\text{H22mO})_2\text{Cu}^{\text{II}}_2]^{2+}$ (**5c**) presents a quasi ideal parallel square-base pyramid arrangement, in contrast to the generally coplanar bases found in literature.⁷ On the other hand, complexes **1c-3c** present an increasing distortion of the square-base pyramid to a trigonal bipyramid geometry for each copper center derived from the increased number of $-\text{CH}_2-$ units in the ligand backbone. This distortion is responsible of the fact

that orbitals from N_3OCu atoms exclusively participate in frontier orbitals for complex **5c**, whereas in complexes **1c**, **2c** and **3c** the participation of atomic orbitals from aromatic carbons is significant (see Table 2).

Figure 2. Drawings of the HOMO and LUMO frontier orbitals (for orbitals contributing more than 1%) with corresponding ΔE Gap values obtained for the cations (A) $[(H32mO)_2Cu^{II}_2]^{2+}$ **1c**, (B) $[(H_2Me33mO)_2Cu^{II}_2]^{2+}$ **2c**, (C) $[(H33mO)_2Cu^{II}_2]^{2+}$ **3c** and (D) $[(H22mO)_2Cu^{II}_2]^{2+}$ **5c**.

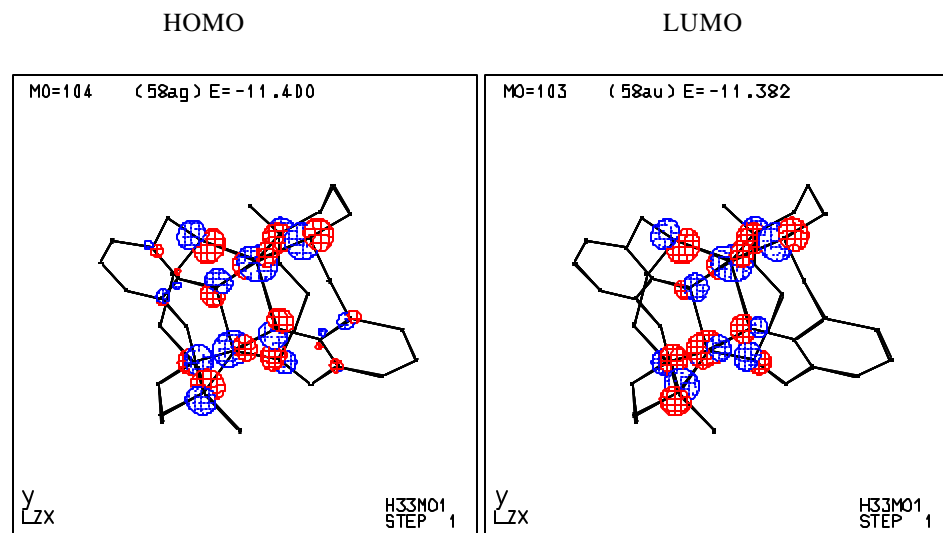


$$\Delta E = 0.048 \text{ eV}$$



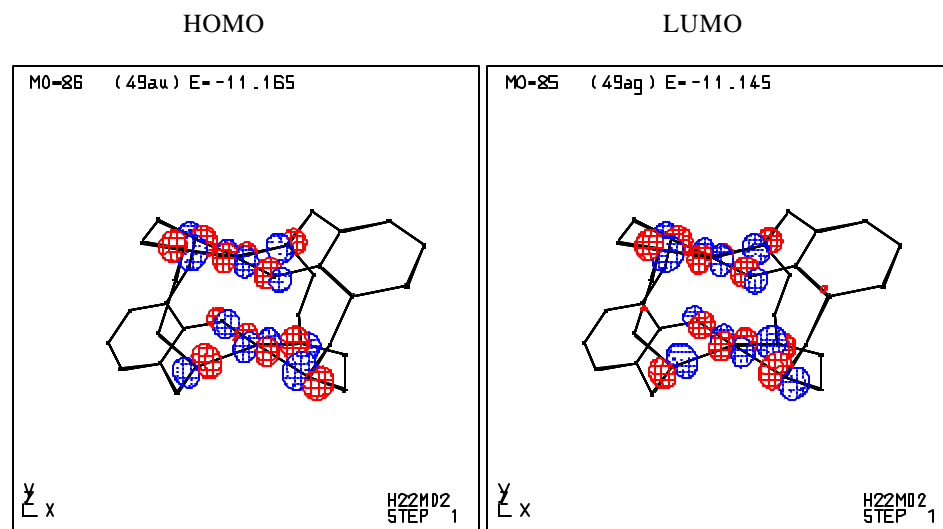
$$\Delta E = 0.018 \text{ eV}$$

C



$$\Delta E = 0.018 \text{ eV}$$

D



$$\Delta E = 0.020 \text{ eV}$$

Table 2. Orbital participation in HOMO and LUMO frontier orbitals for complexes **1c**, **2c**, **3c**, **5c**.

	[(H32mO) ₂ Cu ^{II} ₂] ²⁺		[(H ₂ Me33mO) ₂ Cu ^{II} ₂] ²⁺		[(H33mO) ₂ Cu ^{II} ₂] ²⁺		[(H22mO) ₂ Cu ^{II} ₂] ²⁺	
	1c -(OTf) ₂		2c -(ClO ₄) ₂		3c -(PF ₆) ₂		5c -(PF ₆) ₂	
	HOMO	LUMO	HOMO	LUMO	HOMO	LUMO	HOMO	LUMO
d _{Cu}	34%	40%	33%	36%	32%	38%	42%	38%
p _O	10%	6%	10%	6%	10%	6%	6%	8%
p _N	44%	44%	38%	42%	40%	44%	44%	46%
Σp _{Car} ^a	6%	<1%	6%	<1%	6%	<1%	<1%	<1%

^a Sum of orbital p contributions from aromatic carbon atoms

5.3.3 Magnetic properties

The plots of molar χ_{MT} product vs T for compounds [(H32mO)₂Cu^{II}₂]²⁺ (**1c**), [(H₂Me33mO)₂Cu^{II}₂]²⁺ (**2c**), [(H33mO)₂Cu^{II}₂]²⁺ (**3c**) and [(H22mO)₂Cu^{II}₂]²⁺ (**5c**) are shown in Figure 3. An antiferromagnetic behavior is observed in all of them except in **5c**, which presents a very small ferromagnetic coupling between copper centers.

Experimental data for [(H22mO)₂Cu^{II}₂](ClO₄)₂ (**5c**-(ClO₄)₂) was fitted with the Bleany-Bowers equation for dimeric Cu^{II} species (Eq. 1),¹³ using the Heisenberg isotropic exchange Hamiltonian ($H = -JS_1 \cdot S_2$) for two interacting $S = \frac{1}{2}$ centers,

$$\chi_M = \frac{Ng^2\beta^2}{3kT} \left[1 + \frac{1}{3} \exp\left(\frac{-J}{kT}\right) \right]^{-1} \quad (\text{Eq. 1})$$

where χ_M is expressed in mols per copper atom. The fit was performed by minimizing the function $R = \sum -(\chi_{MT_{calc}} -$

$\chi_{MT_{\text{obs}}}^2 / \Sigma(\chi_{MT_{\text{obs}}})^2$, the best fit parameters being $J = 5.44$ cm^{-1} , $g = 2.177$ with $R = 8.25 \times 10^{-5}$.

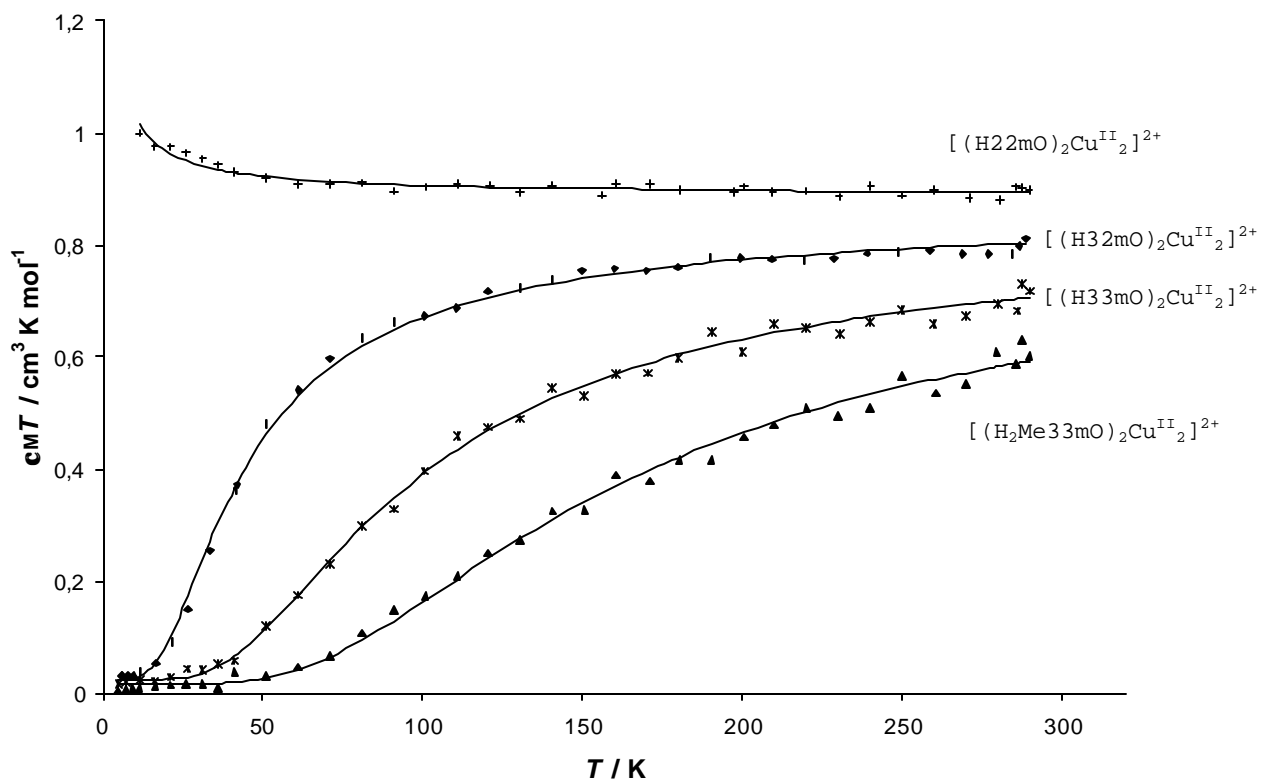
In complexes **1c-3c**, small paramagnetic impurity is found, which slightly disrupts the χ_{MT} vs T curve at low temperatures (below 10 K for **1c**, below 50 K for complexes **2c** and **3c**). Thus, the experimental data were fitted with the Bleaney-Bowers equation (Eq. 2)¹³ for a dinuclear compound containing a small paramagnetic impurity,

$$\chi_M = \frac{Ng^2\beta^2}{3kT} \left[1 + \frac{1}{3} \exp\left(\frac{-J}{kT}\right) \right]^{-1} (1 - \rho) + \frac{Ng^2\beta^2}{4kT} \rho \quad (\text{Eq.2})$$

where χ_M is expressed in mols per copper atoms and ρ is the fraction of monomeric impurity.

The best fit parameters obtained were $J = -55.05$ cm^{-1} , $g = 2.129$, $\rho = 0.0161$ with $R = 2.65 \times 10^{-4}$ for $[(\text{H}32\text{mO})_2\text{Cu}^{\text{II}}_2](\text{OTf})_2$ (**1c**-(OTf)₂); $J = -208.29$ cm^{-1} , $g = 2.122$, $\rho = 0.0102$ with $R = 3.29 \times 10^{-3}$ for $[(\text{H}_2\text{Me}33\text{mO})_2\text{Cu}^{\text{II}}_2](\text{OTf})_2$ (**2c**-(OTf)₂); $J = -125.10$ cm^{-1} , $g = 2.116$, $\rho = 0.1513$ with $R = 3.44 \times 10^{-3}$ for $[(\text{H}33\text{mO})_2\text{Cu}^{\text{II}}_2](\text{PF}_6)_2$ (**3c**-(PF₆)₂).

Figure 3. χ_{MT} vs T plot for complexes (\blacklozenge) **1c**, (\blacktriangle) **2c**, (\ast) **3c** and (\oplus) **5c** in the 4-298 K temperature range



5.4 DISCUSSION

Important differences in magnetic behavior are directly related to structural differences in the Cu_2O_2 core for bisphenoxo complexes. The most important ones are depicted in Figure 1 and listed in Table 1. It has to be mentioned that counteranions do not have a significant influence in structure for our systems¹⁴ and therefore, it is reasonable to compare susceptibility measurements of complex $[(\text{H}_2\text{Me33mO})_2\text{Cu}^{\text{II}}_2](\text{OTf})_2$ (**2c**-(OTf)₂) and crystal structure of **2c**-(ClO₄)₂, as well as magnetism of $[(\text{H}22\text{mO})_2\text{Cu}^{\text{II}}_2](\text{ClO}_4)_2$ (**5c**-(ClO₄)₂) and crystal structure of **5c**-(PF₆)₂.

5.4.1 Magnetostructural correlations

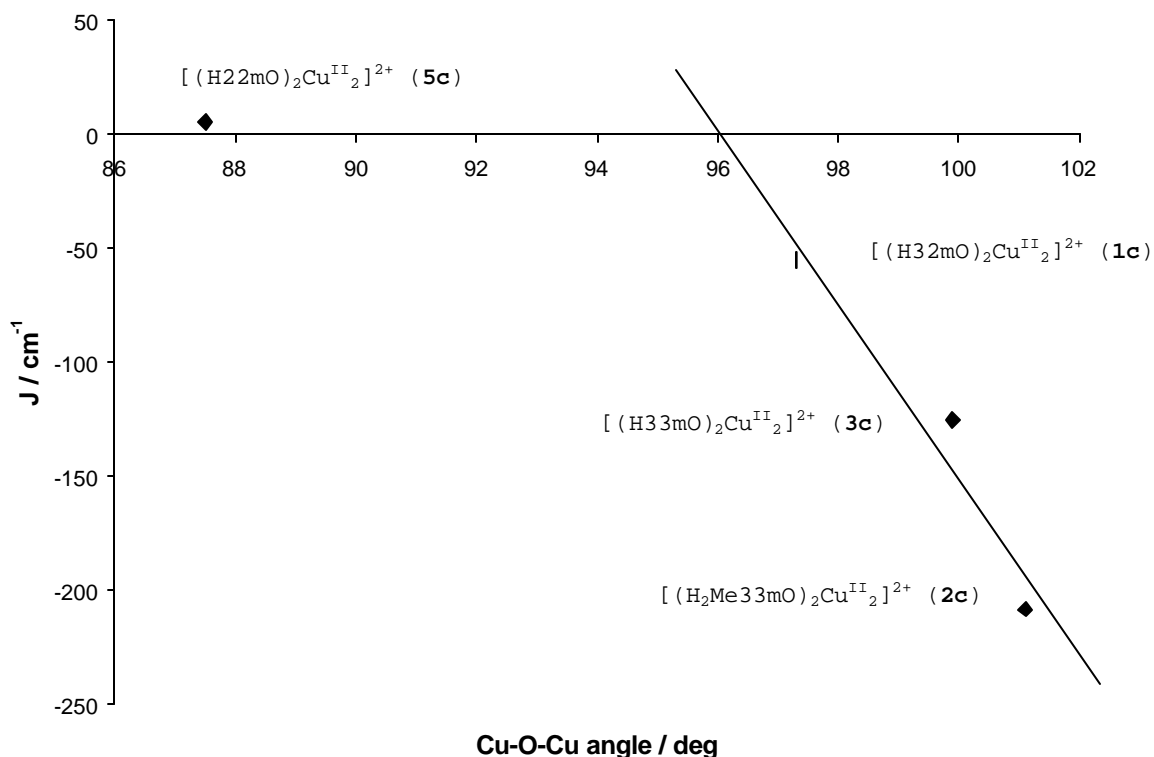
Complex **5c** presents an squared-based pyramidal geometry for copper whereas an important distortion of this geometry towards a trigonal bipyramidal geometry is observed in complexes **1c-3c** (see τ^{15} values in Table 3).¹⁶ This distortion causes a different arrangement of the Cu_2O_2 core, from a rectangular-planar disposition in complex $[(\text{H}22\text{mO})_2\text{Cu}^{\text{II}}_2]^{2+}$ (**5c**) towards a more rhomboidal-planar geometry for $[(\text{H}32\text{mO})_2\text{Cu}^{\text{II}}_2]^{2+}$ (**1c**), and even more for $[(\text{H}33\text{mO})_2\text{Cu}^{\text{II}}_2]^{2+}$ (**3c**) and $[(\text{H}_2\text{Me33mO})_2\text{Cu}^{\text{II}}_2]^{2+}$ (**2c**).

Magnetostructural correlations can only be performed on families of complexes with very similar structural characteristics.^{1,2,7} Thus, Cu-O-Cu angle shows a trend with J value, and a linear correlation is found only among complexes **1c-3c** (see Figure 4 and Table 3). Complex **5c** does not lie under the line because important structural differences preclude a coherent comparison. Linear regression for points concerning the latter complexes gives rise to a straight line where $R^2 = 0.934$ and $J = -38.17(\text{Cu-O-Cu}) + 3666.3$, which is in good agreement with a major

contribution of Cu-O-Cu angle to the magnetic behavior of O-bridged dinuclear copper complexes described in the literature.^{4-6,8-9} The point of accidental orthogonality ($J = 0$)⁸ would be at 96.0° within the set of complexes **1c-3c**.

Table 3. Structural parameters correlated with coupling constant J for complexes $[(\text{H}32\text{mO})_2\text{Cu}^{\text{II}}_2]^{2+}$ (**1c**), $[(\text{H}_2\text{Me}33\text{mO})_2\text{Cu}^{\text{II}}_2]^{2+}$ (**2c**), $[(\text{H}33\text{mO})_2\text{Cu}^{\text{II}}_2]^{2+}$ (**3c**), $[(\text{H}22\text{mO})_2\text{Cu}^{\text{II}}_2]^{2+}$ (**5c**).

Complexes	Cu···Cu distance (Å)	Cu-O-Cu angle (deg)	τ value	Cu-O _{apical} distance (Å)	J value / cm ⁻¹
$[(\text{H}22\text{mO})_2\text{Cu}^{\text{II}}_2]^{2+}$ (5c)	2.864	87.5	0.212	2.202	5.44
$[(\text{H}32\text{mO})_2\text{Cu}^{\text{II}}_2]^{2+}$ (1c)	3.085	97.3	0.556	2.174	-55.05
$[(\text{H}33\text{mO})_2\text{Cu}^{\text{II}}_2]^{2+}$ (3c)	3.103	99.9	0.616	2.122	-125.10
$[(\text{H}_2\text{Me}33\text{mO})_2\text{Cu}^{\text{II}}_2]^{2+}$ (2c)	3.132	101.1	0.611	2.128	-208.29

Figure 4. Correlation of Cu-O-Cu angle vs coupling constant J .

However, Extended Hückel (EH) calculations were performed and molecular orbitals participating in the superexchange pathway were analyzed in detail, in order to understand the J values obtained from susceptibility measurements for all four complexes. The value of the antiferromagnetic contribution is related to the Energy difference between HOMO and LUMO orbitals (Gap value) and also to orbital overlapping in the superexchange pathway. Both parameters can be obtained from EH calculations.

HOMO and LUMO frontier orbitals for all complexes are depicted in Figure 2 along with Energy Gap values and orbital participation for frontier orbitals are listed in Table 2. Energy differences between HOMO and LUMO do not follow the same trend as coupling constant J , so magnetic behavior of bisphenoxo complexes [(H32mO)₂Cu^{II}]₂²⁺ (**1c**),

$[(\text{H}_2\text{Me33mO})_2\text{Cu}^{\text{II}}_2]^{2+}$ (**2c**), $[(\text{H33mO})_2\text{Cu}^{\text{II}}_2]^{2+}$ (**3c**), and $[(\text{H22mO})_2\text{Cu}^{\text{II}}_2]^{2+}$ (**5c**) is not explained by Gap value (see Table 4). However, studying the orbital overlapping in the potential superexchange pathway, it is significant to highlight the orbital disposition in all complexes. In complex $[(\text{H22mO})_2\text{Cu}^{\text{II}}_2]^{2+}$ (**5c**), the Cu metal centers use d_{xy} and d_{xz} type orbitals for a σ^* interaction with p_N and p_O orbitals, all of them placed in the plane formed by the square-base pyramid. Only poor π interaction between the Cu centers, which should take place mainly through the oxygen orbitals, can be deduced from EH calculation, which agrees with slightly ferromagnetic behavior observed for this system.

On the other hand, in complex $[(\text{H32mO})_2\text{Cu}^{\text{II}}_2]^{2+}$ (**1c**) the Cu centers use a combination of d_{xy} , d_{xz} and d_{z^2} orbitals (as a result of the structural distortion away from an square-based geometry) for a σ^* interaction with p_N and p_O orbitals. The same happens in complex $[(\text{H}_2\text{Me33mO})_2\text{Cu}^{\text{II}}_2]^{2+}$ (**2c**), but using a combination of d_{xy} , d_{xz} and d_{yz} orbitals, and in $[(\text{H33mO})_2\text{Cu}^{\text{II}}_2]^{2+}$ (**3c**), where Cu centers use d_{xz} and d_{yz} orbitals for a σ^* interaction with p_N and p_O orbitals. In the HOMO orbital for **1c**, **2c** and **3c**, p_y oxygen orbitals are not in the plane of the pyramid and a π but also a σ interaction with Cu orbitals can be envisioned in some extent.

A graphic analysis of the Mulliken Population Analysis can be carried out through the Molecular Orbital Overlap Population (MOOP) diagram, which displays the overlap population contribution to selected bonds or interactions for each Molecular Orbitals (MOs), within a range of energy, together with the integral value of the MOOP. The Reduced Overlap Population (ROP) value has been obtained for the Cu- O_{apical} bond and used as a measure of the extent

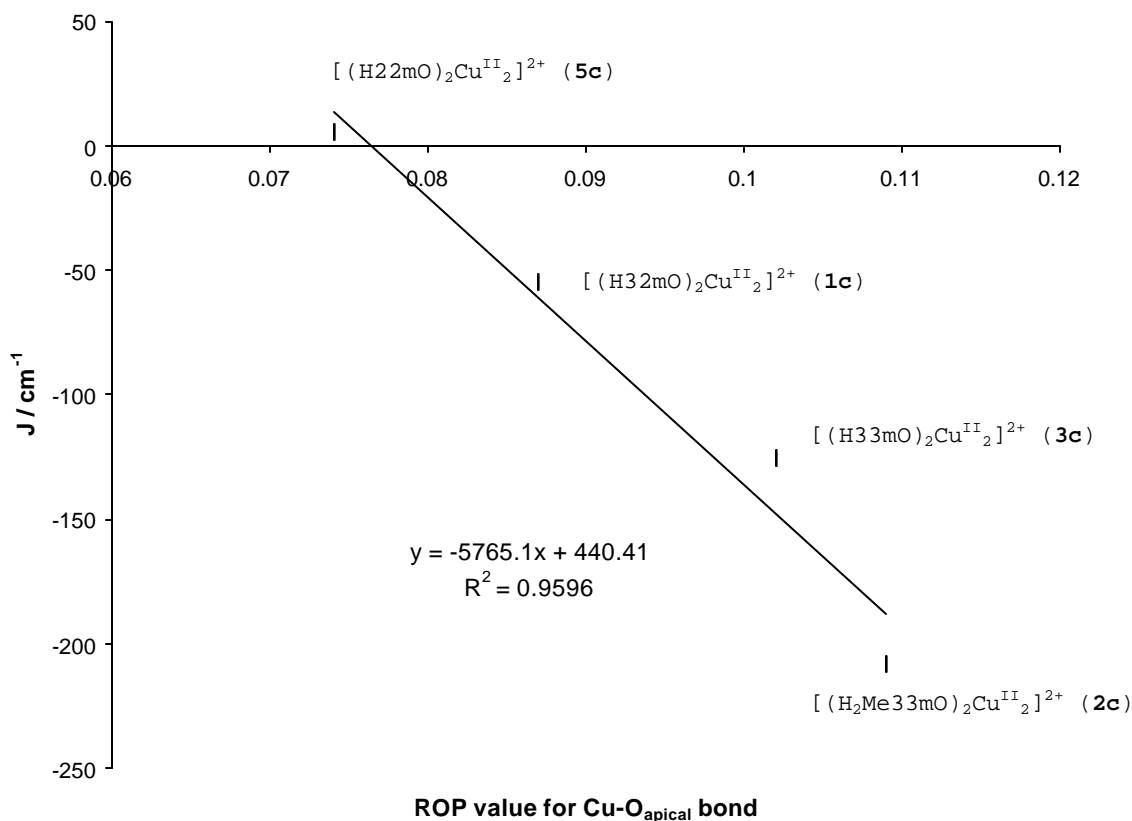
of the interaction between these atoms for all four complexes studied (see Table 4).

A linear correlation is found between the ROP value for the Cu-O_{apical} bond and the coupling constant J of each complex (Figure 5).

Table 4. Correlation of theoretically calculated parameters with J coupling constants for complexes [(H32mO)₂Cu^{II}]₂²⁺ (**1c**), [(H₂Me33mO)₂Cu^{II}]₂²⁺ (**2c**), [(H33mO)₂Cu^{II}]₂²⁺ (**3c**) and [(H22mO)₂Cu^{II}]₂²⁺ (**5c**).

Complexes	ΔE_{H-L} (Gap) / eV	ROP value Cu-O _{apical} bond	J / cm ⁻¹
[(H22mO) ₂ Cu ^{II}] ₂ ²⁺ (5c)	0.020	0.074	5.44
[(H32mO) ₂ Cu ^{II}] ₂ ²⁺ (1c)	0.048	0.087	-55.05
[(H33mO) ₂ Cu ^{II}] ₂ ²⁺ (3c)	0.020	0.102	-125.10
[(H ₂ Me33mO) ₂ Cu ^{II}] ₂ ²⁺ (2c)	0.020	0.109	-208.29

Figure 5. Linear correlation between the ROP value for Cu-O_{apical} bond and coupling constant J for complexes [(H32mO)₂Cu^{II}]₂²⁺ (**1c**), [(H₂Me33mO)₂Cu^{II}]₂²⁺ (**2c**), [(H33mO)₂Cu^{II}]₂²⁺ (**3c**), [(H22mO)₂Cu^{II}]₂²⁺ (**5c**).



Therefore, it can be concluded that magnetostructural correlations can only be performed within families of complexes bearing very similar geometric characteristics. It has also been shown that different number of -CH₂- units in the ligand backbone produce small structural distortions, which are reflected and magnified to obtain large differences in the magnetic behavior. Crystal structure data and Extended Hückel calculations have permitted the rationalization of the magnetostructural correlation displayed by complexes [(H32mO)₂Cu^{II}]₂²⁺ (**1c**), [(H₂Me33mO)₂Cu^{II}]₂²⁺ (**2c**), [(H33mO)₂Cu^{II}]₂²⁺ (**3c**) and [(H22mO)₂Cu^{II}]₂²⁺ (**5c**).

5.5 EXPERIMENTAL SECTION

Complexes. Bisphenoxo compounds $[(H32mO)_2Cu^{II}_2]^{2+}$ (**1c**), $[(H2Me33mO)_2Cu^{II}_2]^{2+}$ (**2c**), $[(H33mO)_2Cu^{II}_2]^{2+}$ (**3c**), $[(H22mO)_2Cu^{II}_2]^{2+}$ (**5c**) are synthesized by methods described in Chapter 4.

Magnetic measurements. From 20 to 30 mg of complexes **1c**, **2c**, **3c** and **5c** were used for variable-temperature magnetic susceptibility measurements in the polycrystalline state, carried out on a MANIC DSM8 equipped with a Bruker BE15 electromagnet and an Oxford CF 1200S cryogenic apparatus. Data were taken in the temperature range 4-300 K with an applied magnetic field of 15000 G.

Theoretical calculations. Molecular Orbital calculations were carried out using CACAO 4.0 (computer-aided composition of atomic orbitals) in its Windows version (WINCACAO),¹² a program based on the Extended Hückel type of analysis.

5.6 REFERENCES

- ¹ (a) W. E. Hatfield, *ACS Symp. Ser.* **1975**, No. 5, 108; (b) R. Malkin, B. G. Malstrom, *Adv. Enzymol.* **1970**, 33, 177.
- ² R. D. Willett, D. N. Hendrickson, *Magnetostructural Correlations in exchange coupled systems*; R. D. Willett, D. Gatteschi, O. Kahn, Eds.; Reidel: Dordrech, 1985; p 389 and 523.
- ³ P. J. Hay, J. C. Thibeault, R. Hoffmann, *J. Am. Chem. Soc.* **1975**, 97, 4884.
- ⁴ (a) L. Merz, W. Haase, *J. Chem. Soc., Dalton Trans.* **1980**, 875; (b) M. Handa, N. Koga, S. Kida, *Bull. Chem. Soc. Jpn.* **1988**, 61, 3853.
- ⁵ Asokan, A.; Manoharan, P. T. *Inorg. Chem.* **1999**, 38, 5642-5654.
- ⁶ (a) Amudha, P.; Kandaswamy, M.; Govindasamy, L.; Velmurugan, D. *Inorg. Chem.* **1998**, 37, 4486-4492. (b) Nishida, Y.; Shimo, H.; Maehara, H.; Kida, S. *J. Chem. Soc., Dalton Trans.* **1985**, 1945.
- ⁷ (a) M. Rodriguez, A. Llobet, M. Corbella, J. Reibenspies, A. E. Martell, *Inorg. Chem.* **1999**, 38, 2328; (b) M. Rodriguez, A. Llobet, M. Corbella, *Polyhedron* **2000**, 19, 2483-2491.
- ⁸ Thompson, L. K.; Mandal, S. K.; Tandon, S. S.; Bridson, J. N.; Park, M. K. *Inorg. Chem.* **1996**, 35, 3117.
- ⁹ Crawford, V. H.; Richardson, H. W.; Wasson, J. R.; Hodgson, D. H.; Hatfield, W. E. *Inorg. Chem.* **1976**, 15, 2107.
- ¹⁰ Ruiz, E.; Alemany, P.; Alvarez, S.; Cano, J. *Inorg. Chem.* **1997**, 36, 3683-3688.
- ¹¹ H. Astheimer, W. Haase, *J. Chem. Phys.* **1986**, 85, 1427.
- ¹² C. Mealli, D. M. Proserpio, *J. Chem. Educ.* **1990**, 67, 399.

¹³ B. Bleaney, K. D. Bowers, *Proc. R. Soc. London* **1952**, A214, 451.

¹⁴ This is supported by the almost equal geometry environment for Copper centers in complex **2c**-(PF₆)(Cl) and **2c**-(ClO₄)₂ (see Chapter 4).

¹⁵ A. W. Addison, T. N. Rao, J. Reedijk, J. V. Rijn, G. C. Verschoor, *J. Chem. Soc., Dalton Trans.* **1984**, 1349

¹⁶ See Chapter 4.

CHAPTER 6

Competitive O₂ activation reactivity driven by steric limitations. Aromatic hydroxylation vs CO₂ fixation by new macrocyclic dinuclear copper complexes

6.1	ABSTRACT.....	293
6.2	INTRODUCTION.....	295
6.3	RESULTS	297
6.3.1	COMPLEX SYNTHESIS.....	298
6.3.2	CRYSTAL STRUCTURES	300
6.3.2.1	$[(\mathbf{m}H33+33mO)Cu^II_2(\mathbf{m}OH)](PF_6)_2 \cdot CH_3CN$ (11-(PF ₆) ₂ ·CH ₃ CN).....	302
6.3.2.2	$[(H33+33m)_2Cu^II_4(\mathbf{m}CO_3)_2](ClO_4)_4 \cdot 4H_2O \cdot 2CH_3COCH_3$ (12-(ClO ₄) ₄ ·4H ₂ O·2CH ₃ COCH ₃).....	306
6.3.2.3	$[(H33+33m)Cu^II_2(CH_3CN)_4](ClO_4)_4 \cdot 2H_2O$ (14-(ClO ₄) ₄ ·2H ₂ O).....	309
6.3.3	MAGNETIC PROPERTIES	311
6.3.3.1	$[(\mathbf{m}H33+33mO)Cu^II_2(\mathbf{m}OH)](PF_6)_2 \cdot CH_3CN$ (11-(PF ₆) ₂ ·CH ₃ CN).....	311
6.3.3.2	$[(H33+33m)_2Cu^II_4(\mathbf{m}CO_3)_2](ClO_4)_4 \cdot 4H_2O \cdot 2CH_3COCH_3$ (12-(ClO ₄) ₄ ·4H ₂ O·2CH ₃ COCH ₃).....	312
6.4	DISCUSSION.....	313
6.4.1	MODULATION OF REACTIVITY.....	313
6.4.2	CRYSTAL STRUCTURES	314
6.4.3	STRUCTURE-REACTIVITY CORRELATION	315
6.4.4	CO ₂ FIXATION CAPABILITY	316
6.4.5	ANTIFERROMAGNETIC COMPOUNDS.....	318
6.4.5.1	$[(\mathbf{m}H33+33mO)Cu^II_2(\mathbf{m}OH)](PF_6)_2 \cdot CH_3CN$ (11-(PF ₆) ₂ ·CH ₃ CN).....	318
6.4.5.2	$[(H33+33m)_2Cu^II_4(\mathbf{m}CO_3)_2](ClO_4)_4 \cdot 4H_2O \cdot 2CH_3COCH_3$ (12-(ClO ₄) ₄ ·4H ₂ O·2CH ₃ COCH ₃).....	319
6.4.6	NEW LIGAND H33+33MOH.....	320
6.4.7	THEORETICAL CALCULATIONS: POSTULATING A PEROXO INTERMEDIATE	320
6.4.8	CONCLUDING REMARKS.....	323
6.5	EXPERIMENTAL SECTION	324
6.6	REFERENCES.....	331

CHAPTER 6

Competitive O₂ activation reactivity driven by steric limitations. Aromatic hydroxylation vs CO₂ fixation by new macrocyclic dinuclear copper complexes.

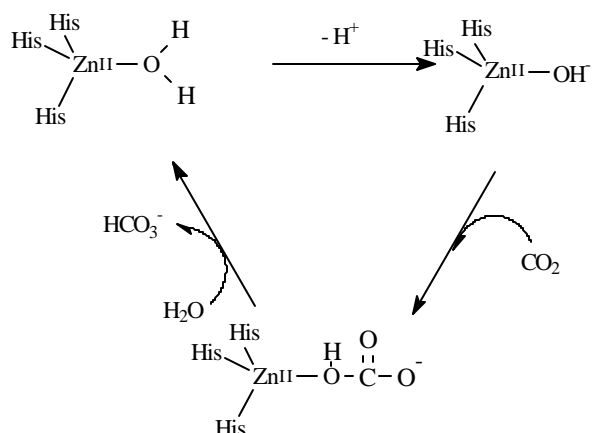
6.1 ABSTRACT

New macrocyclic μ -phenoxo- μ -hydroxo copper(II) complexes $[(\mu\text{-H33+33mO})\text{Cu}^{\text{II}}_2(\mu\text{-OH})](\text{X})_2$ (**11**-(X)₂, X = ClO₄⁻, PF₆⁻) have been obtained by O₂ activation from the dinuclear Cu^I complex $[(\text{H33+33m})\text{Cu}^{\text{I}}_2(\text{CO})_2](\text{X})_2$ (**10**-(X)₂) in 75% isolated yield ($[\mathbf{10}]_i < 4$ mM). Reactivity of O₂ activation intermediates can be redirected towards formation of bis-hydroxo compounds that readily interact with atmospheric CO₂ to finally lead to formation of tetranuclear carbonato complexes $[(\text{H33+33m})_2\text{Cu}^{\text{II}}_4(\mu\text{-CO}_3)_2](\text{X})_4$ (**12**-(X)₄) in a 22% isolated yield ($[\mathbf{10}]_i > 15$ mM). A novel dinuclear Cu^{II} complex $[(\text{H33+33m})\text{Cu}^{\text{II}}_2(\text{CH}_3\text{CN})_4](\text{ClO}_4)_4$ (**14**-(ClO₄)₄) has also been isolated, and it shows an uncommon N₅ ligand-donor set environment for each copper center. Complexes **11**-(PF₆)₂·CH₃CN, **12**-(ClO₄)₄·4H₂O·2CH₃COCH₃ and **14**-(ClO₄)₄·2H₂O have been characterized by XRD. Susceptibility measurements show antiferromagnetic behavior for **11**-(PF₆)₂ ($J = -515.8$ cm⁻¹) and for **12**-(ClO₄)₄ ($J = -169.0$ cm⁻¹).

6.2 INTRODUCTION

A variety of aromatic hydroxylation examples are known in chemical systems modeling tyrosinase activity.¹ A number of xylene-substituted ligands, including amines² and imines,³ have been used to prepare dinuclear Cu^{I} complexes that successfully mimic this reaction. Synthesis of low-molecular weight model complexes is important in order to elucidate the detailed pathways that can lead to the activation of an aromatic C-H bond and therefore has implications in the understanding of metalloenzymes and other catalysts.⁴ Copper-dioxygen intermediates ($\mu:\eta^2:\eta^2$ -peroxy)dicopper(II) and bis(μ -oxo)dicopper(III) isomers are proposed to be responsible of performing this oxygen insertion.⁵

Moreover, if the ligand does not have the adequate geometry, the corresponding copper(I) complexes are not able to catalyze any O insertion, obtaining bis(μ -hydroxo) dinuclear copper complexes as final product as it occurs in many examples in the literature.⁶ Some bis(μ -hydroxo) copper complexes show carbonic anhydrase activity⁷ and present high affinity towards CO_2 fixation, even at low concentration as it occurs in atmosphere.⁸ This reaction is of special interest from an environmental point of view since atmospheric CO_2 elimination is at present an unresolved challenging target. Active site of Carbonic Anhydrase enzymes (CA) presents a single Zn^{II} atom coordinated to three Histidines and a H_2O molecule.⁹

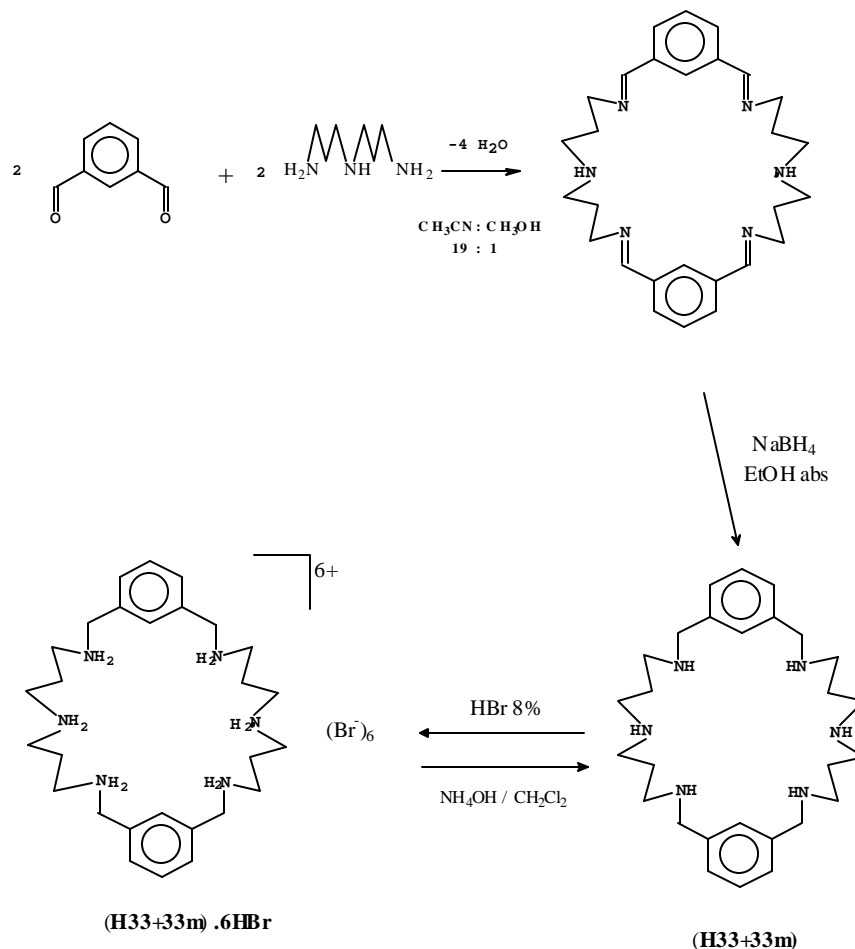


Nucleophilic attack of hydroxide group on a CO_2 molecule is the accepted mechanism for this catalytic reaction, and a similar pathway is thought to take place when the bis(μ -hydroxo) copper complexes react with CO_2 .^{10,8a}

6.3 RESULTS

Synthesis of ligand H33+33m has been reported in literature (see Scheme 1).²⁷ Air-sensitive copper complexes have been obtained using Schlenk techniques. They have been characterized by IR, NMR, ESI-MS, UV-Vis and Elemental Analysis (see Figures S1-S6). Crystal structure of complexes $[(\mu\text{-H33+33mO})\text{Cu}^{\text{II}}_2(\mu\text{-OH})](\text{PF}_6)_2 \cdot \text{CH}_3\text{CN}$ (**11**-(PF₆)₂ · CH₃CN), $[(\text{H33+33m})_2\text{Cu}^{\text{II}}_4(\mu\text{-CO}_3)_2](\text{ClO}_4)_4 \cdot 4\text{H}_2\text{O} \cdot 2\text{CH}_3\text{COCH}_3$ (**12**-(ClO₄)₄ · 4H₂O · 2CH₃COCH₃) and $[(\text{H33+33m})\text{Cu}^{\text{II}}_2(\text{CH}_3\text{CN})_4](\text{ClO}_4)_4 \cdot 2\text{H}_2\text{O}$ (**14**-(ClO₄)₄ · 2H₂O) have been obtained (see section 6.3.2).

Scheme 1. Synthetic procedure for the obtention of ligand H33+33m

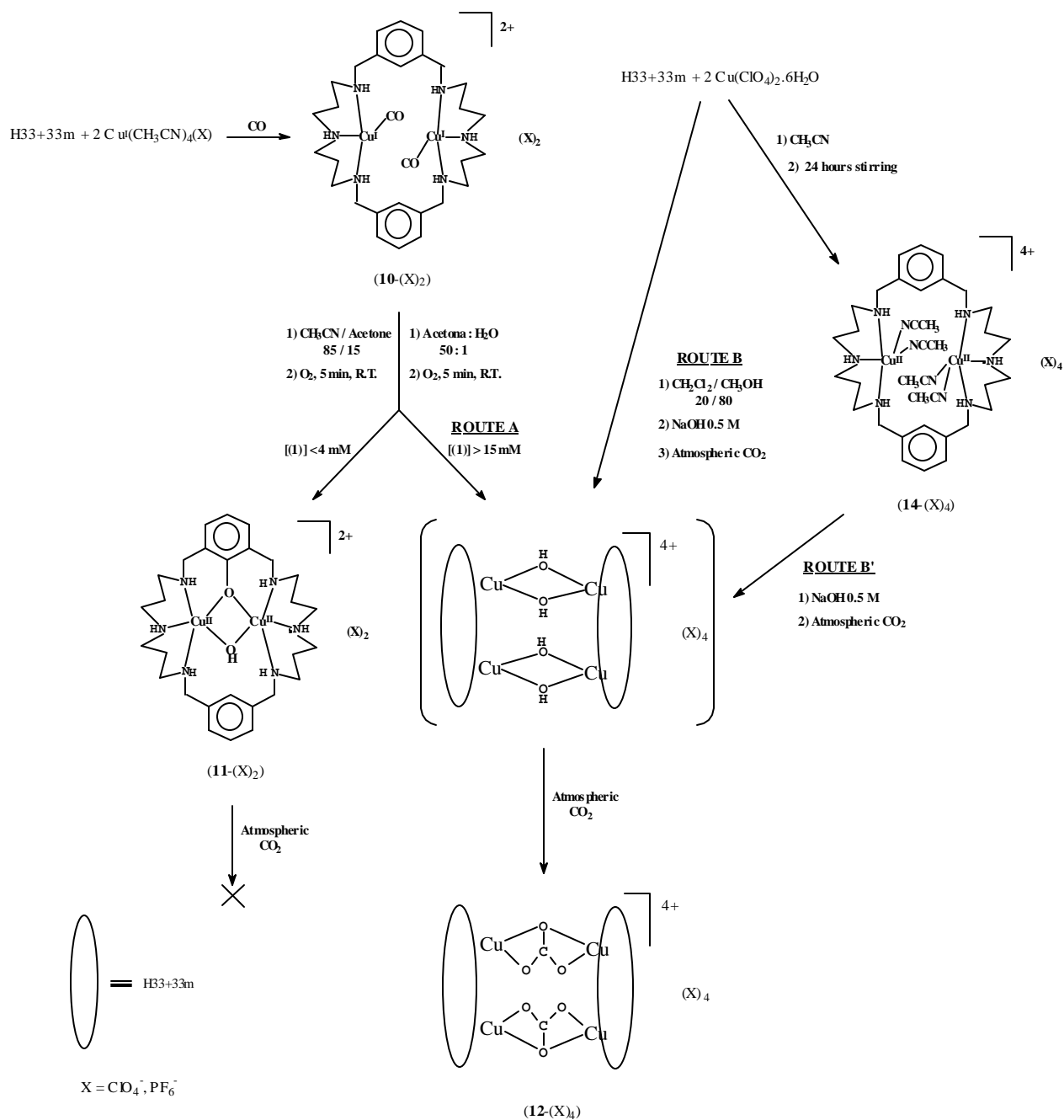


6.3.1 Complex synthesis

The starting complexes used in this work are copper(I) $[(\text{H}^{33}\text{+}^{33}\text{m})\text{Cu}^{\text{I}}_2](\text{X})_2$ ($\text{X} = \text{PF}_6^-$, ClO_4^-) compounds. Their extremely high sensitivity with O_2 and water, even in the solid state, has precluded to work with them under common Schlenk techniques. Therefore, carbon monoxide was used to stabilize Cu^{I} oxidation state forming dinuclear $\text{Cu}^{\text{I}}\text{-CO}$ complexes $[(\text{H}^{33}\text{+}^{33}\text{m})\text{Cu}^{\text{I}}_2(\text{CO})_2](\text{X})_2$ (**10**- $(\text{X})_2$) ($\text{X} = \text{PF}_6^-$, ClO_4^-). These complexes are readily soluble in CH_3CN , CH_3OH , Acetone and CH_2Cl_2 , and mixtures of these solvents are used to perform subsequent reactions with O_2 . A general complex synthesis procedure is depicted in Scheme 2.

Complexes $[(\mu\text{-H}^{33}\text{+}^{33}\text{mO})\text{Cu}^{\text{II}}_2(\mu\text{-OH})](\text{X})_2$ (**11**- $(\text{X})_2$) ($\text{X} = \text{PF}_6^-$, ClO_4^-) are synthesized by bubbling dioxygen to carbonyl Cu^{I} complexes (**10**) solutions at room temperature using a concentration lower than 4 mM. The solution turns green rapidly and diffusion of diethyl ether allows precipitation of green crystals of **11** in 75 % yield. If 8 mM concentration of **10** is used final yield of **11** decreases to 55%, and to 40% if $[\text{10}]_i = 10.3$ mM.

Scheme 2. Synthetic routes to obtain complexes $[(\mu\text{-H33+33mO})\text{Cu}^{\text{II}}_2(\mu\text{-OH})]^{2+}$ (**11**), $[(\text{H33+33m})_2\text{Cu}^{\text{II}}_4(\mu\text{-CO}_3)_2]^{4+}$ (**12**) and $[(\text{H33+33m})\text{Cu}^{\text{II}}_2(\text{CH}_3\text{CN})_4]^{4+}$ (**14**)



As activation of dioxygen is actually achieved and it results into aromatic hydroxylation reaction, attempts were

made to detect and characterize Cu/O₂ intermediates formed in the reaction. UV-Vis monitoring experiments were performed from room temperature to -80°C and no intermediates were found, possibly because of their high instability (see also section 6.4.7).

When the same reaction is run at higher concentrations (>15 mM), no aromatic hydroxylation is detected. Instead, blue crystals of carbonato complex [(H33+33m)₂Cu^{II}₄(μ-CO₃)₂](ClO₄)₄ (**12**-(ClO₄)₄) start to precipitate out from acetone solutions in a final 22% isolated yield. The CO₂ fixation reaction was followed by UV-Vis spectroscopy, showing that show full formation of carbonate tetranuclear complex **12** is achieved in less than 10 minutes (see section 6.4.4).

Same carbonato complex **12**-(ClO₄)₄ can be obtained quantitatively if solution of [(H33+33m)Cu^{II}₂(H₂O)₄](ClO₄)₄ (**13**-(ClO₄)₄) is treated with NaOH 0.5 mM and exposed to open air. Furthermore, complex [(H33+33m)Cu^{II}₂(CH₃CN)₄](ClO₄)₄ (**14**-(ClO₄)₄) is also a good starting material to obtain carbonato complex **12** in 60% yield after addition of one equivalent of NaOH per copper atom and exposure to air.

6.3.2 Crystal structures

X-Ray Diffraction analysis have been performed on complexes [(μ-H33+33mO)Cu^{II}₂(μ-OH)]²⁺ (**11**), [(H33+33m)₂Cu^{II}₄(μ-CO₃)₂]⁴⁺ (**12**) and [(H33+33m)Cu^{II}₂(CH₃CN)₄]⁴⁺ (**14**). A summary of crystallographic data is given in Table 1.

Table 1. Crystal data and structure refinement

	11- (PF ₆) ₂ ·CH ₃ CN	12- (ClO ₄) ₄ ·4H ₂ O	14- (ClO ₄) ₄ ·2H ₂ O · 2CH ₃ COCH ₃
Empirical formula	C ₃₀ H ₄₉ Cu ₂ F ₁₂ N ₇ O ₂ P ₂	C ₆₄ H ₁₁₂ Cl ₄ Cu ₄ N ₁₂ O ₂₈	C ₃₆ H ₆₂ Cl ₄ Cu ₂ N ₁₀ O ₁₈
Fw	956.78	1893.62	1191.84
space group	Pna21	P21/n	Pcca
<i>a</i> , Å	22.107(6)	17.797(4)	24.193(1)
<i>b</i> , Å	18.991(3)	13.879(2)	11.770(1)
<i>c</i> , Å	9.440(2)	19.063(3)	19.488(1)
<i>a</i> , deg	90	90	90
<i>b</i> , deg	90	112.87(1)	90
<i>g</i> , deg	90	90	90
<i>V</i> , Å ³	3962.9(2)	4338.6(1)	5264.3(3)
<i>Z</i>	4	2	4
Data collection instrument	Bruker SMART CCD	Bruker SMART CCD	Bruker SMART CCD
<i>T</i> , K	298(2)	173(2)	298(2)
<i>I</i> Mo-K _α , Å	0.71073	0.71073	0.71073
<i>r</i> (calcd), g cm ⁻³	1.604	1.449	1.504
<i>m</i> , mm ⁻¹	1.249	1.170	1.087
<i>R/Rw</i> ^a	0.0541/0.0803	0.0857/0.1172	0.0696/0.1440

^a $R = \sum |F_0 - F_c| / \sum F_0$ and $R_w = \{\sum [w(F_0^2 - F_c^2)^2] / \sum [w(F_0^2)^2]\}^{1/2}$

6.3.2.1 $[(\mu\text{-H33+33mO})\text{Cu}^{\text{II}}_2(\mu\text{-OH})](\text{PF}_6)_2 \cdot \text{CH}_3\text{CN}$ (**11**-
 $(\text{PF}_6)_2 \cdot \text{CH}_3\text{CN}$)

The molecular structure of **11** consists in a dinuclear Cu^{II} cation $[(\mu\text{-H33+33mO})\text{Cu}^{\text{II}}_2(\mu\text{-OH})]^{2+}$ with a μ -phenoxo bridging group from the macrocyclic ligand backbone and a μ -hydroxo group also bridging the copper atoms. Four perchlorate counteranions are present and one molecule of acetonitrile is found as solvent of crystallization.

No crystallographic symmetry axis is found in the structure. The ORTEP drawing of **11** (Figure 1) shows that each copper center is pentacoordinated to three N and two O atoms in a slightly distorted square-based pyramidal geometry ($\tau = 0.22$)¹¹ with a longer axial coordination (Cu1-N3, 2.32 Å; Cu2-N4, 2.34 Å) to one of the N atoms. Selected bond lengths and angles are listed in Table 2. The phenoxy group acting as a bridge forces the copper atoms to be placed closer to this side of the macrocycle and therefore the N atom in the axial position is the one from the other side of the ligand backbone. The Cu_2O_2 core presents a distorted rhomboidal disposition with short bonds between copper atoms and hydroxo oxygen O2 (Cu1-O2, 1.918 Å; Cu2-O2, 1.920 Å), whereas longer bonds exist between copper centers and O1(phenoxo) (Cu1-O1, 2.032 Å; Cu2-O1, 2.022 Å). Cu1...Cu2 distance is 3.046 Å. The core Cu_2O_2 atoms do not lie in a plane and deviations from mean plane have been calculated (see Table 3). It is also noticeable the formation of four six-membered rings within copper atoms and ligation atoms, that help on the stabilization of the highly constrained structure.

In this structure, the bases of both pyramids share one side (coplanar) but with an important bent angle of 139.42° between planes, which is an uncommon characteristic for this type of geometries. Moreover, the apical N atom for

both copper center is places in a syn fashion (directed to same side) when the most usual disposition is the anti fashion.^{20,21}

Packing cell ORTEP plot for **11** is depicted in Figure S7.

Figure 1. ORTEP diagram of the cationic fragment of complex $[(\mu\text{-H33+33mO})\text{Cu}^{\text{II}}_2(\mu\text{-OH})](\text{PF}_6)_2 \cdot \text{CH}_3\text{CN}$ (**11**- $(\text{PF}_6)_2 \cdot \text{CH}_3\text{CN}$) (50% probability thermal ellipsoids)

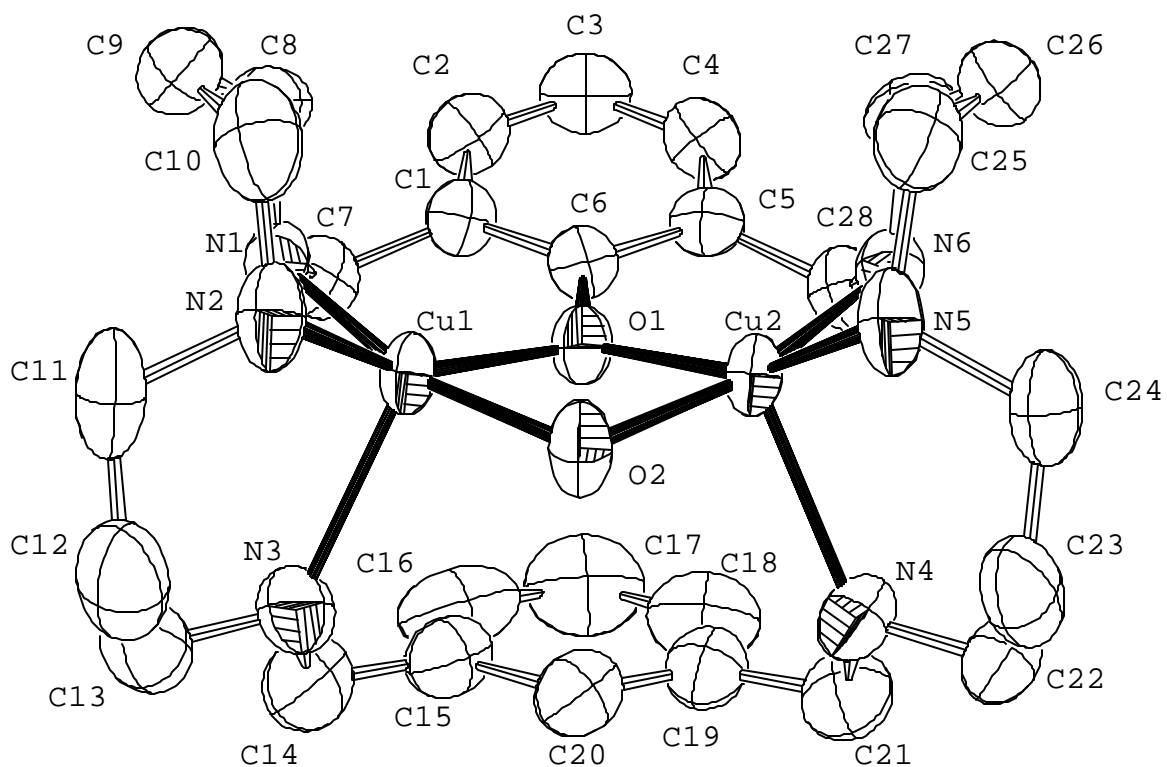


Table 2. Selected Bond Distances (Å) and Bond Angles (deg) for $[(\mu\text{-H33}+\text{33mO})\text{Cu}^{\text{II}}_2(\mu\text{-OH})](\text{PF}_6)_2 \cdot \text{CH}_3\text{CN}$ (**11**- $(\text{PF}_6)_2 \cdot \text{CH}_3\text{CN}$)

Cu1-O2	1.918(4)	Cu2-O2	1.920(4)
Cu1-N1	1.981(5)	Cu2-N6	1.969(5)
Cu1-O1	2.033(4)	Cu2-O1	2.022(3)
Cu1-N2	2.053(4)	Cu2-N5	2.058(4)
Cu1-N3	2.320(6)	Cu2-N4	2.340(5)
Cu1...Cu2	3.046(1)	C6-O1	1.347(6)
O2-Cu1-N1	165.6(2)	Cu1-O2-Cu2	105.0(2)
N1-Cu1-O1	92.9(2)	O2-Cu1-O1	77.1(1)
O2-Cu1-N2	92.7(2)	O2-Cu2-O1	77.3(1)
N1-Cu1-N2	91.6(2)	O2-Cu2-N6	167.5(2)
O1-Cu1-N2	152.2(2)	N6-Cu2-O1	93.9(2)
O2-Cu1-N3	93.4(2)	O2-Cu2-N5	92.2(2)
N1-Cu1-N3	100.2(2)	N6-Cu2-N5	91.7(2)
O1-Cu1-N3	114.6(2)	O1-Cu2-N5	152.8(2)
N2-Cu1-N3	91.5(3)	O2-Cu2-N4	91.9(2)
C6-O1-Cu2	126.8(3)	N6-Cu2-N4	99.8(2)
C6-O1-Cu1	126.9(3)	O1-Cu2-N4	113.0(2)
Cu2-O1-Cu1	97.4(2)	N5-Cu2-N4	92.1(2)

Table 3. Least-squares planes of complex **11**-(PF₆)₂ in cartesian coordinates (esd deviations in brackets).

$$\text{Equation of plane 1 (N1 N2 Cu1 O1 O2)}$$

$$-11.6883 (0.0350) x + 2.7936 (0.0411) y + 7.8910 (0.0101) z = 0.9237 (0.0162)$$

Atom	Deviation from mean plane (Å)
N1	-0.0472 (0.0024)
N2	0.1933 (0.0025)
Cu1	-0.2745 (0.0022)
O1	0.2056 (0.0029)
O2	-0.0772 (0.0027)

Rms deviation of fitted atoms = 0.1807

$$\text{Equation of plane 2 (N5 N6 Cu2 O1 O2)}$$

$$0.8198 (0.0457) x + 10.4113 (0.0299) y + 7.8868 (0.0098) z = 4.7686 (0.0074)$$

Atom	Deviation from mean plane (Å)
N5	0.1940 (0.0025)
N6	-0.0575 (0.0024)
Cu2	-0.2545 (0.0022)
O1	0.2088 (0.0029)
O2	-0.0908 (0.0027)

Rms deviation of fitted atoms = 0.1775

Angle Plane 1 - Plane 2

Angle to previous plane (with approx. esd) = **139.42 (0.16)**

$$\text{Equation of plane 3 (Cu1 O1 Cu2 O2)}$$

$$-7.0018 (0.0268) x + 8.7079 (0.0307) y + 7.8379 (0.0127) z = 3.5404 (0.0059)$$

Atom	Deviation from mean plane (Å)
Cu1	0.1135 (0.0015)
O1	-0.1056 (0.0014)
Cu2	0.1139 (0.0015)
O2	-0.1218 (0.0016)

Rms deviation of fitted atoms = 0.1139

6.3.2.2 $[(H33+33m)_2Cu^{II}_4(m-CO_3)_2](ClO_4)_4 \cdot 4H_2O \cdot 2CH_3COCH_3$ (**12**-
 $(ClO_4)_4 \cdot 4H_2O \cdot 2CH_3COCH_3$)

The molecular structure of **12** consists of a tetranuclear copper(II) complex with two H33+33m ligand molecules, two Cu atoms coordinated to each ligand and two carbonate CO_3^{2-} groups acting as bridges between two copper centers from different ligands. Four perchlorate anions, four water and two acetone molecules are present in the crystal cell.

The molecule sits on a center of symmetry that transform one macrocyclic ligand into the other. The ORTEP drawing of **12** (Figure 2) shows that each copper metal atom is pentacoordinated to a N_3O_2 ligand-donor set in a distorted square-planar pyramidal geometry (with a τ factor of 0.29 for Cu1 and 0.25 for Cu2)¹¹. Selected bond lengths and angles are listed in Table 4. Copper centers are coordinated to one O atom of the carbonato group and three N atoms to form the base of the pyramid, and to another O atom in the axial position in a weaker bond type (Cu1-O1 2.33 Å, Cu2-O1 2.37 Å). Carbonate group is acting as a tridentate ligand coordinating each Cu center in a bidentate and almost symmetrical fashion (see Figure 3), but presenting two longer Cu-O bonds corresponding to the O atom placed in the axial coordination site of each pyramid. Symmetry is also observed on the bond distances between the metal and the carbonato oxygen atoms terminally bound to one side of the metal ion (Cu1-O2, 1.967 Å; Cu2-O3, 1.970 Å). The angle Cu1-O1-Cu2 is bent to 162° in **12**.

Planes described by both carbonato groups are almost parallel with an angle between planes of 4.8°.

Figure 2. ORTEP diagram of the cationic fragment of complex $[(H33+33m)_2Cu^{II}_4(\mu-CO_3)_2](ClO_4)_4 \cdot 4H_2O \cdot 2CH_3COCH_3$ (**12**- $(ClO_4)_4 \cdot 4H_2O \cdot 2CH_3COCH_3$) (50% probability thermal ellipsoids)

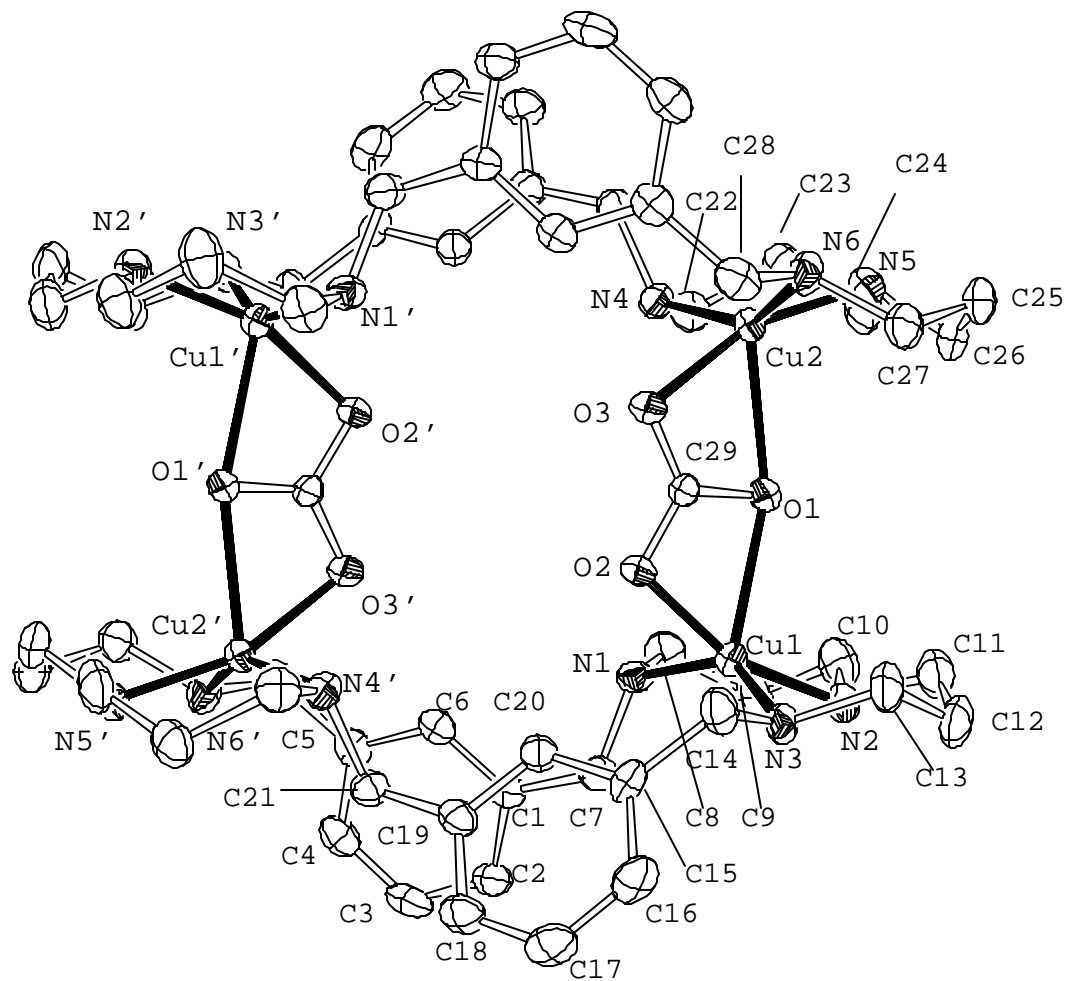


Figure 3. ORTEP diagram of carbonato group bridging the two copper centers in complex $[(\text{H}33+33\text{m})_2\text{Cu}^{\text{II}}_4(\mu\text{-CO}_3)_2](\text{ClO}_4)_4 \cdot 4\text{H}_2\text{O} \cdot 2\text{CH}_3\text{COCH}_3$ (**12**- $(\text{ClO}_4)_4 \cdot 4\text{H}_2\text{O} \cdot 2\text{CH}_3\text{COCH}_3$)

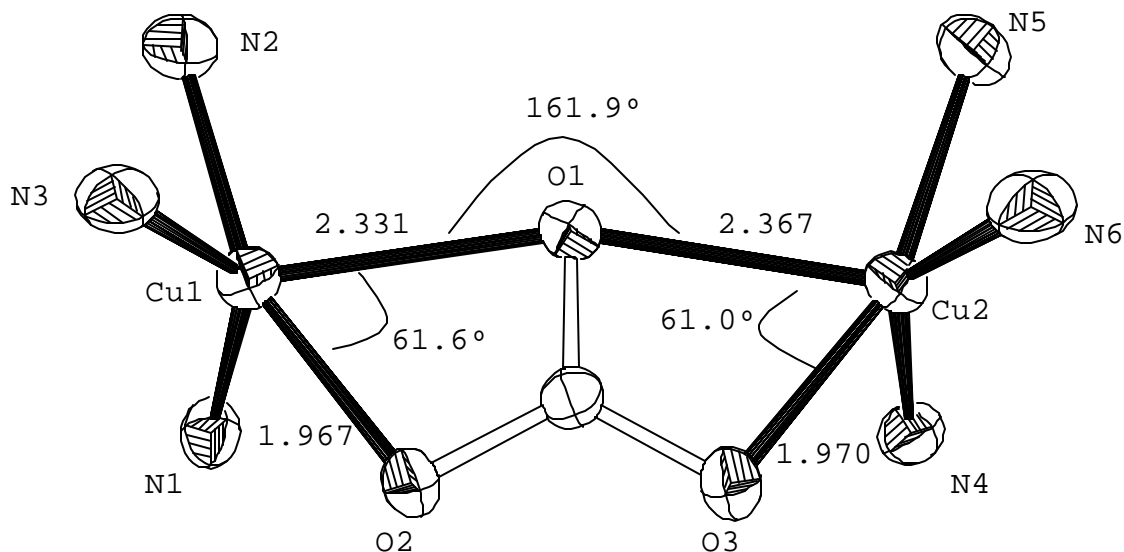


Table 4. Selected Bond Distances (Å) and Bond Angles (deg) for $[(\text{H}33+33\text{m})_2\text{Cu}^{\text{II}}_4(\mu\text{-CO}_3)_2](\text{ClO}_4)_4 \cdot 4\text{H}_2\text{O} \cdot 2\text{CH}_3\text{COCH}_3$ (**12**- $(\text{ClO}_4)_4 \cdot 4\text{H}_2\text{O} \cdot 2\text{CH}_3\text{COCH}_3$)

Cu1-O2	1.967(5)	Cu2-O3	1.971(5)
Cu1-N2	2.008(6)	Cu2-N5	1.999(6)
Cu1-N1	2.049(6)	Cu2-N4	2.047(6)
Cu1-N3	2.051(6)	Cu2-N6	2.056(6)
Cu1-O1	2.331(5)	Cu2-O1	2.368(5)
Cu1...Cu2	4.640(5)	Cu1...Cu1'	8.071(5)
Cu1...Cu2'	6.814(5)	Cu2...Cu2'	8.413(5)
O2-Cu1-N2	159.7(2)	O3-Cu2-N5	160.8(2)
O2-Cu1-N1	88.4(2)	O3-Cu2-N4	87.6(2)
N2-Cu1-N1	95.3(2)	N5-Cu2-N4	97.1(2)
O2-Cu1-N3	95.1(2)	O3-Cu2-N6	94.7(2)
N2-Cu1-N3	94.2(2)	N5-Cu2-N6	91.7(3)
N1-Cu1-N3	142.0(2)	N4-Cu2-N6	145.9(2)
O2-Cu1-O1	61.6(2)	O3-Cu2-O1	61.0(2)
N2-Cu1-O1	98.3(2)	N5-Cu2-O1	99.9(2)
N1-Cu1-O1	105.0(2)	N4-Cu2-O1	101.1(2)
N3-Cu1-O1	109.9(2)	N6-Cu2-O1	109.8(2)

Distances between copper centers bridged by the carbonato group are 4.640 Å, whereas distances between copper atoms from same ligand are 6.814 Å. The latter will have implications in complex magnetic properties (see section 6.3.3.2), as well as the bent Cu1-O1-Cu2 angle and its relatively long Cu-O1 distances.

Packing cell ORTEP plot for **12** is depicted in Figure S7.

6.3.2.3 [(H33+33m)Cu^{II}₂(CH₃CN)₄](ClO₄)₄·2H₂O (**14**- (ClO₄)₄·2H₂O)

Molecular structure of **14** consists in a dinuclear copper(II) complex [(H33+33m)Cu^{II}₂(CH₃CN)₄]⁴⁺ with two acetonitrile molecules coordinated to each copper center. Four perchlorate counteranions are present and two molecules of water are found as solvent of crystallization. The molecule sits on a center of symmetry that transform one copper center and half of the ligand into the rest of the molecule. The ORTEP drawing of **14** (Figure 4) shows that each copper center is pentacoordinated to N₅ ligand-donor set in a strongly distorted square-base pyramidal geometry (with a τ factor of 0.42)¹¹ towards a trigonal bipyramidal geometry. Selected bond lengths and angles are listed in Table 5. This complex presents a rare coordination environment N₅ for copper, bearing two molecules of acetonitrile and coordinated to three secondary amines. One CH₃CN molecule is coordinated in a quasi-linear mode (Cu1-N2S-C3S, 173.9°) whereas the other presents a bent angle (Cu1-N1S-C1S, 144.0°). The distance Cu1-N1S from the bent acetonitrile ligand is longer (2.265 Å) than Cu1-N2S (2.021 Å), so N1S occupies the axial coordination site of the distorted square-planar pyramid.

Copper centers are disposed in a syn mode that places the metals far apart (Cu1...Cu2 distance 7.340 Å).

Packing cell ORTEP plot for **12** is depicted in Figure S7.

Figure 4. ORTEP diagram of the cationic fragment of $[(H33+33m)Cu^{II}_2(CH_3CN)_4](ClO_4)_4 \cdot 2H_2O$ (**14**- $(ClO_4)_4 \cdot 2H_2O$) (50% probability thermal ellipsoids)

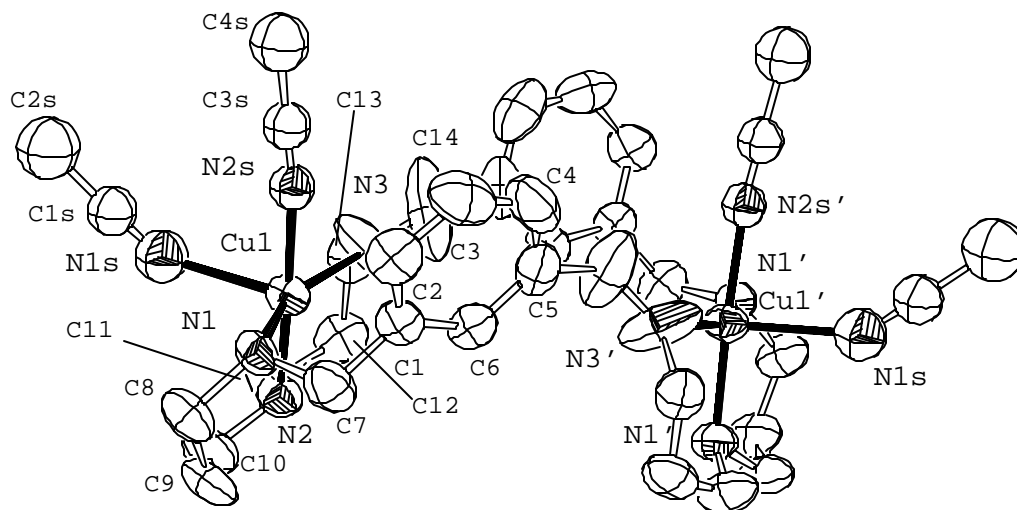


Table 5. Selected Bond Distances (Å) and Bond Angles (deg) for $[(H33+33m)Cu^{II}_2(CH_3CN)_4](ClO_4)_4 \cdot 2H_2O$ (**14**- $(ClO_4)_4 \cdot 2H_2O$)

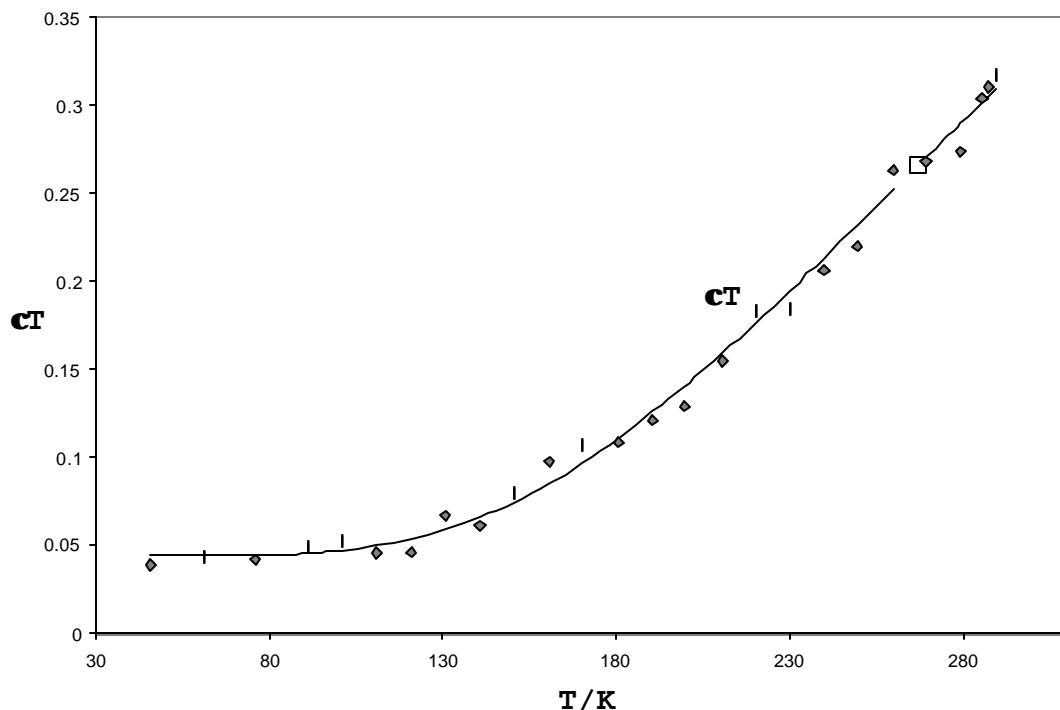
Cu1-N2	2.016(5)	Cu1'-N2'	2.016(5)
Cu1-N2s	2.021(6)	Cu1'-N2s'	2.021(6)
Cu1-N3	2.046(6)	Cu1'-N3'	2.046(6)
Cu1-N1	2.058(5)	Cu1'-N1'	2.058(5)
Cu1-N1s	2.265(7)	Cu1'-N1s'	2.265(7)
Cu1...Cu2	7.340(5)		
N2-Cu1-N2s	176.7(2)	N2-Cu1-N1s	92.4(3)
N2-Cu1-N3	91.9(3)	N2s-Cu1-N1s	84.6(3)
N2s-Cu1-N3	87.9(3)	N3-Cu1-N1s	110.8(3)
N2-Cu1-N1	94.2(2)	N1-Cu1-N1s	96.6(2)
N2s-Cu1-N1	87.5(2)	C1s-N1s-Cu1	144.1(7)
N3-Cu1-N1	151.6(3)	C3s-N2s-Cu1	173.9(7)

6.3.3 Magnetic properties

6.3.3.1 $[(\mu\text{-H33+33mO})\text{Cu}^{\text{II}}_2(\mu\text{-OH})](\text{PF}_6)_2 \cdot \text{CH}_3\text{CN}$ (**11**- (PF_6)₂·CH₃CN)

The temperature dependence of the magnetic susceptibility of $[(\mu\text{-H33+33mO})\text{Cu}^{\text{II}}_2(\mu\text{-OH})](\text{PF}_6)_2$ (**11**-(PF_6)₂) measured in the range 45-300 K is shown in Figure 5. Strong antiferromagnetic behavior is displayed by the complex and χT value decreases already at room temperature. Some paramagnetic impurities causes slight deviation of the curve at low temperatures. Experimental data was fitted to the Bleany-Bowers equation for a binuclear compound containing paramagnetic impurities (see Eq.2 in Chapter 5, section 5.3.3). Best fit parameters derived from Hamiltonian $H = -JS_1S_2$ are $J = -515.8(2) \text{ cm}^{-1}$, $g = 2.40(2)$ and $r = 0.0205$.

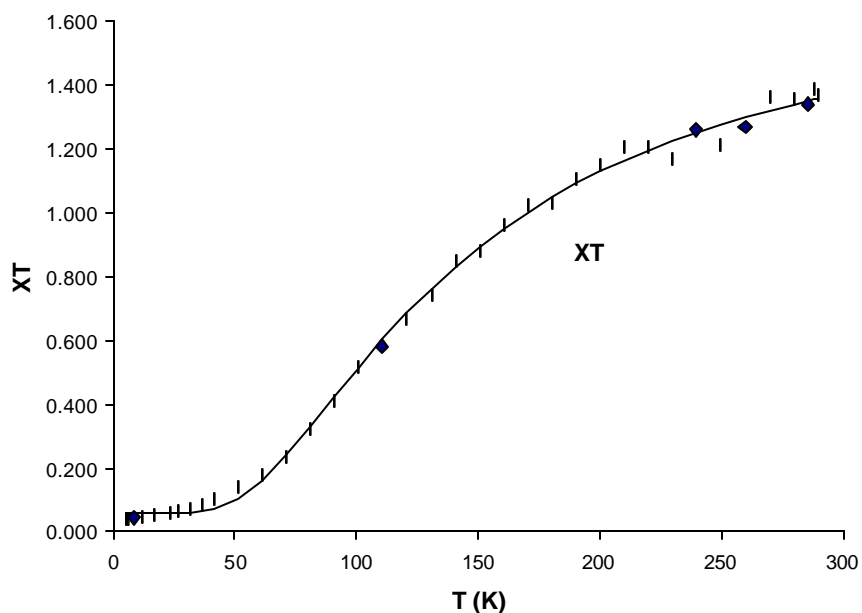
Figure 5. $\chi_M T$ vs T plot in the 45-300 K range of temperatures for complex **11**-(PF_6)₂. Solid line show the best fit indicated in the text



6.3.3.2 $[(\text{H}^{33}\text{+}^{33}\text{m})_2\text{Cu}^{\text{II}}_4(\mu\text{-CO}_3)_2](\text{ClO}_4)_4 \cdot 4\text{H}_2\text{O} \cdot 2\text{CH}_3\text{COCH}_3$ (**12**-
(ClO_4)₄ · 4H₂O · 2CH₃COCH₃)

χT vs T plot measured in the range 4-300 K for complex $[(\text{H}^{33}\text{+}^{33}\text{m})_2\text{Cu}^{\text{II}}_4(\mu\text{-CO}_3)_2](\text{ClO}_4)_4$ (**12**-(ClO_4)₄) is presented in Figure 6. Relatively weak antiferromagnetic behavior is observed for this complex compared to bis(hydroxo) or bis(phenoxo) copper complexes,^{17,20} with best fit parameters derived from the Hamiltonian $H = -JS_1S_2$ are $J = -163.4 \text{ cm}^{-1}$, $g = 2.24$ and $r = 0.092$ (paramagnetic impurities causes slight deviation of the curve at very low T ; see Chapter 5, section 5.3.3).

Figure 6. $\chi_M T$ vs T plot in the 2-300 K range for complex **12**-(ClO_4)₄. Solid line show the best fit indicated in the text



Calculations have been performed considering both carbonato groups as independent units and no coupling is observed between Cu atoms from same ligand.

6.4 DISCUSSION

6.4.1 Reactivity modulation

Reactivity towards atmospheric CO₂ fixation to obtain complex [(H33+33m)₂Cu^{II}₄(μ-CO₃)₂](ClO₄)₄ (**12**-(ClO₄)₄) is attributed to bis(μ-hydroxo) complexes formed through O₂ activation with Cu^I. In high concentration solutions it is reasonable to predict that O₂ activation can take place with two copper atoms from different macrocycles, and therefore, a variety of polymer possibilities arises. The reactivity of this polymeric Cu/O₂ intermediates is unknown and may be the reason why only a 22% of carbonato complex **12**-(ClO₄)₄ is obtained under these conditions. Same carbonato complex **12**-(ClO₄)₄ can be obtained quantitatively if solution of [(H33+33m)Cu^{II}₂(H₂O)₄](ClO₄)₄ (**13**-(ClO₄)₄) or [(H33+33m)Cu^{II}₂(CH₃CN)₄](ClO₄)₄ (**14**-(ClO₄)₄) are treated with 2 eq of NaOH 0.5 mM and exposed to open air. This pathway supports the explanation for low yields in carbonato complex obtained with Cu^I/O₂ route (see Scheme 2).

On the other hand, when solution concentrations below 4 mM are used, interaction of O₂ with both Cu atoms from same ligand is favored and formation of peroxo species Cu^{II}-O₂²⁻-Cu^{II} with an aromatic ring placed close to the core allows aromatic functionalization and formation of phenoxo-bridged complexes [(μ-H33+33mO)Cu^{II}₂(μ-OH)]²⁺ (**11**) in high yields (75%) (see section 6.4.7).

Dinuclear copper(II) complex [(H33+33m)Cu^{II}₂(CH₃CN)₄](ClO₄)₄ (**14**-(ClO₄)₄) structure shows a syn disposition of the two copper centers, which are placed far apart from each other in the solid state (see section 6.3.2.3). This conformation is probably one of the favored also in solution and agrees with oligomeric products formation when high concentrations

are used in O₂ activation by Cu^I systems presented in this work.

6.4.2 Crystal structures

Carbonato complexes with copper and other transition metals have been described in the literature,^{8a,12} presenting the same coordination modes as in complex [(H33+33m)₂Cu^{II}₄(μ-CO₃)₂](ClO₄)₄ (**12**-(ClO₄)₄) but with slightly differences. Normally, the angle Cu1-O1-Cu2 is close to linear (176-178°), and in **12** this angle is bent to 162°. Only one tetranuclear carbonato copper complex has been described very recently in literature:²² it is synthesized with two hexacoordinating non-macrocyclic ligands, presenting two carbonato bridges with a pseudo-bidentate coordination mode (Cu-O distances 2.5-2.7 Å are very long and should be considered only as electrostatic interactions), and an angle Cu1-O1-Cu2 of 151.9° as main differences compared to **12**. In our case, planes described by both carbonato groups are almost parallel with an angle between planes of 4.8°. Complex [(H33+33m)Cu^{II}₂(CH₃CN)₄](ClO₄)₄ (**14**-(ClO₄)₄) presents a particular coordination mode for acetonitrile molecules. One of the CH₃CN molecules is coordinated in a quasi-linear mode whereas the other presents a bent angle. This is probably explained by a particular molecular packing that forces the angle to be bent.

The ligand-donor set N₅ in **14** is only found in two examples in literature (Cambridge Data Base), where a mononuclear copper complex also bears two acetonitriles and three tertiary amines in one case,¹³ and two acetonitriles, a tertiary amine and two benzoimidazole residues in the second case.¹⁴ Dinuclear copper complex **14** resembles the first mentioned example, also presenting a bent

acetonitrile ligand in the axial coordination site of a distorted square-planar pyramid.

6.4.3 Structure-reactivity correlation

It is interesting to compare structures of complexes $[(\mu\text{-H33+33mO})\text{Cu}^{\text{II}}_2(\mu\text{-OH})]^{2+}$ (**11**), $[(\text{H33+33m})_2\text{Cu}^{\text{II}}_4(\mu\text{-CO}_3)_2]^{4+}$ (**12**) and $[(\text{H33+33m})\text{Cu}^{\text{II}}_2(\text{CH}_3\text{CN})_4]^{4+}$ (**14**), specially considering the capability of the ligand H33+33m to adopt different conformations and to suffer significant bendings of the ligand backbone. Thus, complex $[(\text{H33+33m})\text{Cu}^{\text{II}}_2(\text{CH}_3\text{CN})_4]^{4+}$ (**14**), with syn disposition of copper centers, is the most unconstrained complex because no bridging ligands between coppers are present. On the contrary, complex $[(\mu\text{-H33+33mO})\text{Cu}^{\text{II}}_2(\mu\text{-OH})]^{2+}$ (**11**), with the ligand backbone totally bent in the opposite direction compared to (**14**), presents a highly-tensioned structure due to the phenoxo bridging group (Cu1...Cu2 distance is only 3.046 Å). Synthesis of this complex implies formation of a $\text{Cu}^{\text{I}}\text{-O}_2^{2-}\text{-Cu}^{\text{II}}$ peroxo group in a similar fashion as final complex (**11**), as proximity of the aromatic ring is demanded to perform hydroxylation, so conformations with copper centers close to each other must be present before interaction with dioxygen.

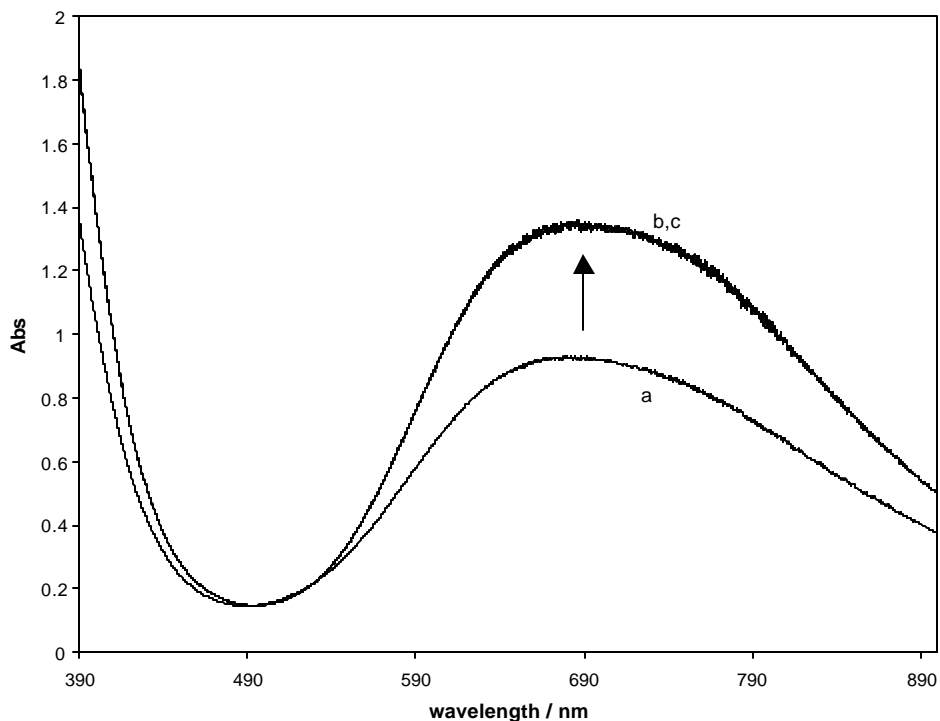
The tetranuclear complex $[(\text{H33+33m})_2\text{Cu}^{\text{II}}_4(\mu\text{-CO}_3)_2]^{4+}$ (**12**) has the ligands positioned in a similar way as in **14** (Cu...Cu distances are 6.814(5) for **12** and 7.340(5) for **14**). Assuming that carbonato complex comes from reaction of bis(μ -hydroxo) intermediate with CO_2 , we can not distinguish whether the latter is dinuclear, dimeric species similar to final carbonato complex, or even oligomeric products. However, it is reasonable to think that molecule aggregation is favored at higher

concentrations so the most reasonable nuclearity for this complex is to be tetranuclear or higher. Once the CO₂ fixation has been achieved, the products rearrange to finally lead to the tetranuclear carbonato complex **12**.

6.4.4 CO₂ fixation capability

Bis(μ -hydroxo) copper intermediates have been proved to be capable of fixing carbon dioxide, even at low partial CO₂ pressure as it occurs in atmosphere (CO₂ concentration in air is 325 ppm).¹⁵ UV-Vis monitoring experiment was performed exposing a solution of the oligomerically presumed complexes $[(H33+33m)_nCu^{II}_{2n}(\mu-OH)_{2n}]^{2n+}$ ($n = 1, 2, 3, \dots$) to open air. Electronic spectrum changed to final carbonato complex typical spectrum in less than 10 minutes. Similar time-scale CO₂ fixation rates are found in literature,^{8a} but those experiments are done using higher concentrations of CO₂ gas.

Figure 7. UV-Vis monitoring study of the CO₂ fixation. a) spectrum for initial bis(hydroxo) species, b) spectrum after 10 min air exposure, c) 15 min. Conditions: CH₃CN, R.T., [H33+33m]= 2.64 mM, [Cu^{II}]= 5.28 mM.



Carbonate bridging groups in complex $[(\text{H33+33m})_2\text{Cu}^{\text{II}}_4(\mu\text{-CO}_3)_2]^{4+}$ (**12**) can be removed if NaOH is added to a acetonitrile solution under Ar atmosphere, to form the corresponding bis(μ -hydroxo) complexes $[(\text{H33+33m})_n\text{Cu}^{\text{II}}_{2n}(\mu\text{-OH})_{2n}]^{4+}$ ($n = 1, 2, 3, \dots$) as seen by UV-Vis analysis. Crystallization of these hydroxo complexes has been pursued without success.

6.4.5 Antiferromagnetic compounds

6.4.5.1 $[(\mu\text{-H33+33mO})\text{Cu}^{\text{II}}_2(\mu\text{-OH})](\text{PF}_6)_2 \cdot \text{CH}_3\text{CN}$ (**11**-
(PF_6)₂·CH₃CN)

Magneto-structural correlations¹⁶ and theoretical calculations¹⁷ establish the relationship between the Cu-O-Cu bridge angle and the magnitude of the exchange coupling constant ($-J$). Complex **11**-(PF_6)₂ is strongly coupled ($J = -515.8(2) \text{ cm}^{-1}$) and falls in the experimental range found for hydroxide-phenoxide bridged complexes ($-J = 300\text{-}700 \text{ cm}^{-1}$), having $\text{Cu}_2\text{N}_4\text{O}_2$ type chromophores with $\text{Cu}\cdots\text{Cu}$ distances of $\sim 3.05 \pm 0.05 \text{ \AA}$ and a $\text{Cu-O}_{\text{hy}}\text{-Cu}$ bridge angle of $103 \pm 2^\circ$.¹⁸ On the contrary, complex **11**-(PF_6)₂, bearing a $\text{Cu}_2\text{N}_6\text{O}_2$ chromophore, should be seen as an exception of the trend observed in several phenoxo-bridged dicopper complexes.¹⁹ These complexes display a $-J > 420 \text{ cm}^{-1}$ for $\text{Cu-O}_{\text{ph}}\text{-Cu}$ bridge angle greater than 99° , and this angle is $\text{Cu-O}_{\text{ph}}\text{-Cu}$ 97.4° for **11**. Therefore, other factors that can affect the J value must be considered, as for instance the degree of distortion from the Cu_2O_2 core planar geometry imposed by the ligand constrains.^{18,20} Usually, flat Cu_2O_2 core disposition favors stronger spin exchange interactions as it is seen in bis(μ_2 -phenoxide)-bridged copper complexes ($-2J = 689\text{-}902 \text{ cm}^{-1}$, $\text{Cu-O}_{\text{ph}}\text{-Cu}$ $98.8\text{-}104.7^\circ$).²⁰ In complex **11**, the core Cu_2O_2 distortion has been calculated as the angle formed by mean planes of both bases from pyramids (see Table 3), which is 139.42° , so Cu_2O_2 core atoms are significantly bent from coplanarity.

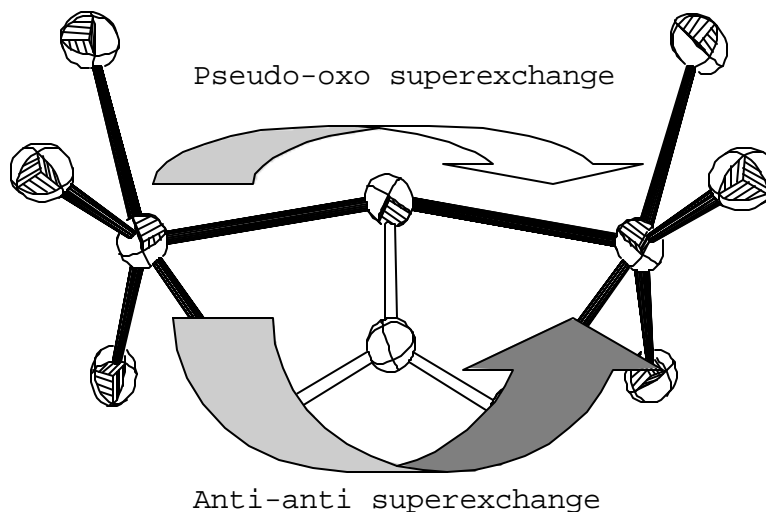
High antiferromagnetic coupling constants are typical for dinuclear copper complexes with bridging chlorides where square-planar pyramids drawn by each copper are sharing one side of the base, as it occurs in **11**.²¹ In complex **11**,

effective orbital overlap through the O-bridging groups allows the strong coupling.

6.4.5.2 $[(H33+33m)_2Cu^{II}_4(m-CO_3)_2](ClO_4)_4 \cdot 4H_2O \cdot 2CH_3COCH_3$ (**12**-
(ClO_4)₄·4H₂O·2CH₃COCH₃)

Magnetic coupling is explained through a superexchange mechanism modulated by the arrangement of the magnetically active atomic orbitals of the metallic ion.^{8d,22} A square-planar rearrangement maximizes the orbital overlap in a situation similar to a single oxo bridge between copper centers.^{23,24} However, examples exist where no Cu-O-Cu bridge is present and magnetic coupling is only active through an anti-anti superexchange pathway. Complex **12** represents a mixed structure with elongated Cu-O1 distances, and both coupling pathways might be present. $J = -163.4 \text{ cm}^{-1}$ for **12** agrees with this consideration and falls in between the $J = -125.5 \text{ cm}^{-1}$ for an anti-anti superexchange pathway example^{8d} and $J = -207.0 \text{ cm}^{-1}$ for pseudo-oxo superexchange pathway example.²⁴

Scheme 3. Possible Cu-Cu superexchange pathways operating through the carbonate bridge



6.4.6 New ligand H33+33mOH

Extraction of monohydroxylated ligand from complex $[(\mu\text{-H33+33mO})\text{Cu}^{\text{II}}_2(\mu\text{-OH})](\text{PF}_6)_2$ (**11**-(PF_6)₂) with ammonia and CH_2Cl_2 allowed the isolation of the novel H33+33mOH compound (see Figure S8), which can be used as a new ligand for the synthesis of complexes.

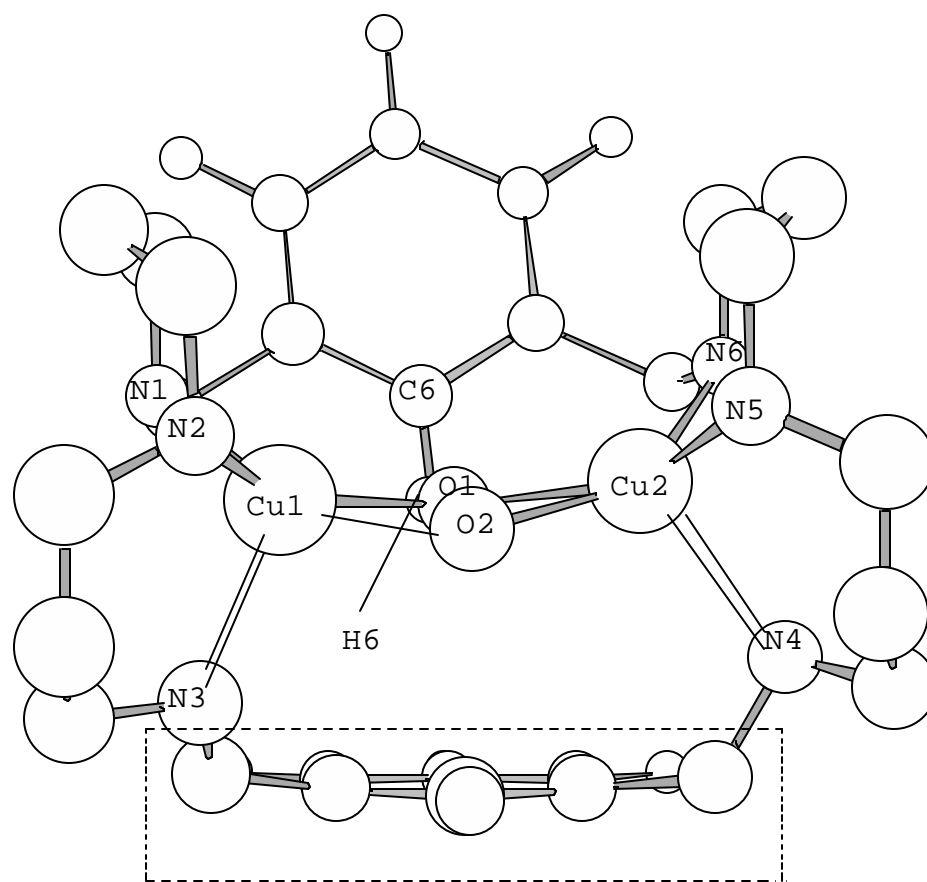
6.4.7 Theoretical calculations: postulating a peroxo intermediate

Aromatic monohydroxylation achieved in this system is one of the multiple examples found in literature. In almost all cases a $\mu:\eta^2:\eta^2$ -peroxo side-on dicopper(II) intermediate is postulated as the active species towards the attack on the aromatic ring. Then, this potential intermediate for our system was modeled by using the Amsterdam density functional (ADF)³¹⁻³³ program with the QM/MM method⁴⁰ to obtain a geometry optimization in order to predict possible interactions with the aromatic ring susceptible to be attacked. QM/MM method applies molecular mechanics to part of the molecule studied in order to reduce the computational time. The accuracy of this methodology for our dinuclear copper complexes was checked by using the crystallographic data of complex $[(\mu\text{-H33+33mO})\text{Cu}^{\text{II}}_2(\mu\text{-OH})]^{2+}$ (**11**) to calculate the optimized geometry. Excellent accurate bond distances are obtained compared with crystallographic data of **11**.

The same crystallographic data of **11** was used to design a preliminary peroxo side-on intermediate $[(\text{H33+33m})\text{Cu}^{\text{II}}_2(\text{O}_2)]^{2+}$ that was used as the starting point for the calculations. Final optimized geometry for the intermediate, depicted in Figure 8, shows that core atoms

Cu_2O_2 lie in a same plane and that the core is in close proximity to both aromatic rings of the macrocycle. Selected bond lengths are listed in Table 6. It is remarkable the disposition of the Cu_2O_2 core pointing towards the carbon C6, and also the short O1-C6 (2.555 Å) and O1-H6 (1.993 Å) distances.

Figure 8. Chem3D view of theoretical calculated geometry for peroxy side-on intermediate $[(\text{H33}+\text{33m})\text{Cu}^{\text{II}}_2(\text{O}_2)]^{2+}$ proposed to be the active species for aromatic hydroxylation. Highlighted the part of the molecule were MM is applied.



The dihedral angle formed by the Cu_2O_2 plane and the aromatic ring is $\sim 45^\circ$, suggesting that the attack of the HOMO of the arene ring is more likely to interact with the

LUMO+1 (which is σ^* type) of the Cu_2O_2 core instead of the LUMO (which is π^* type).^{25,26} Although π^* pathway has been favored in other systems, a better orientation of atoms for a σ^* attack is found in our case, probably due to the ligand constrains in the system.

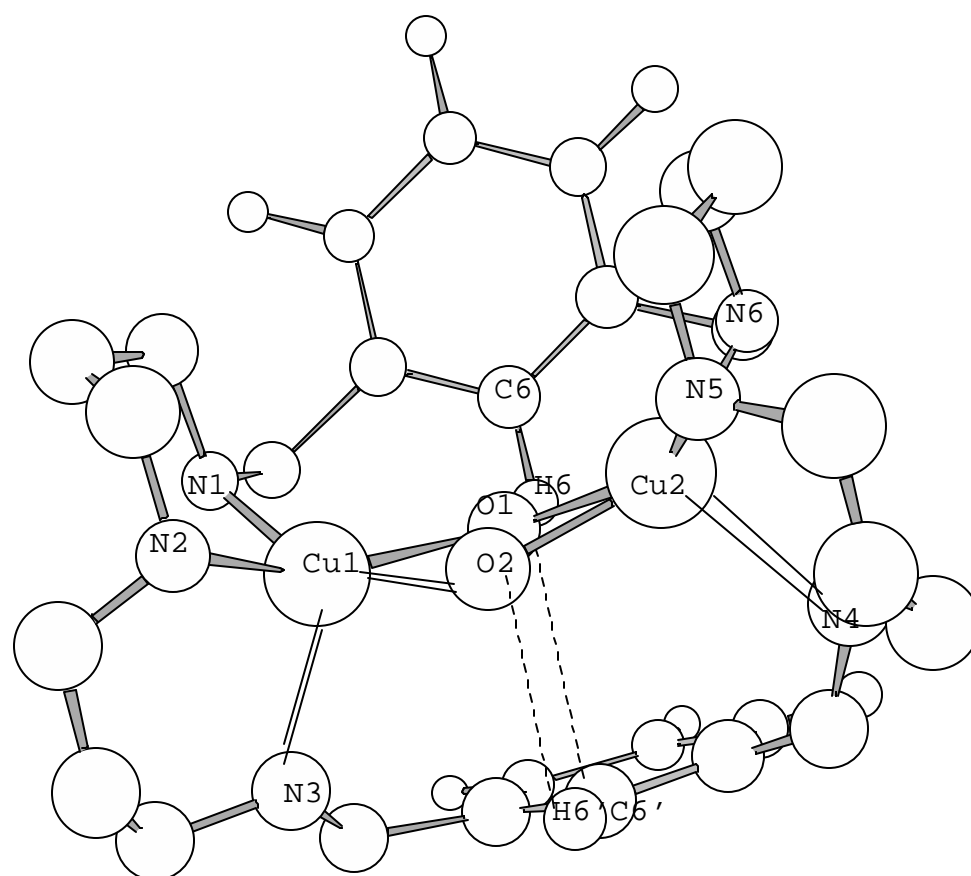
Table 6. Selected bond lengths and angles for optimized geometry of $[(\text{H}33+33\text{m})\text{Cu}^{\text{II}}_2(\text{O}_2)]^{2+}$.

Cu1-O1	1.909	Cu2-O1	1.912
Cu1-O2	2.000	Cu2-O2	1.977
Cu1-N1	2.011	Cu2-N6	2.025
Cu1-N2	1.997	Cu2-N5	1.985
Cu1-N3	2.162	Cu2-N4	2.273
Cu1...Cu2	3.590	O1-O2	1.434
O1...H6	1.993	O1...C6	2.555
O1...C6'	2.933	O2...H6'	2.815
O2-Cu1-N1	144.7	O2-Cu1-O1	43.0
N1-Cu1-O1	106.4	O2-Cu2-O1	43.2
O2-Cu1-N2	102.7	O2-Cu2-N6	144.4
N1-Cu1-N2	95.3	N6-Cu2-O1	106.2
O1-Cu1-N2	140.1	O2-Cu2-N5	99.4
O2-Cu1-N3	101.4	N6-Cu2-N5	96.9
N1-Cu1-N3	106.9	O1-Cu2-N5	136.6
O1-Cu1-N3	109.2	O2-Cu2-N4	117.2
N2-Cu1-N3	95.4	N6-Cu2-N4	91.7
Cu2-O1-Cu1	140.0	O1-Cu2-N4	118.0
Cu1-O2-Cu2	129.0	N5-Cu2-N4	97.1

Another view of the same optimized geometry for $[(\text{H}33+33\text{m})\text{Cu}^{\text{II}}_2(\text{O}_2)]^{2+}$ is depicted in Figure 9 (selected bonds in Table 6). An interesting proximity and orientation of the peroxo core to the other aromatic ring of the macrocycle is found, being placed just below the core and parallel to the O-O axis. Thus, a π - π interaction between

the C6-H6 and O1-O2 atoms could also take place as a possible mechanism.

Figure 9. Chem3D view of peroxo side-on intermediate $[(\text{H33+33m})\text{Cu}^{\text{II}}_2(\text{O}_2)]^{2+}$, highlighting the possible interaction with the arene placed below the Cu_2O_2 core.



6.4.8 Concluding Remarks

The new compound H33+33m is a good dinucleating ligand that provides good coordinative environment for CuI and CuII species. A new example of $\text{Cu}^{\text{I}}/\text{O}_2$ reactivity towards intramolecular aromatic hydroxylation is found in $[(\mu\text{-H33+33mO})\text{Cu}^{\text{II}}_2(\mu\text{-OH})]^{2+}$ (**11**), although detection of the

reactive intermediates formed during the reaction has been elusive. Theoretical calculations on a postulated peroxo intermediate have been performed, showing that a σ^* pathway is favored for the interaction of the peroxo group with one of the arene rings. Moreover, the novel tetranuclear copper(II) complex $[(\text{H33+33m})_2\text{Cu}^{\text{II}}_4(\mu\text{-CO}_3)_2]^{4+}$ (**12**) with two bridging carbonates acting in a bidentate coordination mode has been characterized. It has been proposed that bis(μ -hydroxo) copper species is responsible of CO_2 fixation through a generally accepted hydroxide mechanism. $\text{Cu}^{\text{I}}/\text{O}_2$ interaction can undergo under different reactivity pathways and those can be modulated with control of initial Cu^{I} concentration. H33+33m/ Cu_2 system is the first to our knowledge to display both aromatic hydroxylation and CO_2 fixation reactivities.

Copper(II) complex $[(\text{H33+33m})\text{Cu}^{\text{II}}_2(\text{CH}_3\text{CN})_4]^{4+}$ (**14**) structure has helped on the interpretation of conformation possibilities of these complexes, and represents a new dinuclear example of a rare coordinating ligand-donor set N_5 for Cu^{II} .

6.5 EXPERIMENTAL SECTION

General Information. Amine N-(3-Aminopropyl)-1,3-propanediamine, isophthalaldehyde, $\text{Cu}^{\text{I}}(\text{OTf})_2$, $\text{Cu}^{\text{II}}(\text{ClO}_4)_2 \cdot 6\text{H}_2\text{O}$ where purchased from Aldrich, and all of them used without further purification. Analytical grade solvents were purchased from SDS and dried and distilled under Ar before use. IR, Elemental Analyses, UV-Vis, FAB-MS and NMR spectra were measured on Mattson Satellite FT-IR, Fisons EA-1108, Varian Cary-50 Scan, Fisons VG-Quattro and Bruker DPX-200 MHz instruments, respectively.

Warning: Although we have experienced no problems with the compounds reported herein, perchlorate salts are potentially explosive, and should only be handled in small quantities and never heated in the solid state.

Synthesis of ligand H33+33m. Ligand H33+33m is synthesized by recrystallization of its hexahydrobromic salt²⁷ and subsequent extraction with NH₄OH/CH₂Cl₂. Product is stored under Ar. Final yield starting from the hexahydrobromic salt (0.92 g, 9.66 mmol) is 87% (0.39 g, 8.36 mmol). IR (KBr pellet, cm⁻¹): 3286 (s), 1456 (s), 1335 (s), 1157 (s), 732 (s). ¹H-NMR (**d** in CDCl₃, ppm): 7.33–7.16 (m, 8H), 3.76 (s, 8H), 2.72 (t, 16 H), 2.22 (s, 6H), 1.73 (q, 8H). ¹³C-NMR (**d** in CDCl₃, ppm): 140.4, 128.4, 127.6, 126.9, 53.9, 48.8, 48.2, 29.0. Elemental analysis calcd. for C₂₈N₆H₄₆·0.75CH₂Cl₂: C 65.1 N 15.8 H 9.0; found: C 65.1 N 15.8 H 9.3. FAB-MS: m/z= 467 (M⁺).

Complexes Synthesis.

Cu^I(CH₃CN)₄(X) (X= ClO₄⁻, PF₆⁻) synthesis are reported elsewhere.²⁸

[(H33+33m)Cu^I₂(CO)₂](PF₆)₂ (10-(PF₆)₂). A solution of ligand H33+33m (0.03 g, 0.064 mmol) in CH₂Cl₂ (1 mL) saturated with CO was added to 1 mL CH₂Cl₂ solution of Cu^I(CH₃CN)₄(PF₆) (0.048 g, 0.128 mmol). CO flow is bubbled for 5 minutes under stirring. Solution is filtrated under CO atmosphere over diethylic ether saturated with CO. Cooling the solution allows full precipitation of white compound. Solvent is removed and solid dried under vacuum, obtaining a white powder in 84% yield (0.052 g, 0.054 mmol). IR (KBr pellet, cm⁻¹): 3215 (NH), 2068 (CO), 1459 (C=C ar), 845, 559 (PF₆); ¹H-NMR (**d** in CD₃CN, ppm): 7.52–6.98 ppm (m, 8H),

3.72 (m, 8H), 2.97 (m, 22 H), 1.87–1.76 (m, 8H); elemental analysis calcd. for $\text{Cu}_2\text{C}_{30}\text{H}_{46}\text{N}_6\text{P}_2\text{F}_{12}\text{O}_2 \cdot 0.5\text{CH}_3\text{CN}$ (%): C 38.8, H 5.0, N 9.5; found: C 39.0, H 5.3, N 9.4.

Complex **10**-(ClO₄)₂ is prepared in a similar way and yields. Satisfactory characterization is also achieved.

[(m-H33+33mO)Cu^{II}₂(m-OH)](PF₆)₂ (11-(PF₆)₂). A colorless solution of complex **10**-(PF₆)₂ (0.015 g, 0.016 mmol) in 3.4 mL of CH₃CN/Acetone 85/15 is bubbled with O₂ flow during 5 minutes at room temperature. The deep green resulting solution is filtered and exposed to slow diffusion of diethyl ether under O₂ saturated atmosphere. Green crystals appear after more than 24 hours in 75% isolated yield (0.011g, 0.012 mmol). IR (KBr pellet, cm⁻¹): 3446 (s), 3296 (s), 1596 (w), 1459 (m), 1300 (w), 1080 (w), 844 (s), 558 (s); elemental analysis calcd. for $\text{Cu}_2\text{C}_{28}\text{H}_{46}\text{N}_6\text{O}_2\text{F}_6\text{P} \cdot 0.5\text{H}_2\text{O}$: C 37.2, H 5.1, N 9.7; found: C 37.1, H 5.2, N 9.8; UV-Vis (CH₃CN): λ_{max} (ε) = 342 (3500), 636 (400); ESI-MS: m/z = 769 (M^+ - PF₆⁻).

Complex **11**-(ClO₄)₂ is obtained the same way and in similar yields.

[(H33+33m)₂Cu^{II}₄(m-CO₃)₂](ClO₄)₄ (12-(ClO₄)₄).

Method 1. A solution of complex **10**-(ClO₄)₂ (0.1 g, 0.118 mmol) in 5 mL of Acetone/H₂O 98/2 degassed with Ar is bubbled with O₂ flow during 5 minutes. Green solution is filtered and exposed to open air overnight. Blue crystals appear and are filtered out and washed with acetone, giving the desired product in 22% yield (0.024 g, 0.0126 mmol).

IR (KBr pellet, cm⁻¹): 3245 (s), 1486 (s), 1452 (s), 1117(s), 671 (s); elemental analysis calcd. for $\text{Cu}_4\text{C}_{58}\text{H}_{92}\text{N}_{12}\text{O}_{22}\text{Cl}_4 \cdot 6\text{H}_2\text{O} \cdot \text{CH}_3\text{COCH}_3$: C 39.1, H 5.9, N 9.0; found: C 38.8, H 5.6, N 8.8; UV-Vis (CH₃CN): λ_{max} (ε) = 678 (1540). ESI-MS: m/z = 751 (M^+ - 2ClO₄⁻), 468 (M^+ - 3ClO₄⁻).

Method 2. Ligand H33+33m (0.035 g, 0.075 mmol) and $\text{Cu}^{\text{II}}(\text{ClO}_4)_2 \cdot 6\text{H}_2\text{O}$ (0.054 g, 0.15 mmol) are dissolved in 3 mL of $\text{CH}_2\text{Cl}_2/\text{CH}_3\text{OH}$ 20/80. Degassed solution of NaOH 0.5 mM (0.3 mL, 0.15 mmol) is added and mixture stirred for 10 minutes. Solution is filtered and exposed to open air overnight. Blue crystals are obtained in 94% yield (0.065, 0.035 mmol).

Elemental analysis calcd. for $\text{Cu}_4\text{C}_{58}\text{H}_{92}\text{N}_{12}\text{O}_{22}\text{Cl}_4 \cdot 4\text{H}_2\text{O} \cdot 2\text{CH}_3\text{OH}$: C 39.1, H 5.9, N 9.1; found: C 39.2, H 5.7, N 8.8.

Complex **12**-(PF_6)₂ is prepared in a similar way and yields.

[(H33+33m)Cu^{II}₂(H₂O)₄](ClO₄)₄ (13-(ClO₄)₄). Ligand H33+33m (0.046 g, 0.099 mmol) and $\text{Cu}^{\text{II}}(\text{ClO}_4)_2 \cdot 6\text{H}_2\text{O}$ (0.073 g, 0.2 mmol) are dissolved in 2.5 mL of $\text{CH}_2\text{Cl}_2/\text{CH}_3\text{OH}$ 30/70. After 10 minutes stirring, the blue solution is filtered over diethyl ether to obtain a blue powder. After removing solvent and drying under vacuum blue compound is obtained in 77 % yield (0.085 g, 0.075 mmol). IR (KBr pellet, cm^{-1}): 3433 (s), 3202 (m), 1460 (m), 1144 (s), 1113 (s), 1088 (s), 630 (s); elemental analysis calcd. for $\text{Cu}_2\text{C}_{28}\text{H}_{54}\text{N}_6\text{O}_{20}\text{Cl}_4 \cdot 2\text{H}_2\text{O} \cdot \text{CH}_3\text{OH}$: C 30.8, H 5.4, N 7.4; found: C 30.6, H 5.1, N 7.1; UV-Vis (CH_3CN): λ_{max} (ϵ) = 656 (256).

[(H33+33m)Cu^{II}₂(CH₃CN)₄](ClO₄)₄ (14-(ClO₄)₄). Complex **13**-(ClO₄)₄ (0.041 g, 0.036 mmol) is dissolved in 3 mL of CH_3CN anhydrous and degassed with Ar. 24 hour stirring under Ar and slow diffusion of diethyl ether allowed the formation of blue-violet crystals in 82% yield (0.035 g, 0.03 mmol). IR (KBr pellet, cm^{-1}): 3217 (m), 2251 (w), 1462 (m), 1439 (m), 1144 (s), 1113 (s), 1088 (s), 629 (s); elemental analysis calcd. for $\text{Cu}_2\text{C}_{36}\text{H}_58\text{N}_{10}\text{O}_{16}\text{Cl}_4 \cdot 1.5\text{H}_2\text{O}$: C 36.6, H 5.2, N 11.8; found: C 36.5, H 5.4, N 12.1; UV-Vis (CH_3CN): λ_{max} (ϵ) = 656 (490).

Ligand H33+33mOH. Treatment of complex **11**-(PF₆)₂ (0.016g, 0.017 mmol) with NH₄OH/CH₂Cl₂ and evaporation to dryness of organic layer yielded 0.0076 g (0.0157 mmol, 88% yield) of new hexaaza monohydroxylated ligand H33+33mOH. ¹H-NMR (**d** in CDCl₃, ppm): 7.24 (m, 4H), 6.98 (d, 2H), 6.71 (t, 1H), 3.84 (s, 4H), 3.74 (s, 4H), 2.69 (m, 16 H), 1.68 (m, 8H); ¹³C-NMR (**d** in CDCl₃, ppm): 140.5, 128.8, 127.5, 126.8, 118.5, 53.9, 51.1, 48.6, 48.0, 29.7.

Mass Spectrometry. ESI-MS spectra were performed with a Thermo Quest Finigan Navigator LC/MS, that bears an atmospheric pressure ionization source (API-MS), and using the positive ionization mode (ESI⁺). Typical experimental conditions were: solvent = CH₃CN 100%, source voltage = 30 eV, temperature = 170 °C, Flux = 150 μl/min, mass range = 200-1600, 10-15 scans per LC peak and registration under profile peak format.

FAB-MS spectra were performed with a Fisons VG-Quattro (Cs tube, 10 kV voltage, 3-nitrobenzylalcohol matrix).

UV-Vis experimental procedure. A Varian Cary-50 Scan was used to register electronic spectra. Custom-designed UV-Vis cells were used to perform experiments with air-sensitive samples under controlled N₂ or Ar atmosphere. Cell temperature was thermostated with a Huber CC180 cryostat.

X-ray Structure Analysis. Analyses on a block green crystal of [(μ-H33+33mO)Cu^{II}₂(μ-OH)](PF₆)₂·CH₃CN (**11**-(PF₆)₂·CH₃CN), a plate blue crystal [(H33+33m)₂Cu^{II}₄(μ-CO₃)₂](ClO₄)₄·4H₂O·2CH₃COCH₃ (**12**-(ClO₄)₄·4H₂O·2CH₃COCH₃) and a block blue-violet crystal [(H33+33m)Cu^{II}₂(CH₃CN)₄](ClO₄)₄·2H₂O (**14**-(ClO₄)₄·2H₂O) was carried out on a Bruker SMART CCD area detector single crystal diffractometer with graphite

monochromated Mo $K\alpha$ radiation ($\lambda = 0.71073 \text{ \AA}$) operating in the ω scan method. Cell measurement temperature was 298(2) K for **11** and **14**, and 173(2) K for **12**. Data reduction, Lorentz, polarization and empirical absorption corrections were performed with the Sadabs package. Structures were solved by direct methods using SHELXS-86²⁹ and refined by full-matrix least-squares analysis with SHELXL-93.³⁰ Disordered hexafluorophosphate F atoms are found in complex **11**-(PF₆)₂ and perchlorate O atoms in **14**-(ClO₄)₄. A summary of the crystallographic data is given in Table 1.

Magnetic Measurements. Magnetic susceptibility measurements for complexes $[(\mu\text{-H33+33mO})\text{Cu}^{\text{II}}_2(\mu\text{-OH})](\text{PF}_6)_2$ (**11**-(PF₆)₂) and $[(\text{H33+33m})_2\text{Cu}^{\text{II}}_4(\mu\text{-CO}_3)_2](\text{ClO}_4)_4$ (**12**-(ClO₄)₄) were carried out with a Faraday type magnetometer (MANICS DSM8) equipped with an Oxford CF 1200 S helium continuous-flow cryostat working in the temperature range 4-300 K. Diamagnetic corrections were estimated from Pascal Tables. EPR spectra were recorded at X-band (9.4 GHz) frequencies with a Bruker ESP-300E spectrometer, from room temperature to 4 K.

Computational details. The reported calculations were carried out by using the Amsterdam density functional (ADF) program system, developed by Baerends *et al.*^{31,32,33} The numerical integration scheme employed was that of te Velde and Baerends.³⁴ An uncontracted triple- ζ basis set³⁵ was used for describing the 3s, 3p, 3d, 4s, and 4p orbitals of copper. For carbon (2s,2p), nitrogen (2s,2p), oxygen (2s,2p), and hydrogen (1s), double- ζ basis sets³⁵ were employed and augmented by an extra polarisation function. Electrons in lower shells were treated within the frozen core approximation.^{32a} A set of auxiliary s, p, d, f and g functions,³⁶ centered in all nuclei, was introduced in

order to fit the molecular density and Coulomb potential accurately in each SCF cycle. Geometries were fully optimized within the local density approximation (LDA), which includes the X_α exchange ($\alpha=2/3$),³⁷ together with the electron gas correlation functional in the Vosko-Wilk-Nusair parametrization.³⁸ The analytical gradients implemented by Versluis and Ziegler³⁹ were employed to perform geometry optimizations.

Owing to computational limitations, both geometry optimizations and energy evaluation have been carried out with the QM/MM method available in the ADF program, which includes the standard molecular mechanics force fields in such a way that the QM and MM parts are coupled self-consistently.⁴⁰ The QM/MM model considered in this work is displayed in Figure 8. Basically, the MM part involves the one aromatic ring in the ligand. As for the connection between the QM and MM parts, this occurs by means of the so called "capping" dummy hydrogen atoms, which are replaced in the real system by the corresponding "linking" carbon atom.^{40,41} In the QM/MM optimizations the ratio between the C-N bonds crossing the QM/MM border, and the corresponding optimized C-H distances, was fixed equal to 1.38. A more detailed description of the coupling scheme, as well as further comments on the methodology, can be found in previous papers.^{41,42,43} The AMBER95 force field⁴⁴ was used for the MM potentials, except for Cu, which was treated with the UFF force field.⁴⁵ To eliminate spurious stabilizations from the long-range attractive part of the Lennard-Jones potential,^{43,46} we used an exponential expression fitted to the repulsive part of the Lennard-Jones potential.^{43,47,48,49} The 2000.02 release of the ADF package was used for these calculations.⁵⁰

6.6 REFERENCES

- ¹ (a) R. W. Cruse, S. Kaderli, K. D. Karlin, A. D. Zuberbühler, *J. Am. Chem. Soc.* **1988**, *110*, 6882; (b) K. D. Karlin, M. S. Nasir, B. I. Cohen, R. W. Cruse, S. Kaderli, A. D. Zuberbühler, *J. Am. Chem. Soc.* **1994**, *116*, 1324; (c) L. Casella, E. Monzani, M. Gullotti, D. Caravagnoni, G. Cerina, L. Santagostini, R. Ugo, *Inorg. Chem.* **1996**, *35*, 7516; (d) R. Menif, A. E. Martell, P. J. Squattrito, A. Clearfield, *Inorg. Chem.* **1991**, *29*, 4723; (e) S. Mahapatra, S. Kaderli, A. Llobet, Y. M. Neuhold, T. Palanché, J. A. Halfen, V. G. Young, Jr., T. A. Kaden, L. Que, Jr., A. D. Zuberbühler, W. B. Tolman, *Inorg. Chem.* **1997**, *36*, 6343-6356; (f) S. Ryan, H. Adams, D. E. Fenton, M. Becker, S. Schindler, *Inorg. Chem.* **1998**, *37*, 2134-2140
- ² (a) K. D. Karlin, P. L. Dahlstrom, S. N. Cozzette, P. M. Scensny, J. Zubieta, *J. Chem. Soc. Chem. Commun.* **1981**, 881; (b) T. N. Sorrell, M. L. Garrity, *Inorg. Chem.* **1991**, *30*, 210; (c) T. N. Sorrell, V. Vankai, M. L. Garrity, *Inorg. Chem.* **1992**, *31*, 207; (d) L. Casella, M. Gullotti, R. Radaelli, P. DiGennaro, *J. Chem. Soc. Chem. Commun.* **1991**, 1611
- ³ (a) L. Casella, M. Gullotti, G. Pallanza, L. Rigoni, *J. Am. Chem. Soc.* **1988**, *110*, 4221; (b) L. Casella, M. Gullotti, M. Bartosek, G. Pallanza, E. Laurenti, *J. Chem. Soc. Chem. Commun.* **1991**, 1235
- ⁴ (a) S. Mahapatra, V. G. Young, S. Kaderli, A. D. Zuberbühler, W. B. Tolman, *Angew. Chem. Int. Ed. Engl.* **1997**, *36*, 130; (b) P. L. Holland, K. R. Rodgers, W. B. Tolman, *Angew. Chem. Int. Ed. Engl.* **1999**, *38*, 1139.
- ⁵ (a) J. A. Halfen, S. Mahapatra, E. C. Wilkinson, S. Kaderli, V. G. Young, Jr., L. Que, Jr., A. D. Zuberbühler, W. B. Tolman, *Science* **1996**, *271*, 1397-1400; (b) P. L. Holland, K. R. Rodgers, W. B. Tolman, *Angew. Chem.* **1999**,

111, 1210-1213; *Angew. Chem. Int. Ed.* **1999**, *38*, 1139; (c) V. Mahadevan, R. J. M. K. Gebbink, T. D. P. Stack, *Curr. Opin. Chem. Bio.* **2000**, 228-234

⁶ (a) D. Ghosh, R. Mukherjee, *Inorg. Chem.* **1998**, *37*, 6597-6605. (b) E. Monzani, G. Battaini, A. Perotti, L. Casella, M. Gulloti, L. Santagostini, G. Nardin, L. Randaccio, S. Geremia, P. Zanello, G. Opromolla, *Inorg. Chem.* **1999**, *38*, 5359-5369; (c) A. M. García, J. Manzur, M. T. Garland, R. Baggio, O. González, O. Peña, S. Spodine, *Inorg. Chim. Acta* **1996**, *248*, 247-255; (d) L. Chen, L. K. Thompson, J. N. Bridson, *Inorg. Chim. Acta* **1996**, *244*, 87-93; (e) M. Costas, A. Llobet, unpublished results

⁷ (a) S. J. Dodgson, R. E. Tashian, G. Gros, N. D. Carter, *The Carbonic Anhydrases*; Plenum Press: NY, 1991; (b) D. N. Silverman, S. Lindskog, *Acc. Che. Res.* **1988**, *21*, 30-36.

⁸ (a) N. Kitajima, S. Hikichi, M. Tanaka, Y. Moro-oka, *J. Am. Chem. Soc.*, **1993**, *115*, 5496; (b) N. N. Murthy, K. D. Karlin, *J. Chem. Soc., Chem. Commun.* **1993**, 1236-1238; (c) C. Bazzicalupi, A. Bencini, A. Bianchi, F. Corana, V. Fusi, C. Giorgi, P. Paoli, P. Paoletti, B. Vantancoli, C. Zanchini, *Inorg. Chem.* **1996**, *35*, 5540-5548; (d) A. Escuer, F. A. Mautner, E. Peñalba, R. Vicente, *Inorg. Chem.* **1998**, *37*, 4190-4196; (e) M. Rodríguez, A. Llobet, M. Corbella, M. A. Usón, P. Müller, A. E. Martell, J. Reibenspies, submitted.

⁹ S. Lindskog, *Zinc Enzymes*; I. Bertini, C. Luchinat, W. Maret, M. Zepperauer, Eds.; Birkhauser, Boston, 1986, pp 307.

¹⁰ R. W. Hay, D. T. Richens, G. Wyllie, A. Danby, T. Clifford, *Transition. Met. Chem.* **1995**, *20*, 220.

¹¹ A. W. Addison, T. N. Rao, J. Reedijk, J. V. Rijn, G. C. Verschoor, *J. Chem. Soc., Dalton Trans.* **1984**, 1349.

- ¹² A. R. Davis, F. W. B. Einstein, N. F. Curtis, J. W. L. Martin, *J. Am. Chem. Soc.* **1978**, *100*, 6258.
- ¹³ E. Monzani, L. Casella, G. Zoppellaro, M. Gulloti, R. Pagliarin, R. P. Bonomo, G. Tabbi, G. Nardin, L. Randaccio, *Inorg. Chim. Acta* **1998**, *282*, 180
- ¹⁴ M. J. Scott, S. C. Lee, R. H. Holm, *Inorg. Chem.* **1994**, *33*, 4651
- ¹⁵ J. Heicklen, *Atmospheric Chemistry*; Academic Press: New York, 1976, pp 406.
- ¹⁶ V. H. Crawford, H. W. Richardson, J. R. Wasson, D. H. Hodgson, W. E. Hatfield, *Inorg. Chem.* **1976**, *15*, 2107
- ¹⁷ E. Ruiz, P. Alemany, S. Alvarez, J. Cano, *Inorg. Chem.* **1997**, *36*, 3683-3688
- ¹⁸ A. Asokan, P. T. Manoharan, *Inorg. Chem.* **1999**, *38*, 5642-5654.
- ¹⁹ (a) P. Amudha, M. Kandaswamy, L. Govindasamy, D. Velmurugan, *Inorg. Chem.* **1998**, *37*, 4486-4492. (b) Y. Nishida, H. Shimo, H. Maehara, S. Kida, *J. Chem. Soc., Dalton Trans.* **1985**, 1945
- ²⁰ L. K. Thompson, S. K. Mandal, S. S. Tandon, J. N. Bridson, M. K. Park, *Inorg. Chem.* **1996**, *35*, 3117
- ²¹ M. Rodríguez, A. Llobet, M. Corbella, *Polyhedron* **2000**, *19*, 2483-2491
- ²² P. V. Bernhardt, *Inorg. Chem.* **2001**, *40*, 1086-1092.
- ²³ A. R. Davis, F. W. B. Einstein, *Inorg. Chem.* **1980**, *19*, 1203
- ²⁴ J. S. Sletten, H. Hope, M. Julve, O. Kahn, M. Verdaguer, A. A. Dvorkin, *Inorg. Chem.* **1988**, *27*, 542.
- ²⁵ E. Pidcock, H. V. Obias, C. X. Zhang, K. D. Karlin, E. I. Solomon, *J. Am. Chem. Soc.* **1998**, *120*, 7841-7847
- ²⁶ H. Decker, R. Dillinger, F. Tuczek, *Angew. Chem. Int. Ed.* **2000**, *39*, 1591-1595

- ²⁷ A. Llobet, J. Reibenspies, A. E. Martell, *Inorg. Chem.* **1994**, 33, 5946.
- ²⁸ a) J. V. Rijn, J. Reedijk, M. Dartmann, B. Krebs, *J. Chem. Soc, Dalton Trans.* **1987**, 2579-2591. (b) G. J. Kubas, *Inorg. Synth.* **1979**, 19, 90-92; **1990**, 28, 68-70.
- ²⁹ G. M. Sheldrick, *SHELXS-86: Program for the Solution of Crystal Structures*; University of Göttingen, Germany, 1986.
- ³⁰ G. M. Sheldrick, *SHELXS-93*; University of Göttingen, Germany, 1986.
- ³¹ G. te Velde, F. M. Bickelhaupt, E. J. Baerends, C. Fonseca Guerra, S. J. A. Van Gisbergen, G. J. Snijders, T. Ziegler, *J. Comput. Chem.* **2001**, 22, 931
- ³² (a) E. J. Baerends, D. E. Ellis, P. Ros, *Chem. Phys.* **1973**, 2, 41. (b) E. J. Baerends, Ph. D. Thesis, Vrije Universiteit, Amsterdam, 1975
- ³³ W. Ravenek, *Algorithms and Applications on Vector and Parallel Computers*; H. J. J. te Riele, Th. J. Dekker, H. A. van de Vorst, Eds.; Elsevier: Amsterdam, 1987
- ³⁴ G. te Velde, E. J. Baerends, *J. Comp. Phys.* **1992**, 99, 84
- ³⁵ (a) G. J. Snijders, E. J. Baerends, P. Vernooijs, *At. Nucl. Data Tables* **1982**, 26, 483. (b) P. Vernooijs, G. J. Snijders, E. J. Baerends, *Slater Type Basis Functions for the Whole Periodic System. Internal Report*; Vrije Universiteit of Amsterdam: The Netherlands, 1981
- ³⁶ J. Krijn, E. J. Baerends, *Fit functions in the HFS method. Internal Report (in Dutch)*; Vrije Universiteit of Amsterdam, The Netherlands, 1984
- ³⁷ J. C. Slater, *Quantum Theory of Molecules and Solids*; McGraw-Hill: New York, 1974; Vol. 4
- ³⁸ S. H. Vosko, L. Wilk, M. Nusair, *Can. J. Phys.* **1980**, 58, 1200
- ³⁹ L. Versluis, T. Ziegler, *J. Chem. Phys.* **1988**, 28, 322
- ⁴⁰ F. Maseras, K. Morokuma, *J. Comput. Chem.* **1995**, 16, 1170

-
- ⁴¹ T. K. Woo, L. Cavallo, T. Ziegler, *Theor. Chem. Acc.* **1998**, *100*, 307
- ⁴² L. Deng, T. K. Woo, L. Cavallo, P. M. Margl, T. Ziegler, *J. Am. Chem. Soc.* **1997**, *119*, 6177
- ⁴³ L. Cavallo, T. K. Woo, T. Ziegler, *Can. J. Chem.* **1998**, *76*, 1457
- ⁴⁴ W. D. Cornell, P. Cieplak, C. I. Bayly, I. R. Gould, K. M. J. Merz, D. M. Ferguson, D. C. Spellmeyer, T. Fox, J. W. Caldwell, P. A. Kolmann, *J. Am Chem. Soc.* **1995**, *117*, 5179
- ⁴⁵ A. K. Rappé, C. J. Casewit, K. S. Colwell, W. A. Goddard III, W. M. Shiff, *J. Am. Chem. Soc.* **1992**, *114*, 10024
- ⁴⁶ R. R. Sauers, *J. Chem. Educ.* **1996**, *73*, 1996
- ⁴⁷ K. J. Lee, T. L. Brown, *Inorg. Chem.* **1992**, *31*, 289
- ⁴⁸ T. K. Woo, T. Ziegler, *Inorg. Chem.* **1994**, *33*, 1857
- ⁴⁹ G. Guerra, L. Cavallo, P. Corradini, P. Longo, L. Resconi, *J. Am. Chem. Soc.* **1997**, *119*, 4394
- ⁵⁰ ADF 2000, Vrije Universiteit Amsterdam: Amsterdam, The Netherlands, 2000

SUPPORTING INFORMATION FOR CHAPTER 6

Figure S1. Spectroscopic characterization for ligand H33+33m:
 (a) ^1H NMR and (b) FAB-MS

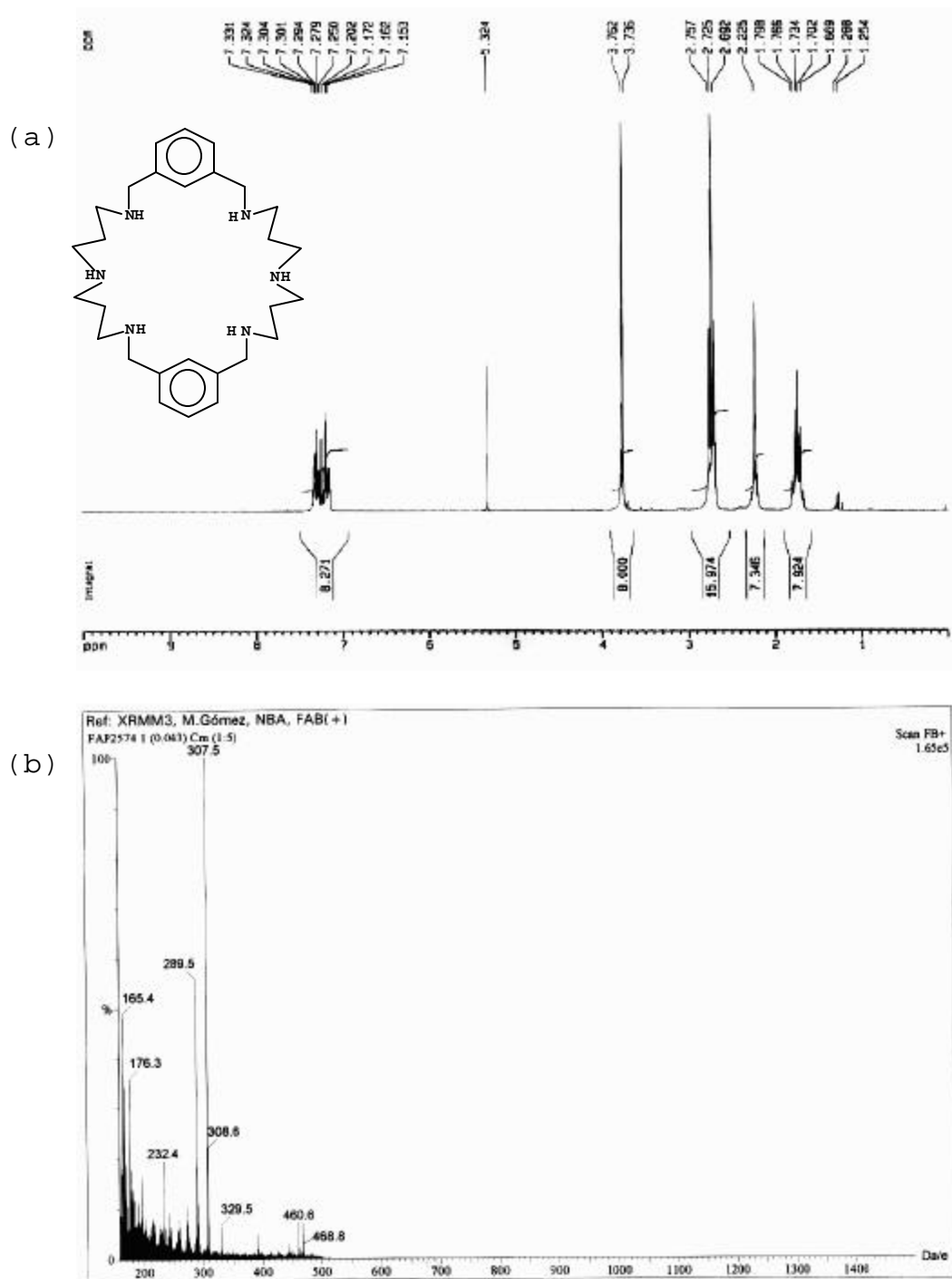
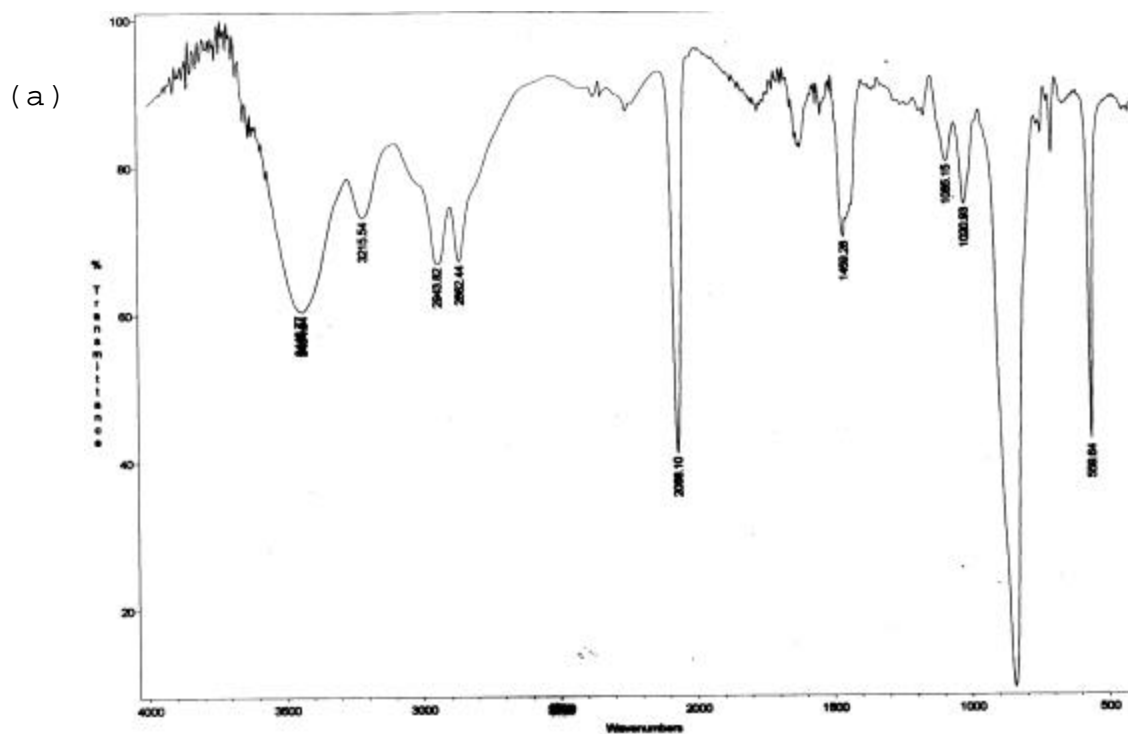


Figure S2. (a) IR and (b) ^1H NMR spectra of complex $[(\text{H}33+\text{H}33\text{m})\text{Cu}^{\text{I}}_2(\text{CO})_2](\text{PF}_6)_2$ (**10**-(PF_6) $_2$)



(b)

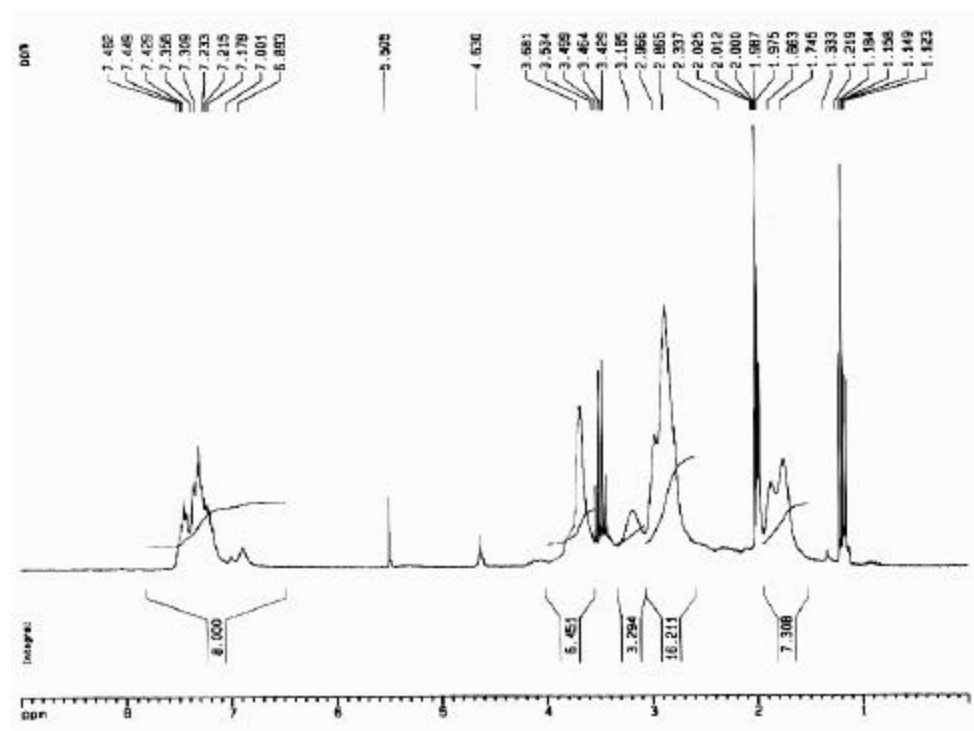


Figure S3. (a) IR and (b) ESI-MS spectrum for complex $[(\mu\text{-H33+33mO})\text{Cu}^{\text{II}}(\mu\text{-OH})](\text{PF}_6)_2$ (**11**- $(\text{PF}_6)_2$) and corresponding simulation for peak fragment.

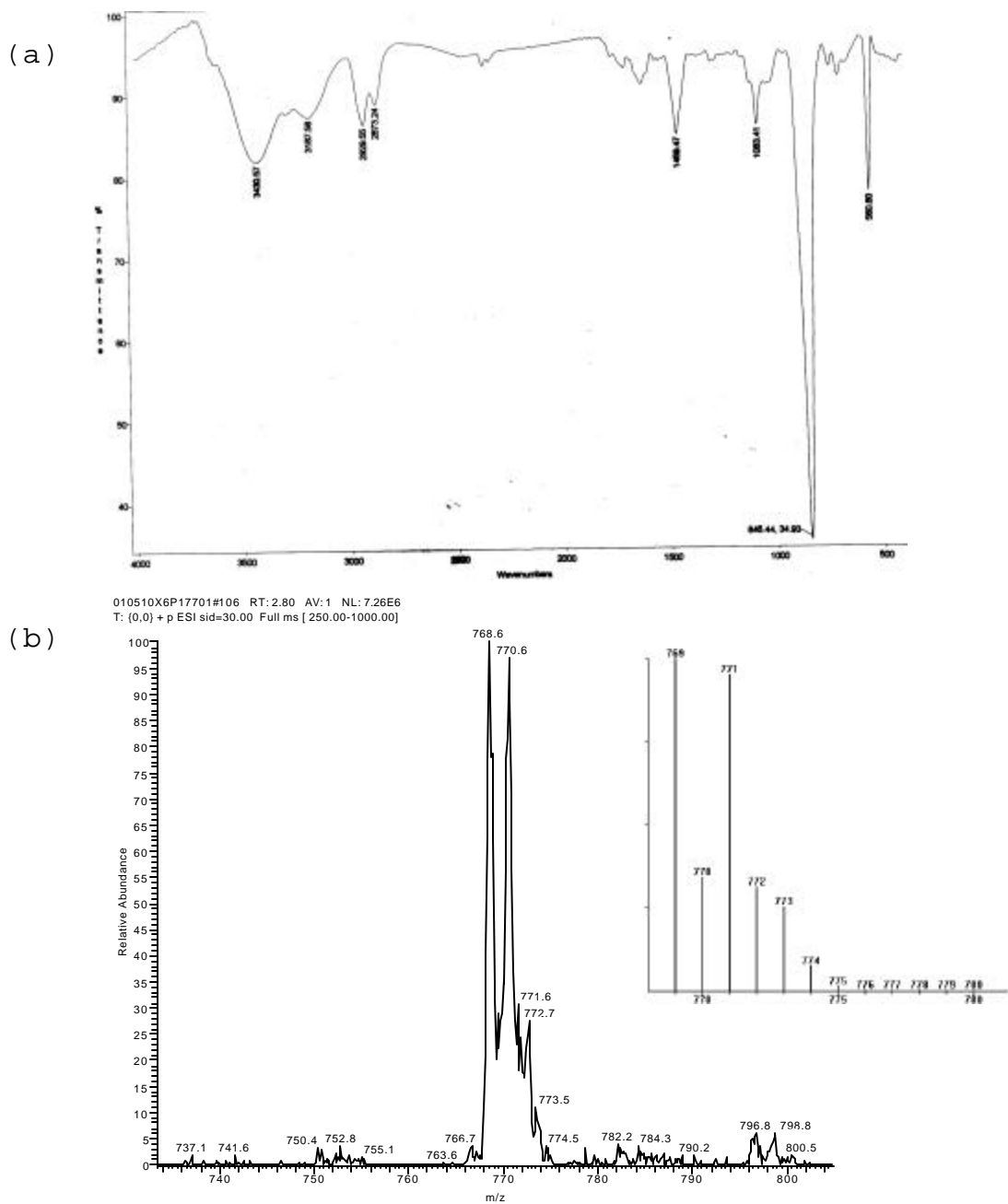
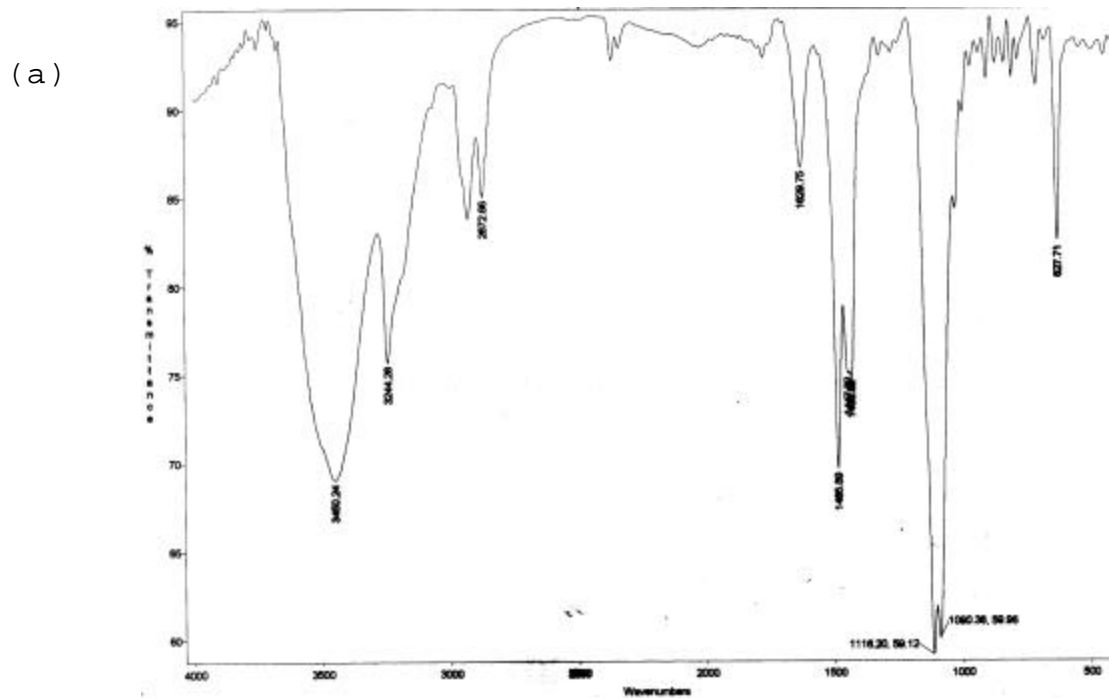


Figure S4. (a) IR and (b) ESI-MS spectrum for complex $[(\text{H}33+33\text{m})_2\text{Cu}^{\text{II}}_4(\mu\text{-CO}_3)_2](\text{ClO}_4)_4$ (**12**- $(\text{ClO}_4)_4$) and amplification of peak for fragment $[(\text{H}33+33\text{m})_2\text{Cu}^{\text{II}}_4(\mu\text{-CO}_3)_2](\text{ClO}_4)_2]^{2+}$.



010510X9P10101#72-78 RT: 3.03-3.28 AV: 7 NL: 2.82E7
T: {0,0} + p ESI sid=30.00 Full ms [421.00-1636.00]

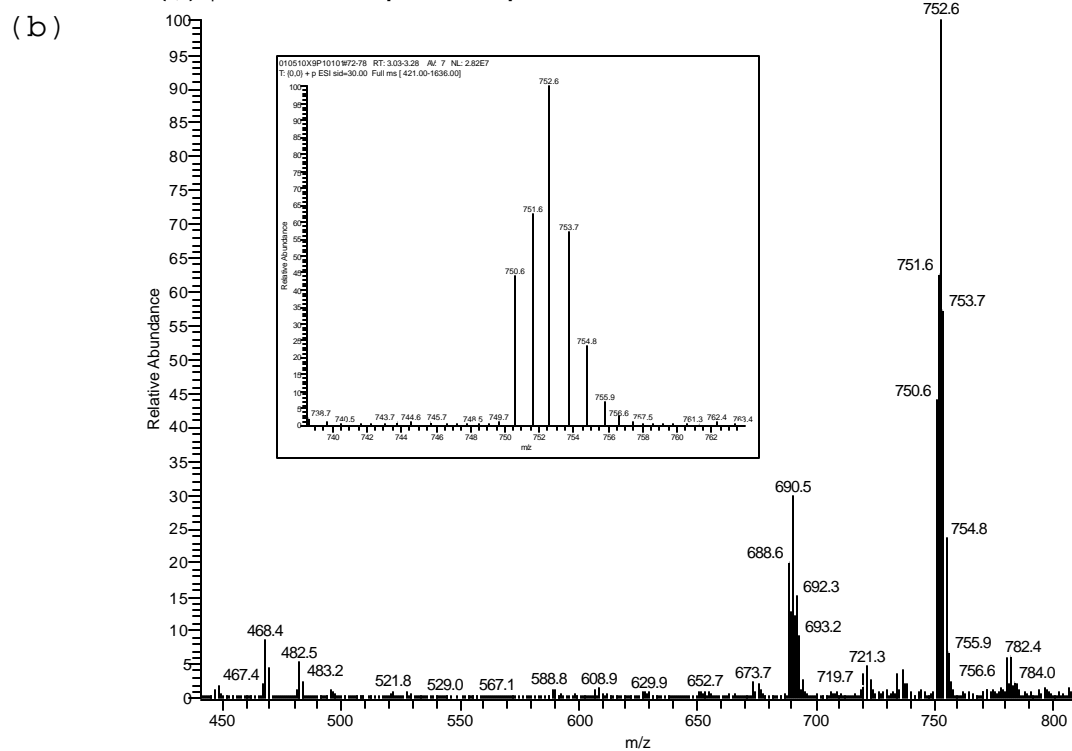


Figure S5. IR spectrum of complex $[(\text{H33+33m})\text{Cu}^{\text{II}}_2(\text{H}_2\text{O})_4] (\text{ClO}_4)_4$ (13-(ClO_4)₄)

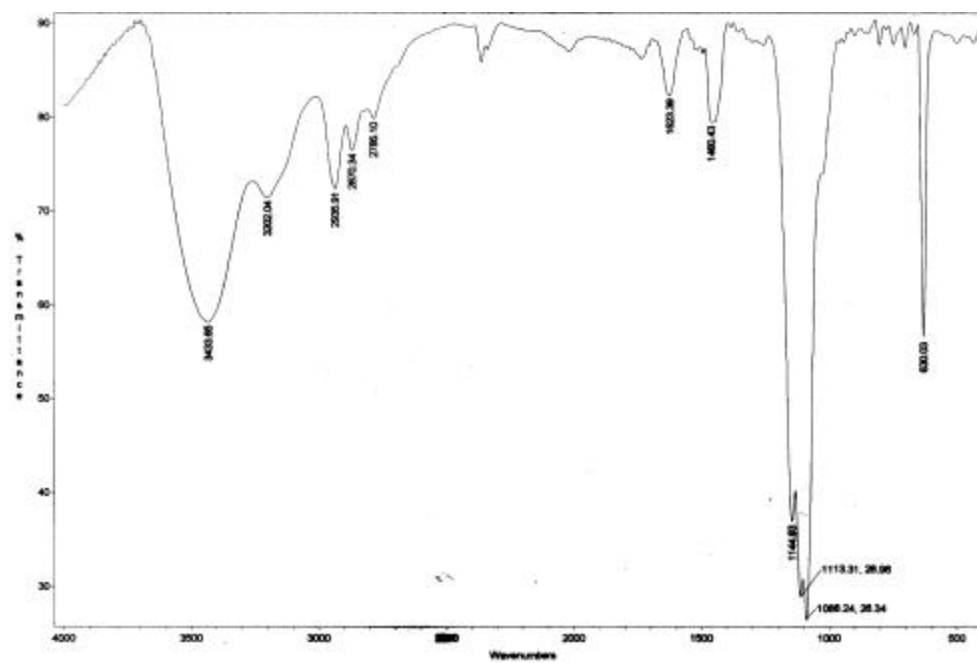


Figure S6. IR spectrum of complex $[(\text{H33+33m})\text{Cu}^{\text{II}}_2(\text{CH}_3\text{CN})_4] (\text{ClO}_4)_4$ (14-(ClO_4)₄)

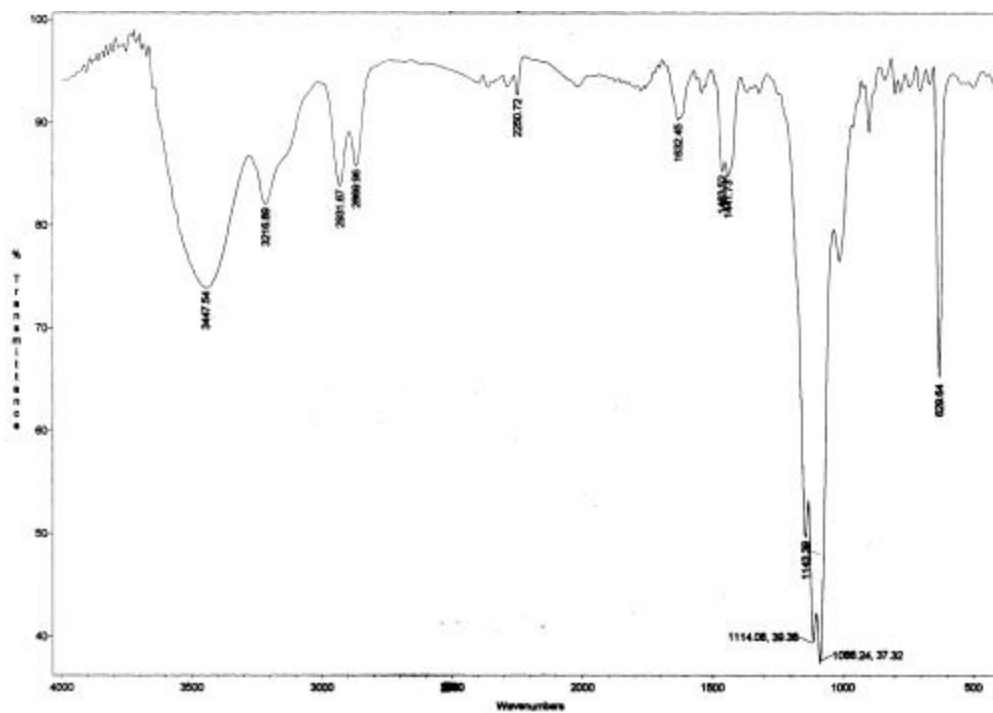
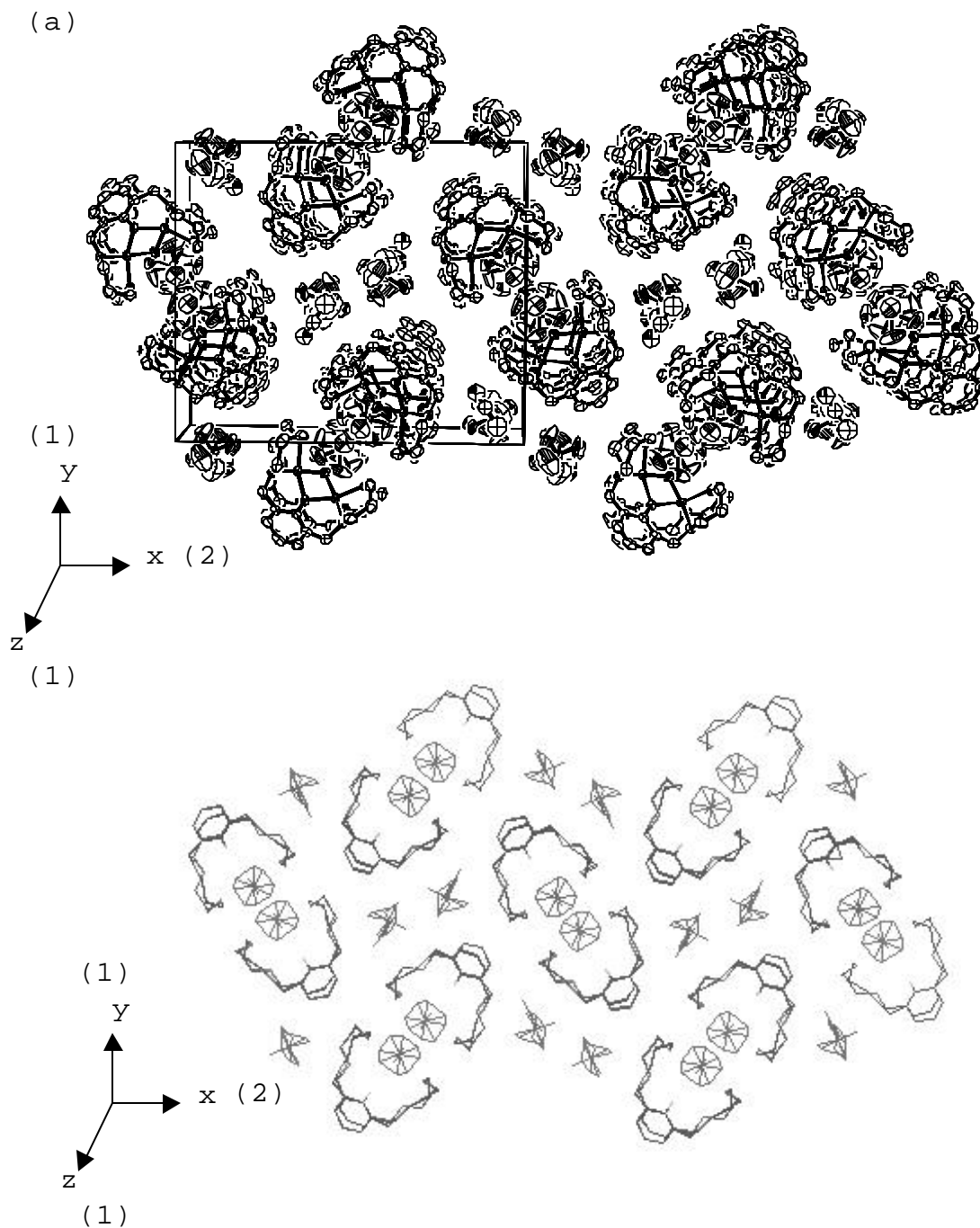
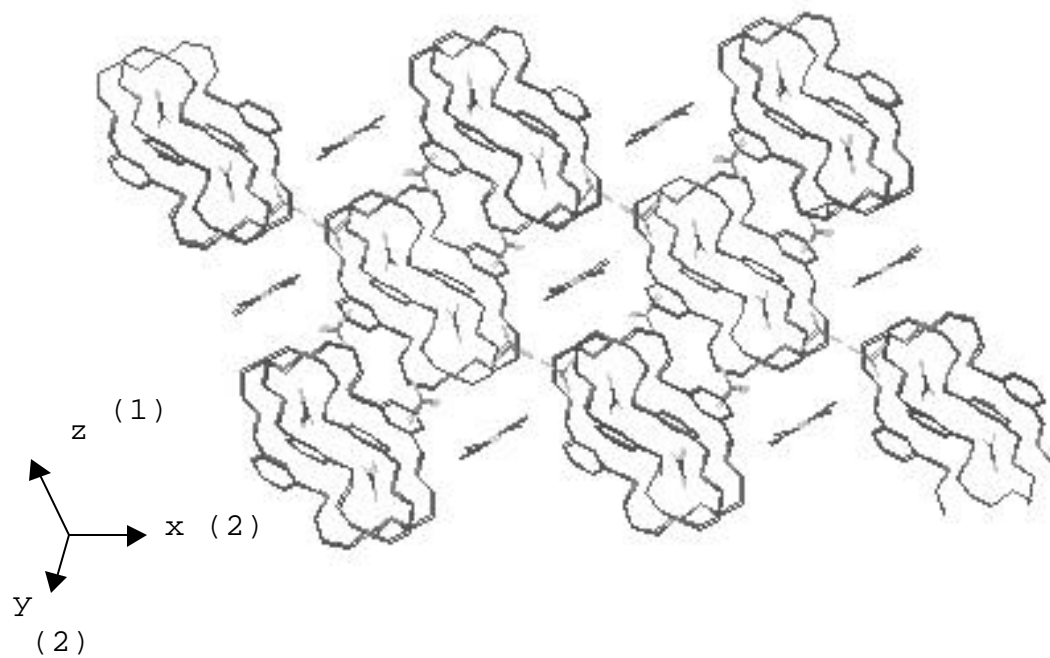
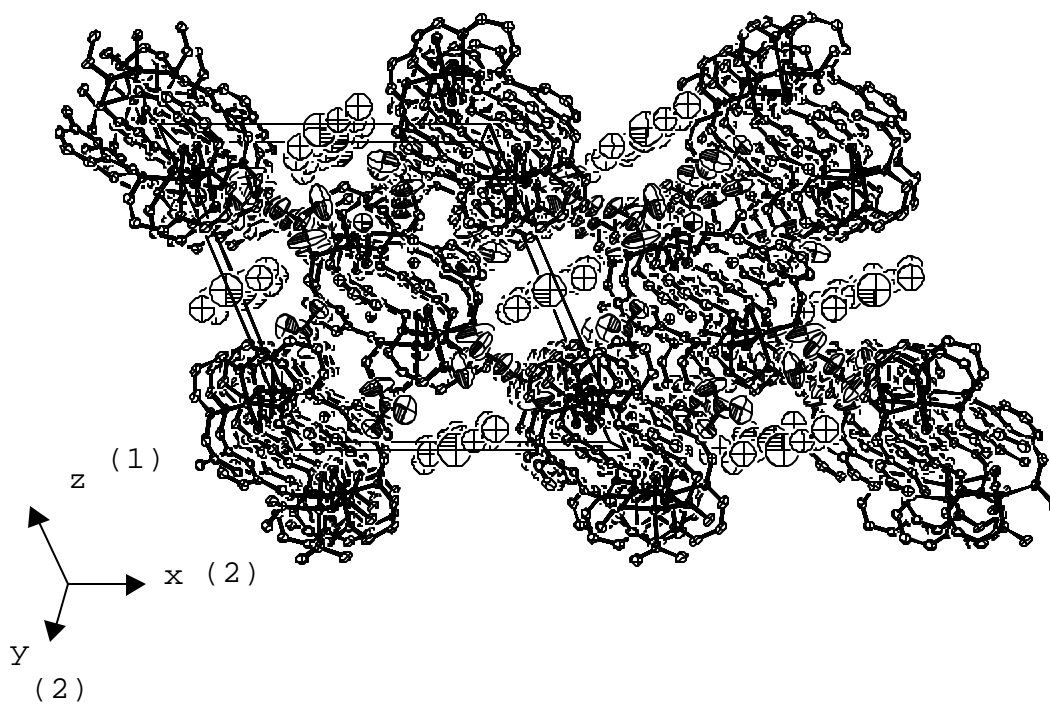


Figure S7. ORTEP and wireframe plots of packing cells for structures of complexes (a) $[(\mu\text{-H33+33mO})\text{Cu}^{\text{II}}_2(\mu\text{-OH})](\text{PF}_6)_2 \cdot \text{CH}_3\text{CN}$ (**11**- $(\text{PF}_6)_2 \cdot \text{CH}_3\text{CN}$), (b) $[(\text{H33+33m})_2\text{Cu}^{\text{II}}_4(\mu\text{-CO}_3)_2](\text{ClO}_4)_4 \cdot 4\text{H}_2\text{O} \cdot 2\text{CH}_3\text{COCH}_3$ (**12**- $(\text{ClO}_4)_4 \cdot 4\text{H}_2\text{O} \cdot 2\text{CH}_3\text{COCH}_3$), (c) $[(\text{H33+33m})\text{Cu}^{\text{II}}_2(\text{CH}_3\text{CN})_4](\text{ClO}_4)_4 \cdot 2\text{H}_2\text{O}$ (**14**- $(\text{ClO}_4)_4 \cdot 2\text{H}_2\text{O}$). Hydrogen atoms are omitted for clarity. Enclosure boxes in each axis indicated in brackets.



(b)



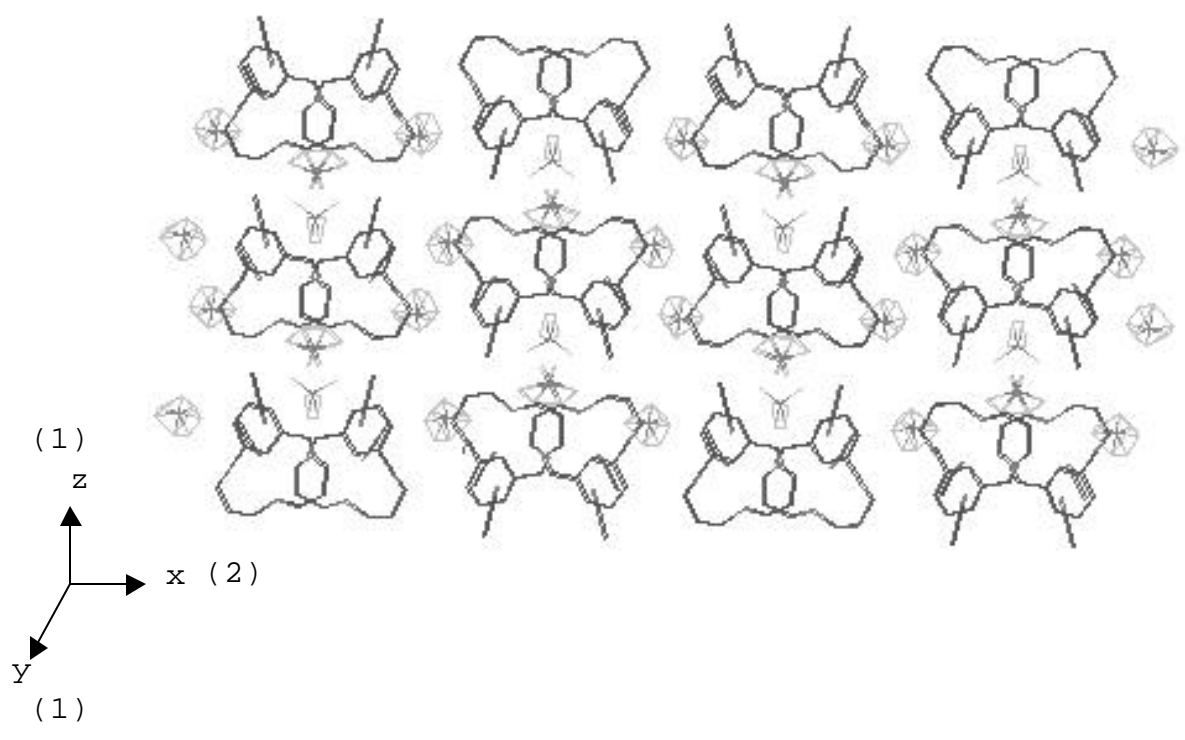
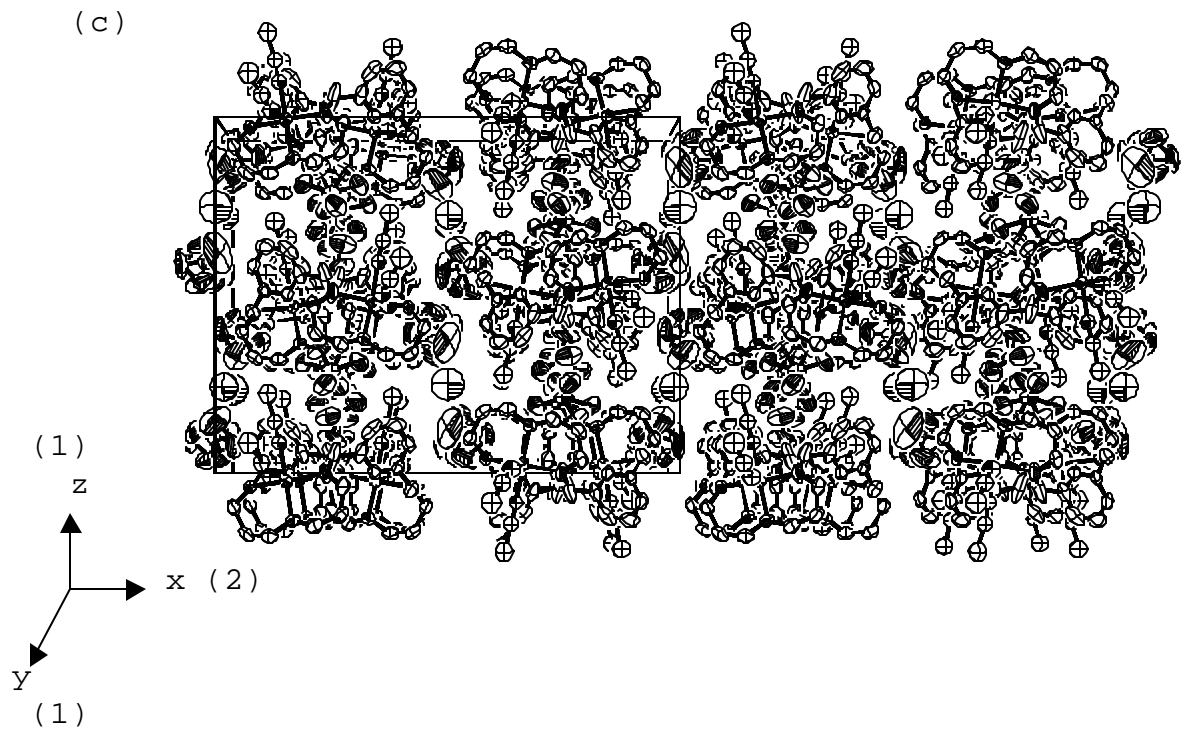
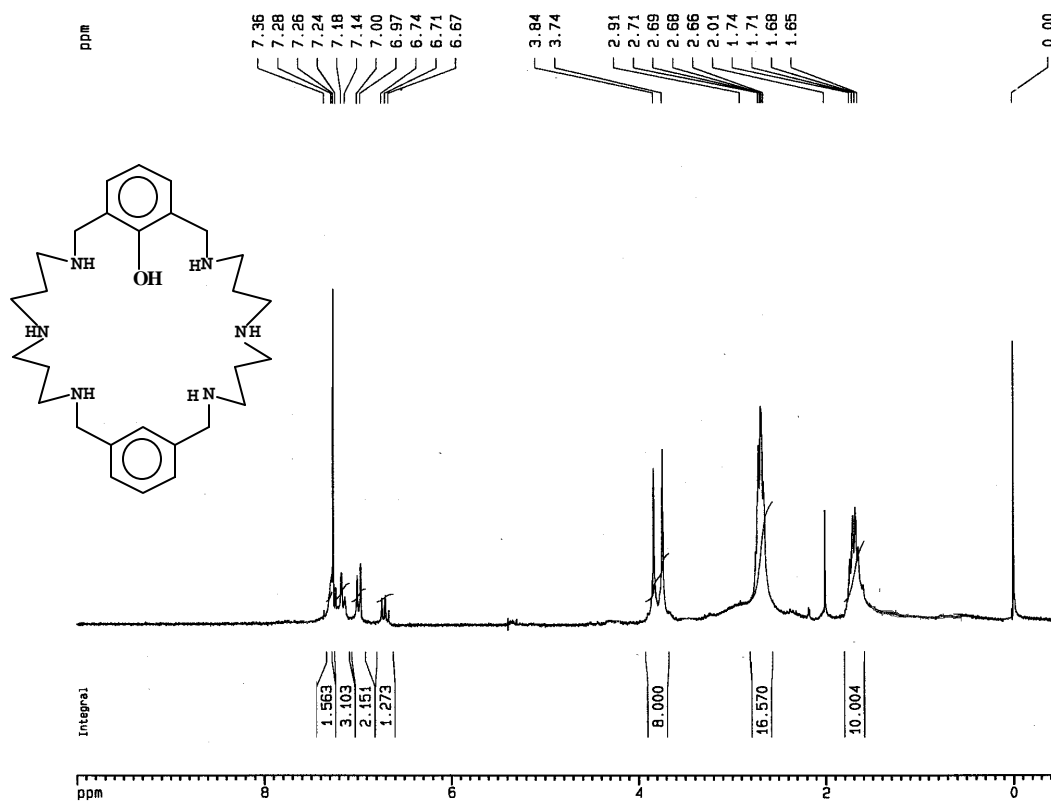


Figure S8. ^1H NMR spectrum of hydroxylated ligand H33+33mOH in CDCl_3 (TMS)



CHAPTER 7

Conclusions

7.1 CONCLUSIONS

Chapter 3

- I. A new family of macrocyclic triazaligands has been synthesized and used to obtain new copper complexes.
- II. A new type of disproportionation reaction has been found to occur quantitatively with ligands H32m, H₂Me33m, H33m and Cu^I salts, yielding new organocopper(III) complexes in 50% isolated yield and Cu^I species in also 50% yield.
- III. New organometallic Cu^{III} complexes [(H32m-C)Cu^{III}]²⁺ (**1**), [(H₂Me33m-C)Cu^{III}]²⁺ (**2**), [(H33m-C)Cu^{III}]²⁺ (**3**) and [(H33m-C)Cu^{III}(Cl)]²⁺ (**4**) have been fully characterized by X-Ray diffraction and XAS techniques.
- IV. Disproportionation reaction occurs through a neat C-H bond activation at room temperature, followed by an electron transfer to give the final organometallic Cu^{III} complexes. C-H activation is found to proceed through an heterolytic pathway assisted by the presence of a base to extract the proton. However, mechanism is not yet fully understood.
- V. Copper(I) complexes with ligands H32m, H₂Me33m and H33m exhibits a complete H/D exchange in [D₆]acetone at room temperature. Isolation of deuterated ligand H33m(D) allows the estimation of the KIE on the reaction with Cu^I. High KIE value indicates that the heterolytic cleavage of the C-H bond is involved in the RDS of the reaction.

- VI. Theoretical DFT calculations show a transient agostic C-H \rightarrow Cu^{II} intermediate, with a significant enlargement of C-H bond length and an important angle deviation of the proton out of the aromatic ring plane, in line with the reactivity observed.
- VII. Organocopper(II) complex $[(\text{H33m-C})\text{Cu}^{\text{II}}]_2(\mu\text{-Cl})(\text{PF}_6) \cdot 6\text{H}_2\text{O} \cdot \text{CH}_2\text{Cl}_2$ (**6-PF₆**) has been isolated from a side reaction. The mechanism of this reaction is not understood. However, this compound is the second crystal structure of a Cu^{II} organometallic complex ever reported.

Chapter 4

- VIII. Organocopper(III) species **1**, **2** and **3** undergo intramolecular aromatic hydroxylation into the previous activated aromatic position to yield bisphenoxo complexes $[(\text{H32mO})_2\text{Cu}_2]^{2+}$ (**1c**), $[(\text{H}_2\text{Me33mO})_2\text{Cu}_2]^{2+}$ (**2c**) and $[(\text{H33mO})_2\text{Cu}_2]^{2+}$ (**3c**), respectively. Crystal structure of bis(phenoxo) complexes have been solved by X-Ray Diffraction.
- IX. Aromatic hydroxylation reaction proceeds slowly at room temperature through meta-stable deep-colored intermediates attributed to deprotonated organocopper(III) species $[(\text{H32m-C})'\text{Cu}^{\text{III}}]^+$ (**1b**), $[(\text{H}_2\text{Me33m-C})'\text{Cu}^{\text{III}}]^+$ (**2b**), $[(\text{H33m-C})'\text{Cu}^{\text{III}}]^+$ (**3b**). The presence of a base and water is demanded for the reaction to occur.

- X. Hydroxylation mechanism seems to involve a partial decoordination of the Cu center from two N groups. The conformation changes proposed are supported by the bis(phenoxo) complex $[(\text{H}_2\text{Me33mO})_2\text{Cu}_2(\text{Cl})_2]$ (**2d**) structure, thought to be an intermediate conformation in the hydroxylation process.
- XI. Reaction of molecular O_2 with Cu^{I} complexes $[(\text{H32m})\text{Cu}^{\text{I}}]^+$ (**7**), $[(\text{H}_2\text{Me33m})\text{Cu}^{\text{I}}]^+$ (**8**) and $[(\text{H33m})\text{Cu}^{\text{I}}]^+$ (**9**) is shown to proceed through the following steps: O_2 activation to form a peroxo dinuclear intermediate, molecular rearrangement to form an aryl- Cu^{III} intermediate and final intramolecular hydroxylation. This reactivity is clearly linked to the aryl- Cu^{III} /base(aq) systems, and represent a new possible mechanism for aromatic hydroxylation performed by tyrosinase and tyrosinase-like chemical models.
- XII. Reactivity with system H22m leads to final bis(phenoxo) complex $[(\text{H22mO})_2\text{Cu}_2]^{2+}$ (**5c**), although aryl- Cu^{III} intermediate detection has been elusive. However, similarities in reactivity and synthesis of the bisphenoxo compound **5c** from Cu^{II} disproportionation and $\text{Cu}^{\text{I}}/\text{O}_2$ routes indicate similar reaction mechanisms.

Chapter 5

- XIII. Susceptibility measurements of bis(phenoxo) compounds **1c**, **2c**, **3c**, and **5c** indicate a trend that correlates the coupling constant value (J) with the geometric Cu_2O_2 core differences of the different

complexes. J values found are in the range of -210 to $+6 \text{ cm}^{-1}$.

XIV. It is found a magnetostructural correlation between the Cu-O-Cu angle and the J value with complexes **1c-3c**. However, important structural differences found in **5c** preclude its correlation with the rest. Extended Hückel calculations were performed to understand the differences in the magnetic behavior, obtaining as a conclusion that the orbital overlap on the Cu-O(apical) bond was the best parameter that correlates with the J values found for the four bis(phenoxo) complexes.

Chapter 6

XV. Dinuclear Cu^{I} complex $[(\text{H33+33m})\text{Cu}^{\text{I}}_2(\text{CO})_2]^{2+}$ (**10**) is capable of performing intramolecular ligand monohydroxylation after molecular O_2 activation, to finally isolate and structurally characterize complex $[(\mu\text{-H33+33mO})\text{Cu}^{\text{II}}_2(\mu\text{-OH})]^{2+}$ (**11**). Hydroxylation is extremely sensitive to initial Cu^{I} complex concentration, obtaining 75% yield when concentration is below 4 mM in CH_3CN . If concentration is higher than 15 mM, no hydroxylated product is detected.

XVI. Reaction of O_2 with Cu^{I} complex **10** in high concentrations favors the dimerization or oligomerization products that preclude the correct disposition of the putative peroxo intermediate in order to react with the ligand. However, O_2 activation is also achieved to yield hydroxo oligomers capable of atmospheric CO_2 fixation to finally obtain the

tetranuclear carbonato complex $[(\text{H}33+33\text{m})_2\text{Cu}^{\text{II}}_4(\mu\text{-CO}_3)_2]^{4+}$ (**12**). Complex **12** has been structurally characterized and shows two dinuclear units linked through copper centers by two CO_3^{2-} bridges. Same product is obtained quantitatively when Cu^{II} complex with ligand H33+33m is treated with two equivalents of OH^- per Cu atom and exposed to air. The latter experiments support a nucleophilic attack of the hydroxo groups to the CO_2 molecule.

XVII. Crystal structure of the dinuclear complex $[(\text{H}33+33\text{m})\text{Cu}^{\text{II}}_2(\text{CH}_3\text{CN})_4]^{4+}$ (**14**) has been obtained, showing an unusual Cu-N₅ ligand-donor set.

XVIII. Control of initial conformations in solution is clue to modulate the reactivity pathway that the reaction will follow, as derived from structure comparison of complexes **11**, **12** and **14**. The way found within this system for this modulation is the control of initial complex concentration.

XIX. Density functional QM/MM calculations on a postulated peroxo intermediate $[(\text{H}33+33\text{m})\text{Cu}^{\text{II}}_2(\text{O}_2)]^{2+}$ indicates a possible electrophilic attack from the peroxo to the aromatic ring, favoring a σ^* pathway in front a π^* pathway.

General conclusions

XX. Ligands H32m, H₂Me33m and H33m have the capability of stabilizing high oxidation states for metals (Cu^{III} , Ni^{III}) and represent a model for the study of a clean and mild C-H bond activation reaction of a

particularly strong C-H bond (aromatic C-H, 109 kcal mol⁻¹).

XXI. Geometric and coordination properties of these ligands converts them to ideal starting complexes for the study of C-H activation reactions by copper and possibly by other metals. Placing the metal really close to the C-H bond that wants to be activated seems to be sufficient for the reaction to occur.

XXII. Dinucleating ligands such as H33+33m and their corresponding copper complexes permit the close proximity of metal centers to obtain metal-metal interactions. This has implications in reactivity and also in magnetic properties of final dinuclear complexes. Ligand design in order to achieve a desired reactivity is an important aspect of the bioinorganic chemistry that has been and will be pursued in the next years.